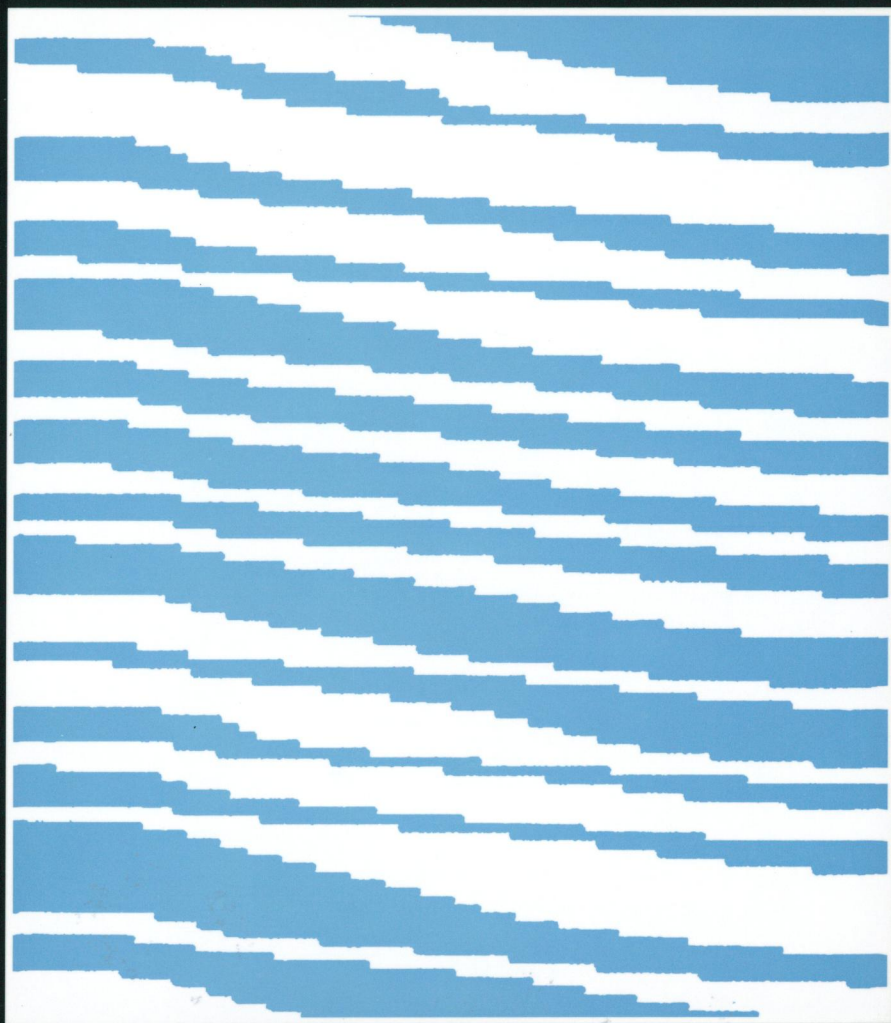


NONLINEAR SCIENCE THEORY AND APPLICATIONS

The dynamics of cellular motility



MASATOSHI MURASE

NONLINEAR SCIENCE THEORY AND APPLICATIONS

Numerical experiments over the last thirty years have revealed that simple nonlinear systems can have surprising but complicated behaviours. Nonlinear phenomena include waves that behave as particles, deterministic equations having irregular, unpredictable solutions, and the formation of spatial structures from an isotropic medium.

The applied mathematics of nonlinear phenomena has provided metaphors and models for a variety of physical processes: solitons have been described in biological macromolecules as well as in hydrodynamic systems; irregular activity that has been identified with chaos has been observed in continuously stirred chemical flow reactors as well as in convecting fluids; nonlinear reaction diffusion systems have been used to account for the formation of spatial patterns in homogeneous chemical systems as well as biological morphogenesis; and discrete-time and discrete-space nonlinear systems (cellular automata) provide metaphors for processes ranging from the microworld of particle physics to patterned activity in computing neural and self-replicating genetic systems.

Nonlinear Science: Theory and Applications will deal with all areas of nonlinear science – its mathematics, methods and applications in the biological, chemical, engineering and physical sciences.

Nonlinear science: theory and applications

Series editor: Arun V. Holden, *Reader in General Physiology,*
Centre for Nonlinear Studies, The University, Leeds LS2 9NQ, UK

Editors: S. I. Amari (Tokyo), P. L. Christiansen (Lyngby),
D. G. Crighton (Cambridge), R. H. G. Helleman (Houston),
D. Rand (Warwick), J. C. Roux (Bordeaux)

Chaos A. V. Holden (*Editor*)

Control and optimization J. E. Rubio

Automata networks in computer science F. Fogelman Soulié, Y. Robert and
M. Tchuente (*Editors*)

Simulation of wave processes in excitable media V. S. Zykov

Introduction to the algebraic theory of invariants of differential equations
K. S. Sibirsky

Mathematical models of chemical reactions P. Érdi and J. Tóth

Almost periodic operators and related nonlinear integrable systems
V. A. Chulaevsky

Oscillatory evolution processes I. Gumowski

Soliton theory: a survey of results A. P. Fordy (*Editor*)

Fractals in the physical sciences H. Takayasu

Stochastic cellular systems: ergodicity, memory, morphogenesis
R. L. Dobrushin, V. I. Kryukov, A. L. Toom (*Editors*)

Chaotic oscillations in mechanical systems T. Kapitaniak

Stability of critical equilibrium states L. G. Khazin and E. E. Shnol

**Nonlinear random waves and turbulence in nondispersive media:
waves, rays, particles** S. N. Gurbatov, A. N. Malakhov and A. I. Saichev

Nonlinear chemical waves Peter J. Ortoleva

Other volumes are in preparation

Dynamics of cellular motility

Masatoshi Murase

JOHN WILEY & SONS

Chichester · New York · Brisbane · Toronto · Singapore

Copyright © 1992 by John Wiley & Sons Ltd,
Baffins Lane, Chichester,
West Sussex PO19 1UD, England

All rights reserved.

No part of this book may be reproduced by any means,
or transmitted, or translated into a machine language
without the written permission of the publisher.

Other Wiley Editorial Offices

John Wiley & Sons, Inc., 605 Third Avenue,
New York, NY 10158-0012, USA

Jacaranda Wiley Ltd, G.P.O. Box 859, Brisbane,
Queensland 4001, Australia

John Wiley & Sons (Canada) Ltd, 22 Worcester Road,
Rexdale, Ontario M9W 1L1, Canada

John Wiley & Sons (SEA) Pte Ltd, 37 Jalan Pemimpin #05-04,
Block B, Union Industrial Building, Singapore 2057

Library of Congress Cataloging-in-Publication Data

Murase, Masatoshi, 1957—

Dynamics of cellular motility / Masatoshi Murase.

p. cm. — (Nonlinear science : theory and applications)

ISBN 0 471 93576 X

1. Contractility (Biology) 2. Cilia and ciliary motion.
3. Flagella (Microbiology) 4. Muscle contraction. 5. Cells —
Motility. I. Series: Nonlinear science.

QH848.M87 1991

574.87'64 — dc20

91-19126

British Library Cataloguing in Publication Data

A catalogue record for this book is available from the British Library

ISBN 0 471 93576 X

Set in 10/12pt Times by Graphicraft Typesetters Ltd, Hong Kong
Printed and bound in Great Britain by Biddles Ltd, Guildford, Surrey

To Yuken and Tomoko

Contents

Preface	xiii
Acknowledgements	xvii
1 Introduction	1
1.1 Temporal order	2
1.1.1 Rhythms out of rhythms	2
1.1.2 Rhythms out of constant flow	3
1.1.3 Noise-induced order out of chaos	8
1.1.4 Birhythmicity	13
1.1.5 Bursting	17
1.2 Spatial order	18
1.2.1 Pattern formation in the two-component system	18
1.2.2 Solitons in the reaction–diffusion system	21
1.2.3 Complex behaviours in the one-component system	23
Part I Oscillatory contraction in muscle	27
2 Muscle structure and function	29
2.1 Introduction	29
2.2 Muscle structure	31
2.2.1 Vertebrate muscle	31
2.2.2 Insect flight muscle	33
2.3 Mechano-chemical cycle of a myosin cross-bridge	34
2.4 Mechanical properties	36
2.4.1 Free-oscillation experiment	36
2.4.2 Driven-oscillation experiment	38
2.4.3 Length-step experiment	41
2.4.4 Tension-step experiment	46
2.5 Advanced experiments on insect flight muscle	47
2.5.1 Oscillation-induced ATPase	47
2.5.2 Double length-step experiment	50

3	Models for muscle contraction	54
3.1	The Huxley (1957) two-state model	54
3.2	Models for stretch activation	57
3.3	The two-state models with reverse rate constants	63
3.4	Three-state model for oscillatory contraction	68
3.4.1	The model	68
3.4.2	Simulation results	72
3.5	Interpretation of stretch activation	80
3.6	Simplified model of muscle contraction	81
Part II	Nonlinear dynamic phenomena in flagella and cilia	87
4	Hierarchy in structure and function	89
4.1	Introduction	89
4.2	Internal structure and physiological function	90
4.2.1	Typical movements of flagella and cilia	90
4.2.2	Typical structure of flagella and cilia	91
4.3	How do individual flagella and cilia move?	96
4.3.1	Hypotheses	96
4.3.2	Reactivation	99
4.3.3	Evidence for active sliding	101
4.4	Functional mechanisms	102
4.4.1	Force-generating mechanisms	102
4.4.2	Control mechanisms	103
4.5	Dynamics of individual flagella and cilia	111
4.5.1	Excitability and oscillations in dynein cycles	111
4.5.2	Excitability, oscillations and bursts in ciliary beat cycles	112
4.5.3	Mechano-sensitivity	112
4.5.4	Quantal steps in angular changes	117
4.5.5	Intermittent flagellar beating	120
4.6	Dynamics of groups of flagella and cilia	123
4.6.1	Synchronism and metachronism	123
4.6.2	Strange behaviour of ciliary activity	129
5	Models of flagella and cilia exhibiting regular behaviour	135
5.1	Introduction	135
5.2	Fluid dynamics of micro-organism propulsion	138
5.2.1	Historical background	138
5.2.2	Externally forced motion and self-propulsive motion	144
5.2.3	Resistive-force theory	146
5.3	Theoretical models for flagella and cilia	150
5.3.1	The basic equations of flagellar dynamics	152

5.3.2	The Machin model	156
5.3.3	The curvature-controlled model	167
5.3.4	The self-oscillatory model	175
5.3.5	The ciliary model	178
5.3.6	Ciliary propulsion	185
6	Molecular mechanism for excitability and oscillations	191
6.1	Theoretical background	191
6.2	Experimental background	193
6.3	Model development	194
6.3.1	Geometric considerations	194
6.3.2	A three-state model for the cross-bridge cycle	196
6.4	Dynamics of a short flagellar segment	200
6.4.1	Kinetic equations for cross-bridge dynamics	200
6.4.2	Equations for sliding motion of a short flagellum	202
6.4.3	Free sliding motion	203
6.4.4	Excitable-oscillatory phenomena	203
6.4.5	Phase-plane analysis	209
6.5	Dynamics of a long flagellum	213
6.5.1	The basic assumptions	213
6.5.2	Self-organization of propagating waves	216
6.5.3	A single wave-propagation	217
6.6	Simulations of asymmetric bending waves	219
7	Simplified models for flagellar dynamics	224
7.1	The simplified excitable dynein model	225
7.2	Dynamics of a segment model	228
7.3	Bend propagation at zero external viscosity	228
7.4	Bend propagation at non-zero external viscosity	230
7.4.1	Boundary conditions for cilia and flagella	233
7.4.2	Bend propagation with clamped-end boundary conditions	235
7.4.3	Bend propagation with free-end boundary conditions	242
7.4.4	Interaction of two waves propagating in opposite directions	247
7.4.5	External viscosity-induced perturbations	249
8	Simplified models for ciliary dynamics	255
8.1	Introduction	256
8.2	Dynamic properties of the opposed dyneins	259
8.2.1	A segment model	260
8.2.2	Excitable behaviour of the segment model	261

8.2.3	Mechano-sensitivity of the segment model to external stimuli	263
8.3	Ciliary dynamics	264
8.3.1	A ciliary model	264
8.3.2	Repetitive beat-cycle	269
8.3.3	Discontinuous beat-cycle	271
8.4	Ciliary dynamics under the influence of fluid flow	273
8.4.1	A modified ciliary model	273
8.4.2	Responsiveness of a quiescent cilium to fluid flow	277
8.4.3	Fluid flow induced beating patterns of quiescent cilia	277
8.4.4	A bridge between experimental observations and simulation results	280
9	Large-amplitude oscillations and bend propagation	282
9.1	Dynein substructure and function	283
9.1.1	Outer dyneins	283
9.1.2	Inner dyneins	285
9.2	Regulation of flagellar oscillations	286
9.3	Brief outline of the previous model	289
9.4	A segment model for large-amplitude motion	291
9.5	Large-amplitude sliding motion	295
9.5.1	Free sliding motion	296
9.5.2	Excitability and oscillations with large amplitude	296
9.6	Bend propagation without curvature control	297
9.7	Essence of the model behaviour	302
9.7.1	Dynamical behaviours of dyneins with multiple active sites	302
9.7.2	Controversy over structure and function of dynein arms	304
9.7.3	Difference between Satir's model and the present model	305
9.7.4	Some future work	305
10	From simple to complex dynamical behaviours in mechano-chemical cycles: hyperoscillations, bursting and chaos	307
10.1	Mechano-chemical hyperoscillations	307
10.2	The model	309
10.2.1	Mathematical description	309
10.2.2	Force–distance relationship	310
10.2.3	Potential-energy surface	312
10.2.4	Phase-plane representation	314
10.3	Excitability and oscillations in the dynein–tubulin system	314
10.3.1	Homoclinic orbit	314

<i>Contents</i>	xi
10.3.2 Dynamic hysteresis loop	318
10.4 Onset and cessation of hyperoscillations	321
10.5 Complex dynamical behaviours	325
10.5.1 Bursting	325
10.5.2 Chaos	326
10.5.3 Discussion	330
References	332
Author index	343
Subject index	347

Preface

This book presents new ideas and theories that account for oscillatory contraction in muscle and the various modes of flagellar and ciliary movements. Despite the great variety of dynamical behaviours, attempts have been made to model some of the specific modes, though not to account for the overall properties. I have tried to develop theoretical models and to interpret nearly all of the dynamical behaviours in terms of these models. This book is intended for students and specialists in biology, physics, chemistry and mathematics, as cellular motility is a subject of interdisciplinary interest.

The book consists of an Introduction, Part I and Part II. Nearly all the chapters are self-contained, so that the reader can start with any of them. Although there are a lot of mathematical equations in this book, the reader need not follow each step, but rather should try to understand the overall concepts behind them. For this purpose, I include more than 200 illustrations.

Chapter 1 gives basic examples of temporal and spatial orders. The problems of these orders are not just restricted to biology, but apply also to mechanics and chemistry.

Part I deals with the mechanical properties of vertebrate skeletal muscle and insect flight muscle. I am concerned with the oscillatory properties of these muscles, as the molecular mechanism for oscillation has been one of the most intriguing subjects for experimentalists and theoreticians.

Chapter 2 describes the experimental observations. Oscillatory contractions have been observed, not only in heart muscle, but in skeletal and insect flight muscle as well. Thus a common molecular mechanism for oscillation might exist in various types of muscle. Starting from the organic structure of muscle, experimental results are outlined.

Chapter 3 discusses some of the mathematical models for muscle contraction. Instead of giving a detailed explanation of each model, its essential features are summarized. After the quick review of these models, I propose a simplified model that accounts for oscillatory contraction. The analogy between the muscle system and the nerve system is discussed, based on this simplified model behaviour.

Part II sketches the self-organization of flagellar and ciliary bending patterns. Like other nonlinear distributed systems, the flagellar system, which is viewed as a one-dimensional array of functional units, gives rise to regular and irregular dynamical behaviours.

Chapter 4 starts with the definition of flagella and cilia, and then describes their internal structure. Functional as well as structural hierarchy is discussed.

Chapter 5 discusses fluid-dynamical principles of flagellar and ciliary motion. Then, the fundamental equation which governs the behaviour of a thin filament through a viscous medium is derived. With these theoretical backgrounds, important mathematical models are discussed, with emphasis on their significance and their status.

Chapter 6 discusses the molecular mechanism underlying bend initiation and propagation. Using computer simulations, the one-dimensional array of excitable units not only shows symmetric beating patterns typical of flagella, but also demonstrates asymmetric beating patterns typical of cilia. Although these simulation results are restricted to the zero external viscosity and small-amplitude oscillations, the two different types of behaviours are demonstrated by using a similar mechanism.

Chapter 7 develops simplified models for flagellar motility, to examine whether the excitable mechanism that was studied in Chapter 6 generates bend propagation of small amplitudes. In the limit of zero external viscosity, simulation results show self-organization of symmetric bends as occurred in the previous chapter. At non-zero external viscosity, the model shows regular base-to-tip and irregular tip-to-base propagating waves, depending on the structural asymmetry along the axoneme.

Chapter 8 develops simplified models for ciliary dynamics at non-zero external viscosity. Besides regular repetitive beating with alternate effective and recovery strokes of small amplitudes, these models exhibit a resting phase called quiescence, and mechano-sensitivity.

Chapter 9 extends the simplified models proposed in Chapter 7, in order to demonstrate large-amplitude oscillations and bend propagation. Recent experimental observations are briefly summarized, and are used to develop new models.

Chapter 10 discusses the various types of dynamical behaviours at the molecular level. Using a simple model of dynein-tubulin interaction, I predict many interesting phenomena.

Like other nonlinear phenomena in biology, such as pattern formation in developmental biology, recognition in neurobiology and immunology, and enzyme reaction in biochemistry, cellular motility has exhibited attractive and interesting phenomena. However, the subject of cellular motility has not drawn interdisciplinary attention, probably because the mathematical models that have been developed are too complicated to deal with, and also because the details of molecular structure and function have not been completely understood.

It is impossible to refer to all of the experimental and theoretical studies. Instead, I prefer to emphasize interesting results from a point of view of nonlinear science, and to develop simple models in order to make qualitative interpretations and predictions rather than quantitative data fittings. Of course, there are many ways to develop theoretical models. My standpoint is 'simple is best'.

I hope that this book stimulates greater interest in cellular motility.

Tokyo, Japan
26 October 1990

Masatoshi Murase

Acknowledgements

I am particularly grateful to Dr A. V. Holden of the Centre for Nonlinear Studies at the University of Leeds, for suggesting that I write this book. I am grateful to Professor H. Shimizu of the University of Tokyo for his constant support and helpful discussions.

This book was partially written while I was a visiting research scientist at the Duke University Medical Center. I am grateful to Professors J. J. Blum and M. Hines for their hospitality during this period and for their valuable discussions.

The book was revised when I was visiting professor of the Department of Mathematics and the Institute of Theoretical Dynamics of the University of California at Davis. I gave a graduate course of 'An Introduction to Mathematical Modelling of Biological Systems' based on this book. I am grateful for the hospitality of Professor A. Krener, Chairman of the Department of Mathematics and Professor J. Keizer, Director of the Institute of Theoretical Dynamics.

I thank Dr D. K. Campbell, Director of the Center for Nonlinear Studies at Los Alamos for inviting me. My visit to Los Alamos was invaluable and it was completely supported by the University of California INCOR Travel Grant Program in Nonlinear Science.

I thank Dr L. M. Simmons, Jr, Executive Vice President of the Santa Fe Institute at New Mexico for inviting me. I had an excellent time there and enjoyed valuable discussions on interdisciplinary subjects.

For the interdisciplinary nature of this book, I had to discuss problems with many scientists. I wish to thank Professors M. Yano, Y. Yamaguchi, S. Kamimura, K. Takahashi, A. Murakami and C. Shingyoji of the University of Tokyo, I. Tsuda of the Kyushu Institute of Technology, M. Mulase, C. Tracy and A. Cheer of the University of California, R. Kamiya of the Nagoya University, Y. Naitoh and K. Sugino of the University of Tsukuba, Y. Kuramoto and S. Shinomoto of Kyoto University, G. Matsumoto of the Division of Information Science at the Tsukuba Science City, M. Kawai of

the University of Iowa, C. J. Brokaw of the California Institute of Technology, J. Rinzel of the National Institute of Health, C. K. Petersen of the University of Leeds and R. Kobayashi of Ryukoku University.

I am grateful to Dr T. Tsumita, Director of the Tokyo Metropolitan Institute of Gerontology (TMIG) and Dr M. Matsuo, Associate Director of TMIG for a financial support.

I thank graduate students in the University of Tokyo and in the University of California at Davis for their valuable discussions.

I also want to thank Mr Lucas Simpson for making my English easier to read.

1 Introduction

One of the important problems in biology is to clarify the mechanisms underlying *self-organization* at various levels. From a thermodynamic point of view, self-organizing phenomena are likely to occur in *non-equilibrium* open systems close to or beyond instability of a stationary state (Nicolis and Prigogine, 1977). States possessing such properties are called *dissipative structures* (Prigogine *et al.*, 1969). Their occurrence depends on (i) specific nonlinear dynamics taking place in each subsystem (i.e. each part of the system), and (ii) the way the subsystems couple.

An example of self-organizing phenomena occurs in a nervous system. Under *space clamp* conditions, where the state of the nerve membrane is spatially uniform or homogeneous, the nervous system exhibits temporal orders such as *excitability*, *oscillations* and *multiple steady-state transitions* in the form of *all-or-none responses* to external stimuli. If one removes the spatially homogeneous condition, to take into account the *electrotonic* coupling of nearby regions of the membrane, the system is no longer uniformly stable; instead, space-dependent patterns like *action potentials* can appear.

Self-organizing phenomena are also observed in biochemical systems, such as metabolic pathways. Under the spatially homogeneous conditions, when the medium is well stirred, time-dependent properties of concentration like excitability and oscillations appear. Without continuous stirring we must take into account *diffusion*, and the system gives rise to space-dependent travelling patterns known as *chemical waves*.

Another example is seen in a mechano-chemical system, such as muscle, cilia or flagella. This system not only exhibits excitability and oscillations, but also shows *bending waves*. Like electrotonic and diffusion coupling, an elastic coupling is responsible for the generation of space-dependent travelling patterns. It seems that these three biological systems may share, in spite of their detailed differences, common principles for the self-organization of spatio-temporal structures. The key requirements for these properties seem to

be: (i) the excitable and/or oscillatory dynamics operating as a functional unit (or subsystem); and (ii) an *attractive* type of interaction between the units (or subsystems).

Recent theoretical and experimental studies, however, have revealed that the above two requirements are not always met. Under spatially homogeneous conditions, the nervous and biochemical systems show complex temporal patterns such as *chaos* and *bursting* oscillations. It will not be surprising if the mechano-chemical system shows similarly complex behaviours, though they have not been studied yet.

Much more complex dynamical behaviours occur when there is a *repulsive* type of interaction in addition to the attractive type. Under these conditions *self-turbulization* phenomena of spatio-temporal structures appear in the one-dimensional case, which leads to spatio-temporal chaos. The most interesting point is that the total system exhibits chaos through two functionally different interactions, even though an individual subsystem persists with its ordered temporal structure in isolation. Some spatio-temporal irregular behaviours have been observed in the flagellar system. These irregular behaviours may probably be interpreted in terms of the destabilization process similar to that found in the self-turbulization phenomena.

The mechano-chemical systems considered in this book provide various types of behaviours. These behaviours are worth studying not only from a physiological, but also from a theoretical point of view. Before considering this system, it is instructive to survey some of the mechanical and biological models which exhibit various types of order and disorder.

In this introduction, we shall begin with a single unit exhibiting temporal structures. Then we will consider spatio-temporal structures in a system which consists of an ensemble of units.

1.1 Temporal order

Periodic behaviours or rhythms seem to be the basis of temporal order in biology, chemistry, physics and mathematics. From a mathematical point of view, it is simple to say that any time-dependent evolution can be described as an algebraic sum of periodic contributions via the *Fourier transform*. Therefore, an understanding of oscillation is necessary before we study more complex temporal phenomena. This section begins with the mechanisms underlying simple temporal order.

1.1.1 Rhythms out of rhythms

The classical example of oscillations is a *parametrically* excited system (i.e. vibration of a swing or a pendulum) whose point of suspension moves harmonically in the vertical direction. Suppose that the support of the pendulum is moved up and down with angular frequency 2ω , then the pen-

dulum is accelerated up and down and finally an oscillation with angular frequency ω is observed.

This system is described by the well-known *Mathieu equation* (see e.g. Struble, 1962; Scarborough, 1965):

$$\frac{d^2\theta}{dt^2} + (\omega^2 - \alpha \sin 2\omega t)\theta = 0 \quad (1.1)$$

where θ is the angle between the vertical line and the pendulum as shown in Figure 1.1. Interestingly the stable oscillation is also obtained under the *inverse pendulum* conditions when particular values for parameters ω and α are chosen.

If the suspension moves in the horizontal direction, equation (1.1) changes to

$$\frac{d^2\theta}{dt^2} + \omega^2\theta = \alpha \sin 2\omega t \quad (1.2)$$

thereby describing the *forced* oscillation. Thus we can distinguish the parametrically excited oscillation described by equation (1.1) from the forced oscillation described by equation (1.2). In the parametric excitation, a definite point in the system is subject to the *indirect action* of inertial forces; while, in the forced oscillation, the *direct action* of the driving force acts on the mass. On the basis of this parametrically excited system, we can postulate that rhythms result from rhythms.

1.1.2 Rhythms out of constant flow

Another well-known system exhibiting oscillatory behaviour can be seen in a mechanical device where the dynamic phenomena depend on *relative dry friction* arising on the surface between a body having mass, m , supported by an elastic spring with spring constant, k , and a uniformly moving band with velocity, v_0 (Fig. 1.2).

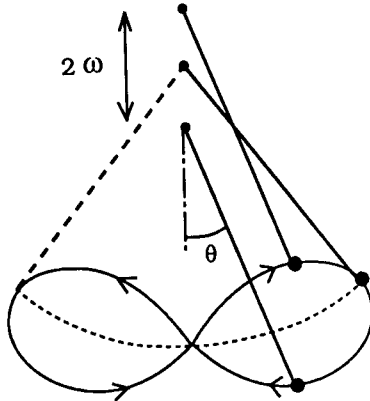
The motion of the system is described by the following equation (cf. Cook, 1986):

$$m \frac{d^2x}{dt^2} + kx = F\left(v_0 - \frac{dx}{dt}\right) \quad (1.3)$$

where x is the displacement of the mass from the equilibrium position at zero band velocity and $F(u)$ is the friction-force function against the relative velocity, u ($= v_0 - dx/dt$), between the mass and the band. This friction force depends on whether the mass is sliding over the belt (slip) or adhering to it (stick) as shown in Figure 1.2B.

Interestingly, the equilibrium position $x = 0$ becomes unstable because of the existence of the region with negative friction (i.e. negative slope of the

(A)



(B)

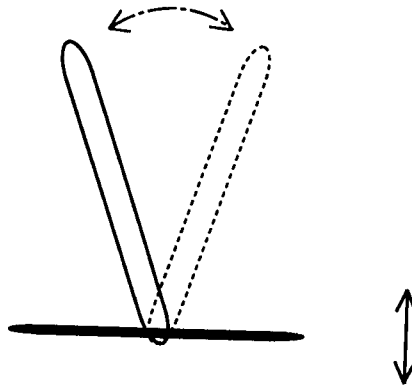


Figure 1.1 A parametrically excited pendulum. (A): The support of the pendulum is moved up and down. The pendulum is accelerated up and down, hence the oscillatory motion. (B): If the pendulum is upside down, we call this the inverse pendulum. This system also shows stable oscillatory modes under certain parameter values.

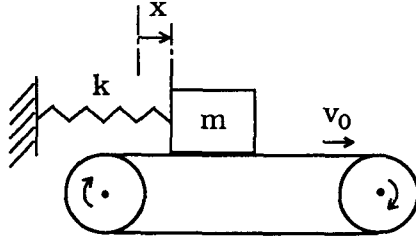
$F(u)$ curve), and then oscillation appears. This system can be described by the *van der Pol* equation¹ (see e.g. Schmidt and Tondl, 1986):

$$\frac{d^2x}{dt^2} - \varepsilon(1 - x^2) \frac{dx}{dt} + x = 0 \quad (1.4)$$

where the damping parameter $\varepsilon(1 - x^2)$ changes sign at $x = \pm 1$. (If $x < 1$, then the system switches on to increase x , and vice versa.) Here, ε plays an important role in determining oscillatory behaviour (Fig. 1.3). The *characteristic* function of equation (1.4) is given by

$$\lambda^2 - \varepsilon\lambda + 1 = 0. \quad (1.5)$$

(A)



(B)

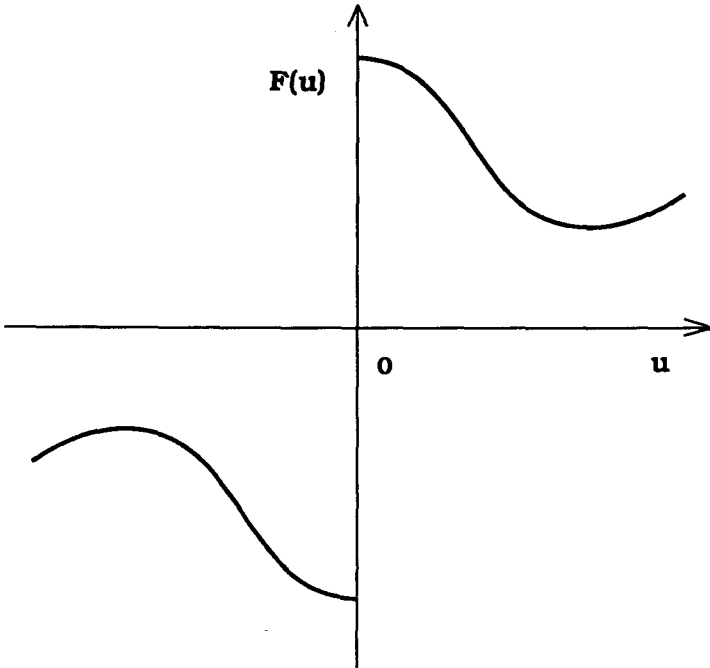


Figure 1.2 (A): A tethered body placed on a moving band. The body has mass, m , supported by an elastic spring with spring constant, k , and a uniformly moving band with velocity, v_0 . The distance x is the displacement of the mass from the equilibrium position at zero band velocity. (B): The friction-force function, $F(u)$, plotted against the relative velocity, $u (= v_0 - dx/dt)$. The value of $F(u)$ depends on whether the mass is sliding over the belt (slip) or adhering to it (stick). The negative slope of $F(u)$ causes instability that leads to oscillations.

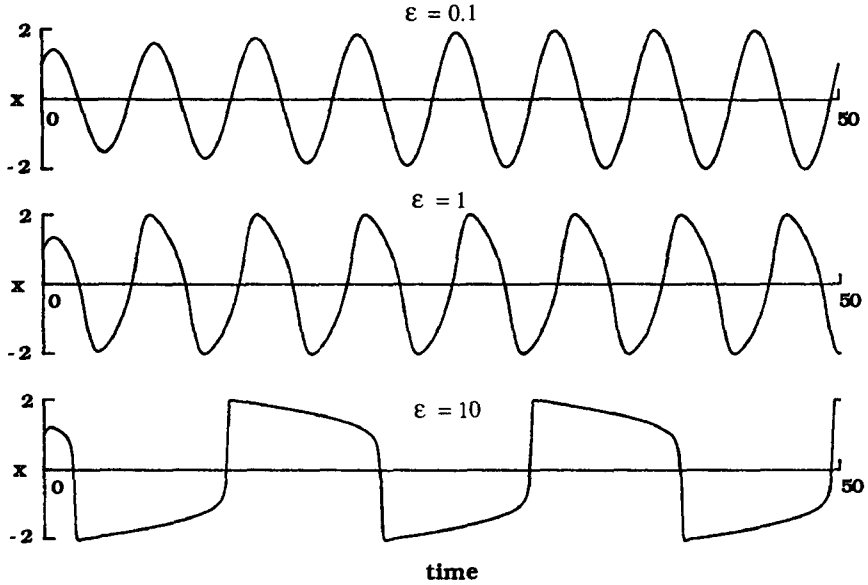


Figure 1.3 Solutions of the van der Pol equation (1.4) for $\epsilon = 0.1, 1$ and 10 . The dynamical behaviour changes from nearly sinusoidal to highly nonlinear relaxation oscillations as ϵ is increased.

The roots of this equation are

$$\lambda = \frac{\epsilon \pm \sqrt{D}}{2} \quad (1.6)$$

where

$$D = \epsilon^2 - 4. \quad (1.7)$$

If ϵ is small (e.g. $\epsilon = 0.1$ or 1 in Fig. 1.3), the *discriminant*, D , is negative and thus we have two complex conjugate roots. In the $(x, dx/dt)$ phase plane, the singular point at the origin becomes an unstable *focus*. The oscillatory pattern is quite simply similar to that of a harmonic oscillator. It is useful to consider the motion of a ball in a potential field in this system. Using polar coordinates (see Haken, 1977, Thompson and Stewart, 1986), the following decoupled first-order equations are obtained

$$\frac{dr}{dt} = -\frac{dU}{dr} \quad (1.8a)$$

$$\frac{d\theta}{dt} = \text{constant} \quad (1.8b)$$

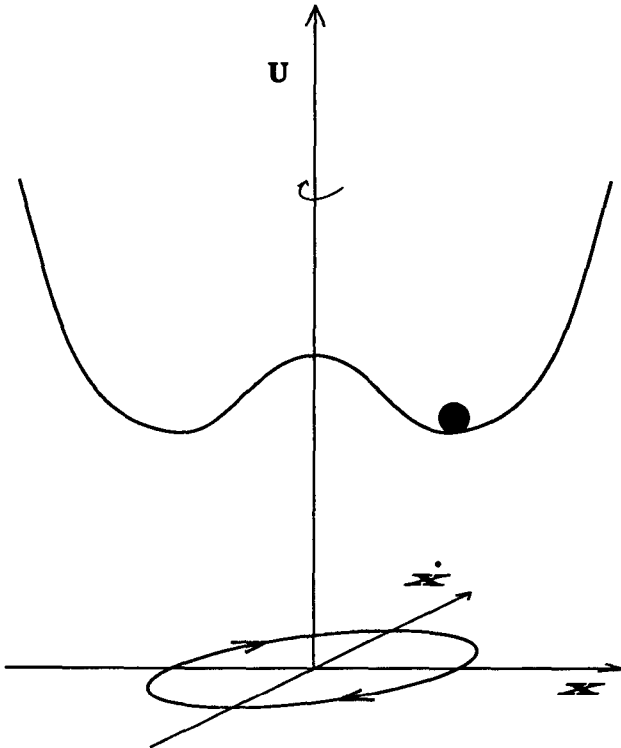


Figure 1.4 The limit-cycle oscillation illustrated by a circle on the $(x, dx/dt)$ plane (below) and the movement of a ball on the rotational potential function (above) for small ϵ values. The temporal oscillations are quasi-sinusoidal because of the small ϵ values. The singular point $(0, 0)$ becomes an unstable focus.

where r is the amplitude, θ is the phase, and U is the potential-energy function which has a vertical axis of rotation (Fig. 1.4). Then we can imagine a ball moving along the wall with the angular velocity $d\theta/dt$.

When ϵ becomes large, highly nonlinear oscillation called *relaxation oscillation* results. In this case, the singular point $(x_0, dx_0/dt) = (0, 0)$ becomes an unstable *node*. By using *Liénard's transformation* (see Minorsky, 1947), the following differential equations are obtained:

$$\frac{dx}{dt} = \epsilon(y - x^3 + x) \tag{1.9a}$$

$$\frac{dy}{dt} = -\frac{1}{\epsilon}x. \tag{1.9b}$$

Since y is a more slowly changing variable than x (except for near the *horizontal isocline* or the *y-nullcline* or $dy/dt = 0$), the potential function is defined over the (x, y) phase plane (Fig. 1.5). According to the motion of a ball acted on by the potential function, we can recognize two processes: the slow change of the energy-accumulating process and the fast change of the energy-supplying process. The relaxation oscillations are characterized by these two distinct processes.

It is interesting to notice the close link between oscillations and excitability. The most famous example of excitability is provided by the nervous system as modelled by Hodgkin and Huxley (1952).² FitzHugh (1961, 1969) and Nagumo *et al.* (1962) developed a simple model, which is described by the following set of differential equations:

$$\frac{dx}{dt} = \epsilon(y - x^3 + x) + Z \quad (1.10a)$$

$$\frac{dy}{dt} = -\frac{1}{\epsilon}(x - a + by) \quad (1.10b)$$

where a and b are fixed parameters and Z is stimulus intensity. Since this model resembled the phase-plane model used by Bonhoeffer to explain the behaviour of passivated iron wires, FitzHugh called it the Bonhoeffer–van der Pol model (BVP for short). When $a = b = Z = 0$, the BVP model described by equations (1.10) can be reduced to the model for the relaxation oscillation described by equations (1.9).

Figure 1.6 shows the typical x - and y -nullclines of the BVP model. When $Z = 0$, the x -nullcline (solid curve) intersects with the y -nullcline (solid line) at the stable point (denoted by s). All trajectories approach this stable point. There is excitability in that movement of the phase point depends on the initial displacement of the phase point from the stable point. Of course, this system exhibits the oscillations under negative constant values of Z . This occurs because the x -nullcline is raised by the negative Z values as shown by the broken curve and the intersection (denoted by u) becomes unstable which leads to limit-cycle oscillation.

Many excitable–oscillatory phenomena (e.g. Belousov–Zhabotinsky reactions, glycolytic systems) can be accounted for by this mechanism (see e.g. Krinsky, 1984 and Zykov, 1987). Here, we can see an interesting analogy between these oscillations and the machine sketched in Figure 1.2. That is, a constant flow causes oscillations.

1.1.3 Noise-induced order out of chaos

Aperiodic dynamics, called chaos in a deterministic system, has been studied in various fields over recent years.³ Since chaos is structurally stable, it can be distinguished from *thermal noise* or *random fluctuation*. This makes sense

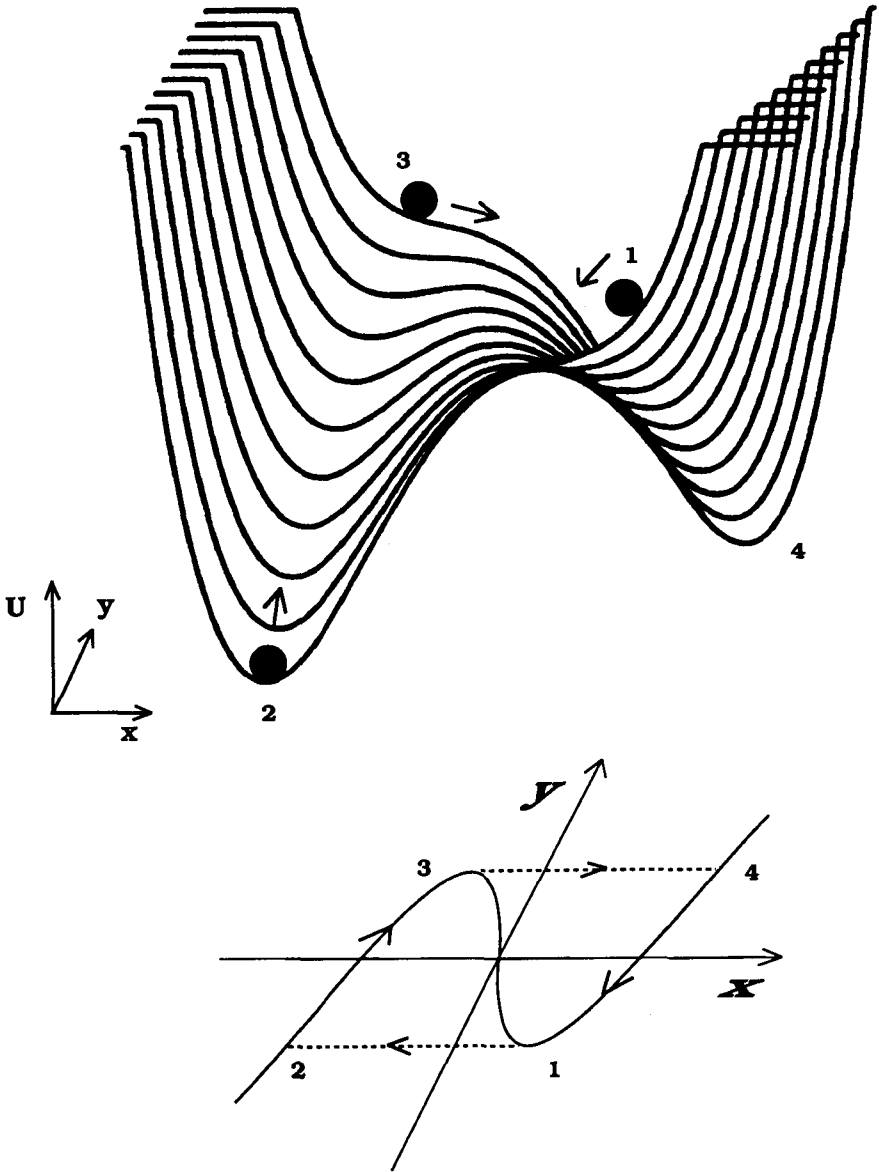


Figure 1.5 The relaxation oscillation illustrated by a bi-phasic path on the (x, y) phase plane (below) and the movement of a ball on the potential function (above) for large ϵ values. There are two distinct time-scales corresponding to the *fast* equation (1.9a) and the *slow* equation (1.9b). The movement of the ball summarizes the trajectory on the phase plane. The numbered balls correspond to the phase points numbered on the trajectory.

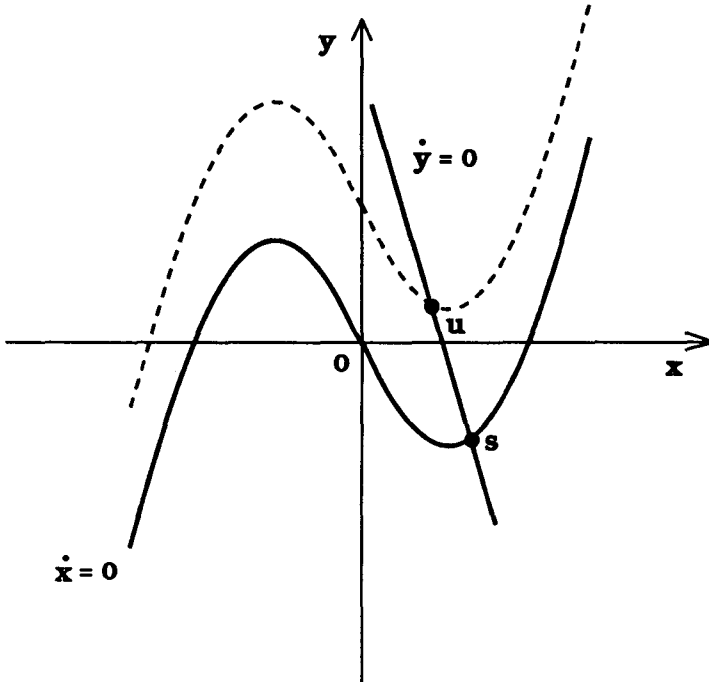


Figure 1.6 x - and y -nullclines of the BVP model described by equations (1.10). When $Z = 0$, the cubic x -nullcline intersects with the straight y -nullcline at the stable point. As Z is decreased from 0, the x -nullcline is raised without any change in the y -nullcline. For certain values of Z , the two nullclines intersect in the region where the x -nullcline has a negative slope. This means that the intersection, or the steady state, becomes unstable, which leads to oscillations.

when both kinds of ‘randomness’ coexist. Matsumoto and Tsuda (1983) noted the interesting phenomenon that under a certain noise level a chaotic orbit becomes unstable and temporal order appears.

They used a simple model that takes into account the Belousov–Zhabotinsky reaction, which explained the bifurcation sequence obtained in experiments. This model is described by

$$\left. \begin{aligned} f(x) &= [-(0.125 - x)^{1/3} + A] \exp(-x) + b & (x < 0.125) \\ f(x) &= [(x - 0.125)^{1/3} + A] \exp(-x) + b & (0.125 < x < 0.3) \\ f(x) &= B \left[10 x \exp\left(-\frac{10}{3} x\right) \right]^{19} \exp(-x) + b & (0.3 < x) \end{aligned} \right\} \quad (1.11)$$

where $A = 0.50607357$, $B = 0.121205692$, and b is the bifurcation parameter (Fig. 1.7).

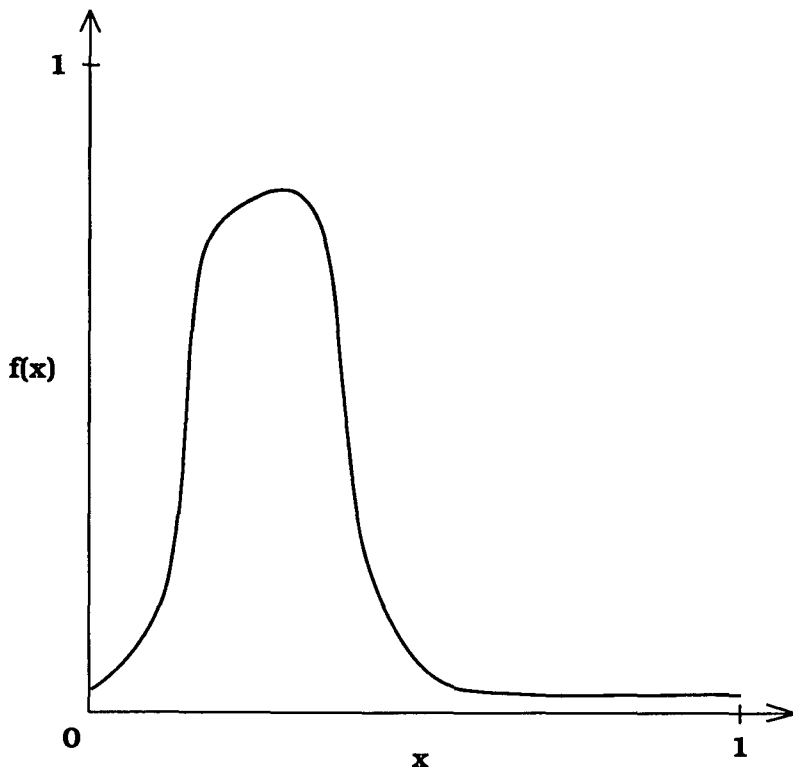


Figure 1.7 Graph of the model for the Belousov–Zhabotinsky reaction described by equations (1.11). Once an initial value for x (say x_0) is specified, a series of x_k values ($k = 1, 2, \dots$) can be defined by successive operation of this model. Depending on the bifurcation parameter, b , the model can show chaotic behaviour.

They studied the power spectrum *with* and *without* noise (Fig. 1.8). In the absence of noise, the model exhibits chaotic behaviour as indicated by the continuous power spectrum. In the presence of large amounts of noise, however, the sharp peak appears. This implies some kind of order. They called this effect *noise-induced order*. This finding suggests that it is very important to distinguish the pure periodic phenomena from noise-induced periodic patterns out of chaos. According to their studies, we can distinguish the above two cases by studying the bifurcation diagram at various noise levels.

Feller (1968), in his famous book (p. 231), pointed out a striking fact about *Bernoulli trials*⁴ with variable probabilities. Suppose that n mutually independent trials succeed with variable probabilities P_k ($k = 1, \dots, n$), such variability of P_k decreases the magnitude of chance fluctuations. In the context of the noise-induced order described by Matsumoto and Tsuda, this

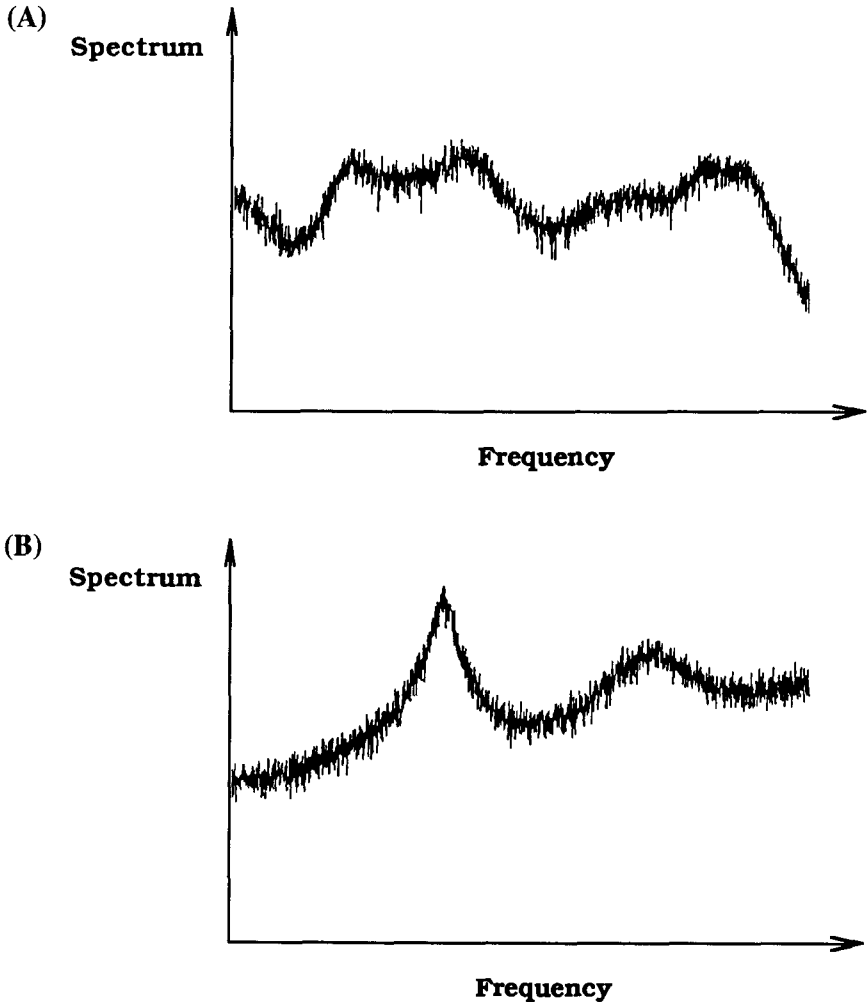


Figure 1.8 Fourier spectrum of the B-Z model for $b = 0.0232885279$. (A): In the absence of noise, the model displays typical chaotic behaviour. (B): In the presence of noise, there is a sharp peak in the spectrum. This proves that chaos is transformed into periodic order. From Matsumoto and Tsuda (1983). Reprinted with permission.

situation means that variability of individual probabilities leads to order in the total number of trials. In relation to this fact, Feller mentioned the following examples:

The number of annual fires in a community may be treated as a random variable; for a given average number, the variability is maximum if all households have the same probability of fire. Given a certain average

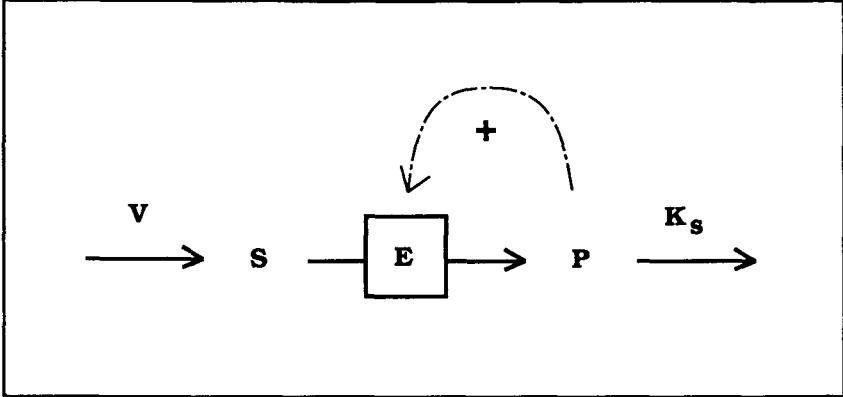


Figure 1.9 Model of autocatalytic enzyme reaction. E denotes the allosteric enzyme. The substrate, S, is constantly supplied with the influx, V. The product, P, is taken away through a first-order reaction, with proportionality constant, K_s . The normalized concentrations of S and P are denoted by α and γ . The normalized parameter values of V and K_s are denoted by v and k_s .

quantity P of n machines, the output will be least uniform if all machines are equal. (An application to modern education is obvious but hopeless.)

1.1.4 *Birhythmicity*

As a simple model of biochemical oscillation and excitability, consider a reaction catalysed by an *allosteric enzyme*,⁵ E, which transforms the substrate, S, into product, P (Fig. 1.9). The system is subject to a constant substrate influx, V, and the product degrades in a linear proportion to its concentration with a proportionality constant, K_s . This model is governed by a set of two kinetic equations for the normalized concentrations of substrate, α , with a normalized influx, v , and product, γ , with a normalized degradation rate, k_s (Goldbeter, 1980):

$$\frac{d\alpha}{dt} = v - \sigma\Phi \tag{1.12a}$$

$$\frac{d\gamma}{dt} = q\sigma\Phi - k_s\gamma \tag{1.12b}$$

where Φ is the rate function of the product-activated allosteric enzyme, E. It is composed of n subunits and behaves according to the concerted transition model of Monod *et al.* (1965) with the allosteric constant, L :

$$\Phi = \frac{\alpha(1 + \alpha)^{n-1}(1 + \gamma)^n}{L + (1 + \alpha)^n(1 + \gamma)^n} \tag{1.12c}$$

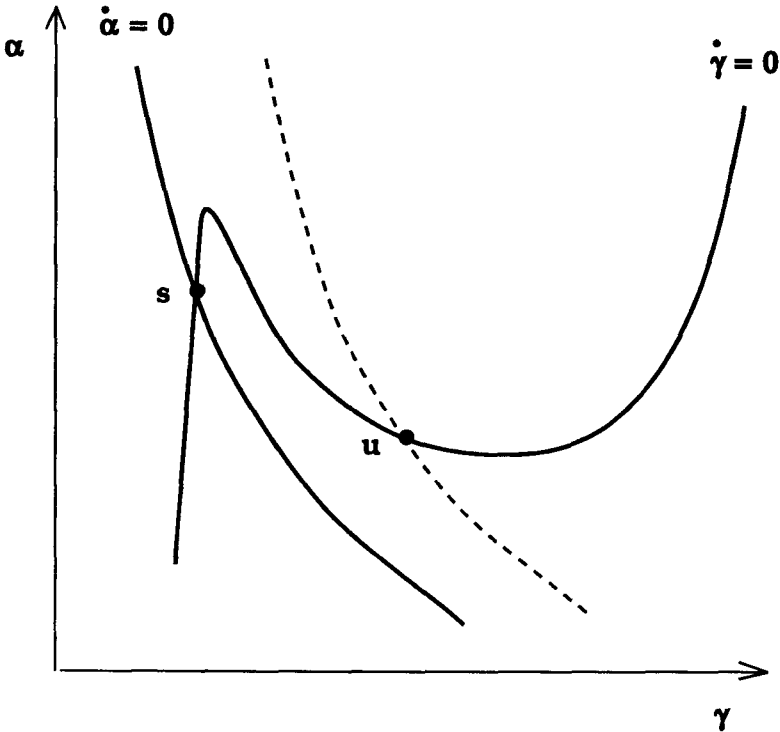


Figure 1.10 The α - and γ -nullclines of the model described by equations (1.12). For a well-defined parameter range, the γ -nullcline is an S-shaped sigmoid. When there is the α -nullcline denoted by a solid curve, the two nullclines intersect at the stable point. This case leads to excitability. When there is the α -nullcline denoted by a broken curve, the steady point becomes unstable. As a result, the limit-cycle oscillations appear.

σ is the normalized maximum activity of the enzyme and q is a constant arising from the normalization process. Figure 1.10 illustrates the α - and γ -nullclines. The γ -nullcline is an S-shaped sigmoid for a well-defined parameter range, which accounts for excitability and oscillations.

As a possible extension of this model, Li and Goldbeter (1989) proposed a simple model for two biochemical reactions coupled in parallel (Fig. 1.11). Each of the two reactions is catalysed by a distinct isozyme transforming, though with different kinetic properties, the given substrate into the same product. This model is described by the following equations:

$$\frac{d\alpha}{dt} = \frac{1}{q}(v - \sigma\Phi) \quad (1.13a)$$

$$\frac{d\gamma}{dt} = \Phi - \frac{k_s}{q\sigma}\gamma \quad (1.13b)$$

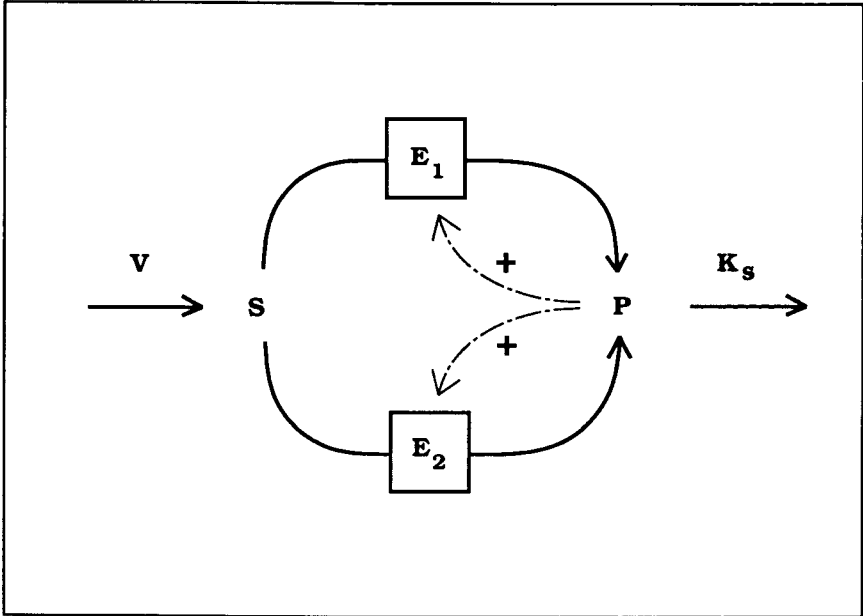


Figure 1.11 Model of two autocatalytic isozyme reactions coupled in parallel. The two enzymes catalyse the same biochemical reaction with different kinetic properties. Similarly to the model in Fig. 1.9, there is a constant influx, V , of the substrate, S , and a degradation of the product, P , with a proportionality constant, K_s . Each of the two enzymes is capable of generating oscillations in isolation.

where

$$\Phi = r_1\phi_1 + r_2\phi_2 \tag{1.13c}$$

$$\phi_i = \frac{c_i\alpha(1 + c_i\alpha)^{n_i-1}(1 + d_i\gamma)^{n_i}}{L_i + (1 + c_i\alpha)^{n_i}(1 + d_i\gamma)^{n_i}}. \tag{1.13d}$$

In equation (1.13c), ϕ_i refers to the rate function of the allosteric enzyme, E_i , which consists of n_i subunits. They assumed that $n_1 = 2$ and $n_2 = 4$. To identify the relative difference in parameters of enzyme E_2 , with respect to the parameters of enzyme E_1 , they assumed that $c_1 = d_1 = r_1 = 1$ and wrote the ratios of the parameters of the enzyme E_2 as $c_2 = c$, $d_2 = d$, and $r_2 = r$. Parameter d plays an important role in producing *birhythmicity*. For small values of d (say $d = 0.0456$), the γ -nullcline has two separate regions of negative slope (Fig. 1.12). There are small- and large-amplitude oscillations (solid closed orbits) separated by an unstable oscillation (broken closed orbit) in Figure 1.12A. The corresponding time variation of α and β is shown in Figure 1.12B. The reversible transition between the two modes of oscillations

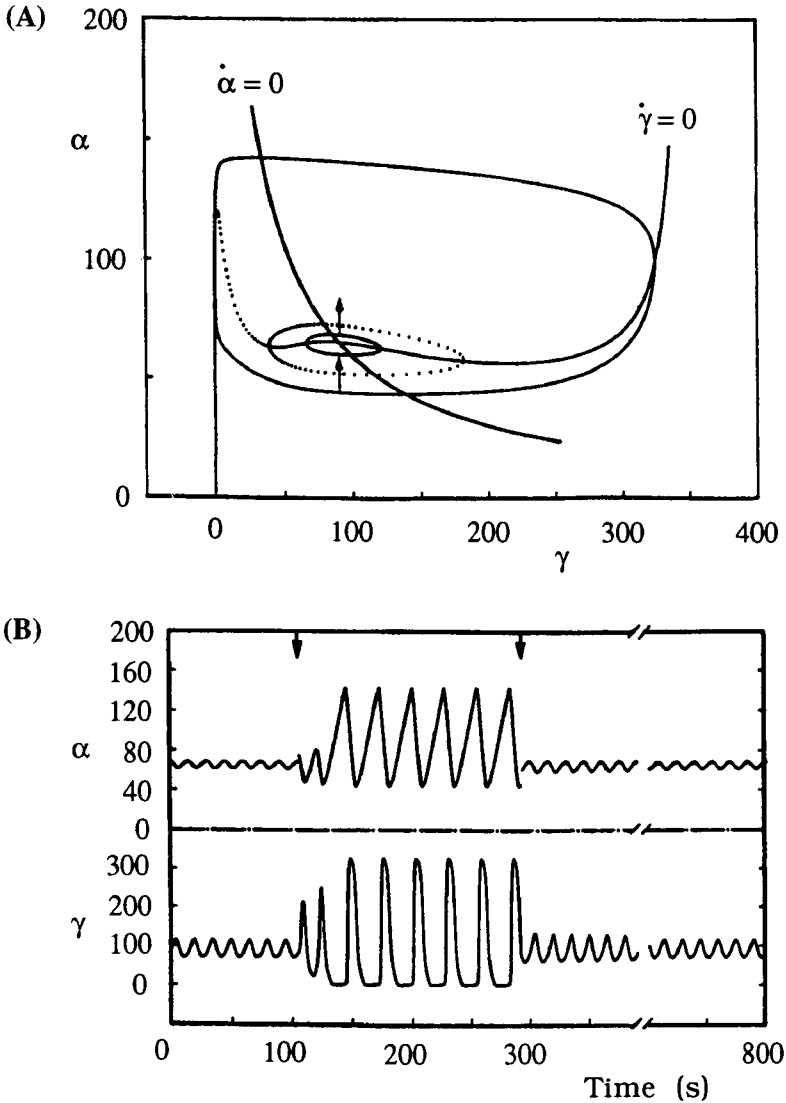


Figure 1.12 (A): Phase-plane demonstration of birhythmicity. The α - and γ -nullclines resemble those in Fig. 1.10 except that the γ -nullcline has two separate regions of negative slope. There are three closed trajectories: two stable limit cycles (solid curves) and one unstable limit cycle (broken curve). The arrows show how the transition from one stable cycle to the other stable cycle can occur in response to the addition of a certain amount of substrate. (B): Transition between the two stable oscillatory modes shown in (A). The transition is induced by an abrupt change in the substrate. The two vertical arrows correspond to the increase of α from 68.5 to 75, and from 45.5 to 60, respectively. From Li and Goldbeter (1989). Reprinted with permission.

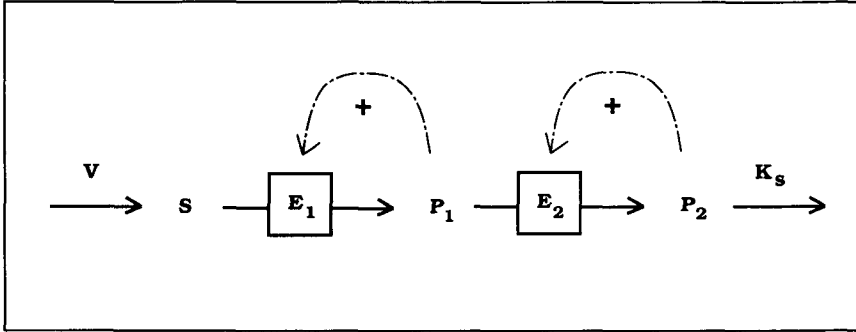


Figure 1.13 Model of two autocatalytic enzyme reactions coupled in series. The normalized concentrations of S, P₁ and P₂ are denoted by α, β and γ.

can be triggered by perturbations of appropriate magnitude in the form of step increases in α at appropriate phases in the cycle.

1.1.5 *Bursting*

As another example of a coupled biochemical system, Decroly and Goldbeter (1987) developed the model of two autocatalytic enzyme reactions coupled in series (Fig. 1.13). This model is described by the following equations:

$$\frac{d\alpha}{dt} = v - \sigma_1\phi_1 \tag{1.14a}$$

$$\frac{d\beta}{dt} = q_1\sigma_1\phi_1 - \sigma_2\phi_2 \tag{1.14b}$$

$$\frac{d\gamma}{dt} = \sigma_2\phi_2 - k_s\gamma \tag{1.14c}$$

where

$$\phi_1 = \frac{\alpha(1 + \alpha)(1 + \beta)^2}{L_1 + (1 + \alpha)^2(1 + \beta)^2} \tag{1.14d}$$

$$\phi_2 = \frac{\beta(1 + \gamma)^2}{L_2 + (1 + \gamma)^2} \tag{1.14e}$$

Similarly to the previous model, this system is driven by a constant input of substrate with the normalized rate, v, and the end product is taken away with a normalized proportionality constant, k_s. σ₁ and σ₂ are the normalized maximum activities of enzymes E₁ and E₂. Their allosteric constants are denoted by L₁ and L₂, and q₁ and q₂ are constants arising from the normalization process.

They assumed the following set of parameter values: σ₁ = σ₂ = 10 s⁻¹, q₁

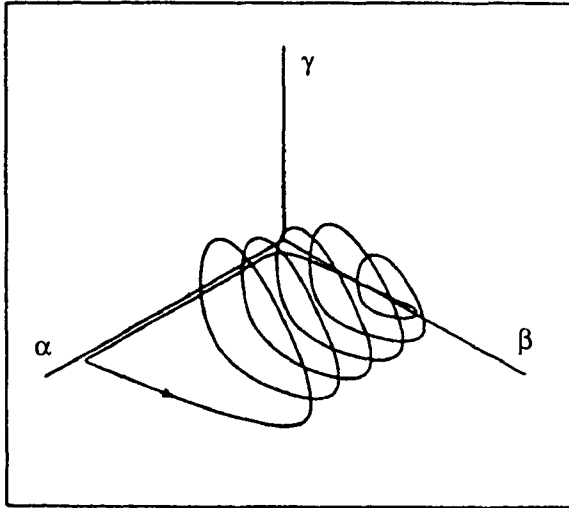


Figure 1.14 Three-dimensional phase-space representation of bursting. Bursting occurs when the $(\alpha - \beta)$ subsystem passes into a region of the phase space where the $(\beta - \gamma)$ subsystem undergoes rapid oscillations. This means that bursting results from the coupling of a fast, spike-generating mechanism with a slow oscillation. From Decroly and Goldbeter (1987). Reprinted with permission.

$= 50$, $q_2 = 0.02$, $L_1 = 5 \times 10^8$, $L_2 = 100$. For these parameter values, the first positive feedback loop, or the $(\alpha - \beta)$ subsystem, undergoes slow oscillations, which are relatively independent of γ because of the small value of L_2 . The second feedback loop, or the $(\beta - \gamma)$ subsystem, gives rise to faster oscillations under the control of the slow oscillatory $(\alpha - \beta)$ subsystem. The parameters ν and k_s determine the dynamical behaviour of this model. Figure 1.14 illustrates the three-dimensional trajectory of the bursting solution to equation (1.14) for $\nu = 0.25 \text{ s}^{-1}$ and $k_s = 5 \text{ s}^{-1}$.

Of course this model also displays chaotic behaviour for $\nu = 0.25 \text{ s}^{-1}$ and $k_s = 1.537 \text{ s}^{-1}$. These complex behaviours such as bursting, chaos and birhythmicity, are also found in the nervous system. Most of the complex behaviours result from different parameter values or *multiple time-scales*.

1.2 Spatial order

1.2.1 Pattern formation in the two-component system

The problems of spatial order were first studied by Rashevsky (1940) and Turing (1952) in the context of *morphogenesis* and *pattern formation*. Their idea was that chemical substances passed through from one cell to its neighbouring cell by diffusion. Suppose that the concentrations of the two

morphogenes in cell r are written by u_r and v_r , and that their reaction rates are $f(u_r, v_r)$ and $g(u_r, v_r)$, respectively, then the following equations describe the changes in u_r and v_r taking into account diffusion as well as the chemical reaction:

$$\frac{du_r}{dt} = f(u_r, v_r) + D_1(u_{r+1} - 2u_r + u_{r-1}) \quad (1.15a)$$

$$\frac{dv_r}{dt} = g(u_r, v_r) + D_2(v_{r+1} - 2v_r + v_{r-1}) \quad (1.15b)$$

where $r = 1, \dots, N$. The second terms of these equations describe the representation of diffusion where D_1 and D_2 are the diffusion constants for u_r and v_r , respectively.

Interestingly, the initial homogeneous (symmetrical) system, being an ensemble of cells, gives rise to inhomogeneous (asymmetrical) structures as the concentrations of chemical substances change due to diffusion. We sometimes call this effect *diffusion instability* or *Turing instability*. Symmetry-breaking phenomena of this kind are very suggestive, not only because they seem to conflict with the general concept that diffusion is likely to cause symmetry, but also because no change appears when we consider the total system instead of the individually divided cell.

Gierer and Meinhardt (1972) (see the book by Meinhardt (1982) for details) developed Rashevsky and Turing's idea into a *reaction-diffusion* system with continuous formulas:

$$\frac{\partial u}{\partial t} = f(u, v) + D_1 \frac{\partial^2 u}{\partial x^2} \quad (1.16a)$$

$$\frac{\partial v}{\partial t} = g(u, v) + D_2 \frac{\partial^2 v}{\partial x^2} \quad (1.16b)$$

where u and v denote concentrations of an *activator* and an *inhibitor*, respectively. Both the activator and inhibitor diffuse, with diffusion coefficients D_1 and D_2 .

It turned out that biologically interesting patterns appeared when an autocatalytic *activation* with a small diffusion coefficient value was coupled with an *inhibition* with a large diffusion coefficient value (Fig. 1.15). The essential point is the combination of *short-range* activation and *long-range inhibition*.⁶ Figure 1.16 illustrates the spatial representation of short-range activation and long-range inhibition.

The diffusion instability responsible for spatial structures is qualitatively interpreted as follows. Consider first the diffusionless reaction. If the activator concentration deviates slightly from its equilibrium value, it grows autocatalytically as time proceeds. This occurrence, however, immediately induces the production of the inhibitor. The accumulated inhibitor in turn

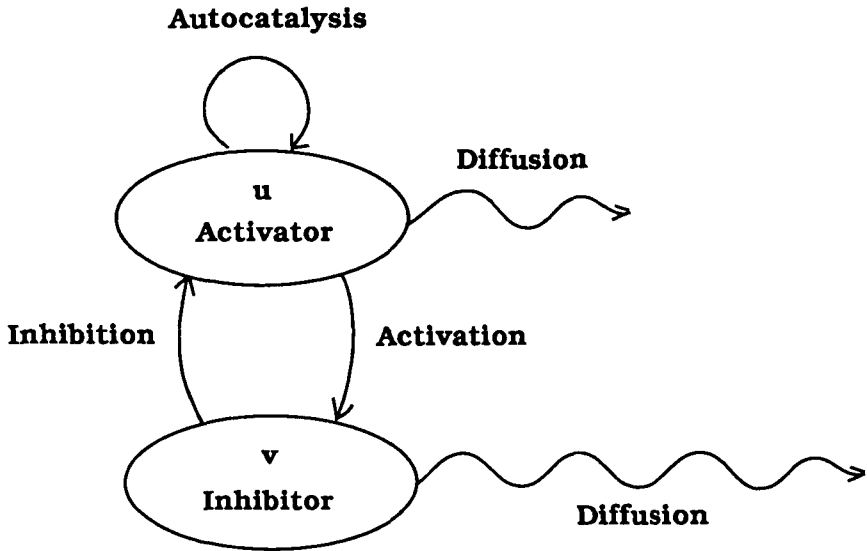


Figure 1.15 Diagram showing the coupling of an autocatalytic activator and an inhibitor with different diffusion coefficients.

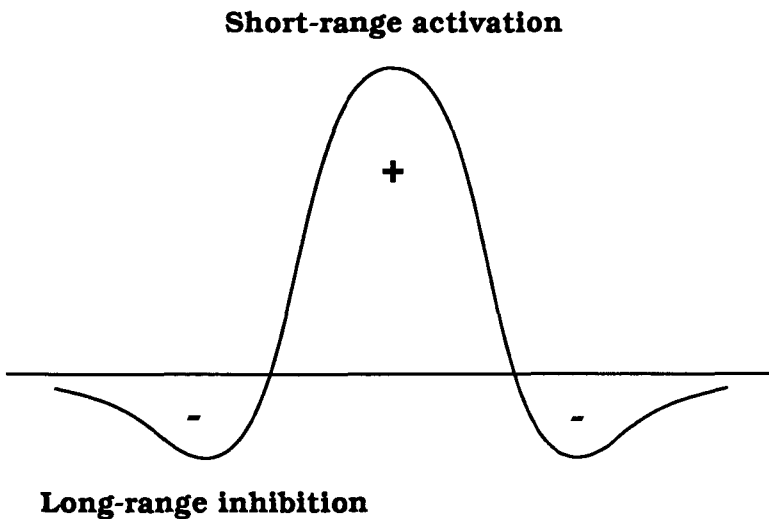


Figure 1.16 Spatial representation of short-range activation and long-range inhibition. The signs + and - indicate the short-range activation (or local activation) and the long-range inhibition (or lateral inhibition), respectively.

suppresses the increase of the activator and leads to a recovery toward its equilibrium value. Due to the intrinsically stable nature of the inhibitor, its concentration returns to its equilibrium value. For small deviations, this stabilization process takes place, so that spatially inhomogeneous structures do not appear.

Now consider what happens when the diffusion is taken into account. If the activator concentration deviates from its equilibrium, it grows autocatalytically as long as it does not diffuse out too rapidly. As a result of the increase in the activator, the inhibitor accumulates in the local region. Since the diffusion of the inhibitor is rapid, the local inhibitor concentration is no longer high enough to suppress the autocatalytic growth of the activator concentration, which consequently leads to spatial structure.

Babloyantz (1977, 1986) developed a theoretical model for pattern formation on the assumption that direct cell–cell interactions affected the rates of reactions between them without the actual passage of chemicals. This model not only generates all the self-organizing phenomena seen in reaction–diffusion systems but also other phenomena previously non-existent, because of the assumption that the direct intercellular contact relaxes the principle of micro-reversibility, i.e. the loss of matter is compensated by the influx of matter from surrounding regions at any point in space.

1.2.2 Solitons in the reaction–diffusion system

As an interesting extension of the reaction–diffusion system, Tuckwell (1980) introduced spontaneous ‘on’ and ‘off’ switches to the reaction rates. The modified system is described by the following equations:

$$\frac{\partial u}{\partial t} = F(u, v) + D_1 \frac{\partial^2 u}{\partial x^2} \quad (1.17a)$$

$$\frac{\partial v}{\partial t} = G(u, v) + D_2 \frac{\partial^2 v}{\partial x^2} \quad (1.17b)$$

where the reaction rates $F(u, v)$ and $G(u, v)$ are the nonlinear functions $F^*(u, v)$ and $G^*(u, v)$ giving rise to excitable phenomena, plus spontaneous ‘on’ and ‘off’ switches which depend on whether the phase point enters the predetermined region on the (u, v) plane. This is mathematically described as follows.

$$F(u, v) = F^*(u, v) + \sum_{i=1}^{10} a_i I_{A_i}(u, v) \quad (1.17c)$$

$$G(u, v) = G^*(u, v) + \sum_{i=1}^{10} b_i I_{A_i}(u, v) \quad (1.17d)$$

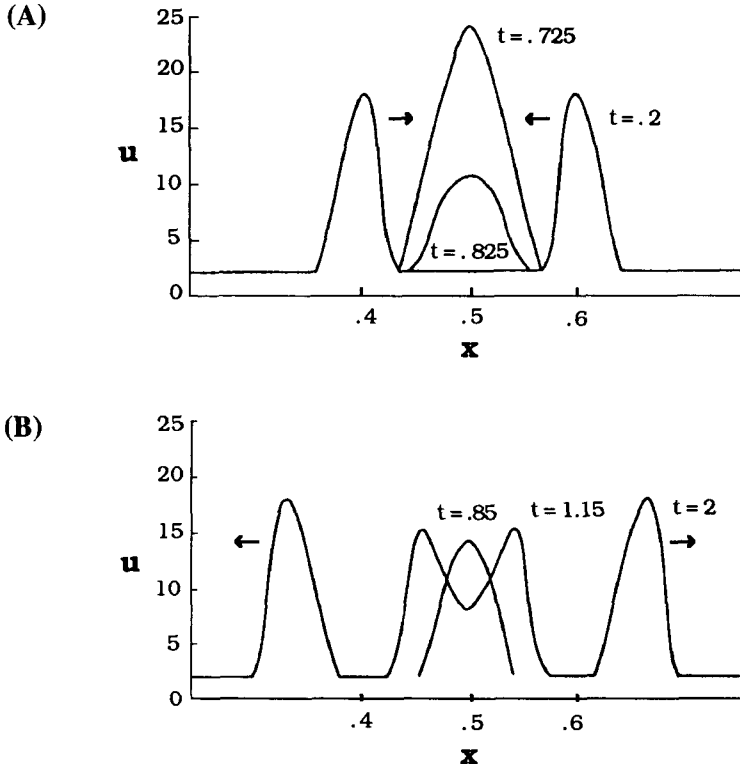


Figure 1.17 (A): Collision of solitons travelling in opposite directions. At $t = 0$ the solitons were at $x = 0.68$ and $x = 0.32$. The collision occurs at about $t = 0.650$. Two solitons merged at $t = 0.725$, and the resultant envelope decreases at $t = 0.825$. (B): Two solitons pass through on collision. From Tuckwell (1980). Reprinted with permission.

where

$$I_{A_i}(u, v) = \begin{cases} 1 & (u, v) \in A_i \\ 0 & (u, v) \notin A_i \end{cases} \quad (1.17e)$$

$$A_i = \{(u, v) \mid u \in (u_i^1, u_i^2), v \in (v_i^1, v_i^2)\}. \quad (1.17f)$$

It is generally accepted that in the reaction–diffusion system the two waves travelling in opposite directions annihilate one another on collision. Tuckwell wanted to adjust the reaction rates described above in such a way that the two waves would pass through on collision like *solitons* (see Scott, 1981; see also books by Jackson, 1990; Olver and Sattinger, 1990; and Infeld and Rowlands, 1990). Figure 1.17 shows the soliton-like solutions of the model described by equations (1.17) with specific parameter values.

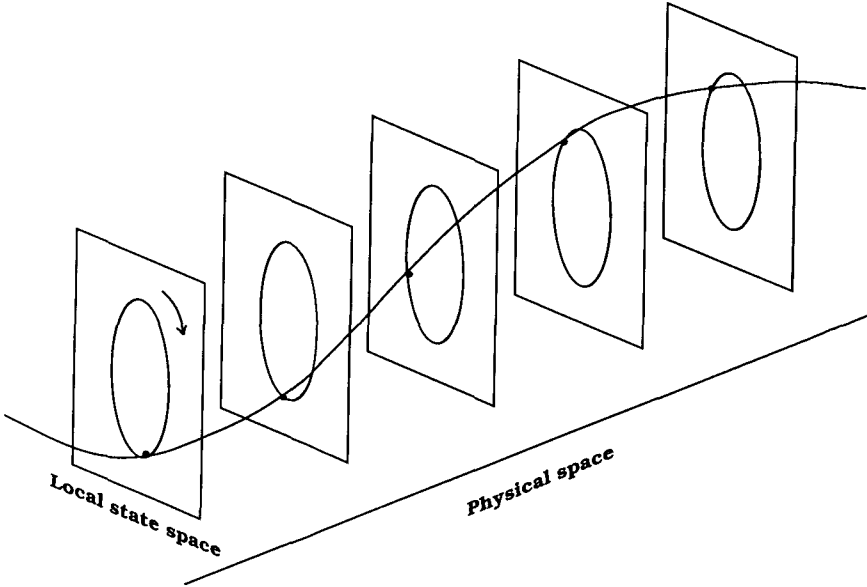


Figure 1.18 A one-dimensional array of coupled limit-cycle oscillators. A limit-cycle oscillator is represented by a closed orbit whose phase is represented by a point in the local state space. Many limit-cycle oscillators are arranged along the physical space to form a one-dimensional array of coupled oscillators. Modified from Kuramoto (1984).

1.2.3 Complex behaviours in the one-component system

Kuramoto (1984) considered a one-dimensional array of diffusion-coupled limit-cycle oscillators (Fig. 1.18). The phase dynamics of this coupled-oscillator system can be described by the following equation:

$$\frac{\partial \phi}{\partial t} = A \frac{\partial^2 \phi}{\partial y^2} - B \frac{\partial^4 \phi}{\partial y^4} + F(\phi) \quad (1.18)$$

where ϕ is a phase of the limit-cycle oscillator in physical space, y , and time, t , and A and B are constants, while $F(\phi)$ is a nonlinear function. *Phase instability* arises when $A < 0$ and $B > 0$, which leads to chaotic behaviours. The same equation not only accounts for the *wavefront instability* of a two-dimensional wave (Kuramoto, 1984), but also explains the *hydrodynamic instability* in a laminar flame (Sivashinsky, 1977; 1979; 1980). Thus equation (1.18) is often called the Kuramoto–Sivashinsky equation.

The essence in equation (1.18) is captured by a *linear stability analysis*. Consider a wave-like solution to the linearized version (say $F(\phi) = 0$) of equation (1.18) in the form

$$\phi(y, t) \propto \exp(\omega t + iky) \quad (1.19)$$

where k is a wave number (i.e. $k = 2\pi/\lambda$, where λ is a wavelength). Substituting solution (1.19) into the linearized equation, we obtain the *dispersion relation* for ω in terms of the wave number k as

$$\omega = -Ak^2 - Bk^4. \quad (1.20)$$

The growth or decay of the solutions is determined by $\exp(\omega t)$ in equation (1.19). If $A < 0$ and $B > 0$, then short waves ($\lambda < \lambda_c$ or $k > k_c$) are stable, and long waves ($\lambda > \lambda_c$ or $k < k_c$) are unstable. The critical wavelength, λ_c , and its critical wave number, k_c , are

$$\lambda_c = \frac{2\pi}{k_c} = 2\pi \sqrt{\frac{B}{-A}}. \quad (1.21)$$

For long waves, the terms of $A < 0$ and $B > 0$ correspond to the destabilization and stabilization processes, respectively. This competing interaction leads to self-turbulization phenomena, in which the ordered structure is replaced by a chaotic structure. This type of instability is quite different from the diffusion instability discussed in Section 1.2.1 as follows. In the previous case, the spatial order results when the spatially homogeneous state is destabilized via diffusion, while in the present case, the ordered state is replaced by a chaotic behaviour via the competing mechanism.

Equations similar to equation (1.18) have also been developed in order to account for population dynamics (Cohen and Murray, 1981) and the morphogenesis of multicellular systems formed by motile cells (Lara Ochoa, 1984). Such equations are often called the *generalized reaction-diffusion* equations. When $A < 0$ in equation (1.18) the first term on the right-hand side corresponds to a negative diffusion coefficient in a Fickian sense or the short-range activation that occurs in system (1.16). In population dynamics, for example, the diffusion coefficient exhibits population pressure which effectively gives a negative diffusion for aggregative behaviour. An example of this is the schooling of fish. The second term on the right-hand side of equation (1.18) accounts for long-range inhibition when $B > 0$.

We have seen that the same type of equation appears in totally different contexts, and that the dynamic variable has different meanings depending on the context. It is not surprising, therefore, that completely different phenomena may have a common nature. In the rest of this book, we will study the muscle system (Part I) and the flagellar system (Part II) in the context of the nonlinear science outlined in this chapter.

Notes

- 1 For van der Pol equation, see van der Pol (1926), and van der Pol and van der Mark (1928).
- 2 For a classical two-factor model of excitation and inhibition, see Rashevsky (1933) and Hill (1936).

- 3 For books see Guckenheimer and Holmes (1983), Bergé *et al.* (1986), Holden (1986), Thompson and Stewart (1986), Moon (1987), Glass and Mackey (1988), Devaney (1989), Jackson (1989, 1990), Baker and Gollub (1990), Rasband (1990), Wiggins (1990) and Schroeder (1991).
- 4 Bernoulli trials refer to repeated independent trials, each of which leads to only one of two possible outcomes (i.e. 'success' or 'failure') with the same probability.
- 5 The term 'allosteric' means that the binding of a ligand molecule to a protein at one site affects the binding of a second, identical or different, ligand, through the mediation of a conformation change in the protein. If the enzyme protein, or *oligomer*, is constructed from several identical subunits, or *protomers*, cooperative interactions between the subunits result. There are two different models for this cooperativity. One is the *concerted* transition model, in which any conformational change occurs simultaneously within all subunits of the oligomer (Monod *et al.*, 1965). The other is the *sequential* transition model, in which the subunit conformational change only occurs as a result of the binding of a ligand molecule (Koshland *et al.*, 1966). Both models lead to similar results.
- 6 The requirement of unequal diffusion constants for two substrates in generating spatially inhomogeneous structures is analogous to the requirement of multiple time-scales in producing temporally complex behaviours.

Part I Oscillatory contraction in muscle

Muscle contraction is the most familiar type of cellular motility. When the muscle shortens the *thin* and *thick* filaments actively slide against each other by the use of the chemical energy of the ATP hydrolysis. This is known as the *sliding filament* mechanism. Although the active sliding between the two filaments occurs *unidirectionally*, the muscle often gives rise to sustained oscillations under appropriate conditions. Wing beats of flying insects and heart beats of living animals are typical examples of such oscillations. Interestingly, oscillatory contraction has also been observed in experiments using the vertebrate skeletal muscle. The oscillatory capability of this muscle can be, therefore, ascribed to the intrinsic property of common muscle components. There arises the problem of what mechanism produces oscillatory contraction in muscles. Part I of this book attempts to solve this problem.

2 Muscle structure and function

This chapter provides experimental observations of various types of muscles. In Section 2.1 the historical background is briefly outlined. Section 2.2 describes the basic structure of vertebrate muscle and compares it with the structure of insect flight muscle. In Section 2.3 two different interpretations of the mechano-chemical cycle underlying muscle contraction are briefly described. The mechanical properties of both vertebrate muscle and insect flight muscle are summarized in Section 2.4. Section 2.5 discusses mechanisms for oscillatory contraction based on measurements of oscillation-induced ATPase activity and stretch-induced changes in stiffness.

2.1 Introduction

Insects fly by beating their wings up and down. Their wing-beat frequencies range from about 5 Hz for butterflies to about 1000 Hz for mosquitos. The wing-movements of some insects result from oscillatory contraction of antagonistic pairs of *direct* flight muscles (Fig. 2.1), while others are produced by *indirect* flight muscles (Fig. 2.2). The direct muscles are inserted into the wing base so that the wing-movements are directly caused by these muscles. The indirect muscles occur in the thorax and they are not connected to the wing base; by distortions of the thorax, the wing-movements are indirectly produced.

Upon the arrival of motor nerve impulses, the muscle cell membrane is excited and causes a contraction. Usually a single nerve impulse or its associated muscle membrane excitation causes a single muscle contraction. Muscles of this type are called *synchronous*.¹ Pringle (1949), however, found that specialized insect flight muscle contracts several times in response to a single electrical stimulus (Fig. 2.3). Such muscles are described as *asynchronous*.² A nerve impulse is necessary to initiate contractions, but subsequent contractions result from intrinsic properties of the muscle itself. Further nervous stimulation is necessary only to maintain the excited state of the

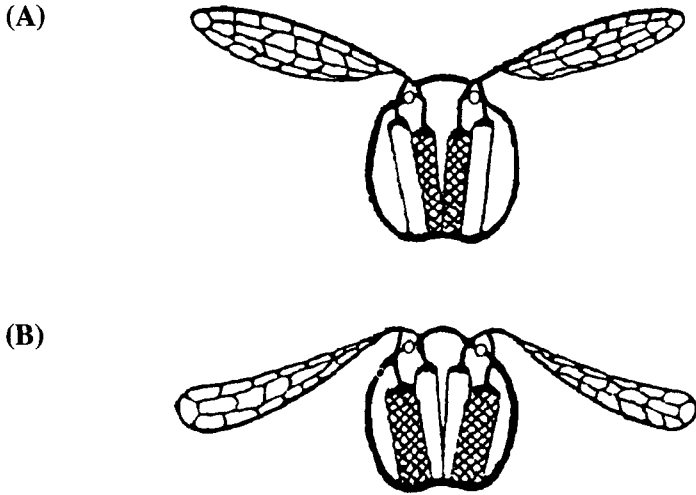


Figure 2.1 Synchronous, direct flight muscles of the type found in dragonflies. The thorax sections show that antagonistic pairs of flight muscles are directly connected to the wing base. The hinges are represented by black circles with white centres. (A): Contraction of the inner pair of muscles raises the wings and stretches the antagonistic pair. (B): Contraction of the outer pair of muscles lowers the wings and stretches the inner pair. Modified from Davydov (1982). Reprinted with permission.

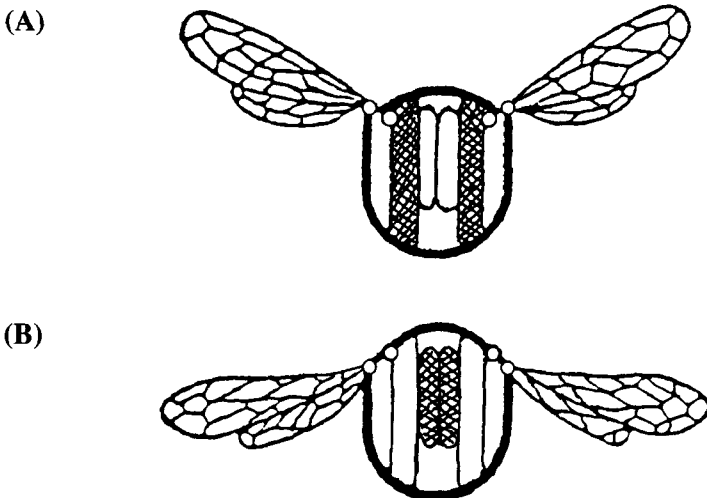


Figure 2.2 Asynchronous, indirect flight muscles of the type found in mosquitos. Antagonistic pairs of flight muscles are not directly connected to the wing base, but are connected to the thorax. The wings are driven up and down via the deformation of the thorax. The hinges are represented by black circles with white centres. (A): The outer pair of muscles contract vertically and raise the wings, stretching the antagonistic pair. (B): The inner pair of muscles contract horizontally and lower the wings, stretching the outer pair. Modified from Davydov (1982). Reprinted with permission.

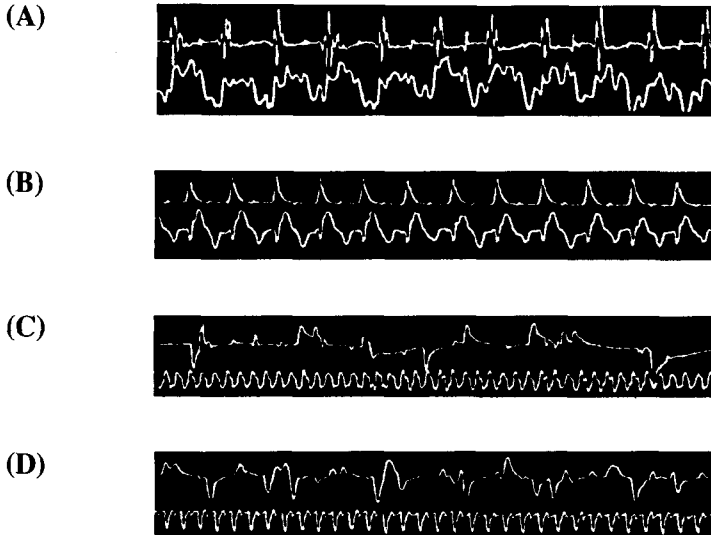


Figure 2.3 Electrical (upper trace) and mechanical (lower trace) records from the thorax of various insects. (A), (B) Synchronous type; (C), (D) asynchronous type. (A) Cockroach; (B) moth; (C) fly; (D) wasp. The wing-beat frequencies are 25, 43.5, 155 and 120 Hz for (A), (B), (C) and (D), respectively. Whereas the wing-beat frequency of insects with synchronous flight muscles is low, not more than about 100 Hz, the frequency is high in insects with asynchronous muscles. From Pringle (1957). Reprinted with permission.

muscle. Asynchronous muscle is, therefore, capable of oscillating at very high frequencies.

Following Pringle's discovery of asynchronous muscle, sustained oscillations were also demonstrated when a glycerol-extracted vertebrate skeletal muscle (rabbit psoas muscle) was coupled to an appropriate inertial load (Goodall, 1956; Lorand and Moos, 1956). These observations revealed that oscillatory contractions were not caused by properties of the structures particular to flight muscles, but resulted from intrinsic properties of the force-generating mechanisms common to different types of muscles.

2.2 Muscle structure

2.2.1 Vertebrate muscle

As a typical example of muscle, the vertebrate muscle is detailed in Figure 2.4. The whole muscle consists of a number of muscle *fibres*. Individual fibres appear striated under a light microscope. An individual fibre is a single muscle cell. This fibre cell contains several nuclei and a large number of mitochondria. Each muscle fibre, in turn, consists of *myofibrils* in a regular

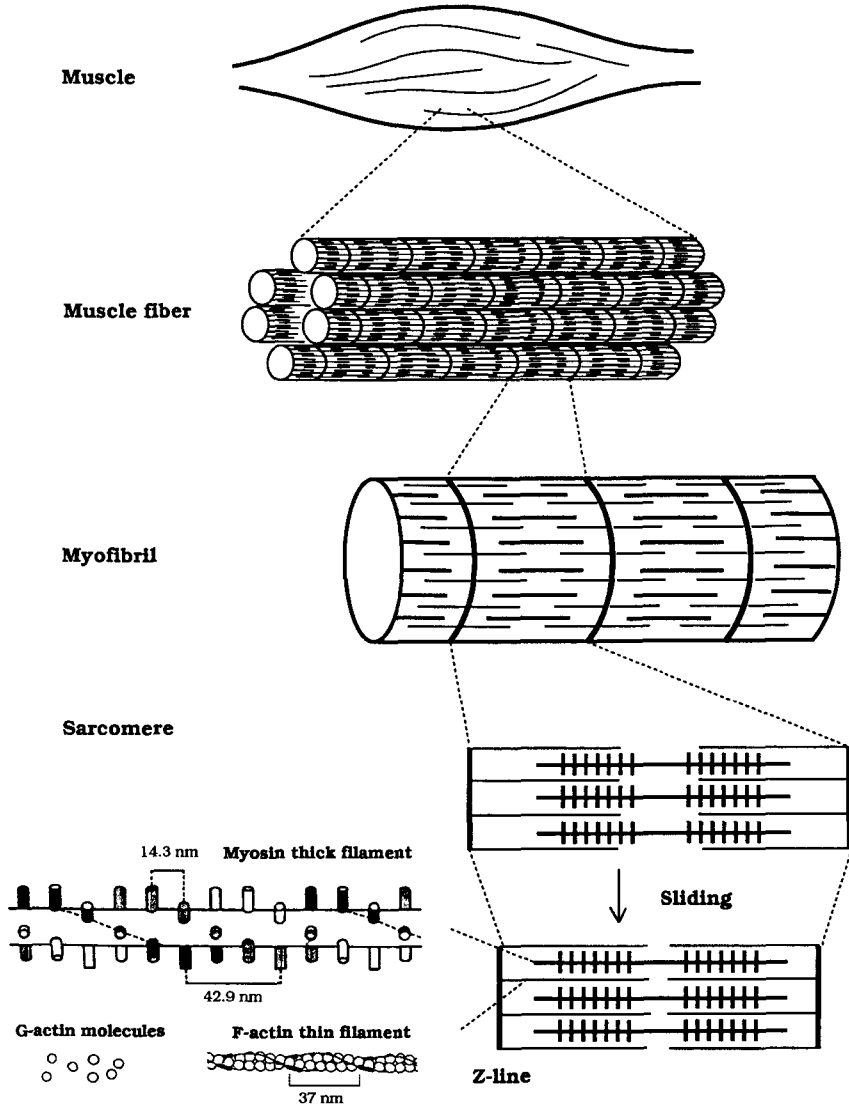


Figure 2.4 Structure of vertebrate muscle. The whole muscle consists of a number of muscle fibres. The motor nerves terminate on the fibres. Each muscle fibre contains many myofibrils. The myofibril has a series of sarcomeres, each of which contains the myosin thick (A) filaments and F-actin thin (I) filaments. There are three helices of projections (shown as white, grey and black) along a single filament. These projections are called cross-bridges. They convert the chemical energy of ATP hydrolysis into the mechanical energy necessary to produce active sliding. The thin filament has two helices, which are formed by G-actins.

parallel arrangement. The myofibril is divided into a series of functional units called *sarcomeres*. The sarcomere can be distinguished by a pair of *Z-lines*.

In each sarcomere, there are two filaments: the thick or *A-filament* and the thin or *I-filament*. These two filaments slide against each other during muscle contraction. The thick filament is formed by three myosin helices; that is, at each level three myosins protrude. These projections are called *cross-bridges*, and can transform the chemical energy of ATP hydrolysis into the mechanical energy necessary to generate active sliding. Adjacent cross-bridges are staggered by 14.3 nm with respect to one another. Since there is a rotation of 60° between successive cross-bridges, the cross-bridges in the same direction occur every 42.9 nm (Huxley and Brown, 1967). The thick filaments reverse polarity at the midline of the sarcomere, because two oppositely oriented sets of myosins come together to form the thick filaments.

The thin filament contains two strands of actin filaments. These actin filaments are called filamentous actin or *F-actin*. The pitch of the F-actin is considered to be 2×37 nm (Huxley and Brown, 1967). Each F-actin is formed by globular subunits, which are known as globular actin or *G-actin*. The thin filaments are polar structures, so that their two ends are different. This polarity determines the direction of active sliding between the thick and thin filaments.

2.2.2 Insect flight muscle

Insect flight muscle and vertebrate muscle have basically similar structures, but differ as follows. First, as illustrated in the upper panels of Figure 2.5, insect flight muscle has relatively longer thick filaments than vertebrate muscle.

Second, insect flight muscle contains another filament, which connects the thick filament and the Z-line (see the upper panel of Fig. 2.5B). This filament is often called a connecting or *C-filament*. The C-filament is responsible for the high stiffness of relaxed insect flight muscle as compared with vertebrate muscle.

Third, as shown in the lower panels of Figure 2.5, the ratio of thin to thick filaments differs in the two muscles. In vertebrate muscle the myofilament array is such that each thick filament is surrounded by six thin filaments and each thin filament by three thick filaments. As a result, the ratio of thin to thick filaments is 2 : 1. In insect flight muscle each thick filament is surrounded by six thin filaments, but each thin filament is placed between two thick filaments. The thin-to-thick ratio is 3 : 1.

Fourth, the thick filaments are different in the two muscles. In vertebrate muscle three myosin cross-bridges protrude at each level of the thick filament (see Fig. 2.4), while in the insect flight muscle there are four cross-bridges at each level (Wray, 1979).

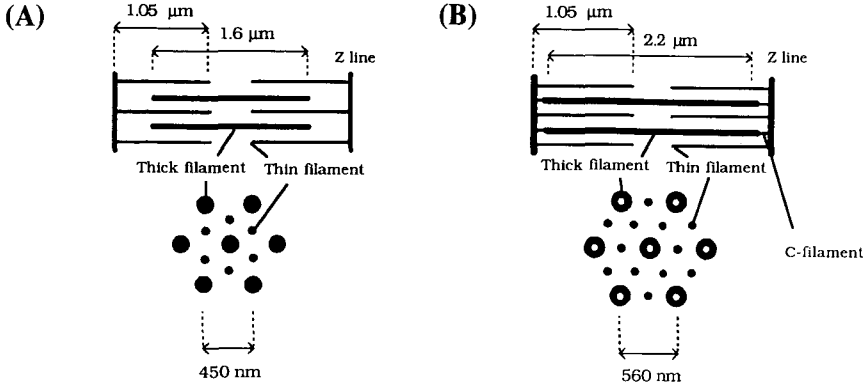


Figure 2.5 The structures of vertebrate muscle (in panel A) and insect flight muscle (in panel B). In both cases, there are thick (A) and thin (I) filaments between the two Z lines forming sarcomeres (upper figures). There is the C-filament between the thick filament and Z line in insect flight muscle. The arrangement of thin filaments around the thick filaments is different in the two muscles: the ratio of thin to thick filaments is 2 : 1 in vertebrate and 3 : 1 in insect flight muscle. From White and Thorson (1973). Reprinted with permission.

2.3 Mechano-chemical cycle of a myosin cross-bridge

It was originally thought that a change in shape or in the angle of cross-bridge attachment to actin produces active sliding between the thick and thin filaments in association with the hydrolysis of ATP (Fig. 2.6). This mechano-chemical cycle is detailed as follows. A molecule of ATP binds to the myosin cross-bridge attached to the thin filament, making it detach (A \rightarrow B). The bound ATP is hydrolysed to ADP + Pi, allowing the cross-bridge to relax (B \rightarrow C), and make contact with the thin filament (C \rightarrow D). This attached cross-bridge undergoes the *power stroke* which causes active sliding, and the subsequent release of ADP + Pi (D \rightarrow A).

The characteristic features of this model are that (i) the distance of one power stroke is at most ~ 10 nm due to the conformation change of the attached cross-bridge and (ii) a single power stroke is associated with one ATP hydrolysis.

Recent experimental observations seem to contradict these two proposed features. Yanagida *et al.* (1985) examined the sliding distance induced by a myosin cross-bridge during one ATP hydrolysis cycle under the conditions of shortening without a load. When the muscle is free from an external load, it contracts by its maximal sliding velocity (cf. Fig. 2.19). The results show that the average sliding distance is more than 60 nm during one ATP cycle. This is much longer than the length of the myosin power stroke. Such a long sliding distance cannot be explained in terms of the cross-bridge cycle shown in Figure 2.6.

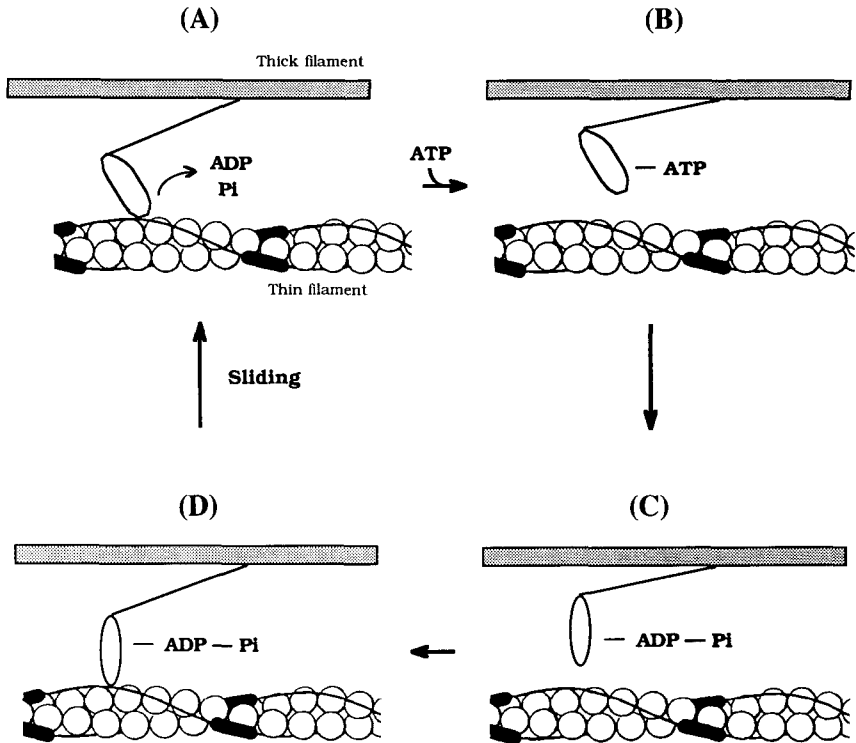


Figure 2.6 A mechano-chemical cycle of a myosin cross-bridge. (A \rightarrow B): After the power stroke, a cross-bridge detaches following the binding of an ATP molecule. (B \rightarrow C): Hydrolysis of the bound ATP to ADP + Pi makes the cross-bridge relax to its original conformation. (C \rightarrow D): The cross-bridge prepares for the next power stroke. (D \rightarrow A): The cross-bridge undergoes a change in conformation accompanied by the release of ADP + Pi. A single power stroke is 'tightly' coupled to one ATP hydrolysis.

Another important experiment was performed by Tsukita and Yano (1985) using the rapid-freezing electron-microscope technique. In isometrically contracting muscles, they found that most cross-bridges protrude from the thick filaments in a perpendicular orientation. This cross-bridge configuration is different from the previously considered one shown in Figure 2.6.

A new mechano-chemical cycle is needed to account for the above experimental observations. Figure 2.7 shows one possible cycle. This cycle contains two important features. First, the active sliding distance induced by one ATP cycle is not restricted to being less than 10 nm. Second, the generation of active force is not associated with the conformation change of the attached cross-bridges.

Unfortunately, similar experimental techniques lead to substantially different conclusions. In reality, the molecular mechanism responsible for muscle

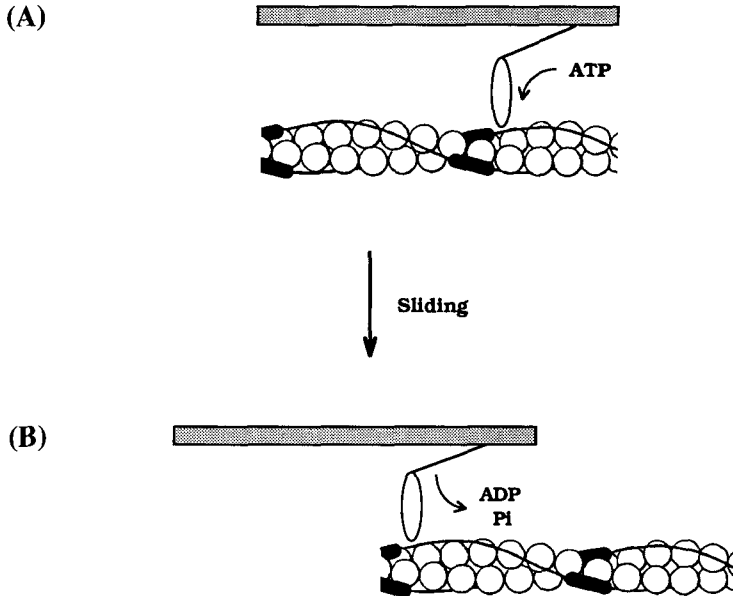


Figure 2.7 The newly proposed mechano-chemical cycle of a myosin cross-bridge. (A \rightarrow B): ATP is hydrolysed to ADP + Pi. Sliding movement is not 'tightly' coupled to this ATP cycle, but instead it is 'loosely' coupled.

contraction is still undetermined. According to the recent review by Huxley (1990), 'it seems that much of the original sliding filament cross-bridge scheme is correct, but there may be some unexpected twists in the tale'.

2.4 Mechanical properties

As we have briefly seen in Section 2.2, muscles are surrounded by a membrane and contain regulatory systems which are activated via the motor nerve stimuli. To investigate the origin of myogenic oscillation, it is very useful to have a 'model system' made up simply of sarcomeres. Such a 'model' was obtained by a *glycerol-extraction* procedure. With the membrane gone, muscles are easily activated by supplying a solution containing Mg-ATP and Ca^{2+} . The merit of using this model system is that any mechanical properties can be ascribed to the well-known structure of the sarcomere.

2.4.1 Free-oscillation experiment

Asynchronous muscles are capable of oscillating at higher frequencies than the rate of electrical stimulation (see Fig. 2.3). The wing-beat frequency of insects with these asynchronous muscles is altered by cutting off the tips

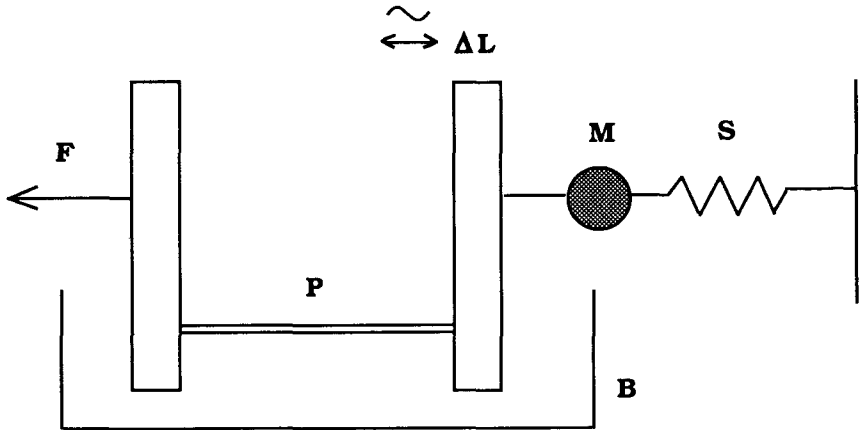


Figure 2.8 Experimental set-up for free oscillation. The preparation (P) is immersed in a bath (B) of ATP salt solution. The resonant lever system has mass M and the elasticity S . Under certain magnitudes of the mass and elasticity, the preparation gives rise to oscillations of amplitude ΔL . From Rüegg (1968). Reprinted with permission of Birkhäuser Verlag AG.

of the wings or by loading them with small amounts of wax. This probably occurs because the frequency of oscillation depends on mechanical parameters such as inertia of the wings and stiffness of the thorax. If this is true, the wing-beat frequency would be determined by the *resonant frequency* of the thorax–wing system.

To ascertain whether the wing-beat frequency was near the resonant frequency, a lever system was developed which involved the mass (M) and the elasticity (S) (Fig. 2.8). The mass and the elasticity corresponded to the inertia of the wings and elasticity of the thorax. By changing either the mass or elasticity, the resonant frequency of the lever system was easily changed.

Jewell and Rüegg (1966) used the indirect muscles of huge tropical waterbugs which had a wing-beat frequency of about 10–20 Hz. A preparation obtained from the glycerol-extraction procedure was attached to the resonant lever system. This preparation gave rise to oscillations when it was immersed in a bath of ATP salt solution with high concentrations of Ca^{2+} (Fig. 2.9). Their results showed that the observed frequency was always near the resonant frequency, over the range of about 5–20 Hz. If the resonant frequency was set to be out of this range, non-oscillatory contraction resulted.

Similarly, the glycerol-extracted vertebrate muscle showed auto-oscillations when coupled with an inertial load (Goodall, 1956; Lorand and Moos, 1956). It appeared that oscillatory capability can be ascribed to the intrinsic properties in the common structure of the muscles as mentioned in Section 2.1.

This *free-oscillation* experiment is, thus, useful for directly demonstrating

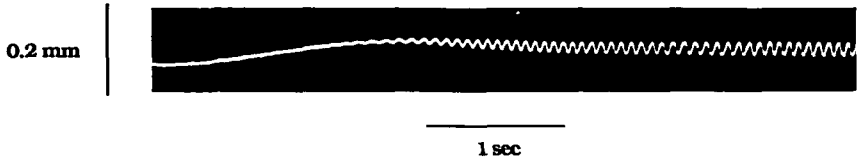


Figure 2.9 Free oscillation of glycerinated insect muscles. This oscillation requires a steady level of free calcium. From Jewell and Rüegg (1966). Reprinted with permission of the Royal Society.

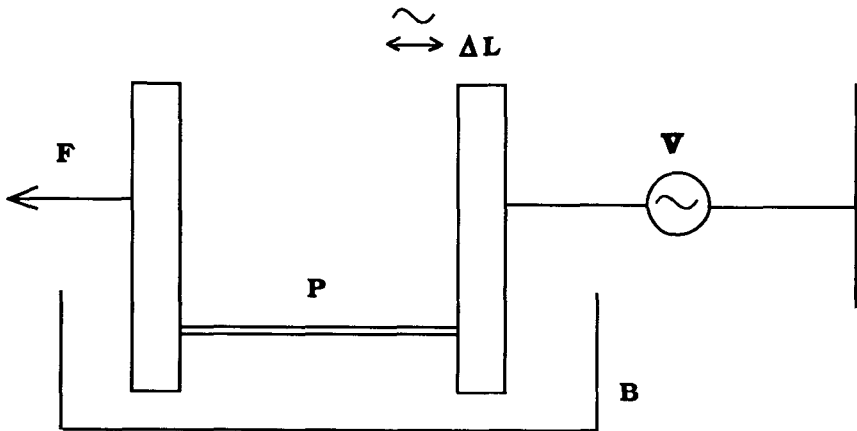


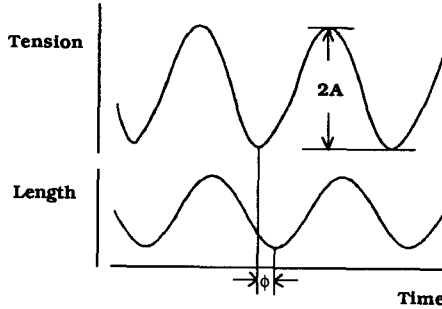
Figure 2.10 Experimental set-up for driven oscillation. The preparation (P) is immersed in a bath (B) of ATP salt solution. The preparation is driven by a sinusoidal wave generator (V), and the tension response is measured. From Rüegg (1968). Reprinted with permission of Birkhäuser Verlag AG.

the possibility of oscillations. However, it is not suitable for analysing the dynamic characteristics of the muscle, because the experimental set-up contains 'artificial' mass and elasticity.

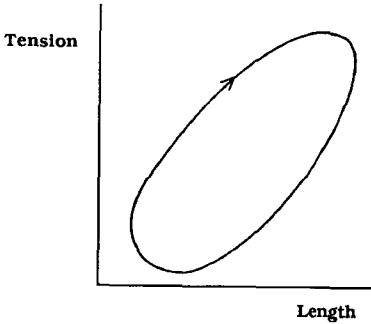
2.4.2 Driven-oscillation experiment

The free-oscillation experiment was soon replaced by a *driven-oscillation* experiment in order to obtain more information about the dynamic properties of muscle (see the review by Pringle, 1978). The muscle is subjected to a sinusoidal length change of small amplitude, and the resulting sinusoidal change in tension is measured (Fig. 2.10). This method is called *sinusoidal analysis*. In response to a sinusoidal length change, the tension also shows a sinusoidal waveform with the same frequency as that of the length change though different in its phase. Therefore, this tension response can be

(A) Sinusoidal analysis



(B) Length-tension loop



(C) Nyquist plot

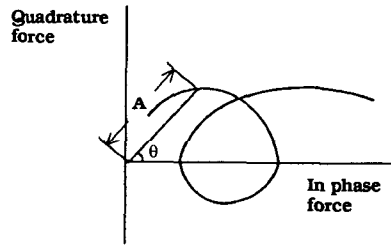


Figure 2.11 (A): Sinusoidal analysis. The length change is imposed sinusoidally at one particular frequency. In response to this length change, tension shows sinusoidal change with the same frequency but with a different phase. This panel shows that the tension change advances the length change by ϕ . (B): Length-tension loop. When the tension is plotted as a function of length, we have a length-tension loop for one frequency. If the phase shift, ϕ , is positive, as occurs in panel A, the direction of rotation on the loop is clockwise. (C): Nyquist plot. The phase shift, ϕ , is converted into the phase angle, θ , through equation (2.1) such that a point is plotted whose distance is equal to the amplitude, A , and whose angle is equal to the phase angle, θ . At different frequencies, these points are plotted and connected by a continuous curve.

characterized by its amplitude and resulting *phase shift* with respect to the length change. Figure 2.11A shows that there is a phase advance, ϕ , of tension on length at a particular frequency.

Depending on the applied frequency of the sinusoidal length change, the amplitude and phase shift of tension responses are altered. In order to obtain a lot of tension response data at different frequencies we must repeat this

sinusoidal analysis with the same amplitude of length changes at various frequencies. One way to express these results is to draw the length-tension loops at different driven frequencies. The shapes of these loops and the direction of their rotation are specified by the amplitude and phase shift of tension response. Figure 2.11B shows that a loop rotates clockwise. This corresponds to the phase advance of tension on length, as shown in Figure 2.11A.

The area of the loop represents work per cycle or *oscillatory work*. If the loop rotates clockwise, the muscle absorbs oscillatory work from the oscillating lever system. If, however, the direction of the rotation is anti-clockwise, the muscle is doing oscillatory work on the lever system. Driven oscillations with *positive* oscillatory work are functionally equivalent to free oscillations against a particular load.

Another way of representing the data obtained from sinusoidal analysis is the *Nyquist plot*. The Nyquist plot is obtained in the following way. At a given frequency, the tension response has either positive or negative phase shift. This phase shift, ϕ , is transformed into the *phase angle*, θ , by the following equation:

$$\theta = 2\pi \frac{\phi}{T} \quad (2.1)$$

where T is the period of the applied oscillation. Then, a point is plotted on a graph at a distance from the origin equal to the amplitude of the tension and at an angle to the abscissa equal to the phase angle. The abscissa and ordinate of this graph now represent the *in-phase* and *quadrature* components, respectively. For one frequency, one point is plotted on the graph. There are many points on the graph corresponding to data at different frequencies. The resulting points are connected to give a complete Nyquist plot as shown in Figure 2.11C.

For convenience, the in-phase and quadrature components of tension are converted into *elastic* and *viscous moduli*, respectively:

$$E_e = \frac{\Delta F_e \cdot L}{A \cdot \Delta L} \quad (2.2a)$$

$$E_v = \frac{\Delta F_v \cdot L}{A \cdot \Delta L} \quad (2.2b)$$

where E_e and E_v are the elastic and viscous moduli, ΔF_e and ΔF_v are the in-phase and quadrature components of the tension response, L is the length of the muscle, ΔL is the amplitude of the length change, and A is the cross-sectional area of the muscle (Machin and Pringle, 1960). The Nyquist plot is now converted into a *vector modulus plot*. This representation is useful in comparing results from different muscles.

An example of the viscous modulus plot was obtained for insect flight

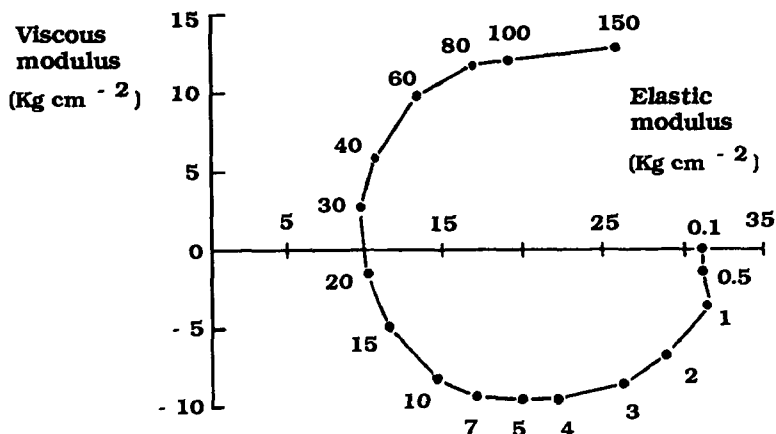


Figure 2.12 Vector modulus plot of glycerinated insect flight muscle. The amplitude of length change is $0.12\% L_0$, where L_0 is the initial fibre length before the length change. From Jewell and Rüegg (1966). Reprinted with permission of the Royal Society.

muscle by Jewell and Rüegg (1966). At relatively high frequencies (~ 30 – 150 Hz), the phase angle was positive; while at relatively low frequencies (~ 0.1 – 20 Hz) it was negative, which means that the muscle performed positive oscillatory work over the range of these frequencies (Fig. 2.12).

Another example was obtained for vertebrate muscle by Kawai and Brandt (1980). At high and low frequencies, the phase angle was positive; while over an intermediate range of frequencies it was negative (Fig. 2.13).

2.4.3 Length-step experiment

Besides the driven-oscillation experiment, Jewell and Rüegg (1966) also performed a quick-release and quick-stretch experiment. As shown in Figure 2.14, there is an initial rapid tension change (phase 1) in phase with a quick length change, followed by an immediate recovery phase (phase 2). The rate of recovery slows down and then reverses (phase 3). This is characterized by a delayed tension fall or *release de-activation* in response to a step decrease in length, and a delayed tension rise or *stretch activation* in response to a step increase of length.

Insect flight muscles occur in antagonistic pairs, so that contraction of one set of muscles stretches the antagonist, which in turn responds with stretch activation. Of course, as we have seen in Section 2.4.1, auto-oscillation appears even in a single set of the antagonistic muscles when connected to the resonant lever system. Nevertheless, by the alternate activation of these two sets of muscles, oscillations of high frequencies are maintained.

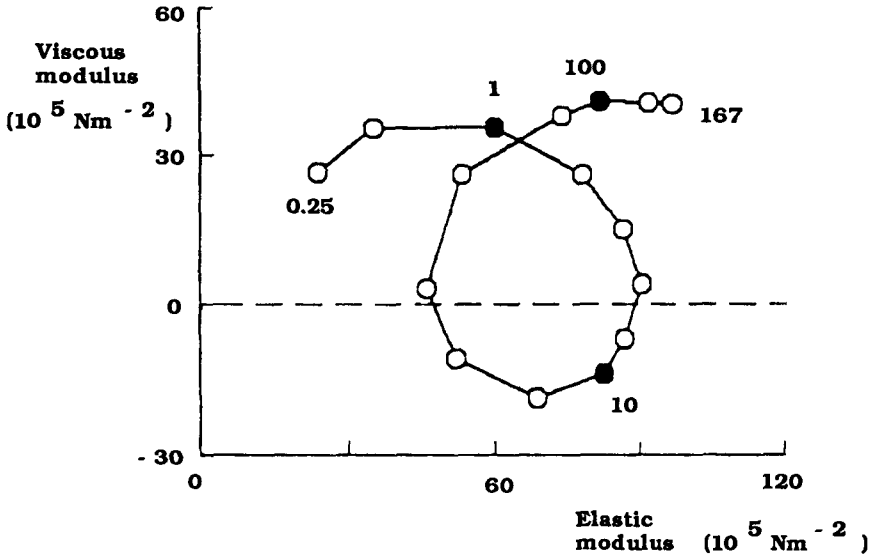


Figure 2.13 Vector modulus plot of glycerinated vertebrate muscle. For simplicity, some of the frequency points are omitted from the plots, and the filled symbols correspond to decade frequencies (1, 10, 100 Hz). The peak-to-peak amplitude of length change is $0.23\% L_0$, where L_0 is the initial fibre length before the length change. From Kawai and Brandt (1980). Reprinted with permission of Chapman & Hall.

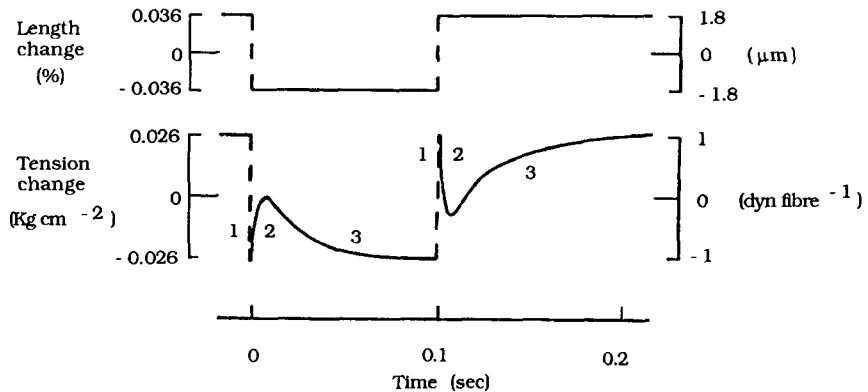


Figure 2.14 Tension transients following quick release and quick stretch of insect flight muscle. Upper panel shows a sequence of release and stretch. Lower panel shows the corresponding tension transients. The tension transients involve three phases: phase 1 is the immediate elastic response; phase 2 is the early tension recovery; and phase 3 is the delayed tension change. From Jewell and Rüegg (1966). Reprinted with permission of the Royal Society.

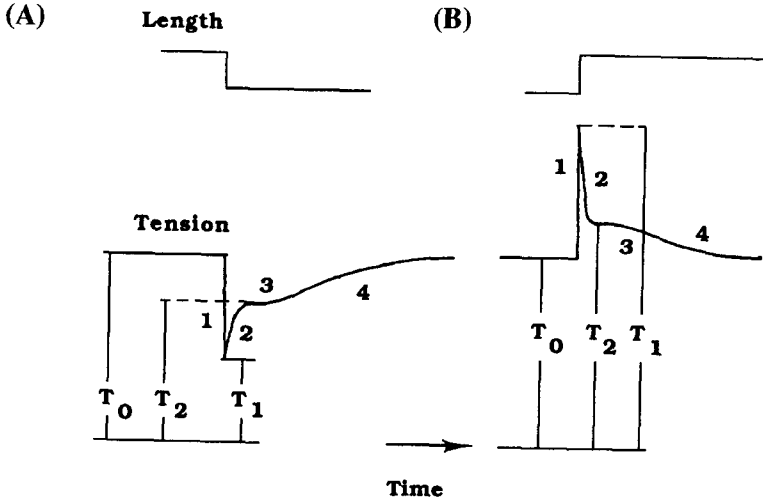


Figure 2.15 Schematic tension transients of skeletal muscle to quick release (in A) and quick stretch (in B). Four phases can be recognized: phase 1 occurs in phase with the change in length, which is ascribed to instantaneous elasticity; phase 2 is the quick recovery of tension; phase 3 is the delayed tension change; and phase 4 is the slow change in tension toward the isometric level. T_0 : isometric tension; T_1 : tension approached at the end of phase 1; and T_2 : tension approached at the end of phase 2. From Heinl *et al.* (1974). Reprinted with permission.

Tension responses to a length-step experiment on vertebrate muscle are schematically represented in Figure 2.15. The tension generated by muscle is called the *isometric tension* T_0 when it is neither shortening nor lengthening. Following the quick tension changes in phase with the quick length changes, three distinct phases (phases 2, 3 and 4) appear successively. The tension is designated T_1 and T_2 at the end of phases 1 and 2, respectively. Phase 3 corresponds to release de-activation (in Fig. 2.15A) or stretch activation (in Fig. 2.15B). While in insect flight muscles the delayed tension is large and functionally significant, in vertebrate muscles it is small and transient. This difference is ascribed to structural differences such as the presence of the C-filament.

It is important to clarify the correlation between the results of sinusoidal analysis and those of length-step analysis. Let us first consider a simple first-order rate process. The Nyquist plot produced by the first-order delay (or advance) becomes semicircular in shape, where the frequency at the lowest (or highest) point is referred to as the *characteristic frequency*. On the basis of a linear-response theory, the rate constant, r_e , of an exponential response in step analysis is related to the characteristic frequency, f_c , by the simple formula:

$$r_e = 2\pi f_c \tag{2.3}$$

(A)

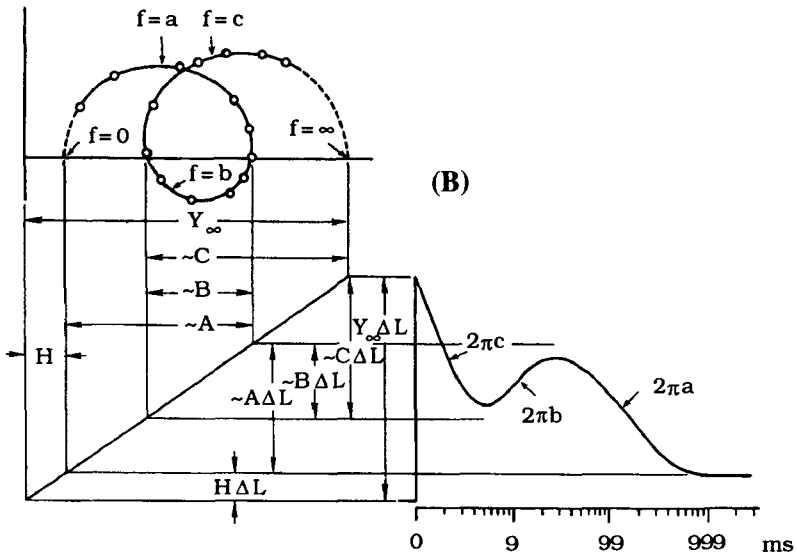


Figure 2.16 Correlation between sinusoidal and length-step analyses. (A): Typical form of a Nyquist plot which consists of three semicircular arcs. Characteristic frequencies, f , for each semicircle are a , b and c , respectively in order from small to large. (B): Tension time-course in response to step-length change. There are four phases in the tension transients. The rate constants of phases 2, 3 and 4 are $2\pi c$, $2\pi b$ and $2\pi a$, respectively. From Kawai and Brandt (1980). Reprinted with permission of Chapman & Hall.

where $2\pi f_c$ is its angular frequency. This formula combines the results of the step analysis with those of the sinusoidal analysis.

Now consider the Nyquist plot obtained from muscle. Generally, the plots are approximately composed of three semicircles, whose characteristic frequencies are quite different in the orders of their magnitudes. We can, therefore, consider that the dynamical response of muscle is approximated by three different first-order rate processes. Each phase appearing in the tension transients after the step-length change corresponds to each semicircle of the Nyquist plot (Fig. 2.16). Since insect flight muscle has no phase 4 in the tension transients (see Fig. 2.14), the related Nyquist plot consists of two semicircles (see Fig. 2.12). Consequently, the delayed tension change in the length-step experiment is related to the phase lag of tension on length in the sinusoidal experiment.

Results of the length-step experiment have been expressed by means of T_1 and T_2 curves as a function of a step change in length (Fig. 2.17A). T_1 is a linear function of the amplitude of stretch but departs from this linear function as the amplitude of release is increased. The slope of this T_1 curve

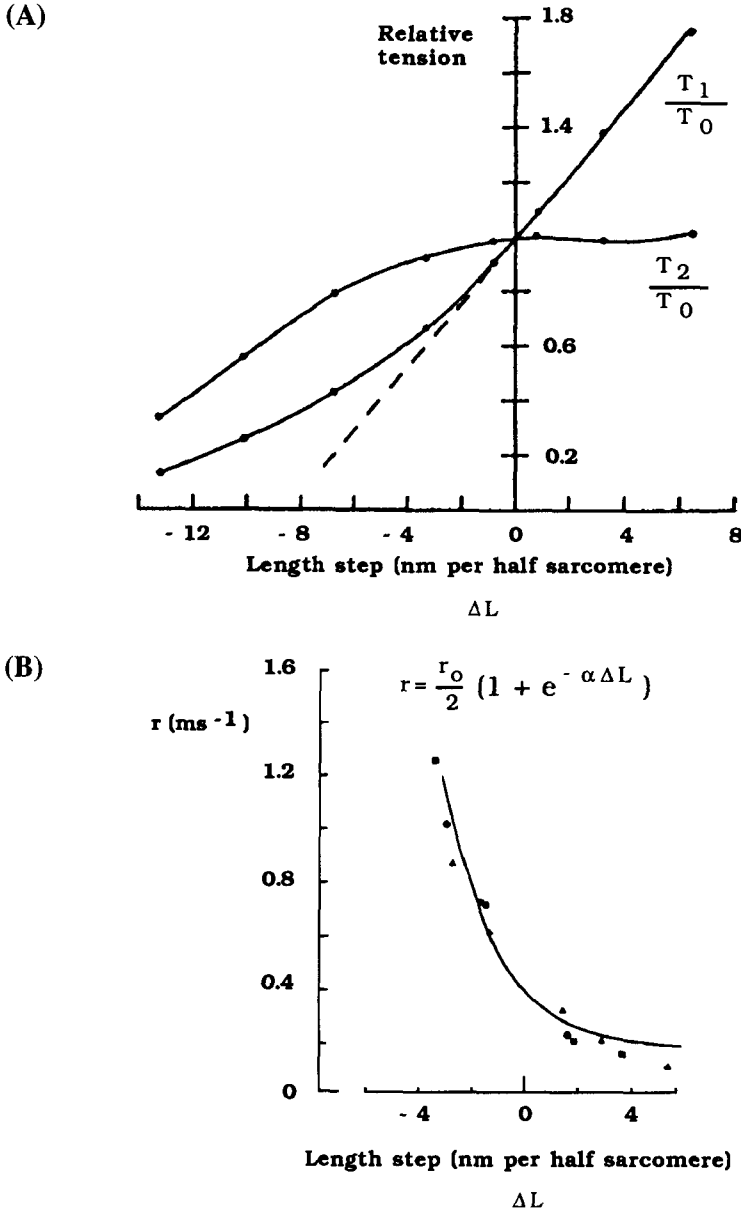


Figure 2.17 Analysis of length-step experiment on vertebrate muscle. (A): T_1 and T_2 values are plotted as a function of the step change in length. (B): Rate constant r of the immediate recovery phase (phase 2) as a function of the amplitude of the length step. The rate of tension recovery is much faster for releases than for stretches. Data from three experiments are plotted. The curve is $r = 0.2(1 + e^{-0.5\Delta L})$. From Huxley and Simmons (1971). Copyright © Macmillan Magazines Ltd. Reprinted with permission.

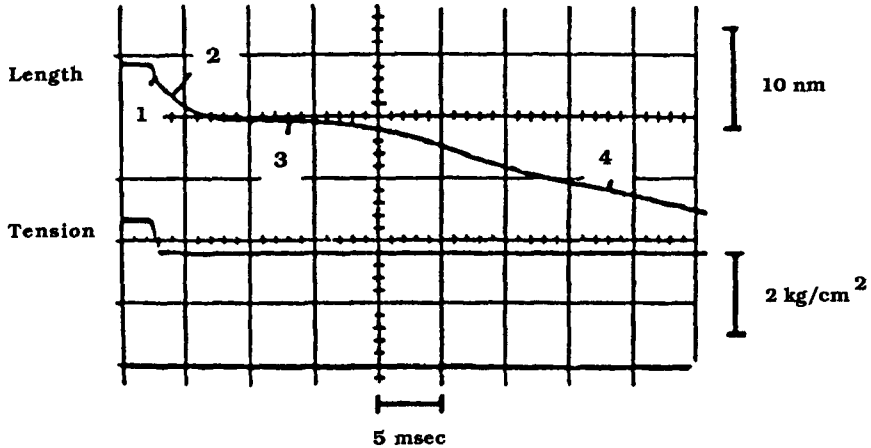


Figure 2.18 Tension-step experiment on single frog muscle fibre. The muscle starts to shorten (upper trace) when the load is suddenly reduced (lower trace). From Huxley (1974). Reprinted with permission.

(or simply the height of phase 1) is considered to be the stiffness of muscle, which in turn corresponds to the number of cross-bridges in the active or attached state. T_2 is an extremely nonlinear function, which is nearly flat in the region of small steps and decreases continuously with releases of moderate size.

Studying the rate constant r of the early tension recovery (phase 2) toward T_2 , Huxley and Simmons (1971) found that this phase occurs much more rapidly in releases than in stretches (Fig. 2.17B). This suggests that there must be an intrinsic *asymmetry* at the level of cross-bridge behaviour. And this provides useful information for developing a mathematical model, which is the subject of Chapter 3.

2.4.4 Tension-step experiment

When the load, which is balanced to the tension generated by the muscle, is suddenly released, the muscle begins to shorten against a constant load with initial transients, before the steady-state shortening. The tension generated by muscle when shortening or lengthening is called the *isotonic tension*. One example of the tension-step experiment on the vertebrate muscle is shown in Figure 2.18. Like the length-step experiment, there are four characteristic phases: in phase 1 there is simultaneous shortening, phase 2 is rapid early shortening, phase 3 is extreme reduction or even reversal of shortening speed, and phase 4 is shortening at a steady speed. Since insect flight muscles have the C-filament which interrupts the steady-state shortening, this kind of

experiment has not been extensively performed to determine properties of these muscles.

Although transients obtained from the tension-step experiment resemble those from the length-step experiment, these transients have not been conventionally expressed on a graph like the T_1 and T_2 curves. Instead, the steady-state shortening phase (phase 4) has been used to characterize the relationship between the load and steady-shortening velocity. The resulting relationship is roughly hyperbolic and is known as the force–velocity relation. This is written as follows (Hill, 1938):

$$(P + a)(V + b) = (P_0 + a)b \quad (2.4)$$

where P is the isotonic tension, V the shortening velocity, and P_0 the isometric tension. The asymptotes of this hyperbola are $P = -a$ and $V = -b$, but not $P = 0$ and $V = 0$. The maximal shortening velocity V_0 is defined as the velocity under no-load conditions as follows:

$$V_0 = \frac{bP_0}{a}. \quad (2.5)$$

The schematic representation of the Hill's force–velocity relationship is shown in Figure 2.19.

2.5 Advanced experiments on insect flight muscle

We have seen that the mechanical properties of muscle can be analysed by many types of experiments such as the driven-oscillation experiment and length-step experiment. It is now clear that the oscillatory capability of muscle can be ascribed to the positive oscillatory work that occurs when the driven-oscillation experiment is performed at particular frequencies, and also ascribed to the stretch activation which appears in the length-step experiment. Although some of these experimental results are simply expressed on graphs, the underlying molecular mechanism is still unclear. This section deals with two other experiments which provide us with an important insight into the basic oscillatory mechanism.

2.5.1 Oscillation-induced ATPase

Steiger and Rüegg (1969) measured the dependence of oscillatory power (i.e. oscillatory work \times frequency) and extra ATPase activity (ATPase activity in excess of that obtained in the absence of oscillation) upon the frequency for applied sinusoidal length oscillations of large peak-to-peak amplitudes (e.g. 2.5% of the fibre length).

At a low Ca^{2+} concentration (10^{-6}M), there is a close correlation between the power output and the extra ATPase activity over a wide range of

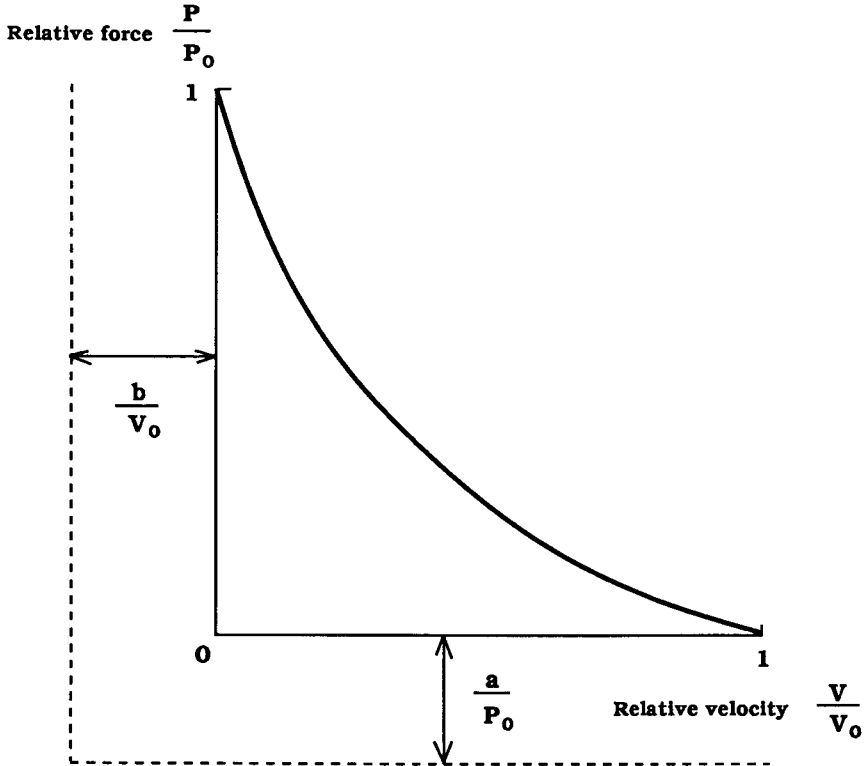
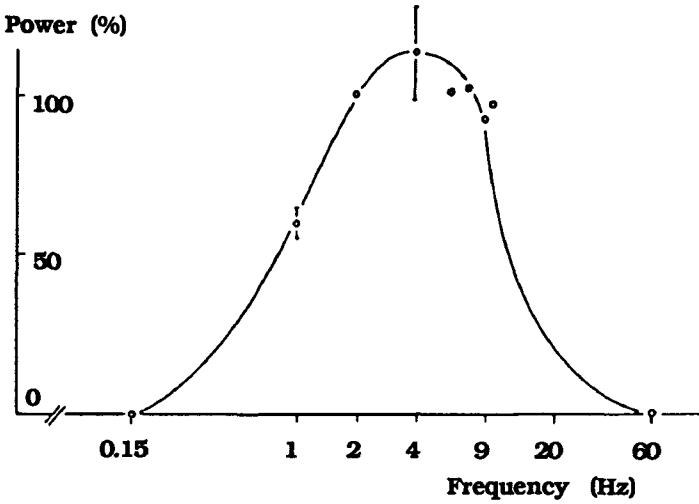


Figure 2.19 The force–velocity curve. P_0 is the isometric tension generated by muscle when its length is held constant. V_0 is the maximal shortening velocity of muscle when there is no load. Relative force, P/P_0 , is plotted against relative velocity, V/V_0 . The asymptotes for the hyperbola are represented by broken lines.

frequencies (Fig. 2.20). Suppose that both power output and extra ATPase activity depend on the rate of actin–myosin interaction. The frequency dependence of the power output and the extra ATPase activity reflects the frequency dependence of actin–myosin interaction rates. As the rate of filament sliding is increased, actin sites slide past to interact with myosin sites more frequently. This results in an increase in the power output and extra ATPase activity. However, if the oscillatory frequency exceeds the optimal value, there is not sufficient time for the actin–myosin interaction to take place. As a result, both power and ATPase activity decrease. The parallel correlation between the power and ATPase activity indicates a ‘tight’ coupling of chemo-mechanical energy conversion.

By contrast, at a high Ca^{2+} concentration (10^{-5}M), the optimal frequencies of the power and ATPase activity differ (Fig. 2.21). This suggests a less ‘tight’ chemo-mechanical coupling. In either case, however, the presence of

(A)



(B)

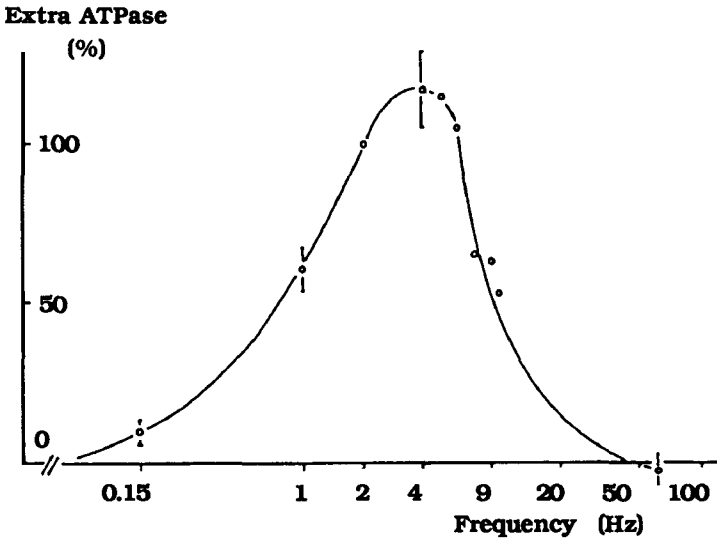


Figure 2.20 Frequency dependence of power output and extra ATPase activity at a low Ca^{2+} concentration. The oscillatory power (in A) and oscillation-induced extra ATPase activity (in B) are represented as a percentage of the power and the extra ATPase activity at the reference frequency 2 Hz. From Steiger and Rüegg (1969). Reprinted with permission of Springer Verlag.

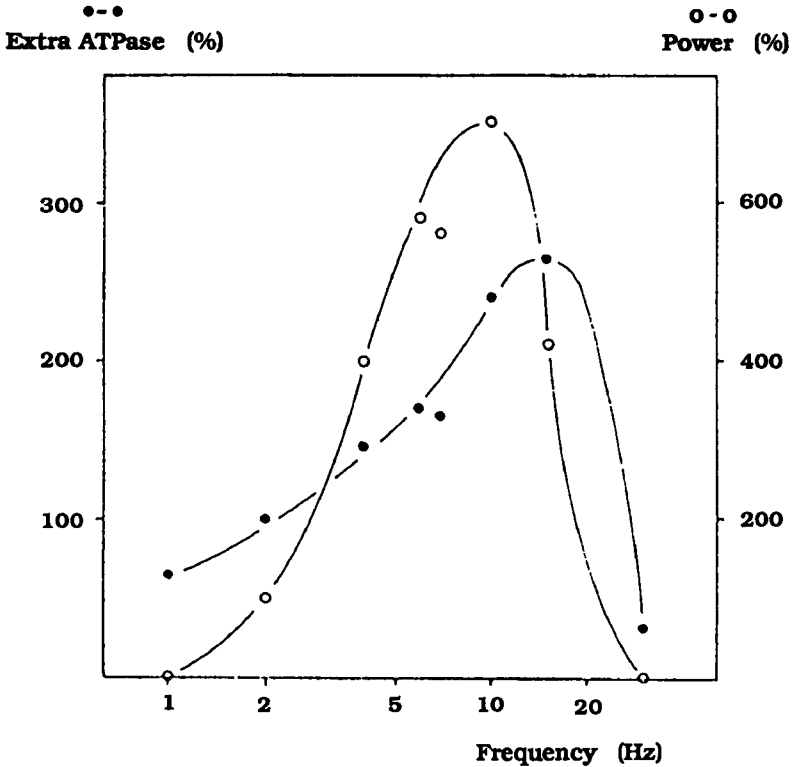


Figure 2.21 Frequency dependence of power output and extra ATPase activity at a high Ca^{2+} concentration. The oscillatory power (○-○) and oscillation-induced extra ATPase activity (●-●) are represented as a percentage of the power and the extra ATPase activity at the reference frequency 2 Hz. From Steiger and Rüegg (1969). Reprinted with permission of Springer Verlag.

optimal frequency probably occurs because of a considerable degree of cross-bridge synchronization (Pringle, 1978).

2.5.2 Double length-step experiment

Stiffness measurements provide useful information about cross-bridge dynamics because stiffness is considered to be proportional to the number of attached cross-bridges (Huxley and Simmons, 1971). The immediate elastic responses, ΔT ($= T_1 - T_0$), obtained in phase with the quick length change, ΔL , are related to stiffness, S , according to the following equation:

$$S = \frac{\Delta T}{\Delta L} \times L_0 \quad (2.6)$$

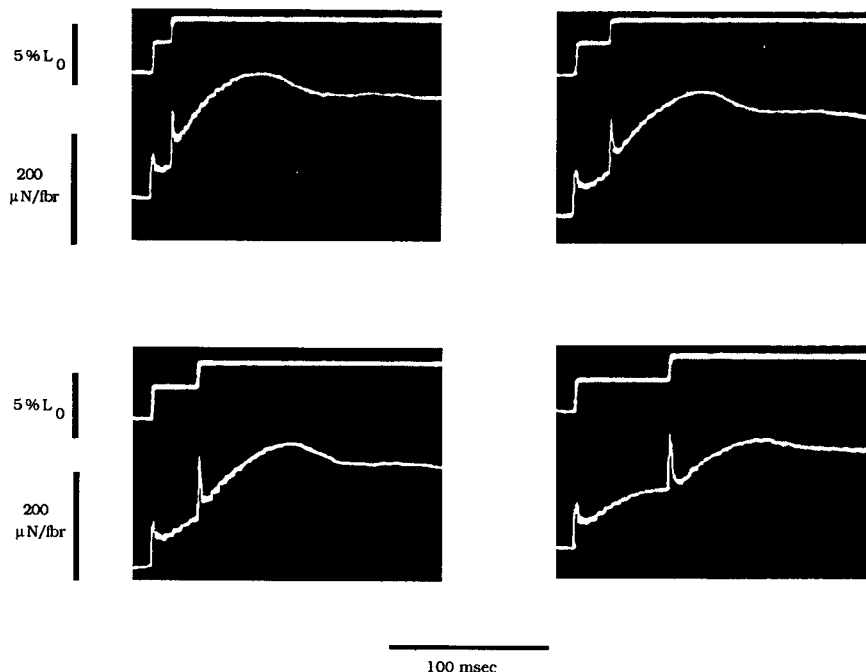


Figure 2.22 Stiffness measurements at various moments during stretch activation (Double length-step experiment). The first length-step is $3\% L_0$, where L_0 is the initial fibre length before the length change. Following this quick stretch, tension transients appear. At a certain moment, the second length-step is applied as a test to measure the stiffness. This corresponds to the peak height of the quick tension change in phase with the quick stretch. Note that this peak height remains constant during the delayed tension development. From Herzig (1977). Reprinted with permission of Elsevier Science Publishers.

where L_0 is the initial fibre length before the length change (Herzig, 1977). Equivalently, stiffness is defined as the slope of the T_1 curve which is a function of the length-step (see Fig. 2.17).

Since the delayed tension change (e.g. stretch activation and release deactivation) following the quick length change is highly responsible for the oscillatory capability of muscle, stiffness measurements during this delayed phase in tension are worth studying. For this purpose, a double length-step experiment was performed, in which the first length-step was applied to induce tension transients during which the second length-step was used to measure the stiffness (Fig. 2.22).

Herzig (1977) examined the time-course of stiffness in detail and concluded that changes in stiffness depend on the amplitude of the first length-step. In response to a quick stretch of less than $1\% L_0$, the delayed tension development is associated with a parallel increase in stiffness (Fig. 2.23A). For a

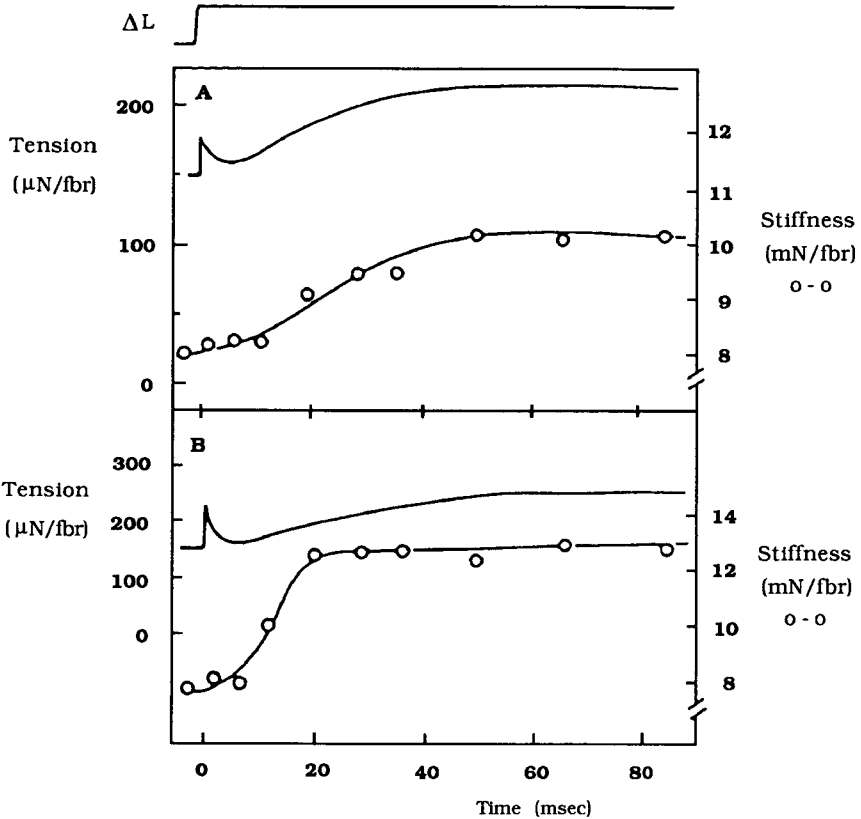


Figure 2.23 Time-course of tension and stiffness. (A): The delayed rise of tension (upper curve) in response to a quick stretch of $0.5\% L_0$ (L_0 : the initial fibre length before the length change) is parallel with the increase in stiffness ($\circ-\circ$). (B): When the size of the quick stretch is $1.5\% L_0$, stiffness ($\circ-\circ$) reaches a plateau immediately after the onset of the delayed tension rise (upper curve). From Herzig (1977). Reprinted with permission of Elsevier Science Publishers.

quick stretch of more than $1\% L_0$, stiffness reaches a plateau phase immediately after the onset of delayed tension development (Fig. 2.23B).

These results suggest an important feature of the cross-bridge behaviour. If there is only one attached or force-generating state for a cross-bridge, the increase in tension is caused by the increase in the fraction of cross-bridges attached. If this is the case, the increase in tension must always be parallel with the increase in stiffness as shown in Figure 2.23A. However, depending on the initial length-step, tension develops even after stiffness reaches its plateau phase (see Fig. 2.23B). This can only be explained if there are two different attached states: a force-generating state and a non-force-generating state. After the large length-step, the fraction of cross-bridges in the non-

force-generating state begins to increase, which causes the increase in stiffness but does not result in tension development. When the transition of these cross-bridges synchronously occurs to the force-generating state, tension develops at the plateau phase of stiffness as shown in Figure 2.23B.

Consequently, at least two mechanically distinguishable states of attached cross-bridges are present during contraction. The critical length-step ($1\% L_0$) may reflect the range of motion of the attached cross-bridges.

Notes

- 1 Since myofibrils are not easily recognized in synchronous muscle, though they are present, it is referred to as *afibrillar* muscle.
- 2 In contrast to synchronous muscle, asynchronous muscle contains easily distinguishable myofibrils so that it is referred to as *fibrillar* muscle.

3 Models for muscle contraction

Many models have been proposed to account for the experimental observations since the A. F. Huxley (1957) model. This chapter discusses some of them. In Section 3.1 the essence of Huxley's two-state model is described. This model mimics the force–velocity curve observed in vertebrate muscle when it is shortening, but does not account for muscle lengthening.

There are two distinct ways to modify this model. One way is to modify it in order to demonstrate oscillatory contraction typical in insect flight muscle, which is discussed in Section 3.2. The other way is to modify the two-state model so that it matches other dynamical properties such as the lengthening region of the force–velocity curve and many transients, in response to length- or tension-step changes. After a further slight change in this modified two-state model, it produces oscillatory behaviour as discussed in Section 3.3.

Despite the attempts to explain all of the mechanical properties of muscle, it turns out that no two-state model can successfully demonstrate these properties. The two-state model is, therefore, replaced by the three-state model. Section 3.4 shows that nearly all the important experimental data are clearly demonstrated by the three-state model. The stretch activation (i.e. the delayed tension development that follows a quick stretch of muscle length) is interpreted in terms of the three-state model in Section 3.5. Section 3.6 provides a simplified model which accounts for the typical dynamical properties of muscle, and then discusses the similarity between the muscle system and the nerve system based on this simplified model.

3.1 The Huxley (1957) two-state model

To explain steady-state muscle contraction, A. F. Huxley (1957) proposed the two-state model (Fig. 3.1). The essential features of this model are summarized as follows:¹

- (i) The cross-bridge dynamics within the half-sarcomere are considered.
- (ii) The sliding coordinate x is defined as the distance of an attachment site on a thin filament from a reference point on a thick filament. Note that increasing x corresponds to release.
- (iii) All the cross-bridges in the half-sarcomere are distributed uniformly (or homogeneously) over the x values (Fig. 3.1D).
- (iv) These cross-bridges are either in the *attached* or *detached* state, depending on the sliding coordinate x (Figs. 3.1A and C).
- (v) The cross-bridges cannot reach out a distance greater than h to make attachment.
- (vi) An active force, $F(x)$, generated by an attached cross-bridge is given by

$$F(x) = -kx \quad (3.1)$$

where k is the ‘spring constant’ of the cross-bridge. Its potential-energy function, $U(x)$, is obtained by the integration of equation (3.1) with respect to x (Fig. 3.1B):

$$U(x) = \frac{k}{2} x^2. \quad (3.2)$$

- (vii) Attachment and detachment of these cross-bridges are represented by a first-order kinetic equation:

$$\frac{dn(x)}{dt} = [1 - n(x)]f(x) - n(x)g(x) \quad (3.3)$$

where $n(x)$ is the fraction of attached cross-bridges, and $f(x)$ and $g(x)$ are the rate constants between the two states (Fig. 3.1A). These rate constants depend only on x . They are asymmetric about $x = 0$: the attachment rate constant is zero in the negative-force generating region $x > 0$, and it exceeds the detachment rate constant in the region $-h < x < 0$. This asymmetry guarantees that the cross-bridges tend to attach in the positive force region, and hence the contraction of muscle (Figs. 3.1C and D).

- (viii) The force–velocity relationship is obtained in the following way. First, the total derivative in equation (3.3) is expanded by the chain rule to become:

$$\frac{dn}{dt} = \frac{\partial n}{\partial t} + \frac{\partial x}{\partial t} \frac{\partial n}{\partial x}. \quad (3.4)$$

Now we assume that $\partial n / \partial t = 0$ and $\partial x / \partial t = V$ (sliding velocity) under the steady-state conditions. Substituting equation (3.4) into equation (3.3) under these conditions, we solve a cross-bridge distribution, $n(x)$, for a given sliding velocity, V . At any time, if $n(x)$ is known, the force produced by all the attached cross-bridges in the half-sarcomere is:

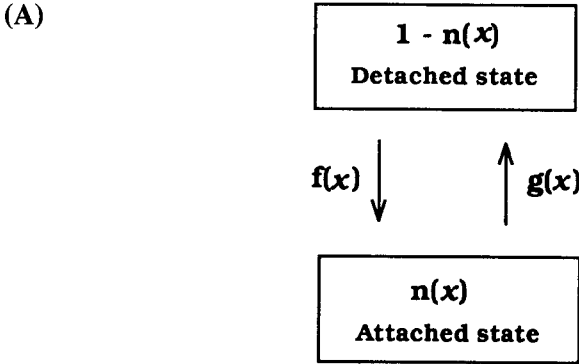
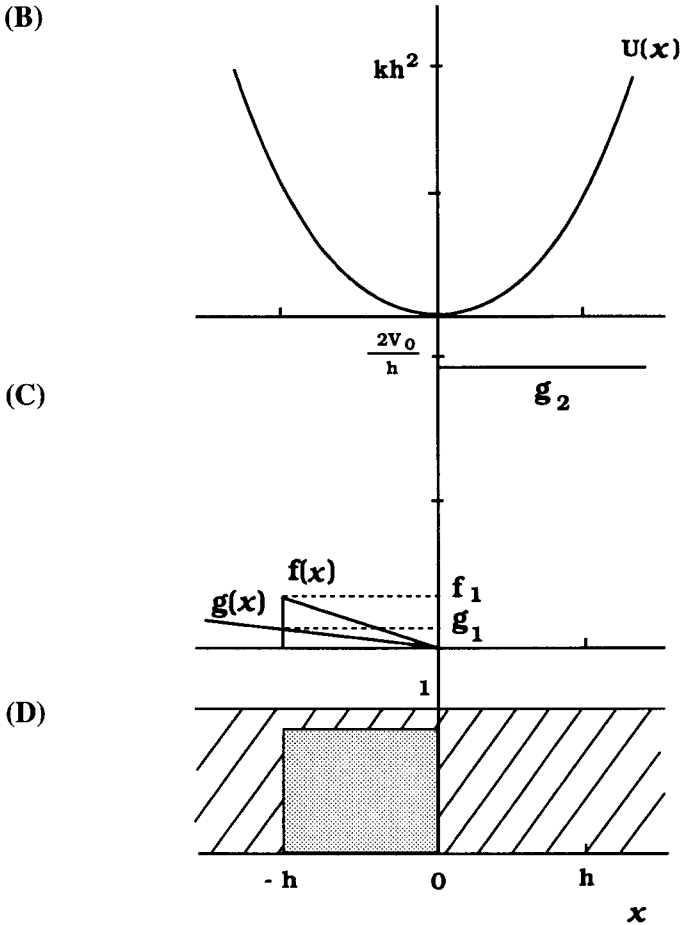


Figure 3.1 A. F. Huxley (1957) two-state model. (A): There are two states: a detached and an attached state, whose fractions are represented by $1 - n(x)$ and $n(x)$, respectively. $f(x)$ and $g(x)$ denote the attachment and detachment rate constants, respectively. (B): Potential-energy function, $U(x)$. A cross-bridge in the region $x < 0$ produces a positive force, whereas that in the other region $x > 0$ generates a negative one. (C): Rate constants for attachment and detachment which are not symmetric about $x = 0$. Now f_1 , g_1 and g_2 are the constants, which are defined by $f_1 = f(h)$, $g_1 = g(h)$ and $g_2 = 3.919(f_1 + g_1)$, and h is the maximum value of x where attachment is permitted during shortening. (D): The cross-bridges are uniformly distributed over all of the x values as shown by the striped region. The distribution of the attached cross-bridges (indicated by a dark rectangle) is positioned in the region $-h \leq x \leq 0$ under the isometric conditions. Note that the increase in x corresponds to release. This correspondence is retained throughout this book, although it was the reverse in the original paper.

$$P = \int_{-\infty}^{\infty} F(x)n(x)dx. \quad (3.5)$$

Figure 3.2 shows the force-velocity relationship obtained by the Huxley model (broken curve) compared with the result obtained in experiments (solid curve).

- (ix) Although the Huxley model was developed in order to account for the steady-state muscle contraction, it is interesting to examine the dynamic properties in response to step-length changes. Under isometric conditions, the steady-state attached cross-bridge distribution is shown at $t = 0$ in Figure 3.3A. Instantaneous stretch of ΔL makes it shift by $x = -\Delta L$ at $t = t_1$, because the lengthening process is so fast that the transition between the attached and detached states is not allowed at this instant. Since the force generated by the attached cross-bridge is proportional to x as defined by equation (3.1), this step stretch causes a spontaneous increase in tension (see the right-hand panel of Fig. 3.3B) Subsequent changes in the distribution occur in two different regions at $t = t_2$: one for region 1 ($-h - \Delta L < x < -h$) and the other for region 2 ($-\Delta L < x < 0$).



From equation (3.1), the tension decrease in region 1 is much larger than the increase in tension in region 2 (see the left panel of Fig. 3.3B). Thus, total tension, obtained by the sum of the two tension changes, always decreases in a monotonic fashion. Consequently, the Huxley two-state model cannot demonstrate the stretch activation or the delayed tension development in its original form.

3.2 Models for stretch activation

Julian (1969) modified the Huxley model such that the resultant model gave rise to a delayed tension change as observed in insect flight muscle. For this purpose, an activation factor, r ($0 \leq r \leq 1$), is introduced to the attachment rate constant $f(x)$ as a regulatory feedback system via Ca^{2+} binding. The

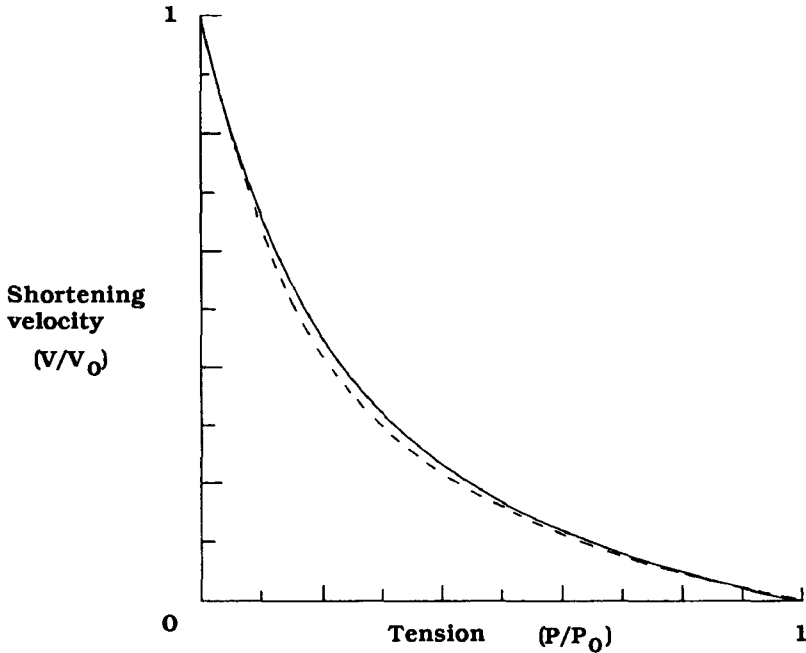


Figure 3.2 Force-velocity relationship. The broken curve shows the result of the Huxley model. The solid curve shows the result of experiments. From A. F. Huxley (1957). Reprinted with permission.

product $rf(x)$ becomes the net rate constant for attachment. In order to account for stretch activation, r is initially reduced such that the steady-state attached cross-bridge distribution under isometric conditions is reduced from that of the Huxley model. Suppose that r is sensitive to length change, and r is increased up to 1 after stretch with a delay, then a large number of cross-bridges begin to attach with a delay.²

After this modification, the model accounts for stretch activation as schematically illustrated in Figure 3.4B. With the step increase in length at $t = t_1$, the attached cross-bridge distribution, n , is shifted to regions where the force generated by the attached cross-bridges is large. This leads to a spontaneous increase in tension, as in the original Huxley model. In region 1 where the detachment rate constant is large, a rapid decay of n occurs which results in a quick fall in tension at $t = t_2$. Since the amount of tension increase caused by the new attachment of cross-bridges in region 2 is larger than that of tension decrease in region 1, a delayed tension development appears following the increase in $rf(x)$.

In the Julian model, r was assumed to be sensitive to length change, while $f(x)$ was constant. Alternatively, it is possible that r could be constant and

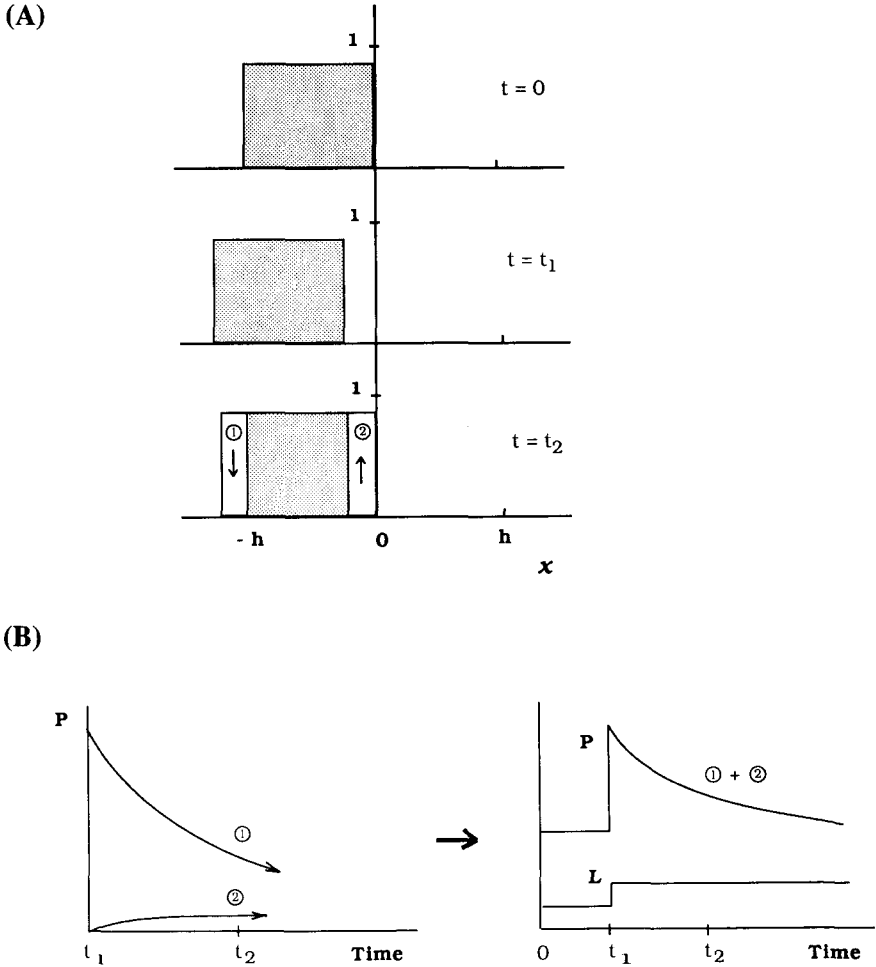
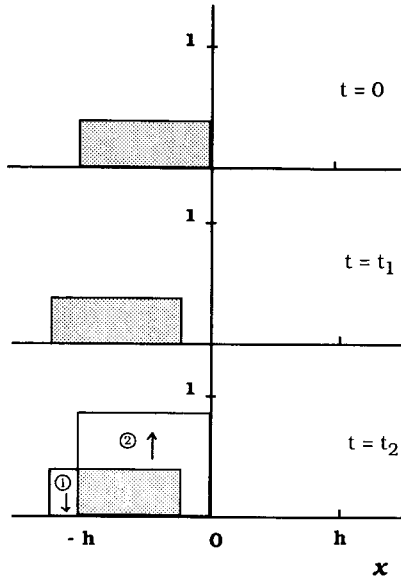


Figure 3.3 Transients in response to a step-length change predicted by the Huxley model. (A): The distribution of attached cross-bridges as a function of x . The top panel: the distribution under isometric steady-state conditions at $t = 0$. The middle panel: the distribution shifted by $-\Delta L$ at $t = t_1$. The bottom panel: the distribution at $t = t_2$, when the detachment (in region 1) and attachment (in region 2) occur. (B): Tension transients as a function of time. The left panel: the tension decreases significantly due to the detachment of cross-bridges in region 1, while the increase in tension caused by the attachment in region 2 is not so large. The right panel: the total tension shows a monotonic decrease as time proceeds.

(A)



(B)

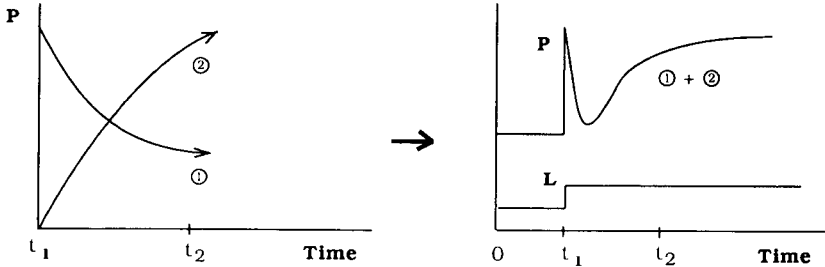


Figure 3.4 Transients in response to a step-length change predicted by the Julian model. (A): The distribution of attached cross-bridges as a function of x . The top panel: the distribution under isometric steady-state conditions at $t = 0$. Since the net attachment rate constant is initially reduced, the distribution is smaller than that of the Huxley model (see Fig. 3.3). The middle panel: the distribution shifted by $-\Delta L$ at $t = t_1$. The bottom panel: the distribution at $t = t_2$, when the detachment (in region 1) and attachment (in region 2) occur. (B): Tension transients as a function of time. The left panel: the tension decreases due to the detachment of cross-bridges in region 1. The increase in tension caused by the attachment in region 2 is very large because a large number of cross-bridges begin to attach under 'full' activation. The right panel: the total tension shows a stretch activation.

$f(x)$ a length-dependent variable. A simple version of this model was proposed by Thorson and White (1969), White and Thorson (1972), and Abbott (1973). The essence of their models is as follows.

- (i) As illustrated in Figure 3.5A, the attachment rate constant, $f(x)$, is influenced by length changes via *strain* of the filaments or *displacement* between the filaments (see Thorson and White, 1983).
- (ii) The rate constants are chosen so that the attached cross-bridges are located at $x = x_0$ under steady-state conditions at $t = 0$. For example, $f(x)$ is positive only at $x = x_0$, while $g(x)$ is constant everywhere. Then the steady-state distribution of attached cross-bridges is positioned at $x = x_0$ as shown in the top panel of Figure 3.5B
- (iii) Similarly to the previous models, step-length changes shift the attached cross-bridge distribution at $t = t_1$. This leads to an instantaneous increase in tension. The rapid fall in tension is caused by detachment in region 1, which is followed by the delayed tension development induced by re-adjustment of attached cross-bridges in region 2.

Consequently, in these models, the critical delay in tension is actually the delay in the re-adjustment of the fraction of attached cross-bridges caused by the change in the rate constant.

It is very useful to derive a phenomenological equation which describes the stretch activation. For simplicity, let us assume the following conditions:

$$\Delta P = Q\Delta n \quad (3.6a)$$

$$f = f_0 + R\Delta L \quad (3.6b)$$

$$g \gg f. \quad (3.6c)$$

Equation (3.6a) shows that the increase in tension, ΔP , is proportional to the fraction of extra attached cross-bridges, Δn . Equation (3.6b) is a possible expression for a length change, ΔL , influencing the attachment rate constant, f , where f_0 is the attachment rate constant in the absence of length change. Equation (3.6c) accounts for the condition where the detachment rate, g , is much larger than the attachment rate, f . Both Q and R are constants. We ignore the x -dependence of f , g and n .

Substituting equations (3.6a, b) into equation (3.3), we obtain the following equation:

$$\frac{d\Delta P}{dt} = \frac{1}{\tau}(G\Delta L - \Delta P) \quad (3.7)$$

where τ ($\approx g^{-1}$) is the relaxation time for the stretch activation and $G = QR/g$. Here we ignore the contribution from f in the second term on the right-hand side of equation (3.3) because of condition (3.6c). Equation (3.7) describes the first-order delay of tension change, following the step-length change, with a time constant, τ .

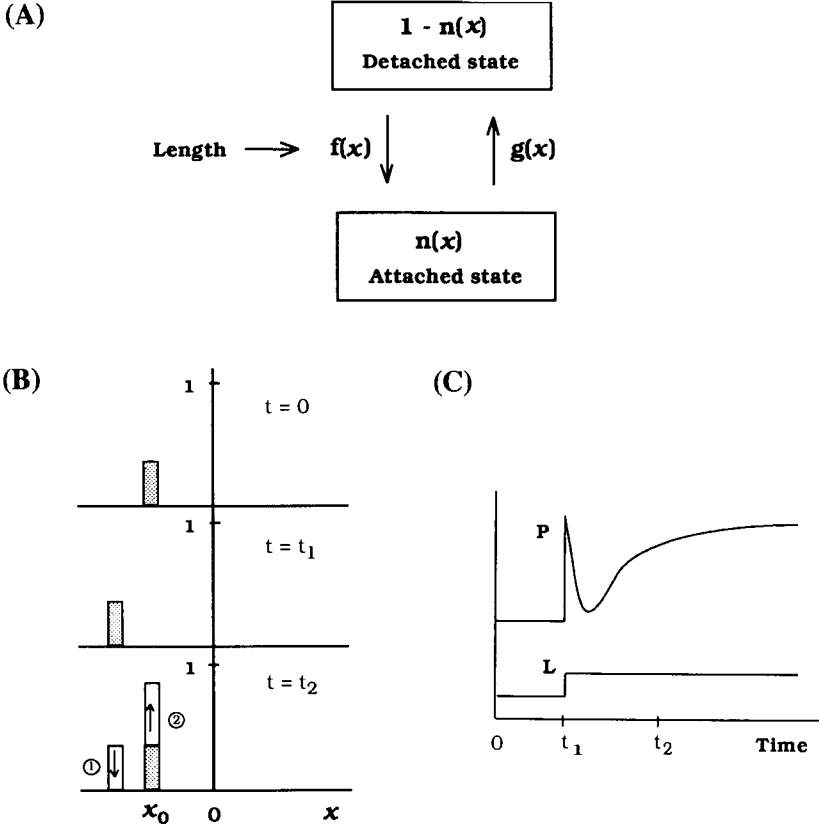


Figure 3.5 The modified two-state model. (A): There are two states: a detached and an attached state, whose fractions are represented by $1 - n(x)$ and $n(x)$, respectively. $f(x)$ and $g(x)$ denote the attachment and detachment rate constants, respectively. $f(x)$ is assumed to be perturbed by the length of muscle. (B): The distribution of attached cross-bridges as a function of x . The top panel: the distribution under isometric steady-state conditions at $t = 0$. Since $f(x)$ is positive only at $x = x_0$, the distribution is localized. The middle panel: the distribution shifted by $-\Delta L$ at $t = t_1$. The bottom panel: the distribution at $t = t_2$, when the detachment (in region 1) and attachment (in region 2) occur. (C): Tension transients as a function of time. As in the Julian model, a stretch activation is observed.

If we consider the tension, P , and the fraction of attached cross-bridges, n , instead of their increments, equation (3.6a) is replaced by

$$P = Qn. \quad (3.6a')$$

In this case, equation (3.7) is replaced by

$$\frac{dP}{dt} = \frac{1}{\tau}(P_0 + G\Delta L - P) \quad (3.7')$$

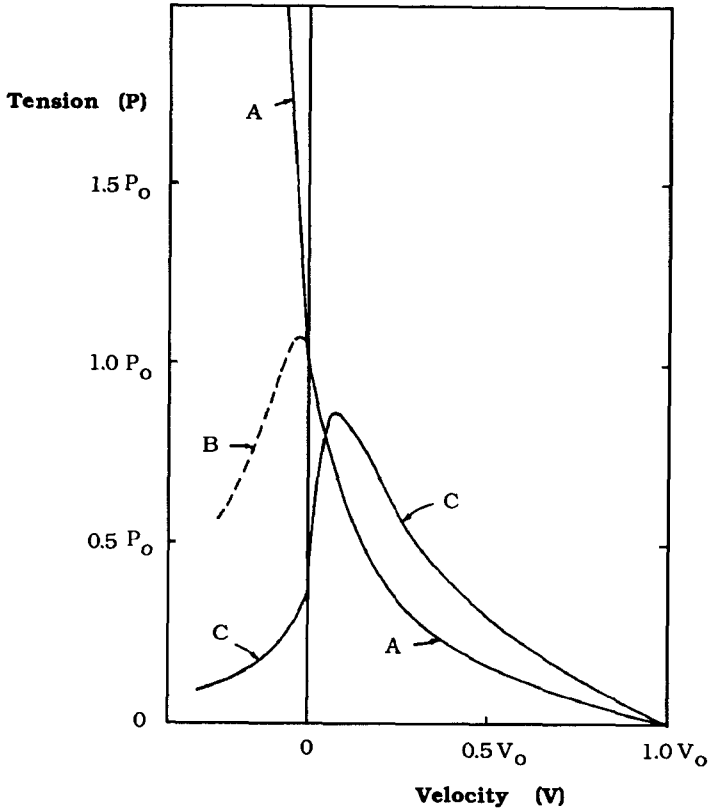


Figure 3.6 Force-velocity relationship of cross-bridge models. Curve A is the relationship of the Huxley (1957) model. Curve B is an relationship of the modified Huxley model which contains the inverse attachment rate, $f'(x)$, as shown in Fig. 3.7A. Curve C is the relationship of the Brokaw (1975) model with rate constants shown in Fig. 3.8A. P_0 is the isometric tension. V_0 is the maximal shortening velocity. From Brokaw (1975). Reprinted with permission.

where P_0 is the isometric steady-state tension at $\Delta L = 0$.

Although equation (3.7) or (3.7') clearly describes how the length change has a delayed influence on the tension, the underlying molecular mechanism is still unclear. Furthermore, we do not know any direct evidence which supports the assumption that length perturbs the rate constants. An alternative interpretation of the stretch activation was proposed by Brokaw (1975; 1976) in order to model the oscillatory behaviour in muscle and flagella. The next section discusses this class of model.

3.3 The two-state models with reverse rate constants

The Huxley model only produced the force-velocity curve in accordance with experimental observation of shortening (curve A in Fig. 3.6). For stretching,

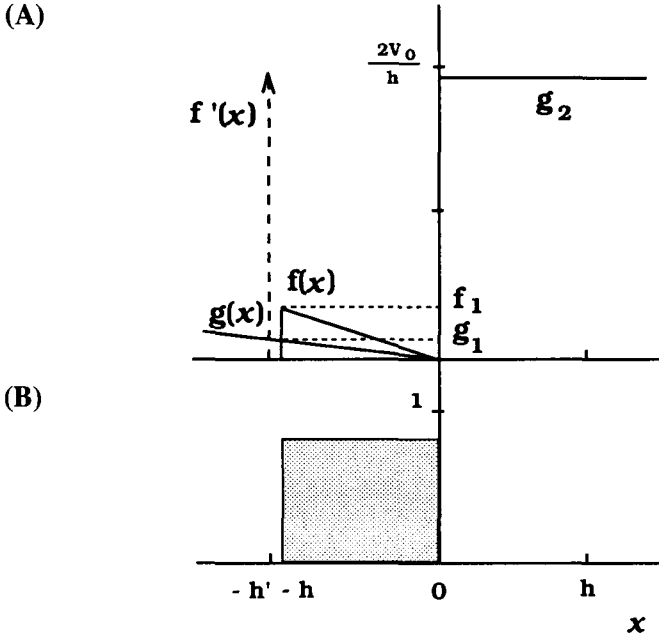


Figure 3.7 The modified Huxley model. (A): The rate functions are the same as those of the Huxley (1957) model except that there is an inverse attachment rate, $f'(x)$. This causes rapid breakage of cross-bridges, when they exceed $-h'$. (B): The distribution of steady-state attached cross-bridges under isometric conditions.

the force calculated by this model increases monotonically with velocity, while experimental data show that its changes are bi-phasic: there is a critical stretching velocity below which the tension is monotonically increased, and above which it is decreased.

This inconsistency was partially removed in the two-state model when the *reverse* rate constants were introduced to the model (Brokaw, 1975). Within the framework of cross-bridge dynamics developed by T. L. Hill and colleagues (1974; 1975), the forms of the reverse attachment rate, $f'(x)$, and the reverse detachment rate, $g'(x)$, are *self-consistently* determined once $F(x)$, $f(x)$, and $g(x)$ are specified. Here we emphasize the effects of $f'(x)$ on the force–velocity curve.

As suggested by Huxley (1957), the more realistic force–velocity curve might be demonstrated by a two-state model when the reversal of the attachment reaction is taken into account during the stretch. Brokaw (1975) introduced $f'(x)$ into the original Huxley model, as shown in Figure 3.7. This model, demonstrated a new force–velocity curve (curve B in Fig. 3.6). Although the peak of the tension during stretch is much smaller than that of

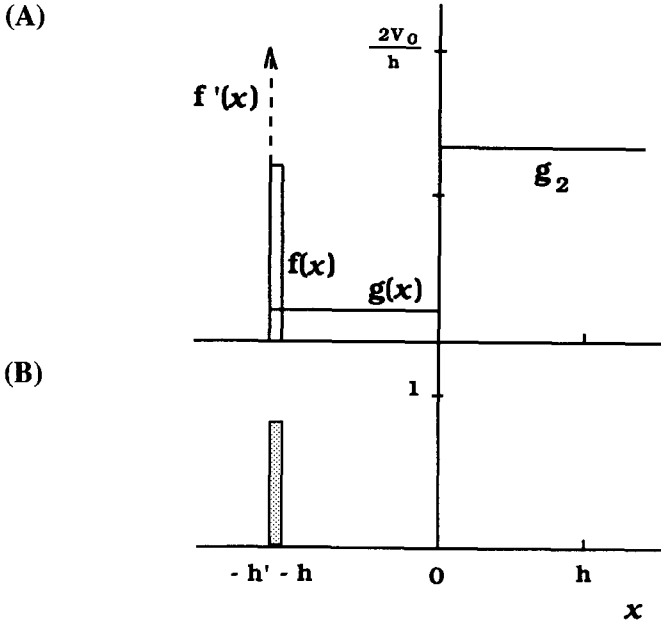


Figure 3.8 The Brokaw (1975) model. (A): $f'(x)$ is incorporated into the Brokaw model in the same way as in the modified Huxley model (see Fig. 3.7). $f(x)$ is positive only in a narrow region. (B): Due to the localized $f(x)$, the distribution of steady-state attached cross-bridges is localized.

the experimental observation, this modification would be the first step in developing a model for self-oscillations.

Brokaw specified the rate constants of the two-state model in such a way that the force-velocity curve had its peak during shortening, but not during stretching (curve C in Fig. 3.6). Figure 3.8A shows a set of rate constants. Since $f(x)$ is positive only in a narrow region, $-h' < x < -h$, the steady-state attached cross-bridge distribution under isometric conditions is localized in that region (Fig. 3.8B).

Now consider what happens in response to step-length changes (Fig. 3.9). Similarly to the previous model behaviour, a step stretch shifts the attached cross-bridge distribution in the direction of decreasing x at $t = t_1$. Now $f'(x)$ is so large that spontaneous detachment occurs, which causes a rapid tension drop at that time. Brokaw called this 'stretch de-activation'. Then detached cross-bridges begin to attach and thus tension is monotonically developed toward the initial level.

As a model of an antagonistic set of muscles, such as insect flight muscles, Brokaw combined two cross-bridge systems with the above properties. The resulting antagonistic pair of cross-bridges gave rise to the net steady-state

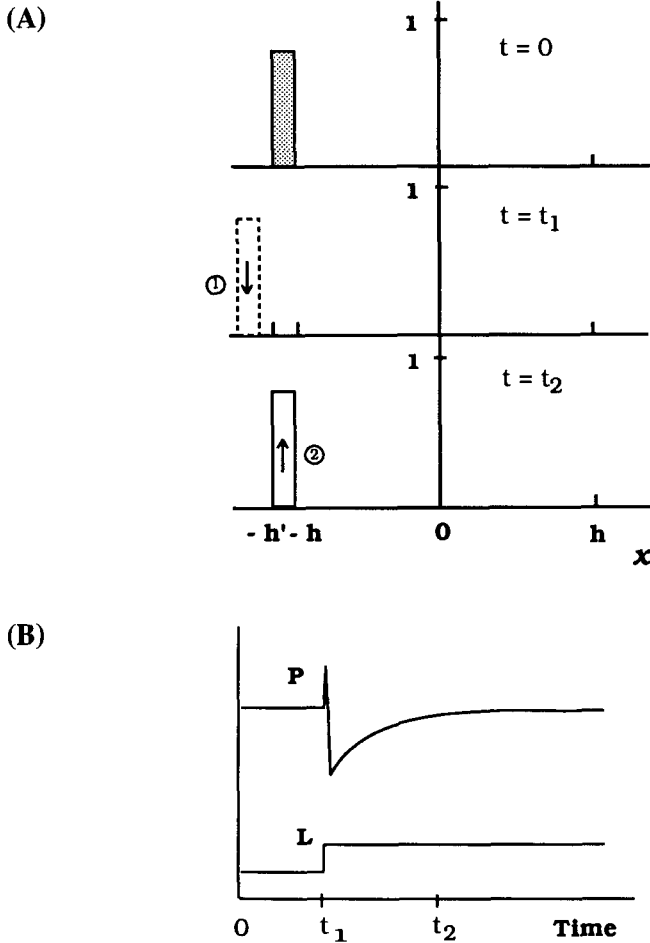


Figure 3.9 Transients in response to a step-length change predicted by the Brokaw model. (A): The distribution of attached cross-bridges as a function of x . The top panel: the distribution under the isometric steady-state conditions at $t = 0$. The middle panel: the distribution shifted by $-\Delta L$ at $t = t_1$. Spontaneous breakage of cross-bridges occur due to $f'(x)$. The bottom panel: the distribution at $t = t_2$. Attachment occurs (in region 2). (B): Tension transients as a function of time. The total tension reverts to its original tension.

force-velocity curve as shown in Figure 3.10A.³ Here the net force, P_a , is given by

$$P_a = P(V) - P(-V). \quad (3.8)$$

In order to investigate whether this force-generating system is capable of demonstrating oscillatory motion, the system was connected to an appropriate

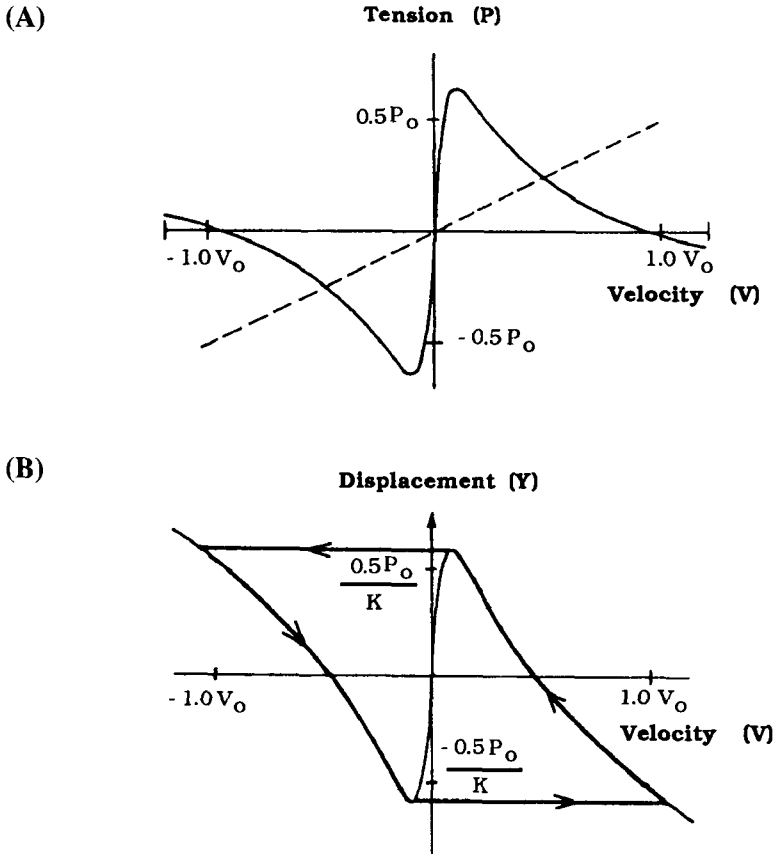


Figure 3.10 Dynamical behaviors of the antagonistic pair of the Brokaw cross-bridge model. (A): Force-velocity behavior of the coupled cross-bridges. The viscous force, γV , is described by a broken line. P_0 and V_0 are the same as in Fig. 3.6. (B): Displacement-velocity plot for the coupled Brokaw models. When combined with a viscous load, γV , and an elastic restoring force, $-KY$, the system will oscillate as represented by the arrows indicating trajectory. From Brokaw (1975). Reprinted with permission.

load which consisted of linear elastic, $-KY$ (Y is defined as displacement), and viscous resistances, $\gamma V (= \gamma dY/dt)$.

The force-balance equation is represented by:

$$\gamma V = P_a - KY. \tag{3.9}$$

In Figure 3.10, γ is equal to $0.5P_0/V_0$. To obtain the displacement-velocity relationship on the (Y, V) plane, equation (3.9) is rewritten as follows:

$$Y = \frac{1}{K}(P_a - \gamma V). \tag{3.10}$$

Figure 3.10B illustrates the Y - V curve, on which a closed trajectory is drawn. This trajectory represents a stable limit cycle. As the peak height of this Y - V curve is inversely proportional to K , the amplitude of oscillation becomes small when the K -value is large, and vice versa.

The Brokaw model was the first that could demonstrate oscillatory behaviour at the molecular level. However, the oscillatory behaviour was demonstrated by the antagonistic pair of cross-bridges. A single site of the cross-bridge system revealed that after step-length change, there was an instantaneous stretch de-activation followed by a delayed tension development (see Fig. 3.9B). These tension transients were quite different from experimental ones. Since the flagellar system was considered to consist of a number of antagonistic cross-bridge pairs, Brokaw extended this model to account for flagellar beating (see Section 5.3.4).

3.4 Three-state model for oscillatory contraction

The models considered in the previous sections assumed only one attached state. These models can account for some of the dynamical properties of muscle such as the force-velocity relationship and delayed tension development. One of the key features of these models is that the early tension recovery after a step-length change (i.e. phase 2 in Figs. 2.14 and 2.15) is interpreted in terms of a very rapid detachment of force-generating cross-bridges. By contrast, Huxley and Simmons (1971) considered that this process is ascribed to the quick transition between the two attached states. This consideration was directly supported by the stiffness measurements, in which stiffness (corresponding to the number of attached cross-bridges) does not change in the early tension-recovery phase (see Section 2.5.2). One may expect, therefore, that the three-state model which contains two attached states and one detached state would mimic many dynamical properties better than the two-state model.

Since the three-state model proposed by Nishiyama *et al.* (1977) demonstrated almost all of the mechanical properties of muscle (Nishiyama and Shimizu, 1979; 1981; Murase *et al.*, 1986), in this section the three-state model is modified so that it accounts for the oscillatory contraction and related properties.

3.4.1 The model

The three-state model assumes the presence of one detached and two attached states denoted by 0, 1 and 2, respectively (Fig. 3.11A). State 1 is a preactive state, in which a cross-bridge produces only a little tension. State 2 is an active state, in which a cross-bridge generates a lot of tension. The cyclic transition among these states ($0 \rightarrow 1 \rightarrow 2 \rightarrow 0$) is considered to be coupled with the hydrolysis of one ATP molecule. The sliding coordinate, x , is

chosen as the distance between an actin and a myosin site with $-d_{\text{att}}/2 \leq x < d_{\text{att}}/2$, where d_{att} (taken as 37.0 nm) is a unit length of two nearest actin sites.

The mechanical potential of each state is defined as a function of sliding coordinate, x (Fig. 3.11B). The analytical form of each potential is written as:

$$\left\{ \begin{array}{l} \text{State 0: } U_0(x) = 0 \end{array} \right. \quad (3.11a)$$

$$\left\{ \begin{array}{l} \text{State 1: } U_1(x) = K_1 \frac{(x - x_1)^2}{2} - U_1^0 \end{array} \right. \quad (3.11b)$$

$$\left\{ \begin{array}{l} \text{State 2: } U_2(x) = K_2 \frac{(x - x_2)^2}{2} - U_2^0 \end{array} \right. \quad (3.11c)$$

where $K_1 = 0.075 \text{ pN nm}^{-1}$, $K_2 = 0.1 \text{ pN nm}^{-1}$, $x_1 = -5.0 \text{ nm}$, $x_2 = 3.0 \text{ nm}$, $U_1^0 = 3.37 \text{ pNnm}$, and $U_2^0 = 49.98 \text{ pNnm}$.

Rate constants of transitions among the three states are also defined as a function of x (Fig. 3.11C). Here, $k_{ij}(x)$ represents the rate constant of the transition from state i to j . There are three important characteristics of these rate constants. First, the rate constants are asymmetric with respect to $x = 0$, which is analogous to the asymmetric rate constants in the Huxley (1957) model. Second, $k_{12}(x)$ and $k_{21}(x)$ are defined as an extremely nonlinear function of x : $k_{12}(x)$ is an exponentially increasing function of x and $k_{21}(x)$ an exponentially decreasing function of x . The form of these rate constants reflects the rate constant for the early tension recovery from T_1 to T_2 , which is expressed by an exponential function of the length step (see Fig. 2.17). That is, the rate constant is low for step increases of length, but increases rapidly with step decreases of length. This is again the intrinsic asymmetry in the transition rate constants. Third, the magnitudes of the rate constants at x_1 (the minimum position of potential U_i) have three different orders: 250 s^{-1} for $k_{12}(x_1)$ and $k_{21}(x_1)$, 10 s^{-1} for $k_{01}(x_1)$ and $k_{20}(x_1)$, and 1 s^{-1} for $k_{10}(x_1)$. This will account for three different rate processes as represented by three arcs of a Nyquist plot (cf. Fig. 2.13).

The analytic form of $k_{ij}(x)$ is given as follows:

$$k_{01}(x) = c_{01} \exp\left[-K_1 \frac{(x-x_1)^2}{2k_B T}\right] \quad \left(-\frac{d_{\text{att}}}{2} \leq x < \frac{d_{\text{att}}}{2}\right) \quad (3.12a)$$

$$k_{10}(x) = c_{10} \quad \left(-\frac{d_{\text{att}}}{2} \leq x < \frac{d_{\text{att}}}{2}\right) \quad (3.12b)$$

$$k_{12}(x) = \begin{cases} c_{12} \exp\left[\frac{K_2(x_2 - x_1)(x + 5)}{k_B T}\right] & \left(-\frac{d_{\text{att}}}{2} \leq x < -3.6\right) \\ c'_{12} & \left(-3.6 \leq x < \frac{d_{\text{att}}}{2}\right) \end{cases} \quad (3.12c)$$

(A)

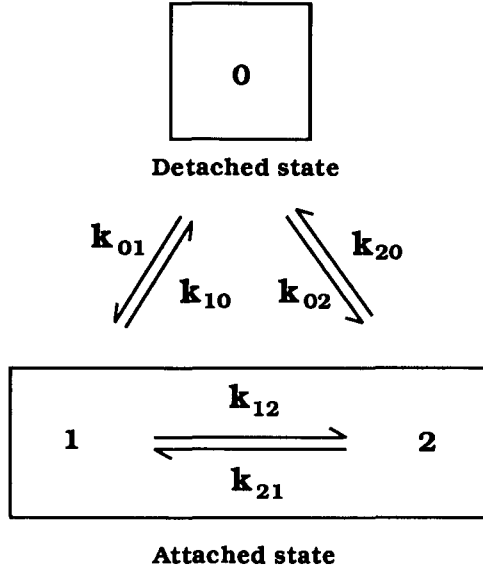
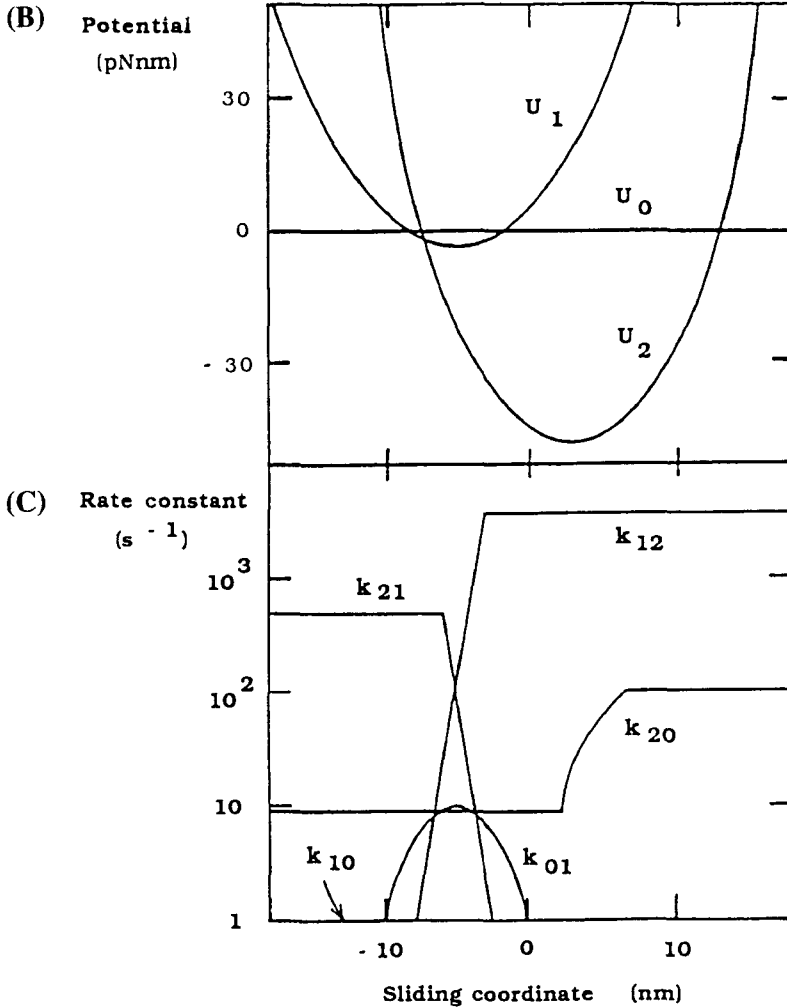


Figure 3.11 Three-state model. (A): There are three states: one detached state (denoted by state 0) and two attached states (denoted by states 1 and 2). k_{ij} denotes the rate constant of the transition from state i to j . (B): Potential-energy functions as a function of x , where U_0 , U_1 and U_2 are the potential functions of states 0, 1 and 2, respectively. From Murase *et al.* (1986). Reprinted with permission of Chapman & Hall. (C): Rate constants as a function of x . From Murase *et al.* (1986). Reprinted with permission of Chapman & Hall.

$$k_{21}(x) = \begin{cases} c_{21} \exp\left[\frac{K_2(x_2 - x_1)(-x - 5)}{k_B T}\right] & \left(-\frac{d_{\text{att}}}{2} \leq x < -6.0\right) \\ c'_{21} & \left(-6.0 \leq x < \frac{d_{\text{att}}}{2}\right) \end{cases} \quad (3.12d)$$

$$k_{20}(x) = \begin{cases} c_{20} & \left(-\frac{d_{\text{att}}}{2} \leq x < 2.0\right) \\ \frac{(c'_{20} - c_{20})(x - 2)}{4} + c_{20} & (2.0 \leq x < 6.0) \\ c'_{20} & \left(6.0 \leq x < \frac{d_{\text{att}}}{2}\right) \end{cases} \quad (3.12e)$$

$$k_{02}(x) = 0 \quad \left(-\frac{d_{\text{att}}}{2} \leq x < \frac{d_{\text{att}}}{2}\right) \quad (3.12f)$$



where $c_{01} = 10 \text{ s}^{-1}$, $c_{10} = 1 \text{ s}^{-1}$, $c_{12} = 250 \text{ s}^{-1}$, $c'_{12} = 4000 \text{ s}^{-1}$, $c_{21} = 62.5 \text{ s}^{-1}$, $c'_{21} = 500 \text{ s}^{-1}$, $c_{20} = 9.375 \text{ s}^{-1}$, $c'_{20} = 100 \text{ s}^{-1}$, $K_1 = 0.075 \text{ pN nm}^{-1}$, $K_2 = 0.1 \text{ pN nm}^{-1}$, K_B is the Boltzmann constant; T is the absolute temperature.

The distributions of cross-bridges in the three states 0, 1 and 2 at the sliding coordinate x and time t are represented by $n_0(x, t)$, $n_1(x, t)$ and $n_2(x, t)$,

respectively. The kinetic equations for the distributions can be written as follows:

$$\frac{dn_0(x, t)}{dt} = k_{10}(x)n_1(x, t) + k_{20}(x)n_2(x, t) - k_{01}(x)n_0(x, t) \quad (3.13a)$$

$$\frac{dn_1(x, t)}{dt} = k_{01}(x)n_0(x, t) + k_{21}(x)n_2(x, t) - [k_{10}(x) + k_{12}(x)]n_1(x, t) \quad (3.13b)$$

$$\frac{dn_2(x, t)}{dt} = k_{12}(x)n_1(x, t) - [k_{21}(x) + k_{20}(x)]n_2(x, t) \quad (3.13c)$$

where

$$n_0(x, t) + n_1(x, t) + n_2(x, t) = 1. \quad (3.13d)$$

In order to obtain simulation results of the sinusoidal analysis (see Section 2.4.2), length change, ΔL , is forced to oscillate at frequency, f :

$$\Delta L = \delta \sin(2\pi ft) \quad (3.14)$$

where δ is the amplitude of sinusoidal length change. In this simulation δ is taken as 2.0 nm per half-sarcomere. As the length change, ΔL , is identical with the change in the sliding coordinate, x , but has opposite sign, x is perturbed as follows:

$$x = -\Delta L = -\delta \sin(2\pi ft). \quad (3.15)$$

When the distributions are specified, tension per cross-bridge, P , the number of elementary cycles per cross-bridge per unit of time, A , and power output per cross-bridge, W , can be calculated:

$$P = \frac{1}{d_{\text{att}}} \int_{-\frac{d_{\text{att}}}{2}}^{\frac{d_{\text{att}}}{2}} dx \left[\left(-\frac{dU_1}{dx} n_1(x, t) \right) + \left(-\frac{dU_2}{dx} n_2(x, t) \right) \right] \quad (3.16a)$$

$$A = \frac{f}{d_{\text{att}}} \int_0^{\frac{1}{f}} dt \int_{-\frac{d_{\text{att}}}{2}}^{\frac{d_{\text{att}}}{2}} dx n_2(x, t) k_{20}(x) \quad (3.16b)$$

$$W = f \int_0^{\frac{1}{f}} dL P. \quad (3.16c)$$

In this model, A is considered to correspond to ATPase activity.

3.4.2 Simulation results

Length–tension relationship. Figure 3.12 shows the length–tension loop of a three-state model in response to sinusoidal length changes. The loop rotates clockwise at high (a) and low (e) frequencies while over an intermediate range of frequencies (c) it rotates anti-clockwise, and a twist of the loop can

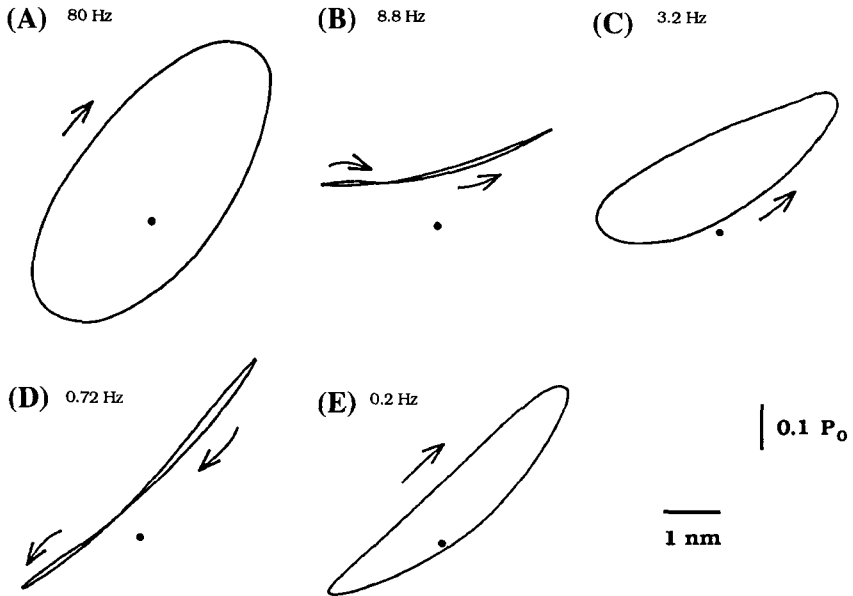


Figure 3.12 Length-tension loop of the three-state model. Tension is plotted vertically and length horizontally. Arrows indicate the direction around the loop. Spots denote the position of the isometric steady state tension, P_0 ($= 5.88 \times 10^{-2}$ pN per cross-bridge). The five loops differ in the frequency of sinusoidal analysis: a, 80 Hz; b, 8.8 Hz; c, 3.2 Hz; d, 0.72 Hz; e, 0.20 Hz.

be seen in the critical ranges of frequencies (b), (d). This reflects that the system absorbs work at high (a) and low (e) frequencies, while it produces positive oscillatory work over an intermediate range of frequencies (c), and the work absorption and production of the system are almost the same at the critical frequencies (b), (d).

A Nyquist plot. Figure 3.13 illustrates the Nyquist plot calculated by using the fast Fourier transform (see Murase *et al.*, 1986). The results are consistent with those obtained by Kawai and Brandt (1980). This plot consists of three arcs with characteristic frequencies of approximately 80, 3.2 and 0.2 Hz. The middle arc with a characteristic frequency of 3.2 Hz corresponds to a change in the phase delay of tension. The other two arcs correspond to high- and low-frequency phase advances.

The power output and the number of elementary cycles. Figure 3.14 shows the calculated power output and the number of elementary cycles per cross-bridge per time at various frequencies. The results are qualitatively similar to those by Steiger and Rüegg (1969) at high Ca^{2+} concentration (see Fig. 2.21).

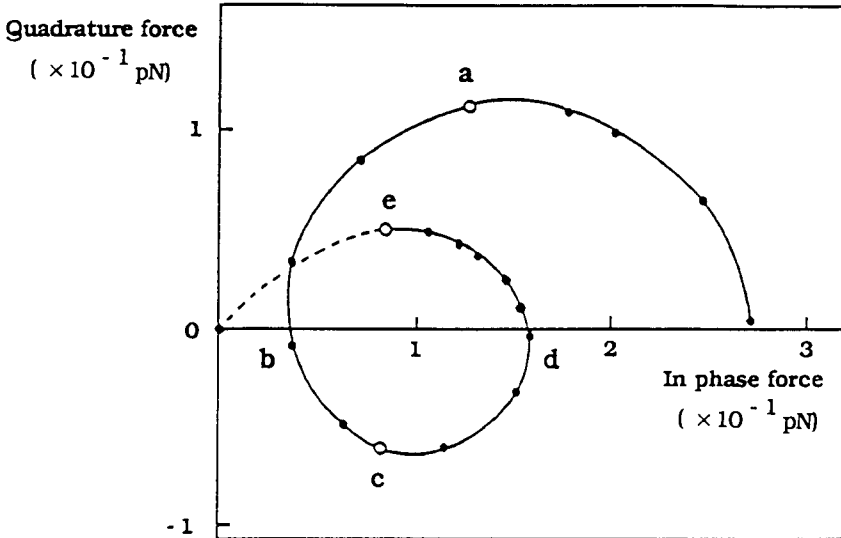


Figure 3.13 A Nyquist plot of the in-phase and quadrature components of the dynamic force. Frequencies are (from right to left): 1273, 400, 159, 120, 80(a), 40, 16, 8.8(b), 4.0, 3.2(c), 2.0, 1.1, 0.72(d), 0.64, 0.55, 0.45, 0.4, 0.3, 0.2(e). Symbols a, c and e at the open circles correspond to the approximate characteristic frequencies. The points extrapolated to the zero frequency and to the infinite frequency correspond to the origin and the value of 2.69×10^{-1} pN on the abscissa. From Murase *et al.* (1986). Reprinted with permission of Chapman & Hall.

Spatio-temporal distributions of attached cross-bridges. Since the Nyquist plot consists of three arcs, we can expect that there should be three distinguishable rate processes in the cross-bridge mechanism. To detail such a mechanism, spatio-temporal cross-bridge distributions are calculated at each characteristic frequency.

Figure 3.15 shows the distributions of attached cross-bridges changing with space and time in response to a sinusoidal length change at 80 Hz. The top panel shows the spatio-temporal distribution of cross-bridges in state 1 and the time course of the force, P_1 , generated by these cross-bridges. We can see that the change in P_1 is almost in phase with the length change, ΔL . The middle panel shows the distribution of cross-bridges in state 2 and the time course of the force, P_2 , generated by these cross-bridges. A large phase advance between P_2 and ΔL can be seen. The bottom panel is the sum of the above two distributions. There is a phase advance between $P (= P_1 + P_2)$ and ΔL , which chiefly results from the phase advance between P_2 and ΔL .

At 80 Hz, the period of oscillation is too fast to allow the cross-bridges to attach and detach, so the total number of attached cross-bridges does not vary significantly. The only effective change is caused by the large rate constants.

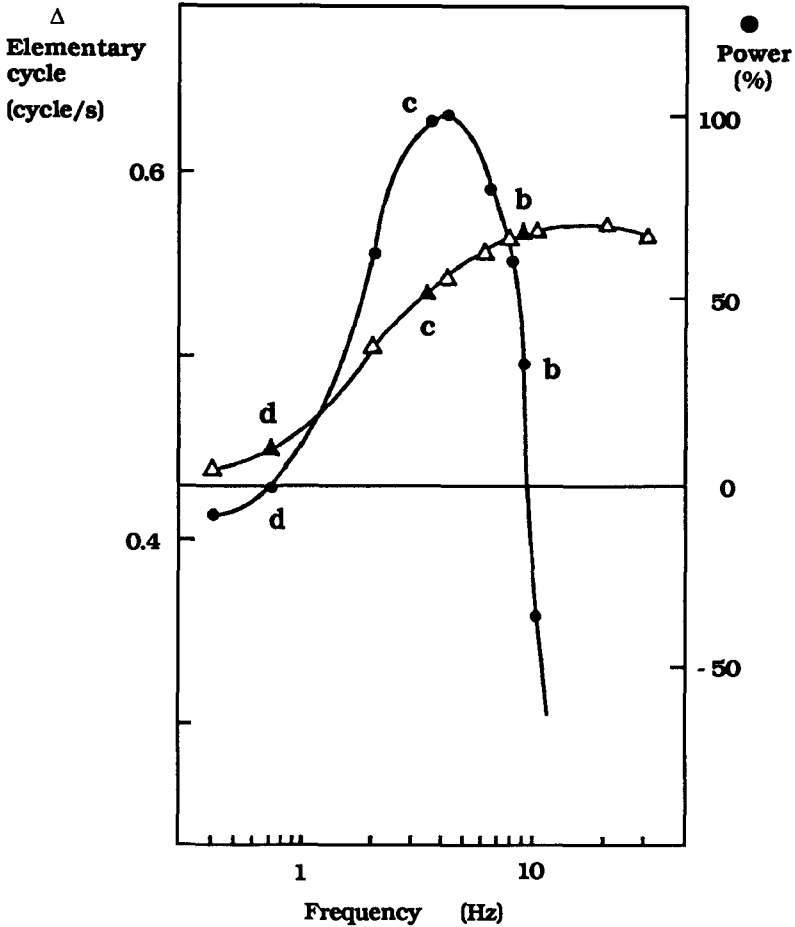


Figure 3.14 The power output per cross-bridge (●) and the number of elementary cycles (Δ). The number of elementary cycles is considered to be proportional to ATPase activity. Symbols b, c and d correspond respectively to those of Fig. 3.13. The maximum power (1.23×10^{-1} pN nm s^{-1} cross-bridge $^{-1}$ at 4.0 Hz) is taken as 100% power. From Murase *et al.* (1986). Reprinted with permission of Chapman & Hall.

This is the transition between states 1 and 2. The kinetic equation describing the tension change of this rate-limiting process is obtained by differentiating equation (3.16a) with respect to t and substituting $dn_1/dt = -dn_2/dt$ (i.e. the total number of attached cross-bridges is almost constant). The equation is represented by:

$$\frac{dP}{dt} = \frac{1}{d_{att}} \int_{-\frac{d_{att}}{2}}^{\frac{d_{att}}{2}} \left[\frac{dU_1}{dx} - \frac{dU_2}{dx} \right] \frac{dn_2}{dt} dx \quad (3.17a)$$

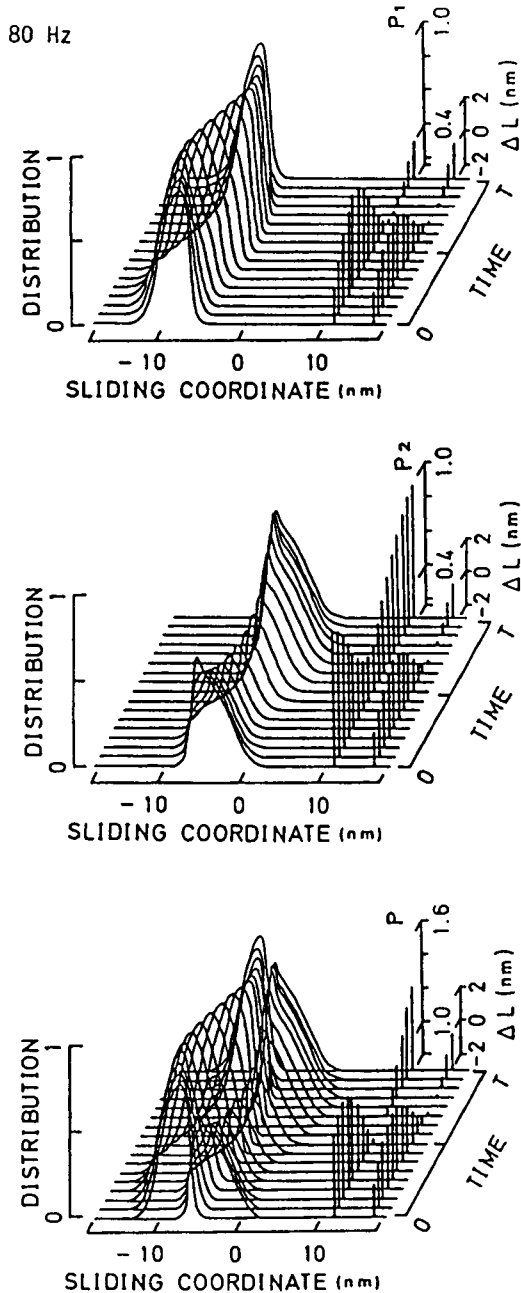


Figure 3.15 Spatio-temporal distributions of attached cross-bridges at 80 Hz. Distributions are plotted as a function of x , during one time period, T . The top panel: the distribution of cross-bridges in state 1 (at the left) and the relationship between P_1 and ΔL (at the right). The middle panel: the distribution of cross-bridges in state 2 (at the left) and the relationship between P_2 and ΔL (at the right). The bottom panel: the distribution of cross-bridges in states 1 and 2 (at the left) and the relationship between P and ΔL (at the right). Note that $\Delta L > 0$ corresponds to stretch, which makes distributions move to the left. From Murase *et al.* (1986). Reprinted with permission of Chapman & Hall.

where

$$\frac{dn_2}{dt} = k_{12}n_1 - k_{21}n_2. \quad (x_1 - \delta \leq x \leq x_1 + \delta) \quad (3.17b)$$

Equation (3.17b) is restricted to the narrow region $x_1 - \delta \leq x \leq x_1 + \delta$, because the transition between states 1 and 2 chiefly occurs in this region. The rate constant of this process is $k_{12} + k_{21}$ with an approximate value in the region $(x_1 - \delta \leq x \leq x_1 + \delta)$ of $\sim 500 \text{ s}^{-1}$. This value is almost equal to the applied angular frequency $2\pi \times 80 \text{ s}^{-1}$. This relationship reflects equation (2.3) in Section 2.4.3, when we substitute $r_e = k_{12} + k_{21}$ and $f_c = 80$.

Figure 3.16 shows the distributions of cross-bridges at 3.2 Hz, when there is a phase delay between P and ΔL . Because rate constants k_{12} and k_{21} are much larger than the rate of length change, the transition between states 1 and 2 reaches a steady state. There is almost zero phase difference between P_1 and ΔL (see the top panel), whereas there is a phase delay between P_2 and ΔL (see the middle panel). As we can see from the bottom panel, there is a phase delay between P and ΔL which results from the phase delay between P_2 and ΔL . After the lengthening phase, the distribution in state 2 increases due to further attachment. This is obvious because the distribution in state 1 has a shoulder, the result of new attachment in the region $x_1 - \delta \leq x \leq x_1$. After the shortening phase, the distribution in state 2 decreases due to detachment.

Consequently, the rate-limiting process is the combination of the attachment to state 1 due to k_{01} with the detachment from state 2 due to k_{20} . The kinetic equation becomes:

$$\frac{dP}{dt} \approx \frac{1}{d_{\text{att}}} \int_{-\frac{d_{\text{att}}}{2}}^{\frac{d_{\text{att}}}{2}} \left[-\frac{dU_2}{dx} \right] \frac{dn_2}{dt} dx \quad (3.18a)$$

where

$$\frac{dn_2}{dt} = k_{01}n_0 - k_{20}n_2. \quad (x_1 \leq x \leq x_1 + \delta) \quad (3.18b)$$

The relaxation rate of this process is obtained as $k_{01} + k_{20}$ ($\sim 20 \text{ s}^{-1}$). This value is almost equivalent to the applied angular frequency $2\pi \times 3.2 \text{ s}^{-1}$. This relationship reflects equation (2.3) in Section 2.4.3, when we substitute $r_e = k_{01} + k_{20}$ and $f_c = 3.2$. Strictly speaking, the right-hand side of equation (3.18a) should contain the contribution of the distribution in state 1 as in equation (3.17a). However, it is not necessary to consider its contribution as it does not produce any force in this region.

Figure 3.17 shows the distribution of cross-bridges at 0.20 Hz. The distribution in state 2 does not change significantly during the oscillation, which reflects the fact that the transitions which occur at x , such as $x \geq x_1$, have reached a steady state. As a result, the change in P_2 is not so large (see the middle panel). We can see that there is a phase advance between P and

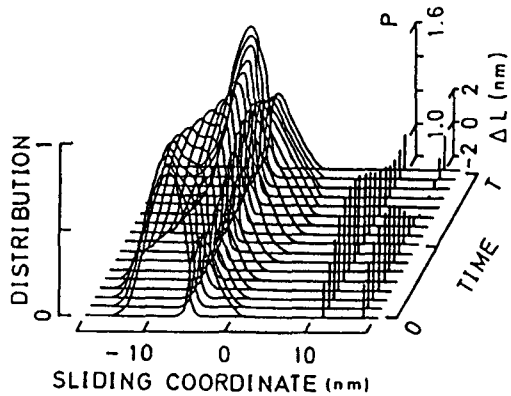
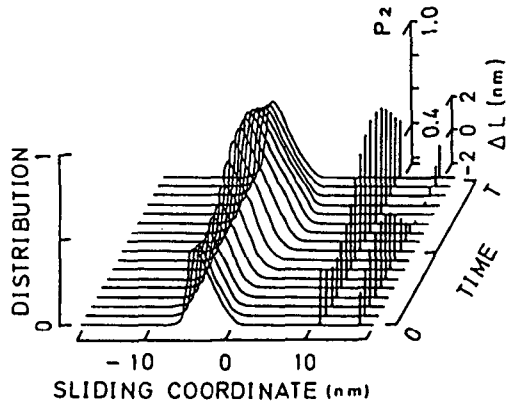
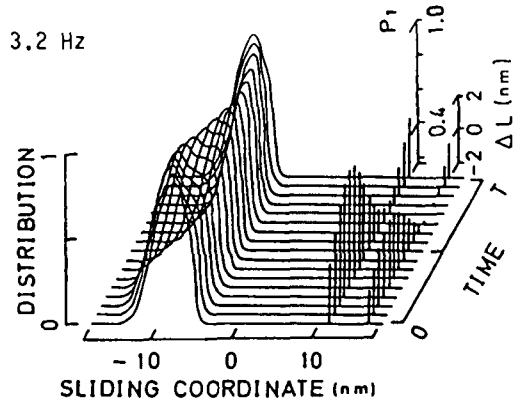


Figure 3.16 Spatio-temporal distributions of attached cross-bridges at 3.2 Hz. The distribution in state 1 has a 'shoulder' when muscle length is stretched, which is caused by further attachment to state 1 (see the top panel). The distribution in state 2 alternately increases and decreases with a phase delay according to sinusoidal length oscillation (see the middle panel). For details see the legend to Fig. 3.15. From Murase *et al.* (1986). Reprinted with permission of Chapman & Hall.

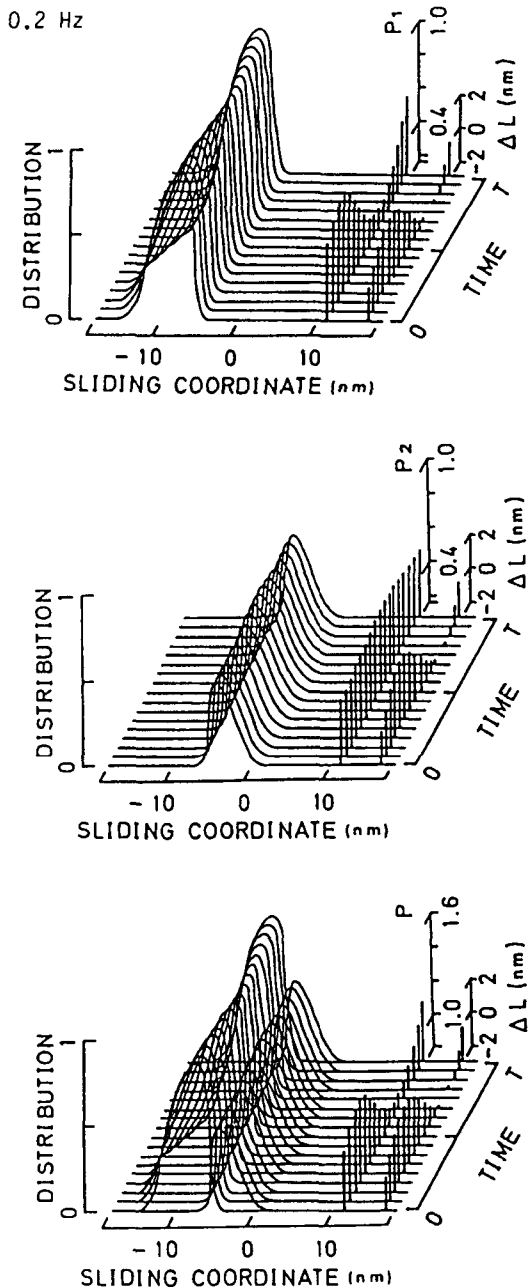


Figure 3.17 Spatio-temporal distributions of attached cross-bridges at 0.20 Hz. The distribution in state 1 changes due to length oscillation in the region $x \leq -10$ nm (see the top panel). The distribution in state 2 shows a steady state (see the middle panel). For details see the legend to Fig. 3.15. From Murase *et al.* (1986). Reprinted with permission of Chapman & Hall.

ΔL (see the bottom panel) which reflects the phase advance between P_1 and ΔL (see the top panel). The most remarkable change appears in the distribution in state 1 for $x \leq -10$ nm, where the transition between states 0 and 1 is a rate-limiting process.

At 0.20 Hz, the kinetic equation is written as:

$$\frac{dP}{dt} \approx \frac{1}{d_{\text{att}}} \int_{-\frac{d_{\text{att}}}{2}}^{\frac{d_{\text{att}}}{2}} \left[-\frac{dU_1}{dx} \right] \frac{dn_1}{dt} dx \quad (3.19a)$$

where

$$\frac{dn_1}{dt} = k_{01}n_0 - k_{10}n_1. \quad (x \leq 10) \quad (3.19b)$$

Since the distribution in state 2 does not change greatly, its contribution to equation (3.19a) is negligible. The rate constant of this process is $k_{01} + k_{10}$ ($\sim 1 \text{ s}^{-1}$), which is approximately equal to the angular frequency $2\pi \times 0.20 \text{ s}^{-1}$. This relationship reflects equation (2.3) in Section 2.4.3, when we substitute $r_e = k_{01} + k_{10}$ and $f_c = 0.2$.

As we have seen, the characteristic frequencies obtained from a sinusoidal analysis are closely related to the transition rate constants at the molecular level. From this close correlation, we can easily modify the calculated Nyquist plot by changing these rate constants, which would mimic the actual Nyquist plot obtained from muscle.

3.5 Interpretation of stretch activation

Let us consider the difference in the explanation of a stretch activation between the three-state model considered in the previous section and the two-state model in Section 3.2. Figure 3.18 illustrates how the three-state model gives rise to the stretch activation. The steady-state attached cross-bridge distribution is shown under isometric conditions in the top panel of Figure 3.18B. Due to a quick stretch in length, the distribution is moved in the direction of decreasing x at $t = t_1$. According to the order of the magnitudes of rate constants, the transition from state 2 to 1 occurs quickly, which corresponds to a quick tension recovery as shown in Figure 3.18C. Then the attachment to state 2 via state 1 occurs. This results in the stretch activation or the delayed tension development. Finally, detachment from state 1 occurs.

The key requirement for the stretch activation in the two-state model is that the attachment rate constant is proportional to the step-length change as simply described by equation (3.6b). As a result, the amount of delayed tension change, ΔP , or the fraction of the excess attached cross-bridges, Δn , is approximately proportional to ΔL :

$$\Delta P = Q\Delta n \approx \frac{QR}{g}\Delta L \quad (3.20)$$

where we assume the condition $g \gg f$. Its rate process is described by equation (3.7).

In the three-state model, as shown in Figure 3.18B, the new attachment to state 2 occurs in order to maintain the equilibrium determined by the rate constants. This rate process is described by equation (3.18b). How much the new attachment occurs depends on how far the distribution is moved by ΔL . It turns out that the amount of the fraction of cross-bridges available for attachment (i.e. $1 - n$) is also roughly proportional to ΔL . Now we know the molecular basis of the stretch activation.

Mathematically, it does not matter whether f or $(1 - n)$ is perturbed by ΔL as long as the first-order rate process like equation (3.3) is considered in the small-signal case ($\Delta L \ll 1$). Consequently, the phenomenological equation (3.7) or (3.7') provides a good approximation to the rate process governed by equation (3.18b) since in both cases the fraction of new attachment of cross-bridges is proportional to the step-length change.

3.6 Simplified model of muscle contraction

It is very interesting to obtain a simplified model that accounts for oscillatory behaviour. As the first step in developing a simplified model, let us start from the force-balance equation:

$$\gamma V = P - Z \quad (3.21a)$$

where γ is the viscous resistance, V the sliding velocity, P the tension of the muscle system, and Z the external load. Since the essential feature necessary for oscillation is the stretch activation, we ignore the initial tension change that appears in T_1 (see Fig. 2.17A). Thus, tension is given as follows:

$$P = T_2(\Delta L) + \Delta P \quad (3.21b)$$

where ΔP is the delayed tension change from the T_2 curve in Figure 2.17A. The T_2 curve is roughly represented by a cubic function of ΔL :

$$T_2(\Delta L) = \Delta L^3 + a \Delta L + P_0 \quad (3.21c)$$

where a is a constant and P_0 is the isometric tension at $\Delta L = 0$. The sign of a depends on the slope of the T_2 curve at $\Delta L = 0$. Whereas a is almost equal to 0 in vertebrate muscle, a can be negative such as in heart muscle (see Figure 3 in Steiger, 1977). ΔP in equation (3.21b) is determined by equation (3.7). From equations (3.21) and (3.7), we have a set of the following equations:

$$\gamma \frac{d\Delta L}{dt} = -(\Delta L^3 + a \Delta L + P_0 + \Delta P) + Z \quad (3.22a)$$

$$\frac{d\Delta P}{dt} = \frac{1}{\tau} (G\Delta L - \Delta P) \quad (3.22b)$$

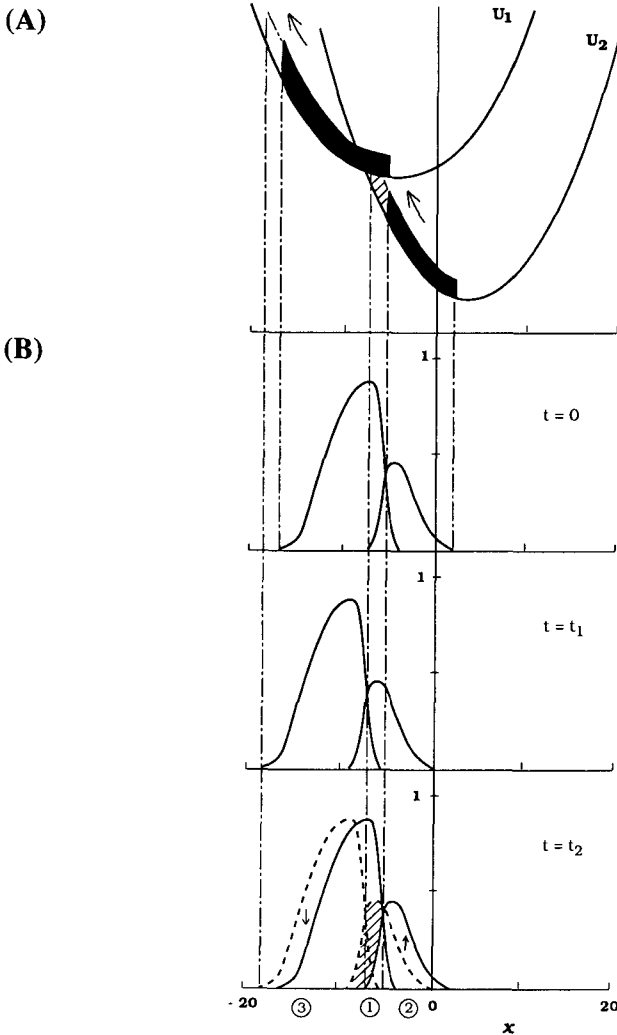
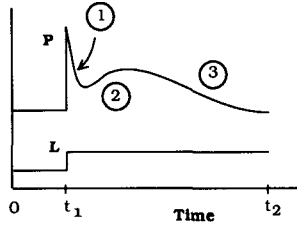


Figure 3.18 Transients of the three-state model in response to a step-length change. (A): Potential-energy functions of states 1 and 2 with cross-bridge distributions. Under isometric conditions, the steady-state distributions are shown as the filled regions. (B): The distributions of cross-bridges in states 1 and 2 as a function of x . The top panel: the steady-state distributions at $t = 0$. The middle panel: the distributions immediately after the stretch at $t = t_1$. The bottom panel: the distributions will revert to their original distributions until $t = t_2$. There are three major changes in the distributions. In region 1, the fast transition from state 2 to 1 occurs as indicated by a shadowed part. In region 2, re-adjustment of cross-bridges in state 2 appears. In region 3, detachment from state 1 slowly occurs. (C): Time course of tension in response to a step-length change. The circled numbers indicate the changes resulting from the changes in the three regions detailed in (B). Modified from Murase *et al.* (1986). Reprinted with permission of Chapman & Hall.

(C)



where γ , a , τ , G and P_0 are constants; and $V = -d\Delta L/dt$. Replacing $P_0 + \Delta P$ by P , we have

$$\gamma \frac{d\Delta L}{dt} = -(\Delta L^3 + a\Delta L + P) + Z \tag{3.23a}$$

$$\frac{dP}{dt} = \frac{1}{\tau} (P_0 + G\Delta L - P). \tag{3.23b}$$

Generally, γ is extremely small compared with τ , so that (3.23a) and (3.23b) are the ‘fast’ and ‘slow’ equations, respectively. The simplified model described by equations (3.23) is equivalent to the BVP model described by equations (1.10).

Using a similar procedure to FitzHugh (1961), we can obtain the $(Z, \Delta L)$ characteristics of the model (Fig. 3.19A). Since equation (3.23a) describes a very fast change compared with the process determined by equation (3.23b), we can tentatively omit the effects caused by equation (3.23b). This is done by setting

$$\left\{ \begin{array}{l} \frac{dP}{dt} = 0 \end{array} \right. \tag{3.24a}$$

$$\left\{ \begin{array}{l} \text{or } P = P_0. \end{array} \right. \tag{3.24b}$$

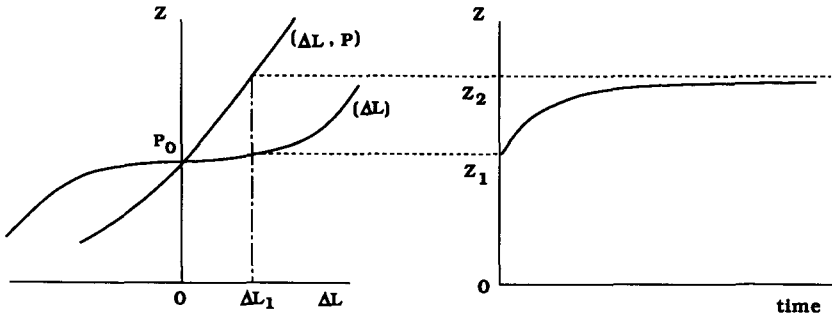
Then the set of equations (3.23) are reduced to just equation (3.23a). According to FitzHugh, this is called the (ΔL) reduced system. The characteristics for the (ΔL) reduced system are obtained by setting

$$\left\{ \begin{array}{l} \frac{d\Delta L}{dt} = 0 \end{array} \right. \tag{3.25a}$$

$$\left\{ \begin{array}{l} \text{or } Z = \Delta^3 L + a\Delta L + P_0. \end{array} \right. \tag{3.25b}$$

To obtain the characteristics for the $(\Delta L, P)$ complete system, equation (3.23b) is allowed to reach its steady state $P = P_0 + G\Delta L$. Substituting this steady-

(A)



(B)

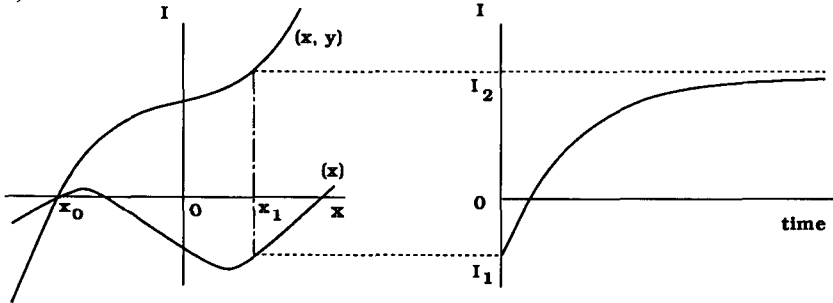


Figure 3.19 Similarity between the muscle system and the nervous system. (A): The simplified model behaviour. The left panel shows the $(Z, \Delta L)$ characteristics for (ΔL) reduced system and $(\Delta L, P)$ complete system. The $(Z, \Delta L)$ characteristics for (ΔL) reduced system corresponds to the T_2 tension-length curve. The right panel shows the delayed tension change after a step stretch by ΔL_1 . (B): The BVP model behaviour. The left panel shows the (I, x) characteristics for the (x) reduced system and (x, y) complete system. The (I, x) characteristics for the (x) reduced system correspond to an N -shaped current-voltage relationship. The right panel shows the time course of the membrane current after a step increase in the voltage by x_1 . This indicates that the inward Na^+ -current is followed by the outward K^+ -current.

state value into equation (3.25a), we obtain the characteristics for the $(\Delta L, P)$ complete system

$$Z = \Delta^3 L + (a + G) \Delta L + P_0. \tag{3.26}$$

The BVP model was originally proposed to account for nerve excitation. It is very instructive to compare the characteristics of the present simplified model and the BVP model, by which we can understand the mathematical similarity between the muscle system and the nervous system. For this purpose, we rewrite the BVP model as follows:

$$\epsilon \frac{dx}{dt} = -(x^3 - x + y) + I \quad (3.27a)$$

$$\frac{dy}{dt} = x + b - cy \quad (3.27b)$$

where I is the membrane current, x the fast variable such as the membrane potential, y the slow variable responsible for refractoriness, and ϵ , b and c are the constants. The (I, x) characteristics of the BVP model are shown in Figure 3.19B.

It is now clear that the tension-length relationship in the muscle system is analogous to the current-voltage relationship obtained by the voltage-clamp experiment in the nervous system. Especially, when a is negative, the T_2 curve in the muscle system is analogous to the N-shaped current-voltage curve mediated by influx of sodium ions.

Under the current-clamp conditions, we know that repetitive firing of the membrane potential occurs. This corresponds to the length oscillations under isotonic conditions as observed by Armstrong *et al.* (1966).

The analogy that has been pointed out seems attractive and would provide us with an important insight into the molecular mechanism underlying these dynamical phenomena. In the nervous system, channel proteins operate to give rise to action potentials; whereas in the muscle system, cross-bridges turn over during contraction. Despite the diversity of biological phenomena at the system level, I believe that the underlying mechanisms can be described by common mathematical terms.

Notes

- 1 In order to avoid confusion, definitions and notations are used consistently throughout this chapter. So detailed descriptions are different from the original papers, but of course the essence is retained.
- 2 Julian (1969) assumed that r is changed with a delay after a step increase in length. However, irrespective of a delay, it is only necessary that r or the product $rf(x)$ is increased after the step stretch. Then, the delayed tension development can result from a delayed re-adjustment of attached cross-bridges.
- 3 The reader should notice the similarity between the force-velocity curve in Figure 3.10A and that in Figure 1.2B.

Part II Nonlinear dynamic phenomena in flagella and cilia

Next to muscle contraction powered by *myosin-actin* mechano-chemical cycles, the best understood type of cellular motility is flagellar and ciliary beating produced by *dynein-tubulin* mechano-chemical cycles. Although it is well established that flagellar and ciliary movements are based on *active sliding* similar to the well-known mechanism in muscle, the flagellar system seems to be more complicated. This is because the muscle system shows only one-dimensional contraction, due to active sliding occurring homogeneously along the muscle filaments, whereas the flagellar system gives rise to rhythmic initiation and propagation of two- or three-dimensional bends, due to a time- and space-dependent pattern of active sliding within the flagellum. One challenging problem that immediately arises is how bending waves are self-organized in cilia and flagella. Structural and functional considerations of cilia and flagella are necessary in solving this problem.

If many such flagella or cilia are close together, they exhibit on a large scale propagating waves known as *metachronal waves*. In ciliated surfaces of protozoa, for example, where beating cilia occur in large numbers, the activity of adjacent cilia is coordinated via hydrodynamic interactions to produce metachronal waves passing over the surface. Another interesting problem then arising is how metachronal waves are self-organized in the ciliated surface. In attempting to solve this problem, it is important to consider the advantage of these wave phenomena from a functional point of view. Through the metachronal coordination of ciliary activity, ciliated systems seem to achieve higher efficiency for the propulsion of fluids than could be achieved by random movement of the cilia.

Of particular interest is the presence of the two self-organizational phenomena on quite different levels. On one hand, the coordination in time and space of mechano-chemical processes *at the molecular level* produces bending waves *at the level of an individual cilium*. On the other hand, the metachronal coordination of such activity in individual cilia in turn generates wave phenomena *at the level of a ciliated system*. This suggests that

regardless of the system level, universal principles may apply to the coordination in time and space of the 'active' processes at the lower level leading to self-organization of temporal, spatial and functional orders at the upper level. Cilia and flagella, thus, provide a good example for studying functional and structural hierarchy. In spite of many studies of the structure, biochemistry and motility of individual organelles, few attempts have been made to identify the universal principles.

Like other nonlinear distributed systems, these motile systems exhibit a large repertoire of self-organizational phenomena at each level. At the individual organelle level, flagella and cilia show regular beating patterns such as oscillations and excitability, with or without the *absolute and relative refractory period*. They also show irregular patterns such as reversal of the direction of wave propagation and *intermittent beating* caused by spontaneous *stopping* and *starting transients*. At the ciliated-system level, groups of cilia show at least four types of regular metachronal waves depending on the relationship between the beat direction of individual organelles and the propagating direction of the metachronal waves. They often show irregular patterns due to a weak metachronism, e.g. sometimes two oppositely propagated metachronal waves collide to disappear (*annihilating waves*) or sometimes they collide to evoke a new metachronal wave (*non-annihilating wave* or *soliton*). Irregular patterns of this kind have been studied less intensively than regular patterns. Recently the presence and role of irregularity, or *chaos*, have been pointed out in various biological systems. This suggests that rather than considering them separately, we should consider both regular and irregular patterns as general phenomena characterized by their degree of order (or the degree of disorder).

In Part II, the above-mentioned phenomena are discussed in detail including consideration of both experimental observations and theoretical calculations. Also attempts are made to answer some of the important problems.

4 Hierarchy in structure and function

This chapter provides a brief overview of experimental observations, which may help us to understand more precisely the mechanisms underlying flagellar and ciliary dynamics, with emphasis on the *hierarchy in structure* as well as *in function*.

A brief introduction to cilia and flagella is made in Section 4.1. Then, the classical definition and the common internal structure for flagella and cilia are described in Section 4.2. Section 4.3 outlines the historical hypotheses and important experimental evidences for the sliding-filament mechanism. Section 4.4 discusses force-generating mechanisms and possible control mechanisms for bending movements in terms of molecular dynamics. In Section 4.5 functional properties of individual cilia and flagella are summarized. Finally, how metachronal waves propagate over groups of cilia is discussed in Section 4.6.

4.1 Introduction

Flagella and cilia are living motile organelles projecting from the surface of eukaryotic cells. They produce bending waves to propel single cells in a medium or to move fluid over the fixed cell surface. Most of them beat at $\sim 10\text{--}40$ Hz, but the form of the beat is quite variable. Their length ranges from $2\ \mu\text{m}$ to several millimetres and the diameter is about $0.2\ \mu\text{m}$. Strictly speaking, flagella and cilia have very diverse ultrastructures depending on the species from which they come (Phillips, 1974), but they are generally similar to one another and have a basic structure of *microtubules* in arrangements called *axonemes* (Warner, 1974). So these different names are merely a matter of definition and the experimental results of one system can be assumed to apply to the other. In most cases, therefore, it is not necessary to distinguish between the two systems.

Confusingly, bacterial flagella share the same name as those of eukaryotes. They will not be considered in this book. For even though many attractive

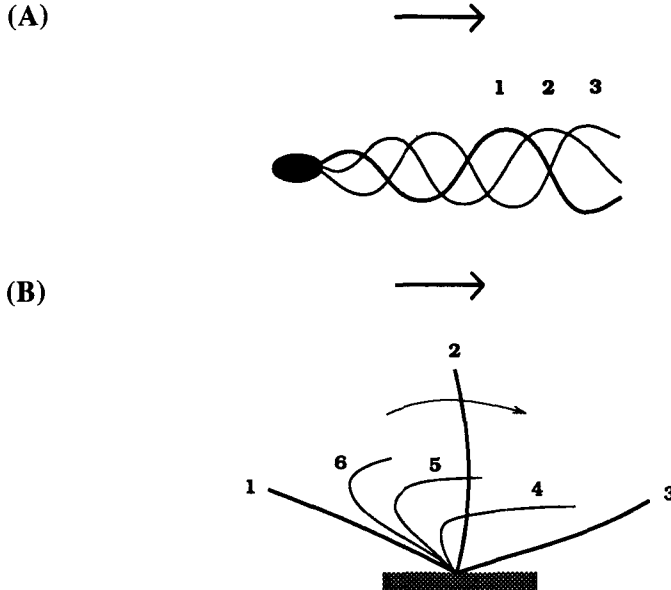


Figure 4.1 Typical beating patterns of flagella and cilia. (A): Successive waves with sustained amplitude (1 – 3) propagated toward the tip of a flagellum move water and thus propel the sperm head forward. (B): The beating cycle of a cilium consists of the effective stroke (1 – 3) in which the extended cilium moves rapidly toward one side by making an ‘oar-like’ movement, and the recovery stroke (4 – 6) in which the cilium moves more slowly back by propagating a bend from the base to the tip. The effective stroke occurs more or less in one plane. The recovery stroke swings either in the same plane or out of the plane. The arrows indicate the water flow caused by activity of the organelles.

problems have arisen from their characteristic properties (cf. Berg, 1983; Murata *et al.*, 1989), they are only 12–20 nm thick and their function is entirely different.

4.2 Internal structure and physiological function

4.2.1 Typical movements of flagella and cilia

The names of flagella and cilia are often used interchangeably, though a fundamental distinction can be made between them, as illustrated in Figure 4.1.

Flagella are very long and occur alone or in small numbers per cell. Sperm tails are typical examples of flagella. They show the propagation of undulatory bending waves with sustained amplitude along the length of the flagellum. The resultant effect is to move water along the flagellar axis and

thus propel the cell in the opposite direction. As Gray (1955) observed, the movement of many flagella is confined to a single plane.

Cilia are short and occur in large numbers per cell where they generate a flow of fluid parallel to the cell surface. They are found on many self-propelling protozoa (e.g. *Opalina*, *Paramecium*), where they are used for locomotion, and also within multicellular animals where they perform transport functions such as mucous transport in the lungs.

Cilia generally show asymmetric beating in a cycle that can be separated into two phases: the *effective stroke* and the *recovery stroke*. During the effective stroke the cilium only bends a little, except near its base, and then swings rapidly around the basal region more or less in one plane. This is followed by the recovery stroke in which a bend is initiated at the base and propagates to the tip of the cilium. As a result, the cilium moves more slowly back to the starting point of the effective stroke. The resultant beat cycle is either planar or three-dimensional depending on whether the cilium recovers in the same plane as the effective stroke.

4.2.2 Typical structure of flagella and cilia

As pointed out before, many flagella and cilia possess an identical axoneme structure in spite of their various beating patterns. Throughout the length of the cilium, nine microtubules are arranged to form a basic structure of the axoneme though its cross-sectional patterns vary with the distance from the tip. To emphasize this 'structural asymmetry' one of the ciliary axonemes, seen in a longitudinal section, and a series of base-to-tip cross-sections at different levels are illustrated in Figure 4.2.

At level (1), nine *singlet* microtubules and a *central pair* of singlet microtubules are arranged. No other specific structures can be seen. At level (2), instead of singlet microtubules, nine outer *doublet* microtubules are arranged around the central pair. This microtubule arrangement is known as the '9 + 2' axoneme (Summers, 1975). Level (3) is the *transition zone* where the central pair terminates. At level (4), instead of doublet microtubules, nine *triplet* microtubules are arranged to form a basal body.

The intact ciliary or flagellar axoneme is surrounded by an extension of the cell membrane and bathed in cytoplasm. This cytoplasmic communication with the cell body, where ATP is produced by mitochondria, provides the necessary channel for supplying the ATP to the motile system of the axoneme. The transport process of the ATP along the flagellum is simple diffusion. A function of the membrane is thus to maintain the proper concentration of ATP and essential ions (e.g. Mg^{2+}) around the axoneme.

9 + 2 axoneme. As illustrated in detail in Figure 4.3, within the 9 + 2 axoneme the nine doublets are in part connected via *radial spokes* to a *sheath* which surrounds the central pair, and in part interconnected via *nexin links* at

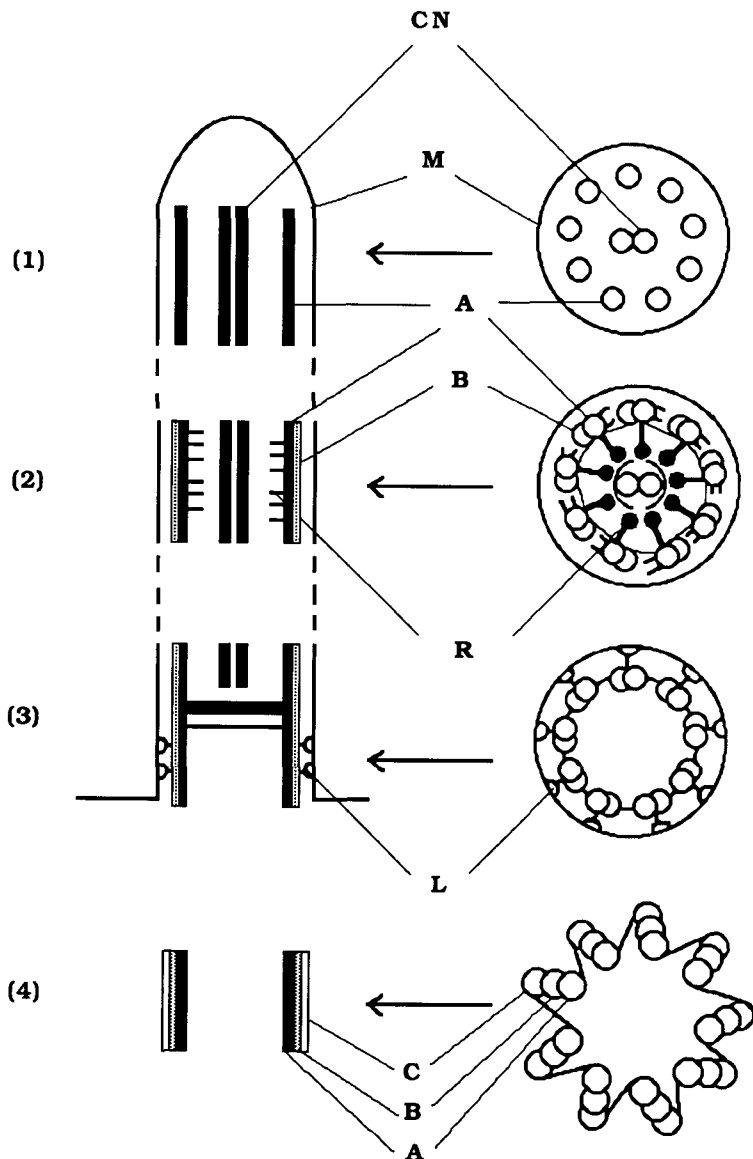


Figure 4.2 Schematic drawing of a median longitudinal section of an axoneme (left), and the cross-section as viewed from base to tip (right) at each level as indicated: A, B and C, are the A-, B- and C-subtubules; CN, the central pair of singlet microtubules; M, the cell membrane; R, radial spokes; L, the ciliary necklace (cf. Gilula and Satir, 1972). (1): At the tip, the B-subtubules disappear, but the A-subtubules remain in the axoneme. (2): The '9 + 2' axonemal structure is retained along most of the length of the flagellum. (3): The transition zone is described as the interval between termination of the central tubules and origin of the C-subtubules. (4): The basal body is composed of nine sets of triplet microtubules, each triplet containing the A-, B- and C-subtubules. Modified from Baba (1974). Reprinted with permission.

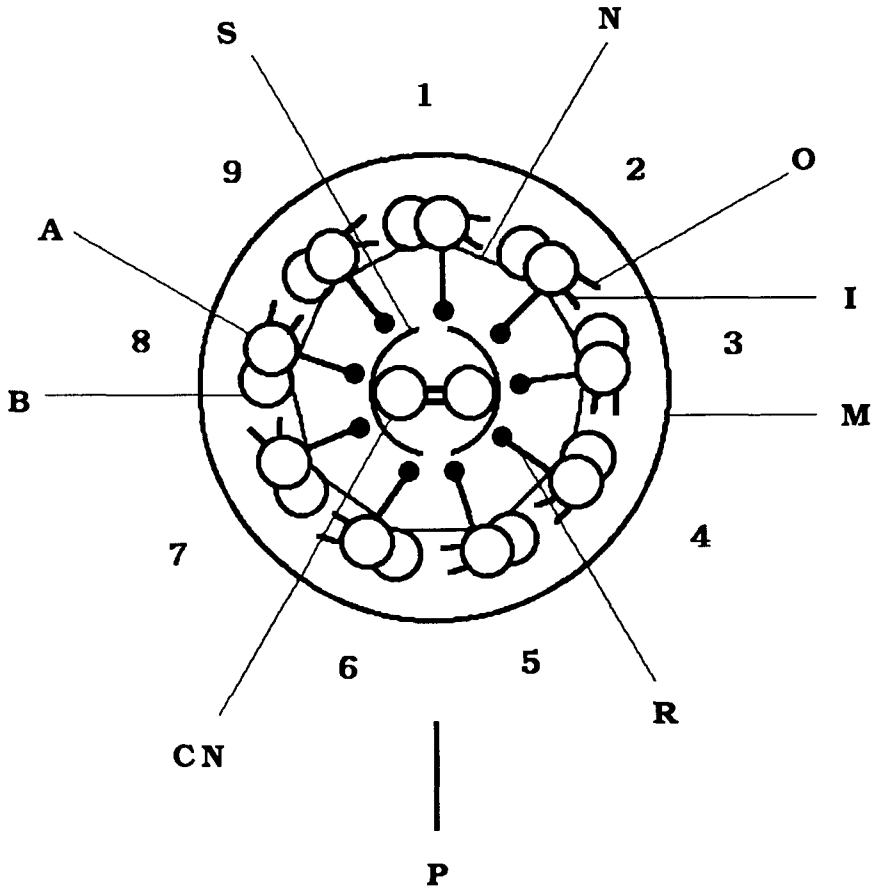


Figure 4.3 Schematic diagram of the 9 + 2 axoneme in cross-section as viewed from base to tip: A and B, the A- and B-subtubules; CN, a central pair of singlet microtubules; O and I, outer and inner arms; M, the cell membrane; N, nexin links; R, radial spokes; S, a sheath. A 'permanent' bridge is often present between doublets 5 and 6, instead of outer and inner arms. A single bend usually occurs in a plane (indicated by P) perpendicular to the plane formed by the central pair of microtubules.

intervals along their length. In addition, the nine doublets possess two rows of arms. The central pair lies in a plane restricting the bend direction of the motile organelle. A single bend prefers to occur in the plane denoted by P in Figure 4.3, which is perpendicular to the central microtubule plane.

Microtubules. The central pair of microtubules are complete, while each of the outer doublets consists of one complete and one partial microtubule – known as the A- and B-subtubules. Figure 4.4 shows a cross-sectional view

(A)

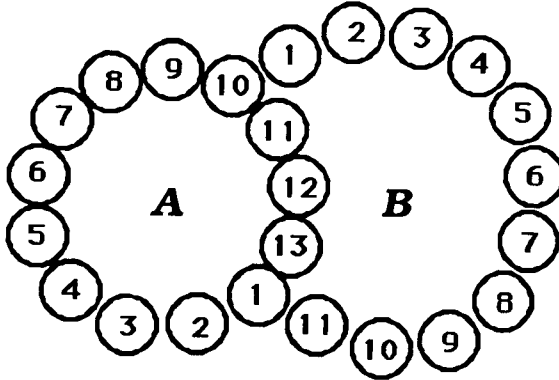
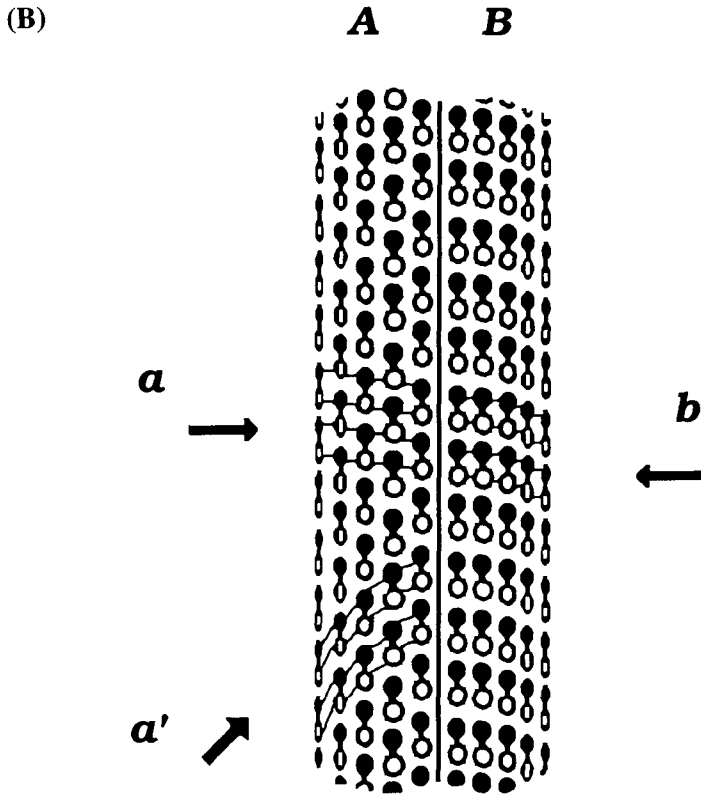


Figure 4.4 (A): Diagram of a doublet microtubule in cross section. A and B are the A- and B-subtubules. The A-subtubule is the complete microtubule composed of 13 protofilaments (in this section 13 globular subunits can be seen), while the B-subtubule is the incomplete microtubule formed from 10 or in this case 11 protofilaments. The 11th subunit is frequently missing. The B-subtubule spans 4 (or 5) protofilaments of the A-subtubule. Modified from Linck and Langevin (1981). Reprinted with permission of the Rockefeller University Press. (B): A proposed model showing the surface lattice of the microtubule doublet in cylindrical form. Each tubulin monomer is represented by a circle (black = α -tubulin, open = β -tubulin). α - and β -tubulin monomers combine to form the $\alpha\beta$ -tubulin heterodimer, giving rise to the dumb-bell-shaped unit. Such heterodimers associate head-to-tail to form protofilaments. Note that both the A- and B-subtubules have the same arrangement of 'monomers' (as marked by the oblique lines indicated by arrows *a* and *b*) but a different 'dimer' lattice. The resultant arrangements of these heterodimers, however, show a right-handed helix for the A-subtubule as marked by the oblique lines (indicated by the arrow *a'*) and a left-handed helix for the B-subtubule (shown by the arrow *b*). Modified from Amos and Klug (1974). Reprinted with permission of the Company of Biologists Ltd.

and a side view of the doublet microtubule. As indicated in Figure 4.4A, the A-subtubule is formed from 13 *protofilaments*, whereas the B-subtubule comprises 10 (or 11) protofilaments sharing a common wall with 4 (or 5) protofilaments of the A-subtubule (Warner, 1974).

Each protofilament is an assembly of *heterodimers* composed of two monomers, α -tubulin and β -tubulin, whose diameters are about 4 nm. Many models have been proposed to account for the doublet microtubule structure (cf. Stephens, 1974). One reliable configuration of the doublet microtubule is illustrated in Figure 4.4B (see Amos and Klug, 1974; Linck *et al.*, 1981; Linck and Langevin, 1981; Mandelkow *et al.*, 1986). It should be noted that each subtubule has the same 4 nm 'monomer' lattice arrangement, but a different 8 nm 'dimer' lattice. This indicates that each subtubule has its particular repeat period based on the helical structure, in addition to inherent 4 nm (monomer) and 8 nm (dimer) longitudinal periodicities.



Dynein cross-bridges and permanent bridge. Two rows of *ATPase* or *dynein cross-bridges* (referred to as *inner* and *outer arms*) extend from each A-subtubule toward the B-subtubule of the adjacent doublet in a clockwise manner, when the axoneme is viewed in transverse section from the base of the organelle to its tip (see Fig. 4.3). These arms are spaced along the microtubule at regular 24 nm intervals. *The presence of ATPase along the entire length of the flagellum strongly suggests that the flagellum itself is composed of active elements.* From a morphological point of view, one question arises: what is the role of two rows of arms whose structures differ slightly? It was found that the outer arms could be selectively removed while the other structures remained intact, and that such axonemes could beat with little change in waveform but at a low frequency (Gibbons and Gibbons, 1973). However, axonemes lacking the entire inner arm were found to be non-motile (Kamiya *et al.*, 1989). This behaviour suggests that inner and outer arms have somewhat different functions in beating axonemes (see Chapter 9).

Some flagella and cilia have a 'permanent' bridge between the two

doublets. This bridge is a useful marker for numbering the doublets. The two bridged doublets are numbered 5 and 6 and doublet 1 lies completely opposite, perpendicular to the central microtubule plane (see Satir, 1974). Other outer doublets are then numbered clockwise when the axoneme is viewed from base to tip (see Fig. 4.3). Using this numbering method, each outer doublet can be assigned a specific unchanging number.

Basal plate and basal body. The two central microtubules end at the level of the cell surface, or a little above it, where there is usually a *basal plate*. While the outer doublet microtubules terminate inside the cell in the *basal body* (see Fig. 4.2). The basal body is composed of nine sets of triplet microtubules that form a short cylinder. Each of the outer doublet microtubules of the axoneme extends into the basal body, where the extra C-subtubule joins part of the doublet microtubules (i.e. the A- and B-subtubules) to form triplet microtubules.

Interestingly, almost all animal cells have *centrioles* in which the ninefold array of triplet microtubules are the same as those in the basal body and are interchangeable in function. For example, the egg does not usually seem to possess active centrioles, while the sperm contains basal bodies that are donated to the egg during fertilization. These sperm basal bodies act as centrioles to organize the mitotic spindle for the first cleavage divisions. A comparable organizing effect can be seen by artificially injecting purified basal bodies from the ciliated protozoan *Tetrahymena* into frog eggs. Further information on their function may be obtained from the review by Pitelka (1974).

4.3 How do individual flagella and cilia move?

The nature of the basic mechanism producing wave phenomena in a cilium (or a flagellum) has been a subject of interest for many years (see books by Gray (1928) and by Sleight (1962); and reviews by Brokaw (1972a, 1989), by Blum and Hines (1979), by Gibbons (1981a), and by Satir (1985)). The investigation of this mechanism provides a lot of information, not only about functioning properties of the individual cilium, but also about dynamic properties of groups of cilia leading to metachronal waves on large scales. Before describing the nature of these metachronal waves (see Section 4.6), we shall first try to understand the underlying mechanism by focusing our attention on the bending movements of flagella and cilia.

4.3.1 Hypotheses

The first important question is whether flagella are 'passive' organelles set in motion by something within the cell, or whether they are 'active' organelles specialized for motility. Three different hypotheses have been proposed: the *passive microtubule mechanism*; the *active contractile microtubule mechanism*; and the *active sliding microtubule mechanism*. Since wave phenomena

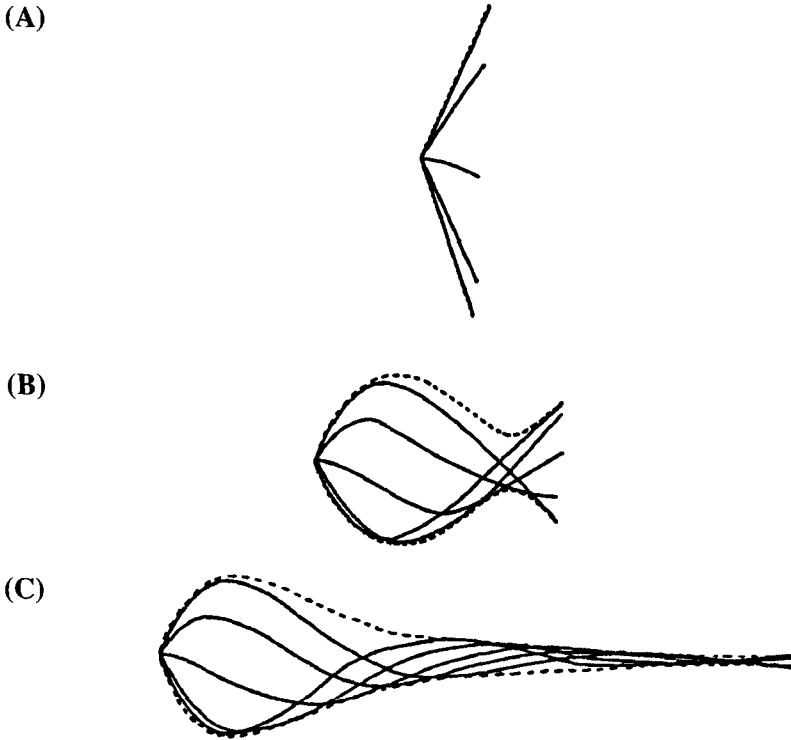


Figure 4.5 Calculated bending waves along a passive flagellum. The boundary conditions are: 'pinned' at the base where movement of the flagellum is constrained to move about a rigid hinge, and 'free' at the tip where the flagellum is completely free to move. In order to initiate successive bends, a forced oscillation is applied to the basal end by angular displacement. The elastic properties of the passive flagellum cause bend propagation. The system sizes are L in (A), $4L$ in (B) and $10L$ in (C), where L is the 'scale length'. When the system size is small (A), the motion is similar to that of a relatively rigid cilium. However, this model cannot account for bend propagation, of sustained amplitude, along a long flagellum (B, C). From Machin (1958). Reprinted with permission of the Company of Biologists Ltd.

in a flagellum are usually ascribed to two processes, *bend initiation* and *bend propagation*, we shall discuss the three hypotheses in terms of the two processes.

Passive microtubule mechanism. The flagellum is considered to be a *passive* cellular appendage whose components, microtubules, lack *autonomous* motility. It is therefore assumed that the bend initiation is triggered by an active process at its proximal end within the cell, and that as a result of elastic properties of the microtubules bend propagation can occur. However, since Machin (1958) showed that the amplitude of such a wave decreases exponentially along the length of the flagellum (Fig. 4.5), it is difficult to

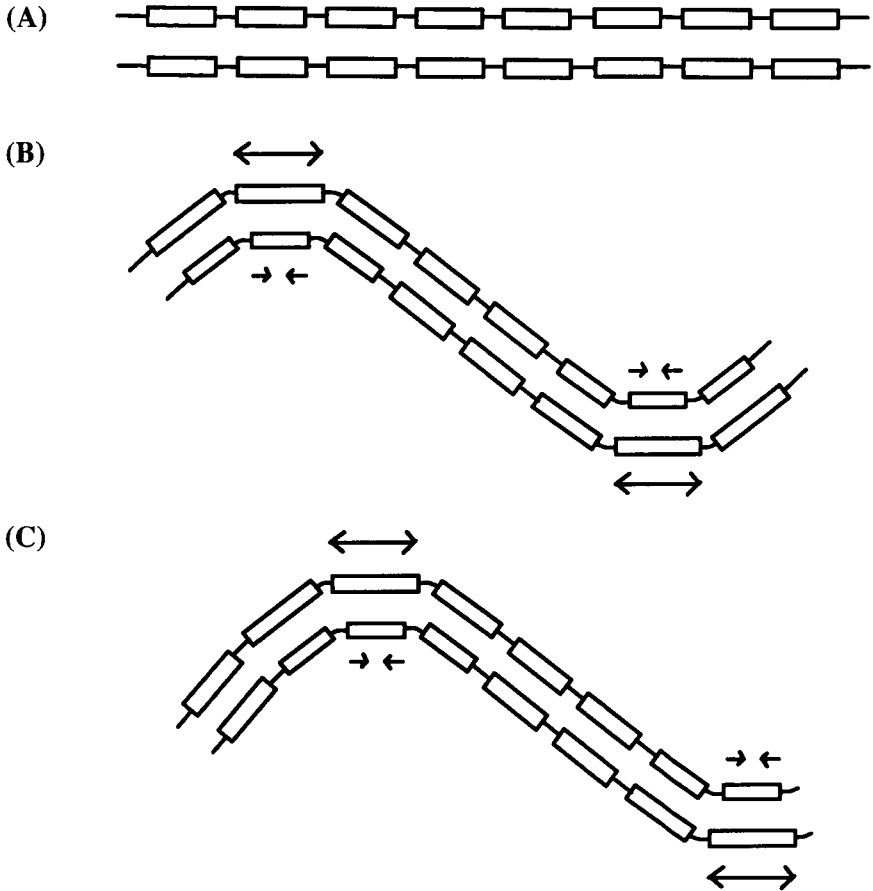


Figure 4.6 Diagrams showing how local contraction causes a bend in a simple flagellum represented by a series of bilaterally arranged contractile elements. (A): Before active contraction, each element is at its equilibrium length and the flagellum is straight. (B): Elements on one side are actively contracting and elements on the other side are stretching in a particular region (indicated by arrows). A local bend is thus produced in the region where an active process takes place. (C): The bend propagation is achieved by the propagated wave of contraction in phase with the active region.

explain the observed wave propagation by this passive mechanism. Instead, the hypothesis that flagella are active organelles appears to be attractive.

Active contractile microtubule mechanism. The flagellum is assumed to be composed of *active* contractile microtubules (Machin, 1958; 1963). When the microtubules change their length actively, relative to one another, they produce local contraction at a particular point along the length of the flagellum, and a local bending is initiated at that point (Fig. 4.6). The

characteristic feature of this mechanism is that *the bending region is a direct reflection of the active region within the flagellum*. A bend propagation is, therefore, achieved by a propagated wave of contraction in phase with the active region. This may be similar to the bending movements of eels and snakes.

Active sliding microtubule mechanism. This hypothesis was suggested on the basis of the analogy of the muscle system with the flagellar system after the discovery of 'arms' projecting from the outer doublets (Afzelius, 1959). It is considered that the microtubules do not change their length but *slide actively* relative to one another (Fig. 4.7). When such sliding occurs *inhomogeneously* along the flagellum, bend initiation occurs between points that have different shear (Brokaw, 1971; Shingyoji *et al.*, 1977). This means that *the bending region is not a direct reflection of the active region, but is the result of sliding processes occurring throughout adjacent regions of the flagellum*. Consequently, a propagated bending wave is associated with a propagated wave of active sliding, but they are out of phase.

4.3.2 Reactivation

To study details of the mechano-chemistry of flagellar dynamics, it was necessary to have a 'model system' that could be subjected to well-controlled conditions. Such a 'model' was developed by Hoffmann-Berling in the early 1950's. First glycerin was added to flagella and then it was washed away. The resulting model was then reactivated by adding chemical energy, ATP, and the necessary ions, Mg^{2+} . ADP was also effective in reactivating the model due to its conversion into ATP-AMP by a kinase present on the axoneme. It was seen, afterwards, that the glycerin had destroyed the flagellar membrane and the cell, but had left the 9 + 2 axonemes intact.

It is of great importance that this treatment often resulted in the separation of sperm tails from the cell, because such isolated flagella were useful in directly answering the question of whether or not flagella are 'active' organelles. Since Brokaw (1961) observed that the isolated flagella could beat and swim through a medium, the idea that flagella are 'active' organelles, which do not require any structures within the cell for movement, has turned out to be true.

The goal, to get a good 'model' which can be reactivated to beat when supplied with ATP and certain ions, is 'complete' disruption of the membrane without changing any other structures. Unfortunately the glycerin procedures caused 'partial' disruption of the membrane leading to two main shortcomings: a low percentage of reactivation and an often somewhat abnormal waveform. Gibbons and Gibbons (1972) extended this 'extraction' technique using a detergent, Triton X-100, to overcome these shortcomings. The Triton-extracted 'model' flagella move just like a living organelle and their beating frequency is determined by the concentration of ATP.

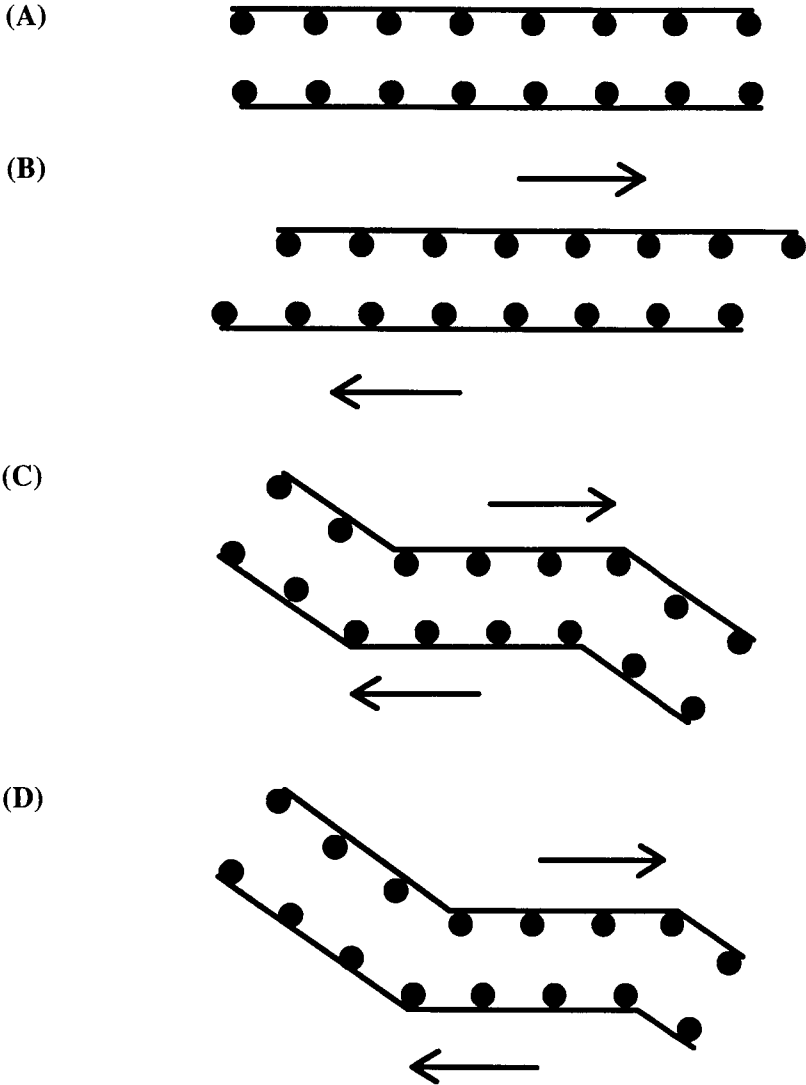


Figure 4.7 Diagrams showing how active sliding causes a bend in a flagellum consisting of two inextensible filaments. (A): The flagellum is straight and no bending occurs without active sliding. (B): No bending is initiated when active sliding occurs *homogeneously* (or *equally*) throughout the length of the flagellum. (C): If there is resistance to sliding at both ends, two bends are formed in opposite directions on either side of the region of active sliding. There is a phase shift between the active region and the bending region. The arrows indicate the active sliding direction of each filament. (D): The resultant bends propagate in accordance with the propagated wave of active sliding with some phase shift. Modified from Shingyoji *et al.* (1977). Copyright © Macmillan Magazines Ltd. Reprinted with permission.

4.3.3 Evidence for active sliding

It is clear that flagella are active motile systems. The next question is which of the two proposed mechanisms is responsible for movement: the contractile microtubule mechanism, by which microtubules actively change in length at a particular point along the length of the axoneme to generate a bend at the same point; or the sliding microtubule mechanism, wherein microtubules remain at a constant length but move longitudinally relative to one another in some region, to cause a bend in adjacent regions.

As pointed out by Brokaw (1972a), this difference is of great importance particularly in cilia, because a cilium beats against the greatest viscous resistance during its effective stroke, where its bending is restricted to a relatively short region near its base. A contractile microtubule mechanism requires very high energy liberation in the bending region, whereas a sliding microtubule mechanism allows this energy liberation to take place along most of the cilium.

In addition to the above difference, each mechanism predicts the characteristic relationship between ciliary stroke positions and changes in the microtubule configuration at the tip of the cilium, on the assumption that the distance between the adjacent microtubules is constant along the whole length of the cilium and the positions of the microtubules remain fixed at the base. A contractile microtubule mechanism predicts that the microtubule on the outer, convex, side of a bend will change in position tipward relative to that on the inner, concave, side of a bend because of the contraction occurring on this side (see Fig. 4.8B).

On the contrary, a sliding microtubule mechanism has the microtubule on the inner side of the bend sliding tipward and results in a displacement different from that of the contractile microtubule mechanism (see Fig. 4.8C). Electron-microscope observations of microtubule configuration strongly support the configuration predicted by the sliding microtubule mechanism (Satir, 1965; 1968).

Much more direct evidence for the occurrence of active sliding between flagellar microtubules is provided by Summers and Gibbons (1971), who isolated Triton-extracted flagellar axonemes from sea-urchin sperm and treated them briefly with *trypsin* (Fig. 4.9). This technique is excellent because the radial spokes and the intermicrotubule nexin links, which are considered to provide the shear resistance, are sensitive to disruption by trypsin, while the dyneins and the microtubules themselves are relatively resistant to a brief treatment with trypsin. The subsequent addition of ATP and Mg^{2+} causes active sliding of the microtubules leading to a disintegration of the axoneme into separated microtubules. As a result of this disintegration, dark-field micrographs showed that the axoneme grows up to eight times longer than the original axonemal fragment.

It is therefore concluded that active sliding generated by ATP-induced

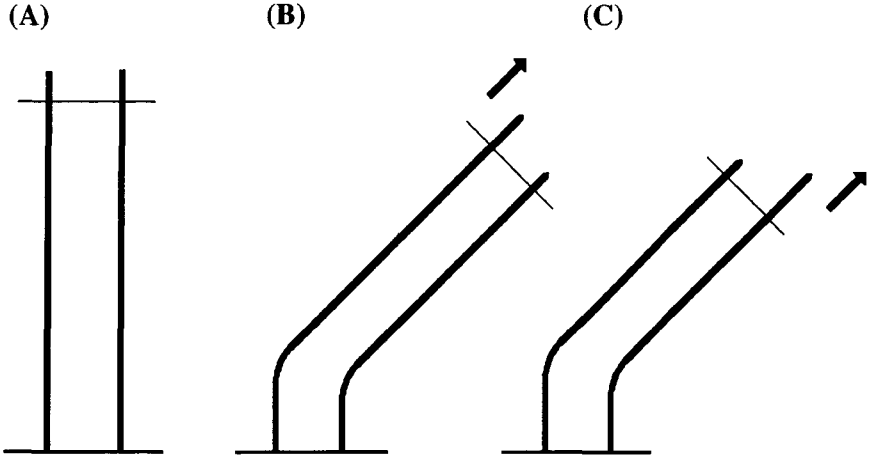


Figure 4.8 Comparison of a typical relationship between microtubule position and bending pattern: (A) straight up; (B) bent by the 'contractile microtubule mechanism'; and (C) bent by the 'sliding microtubule mechanism'. The contractile microtubule mechanism suggests that the microtubule on the outer side of a bend will change its position tipward relative to that on the inner side (shown by the arrow). The outer side of the microtubule will stretch and the inner side will relatively contract, to cause a bend. In contrast the sliding microtubule mechanism predicts that the microtubule on the inner side of a bend will slide tipward (shown by the arrow) to form the bend.

dynein-tubulin interaction is converted into bending by the series of inter-microtubule connections within the axoneme which are chiefly destroyed by trypsin.

4.4 Functional mechanisms

4.4.1 *Force-generating mechanisms*

Although it has been established that ATP-induced force generation by dynein cross-bridges causes active sliding between a pair of doublet microtubules, little information is available on whether or not the active sliding occurs only in one direction. Investigation of this problem provides insight into not only how cilia and flagella beat but also how dynein cross-bridges undergo the mechano-chemical cycle.

Unidirectional active sliding. Sale and Satir (1977) followed the method of Summers and Gibbons (1971) by using electron microscopy to examine a 'polarity' of active sliding between a pair of doublets. In the pair of doublets, the dynein cross-bridges extend from the A-subtubule of one doublet (conventionally referred to as *N*) and point toward the B-subtubule of

the adjacent neighbouring doublet (conventionally referred to as $N + 1$) as illustrated in Figure 4.10.

The active sliding occurs between the two doublets due to the mechano-chemical cycle of the dynein cross-bridges on doublet N . For lack of doublet $N + 2$, the dynein cross-bridges on doublet $N + 1$ would not contribute to the sliding interaction. The relative movement thus depends only on whether the direction of force generation of dynein is toward the tip or toward the base. If the direction of force generation of dynein is from base to tip, doublet $N + 1$ will move toward the tip relative to doublet N (Fig. 4.10B). If, on the other hand, the direction of force generation is from tip to base, doublet $N + 1$ will move toward the base relative to doublet N (Fig. 4.10C).

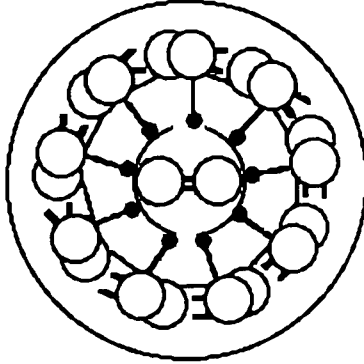
Sale and Satir found that the case shown in Figure 4.10B always occurs such that *the dynein cross-bridges on doublet N push the doublet $N + 1$ toward the tip of the axoneme*. This strongly suggests that there is a single polarity for active sliding, and that active sliding cannot reverse along the same pair of doublets. That is, active sliding occurs 'unidirectionally', but not 'bidirectionally'.

Unidirectional mechano-chemical cycle. The polarity of dynein force generation is analogous to that of myosin force generation, which facilitates the sliding of filaments in striated muscle. Figure 4.11 shows major features of the mechano-chemical activity of dynein-tubulin interactions summarized by Satir *et al.* (1981). A cross-bridge on doublet N is attached to doublet $N + 1$ (A). ATP binds to the cross-bridge, causing it to be detached (B). Hydrolysis of ATP to ADP + Pi relaxes the cross-bridge to its original conformation (B \rightarrow C). The cross-bridge re-attaches to doublet $N + 1$ (D). Sliding movement is generated when the attached cross-bridge performs a unidirectional 'power stroke' to return to its equilibrium position accompanied by the release of ADP + Pi (D \rightarrow A).

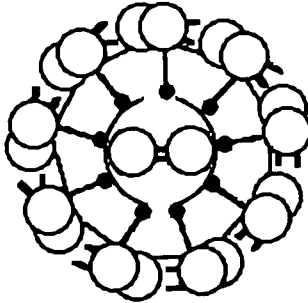
4.4.2 Control mechanisms

It is now clear that the forces in cilia and flagella are produced by a sliding microtubule mechanism, similar to that of striated muscle. However, to produce the observed motion in cilia and flagella, forces have to be developed in the right sequence in time and at the right location in space. This suggests the presence of *temporal* and *spatial control mechanisms*. Without such control mechanisms all dyneins would operate at once – since every dynein arm is potentially identical and every microtubule slides in the same way – and the resultant forces would cancel and no movement would occur (Satir, 1984). Thus one apparent question arises: How is the activity of dyneins coordinated in time and in space?

(A)



(B)



(C)

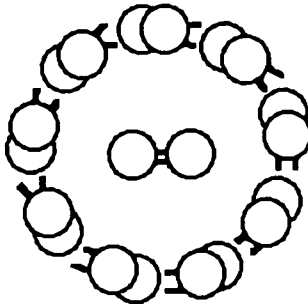
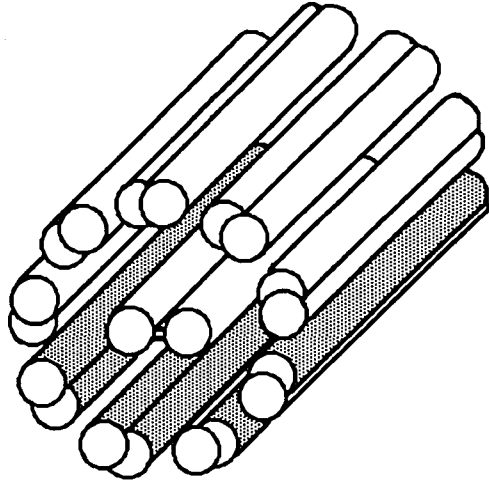
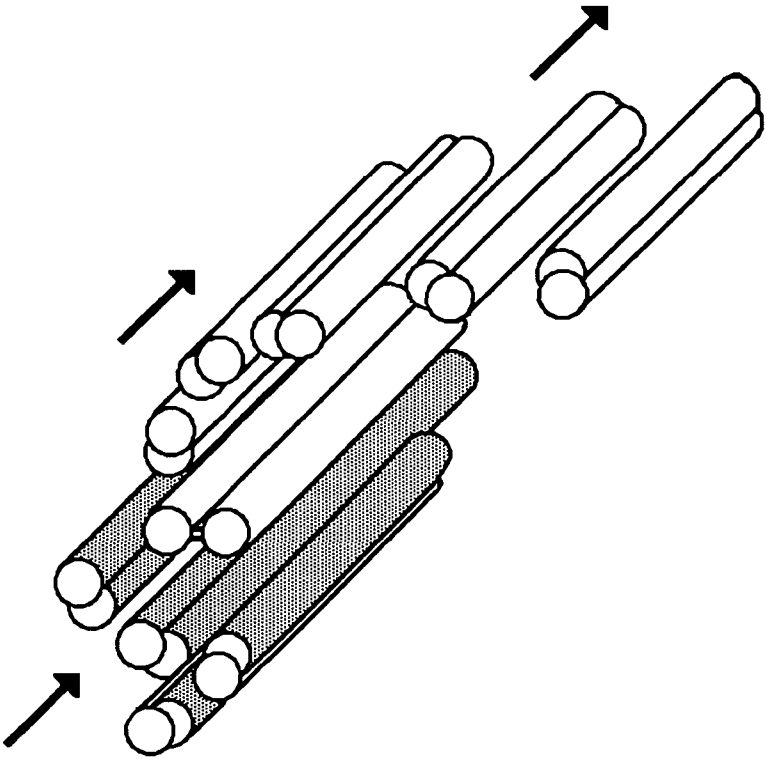


Figure 4.9 Schematic representation of axoneme: (A) intact; (B) demembrated by Triton; (C) followed by a brief treatment with trypsin; (D) before ATP addition; and (E) after ATP addition. Since the radial connections, i.e. nexin links and radial spokes, are partially destroyed by the treatment with trypsin, a disintegration of the axoneme into separated microtubules occurs due to active sliding of the microtubule (as indicated by the arrows).

(D)



(E)



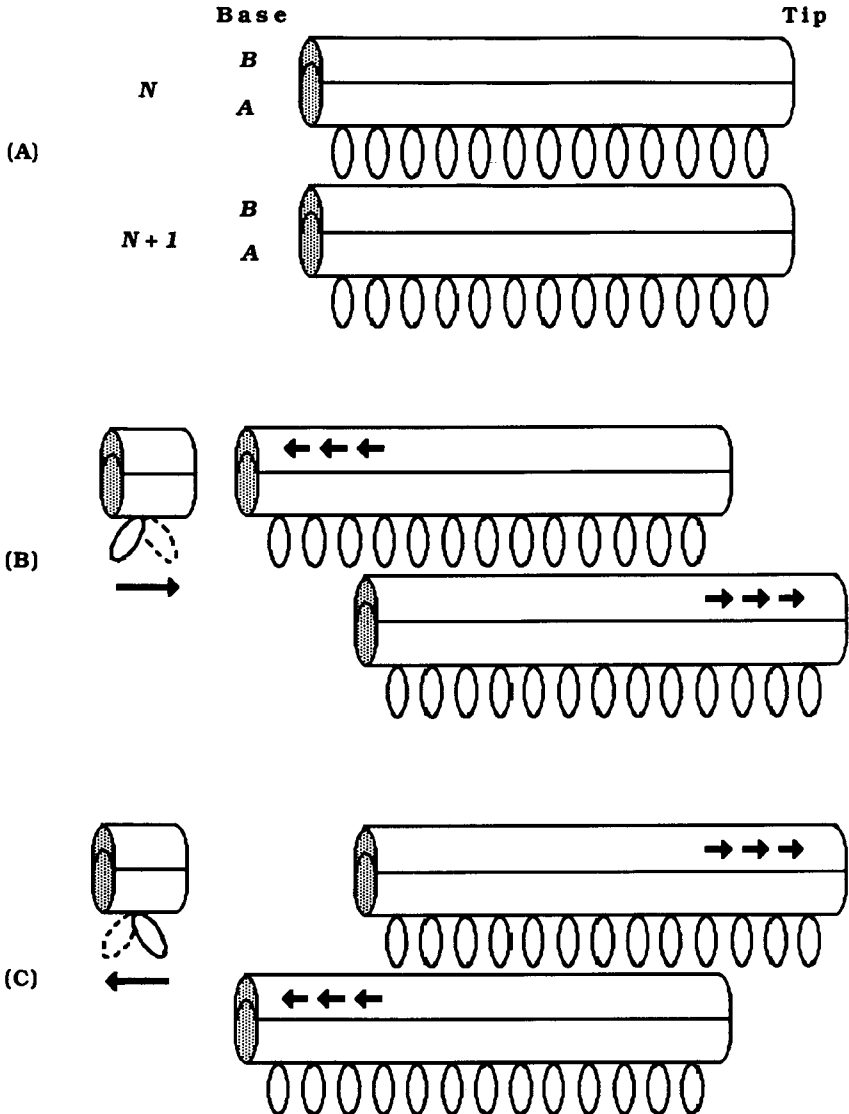


Figure 4.10 Diagram showing a single pair of doublets. (A): Before adding ATP. The upper doublet is conveniently numbered N and the adjacent doublet $N + 1$. The dynein cross-bridges extend from the A-subtubule of doublet N toward the B-subtubule of doublet $N + 1$. Base and tip correspond to left and right. (B): If the direction of force generation of dynein is from base to tip (indicated by the arrow on the left panel), doublet $N + 1$ moves toward the tip relative to doublet N (indicated by the arrow). (C): If the direction of force generation is from tip to base, doublet $N + 1$ moves toward the base relative to doublet $N + 1$. Experimental results always show the case (B).

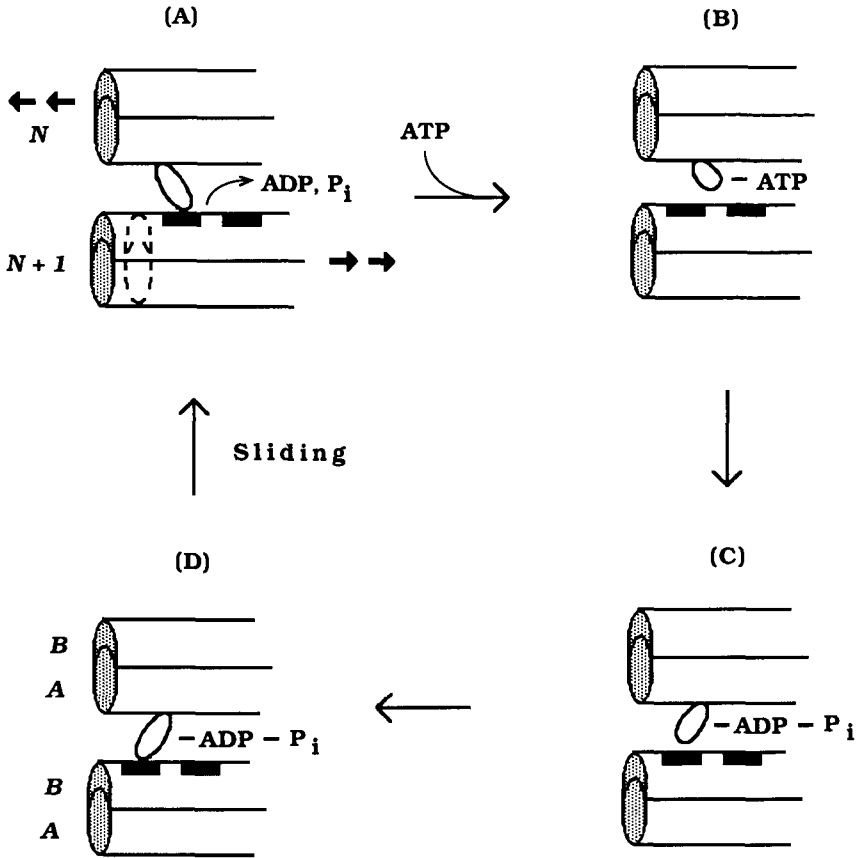


Figure 4.11 Mechano-chemical cycle of dynein cross-bridge. Two successive binding sites on the B-subtubule of doublet $N + 1$ are indicated by filled rectangles. (A): A cross-bridge on the A-subtubule of doublet N attaches to the B-subtubule of doublet $N + 1$. (B): ATP binds to the cross-bridge, which causes the release of the attached dynein. (C): During hydrolysis of ATP to ADP + P_i , the detached dynein changes conformation. (D): Re-attachment of the dynein to the B-subtubule of doublet $N + 1$ occurs. Subsequently, a sliding motion takes place between the two doublets upon the release of ADP + P_i .

Temporal control mechanism. Active sliding between each pair of outer doublets only occurs in one direction (Sale and Satir, 1977) due to a unidirectional dynein power stroke (Satir *et al.*, 1981). Because of the closed ring of doublets, backward sliding of the same pair of doublets is passively induced by active sliding of other pairs in the axoneme. Assuming that bending occurs in a single bend plane, the $9 + 2$ axoneme would behave as if it were only a two-filament system as illustrated in Figure 4.8.

For convenience, the two sides of the axoneme are identified by the

orientation of the dyneins projecting into the bend plane: one is the left half (doublets 6–9) of the cross-section of the axoneme at which all dyneins project into the plane incline in the same direction, and the other is the right half (doublets 1–5) of the axoneme at which all dyneins incline in the opposite direction.

As illustrated in Figure 4.12A, if dyneins on the right half of the axoneme (especially dyneins on doublet 3) are active, unidirectional active sliding takes place between doublets 3 and 4. The two-filament model assumes that 9 doublets are divided into two groups with respect to their direction of relative sliding. One is the upper half (doublets 8–3) of the axoneme, which slides toward the base, and the other is the lower half (doublets 4–7), which slides toward the tip.

Of course ‘doublet subsets’ of the upper and lower halves can be rather arbitrary, i.e. the axoneme can be divided into different subsets of doublets. But such arbitrariness does not matter as long as one assumes the two-filament system to account for planar beating. Although sliding between doublets 3 and 4 is ‘active’, sliding between doublets 7 and 8 is completely ‘passive’. It is passive because the sliding direction is opposed to the ‘preferred’ direction of the dynein power stroke. The sliding movement of doublets causes the cilium to bend to one side (or downward in this figure).

If dyneins on the left half of the axoneme (especially dyneins on doublet 7) are active, the upper half moves relative to the tip and the lower half relative to the base as illustrated in Figure 4.12B. In this case sliding between doublets 7 and 8 is ‘active’, whereas sliding between doublets 3 and 4 is ‘passive’. Thus the cilium bends toward the opposite side (or upward).

The temporal control mechanism, therefore, seems to be an ‘on’ and ‘off’ switch for the activity of dyneins attached to doublets at each side (doublets 1–5 and doublets 6–9) of the axoneme (see Satir, 1984; 1985). Since this control mechanism is allowed to initiate active sliding in the proximal direction and in the distal direction alternately, it may have profound effects on the beat frequency.

Spatial control mechanism. The temporal control mechanism produces alternate active sliding and is probably responsible for the successive changes of bend angle of a cilium between the two opposing stroke positions. However this mechanism cannot produce a typical ciliary cycle which alternates between effective and recovery strokes (see Fig. 4.1).

As illustrated in Figure 4.13, these different beating patterns seem to reflect the strength of microtubule interaction along the length of the cilium – the *spatial control mechanism*. According to the relationship between the geometry of the bent cilium and the sliding displacement of the microtubules, the effective stroke must involve *synchronous sliding*, where simultaneous sliding occurs throughout the length of the axoneme except near its base. The recovery stroke, however, must involve *metachronous sliding*, where sliding occurs in

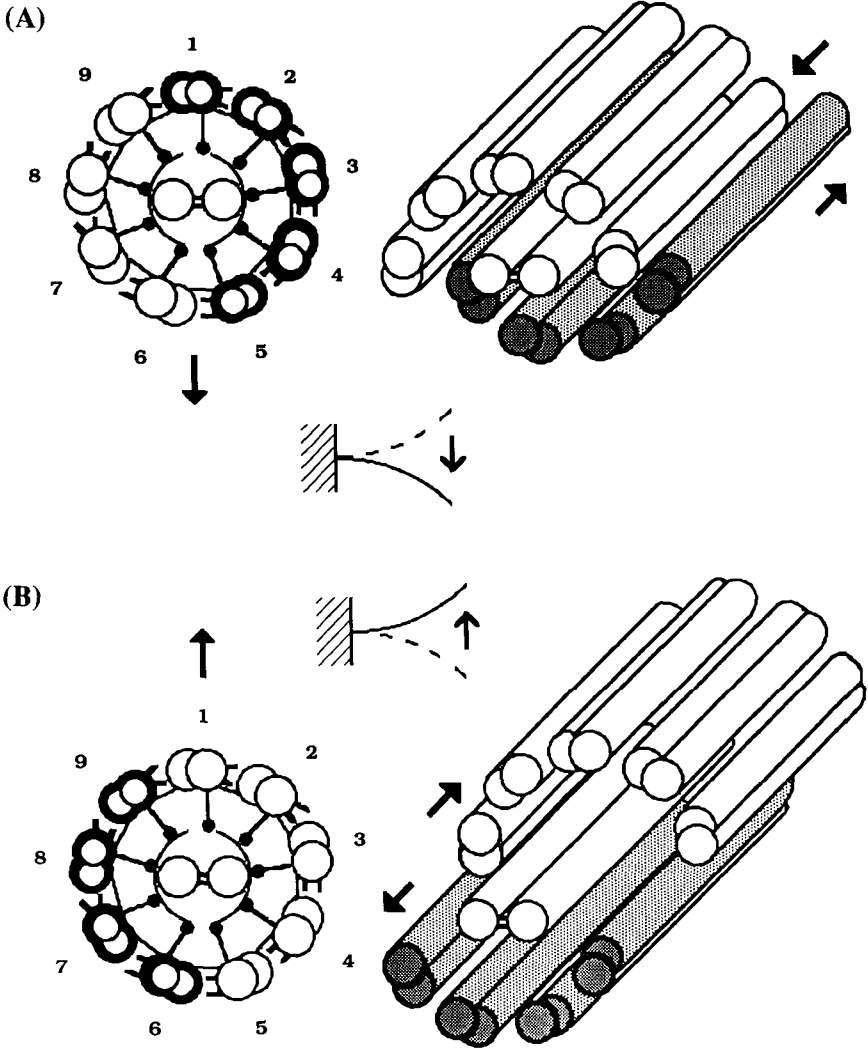
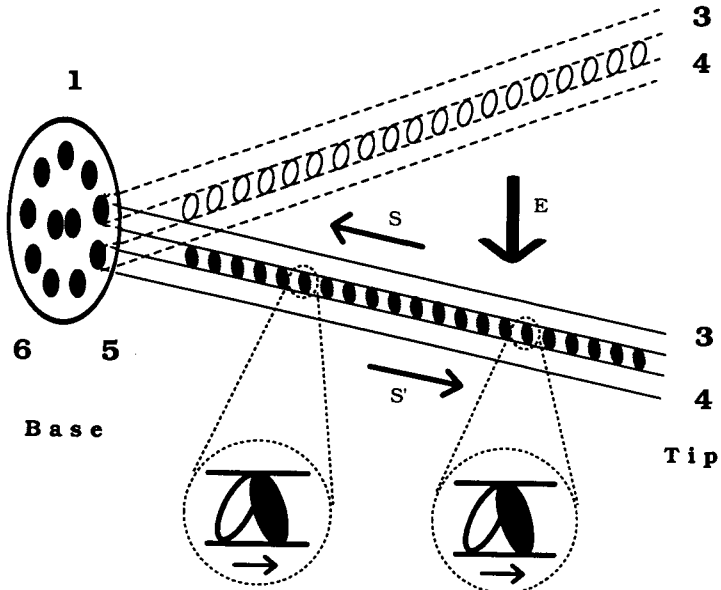


Figure 4.12 Correlations among the activity of dyneins on 9 outer doublets (left), the resultant sliding of doublets (right) and the related configuration of the cilium (middle). (A): If dyneins on the right half (doublets 1–5) of the cross section of the axoneme, especially dyneins on doublet 3, are active (as seen from base to tip, where bending direction is indicated by the arrow), ‘active’ sliding occurs between doublets 3 and 4 and at the same time ‘passive’ sliding occurs between doublets 7 and 8. Assuming that beating occurs in a plane, these 9 outer doublets are divided into two subsets according to the direction of sliding: the upper half (doublets 8–3) and the lower half (doublets 4–7) of the axoneme. The resultant planar bending is shown in the middle panel. (B): If dyneins on the left half (doublets 6–9) of the axoneme, especially dyneins on doublet 7, are active, the sliding direction is reversed and the cilium bends toward the opposite side.

(A)



(B)

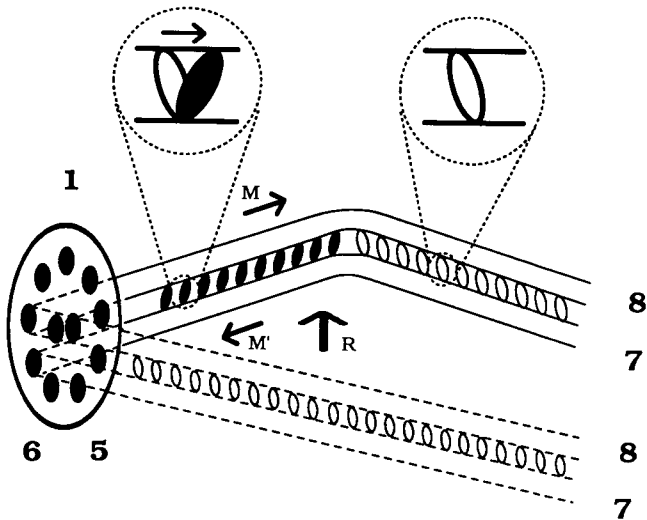


Figure 4.13 Correlations between the strength of 'triggering' interaction and the beating pattern of the cilium. (A): The power stroke of most of the dyneins on doublet 3 is triggered at once (as shown by the dark circles), when there is strong coupling between dyneins along the length of this doublet. Synchronous sliding results (indicated by arrows S and S') and the effective stroke is produced (indicated by arrow E). (B): When dyneins on doublet 7 are weakly coupled, the power stroke of the dyneins (shown by dark circles) is triggered in the restricted region of the doublet. As a result of this local activation, metachronous sliding occurs (indicated by arrows M and M') and the recovery stroke is generated (indicated by arrow R). Flagellar beating patterns are ascribed to this type of metachronous sliding alternately occurring on the two halves of the axoneme.

a restricted region along the length of the cilium to form a bend (Sleigh and Barlow, 1982).

One can expect that synchronous sliding occurs when the active processes of most dyneins on the same doublet are strongly coupled by the sliding movement of the doublet itself, and undergo their mechano-chemical cycles almost as a unit. Metachronous sliding, however, takes place when there is weak coupling between dyneins and they perform the mechano-chemical cycles in a limited region. This suggests that activation of dyneins may be triggered in two different ways, one essentially local and one occurring almost simultaneously throughout most of the length of the axoneme (Rikmenspoel and Sleigh, 1970; Sleigh and Barlow, 1982).

4.5 Dynamics of individual flagella and cilia

4.5.1 Excitability and oscillations in dynein cycles

In the preceding section, we examined how molecular dynamics is amplified into the macroscopic behaviour of flagella and cilia. However, we have not examined what properties are essentially important for generating bending waves. Investigation of the ability of 'modified' flagella to initiate and propagate bending waves is helpful in answering this question. Flagella are modified by damaging and constraining local regions, or inversely reactivating a specific region. Using this technique we can focus on the function and role of particular regions of the flagellum.

The pulsed-laser microbeam is one possible method of modifying a flagellum as it causes an almost instantaneous lesion or break. Goldstein (1969, 1974) amputated sea-urchin sperm flagella during steady-state bending and observed that pre-existing bends in an amputated flagellum propagated more or less normally to the tip, but that no new bends were initiated by the amputated flagellum. Mechanical constraint by a microneedle during the bending movement gave similar results (Okuno and Hiramoto, 1976). It was also found that bends, passively initiated by a microneedle, propagated to the tip with a constant bend angle (Okuno and Hiramoto, 1976).

Instead of inhibiting them, reactivating particular regions of a flagellum reveals other aspects of flagellar function. Triton-extracted 'model' flagella were placed in a reactivation solution without ATP but local reactivation was achieved by iontophoretic application of ATP (Shingyoji *et al.*, 1977). Some amount of ATP applied to a relatively straight region of the axoneme caused a local bend, while a much smaller amount of ATP was enough to straighten this bend with consequent displacement of the bend in the distal direction. On the basis of these results, Shingyoji *et al.* (1977) speculated that a bend was able to propagate even in a low concentration of ATP once it was formed, though a new bend would not be initiated at this concentration.

All these observations suggest that the process of bend initiation is different from the process of bend propagation. When considering self-

organization in non-equilibrium thermodynamics *excitability* is defined as the capability of a system, initially at a 'resting' state, to trigger an 'action' in response to superthreshold perturbations, while *oscillations* are considered to be sustained autonomous phenomena. Bend propagation and bend initiation may be interpreted in terms of excitability and oscillations in dynein mechano-chemical cycles, respectively. In the following chapters theoretical models are developed to account for flagellar and ciliary movements based on these assertions.

4.5.2 *Excitability, oscillations and bursts in ciliary beat cycles*

Oscillations and excitability are much more obvious when we consider the behaviour at the level of an organelle. Detailed experimental observations identify many 'oscillatory' and 'excitable' cilia.

'Oscillatory' cilia exhibit repetitive beat cycles, where ciliary activity is normally continuous over many cycles alternating between effective and recovery strokes. Cilia of protozoa such as *Opalina* and *Paramecium* belong to the 'oscillatory' type. 'Excitable' cilia, however, normally rest every cycle at the end of either the recovery or the effective stroke. Compound cilia (or comb plates) of ctenophores *Pleurobrachia* (Sleigh and Jarman, 1973) are examples of 'excitable' cilia that rest at the end of the recovery stroke and commence the beat cycle with a full effective stroke. Cilia of mammalian tracheal epithelium and similar mucus-propelling cilia (Sanderson and Sleigh, 1981) are the other examples of 'excitable' cilia which rest at the end of the effective stroke.

Unlike the above-mentioned cilia the macrocilia of the ctenophore *Beroë* stop at two different positions: the end of the effective stroke and the end of the recovery stroke (Tamm, 1983). The resting phase at the end of the effective stroke is the more stable, because initiation of the recovery stroke requires a mechanical stimulus though the effective stroke is initiated spontaneously after a rather constant time delay without external stimuli. Of course, it is possible for mechanical stimulation to trigger this effective stroke at an earlier time.

The anal cirri of *Euplotes* show *bursts* of repeated cycles of beating. They rest between bursts in a fully extended position, about half-way through their effective stroke (see Sleigh and Barlow, 1982).

4.5.3 *Mechano-sensitivity*

Absolute and relative refractory period. Like other excitable and oscillatory systems, e.g. nerve membranes, cilia show a *refractory period* of insensitivity to mechanical stimuli before responding with an active stroke. On running photographic film through a slit camera Murakami (1963) recorded the movement of motile cilia in ciliary pads of *Mytilus* gill.

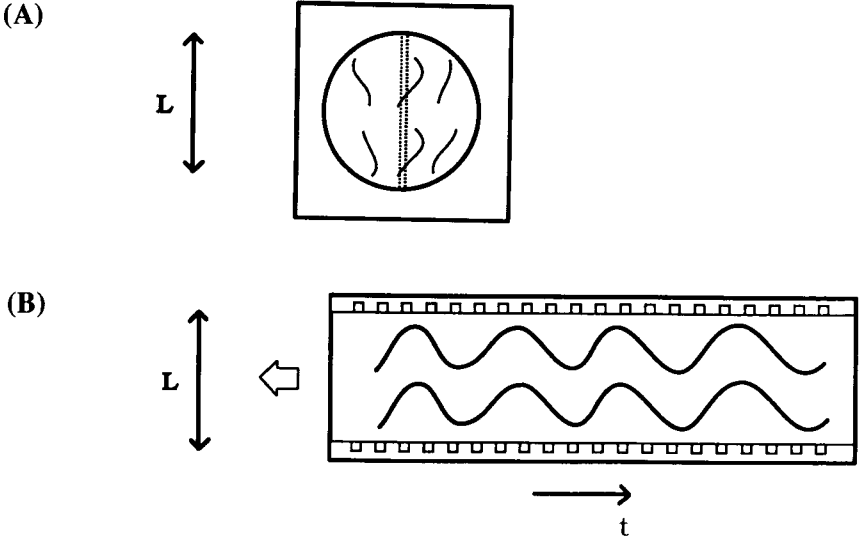


Figure 4.14 Schematic diagrams showing how the movement of cilia is recorded by the slit camera. (A): An image of the surface of cilia within a ciliary pad is projected through a narrow slit (indicated by dot lines) of a microscope onto the screen. (B): The image of the moving cilia is recorded on photographic film running at a constant speed to the left (indicated by an open arrow). On the image, an abscissa (t -axis) corresponds to time elapsed and an ordinate (L -axis) corresponds to the surface of the cilia seen through the slit. Two wave-like traces thus represent the movements of two rows of cilia parallel to the slit.

Figure 4.14 illustrates how the microscopic image was projected onto photographic film running at a constant speed. Cilia are illuminated so that each cilium appears to be a light spot at a given time. When such microscopic images were projected onto the running film, wave-like traces were recorded. Note that this device records exclusively the component of ciliary movement parallel to the slit. Thus measurement of amplitude, frequency and the conduction velocity of metachronal waves record the movement in this component.

Murakami investigated temporal responsiveness of motile cilia to mechanical stimuli. *During the recovery stroke* he made a momentary shift of a microneedle *in the direction of the effective stroke*. In response to this stimulation, the cilia showed an extra effective stroke. As shown in Figure 4.15, the magnitude of the resulting effective stroke depended on the timing when the stimulation was given to cilia exhibiting the previous recovery stroke. Such temporal responsiveness (or ‘graded’ responsiveness) can be interpreted as the absolute or relative refractory period during which mechanosensitivity of motile elements is lost or reduced, respectively.

Since the extra effective stroke was not initiated *during the recovery stroke*

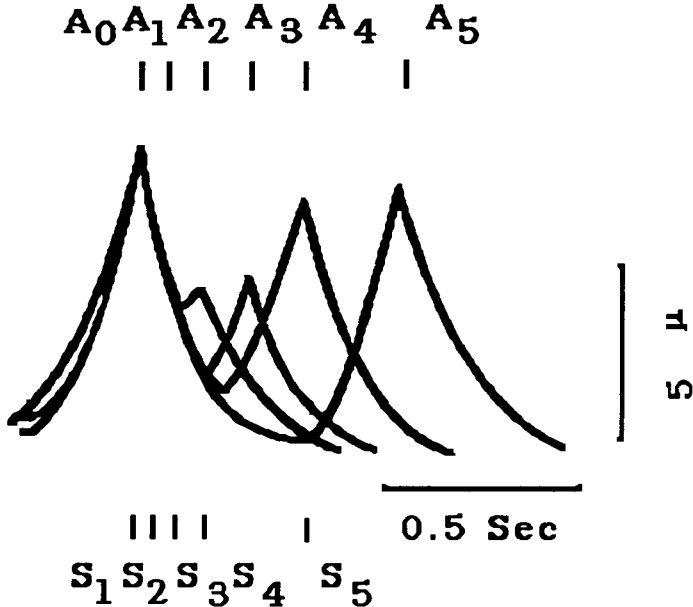


Figure 4.15 Temporal responsiveness of motile cilia to mechanical stimuli. Each mechanical shock S_i induces a corresponding response A_i ($i = 1, 2, 3, 4$ and 5). A_0 indicates normal stroke before stimulation. The stimulation signals indicate the moments of microneedle, $10 \mu\text{m}$ per 0.1 s . From Murakami (1963). Reprinted with permission.

by a mechanical stimulus *in the direction of the recovery stroke* (Murakami, personal communication), the effectiveness of a stimulus seems to be a function of its direction. However, the situation is much more complicated because no extra recovery stroke was ever triggered *during the effective stroke*, irrespective of the direction of stimulation (Murakami, 1963). This means that the mechano-sensitivity of motile cilia to stimuli depends, not only on the direction of the stimulus, but also on the direction of the beating cilia (Fig. 4.16).

Since cilia in a ciliary pad possess an intrinsic rhythm (i.e. 'oscillatory' property), the effects of pre-existing beating makes it difficult to investigate directional mechano-sensitivity. For this reason, 'excitable' cilia are more suitable for this investigation.

Directional mechano-sensitivity. Tamm (1983) used macrocilia of the ctenophore *Beröe* resting *at the end of the effective stroke* to study directional sensitivity (Fig. 4.17A). These compound cilia are $35\text{--}40 \mu\text{m}$ in length and contain many thousands of axonemes within a common membrane.

When the mechanical stimulus by a microneedle is applied to the 'excitable' macrocilia *in the direction of recovery stroke*, a recovery stroke is

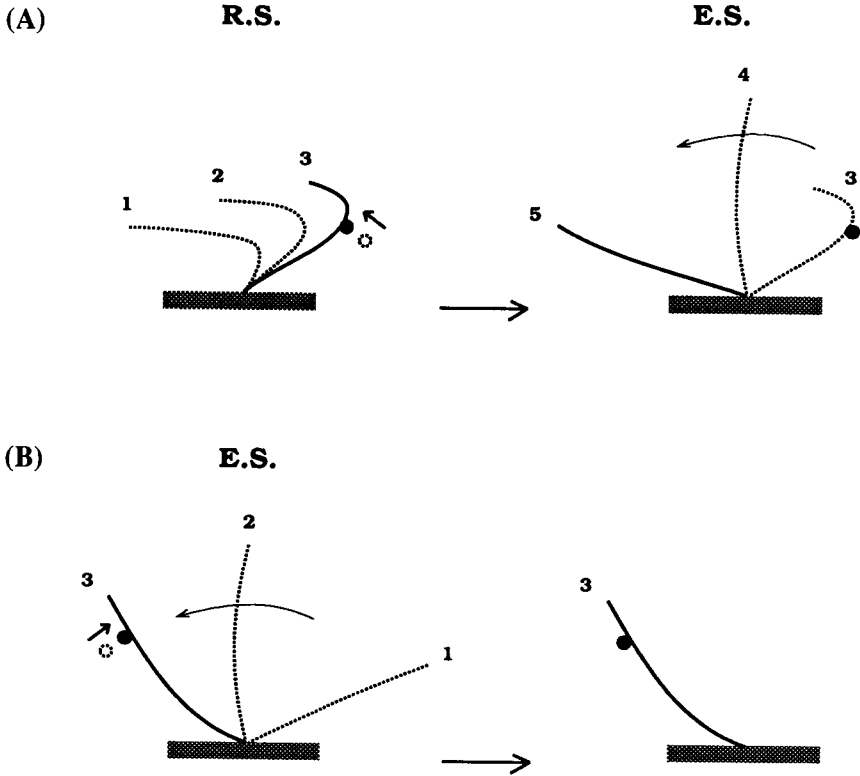


Figure 4.16 Schematic illustrations showing directional sensitivity of 'beating' cilia to mechanical stimuli. (A): Effective stroke (E.S.) is triggered during recovery stroke (R.S.) when a microneedle (black cross-section) is moved in the direction of the effective stroke. (B): Recovery stroke is not initiated by a microneedle irrespective of the direction of stimulation.

triggered. However, movement of the microneedle in the opposite direction does not stimulate the recovery stroke. Similarly macrocilia *resting at the end of the recovery stroke* (although this state is less stable than that at the end of the effective stroke) can generate an effective stroke in response to a mechanical stimulus in the direction of the effective stroke. Therefore the direction of the active bending response reflects the direction of the stimulus.

As bending in opposite directions is considered to result from the activation of doublet sliding alternately in two halves of the axoneme, the directional sensitivity of the cilia to mechanical stimuli indicates that each set of microtubules can be activated independently by mechanical stimuli applied in the direction of force generation.

In contrast, the compound cilia of the ctenophore *Pleurobrachia* resting at the end of the recovery stroke showed different mechano-sensitivity to

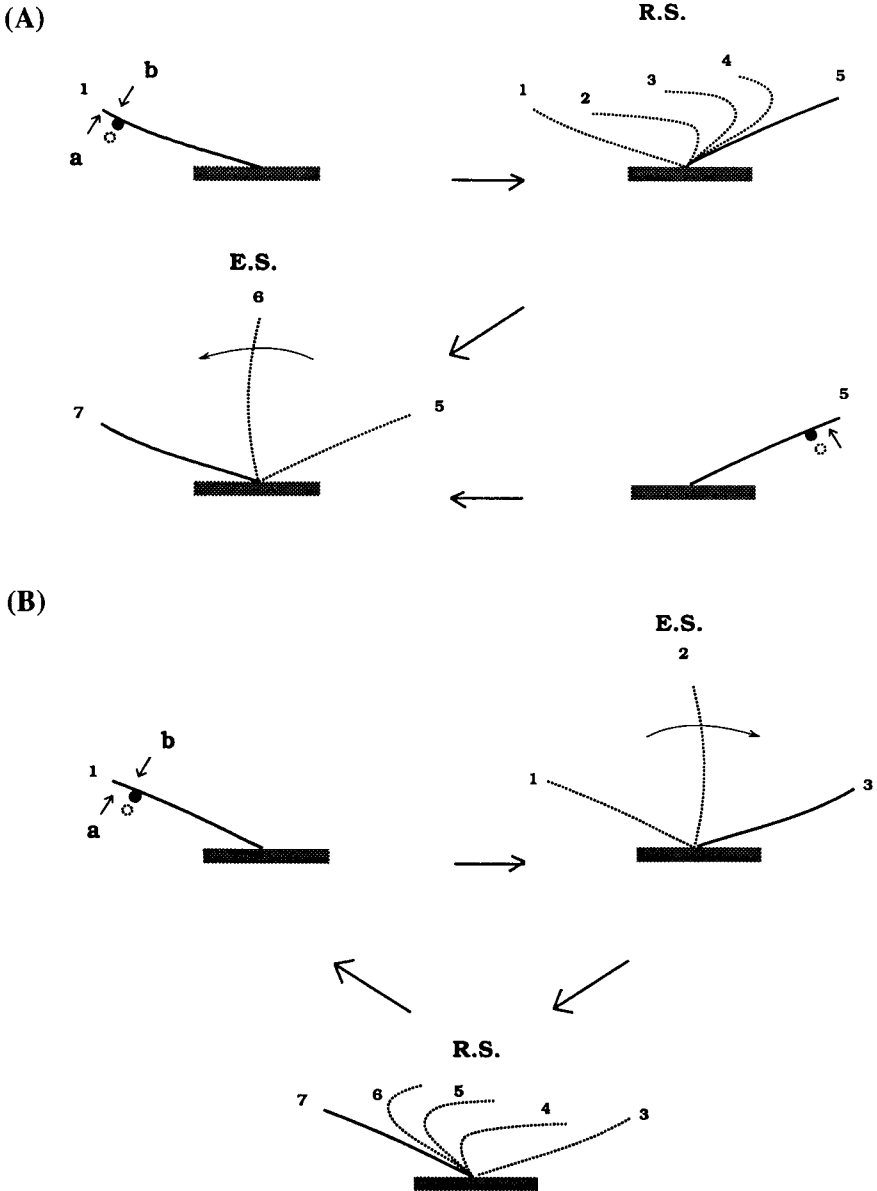


Figure 4.17 Schematic illustrations showing directional sensitivity of 'quiescent' cilia to mechanical stimuli. (A): Compound cilia of ctenophore *Beröe* resting at the end of the effective stroke (E.S.) as well as at the end of the recovery stroke (R.S.). Mechanical stimuli in the direction of the recovery stroke (shown by *a*) cause the recovery stroke, while mechanical stimuli in the opposite direction (shown by *b*) produce no effect on the initiation of the recovery stroke (upper left). At the end of the recovery stroke cilia exhibit a resting phase, though it is not very stable, as an effective stroke is intrinsically triggered (from upper right to lower left). Mechanical stimuli applied before the intrinsic returning phase can initiate the effective stroke (from lower right to lower left). (B): Compound cilia of the ctenophore *Pleurobrachia* resting at the end of the recovery stroke. Mechanical stimuli in either direction (shown by *a* and *b*) can stimulate the effective stroke. The recovery stroke occurs automatically.

external stimuli (Sleigh and Jarman, 1973). A single beat cycle, consisting of the effective and recovery strokes, is triggered by the shift of a microneedle, irrespective of the direction of the stimulus (Fig. 4.17B).

4.5.4 *Quantal steps in angular changes*

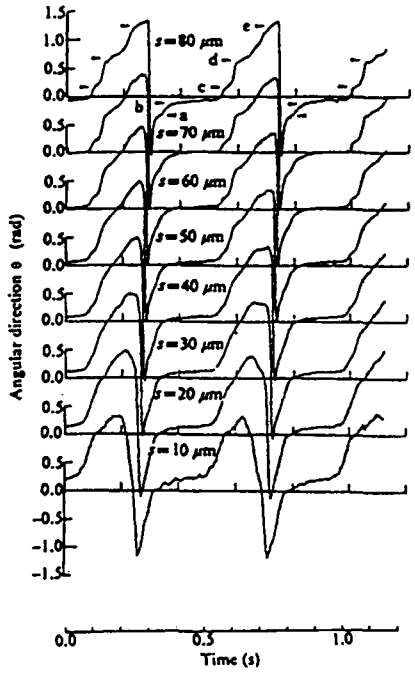
Large abfrontal cilia (giant compound cilia) of *Mytilus* gill are suitable for cinematographic analysis, because they exhibit planar and slow beat cycles. Baba (1979) examined successive beat cycles and found that the effective stroke consists of alternating rapid and slow phases of angular changes particularly in the most distal part of the cilium.

Figure 4.18A shows changes in angular direction as a function of time at different points (indicated in the figure) along a cilium. The effective stroke is interrupted five times by slow phases of various durations (indicated by arrowheads a, b, c, d and e). Figure 4.18B shows a histogram of the slow phases over four successive beats. Five peaks appear in this histogram corresponding to the five slow phases during the effective stroke. These observations suggest that the microtubules slide in quantal steps or, simply stated, with 'intermittent' movements.

The reason why such intermittent movements occur particularly in the distal part of a cilium is as follows. Supposing that active sliding takes place simultaneously between doublets on one side of the axoneme, a single large bend and hence an effective stroke is formed (cf. Fig. 4.8C). However, this is not always the case when the effective stroke begins earlier in the proximal region. A space-dependent change in angular movement results and two bends are formed: the proximal bend pointing in a forward direction and the distal bend pointing backward. Gibbons and Gibbons (1972) referred to the resultant proximal and distal bends as *principal* and *reverse bends* respectively, noting that the proximal bend was sharper than the distal bend. (In asymmetric bending waves the bends with larger angles are usually defined as the principal bends.) The effective stroke is performed with a continuous increase in the principal bend, whereas the reverse bend initiates and propagates to counteract the resultant rapid motion in the distal region. This alternating initiation and propagation of the reverse bend in the distal region may be responsible for the slow- and rapid-phase angular changes observed in the distal part.

Baba (1979) interpreted these abrupt changes in sliding speed (or angular velocity) in terms of axonemal substructures. The sliding speed is essentially determined by the balance between the active force generated by dyneins, and the resistive force due to the strength of the radial link systems such as the strength of radial spokes. When dyneins are activated to generate force in the proximal region, the microtubules in this region slide to form the principal bend near the base. However, dyneins in the distal region are not active enough to cause sliding, reflecting the fact that the angular direction of

(A)



(B)

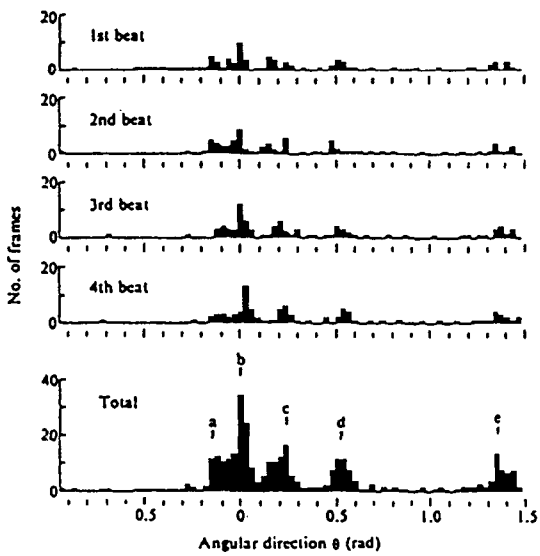


Figure 4.18 Changes in angular direction of large abfrontal cilia of *Mytilus* gill. The length of the cilium is $90 \mu\text{m}$. (A): The angular direction is plotted against time at $10 \mu\text{m}$ intervals along the cilium. Arrowheads a, b, c, d and e show slow phases during the effective stroke. s is the distance from the base along the cilium. (B): Histogram of angular direction of the distal part of a cilium during the effective stroke. The upper four histograms plot the four successive effective strokes. Each histogram represents the relationship between the number of frames and the angular direction, within a range of 0.03 rad widths. The framing speed is 270 frames per second. The bottom histogram is a combination of the four histograms. From Baba (1979). Copyright © Macmillan Magazines Ltd. Reprinted with permission.

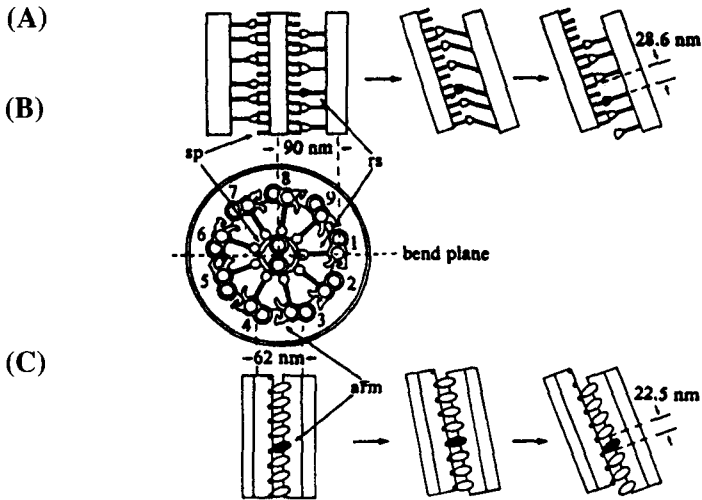


Figure 4.19 Schematic diagrams showing the dynamic relationship between the axonemal substructures and the bent cilium. (A): A side view of a segment of the axoneme showing the relationship between doublet 1 and the central tubule. The stroke distance of the radial spokes (rs) during interactions with the central sheath projections (sp) corresponds to 28.6 nm. This stroke distance causes the segment to change its direction by 0.32 rad, on the assumption that the vertical centre-to-centre distance between the doublet 1 and the central tubule is always 90 nm. (B): A cross-sectional view of the axoneme. (C): A side view showing the relationship between doublets 3 and 4. Dyneins on doublet 3 undergo a complete cycle of attachment–detachment interactions with doublet 4 to slide by 22.5 nm. This causes the segment to change direction by 0.36 rad on the assumption that the centre-to-centre distance of adjacent doublets is 62 nm. From Baba (1979). Copyright © Macmillan Magazines Ltd. Reprinted with permission.

this region is in its slow phase at this stage. As a result, the reverse bend appears in the distal region. The rapid phase appears when the force generated by dyneins, plus the elastic force of the bent cilium, overcomes the resistance in the distal region in accordance with the propagation of sliding toward the tip. This releases the energy stored in the elastic components, thus sliding in the distal region tends to cease again. This effect appears as the second slow phase. At this time, dyneins and radial spokes on the sliding doublet change position relative to their sites of interaction on the adjacent doublet and the central tubules, respectively. This suggests a cyclic regulation of the force generation and resistance (Fig. 4.19).

For simplicity, let us consider dyneins on doublet 3 and spokes on doublet 1, since they are efficient in generating force and resistance due to their location relative to the bend plane (see Fig. 4.19B). During one cycle of interaction, dyneins and radial spokes are thought to slide by 22.5 nm (see Takahashi and Tonomura, 1978) and 28.6 nm (see Warner and Satir, 1974),

respectively. Assuming a basic relationship of $\theta = u/h$ where θ is the bend angle, h the centre-to-centre distance between interacting filaments, and u the net sliding displacement. These sliding displacements in turn correspond to 0.36 rad for dyneins on doublet 3 and 0.32 rad for radial spokes on doublet 1.

An interesting fact is that the observed minimum change in angle (about 0.2–0.3 rad) corresponds to the theoretical minimum change in angle (say, 0.32 rad for radial spokes). This suggests that multiple stable states are possibly induced by the periodic arrangement of dyneins and spokes within the axoneme, which may in turn account for movement of the cilia.

Of course, further investigations using ‘simple’ cilia are necessary to clarify whether the intermittent bending movements of *Mytilus* ‘compound’ cilia reflect an inherent property of the axoneme or interactions of many component cilia.

4.5.5 Intermittent flagellar beating

The distally propagating waves, typical of flagella of protozoa and spermatozoa, propel the cell through a medium. However, flagella of trypanosomatids, *Crithidia oncopelti* (Holwill, 1965) or *Leishmania* (Alexander and Burns, 1983), show an unusual ability to propagate bending waves from either the base or the tip. Normally these flagella propagate bending waves from tip to base, by which the cell is pulled in the direction of the flagellum. This proximally directed wave propagation is intermittently replaced by a distally directed wave propagation in response to mechanical, chemical, or electrical stimuli (Holwill, 1965; Holwill and McGregor, 1974).

Without such stimuli, these flagella could show an ability to reverse the direction of wave propagation (Holwill, 1965). Figure 4.20 shows such intermittent movements of a *Leishmania* promastigote. The flagellar-like tip-to-base waveforms are intermittently interrupted by five successive ciliary-like base-to-tip waveforms. Each ciliary-like beat is initiated with an effective followed by a recovery stroke and has the effect of rotating the animal by ~10–30°. As a result, the cell rotates about 180°. This alternating pattern of beating thus seems to be an avoiding reaction that allows the organism to reverse its direction of movement.

In abnormal conditions where the viscosity of the medium is increased (Holwill, 1965) or some chemical agent is added (Alexander and Burns, 1983), it is found that two waves travel in opposite directions. When the two waves pass each other the flagellum appears to be frozen. The following wave propagates along the flagellum from tip to base (Holwill, 1965). This phenomenon may be somewhat analogous to the non-annihilating metachronal waves propagating over a mat of cilia (see Subsection 4.6.2).

Since there are no special structures at the tip that are initiating the tip-to-base bending waves, the reversal of the direction of propagating waves

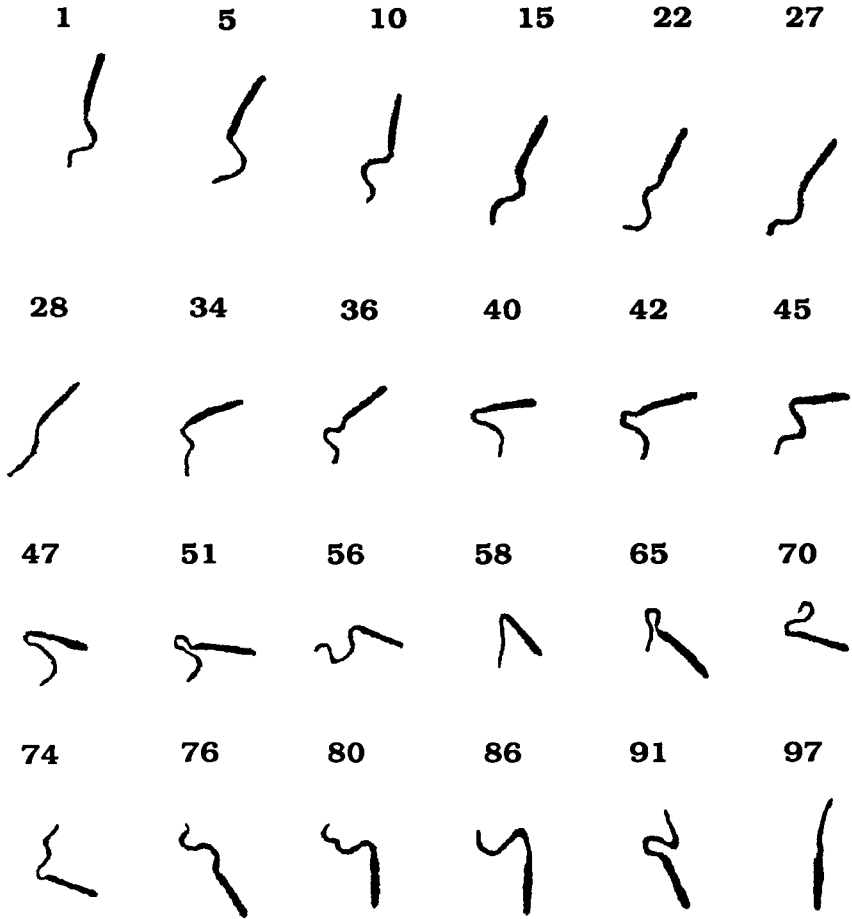


Figure 4.20 Movement of a free-swimming *Leishmania* promastigote. The cell is being propelled forward ($70 \mu\text{m/s}$) by the flagellar-like tip-to-base waveform (frames 1–27). These forward movements are suddenly interrupted by five successive ciliary-like base-to-tip beats (frames 28–36, 36–45, 45–56, 56–74 and 74–91). The framing speed is 50 frames per second. From Alexander and Burns (1983). Copyright © Macmillan Magazines Ltd. Reprinted with permission.

remains a mystery to be solved. Attempts have been made to solve the mystery by isolating the flagellum from the cell by laser irradiation (Goldstein *et al.*, 1970; Goldstein, 1974). Interestingly, the amputated flagellar segments could beat, not only from the tip or the irradiated point, but also first from the tip and then from the irradiated point (Fig. 4.21) or vice versa. This indicated that the influence of the cell was not important in the reversal of wave propagation.

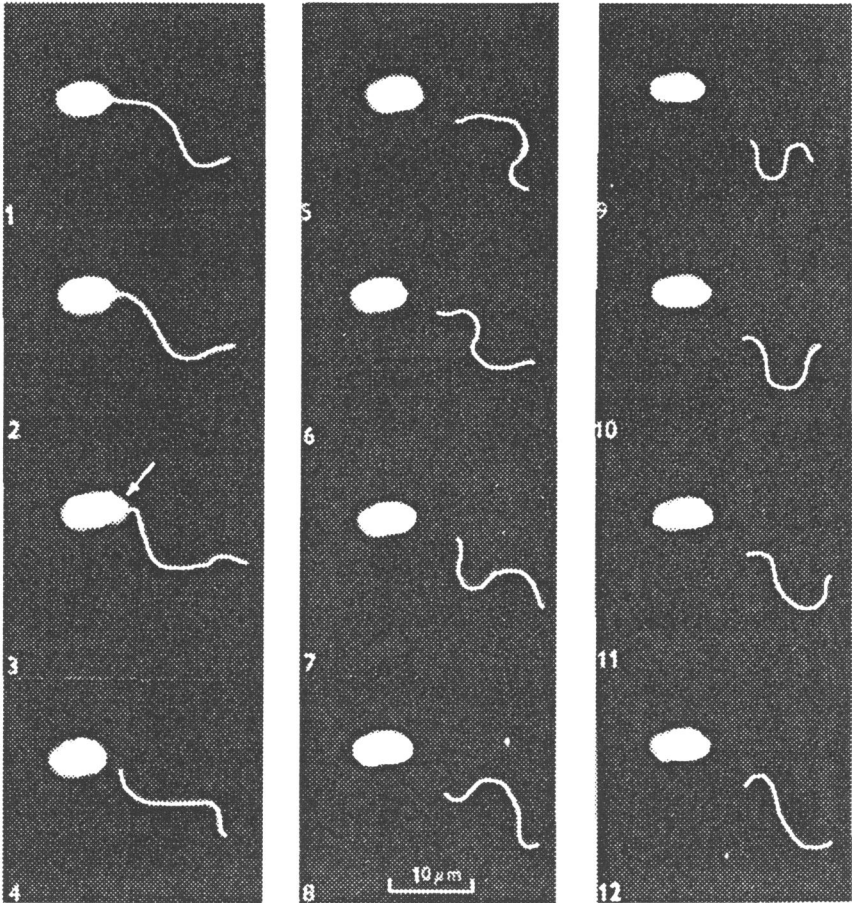


Figure 4.21 Selected frames illustrating the effect of laser radiation on a flagellum of *Crithidia oncopelti*. Panels 1 and 2: Tip-to-base waves are observed before irradiation. Panels 3 and 4: The laser beam hits a basal region. The flagellum is completely severed from the cell. The disturbance produced by the laser beam is indicated by the arrow. Panels 5–8: After irradiation, bends continue to propagate from the tip of the isolated flagellum. Panels 9–12: At a later time (about 1 s), bends are now traveling toward the tip. Elapsed time (ms): Panel 1, 0; 2, 10; 3, 20; 4, 30; 5, 120; 6, 160; 7, 200; 8, 230; 9, 900; 10, 930; 11, 970; 12, 1020. From Goldstein *et al.* (1970). Reprinted with permission of the Company of Biologists Ltd.

Further understanding came from an investigation of demembrated model flagella under various chemical conditions (Douglas and Holwill, 1972; Holwill and McGregor, 1975). The results suggested that Ca^{2+} was able to control the direction of the bend propagation, because at low concentrations of Ca^{2+} (less than 10^{-7} M) only tip-to-base waves were observed, whereas

at higher concentrations only base-to-tip propagations were seen (Holwill and McGregor, 1975; 1976). There is always the possibility, however, that the control mechanism suggested by these model systems may be different from the intact mechanism in the living cell.

Intermittent swimming of sea-urchin sperm of *Tripneustes gratilla* (a Hawaiian species) was observed in both living cells (Gibbons, 1980; 1981b; Gibbons and Gibbons, 1980b) and demembrated models in a reactivation medium containing Ca^{2+} (Gibbons, 1986). This phenomenon involves the *stopping* and *starting transients* of flagellar movement (Fig. 4.22). The stopping transients are triggered by the abrupt failure of a reverse bend to be developed at the basal end of the flagellum at the expected time in the beat cycle. As a result, the preceding principal bend remains at the base and the flagellum becomes *quiescent*, maintaining a shape that resembles a cane with a sharp bend in the basal region and little curvature in the rest of the flagellum (Gibbons and Gibbons, 1980a). The starting transients begin when a reverse bend is initiated at the base. Comparison of the timing of the peaks and the valleys in θ_{tip} before and after the quiescent episode indicates that the flagellar oscillation does not maintain its phase but shifts by about half a cycle corresponding to the quiescent interval (Fig. 4.22B).

Intermittent oscillations were also observed in the bending pattern of short demembrated sea-urchin sperm flagella (Brokaw, 1982). The sperm head was attached to a microscope slide and no movement of the head was allowed. As illustrated in Figure 4.23, flagella shorter than $4\ \mu\text{m}$ were usually observed to beat with irregular duration of pauses before initiation of new bends (i.e. onset of sliding reversals). It is interesting to note that pauses in bend initiation are also evident in the discontinuous beating cycle of 'excitable' cilia, as mentioned in the preceding sections.

From the above evidence, I suspect that intermittent bending movements are not 'species specific', but are common to all cilia and flagella (see Chapters 7 and 8).

4.6 Dynamics of groups of flagella and cilia

4.6.1 Synchronism and metachronism

It has been observed that two or more nearby flagella, originally beating with different frequencies, tend to beat with a common frequency and wavelength due to mechanical coupling via moving fluid near the flagella (Fig. 4.24). Such behaviour is typical of a certain class of nonlinear oscillators and is called *synchronization*.

As pointed out by Gray (1928), a well-known example of this phenomenon is given by two pendulum clocks hung on a common support. Because each clock transmits its vibrations to the support and at the same time receives from the support vibrations set up by the other, the pendulum of the slower

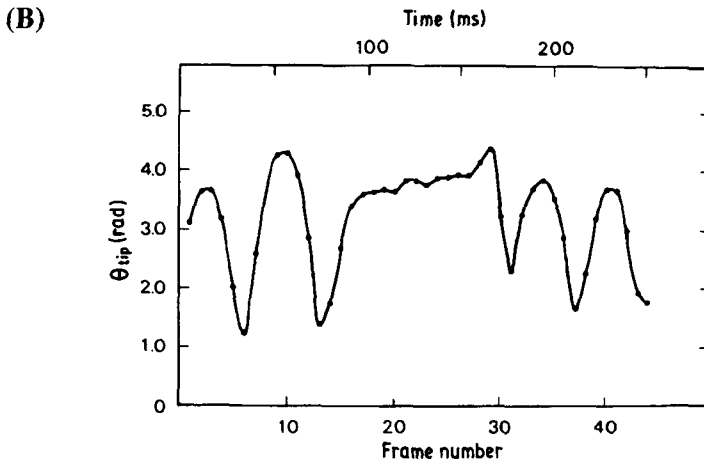
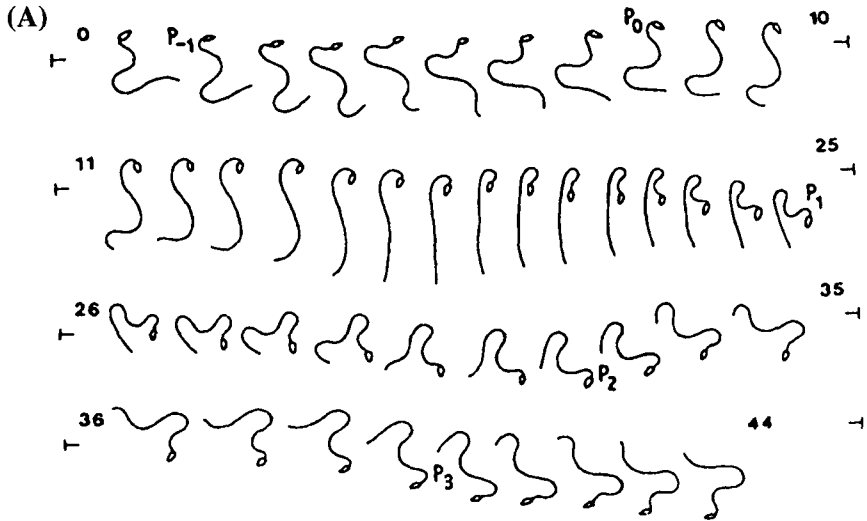


Figure 4.22 Intermittent swimming of sea-urchin sperm of *Tripneustes gratilla*. (A): Tracings of flagellar waveforms showing the stopping transient (frames 8–16), brief quiescence (16–17) and the subsequent starting transient (18–32). The angular orientation and vertical position of each tracing are fixed, though the relative horizontal positions are arbitrary. The framing speed is 170 frames per second. (B): The total angle between the central axis of the sperm head and the tangent to the flagellum at its tip, θ_{tip} , as a function of time. Non-zero mean value of θ_{tip} indicates the degree of asymmetry inherent in the flagellar waveform. From Gibbons (1986). Reprinted with permission of Chapman & Hall.

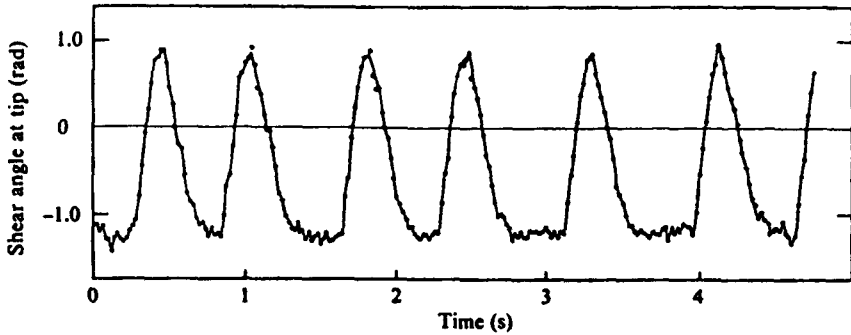


Figure 4.23 The total angle between the axis of the sperm head and the distal 0.5 μm of a very short sperm flagellum with a length of only about 3 μm as a function of time. The movement is asymmetrical with respect to the axis of the sperm head: the bend in one direction is larger (about 1.2 rad) than in the other (about 0.9 rad). Brokaw (1982). Reprinted with permission of Cambridge University Press.

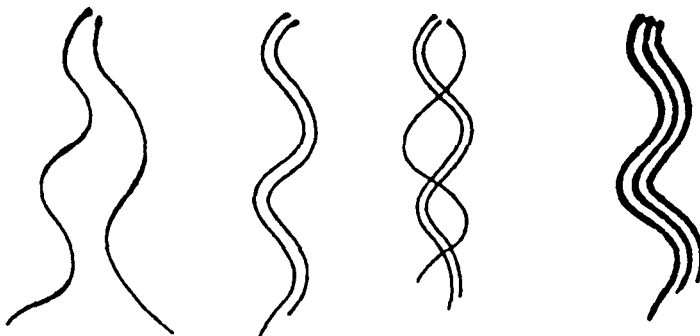


Figure 4.24 *Spirochaeta balbianii* exhibiting synchronism and metachronism. Each individual flagellum has a different waveform. When positioned close to each other, their movements tend to be coordinated by hydrodynamic interaction. Forces generated in the transverse direction (horizontal direction in the figure) presumably exceed those in the main axis of the flagellum (vertical direction in the figure). As a result, synchronization occurs parallel to the transverse forces. Metachronal waves propagate perpendicular to the direction of synchronization. From Gray (1928). Reprinted with permission.

clock is forced to swing by the faster clock resulting in acceleration of its vibrations. This example is simpler than the case of flagella because clocks counting time give rise to only ‘temporal’ synchronization whereas flagella generating bending waves exhibit both ‘temporal’ and ‘spatial’ synchronization.

Like other wave phenomena, populations of synchronized flagella transmit wave fronts and possess two coordinates: one along which all elements

oscillate in phase (i.e. zero phase-shift) leading to synchronization and another, perpendicular to the first coordinate, along which elements beat out of phase (i.e. maximal phase-shift) and cause metachronal waves with a particular wavelength (see Machemer, 1975). In Figure 4.24, the coordinates of *synchronism* and *metachronism* correspond to the horizontal and vertical axes, respectively.

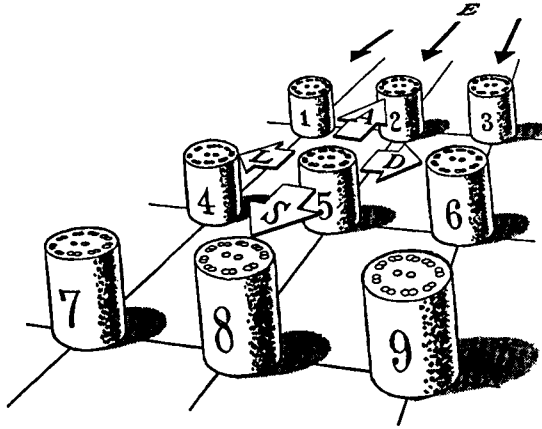
Synchronism and metachronism are also found in populations of cilia. Cilia are generally arranged in rows across and along the cell surface of protozoa and on respiratory-tract epithelia. The movements of adjacent cilia are synchronized to beat in phase along one direction, but out of phase along another direction which is at right angles (often perpendicular) to the lines of synchronism. Waves of ciliary movements, known as metachronal waves, propagate along this out-of-phase direction. The metachronal waves passing across the ciliated surface would look something like the waves of motion of wheat when the wind blows over a field. The advantages of the metachronal coordination of cilia are to increase the amount of fluid propelled and to maintain continuity of flow (see Sleight, 1976).

Individual ciliary movement takes a different form depending on the ciliary system (e.g. planar, helical, oscillatory, or excitable beating). Thus, as shown in Figure 4.25, at least four main patterns of metachronism have been recognized according to the relationship between the direction of the effective stroke of the ciliary beat and the direction of propagation of the metachronal waves (Knight-Jones, 1954). When metachronal waves travel in the same direction as the effective stroke, this is called a *symplectic* metachronism. The coordination is called *antiplectic* when metachronal waves and the effective stroke point in opposite directions. When an observer, looking in the direction of metachronal wave transmission, observes an effective stroke toward the right perpendicular to the wave direction, it is called a *dexioplectic* metachronism. The mirror-image of this configuration is called *laeoplectic*.

The latter two types of metachronism are due to the three-dimensional beat cycle of the cilium. In dexioplectic and laeoplectic metachronism, the ciliary beat cycle consists of a relatively faster effective stroke, in which the cilium is extended and rotates in a vertical plane about its base, and a relatively slower recovery stroke, in which the cilium bends closer to the cell surface and rotates in a horizontal plane, either anti-clockwise or clockwise as viewed from above the plane. This sideways recovery stroke is of great advantage in reducing the resistive forces which may interfere with the continuity of the forward flow generated by the effective strokes.

Figure 4.26 illustrates the fluid volume influenced by the movement of a cilium (termed 'envelope of flow') exhibiting a beat cycle typical of the lateral cilia of *Mytilus* gill and the corresponding laeoplectic metachronal wave. Strong viscous coupling takes place between cilia in the plane of the effective stroke, as the envelope of flow of the effective stroke is more extensive than that of the recovery stroke (producing faster fluid flows during

(A)



(B)

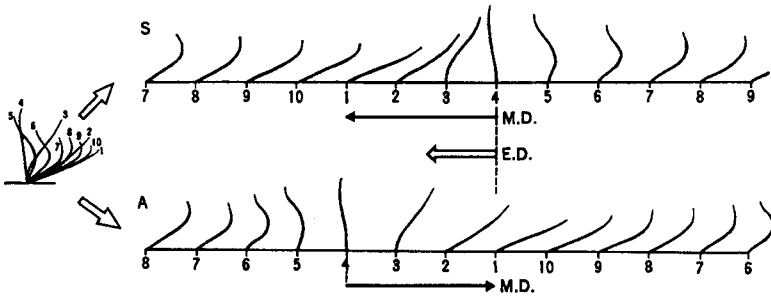


Figure 4.25 Diagram showing metachronal waves. (A): Cilia are arranged in rows across and along the cell surface. The arrow E shows the direction of the effective stroke. The arrows S, A, L and D represent the directions of symplectic, antiplectic, laeoplectic and dexioplectic metachronal waves. In the case of symplectic or antiplectic metachronism, cilia in lines (1,2,3), (4,5,6) and (7,8,9) beat synchronously. In the case of laeoplectic or dexioplectic metachronal waves, cilia in lines (1,4,7), (2,5,8) and (3,6,9) beat synchronously. (B): The full cycle of a typical ciliary beating position at equal intervals in time (left) and the position of an array of cilia at a given time (right). The upper array (denoted by S) and lower array (denoted by A) represent symplectic metachronism and antiplectic metachronism, respectively. M.D. and E.D. represent the direction of metachronal waves and the effective stroke, respectively. Each cilium has the same number assigned to the identical bending position during a cycle. From Murakami (1974). Reprinted with permission.

the effective stroke than during the recovery stroke). Moving cilia in this plane synchronize when the large envelopes of the effective strokes overlap extensively in the plane of beat. Perpendicular to the plane of the effective stroke, relatively weak coupling takes place between adjacent motile cilia because the cilia move to one side in their recovery stroke and the envelope of flow in the recovery stroke will be asymmetrical with respect to the plane

(A)

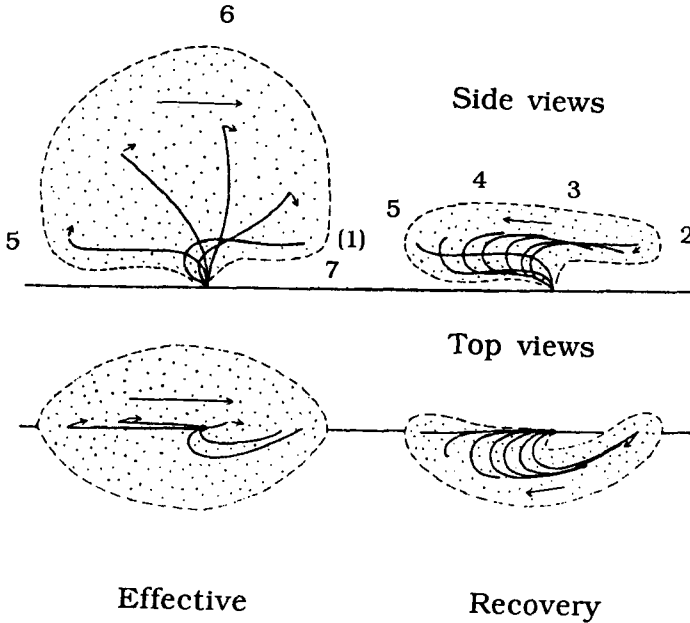


Figure 4.26 (A): The shape and relative size of the 'envelopes of flow' formed by the effective and recovery strokes of a ciliary beat. The dotted area is a rough image of the extent of the envelope. During the recovery stroke the cilium moves back in a clockwise direction (as shown in the view from above), causing asymmetry in the recovery stroke. The resulting asymmetry provides viscous coupling between adjacent motile cilia, perpendicular to the plane of the effective stroke. Every other stage in the beat cycle is numbered. The recovery stroke starts at stage 2 and ends at stage 5, followed by the effective stroke which starts at stage 5 and ends at stage 7 (or 1). From Sleight (1976). Reprinted with permission. (B): Laeoplectic metachronal waves. The cilia in row 1 (identical to row 7) are at the end of their effective stroke. The numbers assigned to the various stages of the beat cycle are the same for Fig. 4.26A and B. E.D. and M.D. indicate the direction of the effective stroke and that of the propagation of the metachronal wave, respectively. From Satir (1974). Copyright Scientific American, Inc., George V. Kelvin, all rights reserved. Reprinted with permission.

of the synchronism. Through this asymmetrical viscous coupling, the lateral movement of one cilium in its recovery stroke can interact with the lateral movement of the adjacent cilium in the direction of the sideways recovery stroke. Consequently, adjacent cilia will be out of phase with one another, hence the metachronism.

Table 4.1 shows examples of the activity of cilia and the types of metachronism in the ciliary systems. *Opalina* is an example of an organism showing the symplectic metachronism, the comb plates of ctenophores *Pleurobrachia* show the antipectic type; the metachronism of *Paramecium* is regarded as a dexioplectic type; and the lateral cilia of *Mytilus* gill display laeoplectic metachronal waves (see Sleight, 1976).

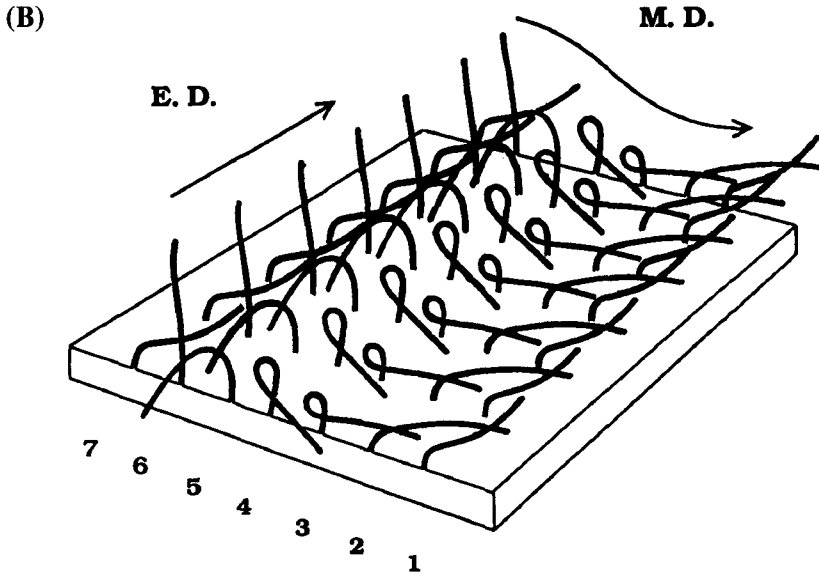


Table 4.1 Examples of cilia showing metachronal waves

Type of ciliary system	Arrangement	Type of cilium	Metachronal type	Ciliary activity
<i>Opalina</i>	Field	Simple	Simplectic	2-D Oscillatory
Ctenophore <i>Pleurobrachia</i>	Single row	Compound	Antiplectic	2-D Excitable-R
<i>Paramecium</i>	Field	Simple	Dexioplectic	3-D Oscillatory
<i>Mytilus</i> lateral cilia	Band	Simple	Laeoplectic	3-D Excitable-R
Rabbit tracheal cilia	Field	Simple	Antilaeoplectic	3-D Excitable-E

2-D and 3-D represent 2-dimensional and 3-dimensional beats, respectively. Excitable-R and Excitable-E represent properties of cilia resting at the end of the recovery stroke and at the end of the effective stroke, respectively.

4.6.2 Strange behaviour of ciliary activity

Cilia often exhibit irregular spatio-temporal orders over the ciliated surface. In order to understand mechanical interaction between individual cilia, it is useful to get a 'model' system for a dense mat of cilia by using micro-

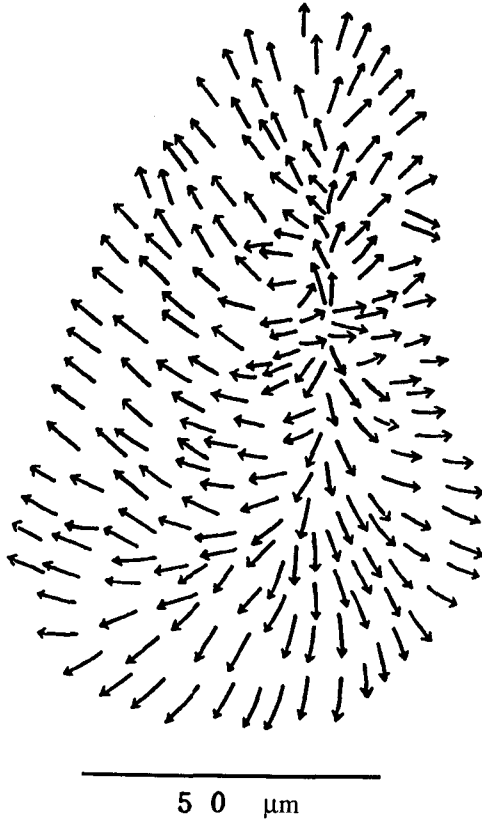


Figure 4.27 Tracings showing the surface view of motile cilia in a ciliary pad of *Mytilus* gill. Each arrow indicates the direction of the effective stroke produced by an individual cilium. From Murakami (1963). Reprinted with permission.

surgery techniques. Two typical ciliary model systems are given: one comes from water-propelling cilia and the other from mucus-propelling cilia.

Water-propelling cilia. Murakami (1963) isolated a ciliary pad from *Mytilus* gill and found that four types of metachronal waves passed across the same part of the pad although the beating direction of each cilium remained constant (Fig. 4.27). This means that the type of metachronism (i.e. the relation between the direction of metachronal wave propagation and the beating direction of cilia) is controlled 'extrinsically' rather than 'intrinsically'.

Figure 4.28 shows the successive collisions of two sets of naturally occurring symplectic and antiplectic metachronal waves. The first collision between the two waves results in their mutual annihilation; however, the

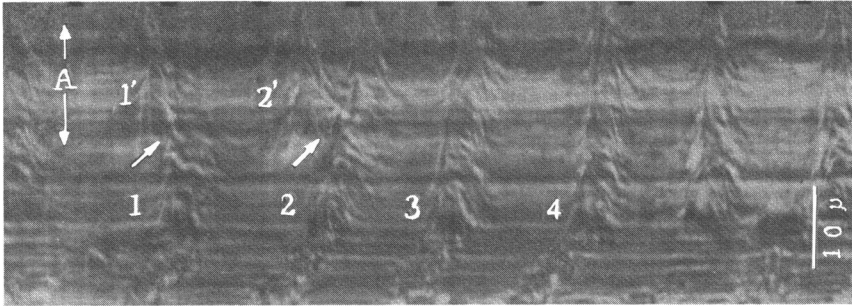


Figure 4.28 A photographic record showing the collision of two types of metachronal waves (i.e. symplectic and antiplectic waves) by using a slit camera. The slit is set up to be parallel to the vertical axis in Fig 4.27. The movements recorded in this photograph represent the component parallel to this axis (see Fig. 4.14). The symplectic metachronal waves are represented by 1, 2, 3 and 4. The antiplectic waves are indicated by 1' and 2'. Two metachronal waves (1 and 1') propagate in opposite directions. When the two waves meet, annihilation of the waves occurs on the first collision. However, after the second collision (2 and 2') a new symplectic wave emerges and the symplectic metachronal waves become dominant. The arrows indicate the collision point of the two waves. From Murakami (1963). Reprinted with permission.

second collision evokes a new symplectic wave. The type of the first collision is analogous to annihilation of action potentials in the nerve membrane, where the two oppositely propagated impulses disappear on collision (Tasaki, 1949). It is believed that the refractoriness left behind by the impulses blocks the further transmission of the impulses.

The type of the second collision is more interesting because it suggests the properties of 'soliton' or non-annihilating waves. A soliton is usually defined as a solitary wave which asymptotically maintains its shape and velocity even after a collision with other solitary waves (see Scott, 1981; see books by Jackson, 1990; Olver and Sattinger, 1990; and Infeld and Rowlands, 1990). Although the detailed mechanism for metachronal waves is different from that of waves generated in 'reaction-diffusion' systems, the numerical computations for the modified reaction-diffusion systems not only show that two identical waves can pass through on collision as in the soliton but also that one wave more or less destroys the other and continues to propagate after the collision when two asymmetric waves collide (see Section 1.2.2).

In the case of ciliary metachronal waves, the emphasis is made on directional mechano-sensitivity of beating cilia to hydrodynamic forces imposed by adjacent cilia, because a symplectic wave always emerges after the collision of symplectic and antiplectic waves.

Mucus-propelling cilia. Sanderson and Sleight (1981) cultured rabbit tracheal epithelium to investigate ciliary activity of mucus-transporting epithelia.

(A)

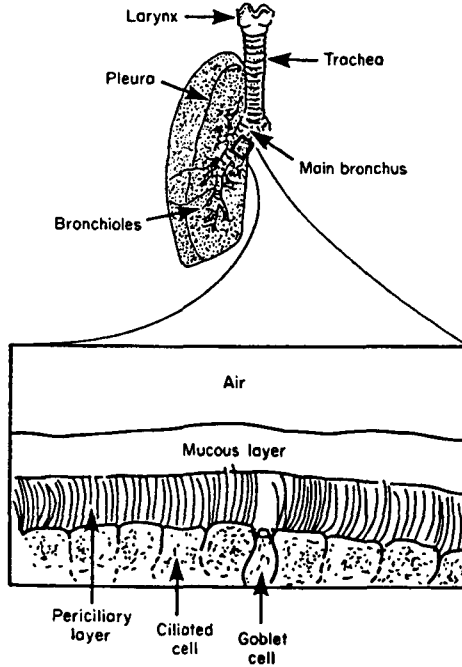


Figure 4.29 (A): Schematic illustration of the muco-ciliary system in the human lung (upper panel) and cross-sectional view of a major bronchiole. This muco-ciliary system has two layers: a mucous layer, and an underlying periciliary (or serous) layer, within which the cilia beat. Mucus is secreted by goblet cells. From Fluford and Blake (1986). Reprinted with permission, (B): A side view of the three-dimensional beat cycle of rabbit tracheal cilia. The cilium rests at the end of the effective stroke. After stimuli, the cilium shows the recovery stroke (0–5) followed by the effective stroke (6–9). If we observe this beat cycle from above, the recovery stroke shows a clockwise rotation. From Sanderson and Sleigh (1981). Reprinted with permission of the company of Biologists Ltd. (C): The spatial relationships of cilia on an epithelial surface. All cilia are equally spaced and the assigned number for each one represents the phase of the cilium in its beat cycle in panel B. The metachronal wave originates from a single cilium as it triggers its recovery stroke. This stroke has two components of hydrodynamic interactions which in turn trigger the recovery stroke of neighbouring cilia. The short arrows indicate the directions of these two interactions. As a result, the metachronal waves propagate in the direction indicated by the arrow, *m*. The effective stroke returns the cilia to the initial resting phase by moving in the direction indicated by the arrow, *e*. The line, *s*, shows the cilia beating synchronously. From Sanderson and Sleigh (1981). Reprinted with permission of the Company of Biologists Ltd.

Muco-ciliary clearance is of great importance to normal lung function as a defence system. The continually secreted mucus provides a protective barrier against dust and bacteria and is transported toward the oropharynx from the lung by the underlying cilia. Foreign particles once trapped can be removed from the airways. The muco-ciliary transport system has two layers: the mucous layer, containing viscoelastic secretion, and the underlying serous layer, of low viscosity within which the cilia beat back and forth.

Mucous-propelling cilia are shorter (with lengths approximately 5–6 μm) than most water-propelling cilia (10–20 μm) but perform an essentially similar beat, composed of a fast effective stroke and a slower recovery stroke (Fig. 4.29). This beat cycle is three-dimensional and involves a resting phase at the end of the effective stroke. Fluid is propelled in the direction of the effective stroke. For an observer facing in the direction of metachronal wave propagation, this direction is toward the back and to the left resulting in the metachronism called *antilaeplectic* (Sanderson and Sleight, 1981).

In contrast to the prominent metachronal waves of water-propelling cilia, this metachronism is observed only in small patches distributed over the epithelial surface. This is partly because the cilia are shorter in length, partly because the clefts provide the discontinuities in the ciliated surface and partly because viscoelastic mucus covers the ciliated surface.

The areas of ciliary activity are observed through numerous beat cycles with little change in their orientation or position. Since adjacent areas of ciliary activity do not seem to influence each other, metachronal fields of activity are functionally independent. However, the discontinuous areas of ciliary activity may enhance the transport efficiency of the more 'solid' mucus.

5 Models of flagella and cilia exhibiting regular behaviour

We have observed different types of dynamical behaviour in cilia and flagella – for example, normal base-to-tip wave propagation typical of flagella, the repetitive beat cycle typical of cilia with its effective- and recovery-stroke phases, intermittent flagellar movement involving stopping and starting transients, excitable–oscillatory dynamics with or without mechano-sensitivity in cilia, and other irregular behaviour. Now we need to understand these observations in terms of mathematical models. There are many models that should be discussed, though they have been developed to account for regular behaviour.

Section 5.1 provides a brief introduction to Reynolds numbers. In Section 5.2 we will discuss the principles of fluid dynamics in flagellar and ciliary motion, and then derive the basic equation governing the behaviour of a thin filament through a viscous medium within the framework of Newton’s laws. After the overview of this theoretical background, mathematical models displaying some of the regular dynamics are discussed, with emphasis on their significance and their status in Section 5.3.

5.1 Introduction

We are familiar with the propulsion of larger and faster organisms such as fish, birds and insects. They propel themselves in water or air by using the *volume* forces such as inertial effects, set up in the surrounding fluid. The dynamics of their motion is ascribed to the dual effects of (i) a propelling mechanism pushing the fluid backward, and (ii) resistance of the body giving the fluid a forward momentum. By considering these two effects separately, an analysis of their motion can be made. For example, consider a swimming fish that is initially held and then released. Its motion will accelerate until the backward and forward momenta balance exactly. The viscosity of the fluid, which is important only in the boundary layer, hardly affects the resulting motion.

This is not the case, however, for the propulsion of ciliated micro-organisms or of spermatozoa. Because they are very small and move with slow velocities their propulsion is caused by the *surface* forces – pressure and viscous stress. It is no longer possible to consider the propulsive effects and fluid resistance separately. Because the motion of fluid around the body follows the same rule as the motion of the micro-organism itself the motions of both the fluid and the body should be considered at once. This means that momentum is instantly diffused throughout the fluid; and thus, the forces on any particle of fluid are in equilibrium.

The two extremes above suggest that the motion of a body depends on the ratio between the viscous and inertial effects. It is the *Reynolds number*, Re , that indicates the non-dimensional ratio between these two effects. The Reynolds number is defined by

$$Re = \frac{\rho UL}{\mu} = \frac{UL}{\nu}, \quad (5.1)$$

where U and L are the velocity and some characteristic length of the body; ρ , μ and ν ($= \mu/\rho$) are the density, the viscosity and the *kinematic viscosity* of the fluid, respectively.

To understand the fluid-mechanical concept of the Reynolds number, it is instructive to illustrate the types of flow fields around a moving cylinder of circular cross-section at different Reynolds numbers (Fig. 5.1). (A). When the Reynolds number is small, about 10^{-2} , the viscous effects are dominant and the flow field is symmetric. (B). At a Reynolds number of about 20, a pair of stationary vortices appears. (C). At a Reynolds number of about 10^2 , the inertial effects dominate and the asymmetries are realized in the flow field past the cylinder, resulting in *Karman vortices*. (D). The *turbulent flow* appears at Reynolds numbers greater than about 10^4 .

From this illustration, we can expect the fluid dynamics of flows, or more generally, dynamical problems in nature, to conform to an elementary classification in terms of the Reynolds number. Indeed, organisms exist throughout the range of Reynolds numbers. For example, values of this quantity range on one hand from about 10^{-6} for bacteria to about 10^{-2} for spermatozoa (cf. Brennen and Winet, 1977), and on the other hand from about 10^4 for flying insects to about 10^5 for flying birds. Thus the motion of micro-organisms and that of relatively large bodies such as insects and birds can be roughly characterized by the magnitude of their Reynolds number. Of course, small insects exist that show neither a large nor small Reynolds number. Consideration of this phenomenon is found in Chapter 11 of the book by Childress (1981).

In this book, we restrict ourselves to the swimming micro-organisms characterized by extremely small Reynolds numbers. A typical feature of such a swimming micro-organism is that the mean propulsive motion of the body is associated with the oscillatory movements of cilia or flagella. The

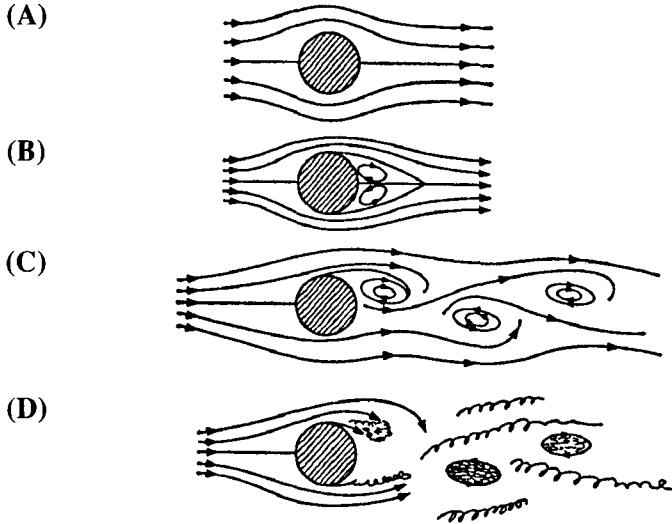


Figure 5.1 Schematic illustrations showing streamlines around a circular cylinder at different Reynolds numbers. (A): At $Re \approx 10^{-2}$, the flow field is symmetric. (B): At $Re \approx 20$, a pair of stationary vortices appear. (C): At $Re \approx 10^2$, the asymmetries are realized in the flow field past the cylinder, resulting in Karman vortices. (D): At $Re > 10^4$, the turbulent flow appears. From Feynman *et al.* (1964). Copyright © Addison-Wesley Publishing Co., Inc. Reprinted with permission.

flow fields around the body are, therefore, characterized by (i) the fluid motion due to the mean propulsion of the organism, and (ii) the fluid field occupied by the beating organelle (cilium or flagellum). For each motion, it is useful to define a particular Reynolds number.

The Reynolds number concerned with (i) is already given by definition (5.1), where U and L must be replaced by the velocity of propulsion and the length of the micro-organism, respectively. An alternative Reynolds number based on (ii), often called an oscillatory Reynolds number R_ω , is defined by

$$R_\omega = \frac{\rho \omega l^2}{\mu} = \frac{\omega l^2}{\nu}. \quad (5.2)$$

Here ω is the angular beating frequency of the organelle (cilium or flagellum) and l is its typical length. The oscillatory Reynolds numbers of the cilium or the flagellum are very small, of the order of 10^{-3} (cf. Brennen and Winet, 1977). Thus, as pointed out before, inertial forces are less important when studying the motion of micro-organisms as the viscous forces dominate the fluid motions around the micro-organisms.

One of the interesting problems for fluid dynamicists to consider is the effect of the combination of the two flow fields. This problem is discussed deeply in the review by Lighthill (1976).

5.2 Fluid dynamics of micro-organism propulsion

The problem is how a flagellum or a ciliated micro-organism can propel itself in a viscous fluid characterized by extremely small Reynolds numbers. To answer this problem, it is necessary to specify the force with which the fluid acts on the flagellum or the cilium. Once the *external* viscous force is specified, we can investigate the *internal* mechanisms responsible for flagellar or ciliary motion.

5.2.1 Historical background

The Stokes equations. An analysis of low-Reynolds-number fluid motion is made by using the *Stokes equations* which describe the stationary nature of an incompressible inertialess fluid of viscosity μ .¹ They consist of a continuity condition on the velocity field $\mathbf{u} = (u(\mathbf{r}, t), v(\mathbf{r}, t), w(\mathbf{r}, t))$,

$$\nabla \cdot \mathbf{u} = 0 \quad (5.3)$$

and a condition of force equilibrium

$$\nabla p - \mu \nabla^2 \mathbf{u} = 0 \quad (5.4)$$

containing the pressure field, $p(\mathbf{r}, t)$, where $\mathbf{r} = (x, y, z)$ stands for vector displacement from the origin and t is time. These equations have the merit of being linear, which allows us to use linear superposition of singular solutions. The problem is thus to search the singular solutions appropriate to the given boundary conditions (see e.g. Lunec, 1975). Before attempting to obtain and analyse the singular solution, we shall start with an analysis by Taylor (1951) to find a relatively straightforward solution to the Stokes equations.

Swimming-sheet model. From a mathematical point of view, Taylor (1951) was the first to answer the problem concerning the self-propulsion of a body in a viscous fluid. He developed a two-dimensional sheet model that underwent propagating waves to investigate whether such waves give rise to viscous forces that drive the sheet forward (Fig. 5.2). The sheet model was originally designed to model flagellar propulsion and so it was taken to be *inextensible*. Unfortunately, this sheet model was based on two-dimensional geometry, which being unrealistic, restricted its application to one-dimensional flagella.

The model was, however, successfully extended to examine the behaviour of a population of cilia as a two-dimensional *envelope model*, whose surface 'particle' was assumed to be roughly equivalent to the locus of the tip of an individual cilium (see Fig. 5.30). Thus the application of the sheet model to ciliary propulsion has meant that both extensibility and two-dimensional geometry of the envelope can be used. In Section 5.3.6, an *extensible* envelope model is discussed in the context of metachronal waves propagating over the surface of numerous oscillating cilia.

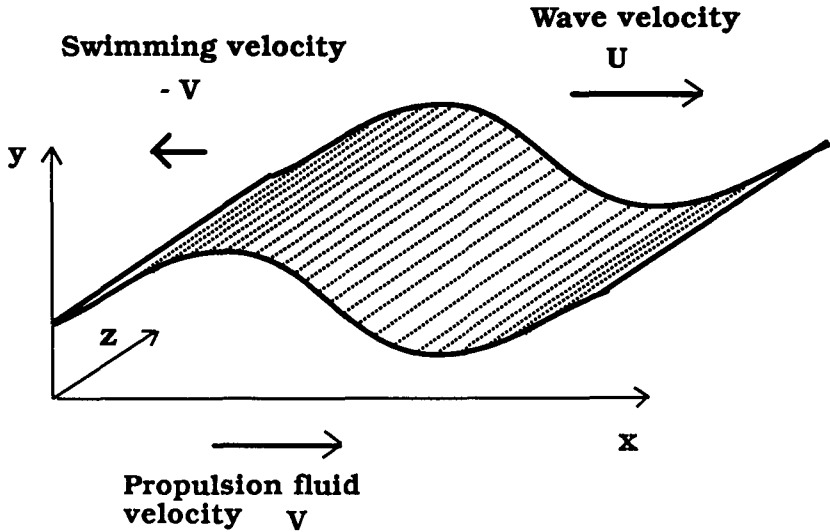


Figure 5.2 Two-dimensional swimming-sheet model. The waves propagate in the positive x -direction with a wave velocity U . When the velocity of the fluid at infinity is V (i.e. the propulsion fluid velocity), the sheet will swim in the negative x -direction with velocity, $-V$.

Without loss of generality, we consider here the swimming of the extensible sheet. To simplify the analysis, we further assume that the sheet is infinite and in contact with the fluid on one side only. A point (x_s, y_s) on the surface of the extensible sheet is thus represented by

$$x_s = x + a \cdot \cos(kx - \omega t - \phi) \tag{5.5a}$$

$$y_s = b \cdot \sin(kx - \omega t) \tag{5.5b}$$

where a and ϕ are the amplitude and a phase shift of the *longitudinal motion*, b the amplitude of the *transverse motion*, λ ($= 2\pi/k$) the wavelength, and f ($= \omega/2\pi$) is the frequency. It should be noted that for flagellar propulsion these parameters correspond to those of ‘flagellar waves’, while for ciliary propulsion they correspond to those of ‘metachronal waves’.

The velocity field (u, v) at the point (x_s, y_s) on the sheet is given by

$$u(x_s, y_s) = \frac{dx_s}{dt} = a\omega \cdot \sin(kx - \omega t - \phi) \tag{5.6a}$$

$$v(x_s, y_s) = \frac{dy_s}{dt} = -b\omega \cdot \cos(kx - \omega t). \tag{5.6b}$$

To find the velocity field and swimming motion of the sheet, we will solve the two-dimensional version of the Stokes equations:

$$\frac{\partial u}{\partial x} + \frac{\partial v}{\partial y} = 0 \quad (5.7a)$$

$$\frac{\partial p}{\partial x} - \mu \nabla^2 u = 0 \quad (5.7b)$$

$$\frac{\partial p}{\partial y} - \mu \nabla^2 v = 0. \quad (5.7c)$$

To satisfy (5.7a), we introduce a stream function ψ such that components of velocity are

$$u = \frac{\partial \psi}{\partial y} \quad (5.8a)$$

$$v = \frac{\partial \psi}{\partial x}. \quad (5.8b)$$

By taking the cross-derivatives of (5.7b) and (5.7c) and eliminating the pressure, we get

$$\nabla^4 \psi = 0. \quad (5.9)$$

Provided that bk (or ak) is small (i.e. the amplitude, b , (or a) is small compared with the wavelength, λ), the solution is sought as a power series in bk (or ak) satisfying both equation (5.9) and the following boundary conditions at $y \rightarrow \infty$:

$$\frac{\partial \psi}{\partial x} \rightarrow 0 \quad (\text{as } y \rightarrow \infty) \quad (5.10a)$$

$$\frac{\partial \psi}{\partial y} \rightarrow V \quad (\text{as } y \rightarrow \infty). \quad (5.10b)$$

(5.10a) indicates that the sheet moves uniformly along the x -axis. (5.10b) defines the velocity of the fluid at infinity, V , so that if V has a finite and positive value the waving sheet will swim to the left with velocity $-V$ relative to the fluid at infinity (Fig. 5.2).

Skipping several steps (for details see Taylor, 1951 and Childress, 1981), we finally have

$$\frac{V}{U} = \frac{1}{2} k^2 (b^2 + 2ab \cdot \cos \phi - a^2) \quad (5.11)$$

where V is the second-order velocity of propulsion and U is the wave velocity ($= \omega/k$). The formula (5.11) indicates that whether the sheet swims to

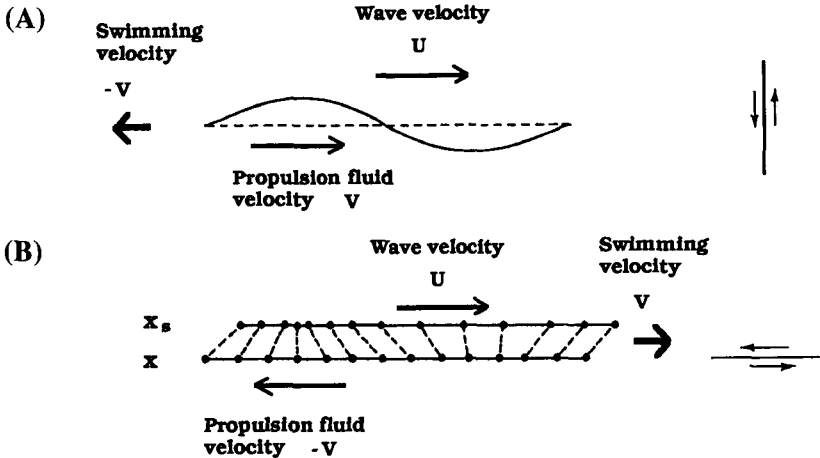


Figure 5.3 Surface shapes (left) and corresponding orbits (right) of swimming sheets together with wave velocity, propulsion fluid velocity and swimming velocity. (A): The simple transverse wave (i.e. $a = 0$) travels along the sheet when the orbit is parallel to the y -axis. The sheet is propelled in the opposite direction to the wave movement. Note that for flagellar propulsion with relatively large amplitudes, the orbit is not a straight line as indicated in the right panel, but is in fact a figure of 8. (B): The longitudinal wave (i.e. $b = 0$) occurs when the orbit is parallel to the x -axis. The sheet is propelled in the same direction as the wave. Modified from Blake and Sleight (1974). Reprinted with permission.

the left or the right depends on the orbit defined by (5.5). From a point of view of ciliary metachronism this formula is worth investigating, as the metachronism is interpreted in terms of the path of movement of the ciliary tip. Since details of the formula (5.11) are given in Section 5.3.6, we will consider two extremes; one is the *transverse wave* (i.e. $a = 0$) and the other the *longitudinal wave* (i.e. $b = 0$).

The simple transverse wave is obtained when $a = 0$ (i.e. the orbit is a vertical line); the sinusoidal wave travels in the positive x -direction with a wave velocity, U (Fig. 5.3A). This case approximates the flagellar propulsion.² Then, (5.11) becomes

$$\frac{V}{U} = \frac{1}{2} k^2 b^2. \tag{5.12}$$

This means that the sheet moves at velocity $-V$ as waves travel down the sheet with velocity $+U$.

By contrast, the pure longitudinal wave occurs when $b = 0$ (i.e. the orbit is a horizontal line); the sheet, remaining in its plane, shows compression and extension alternately (Fig. 5.3B). In this case the formula (5.11) becomes

(A)

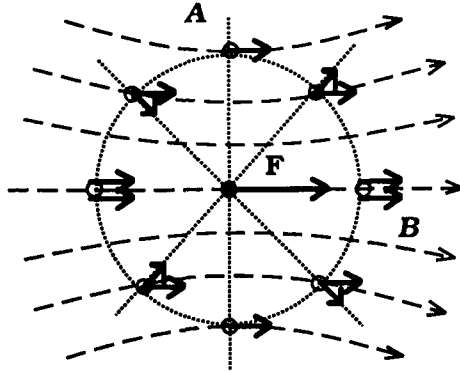


Figure 5.4 (A): Streamlines for the flow due to a single point-force, \mathbf{F} . A parallel field and a radial field of the Stokeslet are indicated at points on the circle. (B): As a result of the direction-dependent velocity field, the induced velocity at point A is U , while that at point B is $2U$, even though both points are equidistant from the origin at which the external force is applied. (C): The force distribution along an elongated body moving (i) in the normal direction, or (ii) tangentially. The force distribution, \mathbf{F} , needed to satisfy the no-slip condition on the elongated body moving tangentially at velocity U , is half that, $\mathbf{F}/2$, for movement in the normal direction at the same velocity.

$$\frac{V}{U} = -\frac{1}{2}k^2 a^2, \quad (5.13)$$

and the sheet swims in the same direction as the wave.

It is clear from the above considerations that the sheet will swim in a viscous medium whose swimming direction is closely related to the orbit of the surface particle.

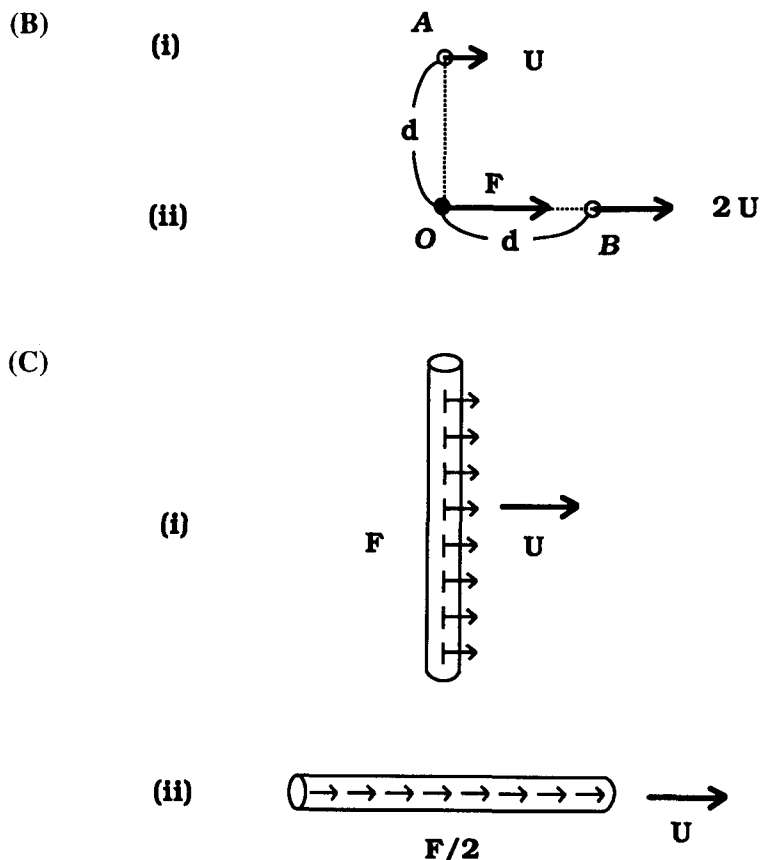
Stokeslet. Now we seek a singular solution to the Stokes equations, called a *Stokeslet*, due to a concentrated external force \mathbf{F} at the origin in an infinite fluid. Technically, we must solve the modified force-balance equation

$$\nabla p - \mu \nabla^2 \mathbf{u} = \mathbf{F} \delta(\mathbf{r}) \quad (5.14)$$

where $\delta(\mathbf{r})$ is the Dirac delta function. The resulting Stokeslet velocity field is obtained as the sum of a *parallel field* and a *radial field* as follows (Lighthill, 1976):

$$\mathbf{u} = \frac{r^2 \mathbf{F} + (\mathbf{F} \cdot \mathbf{r}) \mathbf{r}}{8\pi\mu r^3}. \quad (5.15)$$

Both components in the Stokeslet velocity field (5.15) fall off inversely with the distance from a single point force (i.e. r^{-1} -dependence). The first term (corresponding to the parallel field) shows a simple r^{-1} -dependence in every direction, while the second term (corresponding to the radial field) modifies



the first one to indicate the preferred direction of fluid motion (i.e. in the direction of the force).

Figure 5.4A illustrates the streamlines for the flow caused by a single point-force, on which a parallel component and a radial component of the velocity field (5.15) are superimposed at points equidistant from the origin. Clearly the parallel field at any point on a circle is independent of the angle between the direction of the force and the radial direction at that point; however, the radial field is closely related to the angle. As a result, the induced velocity at point A is U while the velocity at point B is $2U$, which is twice that at A , even though both points are equidistant from the origin (Fig. 5.4B).

The resulting factor 2 is important when considering the distribution of line forces along an elongated inert body moving (i) in the normal direction, or (ii) tangentially (Fig. 5.4C). Known as the *no-slip* boundary condition, the

layer of fluid adjacent to the surface of the body follows the movement of the corresponding part of the body itself: the velocity of the fluid on the surface must be equal to the velocity of the surface of the body itself. Under the no-slip condition, the induced velocity at any one point along the body, due to a force at a different point on the body, is U for the normal motion but $2U$ for the tangential motion. Inversely, the force distribution along an elongated body necessary to maintain the motion in the normal direction is \mathbf{F} , but that for the tangential motion at the same velocity is $\mathbf{F}/2$.

This discussion provides the basis for the theory of Gray and Hancock (1995) for specifying the *force distribution* along a flagellum. It should be noted that the above discussion applies to the force distribution along an elongated body not the *fluid motion* around the body. To get some feeling for the velocity field near the body, one must integrate all the contributions (see Blake and Sleight, 1974).

5.2.2 Externally forced motion and self-propulsive motion

In the previous section, we first treated the problem of self-propulsion of a waving sheet and later dealt with the problem of externally forced motion of an elongated inert body. To apply the concept of an elongated inert body to the model of self-propelling micro-organisms, we will make clear the distinction between them.

We shall begin by comparing a *self-propelling* body, e.g. a ciliated micro-organism, with an *inert* body of a similar shape (Fig. 5.5). By Newton's laws the total forces on a body must be zero. This constraint is valid for both inert and self-propelling bodies. For an inert body, an external force must be balanced to the forces *dragging* a large bulk of fluid with it. By contrast, no external force is needed for a self-propelling body: the organism provides equal but opposite *thrusting* and *dragging* forces. That is, the fluid close to the organism is pulled along with it, whereas the fluid slightly distant from it moves in the opposite direction.

Next we consider a thin, flexible body such as a flagellum. We assume that the flagellum consists of a finite number of segments each of which moves in a similar fashion to a rigid elongated inert body moving with the same velocity and direction. According to Newton's laws, the sum of all the forces in the segments and the head must equal zero.³ This approach was achieved by Gray and Hancock (1955) when they evaluated the force exerted by flagella. However, since the translational motion of a flagellum through the fluid is combined with undulatory motions, the problem is rather complicated.

As a good introduction to the Gray and Hancock approach, it is useful to consider the *classical paradox* of a transverse undulation passing along a rope. Supposing that the left end of a rope is shaken rhythmically, transverse waves pass along the rope (Fig. 5.6). Although at any point no net displacement to the right occurs, we recognize some motion toward the right.

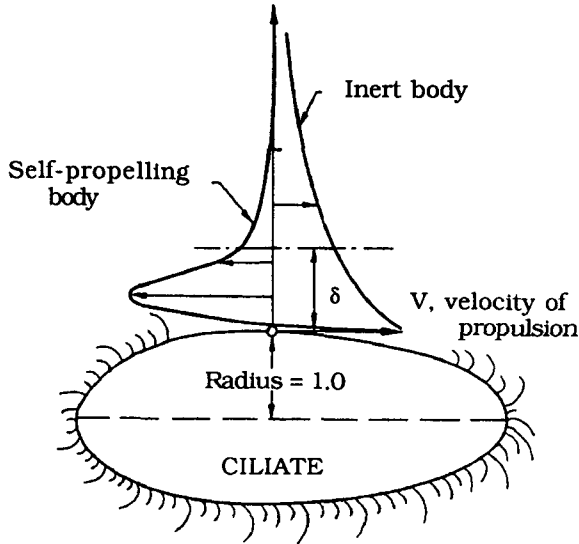


Figure 5.5 Schematic illustration showing the velocity profile for an inert and a self-propelling body. Although both the inert and self-propelling bodies must obey Newton's laws, i.e. the sum of all the forces must be zero, there is an important difference between them. For an inert body, a large bulk of fluid is dragged with it and the velocity decays monotonically with the distance from the inert body; whereas for a self-propelling organism there is a change of sign in the gradient of the velocity profile. From Blake and Sleight (1974). Reprinted with permission.

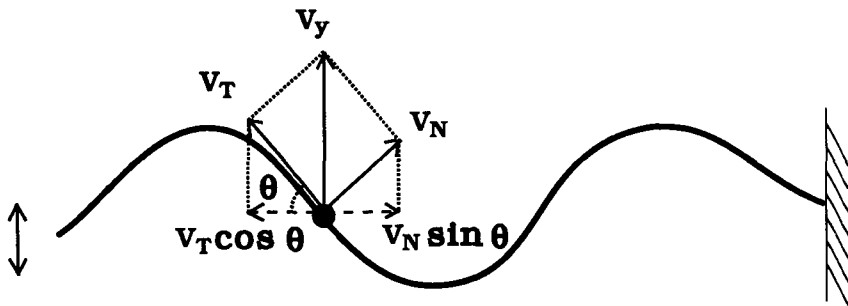


Figure 5.6 Transverse waves passing along a rope. When the left end of a rope is shaken rhythmically, waves are initiated and propagate toward the right end. Although there appears to be some motion toward the right, no net displacement occurs because the average normal and tangential motions are cancelled out. V_y is the transverse velocity; V_T and V_N are the tangential and normal components of V_y ; θ is the angle between the horizontal axis and the tangent to the rope.

This *illusion* occurs because we are very sensitive to motions of the rope normal to itself but not to tangential motions and consequently a left-to-right component in the normal resultant velocity is emphasized. However, since the average normal resultant pointing from left to right must be equal to the average tangential resultant pointing in the opposite direction, the net velocity is zero and no net displacement to the right occurs.

Similarly to the above example, the undulating flagellum generates average normal motions in the direction of propagation, which are accompanied by equal, and oppositely directed, average tangential motions. In the next section, we extend this idea to help us understand the Gray and Hancock approach.

5.2.3 Resistive-force theory

Gray and Hancock approach. At low Reynolds numbers the force exerted on a segment of the elongated body is proportional to the local velocity. On the basis of this characteristic at low Reynolds numbers, Gray and Hancock (1955) assumed that the local velocity of each element, ds , of the flagellum and the force on that local element decomposed into normal and tangential components, V_N , V_T , dF_N and dF_T , respectively. They were represented by

$$dF_N = -C_N V_N ds \quad (5.16a)$$

$$dF_T = -C_V V_T ds \quad (5.16b)$$

where C_N and C_V are the viscous drag coefficients determined from the geometry alone. The values for coefficients proposed by Gray and Hancock are

$$C_T = \frac{2\pi\mu}{\ln \frac{2\lambda}{A} - \frac{1}{2}} \quad (5.17a)$$

$$C_N = 2C_T \quad (5.17b)$$

where A is the cross-sectional radius of the flagellum and λ the wavelength.⁴

Applications of the resistive-force theory. We will consider the application of the resistive-force theory to a self-propelling flagellum, to understand how the flagellum generates undulating motions and swims through a viscous fluid. Suppose that a self-propelling flagellum generates planar waves. We must consider two motions separately: one is the transverse motion with velocity V_y and the other is the propulsive motion with velocity V_x (Fig. 5.7). The formulas (5.16a, b) are rewritten as:

$$dF_N = -C_N(V_y \cdot \cos\theta - V_x \cdot \sin\theta) ds \quad (5.18a)$$

$$dF_T = -C_T(V_y \cdot \sin\theta + V_x \cdot \cos\theta) ds. \quad (5.18b)$$

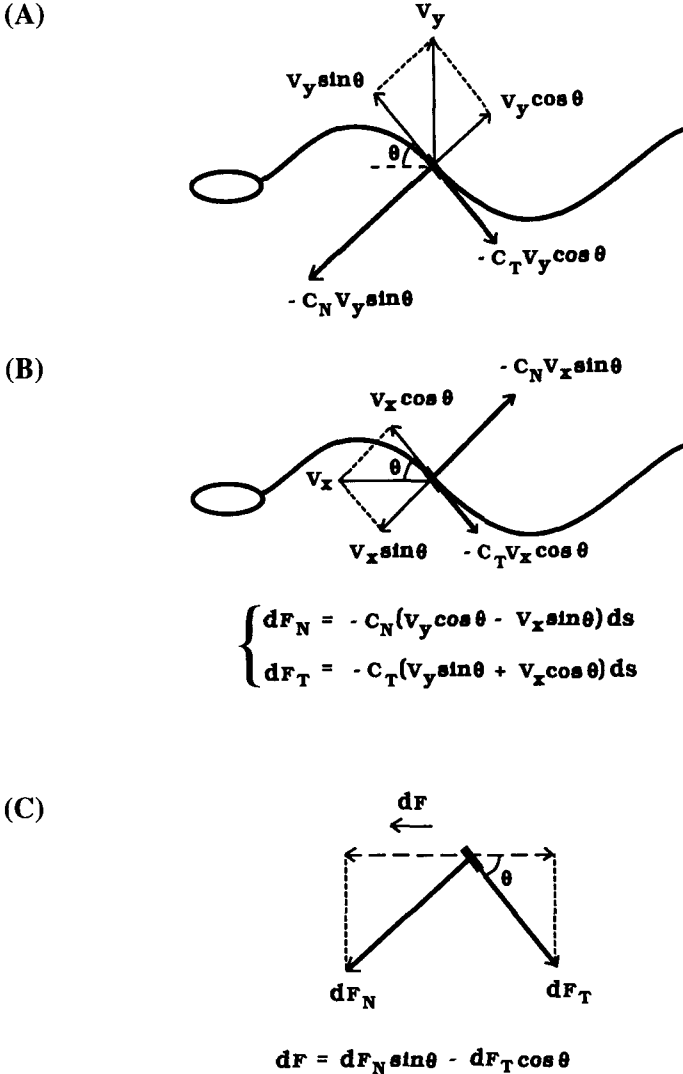


Figure 5.7 Diagrams showing the forces acting on an element, ds , of a flagellum. (A): When the flagellum is moving transversely at velocity V_y , the resistive forces acting normally and tangentially on the element are $-C_N \cdot V_y \cdot \cos \theta$ and $-C_T \cdot V_y \cdot \sin \theta$, respectively. θ is the angle of inclination of the element to the horizontal axis. (B): In addition to the transverse motion, the flagellum is moving along the horizontal axis at velocity, V_x . The normal and tangential components of the resistive forces are $-C_N \cdot V_x \cdot \sin \theta$ and $-C_T \cdot V_x \cdot \cos \theta$, respectively. (C): The net propulsive thrust, dF , is the result of these transverse and forward movements. Modified from Gray and Hancock (1955). Reprinted with permission of the Company of Biologists Ltd.

The resultant forward thrust (dF) is

$$dF = dF_N \cdot \sin\theta - dF_T \cdot \cos\theta \quad (5.19a)$$

$$= [(C_N - C_T)V_y \sin\theta \cos\theta - V_x(C_N \sin^2\theta + C_T \cos^2\theta)] ds \quad (5.19b)$$

$$= \left[\frac{(C_N - C_T)V_y \tan\theta - V_x(C_T + C_N \tan^2\theta)}{1 + \tan^2\theta} \right] ds. \quad (5.19c)$$

If $\theta \ll 1$ (i.e. $\tan^2\theta \ll 1$), equation (5.19c) can be reduced to

$$dF = [(C_N - C_T) V_y \tan\theta - C_T V_x] ds. \quad (5.20)$$

Suppose $V_y = dy/dt$, $\tan\theta = dy/dx$ and $dx/ds \approx 1$, equation (5.20) becomes

$$\frac{dF}{dx} = (C_N - C_T) \frac{dy}{dt} \frac{dy}{dx} - C_T V_x. \quad (5.21)$$

For simplicity, we consider a flagellum generating a sinusoidal wave

$$y = b \cdot \sin(kx - \omega t) \quad (5.22)$$

where b is the amplitude, $\lambda (= 2\pi/k)$ the wavelength and $U (= \omega/k)$ is the wave velocity of the propagating wave. By substituting (5.22) into (5.21) and using $dF/ds \approx dF/dx$, the total thrust, F , exerted by the flagellum over one wavelength ($0 \leq x \leq \lambda$) is

$$F = \int_0^\lambda dF = \frac{2\pi^2 b^2 U (C_N - C_T)}{\lambda} - C_T \lambda V_x. \quad (5.23)$$

When a flagellum without a head is propelling itself through the fluid (i.e. the *zero-thrust* swimming condition), the ratio of V_x/U is obtained by making $F = 0$,

$$\frac{V_x}{U} = \frac{2\pi^2 b^2 (C_N - C_T)}{\lambda^2 C_T}. \quad (5.24)$$

This equation predicts that (i) the flagellum will swim in the 'opposite' direction of propagation of the wave when $C_T < C_N$, and (ii) the flagellum will swim in the 'same' direction of propagation of the wave when $C_T > C_N$. Of course, normal flagella move through the fluid in the opposite direction of wave propagation as in case (i). However, there are some species (*Ochromonas*) whose flagella move through the fluid in the same direction of wave propagation as in case (ii). These flagella have rigid projections known as *mastigonemes* (Fig. 5.8). A simple explanation for this phenomenon is that the hydrodynamic effect of the mastigonemes results in values of C_T greater than C_N .

It should be noted that if $C_N = 2C_T$, (5.24) can be reduced to

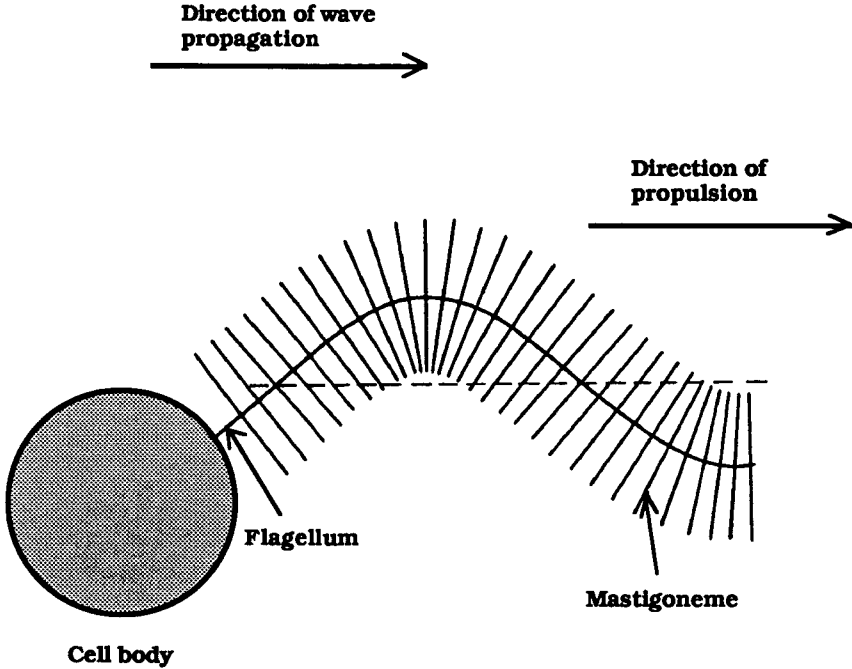


Figure 5.8 The flagellum with projecting mastigonemes. The cell body is pulled forward by the undulations passing along an anterior flagellum *from base to tip*. That is, the direction of propulsion is the same as that of the wave propagation. The reader should notice the essential difference between the flagellum with mastigonemes and a 'smooth' flagellum, such as a trypanosomatid flagellum (see Fig. 4.20). The trypanosomatid flagellum is not only pulled forward by the undulations passing along the anterior of the flagellum, *from tip to base*, but also pushed forward by undulations passing along the posterior of the flagellum, *from base to tip*. That is, the direction of propulsion is *always* opposite to that of the wave motion. From Brennen and Winet (1977). Reprinted with permission.

$$\frac{V_x}{U} = \frac{1}{2} k^2 b^2 \tag{5.25}$$

which is identical with equation (5.12) derived from the Taylor model. If the head of the flagellum is propelled, we use $F = 6\pi\mu BV_x$ (where B is the radius of the head) instead of $F = 0$. Then equation (5.24) is slightly modified, but its essential feature is retained.

Improvement of the resistive-force theory. (1). Lighthill (1976) considered a simple flagellum without its cell body generating planar bending waves of small amplitude. The calculated coefficients for this case were:

$$C_T = \frac{2\pi\mu}{\ln \frac{2q}{A}} \quad (5.26a)$$

$$C_N = \frac{4\pi\mu}{\ln \frac{2q}{A} + \frac{1}{2}} \quad (5.26b)$$

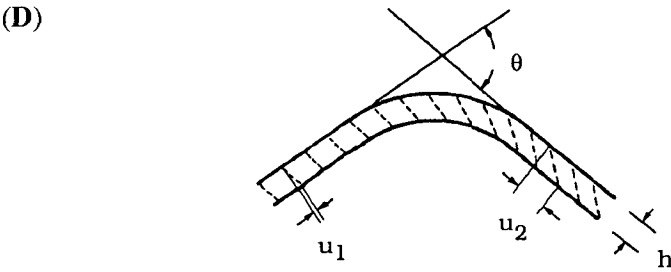
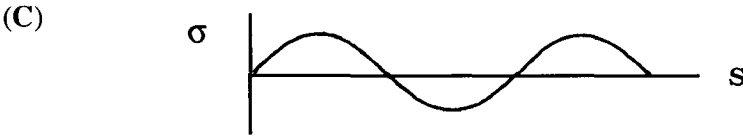
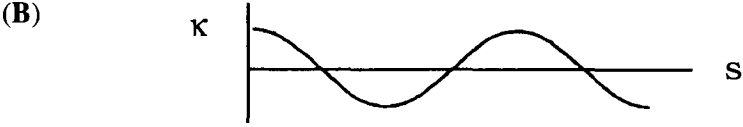
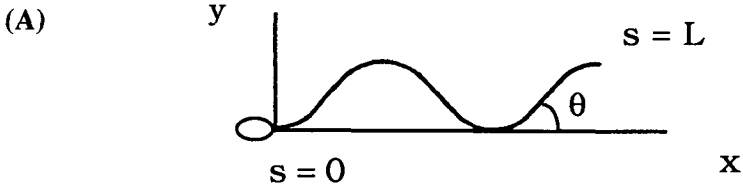
where $q = 0.09\Lambda$ (Λ : the wavelength measured along the centre-line of the flagellum). For a typical wave, $C_N/C_T = 1.8$ and the value of C_N defined by Lighthill is about 40% greater than that of C_N , as originally defined by Gray and Hancock.

(2). The resistive-force theory is concerned with the local hydrodynamic interactions. However, as pointed out by Lighthill (1976), there are long-range hydrodynamic interactions in the viscous fluid. According to Johnson and Brokaw (1979), these interactions are divided into two categories: (i) flagellum–flagellum interactions, and (ii) cell-body–flagella interactions. To evaluate these long-range interactions they used the *slender-body theory* in which the local force is obtained from integration of all the forces distributed along the flagellum and the cell body. After a comparison between the resistive-force theory and the slender-body theory with respect to the distributions of the forces and moments along the length of the flagellum, they found that the resistive-force theory was completely satisfactory when the flagellum had no cell body, the magnitude of the classical drag coefficient was increased up to about 35%, and the ratio $C_N/C_T = 1.8$ was adopted. To facilitate accurate analysis when the flagellum has a large cell body, we must use the slender-body theory instead of the resistive-force theory.

5.3 Theoretical models for flagella and cilia

To simplify the analysis, we restrict our attention to a flagellum generating planar bending waves. Using Gray and Hancock approximation, we can specify the external viscous forces acting on a flagellum as it moves through a viscous medium. The next step in developing a theoretical model is to identify the configuration of the flagellum. There are two ways to describe the form of a flagellum. One way is to directly describe the flagellum in terms of the (x, y) coordinates (see Fig. 5.9A) similar to Taylor (1951) (see Fig. 5.2 and equations (5.5)) or Gray and Hancock (1955) (see Fig. 5.7 and equation (5.22)).

The other way concentrates on a ‘wave-generating function’ defined in the (s) coordinate, in which the curvature, κ (Fig. 5.9B), or the corresponding *shear angle*, σ (Fig. 5.9C), is defined as a function of length, s , measured along the flagellum. As illustrated in Figure 5.9D, the bend angle θ between two different points is given by $(u_2 - u_1)/h$, where h is the distance between the



$$\theta = \frac{u_2 - u_1}{h} = \Delta \sigma$$

$$\kappa = \frac{d\theta}{ds} = \frac{d\sigma}{ds}$$

Figure 5.9 Descriptions of the flagellar configuration. (A): The flagellar shape is plotted against an (x, y) coordinate system with its origin at the anterior end of the flagellum. Only movements in the (x, y) plane are considered. $\theta(s)$ is the angle between the tangent to the flagellum at a point s and the x -axis, where s is distance measured along the flagellum from the origin of the (x, y) coordinate system. (B): The curvature, κ , as a 'wave-generating function' is plotted as a function of distance, s . The variables used for calculation are defined on this (s) coordinate. (C): An alternative wave-generating function is the shear, σ , which is plotted as a function of s . (D): When the filaments are inextensible, the bend angle, θ , between two different points is proportional to the net sliding displacement, Δu ; that is, $\theta = (u_2 - u_1)/h = \Delta u/h = \Delta \sigma$, where h is the distance between the two filaments. From this simple relationship, if the filaments are tied together at the base, $\theta(s) = \sigma(s)$ holds (see Section 7.4.1). However this is not the case when the filaments are allowed to slide at the base. Modified from Brokaw (1972a). Copyright © the American Association for the Advancement of Science. Reprinted with permission.

two filaments and u_2 and u_1 are the *sliding displacement* (or *shear displacement*) at the points. Note that $\kappa = d\theta/ds = d\sigma/ds$ since the filaments are inextensible, and that $\sigma(s) = \theta(s)$ if the filaments are tied together at the base.⁵

Of course, the x and y coordinates of the point are obtained from the following integrals:

$$x = \int_0^s \cos\theta \, ds \quad (5.27a)$$

$$y = \int_0^s \sin\theta \, ds. \quad (5.27b)$$

Thus data on flagellar configuration in the (x, y) coordinate can be interpreted in terms of the (s) coordinate.

5.3.1 The basic equations of flagellar dynamics

The essence of flagellar dynamics is described by a simple version of equations on the assumption of small amplitude and planar waveforms. We will derive the basic equations for this simple case.

Consider an arbitrary region of the flagellum with length ds . When this region is treated as a free body, Newton's laws require that the total force and moment on the body must be zero. Let f_N denote an external viscous force per unit length, F_N the normal component of the external viscous force and M_v the external viscous moment. Figure 5.10 illustrates a segment of the flagellum together with the forces and moments necessary to maintain equilibrium during planar bending. Conventionally, positive F_N on a positive 'face' produces a counter-clockwise rotation about a point proximal to the point of application of the force. This is appropriate for a positive M_v . Ignoring *rotational inertia*, we obtain the moment-balance equation in the limit of $ds \rightarrow 0$:

$$\frac{\partial M_v}{\partial s} + F_N = 0. \quad (5.28)$$

The force-balance equation in an equilibrium condition is:

$$\frac{\partial F_N}{\partial s} = f_N. \quad (5.29)$$

The external viscous moment, M_v , must be equal and opposite to the internal moment, which is the sum of active moment, M_a , and elastic moment, M_e :

$$-M_v = M_a + M_e. \quad (5.30)$$

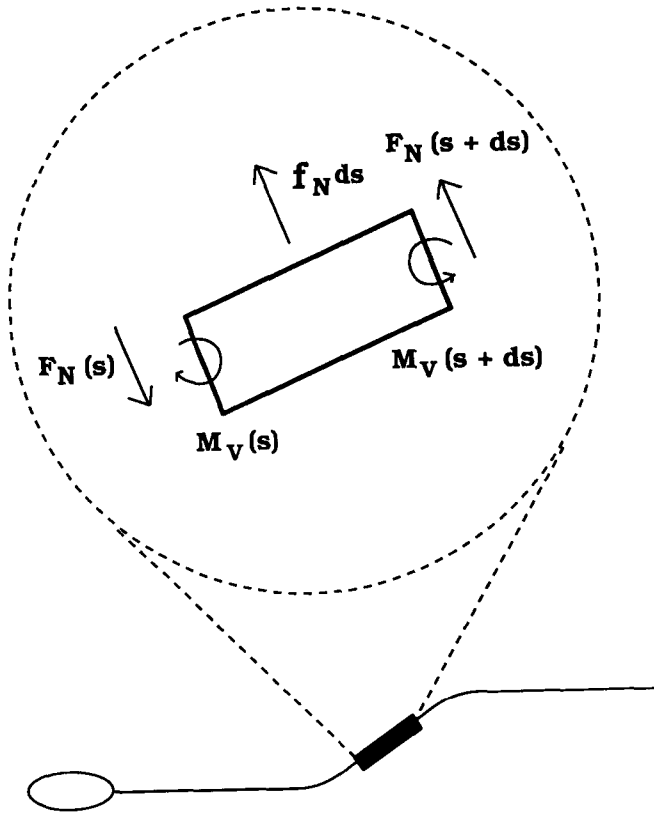


Figure 5.10 Diagram showing the force and moment equilibrium in a segment of a flagellum during planar bending. Applying Newton's laws to the segment of the flagellum, we obtain the force and moment equilibrium of the segment between s and $s + ds$. The forces and moments necessary for equilibrium are shown. Conventionally, positive F_N on a positive side produces a counter-clockwise rotation (corresponding to positive moment, M_v) about a point proximal to the point of application of the force.

Equation (5.30) is equivalent to Brokaw's formalism (see e.g. equation (7) of Brokaw (1971)).

To complete the description of the flagellar motion, we must specify each moment. Specification of the external viscous moment is given by the Gray-Hancock approximation:

$$f_N = -C_N V_N. \tag{5.31}$$

The elastic moment is defined by the bending resistance, E_B :

$$M_e = E_B \kappa. \tag{5.32}$$

From equations (5.28)–(5.32), we get the following basic equation for flagellar dynamics:

$$\frac{\partial^2 M_a}{\partial x^2} + E_B \frac{\partial^4 y}{\partial x^4} + C_N \frac{\partial y}{\partial t} = 0. \quad (5.33)$$

Here, we use $V_N = dy/dt$, $\kappa = d^2y/dx^2$ and $dx/ds \approx 1$.

This equation, equivalent to the equation by Machin (1958; 1963), can be applied to both the local contraction mechanism and the sliding-filament mechanism (see Section 4.3.1 and also Lubliner, 1973).

In the case of the sliding-filament mechanism, we must define the active shear force, S_a , arising from cross-bridge dynamics. For small-amplitude approximations, we can assume that $dx/ds \approx 1$ and $dy/ds \approx \theta$. Suppose that a positive shear force is defined to cause a positive shear; that is, a microtubule on the top side moves distally (Fig. 5.11). As illustrated in Figure 5.11A, we have

$$\frac{\partial M_a}{\partial s} = S_a. \quad (5.34)$$

Upon differentiating equation (5.33) with respect to x ($\approx s$), and substituting (5.34), we have

$$\frac{\partial^2 S_a}{\partial s^2} + E_B \frac{\partial^4 \theta}{\partial s^4} + C_N \frac{\partial \theta}{\partial t} = 0. \quad (5.35)$$

More generally, besides the active shear force generated by the cross-bridge system, S_a , passive elastic shear force, S_p , arises from other link systems such as nexin and radial spokes. Internal viscous shear force, S_v , arises from internal viscous resistance, so that M_a and S_a in equations (5.33), (5.34) and (5.35) are replaced by the (total) shear moment, M_s , and the (total) shear force, S_s , respectively.⁶ For convenience, the general equations for basic flagellar beating are written as:

$$\frac{\partial^2 S_s}{\partial s^2} + E_B \frac{\partial^4 \theta}{\partial s^4} + C_N \frac{\partial \theta}{\partial t} = 0 \quad (5.36a)$$

$$S_s = S_a + S_p + S_v, \quad (5.36b)$$

or

$$\frac{\partial^2 M_s}{\partial x^2} + E_B \frac{\partial^4 y}{\partial x^4} + C_N \frac{\partial y}{\partial t} = 0 \quad (5.37a)$$

$$\frac{\partial^2 M_s}{\partial s} = S_s. \quad (5.37b)$$

The problem in finding the underlying mechanism(s) for flagellar dynamics is how to specify M_a , S_s , or M_s in equations (5.33), (5.36), or (5.37), respec-

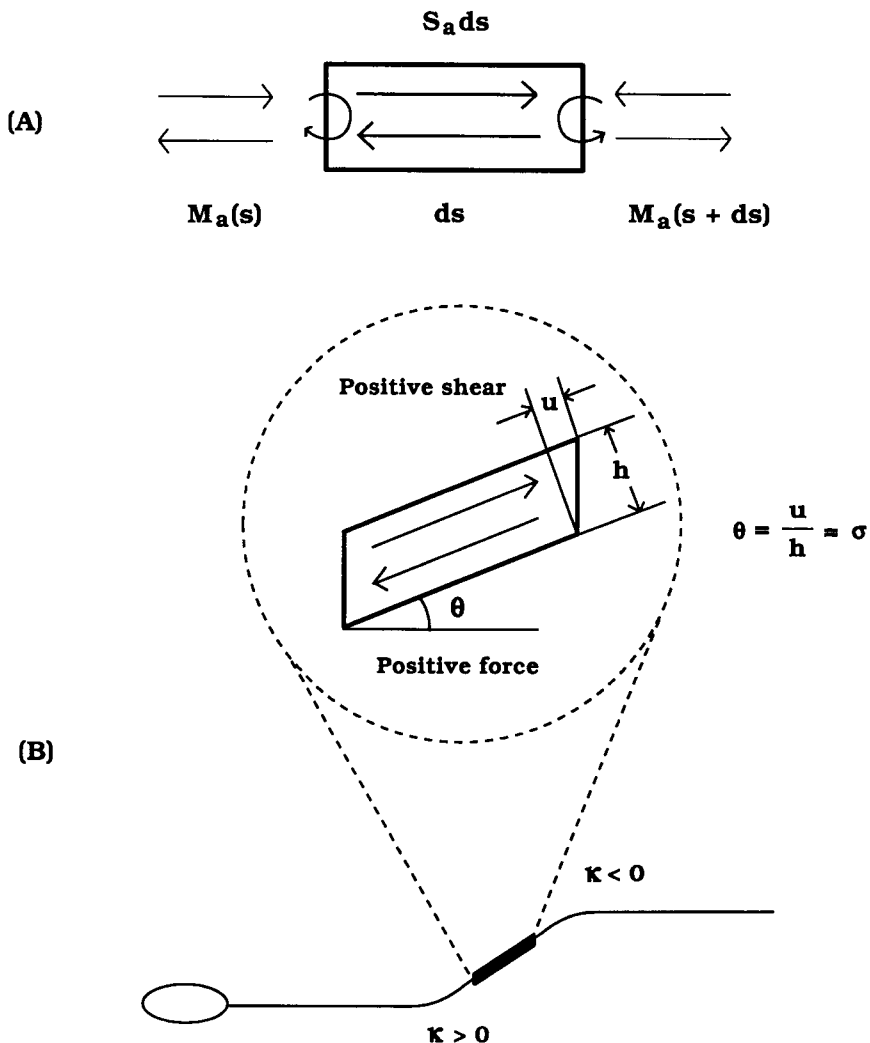
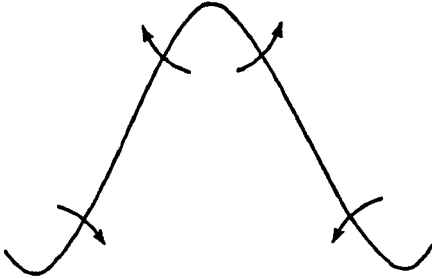


Figure 5.11 (A): The balance of active moment, M_a , on a segment between s and $s + ds$ of a flagellum. An active shear moment, $S_a ds$, is generated in the segment. (B): A positive shear force is defined as one that produces positive shear displacement, u , as indicated by the arrows. As a result, a microtubule on the positive side of the flagellum moves distally relative to that on the opposite side. When the filaments are tied together at the base (i.e. $\theta(0) = \sigma(0) = 0$), there is a simple relationship between the shear displacement u , the shear angle σ , and the bend angle θ as indicated in the figure. As a result of positive shear in the segment, positive curvature ($+\kappa$) and negative curvature ($-\kappa$) occur to the left and to the right of the segment, respectively.

(A)



(B)

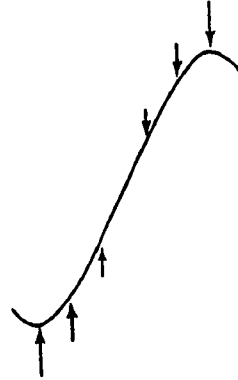


Figure 5.12 Forces acting on a flagellum illustrated in an (x, y) plane (see Fig. 5.9A). (A): The elastic forces, due to the bending resistance, tend to straighten the flagellum. The resultant bending moment is at its maximum at the point of maximum curvature. (B): The viscous forces produce a maximum moment at the point of zero curvature. Therefore there is a $(1/4)$ -cycle phase-difference between the viscous and elastic bending moments. From Machin (1958). Reprinted with permission of the Company of Biologists Ltd.

tively. To understand how this problem is difficult to solve, it is useful to illustrate two different moments: the elastic bending moment and the viscous bending moment (Fig. 5.12). The elastic moment, M_e , is at its maximum at the point of maximum curvature; while the viscous moment, M_v , is at its maximum at the middle point of the straight region. This means that the shear moment, M_s , must have two components corresponding to these moments. Since each component differs in phase, specification of the shear moment that satisfies this constraint is not straightforward.

5.3.2 The Machin model

Machin (1958; 1963) assumed that a flagellum consists of a series of bilaterally arranged contractile elements (Fig. 5.13) and that each element has a *delayed elasticity* in which, after a time delay, a change in the length of the element causes a change in tension. As a result of this delayed elasticity, bending waves arise spontaneously along the flagellum. Although this 'contractile microtubule' model has been replaced by the 'sliding microtubule' model, the Machin model predicts many important phenomena. Its most interesting prediction is that the propagation direction of the wave is determined by the *mechanical impedance* at the base. This prediction suggests the physiological importance of the presence of the head at one end of

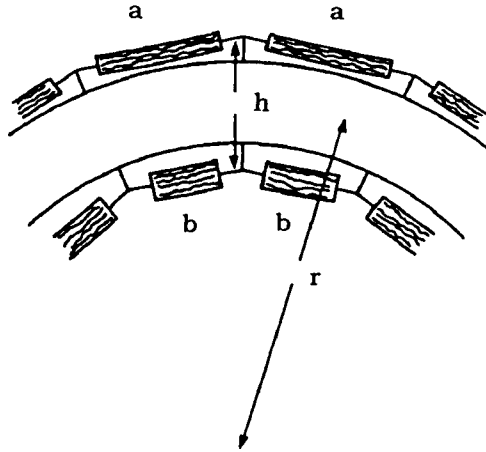


Figure 5.13 The Machin model composed of active contractile elements. The flagellar configuration is illustrated in an (x, y) plane (see Fig. 5.9A). The elements a and b are separated by distance, h . Their local radius of curvature is given by r . From Machin (1963). Reprinted with permission.

the flagellum because it might be responsible for mechanical impedance. This section will detail the Machin model.

Suppose that T_a and T_b are the tensions in elements a and b. The active bending moment, M_a , can be expressed as

$$M_a = h(T_a - T_b) \tag{5.38}$$

where h is the distance between the adjacent microtubules. Now it is necessary to define the form of each element in relation to the flagellar configuration. Let L_0 be the length of an element when the flagellum is straight, and r the local radius of curvature representing a part of the flagellar configuration. Then the lengths, L_a and L_b , of the elements are

$$L_a = L_0 \left(1 + \frac{h}{2r} \right) \tag{5.39a}$$

$$L_b = L_0 \left(1 - \frac{h}{2r} \right) \tag{5.39b}$$

where

$$\frac{1}{r} = \frac{\partial^2 y}{\partial x^2}. \tag{5.39c}$$

The next step is to combine the tension in the element in equation (5.38) and the length of the element in equations (5.39). For this purpose, Machin

considered an oscillatory element in which both tension and length change with time. A typical example is the self-oscillation observed in insect flight muscle and skeletal muscle (see Part I of this book). This property is interpreted in terms of *stretch activation* (i.e. *delayed elasticity*) or *positive oscillatory work*. The term ‘stretch activation’ is due to the observation that a sudden change of length is followed by a tension development after a time delay. A system containing this property is capable of producing positive work output (i.e. oscillatory work) when the length is forced to oscillate at some appropriate frequency. In an attempt to express such a dynamic tension–length relationship, Machin considered two possible cases: (i) a linear tension–length relationship under small-amplitude conditions, and (ii) a nonlinear relationship for large amplitudes.

(i) *Linear tension–length relationship.* First let us consider the case for small amplitudes, where a linear approximation is used. An operator ϕ is introduced to express a tension–length relationship written as

$$T - T_0 = \phi(L - L_0), \quad (5.40)$$

where ϕ is formally a function of $\partial^n/\partial t^n$, thus ϕ becomes a function of $i\omega$ ($i = \sqrt{-1}$) when the length is forced to change sinusoidally at frequency $\omega/2\pi$. We call ϕ a *transfer function* which represents a complex frequency-dependent quantity (see Machin, 1964). In the linear case, ϕ is taken to be constant so that k is automatically determined once ω is given (see Fig. 5.14).

From equations (5.38) to (5.40),

$$M_a = \Phi \left(\frac{\partial^2 y}{\partial x^2} \right) \quad (5.41a)$$

where

$$\Phi = h^2 \phi. \quad (5.41b)$$

Since Φ is independent of x , we have the following equation by substituting (5.41a) into (5.33),

$$\Phi \frac{\partial^4 y}{\partial x^4} + E_B \frac{\partial^4 y}{\partial x^4} + C_N \frac{\partial y}{\partial t} = 0. \quad (5.42)$$

The solution of this equation is represented by a small-amplitude sinusoidal bending wave as follows:

$$y = Ae^{i\omega t - ikx} \quad \text{or} \quad A \cos(\omega t - kx). \quad (5.43)$$

Substituting (5.43) into (5.42), we obtain

$$\Phi = -\frac{i\omega C_N}{k^4} - E_B. \quad (5.44)$$

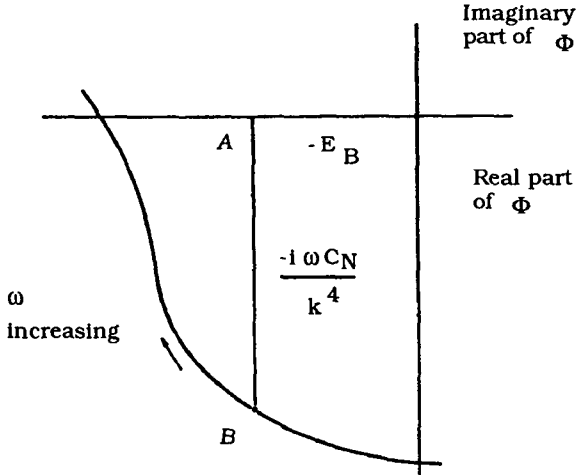


Figure 5.14 A Nyquist plot. The real and imaginary parts of Φ are plotted against each other with ω as the parameter. The vector AB represents $i\omega C_N/k^4$. Of particular interest is the case where AB is vertical; that is, ω and k^4 are real. As shown in Fig. 5.14 and Fig. 5.15, the effect of nonlinearity allows the system to adjust itself to this condition. The curve is purely illustrative. From Machin (1963). Reprinted with permission.

Equation (5.44) is represented on a complex plane as shown in Figure 5.14, in which the real and imaginary components of Φ are plotted against each other, with ω as the parameter. Of particular interest is the case where the vector AB (represented by $i\omega C_N/k^4$) is vertical, i.e. ω and k^4 are real. In this case the general solution is given by

$$y = e^{i\omega x}(Ae^{-ikx} + Be^{-kx} + Ce^{ikx} + De^{kx}). \tag{5.45}$$

Here the first term represents a propagating wave in the direction of increasing x with wavelength $2\pi/k$, the second term an exponential that decays with increasing x , and the remaining two terms represent ‘reflections’ of them.

Once the frequency of oscillation (i.e. $\omega/2\pi$) is given, the point on the curve is fixed and the associated wavelength ($2\pi/k$) is determined. Fundamentally, any frequency of oscillation is possible, but in a flagellum with finite length only certain modes of oscillation are possible. Three constraints placed on the proximal end are possible: (i) *free* end (i.e. zero force and zero moment at $x = 0$); (ii) *clamped* end (i.e. zero displacement and zero angle at $x = 0$); and (iii) *pinned* end (i.e. zero displacement and zero moment at $x = 0$). These conditions can be conveniently expressed in terms of the *mechanical impedance* of the constraints. The mechanical impedance is defined as the ratio of the alternating component of force to the alternating

Table 5.1 Boundary conditions of the axoneme at the base. Conditions in the middle column directly represent the fact that the basal end is either free, clamped or pinned. These conditions are also represented in terms of the transverse mechanical impedance, Z_t , and the angular mechanical impedance, Z_a , as shown in the right-hand column.

Free	$\begin{cases} \frac{\partial^3 y(0)}{\partial x^3} = 0 \\ \frac{\partial^2 y(0)}{\partial x^2} = 0 \end{cases}$	or	$\begin{cases} Z_t(0) = 0 \\ Z_a(0) = 0 \end{cases}$
Clamped	$\begin{cases} y(0) = 0 \\ \frac{\partial y(0)}{\partial x} = 0 \end{cases}$	or	$\begin{cases} Z_t(0) = \infty \\ Z_a(0) = \infty \end{cases}$
Pinned	$\begin{cases} y(0) = 0 \\ \frac{\partial^2 y(0)}{\partial x^2} = 0 \end{cases}$	or	$\begin{cases} Z_t(0) = \infty \\ Z_a(0) = 0 \end{cases}$

component of velocity. Two mechanical impedances are defined, one is the *transverse mechanical impedance* Z_t :

$$Z_t = \frac{F_N}{\frac{\partial y}{\partial t}} \quad (5.46a)$$

and the other is the *angular mechanical impedance* Z_a :

$$Z_a = \frac{M_a}{\frac{\partial}{\partial t} \left(\frac{\partial y}{\partial x} \right)}. \quad (5.46b)$$

Table 5.1 expresses boundary conditions at the proximal end in two different ways.

For convenience, equation (5.45) is transformed into

$$y = e^{i\omega t} (a \cosh kx + b \sinh kx + c \cos kx + d \sin kx) \quad (5.47a)$$

where

$$a = D + B, \quad b = D - B, \quad c = C + A, \quad d = i(C - A). \quad (5.47b)$$

Differentiating equation (5.47a), we obtain the values of $\partial y / \partial t$ and $\partial(\partial y / \partial x) / \partial t$; while, integrating equation (5.33), we get M_a and $F_N (= -\partial M_a / \partial x)$. Note that due to symmetry the constants of integration are set at zero.

Finally,

$$Z_t = \frac{(E_B k^4 + i\omega C_N) (a \sinh kx + b \cosh kx + c \sin kx - d \cos kx)}{i\omega k (a \cosh kx + b \sinh kx + c \cos kx + d \sin kx)} \quad (5.48a)$$

$$Z_a = -\frac{(E_B k^4 + i\omega C_N) (a \cosh kx + b \sinh kx - c \cos kx - d \sin kx)}{i\omega k^2 (a \sinh kx + b \cosh kx - c \sin kx + d \cos kx)}, \quad (5.48b)$$

At the proximal end (i.e. $x = 0$),

$$Z_t = \frac{(E_B k^4 + i\omega C_N)}{i\omega k} P \quad (5.49a)$$

$$Z_a = -\frac{(E_B k^4 + i\omega C_N)}{i\omega k^3} Q \quad (5.49b)$$

where

$$P = \frac{b - d}{a + c} \quad (5.49c)$$

$$Q = \frac{a - c}{b + d}. \quad (5.49d)$$

Suppose that the two ends of the flagellum are both free. Equation (5.44) provides us with

$$E_B k^4 + i\omega C_N \neq 0. \quad (5.50)$$

From equation (5.50) and $Z_t = Z_a = 0$ at $x = 0$:

$$b - d = 0 \quad (5.51a)$$

$$a - c = 0. \quad (5.51b)$$

From $Z_t = 0$ and $Z_a = 0$ at $x = L$ because of the free distal end, where L is the length of the flagellum:

$$a \sinh kL + b \cosh kL + c \sin kL - d \cos kL = 0 \quad (5.52a)$$

$$a \cosh kL + b \sinh kL - c \cos kL - d \sin kL = 0. \quad (5.52b)$$

From equations (5.51) and (5.52), we get

$$\frac{c}{b} = \frac{a}{d} = \frac{\cos kL - \cosh kL}{\sinh kL + \sin kL} = \frac{\sin kL - \sinh kL}{\cosh kL - \cos kL}. \quad (5.53)$$

If b is real, then a , c and d must also be real from equations (5.51) and (5.53). Certain values for k are determined from the second half of equation (5.53). Now the amplitudes A and C of the progressive waves are represented by

$$A = \frac{1}{2}(c + id), \quad C = \frac{1}{2}(c - id), \quad (5.54)$$

so that

$$|A| = |C|. \quad (5.55)$$

This means that the amplitudes of the forward-propagating and backward-propagating waves are equal; that is, the two equal and opposite waves generate *standing-wave* modes with certain wavelengths. For all combinations of boundary conditions at the two ends (e.g. free, clamped or pinned conditions), such standing-wave modes can occur.

Since there is no net energy transfer along the flagellum when standing waves are present, no propulsive motion occurs. In other words, propulsion requires the presence of an imbalance in the amplitudes of the two opposite progressive waves. Now suppose that $c = id$ (i.e. $C = 0$). This particular condition is retained as long as $P = i$ and $Q = -i$. From equation (5.49), it is found that Z_i and Z_a lie in the *first quadrant* of the complex plane, which implies that the energy source, in the form of springs of *negative stiffness*, is combined with energy absorption (or energy dissipation) due to the viscous-type mechanism. On the contrary, where $P = -i$ and $Q = i$ lead to $c = -id$, Z_i and Z_a lie in the *third quadrant*. This case implies that energy absorption in the form of positive springs is combined with energy sources of negative viscous components. Table 5.2 summarizes the relationship between the impedances at the base and the direction of the wave propagation.

(ii) Nonlinear tension-length relationship. For large amplitudes ϕ is not constant but instead it changes, which indicates the onset of nonlinear effects. Conveniently, this situation is expressed by assuming a constant operating on a power series in $(L - L_0)$:

$$T - T_0 = \phi\{(L - L_0) - \xi(L - L_0)^2 - \gamma(L - L_0)^3 \dots\}. \quad (5.56)$$

Since the even terms cancel out because of the symmetry of the contractile structure, equation (5.56) leads to

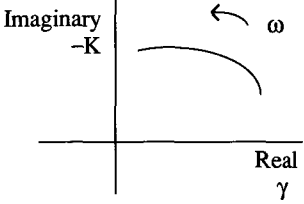
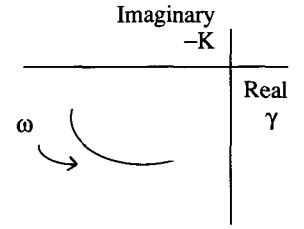
$$M_a = \Phi \left\{ \left(\frac{\partial^2 y}{\partial x^2} \right) - \gamma \left(\frac{\partial^2 y}{\partial x^2} \right)^3 \dots \right\}. \quad (5.57)$$

Here we ignore all terms after the cube. Now suppose that a flagellum carries both distally and proximally propagating waves,

$$y = A \sin(\omega t - kx) + C \sin(\omega t + kx) \quad (5.58)$$

where ω and k are real and positive. When the origin of t is properly chosen, A and C become real. Of course, harmonics of these waves must be present in this nonlinear system, but cross-products between them are ignored on the assumption that their amplitudes are relatively small. Equation (5.58) is substituted into equations (5.33) and (5.57), then the terms in $(\omega t - kx)$ and

Table 5.2

Proximal impedance	Wave direction
 <ul style="list-style-type: none"> • Positive viscous components (energy sinks) • Negative springs (energy sources) 	<p>From base-to-tip</p>
 <ul style="list-style-type: none"> • Negative viscous components (energy sources) • Positive springs (energy sinks) 	<p>From tip-to-base</p>

The mechanical impedance Z has the form $\gamma + iK$, where γ and K are real. According to the equations (5.46), γ and K correspond to the viscous resistance and the spring stiffness, respectively. Conventionally, the mechanical impedance Z is plotted against a $(\gamma, -K)$ plane so that it lies in the first quadrant when γ and K are both positive (cf. Cole, 1968). Therefore mechanical impedance in the first quadrant means the presence of negative stiffness and positive viscous resistance (upper panel). Inversely mechanical impedance in the third quadrant means the presence of positive stiffness and negative viscous resistance (lower panel).

$(\omega t + kx)$ are compared separately to obtain the relationship between parameters. Finally, for the terms in $(\omega t - kx)$,

$$A \left[\Phi \left\{ 1 - \frac{3\gamma k^4}{4} (A^2 + 2C^2) \right\} + E_B + \frac{i\omega C_N}{k^4} \right] = 0 \tag{5.59a}$$

where i comes from the term of $\cos(\omega t - kx)$. Similarly for the terms in $(\omega t + kx)$,

$$C \left[\Phi \left\{ 1 - \frac{3\gamma k^4}{4} (C^2 + 2A^2) \right\} + E_B + \frac{i\omega C_N}{k^4} \right] = 0. \tag{5.59b}$$

When only the distally propagating wave is present (i.e. $C = 0$), equation (5.59b) becomes trivial and equation (5.59a) gives $A = A_0$ where

$$\frac{3\gamma k^4}{4} A_0^2 = 1 + \frac{E_B + \frac{i\omega C_N}{k^4}}{\Phi}. \tag{5.60}$$

In the limit of $A_0 \rightarrow 0$, this equation becomes identical with equation (5.44) for the linear case. Formally we rewrite equations (5.59a) and (5.59b) as follows

$$A(A^2 + 2C^2 - A_0^2) = 0 \quad (5.61a)$$

$$C(C^2 + 2A^2 - A_0^2) = 0. \quad (5.61b)$$

There are two stable solutions $(A, C) = (0, A_0)$, $(A_0, 0)$ and one unstable solution $(A, C) = (A_0/\sqrt{3}, A_0/\sqrt{3})$. Since any small disturbance in the unstable solution results in either stable solutions, the evoked wave propagating in one direction suppresses the wave propagating in the opposite direction.

Stability. We have assumed that ω and k are real. Even though ω and k are not real, the corresponding solutions are unstable and will tend toward the stable condition when ω and k are real. This self-adjacent property of the nonlinear system can be visualized by the change of Φ on the complex plane.

Consider the case where k^4 is real but ω is not real. We shall show that the only stable solution occurs when ω is real. Suppose that $\omega = \omega' + i\omega''$, then curves of Φ plotted on the complex plane form an orthogonal net (Fig. 5.15A). For convenience, equation (5.60) is rewritten

$$\Phi = -\frac{E_B + \frac{i\omega C_N}{k^4}}{1 - \frac{3}{4}\gamma k^4 A_0^2}. \quad (5.62)$$

Suppose $\omega'' < 0$: such a solution is illustrated in Figure 5.15B. Since $\omega'' < 0$ implies that a corresponding amplitude increases exponentially with time,⁷ the value of A_0 must increase after a short time (Fig. 5.15C). As a result, the value of $(-\omega'')$ becomes small, and consequently, the exponential rate of increase of amplitude also becomes small. This brings about the steady state as shown in Figure 5.15D. Starting with the assumption of $\omega'' > 0$, similar arguments can be applied.

Next consider the case when k is not real (i.e. $k = k' + ik''$). Suppose $k'' < 0$: a corresponding wave decreases its amplitude exponentially with increasing x . At a certain point (say x_0), ω is real (Fig. 5.16A). Therefore at a point $x > x_0$, the value of A_0 becomes smaller, which in turn implies the case where ω is not real with $\omega'' < 0$ (Fig. 5.16B). According to the previous argument, A_0 increases to a steady value that is the same as A_0 at x_0 . Consequently, the amplitude of the wave at all points is the same (i.e. $k'' = 0$) when the steady state is obtained.

Synchronization. Synchronization is observed among spermatozoa. Flagella that are close together beat with a common frequency and wavelength even though their original values in the isolated individuals are different (see Fig.

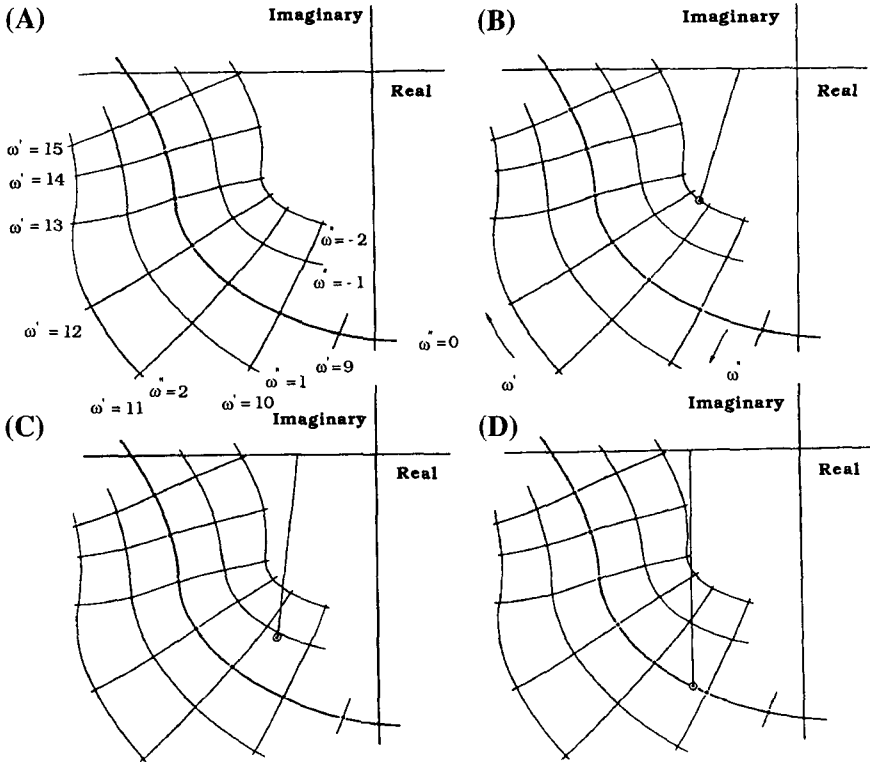


Figure 5.15 The Nyquist plot generalized to include complex frequencies. (A): When ω is complex (i.e. $\omega = \omega' + i\omega''$), curves of Φ form an orthogonal net on the complex plane. (B): A solution for ω'' negative. (C): A solution for ω'' negative after a short time. The amplitude, A_0 , increases exponentially. (D): A steady-state solution when ω is purely real. As a result of the increase in A_0 , the value of $(-\omega'')$ eventually decreases and a steady-state solution is attained. The effect of the nonlinearity operates through A_0 to make ω purely real. From Machin (1963). Reprinted with permission.

4.24). To consider this problem, we will assume a moving flagellum carries a wave

$$y = N \sin(\omega_1 t - k_1 x). \tag{5.63}$$

The force-balance equation (5.29) must be modified

$$\frac{\partial F_N}{\partial s} = f_N + \beta N \cos(\omega_1 t - k_1 x) \tag{5.64}$$

where β will be real and positive and will depend on the characteristics of two flagella such as ω_1 , k_1 and their distance apart. Thus the basic equation (5.33) becomes

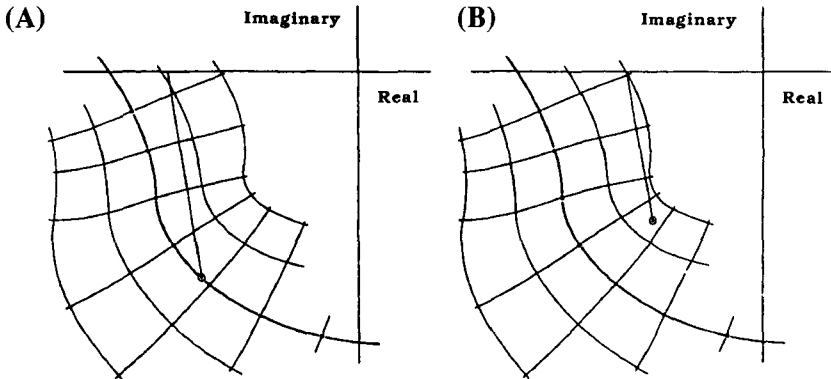


Figure 5.16 The Nyquist plot generalized to include complex wave numbers. (A): A solution for k complex and ω real at a point x_0 . (B): The solution at a point $x > x_0$. The amplitude decreases with an increase in x , which in turn implies $\omega'' < 0$. From Machin (1963). Reprinted with permission.

$$\frac{\partial^2 M_a}{\partial x^2} + E_B \frac{\partial^4 y}{\partial x^4} + C_N \frac{\partial y}{\partial t} = \beta N \cos(\omega_1 t - k_1 x). \quad (5.65)$$

Applying a similar technique to that discussed previously, we assume

$$y = A \sin(\omega t - kx) + B \sin(\omega_1 t - k_1 x). \quad (5.66)$$

After substituting this solution, terms in $(\omega t - kx)$ are compared to get

$$A \left[\Phi_\omega \left\{ 1 - \frac{3\gamma}{4} (k^4 A^2 + 2k_1^4 B^2) \right\} + E_B + \frac{i\omega C_N}{k^4} \right] = 0 \quad (5.67a)$$

and from terms in $(\omega_1 t - k_1 x)$

$$B \left[\Phi_{\omega_1} \left\{ 1 - \frac{3\gamma}{4} (k_1^4 B^2 + 2k^4 A^2) \right\} + E_B + \frac{i\omega_1 C_N}{k_1^4} \right] = i\beta N. \quad (5.67b)$$

Note that Φ is defined as a function of ω .

When $B = 0$ and $A = A_0$, we get

$$A[k^4(A_0^2 - A^2) - 2k_1^4 B^2] = 0. \quad (5.68)$$

The value of A must always be real, so that

$$A^2 = A_0^2 - 2 \left(\frac{k_1}{k} \right)^4 B^2 \quad (\text{if } k^4 A_0^2 > 2k_1^4 B^2) \quad (5.69a)$$

$$A = 0 \quad (\text{if } k^4 A_0^2 < 2k_1^4 B^2). \quad (5.69b)$$

Since the right-hand side of equation (5.67b) is not zero, a real solution for B can be obtained whatever the value of A . In other words, the flagellum

being self-oscillating always involves a wave of frequency ω_1 . However, the free oscillation is completely suppressed when the amplitude of this component increases to satisfy the inequality (5.69b). This is the phenomenon of synchronization.

The mathematical theory predicts that synchronization will occur even if the two waves propagate in opposite directions, since only even powers of k appear in the equations (5.69) though in a natural situation two spermatozoa travelling in opposite directions are unlikely to come close enough to each other for synchronization to occur.

5.3.3 The curvature-controlled model

The Brokaw (1972b) model. Although the Machin model has provided many interesting features, such as the importance of mechanical impedance in determining the direction of wave propagation and synchronization between two nearby flagella, the model is not complete as the transfer function Φ is not specified. Using a sliding-microtubule mechanism, Brokaw (1971) tried to specify the feedback relationship between the active process and flagellar shape. For this purpose Brokaw assumed small-amplitude sinusoidal waves travelling distally on a flagellum of infinite length. Due to the small-amplitude waves, x and s were considered to be identical, and in assuming infinite length, the boundary conditions at the two ends of the flagellum were ignored. To get a simple relationship between the active process and flagellar shape, Brokaw also assumed that the elastic bending moment, M_e , is negligible in comparison with the active bending moment, M_a , and the viscous bending moment, M_v . Thus the moment-balance equation (5.30) becomes

$$M_a + M_v = 0. \tag{5.70}$$

Consider a flagellum carrying distally propagating waves only. Small-amplitude sinusoidal bending waves on a flagellum will be described by

$$y = be^{i\omega t - ikx} \quad \text{or} \quad b\cos(\omega t - kx). \tag{5.71}$$

From equations (5.28), (5.29) and (5.31), the viscous bending moment, M_v , is given by

$$\frac{\partial^2 M_v}{\partial x^2} = C_N \frac{\partial y}{\partial t}. \tag{5.72a}$$

Substituting (5.71) into (5.72a), we obtain

$$\frac{\partial^2 M_v}{\partial x^2} = iC_N \omega b e^{i\omega t - ikx}. \tag{5.72b}$$

On the other hand, using equations (5.34) and (5.70), we get

$$\frac{\partial M_v}{\partial x} = -S_a. \tag{5.73a}$$

Integration of equation (5.72b) leads to

$$S_a = \frac{C_N \omega b}{k} e^{i\omega t - ikx}. \quad (5.73b)$$

For sinusoidal movement, the curvature of the flagellum, κ , is given by

$$\kappa = \frac{\partial^2 y}{\partial x^2}. \quad (5.74a)$$

Substituting (5.71) into (5.74a), we obtain

$$\kappa = -k^2 b e^{i\omega t - ikx}. \quad (5.74b)$$

A comparison of equations (5.73b) and (5.74b) suggests a relationship between the active process and flagellar shape written as

$$S_a = -\frac{C_N \omega}{k^3} \kappa. \quad (5.75)$$

This relationship implies that S_a varies in phase with $-\kappa$. However this simple relationship holds only if the elastic bending moment is negligible. As illustrated in Figure 5.12, there is a (1/4)-cycle phase difference between M_e and M_a . The active moment, M_a , must have a component to cancel the elastic bending moment. If this occurs, the moment-balance equation (5.30) is satisfied. For this purpose, Brokaw (1972b) introduced a time delay, τ , in the control process:

$$S_a = -S_0 \kappa(t - \tau) \quad (5.76)$$

where S_0 is a constant. In the case of the sliding-filament mechanism, internal shear resistances are taking place during bend initiation and propagation. Thus Brokaw (1972b) introduced the internal shear moment, M_s , given by

$$\frac{\partial M_s}{\partial s} = S_a - E_s \sigma - C_s \frac{\partial \sigma}{\partial t} \quad (5.77)$$

where σ is shear. This equation corresponds to the combination of equations (5.34) and (5.36b). The first term on the right-hand side of this equation shows the active shear force. The second and third terms represent elastic shear resistance and viscous shear resistance, respectively. In the absence of these internal resistances, equation (5.77) is reduced to equation (5.34).

Since the active shear force is proportional to curvature and does not saturate, the elastic resistance, say E_s , must be nonlinear. For small shear displacement, the active shear force is stronger than the elastic shear resistance, thus the shear increases until the shear resistance balances the active shear force. Brokaw introduced nonlinearity in the form of cubic elastic resistance, as indicated by $E_s \sigma \propto \sigma^3$. Alternatively, to get stable bend amplitudes it is necessary to introduce nonlinearity in the form of saturation in an active shear force, together with linear shear resistance.

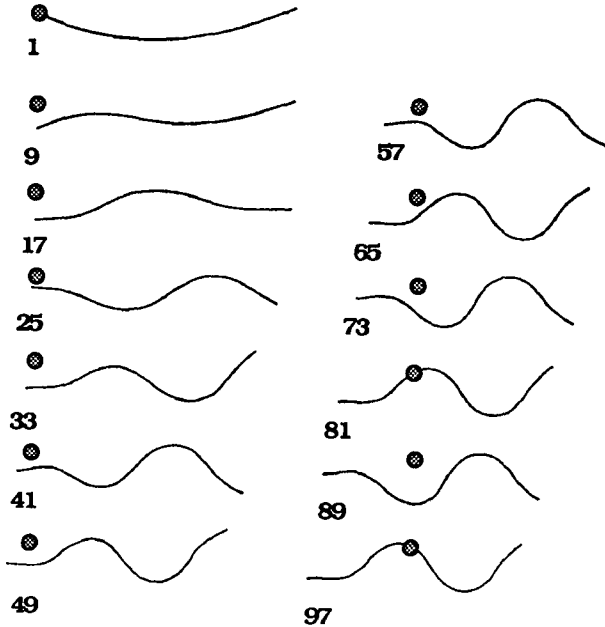


Figure 5.17 Self-organization of a bending-wave propagation on a flagellar model. The model is initially given the shape numbered 1 where the basal end of the model is indicated by a dark circle. As the model produces bending waves propagating toward the right, it will swim toward the left. Each image is then plotted relative to this circle. There are eight time-steps, or 1/2 beat cycle, between each successive image. From Brokaw (1972b). Reprinted with permission of the Biophysical Society.

Brokaw combined the internal shear moment, M_s , with the viscous moment, M_v , and the elastic bending moment, M_e , to demonstrate bending wave propagation in computer simulations. The moment-balance equation that Brokaw used is a more general equation than the simple version derived previously and can analyse the large-amplitude bend propagation. One of his results is shown in Figure 5.17. A nearly straight flagellum starts beating and reaches steady-state bending waves after two or three beat cycles. The stable movement pattern is independent of the initial condition, but in its present form the model will not beat from a completely straight position.

The Hines–Blum (1978) model. Hines and Blum (1978) replaced the explicit time delay by a smooth first-order rate process, without changing the essential features of the Brokaw (1972b) model. This change allows for greater stability in the numerical simulation. Their expression of S_a is given by

$$\frac{\partial S_a}{\partial t} = \frac{1}{\tau} (-S_0 \kappa - S_a) \tag{5.78}$$

where S_0 is a constant, κ is the curvature of the flagellum and τ is the relaxation time of this active process. Incorporating this active process into the general form of moment-balance equations (see Hines and Blum, 1978), they demonstrated stable travelling waves. To get stable amplitudes, they also used cubic nonlinear elastic resistance.

The essential feature of the curvature-controlled model can be understood analytically and graphically. By omitting all the nonlinear terms from the equations, we can use a *linear stability analysis* (see Section 1.2.3 of this book; and also e.g. Chapter 9 of the book by Babloyantz (1986)). The linearized equations (5.35) and (5.78) are described as follows:

$$\frac{\partial}{\partial t} \begin{pmatrix} \theta \\ S_a \end{pmatrix} = \begin{pmatrix} -\frac{E_B}{C_N} \frac{\partial^4}{\partial s^4} - \frac{1}{C_N} \frac{\partial^2}{\partial s^2} \\ -\frac{S_0}{\tau} \frac{\partial}{\partial s} \quad -\frac{1}{\tau} \end{pmatrix} \begin{pmatrix} \theta \\ S_a \end{pmatrix}. \quad (5.79)$$

For simplicity, we assume a flagellum of infinite length, and we set

$$\begin{pmatrix} \theta \\ S_a \end{pmatrix} = \begin{pmatrix} \theta^0 \\ S_a^0 \end{pmatrix} e^{\omega t - i k s}, \quad (5.80)$$

where k is a real number corresponding to the wave number of the flagellum. The characteristic equation of ω is given by

$$\omega^2 + A\omega + B - iC = 0 \quad (5.81)$$

where

$$A = \frac{1}{\tau} + \frac{k^4}{C_N} E_B \quad (5.82a)$$

$$B = \frac{k^4}{C_N \tau} E_B \quad (5.82b)$$

$$C = \frac{k^3}{C_N \tau} S_0. \quad (5.82c)$$

Let ω be complex (i.e. $\omega = \omega' + i\omega''$), and from real and imaginary parts of equation (5.81) we get

$$\begin{cases} \omega'^2 - \omega''^2 + A\omega' + B = 0 & (5.83a) \\ 2\omega'\omega'' + A\omega'' - C = 0. & (5.83b) \end{cases}$$

From equation (5.83a),

$$\omega''^2 = \omega'^2 + A\omega' + B \geq 0. \quad (5.84a)$$

The solution we are interested in is $\omega' > 0$. In this case, a travelling wave can be initiated. For the critical condition (i.e. $\omega' = 0$), $\omega'' = +\sqrt{B}$, or $-\sqrt{B}$. Suppose

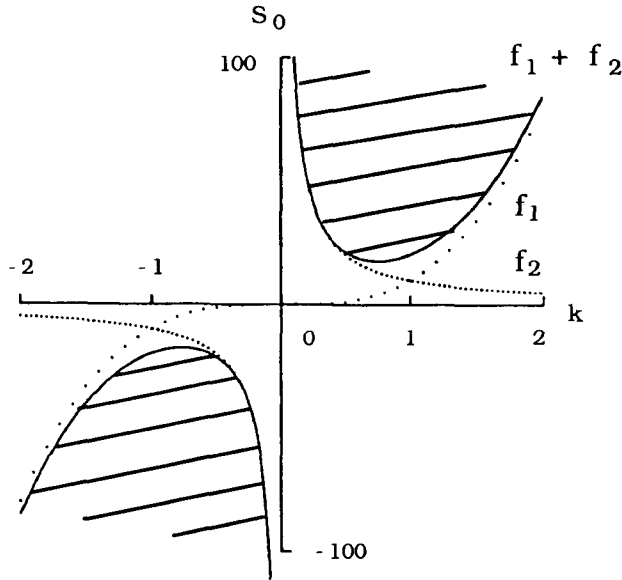


Figure 5.18 The unstable region causing bend propagation plotted as a function of wave number, k . In the figure, $f_1 = \alpha k^3$ and $f_2 = \beta/k$ are represented by broken curves. The sum of f_1 and f_2 is indicated by a continuous line. The shadowed regions satisfy the condition (5.86); that is, $S_0 \geq f_1 + f_2$, where $\alpha = \beta = 10$. For some positive values of S_0 , instability occurs only if $k > 0$, whereas for some negative values of S_0 instability occurs only if $k < 0$. This means that the direction of the bend propagation completely depends on the sign of S_0 in equation (5.78).

$\omega'' = +\sqrt{B} > 0$: the critical condition becomes $\omega' \omega'' \geq 0$. From equation (5.83b), this means

$$C \geq A\sqrt{B}. \tag{5.85}$$

Substituting A and C , and then dividing by k ,

$$S_0 \geq \alpha k^3 + \beta \frac{1}{k} \tag{5.86}$$

where

$$\left\{ \begin{aligned} \alpha &= \frac{E_B}{C_N} \sqrt{E_B C_N \tau} \end{aligned} \right. \tag{5.87a}$$

$$\left\{ \begin{aligned} \beta &= \frac{1}{\tau} \sqrt{E_B C_N \tau}. \end{aligned} \right. \tag{5.87b}$$

(If instead $\omega'' = -\sqrt{B} < 0$, equation (5.83b) cannot be satisfied.) Figure 5.18 shows that distally propagating waves (i.e. $k > 0$) will appear if $S_0 > 0$, and that proximally propagating waves (i.e. $k < 0$) appear if $S_0 < 0$.

If there is no time delay (i.e. $\tau = 0$), from equation (5.78) we get $S_a = -S_0 \partial\theta/\partial s$, where $\partial\theta/\partial s = \kappa$. Substituting this relation into equation (5.79), we get $\omega' < 0$ for any values of k . Therefore, traveling waves can never occur in the curvature-controlled mechanism without a time delay.

The importance of the presence of a time delay between the curvature of a flagellum and the active shear force is illustrated in Figure 5.11. When active shear force is produced in the region where the curvature of the flagellum is negative after appropriate time delay, the bending wave will propagate toward the distal end.

It is interesting to investigate the 'stretch-activation' mechanism, instead of the curvature-controlled feedback mechanism, in generating travelling waves. The stretch-activation feedback (see equation (3.7)) is described by

$$\frac{\partial S_a}{\partial t} = \frac{1}{\tau} (S_0 \sigma - S_a). \quad (5.88)$$

For simplicity σ is considered to be equivalent to θ . The characteristic equation obtained from equations (5.35) and (5.88) is

$$\omega^2 + A\omega + B' = 0 \quad (5.89)$$

where

$$\left\{ \begin{array}{l} A = \frac{1}{\tau} + \frac{k^4}{C_N} E_B \\ B' = \frac{k^4}{C_N \tau} E_B - \frac{k^2}{C_N \tau} S_0. \end{array} \right. \quad (5.90a)$$

$$(5.90b)$$

For $\Re(\omega) > 0$, B' must be negative (i.e. $B' < 0$) from equation (5.89). As illustrated in Figure 5.19, both distally and proximally propagating waves would occur when $B' < 0$. When the time delay is absent (i.e. $\tau = 0$), $S_a = S_0 \sigma = S_0 \theta$. Then the characteristic equation shows $\omega = -B'$, so that the condition of $B' < 0$ indicates instability leading to travelling wave patterns. In other words, the presence of a time delay is not essential in the case of a shear-controlled feedback mechanism. As discussed in Section 7.4.5, there is an instability leading to bend propagation even in the absence of the time delay.

The Brokaw (1985) model. In the previous model by Brokaw (1972b), linear active shear force is combined with nonlinear shear resistance to obtain the stable bend amplitude. When active shear force saturates, linear elastic shear resistance is sufficient to maintain stable bending waves. For this purpose, equation (5.78) which describes the feedback relationship is modified as follows:

$$\frac{\partial S_a}{\partial t} = \frac{1}{\tau} (S_0 - S_a) \quad (5.91)$$

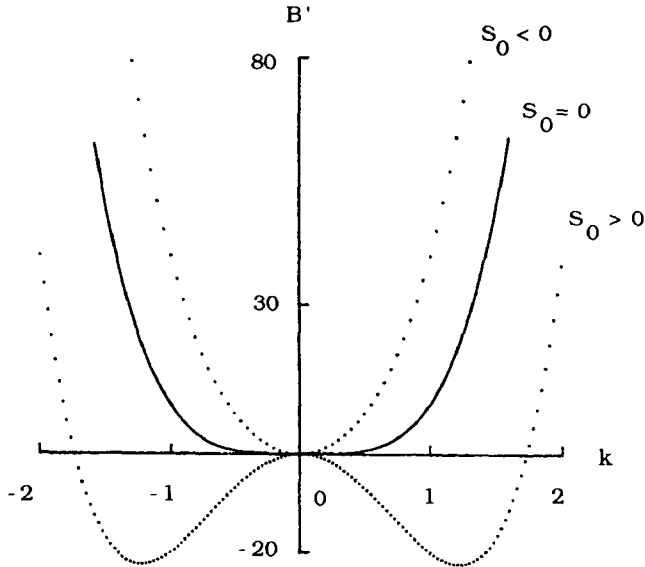
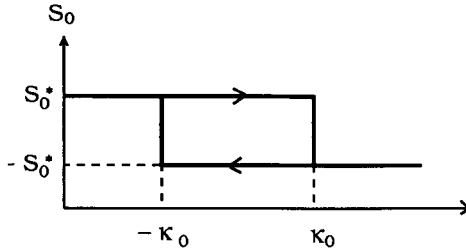


Figure 5.19 The unstable region causing bend propagation plotted as a function of wave number, k . We plot B' of equation (5.90b) (here, $B' = 10k^4 - 30k^2$) against k . For some values of parameters (e.g. τ, E_b, S_0 in equation (5.90b)), B' can be negative. In contrast to Fig. 5.18, instability occurs for $k < 0$ and $k > 0$. The model can, therefore, produce proximally travelling waves ($k < 0$) as well as distally propagating waves ($k > 0$).

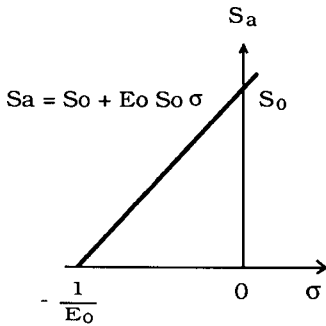
where the value of S_0 is switched between two constant values, say S_0^* and $-S_0^*$ as illustrated in Figure 5.20A. When the curvature falls below $-\kappa_0$, S_0 becomes $+S_0^*$, and when the curvature rises above $+\kappa_0$, S_0 becomes $-S_0^*$. In this way, the curvature feedback mechanism is incorporated into the model.

Besides the above nonlinearity in the feedback control mechanism, Brokaw incorporated two additional characteristics which are essential for the cross-bridge force-generating system: the force-length relationship and the force-velocity relationship (see Fig. 5.20B and C). Although the force-length relationship changes dynamically in response to a quick change in length as time develops (see Fig. 2.17), Brokaw incorporated two more characteristics: (i) In the absence of sliding, the active shear force, S_a , was considered to be equal to a constant value, S_0 (i.e. isometric force). (ii) In response to a quick change in shear, the force-generating system produced only a simple elastic shear resistance determined by a simple coefficient, E_0 . (E_0 was independent of S_a .) The actual shear resistance was the product of E_0 and S_0 . This property mimics the response of a real cross-bridge system. The stiffness in response to quick change in shear reflects the stiffness of attached cross-bridges as

(A)



(B)



(C)

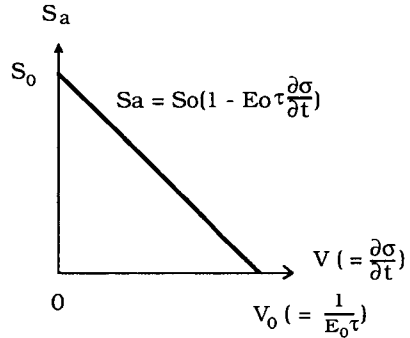


Figure 5.20 Diagrams showing the Brokaw (1985) model. (A): The active force is switched between two discrete values, S_0^* and $-S_0^*$, depending on the curvature, κ . Note that hysteresis switching occurs, in which the critical value for switching is dependent on the direction of the system. (B): The spontaneous force-length relation. This is analogous to the T1 curve obtained in muscle (see Fig. 2.17A). S_0 corresponds to ‘isometric tension’ in the force-generating system. This is analogous to the force-velocity curve in muscle (see Figs. 2.19 and 3.2). (C): The force-velocity relation. V_0 indicates ‘maximum sliding velocity’ at zero force.

there is no time for cross-bridges to detach and re-attach during the rapid shear change.

The force-velocity relationship describes the decrease in active force generated by the muscle as the shortening velocity increases. From the point of view of the molecular mechanism, this relationship is interpreted as follows: the faster the velocity of muscle contraction, the smaller the interacting cross-bridges and hence the smaller the active force generated by the muscle. Of course, detailed models that include the kinetics of cross-bridge attachment and detachment can mimic such a force-velocity relationship. To avoid many difficulties in dealing with such detailed models, Brokaw used

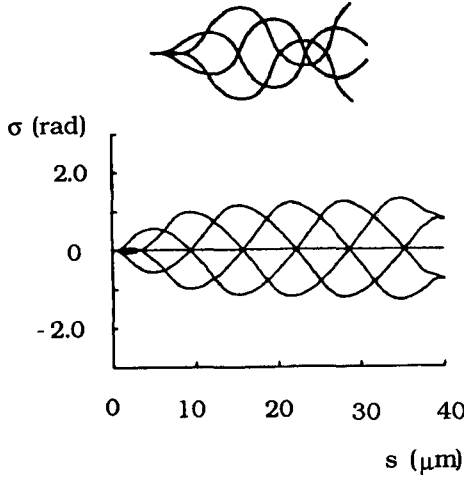


Figure 5.21 Behaviour of a flagellar model. The upper panel shows the configuration of the model in the (x, y) plane at time intervals separated by $1/4$ beat cycle. The basal end of the model is arbitrarily maintained in a fixed position and orientation. The lower panel shows successive shear, σ , as a function of arc length, s , of the flagellum. From Brokaw (1985). Reprinted with permission of the Biophysical Society.

a phenomenological equation to describe the properties of a cross-bridge system as follows:

$$\frac{\partial S_a}{\partial t} = -E_0 |S_0| \frac{\partial \sigma}{\partial t} + \frac{1}{\tau} (S_0 - S_a). \quad (5.92)$$

For the quick change in shear (i.e. $\partial \sigma / \partial t \gg 1$), equation (5.92) gives $|\partial S_a / \partial \sigma| = E_0 |S_0|$. For the steady-state length change (i.e. $\partial S_a / \partial t = 0$), equation (5.92) gives the force–velocity relationship:

$$S_a = S_0 \left(1 - E_0 \tau \frac{\partial \sigma}{\partial t} \right). \quad (5.93)$$

As we first expected, this simple model, which involves nonlinear active force-generating processes, produces stable oscillation and bend propagation with linear elastic shear resistance, E_s . In the absence of the shear resistance or external viscous resistance, this model also produces stable bend propagation (see Fig. 5.21).

5.3.4 The self-oscillatory model

Although an active force-generating system that involves a feedback control by the curvature of the flagellum shows oscillation and wave propagation,

there is no direct experimental evidence supporting the curvature control mechanism. In the light of the Machin model, which contains self-oscillatory contractile elements distributed along the length of the flagellum, a search for the self-oscillatory properties of an active sliding system seems to be appropriate. It seems, in the absence of the curvature feedback control, that the distributed shear oscillators coupled throughout the microtubule will produce metachronous shear oscillations that are responsible for the propagated bending waves. Observation of localized oscillatory bending in short regions locally activated with ATP has also stimulated this idea. Thus the problem is to search for the oscillatory mechanism used in the active sliding system.

One possible explanation is based on the actin–myosin sliding system for vibration typical of insect flight muscle (see Chapter 2). The oscillatory properties of such muscle are ascribed to a *delayed stretch-activation* (i.e. a delayed development of active force after a quick change in length). This delayed stretch-activation can be phenomenologically expressed by equation (5.88).

In opposition to this mechanism, Brokaw (1975) proposed a *stretch de-activation* mechanism that enabled the force during stretch to fall below the isometric force, S_0 , for $V = 0$. In addition, the force during shortening is set to be greater than the isometric force. When two such active sliding systems are combined together to form an antagonistic pair, the net steady-state force–velocity relationship is characterized by a positive slope in the region around $V = 0$, leading to instability, and a negative slope outside this region is required for stability.

For simplicity, Brokaw used a piecewise-linear force–velocity relationship given by the following specification (Fig. 5.22A):

$$S_a = \begin{cases} S_0 \left(-1 - \frac{V}{V_0} \right) & (V < -0.2V_0) \\ 4S_0V & (-0.2V_0 \leq V \leq 0.2V_0) \\ S_0 \left(1 - \frac{V}{V_0} \right) & (0.2V_0 < V). \end{cases} \quad (5.94)$$

When this active force-generating system is connected to a simple linear viscoelastic load with the elastic resistance, K , and the viscous resistance, γ , spontaneous oscillation can result (Fig. 5.22B). As shown in the (σ, V) plane (here, $V = \partial\sigma/\partial t$), a trajectory appears to be relaxation oscillation. It is found that a flagellar model containing distributed local shear oscillators produces bend propagation (Fig. 5.23).

Instead of using the steady-state force–velocity relationship, Hines and Blum (1979) and Brokaw (1982) have made attempts to investigate molecular mechanisms producing both steady-state behaviour and transient behaviour.

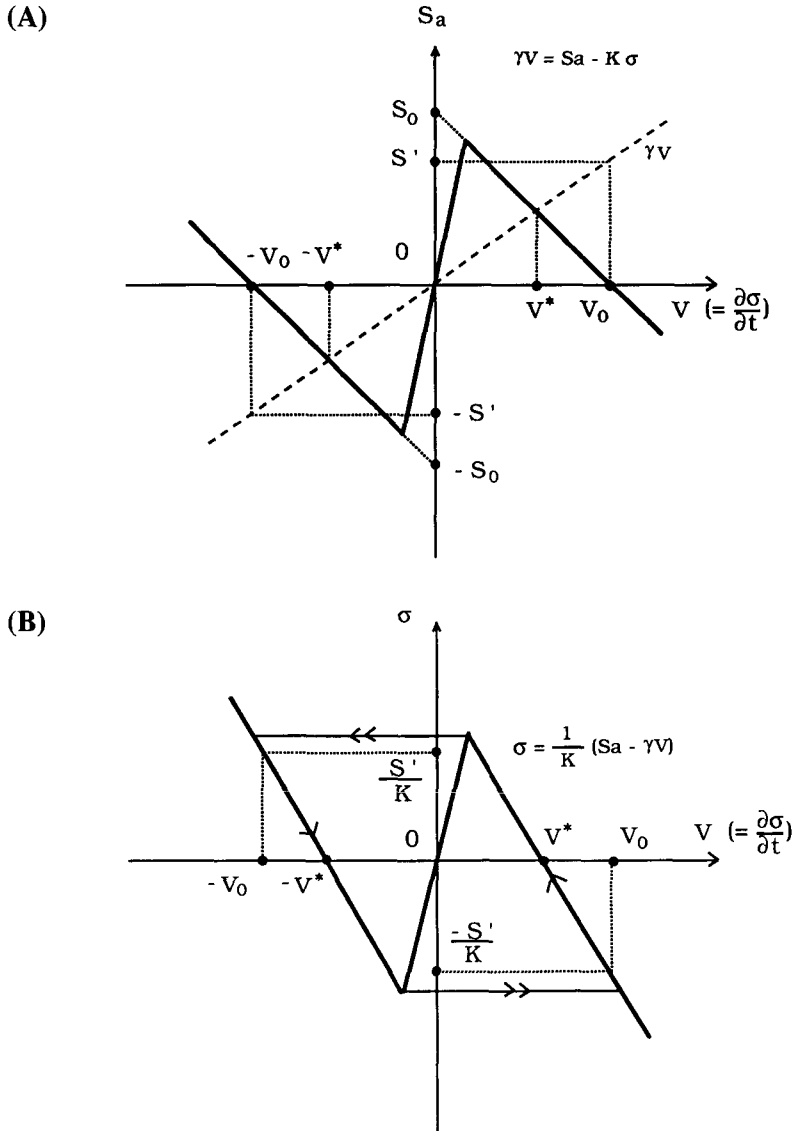


Figure 5.22 (A): The force-velocity relationship that corresponds to the antagonistic force-generating system. The force-balance equation is given by $\gamma V = S_a - K\sigma$, where $V = \partial\sigma/\partial t$. Here S_a is represented by solid lines. The dotted line indicates γV . The passive shear force ($-K\sigma$) does not appear in the (S_a, V) plane. (B): Displacement-velocity plot for the model. From the force-balance equation, $\sigma = (S_a - \gamma V)/K$ is plotted against V . The system will oscillate in the stable limit cycle (indicated by the trajectory) due to a viscous load (γV) and an elastic restoring force ($-K\sigma$). (See Section 3.3.)

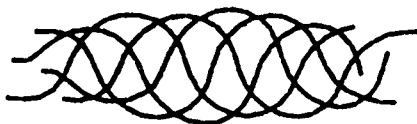


Figure 5.23 Behaviour of a flagellar model. The configuration is plotted in the (x, y) plane. As the model produces distally travelling waves toward the right, it moves toward the left. From Brokaw (1975). Reprinted with permission.

Their results suggest that stable bend propagation occurs either with internal viscous resistance in the absence of curvature feedback control, or with curvature-controlled rate constants determining the states of cross-bridges in the absence of internal viscous resistance. This type of model, however, has not yet demonstrated a realistic bend propagation in the viscous medium without curvature control mechanism, and also without internal viscous resistance.

5.3.5 The ciliary model

Since cilia and flagella possess an identical axonemal structure, the model that accounts for symmetrical wave propagation typical of flagella should produce asymmetric effective strokes plus recovery strokes typical of cilia, after a slight change in the motile system. Solving this problem may result in a good understanding of the internal mechanism. However, there are many difficulties, in attacking this problem.

The modified flagellar model. It was found that the form of the beat changed from the symmetrical to the asymmetrical mode when the severed end of the flagellum was stuck onto a glass surface (Douglas and Holwill, 1972). This observation suggests that the change of the boundary conditions at the proximal end to those appropriate for a cilium attached to a cell surface causes the change of beating patterns characteristic of such cilia.

Blum and Hines (1979) examined the effects of 'clamped' boundary conditions at the proximal end (i.e. $V(0, t) = \theta(0, t) = 0$). Figure 5.24 shows results using the curvature-controlled model by Hines and Blum (1978). The effects of the length of the flagellum, L , appear to be essential in producing bending wave propagation. Although bend propagation can occur under free-end boundary conditions, no motion occurs at $L = 10 \mu\text{m}$ even with identical parameters. Increasing L to $15 \mu\text{m}$ allows the flagellum to beat and distally propagating waves appear. Increasing L further to $20 \mu\text{m}$ allows the flagellum to beat similarly to the flagellar motion with two free ends. These results suggest that the effect of the constraint at the basal end is felt for up to $10 \mu\text{m}$ from the basal end, and that merely changing boundary conditions appropriate for a fixed cilium does not help to initiate ciliary motion.

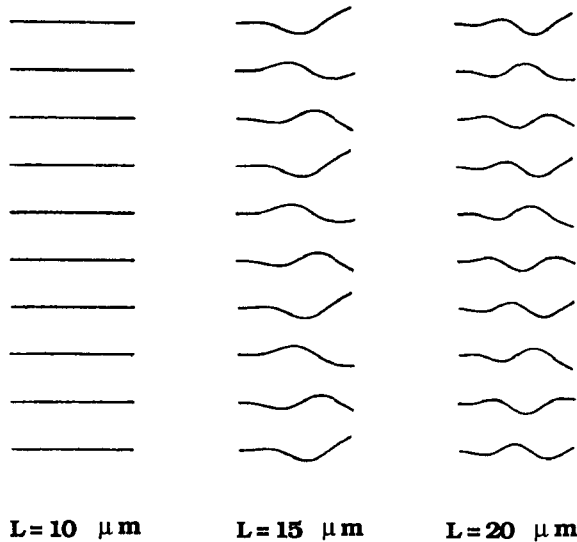


Figure 5.24 Effects of clamped-end boundary conditions on curvature-controlled flagellar models of different lengths. The proximal (left) end of each flagellum is clamped (i.e. $V(0, t) = \theta(0, t) = 0$). No bending motion occurs at $L = 10 \mu\text{m}$. Increasing L from 10 to $20 \mu\text{m}$ allows the flagellum to beat and symmetric bending waves appear. From Blum and Hines (1979). Reprinted with permission.

In contrast to the curvature-controlled model, Blum and Hines also tested the ability of the self-oscillatory model (Hines and Blum, 1979) to produce ciliary motion under the clamped boundary conditions (i.e. $V(0, t) = \theta(0, t) = 0$) without curvature control (Fig. 5.25). At $L = 10 \mu\text{m}$, the ‘cilium’ is short enough to generate a part of its bend during a cycle. This partly resembles an effective stroke. Increasing L to $15 \mu\text{m}$ allows the system to develop more waves, but these waves initiate at the tip and propagate to the base. At $L = 20 \mu\text{m}$, proximally propagating waves are clearly observed. These results are very interesting in comparison with the analytical prediction by Machin (1963) in the sense that the direction of bend propagation may be influenced by the boundary condition at the proximal end (see Table 5.2).

Although experimental studies show that a change of boundary conditions at the proximal end is sufficient to change motion from a flagellar to a ciliary type, the simulation results do not reproduce the experimental results. This means that we may be ignoring some important features responsible for asymmetric beating patterns typical of cilia, and that changing boundary conditions also affects some internal operating mechanism.

The catastrophe model. Varela *et al.* (1977) applied René Thom’s catastrophe theory to ciliary motion as a tool to facilitate *top-down* description

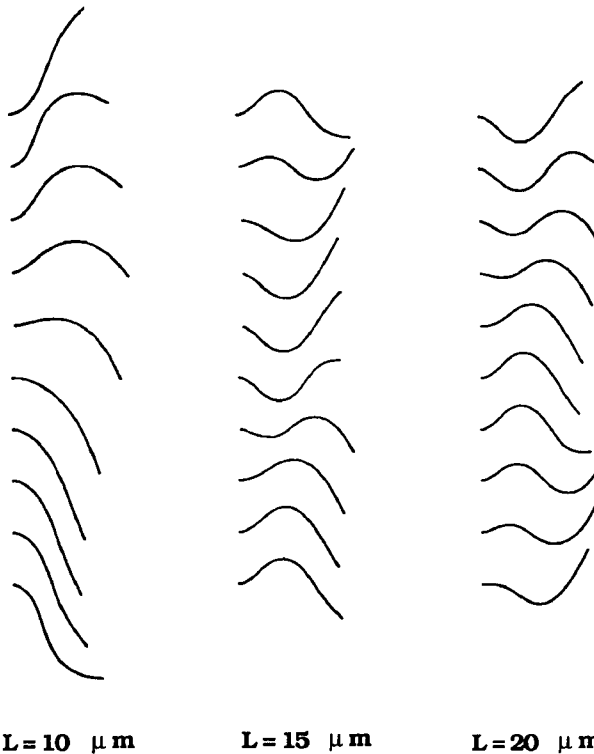


Figure 5.25 Effects of clamped-end boundary conditions on self-oscillatory flagellar models of different lengths. The same boundary conditions are used. At $L = 10 \mu\text{m}$, the 'cilium' is short enough to generate a part of its bend during a cycle, which partially resembles an effective stroke. Increasing L to 15 or $20 \mu\text{m}$ allows the system to develop more waves. These waves initiate at the tip and propagate to the base. From Blum and Hines (1979). Reprinted with permission.

of global qualitative behaviour. From a mechanical point of view, they summarized the basic events during the ciliary beat.

- (i) There is an initial or resting position.
- (ii) A mechanical or biochemical stimulus can trigger an initiation of the effective stroke.
- (iii) Following the effective stroke, the system returns to its initial resting position by exhibiting the recovery stroke.

These three properties are characterized by the following dynamic behaviour:

- I Equilibrium state.
- II Threshold for an action.
- III Return of equilibrium.

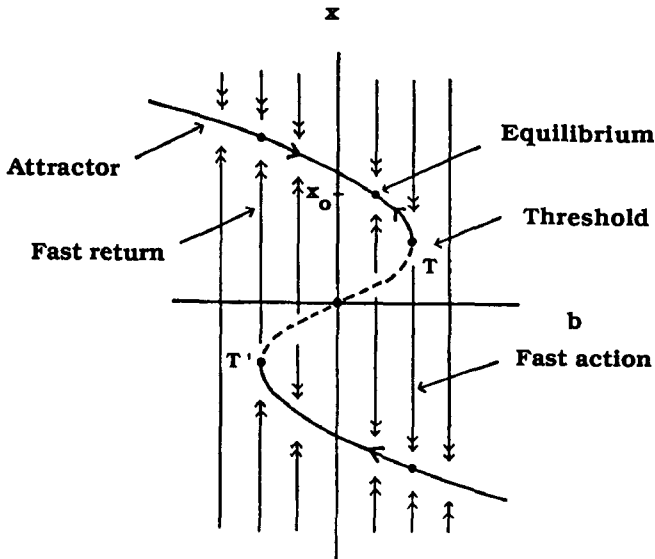


Figure 5.26 The behaviour of the coupled first-order differential equations (5.95). For $a = -1$, the slow manifold (given by $dx/dt = 0$) is seen in the phase plane (x, b) . From Varela *et al.* (1977). Reprinted with permission.

As Zeeman (1972) pointed out, the three properties are commonly observed in various biological systems such as nerve impulses and heart beats. Let x be a state variable which monitors the temporal events related to the action, and a and b the control parameters which change more slowly than x . The simplest pair of equations is

$$\begin{cases} \epsilon \frac{dx}{dt} = -(x^3 + ax + b) & (5.95a) \\ \frac{db}{dt} = x - x_0. & (5.95b) \end{cases}$$

When a is fixed, say $a = -1$, and $x_0 > 0$ and $\epsilon \ll 1$, the behaviour of this equation is seen in the (x, b) phase plane (Fig. 5.26). Suppose that the system is initially at the equilibrium position, $x = x_0$. If b changes externally beyond a threshold value, x will cause a fast action approaching the lower attractor surface where x will change slowly due to the coupling of b and x . But at T' the system will show a fast return; consequently an equilibrium state is retained.

This behaviour is shown in the more general scheme where the equilibrium

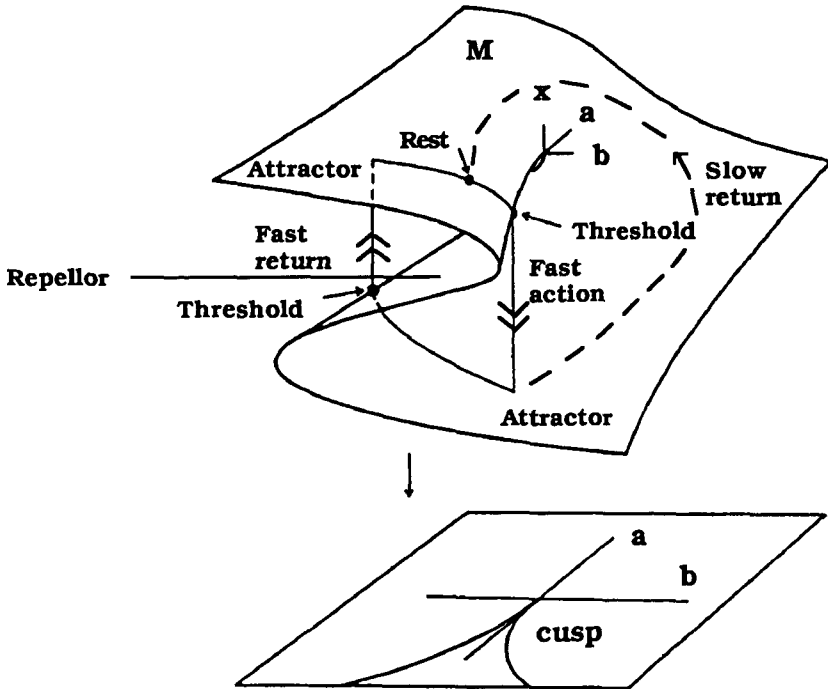


Figure 5.27 The slow manifold surface (upper panel) and the projection of its fold onto the (a, b) plane. The cusp-shaped distribution of the catastrophe points is shown. From Varela *et al.* (1977). Reprinted with permission.

surface is defined by control space (a, b) (see Fig. 5.27). This surface, called a *manifold*, is given by

$$f(x, a, b) = x^3 + ax + b = 0. \quad (5.96)$$

The line of two thresholds is defined by

$$\frac{df(x, a, b)}{dx} = 3x^2 + a = 0. \quad (5.97)$$

On the control plane (a, b) , the cusp-shaped curve is obtained from equations (5.96) and (5.97). It is represented by

$$4a^3 + 27b^2 = 0. \quad (5.98)$$

Thus the folds of the surface are referred to as the *cusp catastrophe*.

Suppose that a is also allowed to vary. Equations (5.95) are modified as follows:

$$\left\{ \begin{array}{l} \varepsilon \frac{dx}{dt} = -(x^3 + ax + b) \end{array} \right. \quad (5.99a)$$

$$\left\{ \begin{array}{l} \frac{da}{dt} = -2a - 2x \end{array} \right. \quad (5.99b)$$

$$\left\{ \begin{array}{l} \frac{db}{dt} = -a - 1. \end{array} \right. \quad (5.99c)$$

Then, a smooth return to the initial equilibrium is possible similar to that of a nerve impulse (Zeeman, 1972).

Varela *et al.* assigned x as the average angular displacement, b as the total displacement and a as the ATP concentration (= constant). These assignments give some insight about the underlying mechanism for ciliary beating. However, there is room to improve this model as Varela *et al.* pointed out. First, this model cannot account for bend initiation and propagation as it contains no space variable, s . We must use the partial differential equations such as (5.36) or (5.37) instead of the ordinary differential equations. Secondly, instead of angle, angular velocity may be a more adequate variable to describe ciliary motion, because angle is proportional to sliding displacement at a point and they are not mutually independent variables.

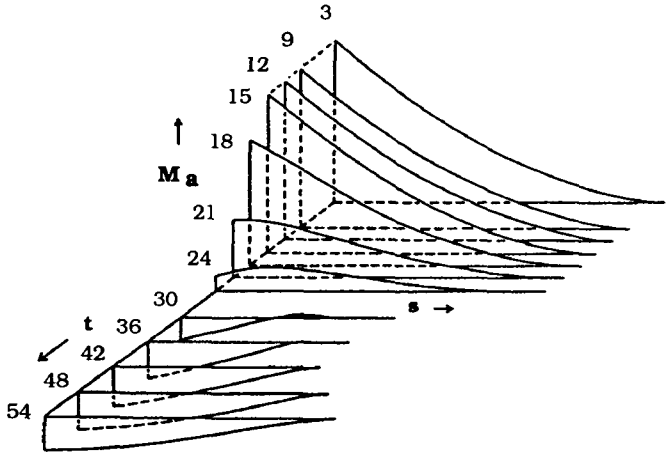
The internal-clock model. Rikmenspoel and Rudd (1973) found a forcing function responsible for the realistic ciliary motion (Fig. 5.28). It was found that simultaneous active sliding is necessary to generate the effective stroke, while for the recovery stroke the forcing function must involve travelling properties (Fig. 5.28A). In addition, the elastic bending resistance, E_B , is assumed to vary during the cycle of a beat, which may reflect the change of the number of attached cross-bridges (Fig. 5.28B). However, this assumption is not acceptable since attached cross-bridges would contribute to the shear resistance but not to the bending resistance (Blum and Hines, 1979).

Rikmenspoel (1982) also attempted to demonstrate flagellar beating patterns by using this technique. He finally succeeded in reproducing the 'spontaneous transitions' from rest to motion observed in real flagella in Rikmenspoel (1978).

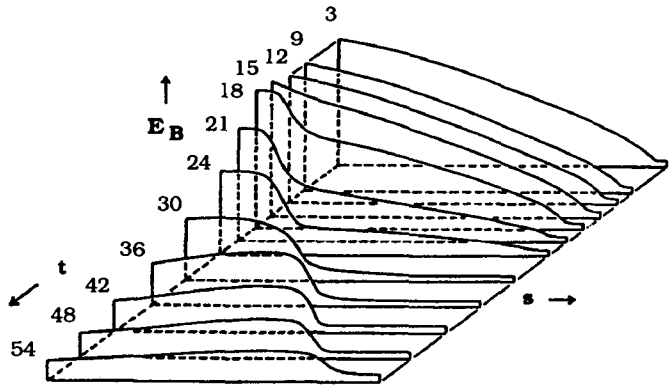
In the context of ciliary and flagellar bending waves, Rikmenspoel's approach of using a forcing function, is an interesting attempt to establish an identical internal force-generating mechanism. However, the models do not explicitly explain the underlying molecular mechanisms for cross-bridge interactions. The step still remaining to be done is to specify the forcing function based on the cross-bridge dynamics.

The Sugino–Naitoh model. Sugino and Naitoh (1982) found active sliding patterns occurring among the nine outer microtubules that reproduce the

(A)



(B)



(C)

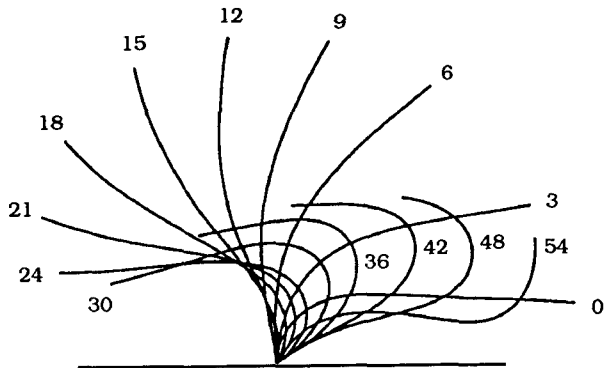


Figure 5.28 (A): Contour plot of the active moment during a full cycle. M_a is plotted as a function of time, t , and position, s . (B): Contour plot of the stiffness during a full cycle. E_B is plotted as a function of t and s . (C): The ciliary shape of the model. The numbers assigned to each stage correspond to time, t , in ms. From Rikmenspoel and Rudd (1973). Reprinted with permission of the Biophysical Society.

three-dimensional beat cycle as seen in *Paramecium*. The patterns were obtained by *trial and error* on the assumption that the cilium is fixed at the base and that elastic bending resistance is ignored.

Figure 5.29 shows 41 successive changes in the sliding pattern (upper part) and the corresponding successive changes in the shape of a cilium (lower left, side view; lower right, top view) during a single beat cycle. The active sliding is localized in each pair of doublets as shown by the dark region. In a single pair of the doublets, the local activation starts at the basal end, travels up along the doublets, and finally disappears at the tip. Within the ring of nine paired doublets, activation is triggered from one pair to the adjacent pair ($n \rightarrow n + 1$).

There is a long interval between the start of activation at the 4–5 pair (No.37) and that in the 5–6 pair (No.15). This indicates that the cyclic activation in the nine pairs of doublets starts at the 5–6 pair and terminates at the 4–5 pair. Since initiation of activation in the 5–6 pair corresponds to the start of the recovery stroke, it is suggested that the recovery stroke precedes the effective stroke.

Although the Sugino–Naitoh model clearly identifies the relationship between the sliding patterns in the nine pairs of doublets and the three-dimensional ciliary beating, the fundamental mechanism generating such spatio-temporal sliding patterns is still a *black box*.

5.3.6 Ciliary propulsion

The envelope model. The *envelope model* has its origins in Taylor's swimming-sheet model for flagellar propulsive motion. When waving cilia are closely packed over the relatively flat cell surface, the motion of ciliary tips is replaced by a waving envelope (Fig. 5.30A). Taylor's sheet is not allowed to stretch and release due to the geometrical constraint of the flagellum. However, the envelope is free from this constraint as it represents loci of ciliary tips, in which an individual tip performs a simple harmonic motion of amplitude, a , tangential to the surface, and a simple harmonic motion of amplitude, b , normal to the surface (Fig. 5.30B). The model assumes that the envelope is infinite and the undulations two-dimensional, and that the envelope is impermeable to fluid (although this is not true).

Recalling equation (5.11),

$$\frac{V}{U} = \frac{1}{2} k^2 (b^2 + 2ab \cdot \cos\phi - a^2) \quad (5.11)$$

we get the expressions for the ratio of swimming speed, $-V$, and wave velocity, U . Evaluations of the velocities of propulsion using this formula (5.11) are valid when kb and ka are small; that is, amplitudes b and a are small compared with the metachronal wavelength, $\lambda (k = 2\pi/\lambda)$. For convenience, equation (5.11) is rewritten as

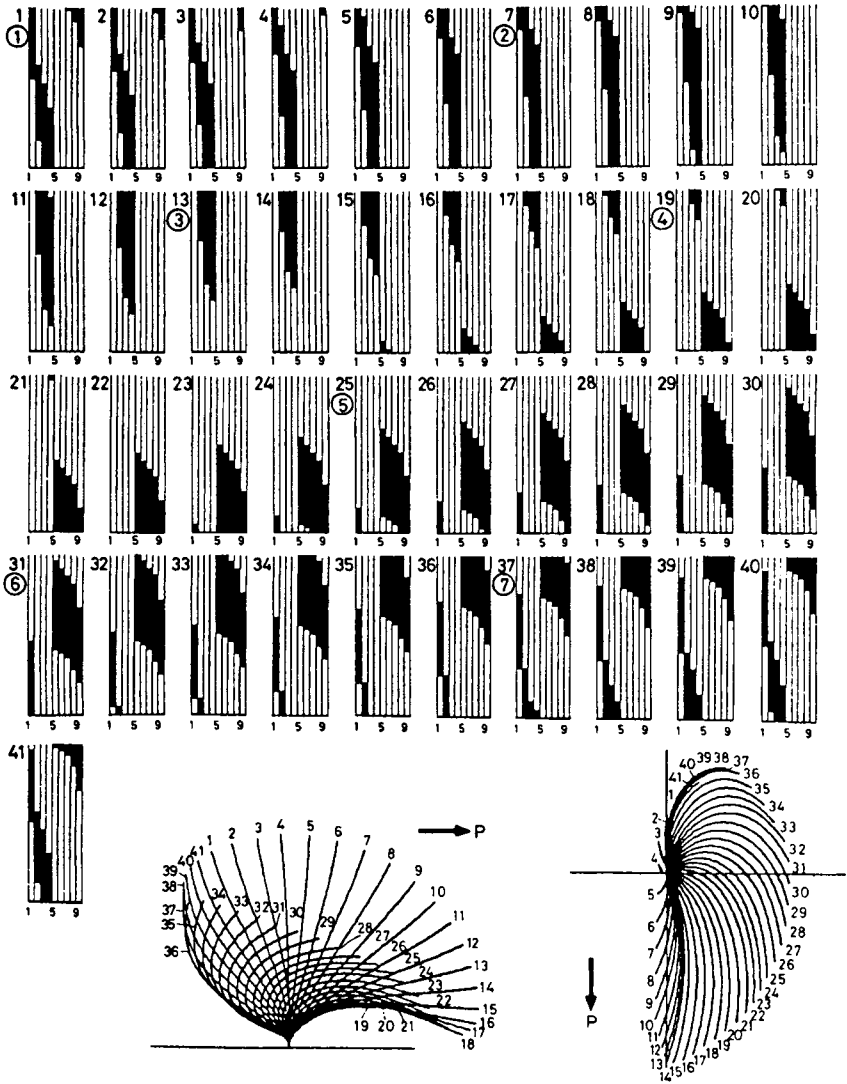


Figure 5.29 Upper part: Spatio-temporal active sliding patterns during a single beat cycle. The nine doublets are shown schematically in a plane as ten vertical lines numbered at their bases (1, 5 and 9). Lines 1 and 10 correspond to doublet No.1. Dark regions between the vertical lines represent the active sliding regions. Lower part: The change in the shape of a cilium during a single beat cycle. Each shape is simulated according to each active sliding pattern shown in the upper part. On the left is the side view and on the right the top view. From Sugino and Naitoh (1982). Copyright © Macmillan Magazines Ltd. Reprinted with permission.

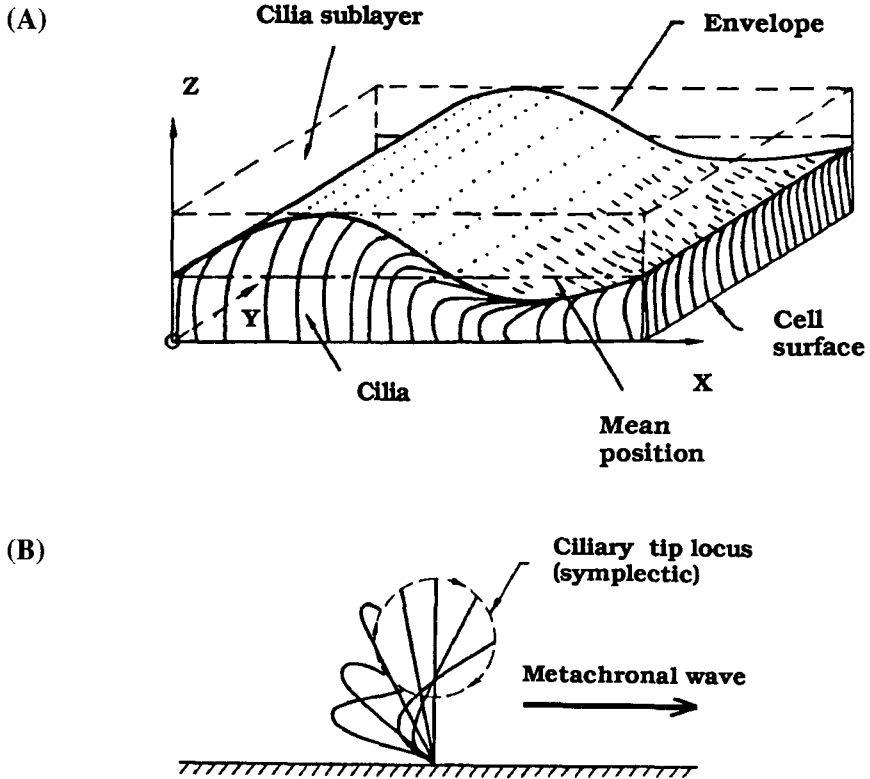


Figure 5.30 (A): The envelope model of ciliary propulsion. The ciliary tips are replaced by the continuous envelope. From Blake (1975). (B): A typical pattern of a ciliary tip locus (symplectic). From Brennen and Winet (1977). Reprinted with permission.

$$\frac{V}{U} = \frac{1}{2} k^2 (a^2 + b^2) \left[\sqrt{(1 - G^2)} \cos \phi - G \right] \tag{5.100a}$$

where

$$G = \frac{a^2 - b^2}{a^2 + b^2}. \tag{5.100b}$$

Figure 5.31A shows arbitrary elliptical ciliary tip loci with the parameters G and ϕ . Note that $G = -1$ (i.e. the simple transverse wave with $a = 0$) corresponds to the solution (5.12), whereas $G = +1$ (i.e. the pure longitudinal wave with $b = 0$) corresponds to the solution (5.13). Figure 5.31B depicts the contours of the dimensionless propulsive velocity, $V/Uk^2(a^2 + b^2)$, against the (G, ϕ) parameter plane. The + sign of this velocity indicates that the sheet swims to the left in an opposite direction to the metachronal wave. In

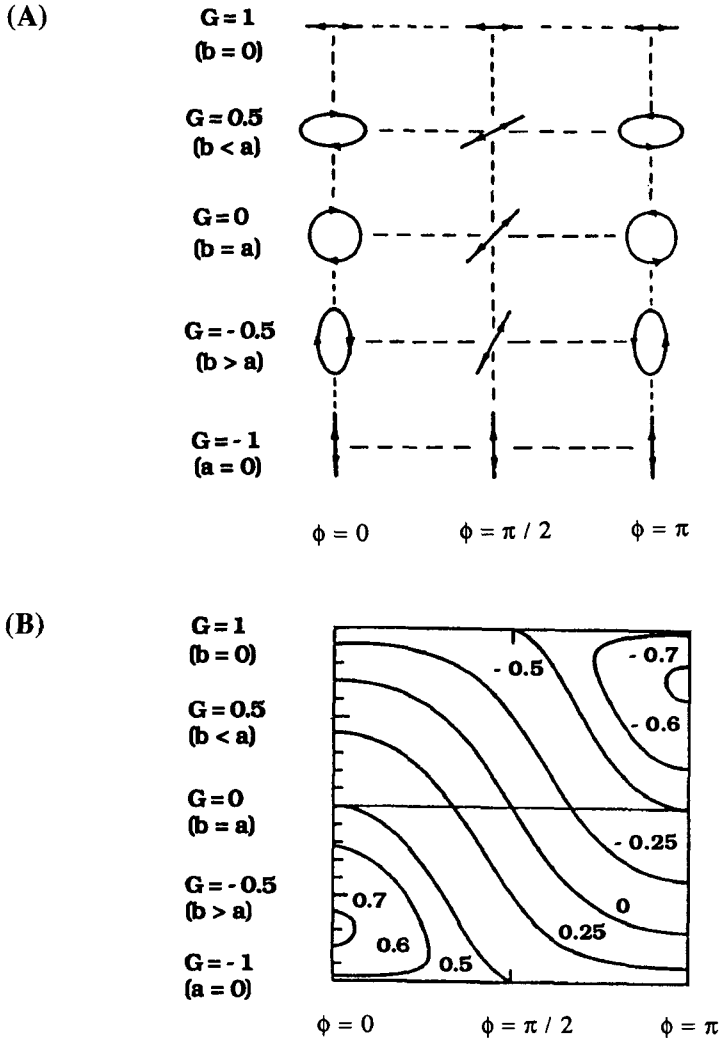


Figure 5.31 (A): Variations of arbitrary elliptical ciliary tip loci with parameters G and ϕ . (B): Contour plot of the dimensionless propulsive velocity $V/UK^2(a^2 + b^2)$ on the (G, ϕ) plane. From Brennen and Winet (1977). Reprinted with permission.

contrast, the $-$ sign suggests that the sheet swims to the right in the same direction as the wave.

The comparison of Figure 5.31A and Figure 5.31B leads to the following two predictions. (i) When the path of a ciliary tip is circular (i.e. $G = 0$ or $a = b$), the direction of propulsion, relative to the wave, depends on whether the ciliary tip moves in a clockwise or counter-clockwise direction. (ii) When the path of a ciliary tip is elliptical, the direction of propulsion depends on

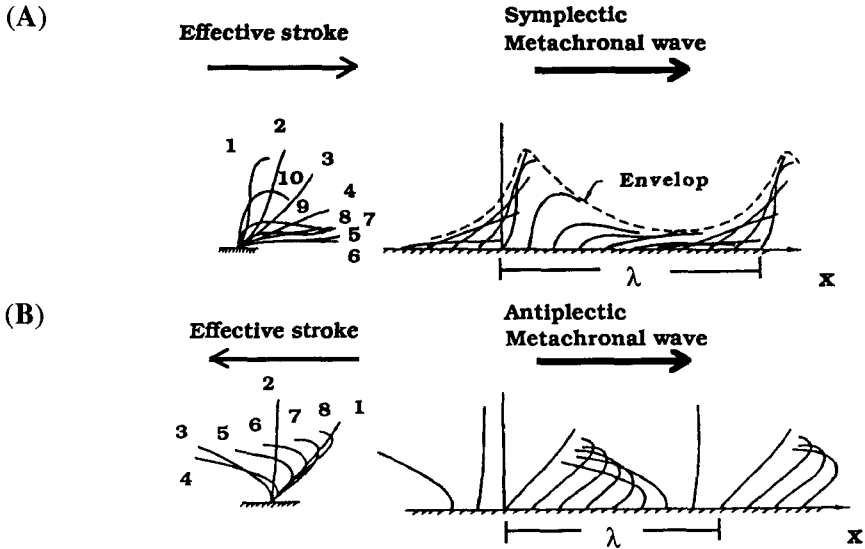


Figure 5.32 (A): Beat patterns and the symplectic metachronism. The ciliary tip moves in a clockwise and predominantly transverse direction. (B): Beat patterns and the antiplectic metachronism. The ciliary tip moves in a counter-clockwise and predominantly longitudinal direction. From Brennen and Winet (1977). Reprinted with permission.

whether the ciliary tip tends toward transverse motion ($G \rightarrow -1$ or $a \rightarrow 0$) or longitudinal motion ($G \rightarrow 1$ or $b \rightarrow 0$) irrespective of the direction of motion along the elliptical path.

As a practical example, consider organisms like *Opalina* whose ciliary tips move predominantly in a transverse and clockwise direction. They are propelled to the left in opposition to the metachronal wave (Fig. 5.32A). Another example is obtained in organisms whose ciliary tips move in a predominantly longitudinal and counter-clockwise direction. They move in the same direction as the wave (Fig. 5.32B).⁸

The cilia sublayer model. The envelope model could mainly explain the symplectic metachronal wave where most of the cilia move closely together to form an 'envelope'. However, for antiplectic metachronism (see Fig. 5.32B), the envelope approximation is not valid because the cilia are spread out during the effective stroke. The *cilia sublayer model* has been proposed to explain the interactions between individual cilia when taking into account the surrounding fluid. But because of a lack of knowledge about the mechanism that causes individual ciliary motion, the observed data or the idealized ciliary forms are used to calculate velocity profiles within the ciliary array (see the review by Blake and Sleight, 1974). A more important and interesting problem is to understand how the metachronal wave arises from individual ciliary motions. This problem has not yet been solved.

Notes

- 1 The Stokes equations are obtained from the more general Navier–Stokes equations by omitting the time-dependent and inertial terms.
- 2 Strictly, the constraint of inextensibility (i.e. $a = 0$ in equation (5.5a)) requires the new form of (5.5a) for waves of relatively large amplitude based on the following geometrical consideration:

$$x_s = x - \frac{b^2}{8} \cdot \sin 2(kx - \omega t). \quad (5.5'a)$$

$$y_s = b \cdot \sin(kx - \omega t). \quad (5.5'b)$$

The equations (5.5') indicate that a point on the surface moves in the form of a figure of 8 (see Fig. 3.2 in Childress (1981)). The corresponding velocity of propulsion calculated up to fourth order is :

$$\frac{V}{U} = \frac{1}{2} k^2 b^2 \left(1 - \frac{19}{16} k^2 b^2 \right). \quad (5.12')$$

- 3 Strictly, since a system under zero resultant force may have a net moment resulting in rotation of the organism, the movement of the flagellum must be consistently determined by requiring that the net force and net moment on the body is equal to zero (see Lighthill, 1976).
- 4 To obtain the values for coefficients in (5.17) we must integrate singular solutions (e.g. 5.15) along the surface of the flagellum (normally taken to be an envelope of spheres of radius A and centre on a certain curved flagellar axis) and identify the coefficients of the normal and tangential forces (see Chapter 6 of the book by Childress (1981)).
- 5 If the filaments are free to slide at the base, $\sigma(s) = \theta(s)$ is no longer correct; instead we must specify $\sigma(0) - \theta(0)$ based on Newton's laws with regard to sliding movement (see Blum and Hines, 1979).
- 6 Internal viscous shear force is not necessary to consider for flagellar and ciliary dynamics (see Hines and Blum, 1978).
- 7 A sinusoid of frequency $\omega/2\pi$ is represented by $\{\exp^{i\omega t} + (\exp^{i\omega t})^*\}/2$, where the asterisk denotes the *complex conjugate*. If ω is now a complex frequency, such as $\omega' + i\omega''$, the 'sinusoid' becomes $\exp(-\omega''t)\cos\omega't$ which is growing exponentially when $\omega'' < 0$.
- 8 The swimming direction of ciliated organisms is opposed to the direction of the effective stroke.

6 Molecular mechanism for excitability and oscillations

In this chapter we restrict ourselves to the *internal mechanisms* underlying flagellar and ciliary dynamics, as studied by Murase and Shimizu (1985b; 1986). Technically, it is assumed that the external viscosity is replaced by a non-zero internal viscosity. The condition with only the external viscosity is different from the condition with only the internal viscosity. Nevertheless we can simplify the basic equation (5.36) through this assumption, and thereby construct a theoretical basis for understanding flagellar and ciliary dynamics.

The simplified equation that we will deal with here is the so-called *reaction–diffusion* equation:¹

$$\gamma \frac{\partial \sigma}{\partial t} = E_B \frac{\partial^2 \sigma}{\partial s^2} + S_a + S_p, \quad (6.1)$$

where γ is the internal viscous resistance, E_B the bending resistance, S_a the dynein active force and S_p the passive restoring force. Thus, the problem is how to specify S_a and S_p in equation (6.1) based on the molecular structure and function and still satisfy travelling-wave solutions.

The key requirement for the propagated dynein activity, which leads to bend propagation along the axoneme, is that dynein molecules be *excitable*, but not *oscillatory*. Of course the real goal of studying flagellar and ciliary behaviour is to understand how they beat in a viscous medium. To do this, we must solve the more complicated equation (5.36), as detailed in Chapters 7, 8 and 9.

Theoretical and experimental background are briefly described in Sections 6.1 and 6.2, respectively. Section 6.3 proposes a flagellar model based on the three-state model. Section 6.4 discusses the dynamics of a short flagellar segment. Symmetric and asymmetric bending waves are demonstrated in Sections 6.5 and 6.6, respectively.

6.1 Theoretical background

The previous chapter has provided two basic classes of models for flagellar beating – the *curvature-controlled* and *self-oscillatory* models (Table 6.1).

Table 6.1 Three different types of theoretical models for flagellar movement

(i) Curvature-controlled models	(ii) Self-oscillatory models	(iii) Excitable dynein models
Brokaw (1971; 1972b) Hines & Blum (1978) Brokaw (1985; 1989)	Machin (1958; 1963) Brokaw (1975; 1976) Blum & Hines (1979)	Murase & Shimizu (1986) Murase, Hines & Blum (1989) Murase (1990) Murase (1991a) Murase (1991b)
Hines & Blum (1979)* Brokaw (1982)*		

* These models possess both curvature-controlled mechanism and self-oscillatory mechanism since the two mechanisms are not mutually exclusive.

The curvature-controlled models of flagellar beating assume that the active sliding process, which causes bending of the flagellum, will in turn be controlled by the resultant bending, or curvature of the flagellum. Normal base-to-tip propagating waves result from the presence of a feedback control between the active process and the curvature (see Fig. 5.17). The recovery phase of ciliary beating, in which a bend is initiated at the base and propagates to the tip, is also generated by a similar feedback control. Unfortunately, such a feedback control mechanism fails to produce the swing of a nearly straight cilium as occurs during the effective stroke, and hence cessation of beating (see Fig. 5.24). Since cilia and flagella do not essentially differ in structure and function – indeed, the same axoneme exhibits both ciliary-like and flagellar-like beats under different conditions (Bessen *et al.*, 1980; Hosokawa and Miki-Noumura, 1987) – the failure of the curvature-controlled models to generate a full cycle of ciliary beating suggests that there may be another mechanism operating in cilia.

Self-oscillatory models seemed to be an attractive alternative at first (Brokaw, 1975; 1976). In these models, elementary oscillators distributed along the axoneme are assumed to cause alternating active sliding. This leads to bend initiation and propagation in flagella when high – unrealistic – internal viscosity is present. Where the length of the axoneme is small enough (or the bending resistance of the axoneme is sufficiently large), oscillators will synchronize with each other through strong coupling. This synchronization of all the oscillators allows simultaneous active sliding within the axoneme to cause a beating form that partially resembles the effective stroke of a cilium. However, in a more realistic situation, in which little or no internal viscosity is present, the self-oscillatory models fail to reproduce the base-to-tip bend propagation that occurs during the recovery stroke of the ciliary beating or during normal flagellar oscillations (Hines and Blum, 1979; Blum and Hines, 1979). Rather, bends seemed to be initiated at the tip and propagate to the base (see Fig. 5.25).

Neither the curvature-controlled nor the self-oscillatory model can completely account for a full cycle of ciliary beating. Thus, it is thought that there is some intermediate (or common) mechanism generating ciliary-like and flagellar-like beats. A search for an identical, force-generating function for both flagella and cilia has been made by Rikmenspoel and colleagues (cf. Rikmenspoel and Rudd, 1973; Rikmenspoel, 1982), though no underlying mechanism has been proposed for this forcing function.

As a third class of models for wave propagation in cilia and flagella, the *excitable dynein* models have been proposed (Table 6.1). These models assumed that dyneins are normally at 'rest' and 'activation' leading to force generation is only triggered by sliding past a threshold. Once superthreshold active sliding is induced by other dyneins, the activity of dyneins is successively triggered along the axoneme as long as sliding persists. Thus, a parameter determining the transition to an 'active' state plays an important role in generating various triggering patterns of dynein activation, and hence various waveforms typical of flagella and cilia. These models operate well at zero external viscosity (this chapter) and also even in the presence of external viscosity (Chapters 7, 8 and 9).

6.2 Experimental background

As we have already detailed in Chapter 4, cilia and flagella show a great variety of dynamical behaviours – for example, the reversal of the direction of wave propagation, intermittent movement, bursting activity and mechanosensitivity. Before attempting to understand some of these complicated behaviours (see Chapter 7), we confine our attention to two main types of dynamics – oscillations and excitability.

The observation that fragments of *Crithidia* flagella as short as 500 nm can beat regularly is of considerable interest (Douglas and Holwill, 1972). Potentially this observation reflects the minimal size of a system necessary to exhibit oscillations. Another interesting observation is that short regions of a flagellum exhibit local oscillations when they are specifically reactivated by ATP (Brokaw and Gibbons, 1973). Rikmenspoel (1978) happened to observe spontaneous transitions from rest to motion in live sperm flagella, which can be interpreted through computer simulations as a result of oscillatory behaviour (Rikmenspoel, 1982). All these observations strongly suggest that *pacemakers* exist which oscillate spontaneously and lead to bend initiation and propagation.

In contrast to these observations there are many others that suggest excitable dynamics. For example, movement of some flagella reactivated with ATP requires either mechanical initiation by a microneedle (Lindemann and Rikmenspoel, 1972) or mechanical constraint at one end of the flagellum by attaching it to a glass surface (cf. Blum and Hines, 1979). In an amputated flagellum, a microneedle stimulation causes a passive bend that propagates

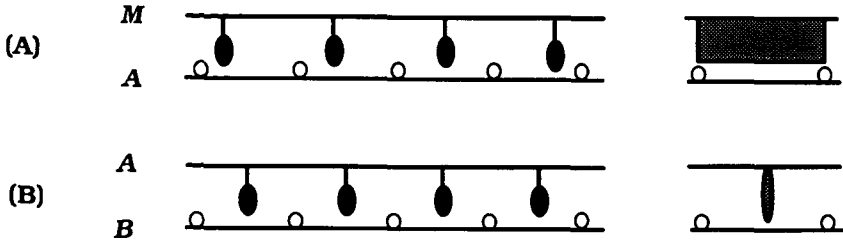


Figure 6.1 Left part: The geometric arrangement of cross-bridges (denoted by arms) and attachment sites (denoted by dots). Right part: The distribution of cross-bridges. (A): In muscle, M and A denote the thick and thin filaments. (B): In flagella, A and B denote the A-subtubule of the N th doublet and the B-subtubule of the $(N + 1)$ th doublet. Modified from Murase and Shimizu (1986). Reprinted with permission.

with a constant bend angle (Okuno and Hiramoto, 1976). Compound cilia of the ctenophore *Pleurobrachia* have low intrinsic activities but show a remarkable sensitivity to mechanical stimuli (Sleigh and Jarman, 1973).

These two types of dynamical behaviour – oscillations and excitability – should not be considered as mutually exclusive phenomena. They are in fact closely related to each other.

6.3 Model development

To formulate theoretical models for flagella and cilia, let us consider the molecular structure and function that leads to excitability and oscillations.

6.3.1 Geometric considerations

Localized cross-bridge distribution. Figure 6.1 illustrates the geometric arrangement of cross-bridges and attachment sites. In muscle the 42.9 nm interval of cross-bridges is different from the 37.0 nm interval of attachment sites (Huxley and Brown, 1967), which leads to homogeneous cross-bridge distribution. In flagella, however, the 24 nm interval of cross-bridges is equivalent to the 24 nm interval of attachment sites (Takahashi and Tonomura, 1978). This suggests that in a straight region the cross-bridge distribution to the attachment sites is not *homogeneous*, but rather it seems to be localized (Murase and Shimizu, 1986). For recent developments in cross-bridge substructure and function see Section 9.1.

Opposing cross-bridge pair system. A real axoneme has nine pairs of doublets. Along each pair two rows of dyneins are distributed corresponding to the presence of inner and outer arms (see Fig. 4.3). For simplicity, only four pairs of doublets are considered: two of the four are named subsystem I and

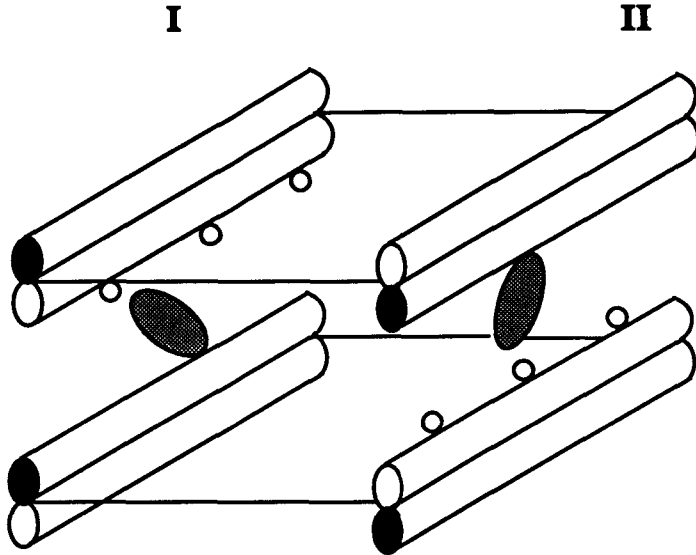


Figure 6.2 A simplified system with four doublets. Cross-bridges in subsystems I and II form opposite pairs of cross-bridges along the flagellum. Modified from Murase and Shimizu (1986). Reprinted with permission.

the other two subsystem II. It is also assumed that the two rows of dyneins are functionally equivalent and that both are represented by a single localized distribution. Reflecting the opposite direction of cross-bridges located on the 6–9 and the 1–4 doublets (see Fig. 4.13), the two subsystems I and II are considered to form an opposing cross-bridge pair (Fig. 6.2).

Radial-spoke system. Warner and Satir (1974) suggested that radial spokes will cause a cycle of attachment and detachment in a similar way to dynein cross-bridges. Baba (1979) observed that the effective stroke of some compound cilia involves several angular steps, which may be interpreted as several sliding units due to the radial-spoke cycle as well as the dynein cross-bridge cycle (see Section 4.5.4). Dynein cross-bridges perform mechano-chemical cycles by the use of chemical energy of ATP hydrolysis similarly to myosin cross-bridges in the muscle system. Dynamics of such dyneins are described by a three-state model as detailed in the next section. In contrast to the dynein system, operation of the radial-spoke system does not require ATP but may be affected by high Ca^{2+} . This system is, therefore, considered as a control system (but not a force-generating system) which facilitates the repetitive progressive bends (Satir, 1984), though details have not yet established.

Usually the radial-spoke system is formulated by a complex function

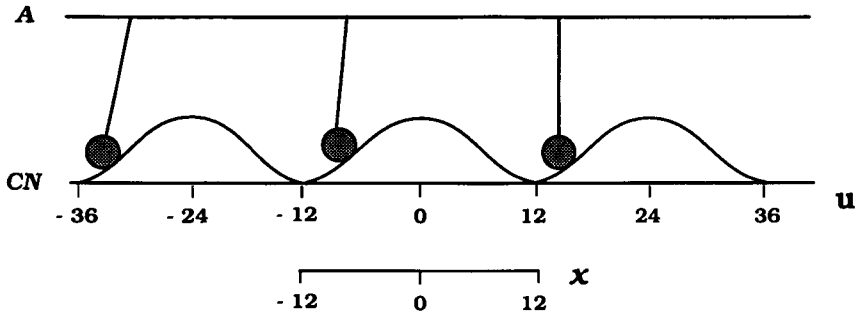


Figure 6.3 A schematic diagram showing a radial-spoke system. Radial spokes (denoted by 'cross-bridges') extend from the A-subtubule (A) to the central sheath surrounding the central pair (CN). The interaction between radial spokes and central sheath is represented by a periodic mechanical potential as a function of the shear displacement, u . The relationship between the shear displacement u and the sliding coordinate x is also shown.

(Lubliner, 1973; Hines and Blum, 1979). We simply assume that there are stable positions periodically located along the filament corresponding to the radial-spoke cycles. Mathematically, a periodic, mechanical potential is defined as a function of *shear displacement*, u , as follows (Fig. 6.3):

$$U_p(u) = \frac{24K_p}{2\pi} \left[1 + \cos \left[\frac{2\pi u}{24} \right] \right]. \quad (6.2)$$

Here K_p is the force coefficient and 24 (nm) represents the stroke distance of the radial spoke.

6.3.2 A three-state model for the cross-bridge cycle

To describe the dynamical behaviour of a dynein cross-bridge, we will use the three-state model originally proposed to account for the dynamics of a myosin cross-bridge (see Chapter 3). Of course we must modify the original three-state model based on the difference in the geometry of molecules in flagella, as mentioned in the previous section.

The three-state model assumes that there are three different states available for a cross-bridge: an *inactive* (i.e. detached) state, a *resting* (i.e. preactively attached) state and an *active* (i.e. actively attached) state denoted by 0, 1 and 2, respectively (see Fig. 6.4A). Using the chemical energy of ATP hydrolysis, a cross-bridge can undergo transitions between the three states. The behaviour of the cross-bridge distribution depends only on a distance, or a *sliding coordinate*, x (in nm), from its nearest-neighbour attachment site, but not on an actual distance, or a shear displacement, u (in nm), between the two filaments. Considering the periodic arrangement of both cross-bridges and sites, the relationship between the sliding coordinate and the sliding displacement

is specified. Mathematically, we take the values of u modulo 24 as follows (see Fig. 6.3):

$$x + C = \text{mod}(u + C, 24), \quad (6.3)$$

where 24 (nm) is a periodicity of attachment sites and C is some arbitrary constant relating to the position of a reference point in measuring the distance between the cross-bridge and site. Equation (6.3) means that any value of x satisfying $0 < x + C < 24$ nm is considered equivalent to $x + C + 24n$, where n is an integer. When $C = 12$ nm, then the sliding coordinate is defined for $-12 \leq x < 12$ nm. If we further restrict our attention to a single sliding unit for $-12 \leq u < 12$ nm, equation (6.3) becomes

$$x = u. \quad (6.3')$$

The mechanical potential of all state and transition rate constants among the three states are defined as a function of x . The analytical form of each potential is written as:

$$\left\{ \begin{array}{l} \text{State 0: } U_0(x) = 0 \quad (6.4a) \\ \text{State 1: } U_1(x) = K_1 \frac{(x - x_1)^2}{2} - U_1^0 \quad (6.4b) \\ \text{State 2: } U_2(x) = K_2 \frac{(x - x_2)^2}{2} - U_2^0. \quad (6.4c) \end{array} \right.$$

where $K_1 = 0.1875$ pN nm⁻¹, $K_2 = 0.25$ pN nm⁻¹, $x_1 = -10$ nm, $x_2 = 12$ nm, $U_1^0 = 5$ pN nm, and $U_2^0 = 60$ pN nm.

Figure 6.4B shows these mechanical potentials. The opposite sign of space derivative for each mechanical potential shows force generated per cross-bridge (i.e. $F_i = -\partial U_i(x)/\partial x$ where $i = 0, 1$ and 2). From this relationship we understand that (i) no active force is generated by a cross-bridge in state 0, (ii) only a small amount of force is produced in state 1, and (iii) a large amount of active force is generated in state 2. The separation in the mechanical potentials between the two stable positions – at x_1 in state 1 and at x_2 in state 2 – reflects the single stroke-distance of the active cross-bridge.

The transition of an individual cross-bridge to the active state affects the sliding motion and the resultant sliding motion in turn influences the behaviour of the cross-bridge. There seems to be a dynamic feedback loop between the cross-bridge behaviour at the molecular level and the macroscopic sliding motion. To describe the dynamic feedback loop, the rate constants are given as a function of x . Figure 6.4C depicts the rate constants. One important assumption is that cross-bridges are allowed to attach to state 1 by k_{01} in the narrow region where $-12 \leq x < 8$ nm, but detach everywhere via k_{10} . This introduces a situation of *local activation* and *global inactivation*, which leads to excitable dynamics of dyneins with *directional sensitivity* (see below). Their analytical forms are given as follows:

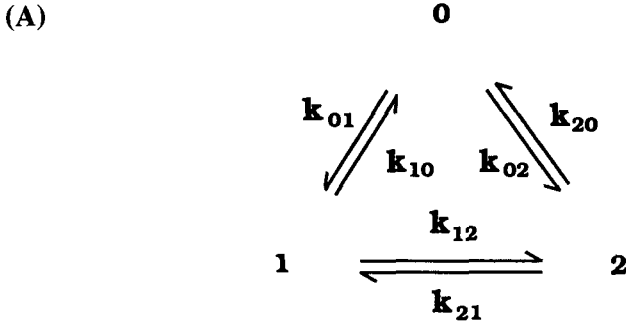


Figure 6.4 (A): A three-state cross-bridge cycle. States 0, 1 and 2 represent an inactive state (or a detached state), a resting state (or a preactively attached state) and an active state (or an actively attached state), respectively. k_{ij} represents the rate constant of transition from state i to j . (B): Mechanical potentials for the three states as a function of x ; U_0 , U_1 and U_2 denote the mechanical potentials of the states 0, 1 and 2, respectively. (C): Rate constants of transitions among the three states as a function of x . Note that in the case of muscle an increase in x corresponds to shortening. Each rate constant is plotted on a log scale. From Murase and Shimizu (1986). Reprinted with permission.

$$k_{01}(x) = \begin{cases} c_{01} \exp\left[-K_1 \frac{(x - x_1)^2}{2k_B T}\right] & (-12 \leq x < -8) \\ 0 & (-8 \leq x < 12) \end{cases} \quad (6.5a)$$

$$k_{10}(x) = c_{10} \quad (-12 \leq x < 12) \quad (6.5b)$$

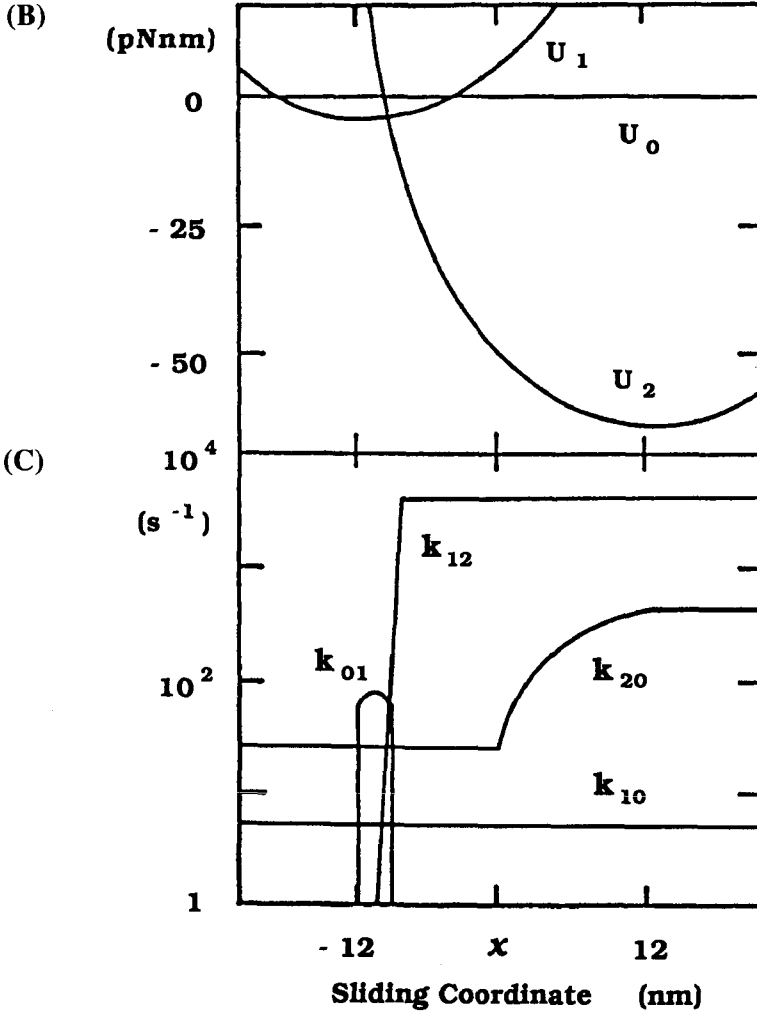
$$k_{12}(x) = \begin{cases} c_{12} \exp[D(x - x_1)] & (-12 \leq x < x_c) \\ c'_{12} & (x_c \leq x < 12) \end{cases} \quad (6.5c)$$

$$k_{21}(x) = 0 \quad (-12 \leq x < 12) \quad (6.5d)$$

$$k_{20}(x) = \begin{cases} c_{20} & (-12 \leq x < 0) \\ \frac{(c'_{20} - c_{20})x}{11} & (0 \leq x < 11) \\ c'_{20} & (11 \leq x < 12) \end{cases} \quad (6.5e)$$

$$k_{02}(x) = 0 \quad (-12 \leq x < 12). \quad (6.5f)$$

where $c_{01} = 80 \text{ s}^{-1}$, $c_{10} = 5 \text{ s}^{-1}$, $c_{12} = 0.0003$ or 0.01 s^{-1} (see Section 6.4.4), $c'_{12} = 4000 \text{ s}^{-1}$, $c_{20} = 20 \text{ s}^{-1}$, $c'_{20} = 400 \text{ s}^{-1}$, $D = 1.423 \text{ nm}^{-1}$, $K_1 = 0.1875 \text{ pN nm}^{-1}$; K_B is the Boltzmann constant; T is the absolute temperature. Note that x_c is calculated from $k_{12}(x_c) = c'_{12}$, which is introduced to limit the maximum value of k_{12} to 4000 s^{-1} .



Let us consider how the three-state model accounts for cross-bridge dynamics. Suppose that an inactive (i.e. a detached) cross-bridge moving into an attachment region ($-12 \leq x < -8$ nm). When a cross-bridge moves into the region from the *left*, attachment begins to occur at $x = -12$ nm by k_{01} . Then that attached cross-bridge in state 1 moves toward $x = -10$ nm due to the active force generated by the cross-bridge itself. The further the cross-bridge

in state 1 moves in a positive (i.e. toward the right) direction the greater the possibility of a transition to state 2, due to the sharply increasing rate function k_{12} . This mechanism is analogous to an *auto-catalytic* process since transition due to k_{12} is catalysed by the sliding movement itself. After the transition to state 2, detachment occurs by k_{20} , before the cross-bridge exceeds $x = 12$ nm. Thus the cross-bridge cycle is completed. When the filaments are free to slide in the positive direction, the *cooperative* sliding movement is accompanied by successive cyclic transition of cross-bridge dynamics (cf. Fig. 6.6).

Now suppose that a detached cross-bridge moves into the attachment region from the *right*. The cross-bridge begins to attach at $x = -8$ nm. If the cross-bridge exceeds $x = -12$ nm, i.e. where the rate constant k_{01} suddenly decreases in the region but the rate constant k_{10} remains unchanged, then detachment occurs by k_{10} . Consequently, the system becomes inactive due to sliding in the 'wrong' direction. This implies that the cross-bridge system exhibits directional sensitivity. As a result, the cross-bridge undergoes a *unidirectional mechano-chemical cycle* (see Section 4.4.1).

The situation in which the passive elastic element (e.g. the nexin or radial-spoke system) combines with the cross-bridge system is of particular interest. If the passive force is directed to the left (i.e. the opposite direction to the active force) and the magnitude of c_{12} is small, a delicate balance appears between these forces. Active sliding does not occur spontaneously but is triggered due to a superthreshold displacement. A response of this kind, in which the behaviour of a system depends on the strength of a stimulus, is called a *threshold phenomenon*. Consequently the magnitude of c_{12} plays an important role in determining the stability of state 1 under a given mechanical constraint.

6.4 Dynamics of a short flagellar segment

Next we consider how the three-state model proposed in the previous section can be incorporated into a model for flagellar movement. For this purpose, a long flagellum is divided into N segments of length Δs making sure that (i) the size of each segment is sufficiently long to include a few hundred cross-bridges, and (ii) it is short enough to be nearly straight.² Assumption (i) ensures that the three-state model can be applied to each segment, and assumption (ii) is necessary to accurately enable us to describe the behaviour of a whole flagellum. In this section, a model of flagellar segment is developed and its dynamic properties are examined.

6.4.1 Kinetic equations for cross-bridge dynamics

The fractions representing the cross-bridges in the three states 0, 1 and 2 at the sliding coordinate x and time t , are represented by $n_0(x, t)$, $n_1(x, t)$ and

$n_2(x, t)$, respectively. The kinetic equations for these fractions are represented by the following form:³

$$\frac{dn_0(x, t)}{dt} = k_{10}(x)n_1(x, t) + k_{20}(x)n_2(x, t) - k_{01}(x)n_0(x, t) \quad (6.6a)$$

$$\frac{dn_1(x, t)}{dt} = k_{01}(x)n_0(x, t) - k_{12}(x)n_1(x, t) - k_{10}(x)n_1(x, t) \quad (6.6b)$$

$$\frac{dn_2(x, t)}{dt} = k_{12}(x)n_1(x, t) - k_{20}(x)n_2(x, t) \quad (6.6c)$$

where

$$n_0(x, t) + n_1(x, t) + n_2(x, t) = \frac{1}{\delta\sqrt{2\pi}} \exp\left[-\frac{(x - \langle x \rangle)^2}{2\delta^2}\right]. \quad (6.6d)$$

Here $\langle x \rangle$ is the mean position of cross-bridge distributions on the sliding coordinate, and δ is the standard deviation. Since $k_{21}(x) = k_{02}(x) = 0$, the related terms are omitted from the equations (6.6a, b, c). The right-hand side of equation (6.6d) is an example of a localized cross-bridge distribution and represents a Gaussian distribution, which satisfies

$$\int_{-12}^{12} \sum_{i=0}^2 n_i(x, t) dx = 1. \quad (6.7)$$

Nexin links form the closed ring structure around an axoneme. These links are responsible for shear resistance (see Fig. 4.3). Rather than *explicitly* taking into account the shear resistance of nexin links we have *implicitly* considered their effect. That is, active cross-bridges in subsystem I cause sliding movement between the filaments in I, and also at the same time between the filaments in II via the nexin links, and vice versa (cf. Summers, 1975). Hence we assume that the change in the mean position of the cross-bridge distribution in I is identical with that in II in accordance with the sliding movement.⁴

Since we are considering a system consisting of subsystems I and II, the fractions for cross-bridges in I and II must be dealt with separately (Fig. 6.5). Hereafter n_i^I and n_i^{II} will be used to denote the fractions for cross-bridges in I and II, respectively. n_i^I satisfies the equations (6.6) as they are, while n_i^{II} satisfies modified equations. These modified equations are similar to equations (6.6) but have rate constants which are reversed with respect to $x = 0$ (i.e. $k_{ij}^I(x) = k_{ij}^{II}(-x)$), depending on the opposite projection of cross-bridges in both subsystems. In the following sections the magnitudes of all parameters c_{ij} in both subsystems I and II are identical, except for c_{12} . As pointed out before, the magnitude of c_{12} plays an important role in determining the stability of state 1 and various situations appear by merely changing this

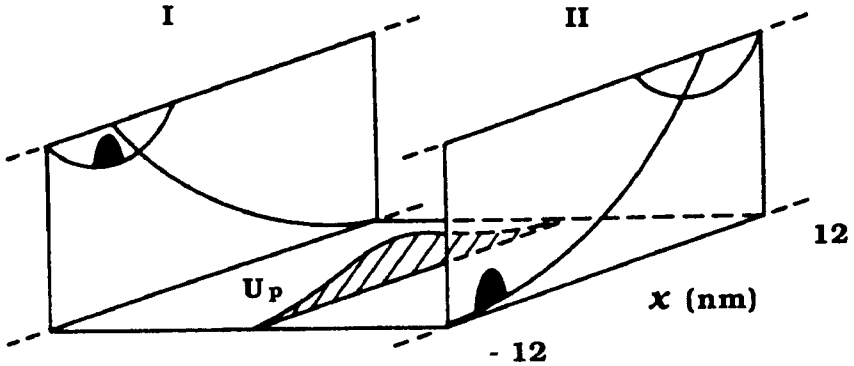


Figure 6.5 A model for a flagellar segment. Mechanical potentials of subsystems I and II are the same, but are opposed to each other in the direction of the sliding coordinate, which corresponds to the opposing pairs of cross-bridges in Figure 6.2. Due to the radial spokes the periodic mechanical potential U_p causes the elastic shear resistance. Dark distributions shown on the mechanical potentials indicate localized cross-bridge distributions in subsystems I and II. From Murase and Shimizu (1986). Reprinted with permission.

parameter. For convenience, c_{12}^I and c_{12}^{II} are used to distinguish c_{12} of subsystem I from that of subsystem II.

6.4.2 Equations for sliding motion of a short flagellum

The sliding motion of a short flagellar segment with a length of Δs is described by the following force-balance equation⁵

$$\gamma' \frac{du}{dt} = Q_I S_I(u, n_1^I, n_2^I) + Q_{II} S_{II}(u, n_1^{II}, n_2^{II}) + S_p(u) \quad (6.8a)$$

where γ' is an internal viscous shear resistance, Q_I (or Q_{II}) is the total number of cross-bridges in subsystem I (or II) in the segment, S_I (or S_{II}) is the active force per cross-bridge in subsystem I (or II), and S_p is the passive elastic force due to the radial-spoke system. Each of the terms on the right-hand side of the equation (6.8a) is given by

$$S_I(u, n_1^I, n_2^I) = -K_1 \int_{-12}^{12} n_1^I(x - x_1^I) dx - K_2 \int_{-12}^{12} n_2^I(x - x_2^I) dx \quad (6.8b)$$

$$S_{II}(u, n_1^{II}, n_2^{II}) = -K_1 \int_{-12}^{12} n_1^{II}(x - x_1^{II}) dx - K_2 \int_{-12}^{12} n_2^{II}(x - x_2^{II}) dx \quad (6.8c)$$

$$S_p(u) = -\frac{dU_p(u)}{du} = K_p \sin\left[\frac{2\pi u}{24}\right]. \quad (6.8d)$$

6.4.3 Free sliding motion

As observed by Summers and Gibbons (1971) (see Section 4.3.3), a flagellum pretreated with trypsin will immediately disintegrate when active sliding of the filaments is induced by addition of ATP. This occurs because the passive elastic elements are sensitive to disruption by trypsin whereas the cross-bridge force-generating system remains intact. As a result, the system shows free sliding. It is very important to examine whether the theoretical model presented here will account for this kind of free sliding motion. For this simulation, the second and the third terms were omitted from equation (6.8a). The results of the simulation show a stepwise sliding motion accompanied by periodic force changes reflecting cyclic transition of cross-bridge dynamics (Murase and Shimizu, 1985a).

Figure 6.6A shows $n_2^I(x, t)$ changing with time and position during active sliding. A population of cross-bridges moves from the left, then attachment to state 1 and subsequent transition to state 2 occurs, leading to active sliding. When the population reaches the right side at $x = 12$ nm, all the attached cross-bridges are turned off, though soon the next population of cross-bridges moves into the attachment region from the left side. This cyclic change induces stepwise sliding motion and periodic force oscillations (Fig. 6.6B and C).

6.4.4 Excitable–oscillatory phenomena

In this section we study the behaviour of a flagellar-segment model where all the terms in equation (6.8a) are considered. As pointed out in Section 6.4.1, parameters c_{12}^I and c_{12}^{II} play a key role in determining the stability of state 1 in subsystems I and II, respectively. Three distinguishable cases are possible according to the combination of c_{12}^I and c_{12}^{II} values: (i) bi-stable behaviour for $c_{12}^I = c_{12}^{II} = 0.0003$ s⁻¹; (ii) mono-stable behaviour for $c_{12}^I = 0.0003$ s⁻¹ and $c_{12}^{II} = 0.01$ s⁻¹; and (iii) oscillatory behaviour for $c_{12}^I = c_{12}^{II} = 0.01$ s⁻¹. Cases (i) and (ii) are regarded as excitable properties because only superthreshold perturbation can trigger active sliding. Case (iii) is referred to as limit-cycle oscillations.

We are interested in the basic behaviour of the flagellar-segment model, so that hereafter we will restrict ourselves to only a single sliding motion (i.e. $-12 \leq u < 12$ nm). Thus x is identical to u (see Fig. 6.3).

Bi-stable behaviour. When $c_{12}^I = c_{12}^{II} = 0.0003$ s⁻¹, there is bi-stability in which state 1 in subsystems I (at $u = -10$ nm) and II (at $u = 10$ nm) are both stable. Figure 6.7 shows the *all-or-none* phenomena (or threshold phenomena or excitable properties) of the cross-bridge dynamics in response to the initial position. Small subthreshold values of $u \leq -9.2$ nm let the system relax to the one stable state at $u = -10$ nm, while superthreshold values of $u > -9.2$

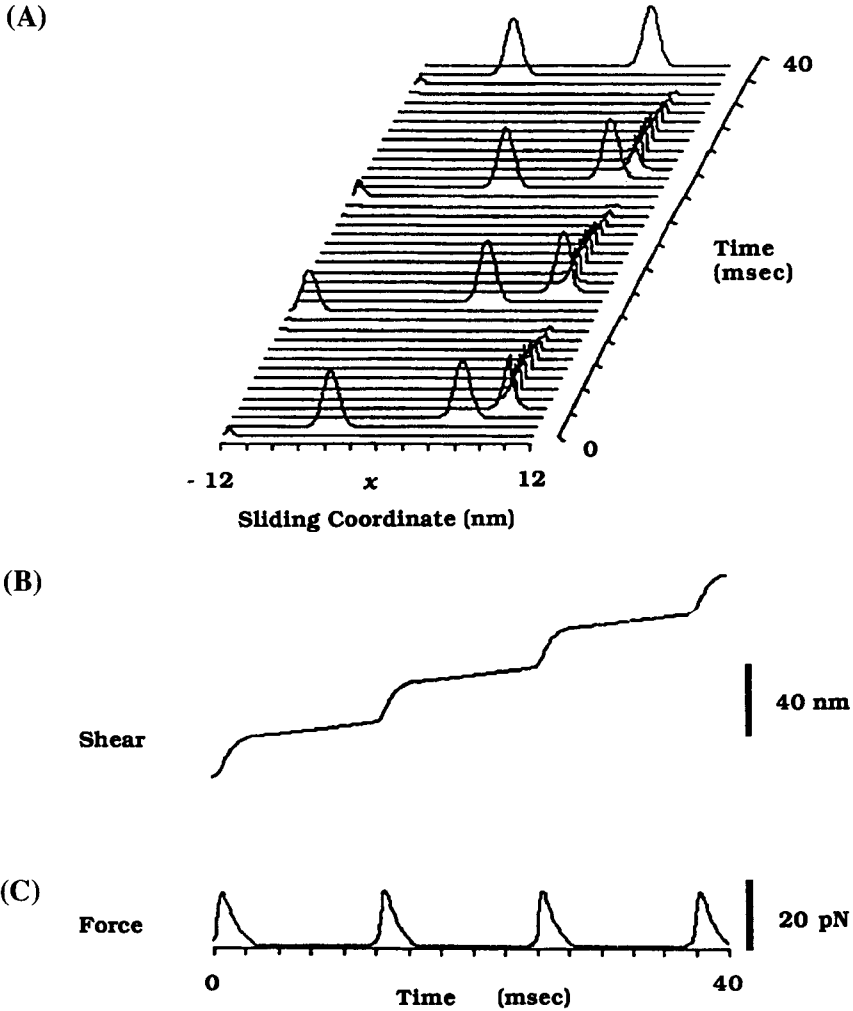


Figure 6.6 (A): The space- and time-dependence of the fraction, $n_2^1(x, t)$. As active sliding takes place, detached cross-bridges move from the left. They first attach to state 1 and then undergo the transition to state 2 due to the space-dependent rate constants of $k_{01}(x)$ and $k_{12}(x)$. When they reach the right side they begin to detach. Re-attachment occurs soon after on the left side. The resulting cyclic transition takes place as long as the sliding motion occurs. (B): The shear displacement, u , plotted as a function of time. According to the cyclic transition of cross-bridges, stepwise sliding motion is observed. (C): The total shear force plotted as a function of time. Periodic change of force reflects the cyclic transition of cross-bridges.

nm cause jump transitions to the other stable state at $u = 10$ nm. These jump transitions are ascribed to conformational changes of the cross-bridges.

As shown in Figure 6.8, this jump transition is accompanied by a spike-like change in the shear force per cross-bridge. The fractions that represent

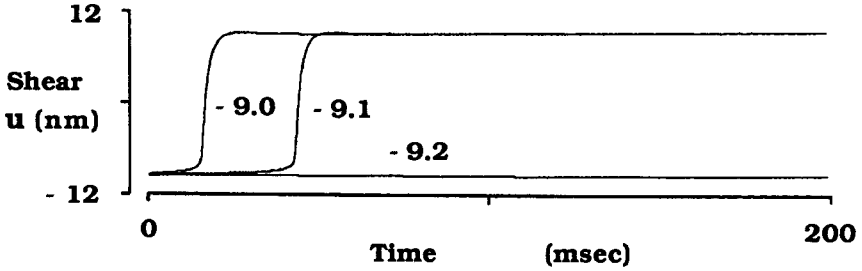


Figure 6.7 Variation of shear, u , as a function of time after a perturbation of u . There is bi-stability in which two stable states are present at $u = -10$ and 10 nm. One of the two states is obtained depending on the initial condition. Subthreshold values of $u \leq -9.2$ nm return the system to $u = -10$ nm. Superthreshold values of $u > -9.2$ nm cause the jump transitions to $u = 10$ nm. The initial conditions for u (nm) are indicated in the figure. From Murase and Shimizu (1986). Reprinted with permission.

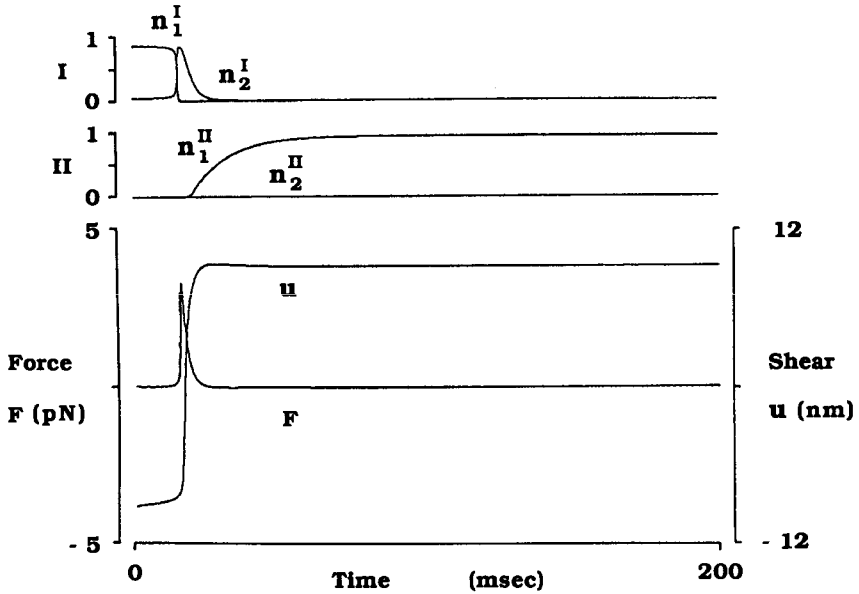


Figure 6.8 The fractions of cross-bridges in subsystems I (n_1^I, n_2^I) and II (n_1^{II}, n_2^{II}), the shear force per cross-bridge, F , and the shear displacement, u , as functions of time. The system exhibits bi-stable behaviour. The initial condition is $u = -9.0$ nm. From Murase and Shimizu (1986). Reprinted with permission.

the attached cross-bridges in subsystems I and II for the two attached states are plotted as a function of time (see upper part of Fig. 6.8). As sliding occurs in the positive direction, n_2^I immediately increases by k_{12}^I , which is accompanied by a sudden decrease of n_1^I , and then decreases subsequently by k_{20}^I . The quick increase and subsequent decrease in n_2^I are interpreted as the *rapid activation* and *slow inactivation* of cross-bridges in subsystem I. After

jump transitions to the other stable state, n_1^{II} increases by degrees because of the localized rate constant k_{01}^{II} . However, n_2^{II} does not increase because the magnitude of c_{12}^{II} is too small.

As the system is symmetric with respect to $u = 0$, active sliding in the opposite direction is also observed for $u < 9.2$ nm at $t = 0$. Whether the sliding occurs in a positive or negative direction depends on the 'history' of the system. As a result, the system exhibits a *hysteresis* in the transition between the two stable states. Katchalsky and Spangler (1968) pointed out an important role of hysteresis.

Hysteresis may be interpreted as a manifestation of the existence of an energy barrier preventing the direct transition from one state to another. If the transition is imposed upon the system, in circumventing the barrier the system will follow the hysteresis cycle. The resultant rotations around the transition barrier appear to the observer as oscillatory phenomena.

To clarify the above statement, we embedded a linear elastic component in the model flagellum instead of using an externally imposed stimulus. For this modification, a term of passive elastic force, S_e , was added to the right-hand side of equation (6.8a). S_e is given as

$$S_e = -K_e(u - u_0) \quad (6.9)$$

where K_e is the force constant for the passive elasticity and u_0 is the equilibrium position of the elastic element. Sustained oscillations occurred over a wide range of K_e values. Figure 6.9 shows the simulation for $K_e = 1.8$ pN nm⁻¹ and $u_0 = 0$ nm.

Mono-stable behaviour. When $c_{12}^{\text{I}} = 0.0003$ s⁻¹ and $c_{12}^{\text{II}} = 0.01$ s⁻¹, a mono-stable state corresponding to a stable 'resting state' is realized. In this case, state 1 in subsystem I is stable and that in II unstable. The all-or-none response is also observed around this resting state (Fig. 6.10). With initial conditions $u > -9.2$ nm, shear shows an action-potential-like change: it initially increases and then decreases (Fig. 6.11). This is essentially different from the case of bi-stable behaviour. The force time-course shows an upward and a subsequent downward spike-like change. The fractions for the cross-bridges in subsystem II change with time as follows. After the sliding in the positive direction, n_2^{II} immediately increases with a time delay, which is coupled with the sudden decrease of n_1^{II} . Then n_2^{II} decreases gradually. The delayed increase and the subsequent decrease of n_2^{II} represent the delayed activation and subsequent inactivation of cross-bridges in subsystem II, respectively. After these transients, the system returns to its initial resting state.

Sustained oscillations were also observed when a linear elastic component was incorporated into the system. Figure 6.12 shows the limit-cycle oscillation for $K_e = 1.26$ pN nm⁻¹. The time-dependence of u is asymmetric with

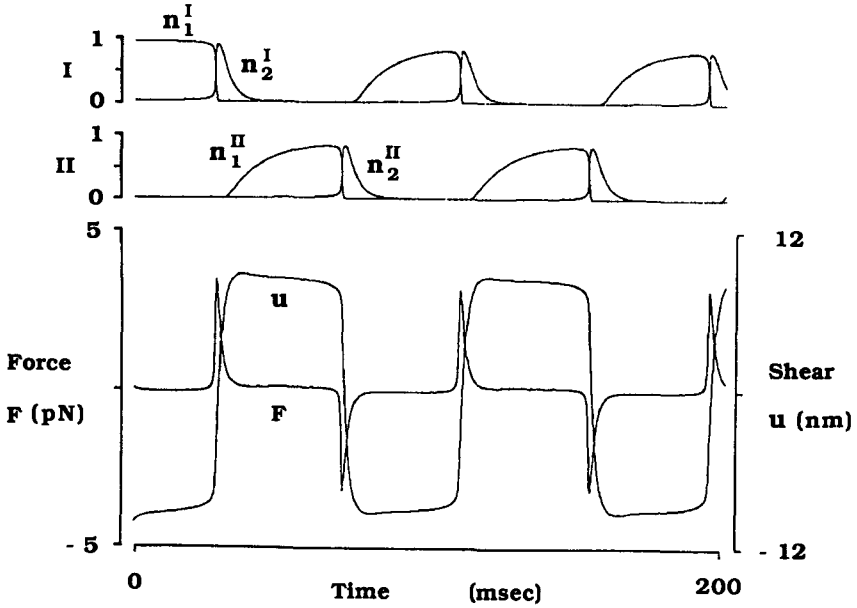


Figure 6.9 The fractions of cross-bridges in subsystems I (n_1^I, n_2^I) and II (n_1^{II}, n_2^{II}), the shear force per cross-bridge, F , and the shear displacement, u , as functions of time. The system shows oscillatory behaviour. The initial condition is $u = -10.0$ nm. From Murase and Shimizu (1986). Reprinted with permission.

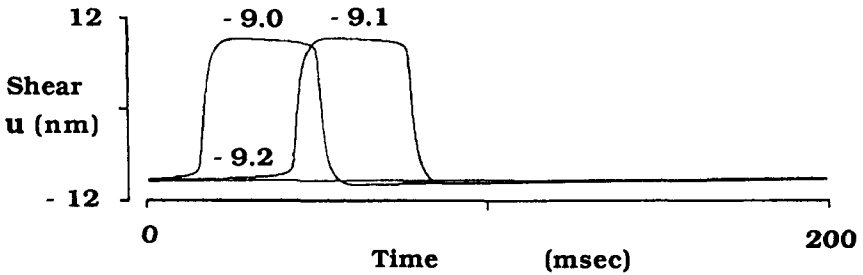


Figure 6.10 Variation of shear, u , as a function of time after a perturbation of u . There is mono-stability in which one ‘resting state’ is present at $u = -10$ nm. Subthreshold values of $u \leq -9.2$ nm return the system to the resting state. Superthreshold values of $u > -9.2$ nm cause changes similar to *action potentials*. The initial conditions for u (nm) are indicated in the figure. From Murase and Shimizu (1986). Reprinted with permission.

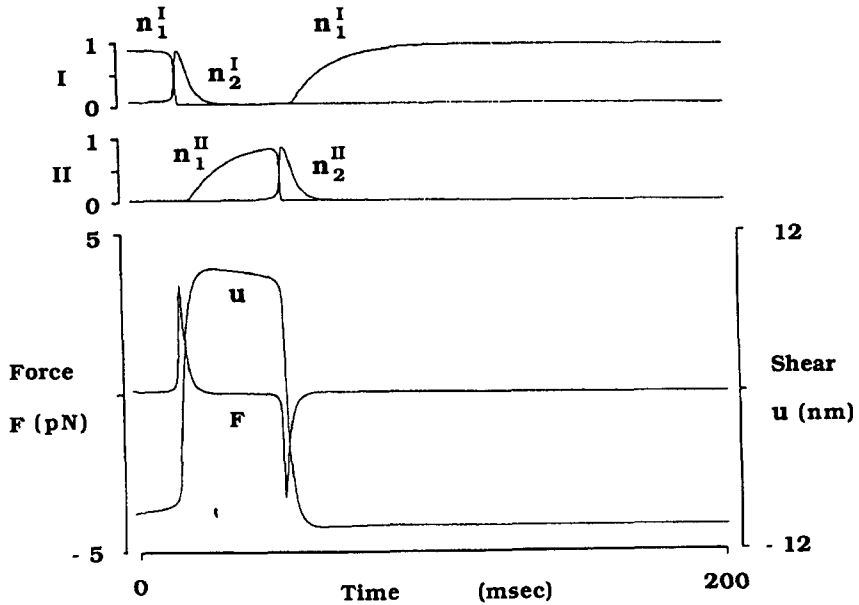


Figure 6.11 The fractions of cross-bridges in subsystems I (n_1^I, n_2^I) and II (n_1^{II}, n_2^{II}), the shear force per cross-bridge, F , and the shear displacement, u , as functions of time. The system shows mono-stable behaviour. The initial condition is $u = -9.0$ nm. From Murase and Shimizu (1986). Reprinted with permission.

respect to $u = 0$ nm, which corresponds to the asymmetric parameters c_{12}^I and c_{12}^{II} .

Limit-cycle oscillation. Instabilities of state 1 in both subsystems I and II occur when $c_{12}^I = c_{12}^{II} = 0.01 \text{ s}^{-1}$. Figure 6.13 shows relaxation oscillation where shear alternately increases and decreases while force changes are represented by upward and downward spikes. Sliding in a positive direction occurs due to both activation of cross-bridges in I and inactivation of cross-bridges in II, whereas sliding in a negative direction is due to both activation of cross-bridges in II and inactivation of cross-bridges in I. Consequently, during oscillation, we can observe switching mechanisms between the inactivation of cross-bridges on one side of the system and activation of those on the other, and also that the 'off' and 'on' of the switching control is separated by a constant time-interval.

Note that there is little difference between Figure 6.9 (or Figure 6.12) and Figure 6.13. It is difficult to make a clear distinction between oscillations resulting from bi-stable (or mono-stable) behaviour and 'true' limit-cycle oscillations. Therefore bi-stable (or mono-stable) behaviour may be one of the most plausible molecular mechanisms for flagellar movement because

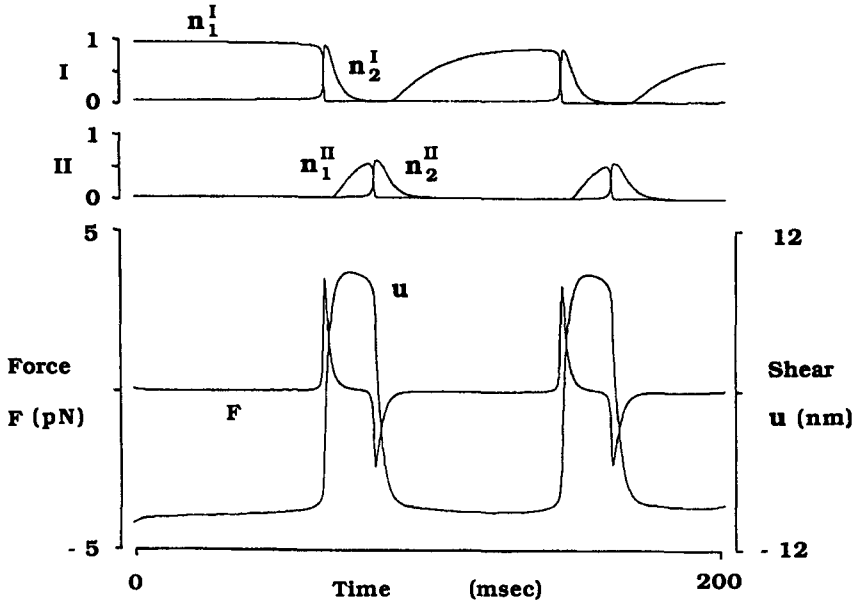


Figure 6.12 The fractions of cross-bridges in subsystems I (n_1^I, n_2^I) and II (n_1^{II}, n_2^{II}), the shear force per cross-bridge, F , and the shear displacement, u , as functions of time. The system shows oscillatory behaviour. The initial condition is $u = -10.0$ nm. From Murase and Shimizu (1986). Reprinted with permission.

it can demonstrate both oscillations and excitability depending on the circumstances.

6.4.5 Phase-plane analysis

An analysis of the flagellar-segment model described by equations (6.4) to (6.8) is carried out by the method of *reduced systems* similar to that used in the analysis of the Hodgkin–Huxley nerve equations (see FitzHugh, 1960). For simplicity we consider the limit $\delta \rightarrow 0$, that is, the Gaussian distribution of the cross-bridges is replaced by the Dirac delta function. Then equation (6.6d) becomes

$$n_0(x, t) + n_1(x, t) + n_2(x, t) = \begin{cases} 1 & \text{for } x = \langle x \rangle \\ 0 & \text{for } x \neq \langle x \rangle \end{cases} \quad (6.10)$$

Substituting equation (6.10) into (6.6b) and (6.6c) at $x = \langle x \rangle$, we get

$$\frac{dn_1}{dt} = k_{01} - (k_{01} + k_{12} + k_{10})n_1 - k_{01}n_2 \quad (6.11a)$$

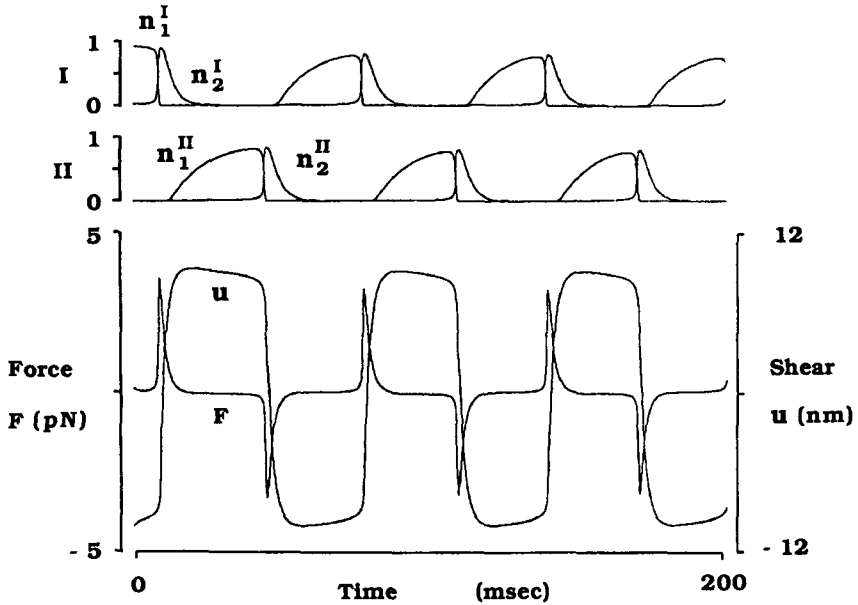


Figure 6.13 The fractions of cross-bridges in subsystems I (n_1^I, n_2^I) and II (n_1^{II}, n_2^{II}), the shear force per cross-bridge, F , and the shear displacement, u , as functions of time. The system shows oscillatory behaviour. The initial condition is $u = -10.0$ nm. From Murase and Shimizu (1986). Reprinted with permission.

$$\frac{dn_2}{dt} = k_{12}n_1 - k_{20}n_2. \quad (6.11b)$$

To understand excitable-oscillatory phenomena, we tentatively consider the simple system composed of force-generating system I, S_1 , and passive force, S_p , due to the radial-spoke system. Then equation (6.8a) is reduced to

$$\gamma' \frac{dx}{dt} = -K_1 Q_1 n_1^I (x - x_1^I) - K_2 Q_1 n_2^I (x - x_2^I) + K_P \sin \left[\frac{2\pi x}{24} \right]. \quad (6.12)$$

Here the integral form can be omitted because of the delta function in the cross-bridge distribution. Note also that $x = u$ in equation (6.8a).

Now we are ready to apply the method of reduced systems. Since the active force is chiefly produced by the cross-bridge in state 2, its fraction, n_2^I , is important in determining the behaviour of the system. Furthermore, x changes relatively rapidly. As a first approximation, the behaviour of x and n_2^I is studied by setting n_1^I constant at a steady state (designated $(n_1^I)^*$ in the limit $t \rightarrow +\infty$). Once the constant value of $(n_1^I)^*$ is specified, the state of this reduced system is completely defined as a phase point on the (x, n_2^I) phase plane.

The equations for the vertical ($\dot{x} = 0$) and horizontal ($\dot{n}_2^I = 0$) isoclines (see FitzHugh, 1960; 1969) are:

$$\dot{x} = 0 \quad n_2^I = \frac{-K_1(n_1^I)^*(x - x_1^I) + \frac{K_p}{Q_1} \sin\left[\frac{2\pi x}{24}\right]}{K_2(x - x_2^I)} \tag{6.13a}$$

$$\dot{n}_2^I = 0 \quad n_2^I = \frac{k_{12}^I}{k_{20}^I} (n_1^I)^*. \tag{6.13b}$$

Figure 6.14 shows the isoclines and a typical trajectory corresponding to bi-stable behaviour. The vertical isocline $\dot{x} = 0$ gives the steady-state value of x as a function of n_2^I , and the horizontal isocline $\dot{n}_2^I = 0$ is the graph of the steady state n_2^I as a function of x .

The intersections of the two isoclines are called the *singular points* (or steady-state points) where $\dot{x} = \dot{n}_2^I = 0$. Figure 6.15 shows singular points P_1 and P_2 as an enlarged detail of Figure 6.14. P_1 is a *stable node* in the sense that solutions approach P_1 as $t \rightarrow +\infty$. P_2 is a *saddle point*. A phase path crossing a saddle point is called a *separatrix*. A stable separatrix exists along which solutions approach P_2 as $t \rightarrow +\infty$ and an unstable separatrix along which solutions approach P_2 as $t \rightarrow -\infty$. All other nearby solutions follow almost hyperbolic paths, i.e. they first approach and then turn away from P_2 . When paths on opposite sides of the stable separatrix diverge from each other, it is called a *threshold separatrix*, as it is responsible for threshold phenomena (see FitzHugh, 1955).

If the vertical isocline $\dot{x} = 0$ is lowered (or the horizontal isocline $\dot{n}_2^I = 0$ is lifted), P_1 moves to the right and P_2 to the left. As a result, P_1 and P_2 approach each other and finally disappear (Fig. 6.16). Then all solutions go away from the original resting state. When two such subsystems are combined together to form a flagellar-segment model, limit-cycle oscillations are observed (Fig. 6.17). The bifurcation of this kind is often called a *saddle-node bifurcation* (or a *fold bifurcation*) (see Fig. 10.9A). This saddle-node bifurcation occurs when c_{12}^I is increased, because it eventually increases $(n_1^I)^*$. Then the vertical isocline $\dot{x} = 0$ is lowered and the horizontal isocline $\dot{n}_2^I = 0$ is raised.

Instead of changing c_{12}^I , similar results are found when a passive elastic component, with sufficient strength, is incorporated into this system. When equation (6.9) is embedded in equation (6.12), the vertical isocline (6.13a) is modified as follows:

$$\dot{x} = 0 \quad n_2^I = \frac{-K_1(n_1^I)^*(x - x_1^I) - \frac{K_e}{Q_1}x + \frac{K_p}{Q_1} \sin\left[\frac{2\pi x}{24}\right]}{K_2(x - x_2^I)}. \tag{6.13'a}$$

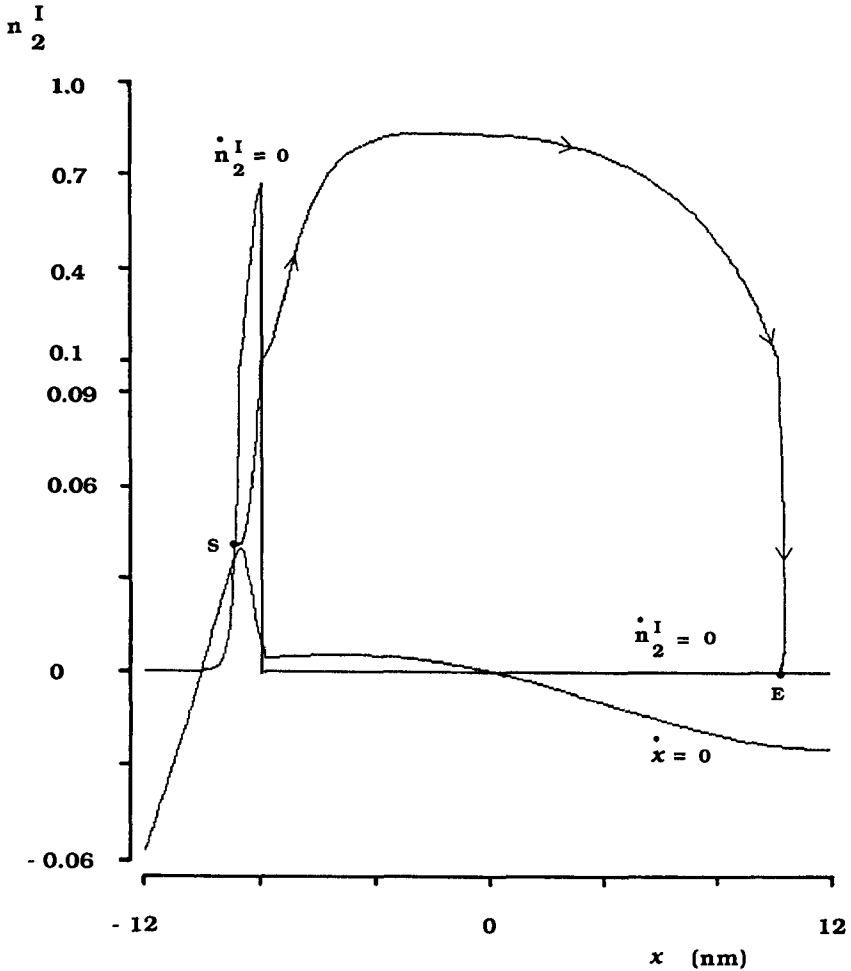


Figure 6.14 (x, n_2^I) phase plane for the reduced system with n_2^I fixed at its steady-state value. A typical solution of equations (6.6) and (6.8) follows the path marked with arrowheads. Starting at point S the system will reach point E which is a stable steady state of subsystem II. Note that on the n_2^I -axis there are two linear scales: one between -0.06 and 0.09 and the other between 0.09 and 1.0 . Vertical and horizontal isoclines are represented by $\dot{x} = 0$ and $\dot{n}_2^I = 0$, respectively.

By introducing $-K_c x/Q_1$, the vertical isocline is lowered, leading to the saddle-node bifurcation. From this viewpoint, oscillatory behaviour in Figure 6.9 (or in Figure 6.12) is essentially identical to that in Figure 6.13.

The *absolute refractory period* is specified as the time interval during which P_2 is absent, because a second excitation never occurs in the absence

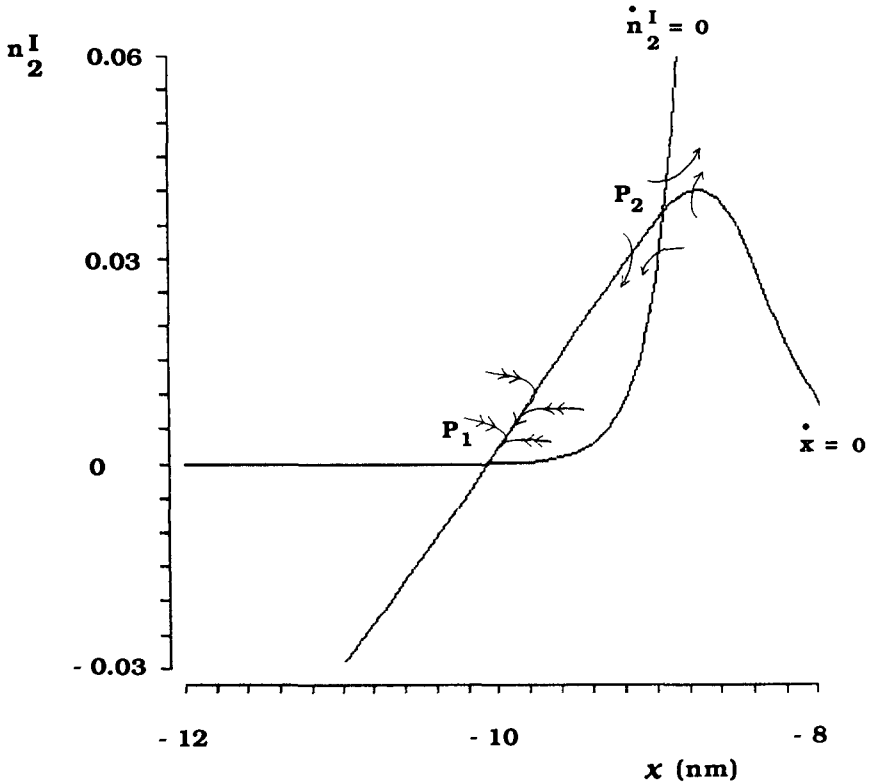


Figure 6.15 Enlarged detail of Figure 6.14. Two singular points P_1 and P_2 occur at the intersections of the isoclines. P_1 is the stable node, P_2 the saddle point. This situation leads to threshold phenomena. Some trajectories are shown by curves with arrowheads.

of the threshold separatrix. After reaching the attachment region it takes time to approach the initial steady state, because of the gradual increase in n_1^I . This transition from state 0 to state 1 is a rate-limiting step and is responsible for the *relative refractory period*.

It should be noted that the paths moving about in the (x, n_2^I) phase plane are different from those in the complete (x, n_1^I, n_2^I) phase space projected onto the (x, n_2^I) phase plane. Nevertheless, the above-mentioned phase-plane analysis provides us with a feeling of how the system works.

6.5 Dynamics of a long flagellum

6.5.1 The basic assumptions

To develop a flagellar model, the following assumptions are made:

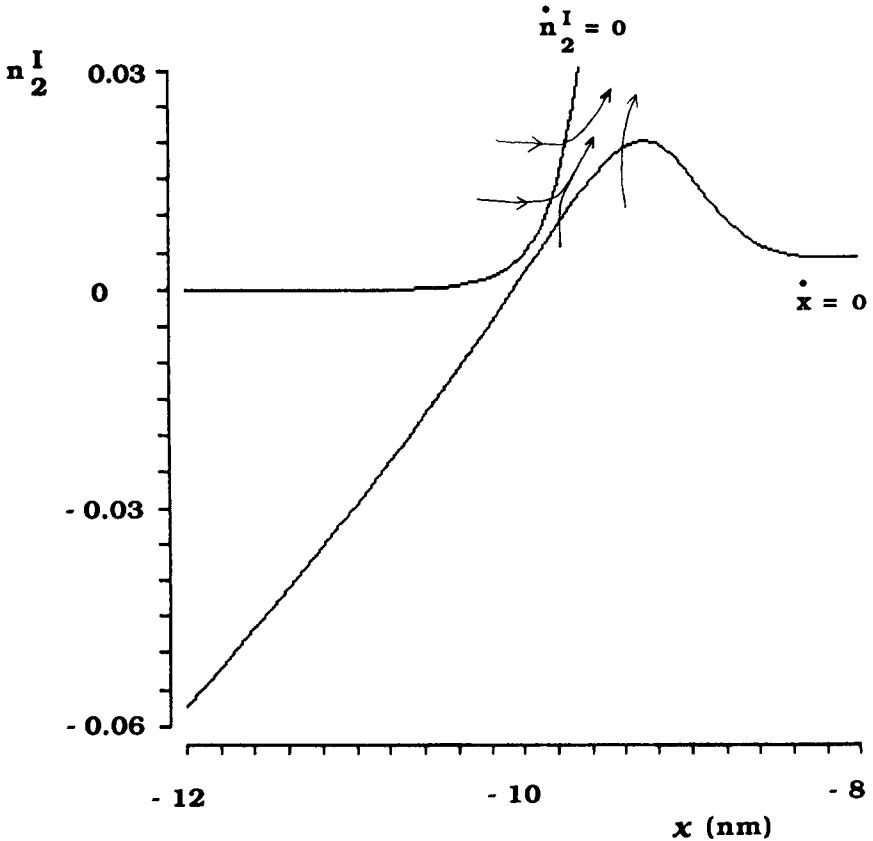


Figure 6.16 Enlarged phase plane for the reduced system like Figure 6.15 except that c_{12}^I is increased from 0.0003 to 0.01 s^{-1} . The vertical isocline $\dot{x} = 0$ is lowered and the horizontal isocline $\dot{n}_2^I = 0$ is raised. As a result, singular points P_1 and P_2 approach each other and vanish.

- (i) The flagellum moves in a plane (Hiramoto and Baba, 1978; Rikmenspoel, 1978).
- (ii) The flagellum is approximated by many straight segments.
- (iii) A linear elastic component similar to equation (6.9) is incorporated at the base, where K_c is taken as 4.5 $pN\ nm^{-1}$. This reflects the fact that the filaments are connected with each other at the base (see Fig. 4.2).
- (iv) The flagellar length L is taken as 30 μm and the number of segments, N , as 40, which leads to 180 pairs of antagonistic cross-bridges in a segment.
- (v) Parameters c_{12}^I and c_{12}^{II} of each segment are taken as 0.0003 s^{-1} , i.e. each segment displays bi-stable behavior.

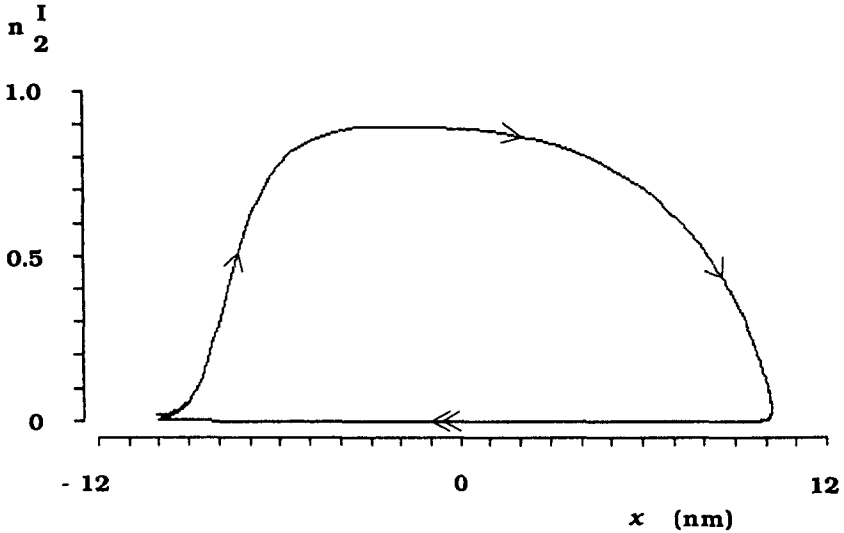


Figure 6.17 Trajectory projected from the complete phase space into (x, n_2) reduced space. The closed trajectory corresponds to limit-cycle oscillation in Figure 6.13.

- (vi) We confine ourselves to considering the case of small amplitude, where the sliding magnitude of a cross-bridge is ascribed to a single stroke-distance.
- (vii) The viscosity of the external medium is neglected to simplify the analysis (see Lubliner and Blum, 1971; 1977; Goldstein, 1979; Crowley *et al.*, 1981), though internal viscosity is introduced instead. The basic force-balance equation is thus rewritten as

$$\gamma' \frac{dx}{dt} = E'_B \frac{\partial^2 x}{\partial s^2} + Q_I S_I + Q_{II} S_{II} + S_P \tag{6.14}$$

where $E'_B = E_B/h$. Equation (6.14) is equivalent to (6.1).

- (viii) Free-end boundary conditions are used, where all the external moments vanish at the proximal and distal ends. Hence

$$M(0, t) = -E'_B \left. \frac{\partial x}{\partial s} \right|_{s=0} = 0; \quad M(L, t) = -E'_B \left. \frac{\partial x}{\partial s} \right|_{s=L} = 0 \tag{6.15}$$

where M is the external bending moment (see equations (5.30) and (5.32)).

- (ix) A straight flagellum is used as the initial condition, i.e.

$$u(s) = -10 \quad (0 \leq s \leq L). \tag{6.16}$$

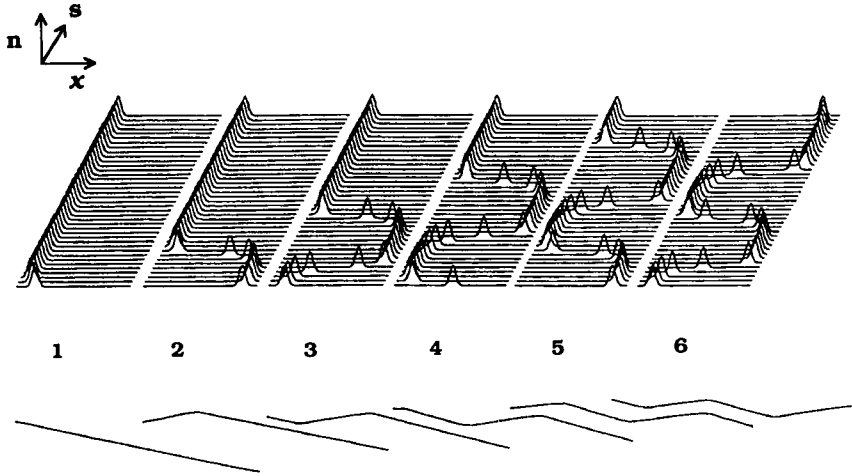


Figure 6.18 Upper part: The total distribution, n , of cross-bridges in subsystems I and II in each of the 39 segments as it changes with time. 39 segments are arranged along an s -axis from the proximal to distal end. The sliding coordinate x is taken for the abscissa with $-12 \leq x < 12$ nm. Time interval between each successive distribution pattern is taken as 20 ms. Lower part: Computer-simulated changes in the shape of a flagellum corresponding to each stage during successive changes of cross-bridge distribution shown in the upper part. The proximal end is situated on the left of the flagellum. From Murase and Shimizu (1986). Reprinted with permission.

This initial condition means that cross-bridges in all segments are situated in stable positions and the initial stretching of the basal elastic component is -10 nm, since the stable position at the base is at $u_0 = 0$ nm (cf. equation (6.9)).

6.5.2 Self-organization of propagating waves

The lower part of Figure 6.18 shows the development of the flagellar shapes at 20 ms intervals. The flagellum numbered 1 is obtained after 10 ms from the initial condition. A single bend begins to form due to the initial stretching of the elastic component at the base and then propagates. A steady-state waveform is attained when the first bend reaches the tip. The transient movements of this type were also observed by Goldstein (1979).

Bend initiation cannot be triggered without the elastic component at the base because the initial positions of cross-bridge distributions along the flagellum are all stable. But once such a flagellum is perturbed by an external stimulus, a bend is generated and propagated. These properties are consistent with the observations that a bending wave propagates along isolated flagellar segments when a mechanical stimulus is added by a microneedle (Lindemann

and Rikmenspoel, 1972; Okuno and Hiramoto, 1976). The next section provides a concrete demonstration of these observations.

The upper part of Figure 6.18 shows successive changes of cross-bridge distribution in each segment against the (x, s) plane. Nonlinear waves of cross-bridge distribution are successively generated, due to the elastic component at the proximal end, and propagate toward the distal end. Active sliding in the positive and negative directions is alternately triggered with a time delay at the proximal end. This alternate active sliding results from the mutually delayed activation of opposing pairs of cross-bridges under the influence of the elastic component. Active sliding, say in a positive direction initiated at the proximal region, induces the key transition from state 1 to 2 of cross-bridges on its distal side along the filaments on one side of the flagellum. Shimizu (1979) called such successively triggering events '*dynamic cooperativity*'. As a result, the region actively sliding in a positive direction propagates toward the distal end with a constant velocity.

6.5.3 A single wave-propagation

The possibility that a bend propagates along an isolated flagellum is studied by using the model described in the preceding section. To reproduce completely symmetrical beating, bi-stable segments are arranged along the axoneme. However, it is possible that there may be some asymmetry in real flagella with respect to the structure and/or function. Here we make one major change to the rate constant. That is, we use $c_{12}^I = 0.0003 \text{ s}^{-1}$ and $c_{12}^{II} = 0.01 \text{ s}^{-1}$. With rate constants of this magnitude, each segment shows mono-stable behaviour (see Fig. 6.11).

Since this model serves as a mono-stable system exhibiting an all-or-none response to the initial magnitude of the sliding, an instability leading to active sliding of filaments does not appear without a superthreshold stimulus in the form of imposed sliding. Bend initiation does not occur as long as the flagellum is straight and the system is in its resting state. However, once a local bend is initiated by imposed sliding at the base, the resultant bend propagates toward the tip.

Figure 6.19 shows computer-simulated changes in the shape of a flagellum when E_B is taken as $600 \text{ pN } \mu\text{m}^2$. Flagellar shapes are successively displaced downward at 20 ms time-intervals. At $t = 0$, a superthreshold sliding magnitude is imposed at the left end of the flagellum. A local bend is initiated and then propagates toward the right. The velocity of the propagation is approximately constant at $450 \mu\text{m/s}$.

Figure 6.20 shows corresponding successive changes of fractions for cross-bridges in subsystems I and II as well as the shear displacement during bend propagation. At $t = 0$ the flagellum is straight except for the basal region, and cross-bridges in subsystem I are attached in state 1. Active sliding occurs in the basal region at $t = 20 \text{ ms}$. An impulse-like change appears at $t = 60 \text{ ms}$.

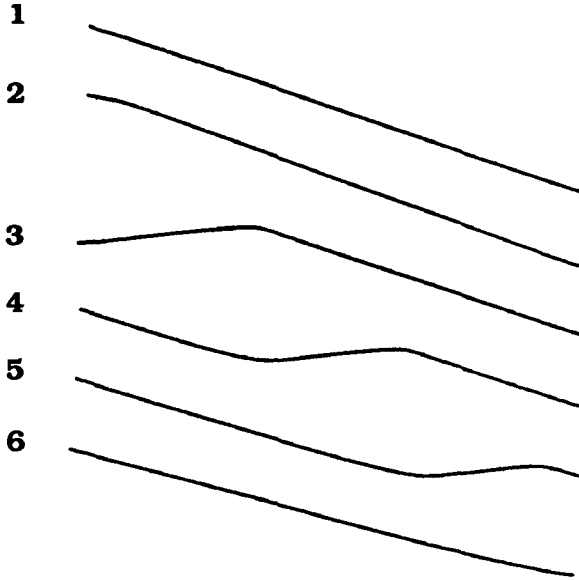


Figure 6.19 Computer-simulated changes in the shape of a flagellum without an elastic component at the base. Time interval between each successive flagellar shape is 20 ms.

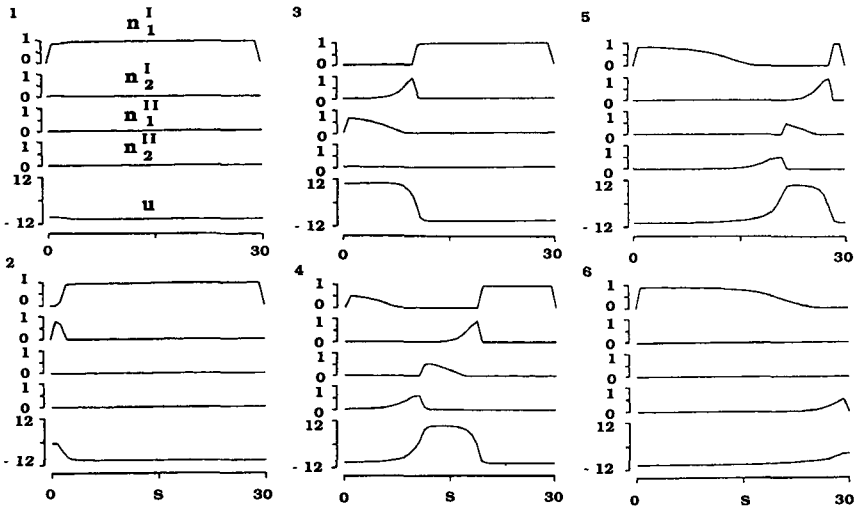


Figure 6.20 The fractions of cross-bridges in subsystems I (n_1^I, n_2^I) and II (n_1^{II}, n_2^{II}), and the shear displacement, u , as functions of space at 20 ms intervals. The number in each panel corresponds to that in Figure 6.19.

This impulse can be described as follows: (i) A sharp ‘wave front’ corresponds to a rapid increase in the shear displacement, which is caused by the transition from state 1 to 2 (i.e. ‘activation’) of cross-bridges in subsystem I. (ii) An almost ‘plateau’ phase appears during the transition from state 2 to 0 (i.e. ‘inactivation’) of cross-bridges in subsystem I and the transition from state 0 to 1 (i.e. ‘attachment’) of cross-bridges in subsystem II. (iii) A rapid decrease in the sliding magnitude is produced by the transition from state 1 to 2 of cross-bridges in subsystem II. (iv) A subsequent ‘refractory’ phase occurs due to a lack of attached cross-bridges in state 1 in subsystem I. This is the recovery process that forces the system to return to its original resting state. The impulse travels distally with an almost constant waveform at $t = 80$ ms. After the impulse passes through, the refractory phase begins to disappear and the system returns to its initial state at $t = 100$ ms. It should be noted that two different time-scales are found during the development of this impulse. That is, processes (i) and (iii) change rapidly relative to processes (ii) and (iv) because of the different magnitudes of the transition rate, constants.

Simulation studies of this kind are consistent with the experimental observations that a local bend initiated by a stimulus (say, direct contact with a microneedle or local application of ATP) is propagated along the flagellum toward the tip (Lindemann and Rikmenspoel, 1972; Shingyoji *et al.*, 1977). Since this system is homogeneous, bending waves can travel in both directions. If one applies a stimulus in the form of imposed sliding to the tip of the flagellum, a bend travels away from the tip toward the base along the flagellum at a constant propagation velocity. Actually, in some flagella, bending waves can be propagated either from the base or tip, depending on the mechanical constraint of the flagellar tip (Holwill and McGregor, 1974). Therefore, it appears that the present model provides a plausible basis for bend propagation along an isolated flagellum.

6.6 Simulations of asymmetric bending waves

Flagella and cilia have a common structure, so that the same mechanism may account for both flagellar and ciliary beating patterns. In this section we examine the ability of the present model, with its excitable properties, to generate asymmetric motion typical of cilia.

Recalling equation (6.9), we assumed a basal elastic component (with $u_0 = 0$), combined to bi-stable flagellar segments, in order to demonstrate symmetric bending waves. Similarly mono-stable segments produced repetitive beating when a basal component was incorporated into the system, though the simulations were not shown. In this section, we make two major changes to produce asymmetrical beating patterns typical of cilia.

- (i) The stable position at the base, u_0 , is shifted from 0 to 12 nm to amplify the structural asymmetry of the model.

- (ii) To increase the interaction between flagellar segments, the bending resistance, E_B , is increased to $12\,000\text{ pN }\mu\text{m}^2$.

Before demonstrating numerical results, let us consider the effects of these changes. The effects of (i) can be interpreted as follows. Each mono-stable segment has only one stable position at $u = -10\text{ nm}$, while a stable position at the base is at $u = 12\text{ nm}$ which is significantly different from that of the flagellar tail. This situation causes 'mutual instability'. On one hand a part of the system (i.e. the elastic component at the base) causes sustained stimuli to the remainder of the system and triggers active sliding in that region; on the other hand the remainder (i.e. mono-stable segments) works on the basal region to cause sliding against the passive force of the elastic component at the base. Thus the total system behaves as if it were a sustained oscillator changing with distance as well as time, and a typical cycle of asymmetric bending patterns is coordinated in time and space.

The effects of (ii) are as follows. From equation (6.14), it turns out that E_B determines the strength of the interaction between adjacent flagellar segments. For $E_B = 600\text{ pN }\mu\text{m}^2$, this interaction is so weak that the bend does propagate at a low speed, which results in a full development of the bend (see Fig. 6.19). Increasing E_B to $12\,000\text{ pN }\mu\text{m}^2$ strengthens the interaction, so that there is little room for a bend to develop along the axoneme with its limited length by the high velocity of the bend. Then a partial bend similar to ciliary beating appears (see Fig. 6.21). Thus, increasing E_B is in effect equivalent to decreasing the flagellar length, L .

The left panel of Figure 6.21 shows the spatio-temporal cross-bridge distribution during a full cycle. One finds that the sliding patterns consist of both metachronous (1–5) and synchronous sliding (6–9). The right panel of Figure 6.21 shows the development of the asymmetric bending waves that correspond to each stage of the left part. This type of movement resembles ciliary beating patterns: a 'recovery' stroke, in which metachronous sliding of the microtubules occurs, is followed by an 'effective' stroke which involves synchronous sliding. To emphasize the striking analogy with ciliary motion, each shape is drawn as if its basal end were pinned at a point.

Indeed, using a flagellar model containing the two-state cross-bridge cycle with 'ciliary' (i.e. clamped-end) boundary conditions, Blum and Hines (1979) showed that decreasing L reduces the number of bending waves, and furthermore when the length is short enough, a bend resembling an effective stroke of ciliary motion is realized. However, their model failed to simulate a recovery stroke under 'ciliary' boundary conditions (see Fig. 5.25). This is because the model has an axoneme with a symmetric structure resulting in an identical bend-propagation velocity for each half of the cycle. This means that although decreasing L (or increasing E_B) is sufficient to generate an effective stroke another possibility, besides introducing 'ciliary' boundary conditions, should be considered to model a full cycle of ciliary beats.

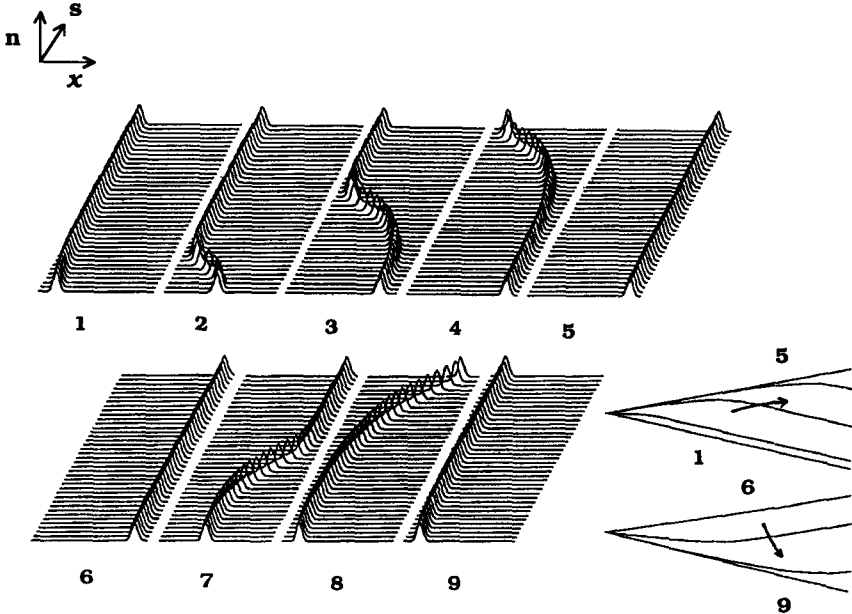


Figure 6.21 Left part: The total distribution, n , of cross-bridges in subsystems I and II in each of the 39 segments changing with time. 39 segments are arranged along an s -axis from the proximal to the distal end. The sliding coordinate x is taken as an abscissa with $-12 \leq x < 12$ nm. Right part: Computer-simulated changes in the shape of a cilium corresponding to each stage during successive changes of cross-bridge distribution shown in the left part. Successive changes of flagellar shapes (1–5) and (6–9) are presented at 5 ms intervals. The time interval between stages 5 and 6 is 12.5 ms.

It was for this reason that we incorporated a linear elastic component into the basal region of the model, with a stable position at $u_0 = 12$ nm. Since a stable position at the base is quite different from that of the flagellar tail, active sliding of cross-bridges in subsystem I (i.e. active interfilament sliding on one side) of each flagellar segment is successively triggered by the passive sliding caused by the elastic component at the base, and, after a time-interval, active sliding of cross-bridges in subsystem II (i.e. active sliding on the other side) spontaneously occurs against the passive force at the base. After the system returns to its original condition another time-interval follows, and thus a single beat-cycle is completed. Because the propagation velocity of the former sliding pattern (i.e. $2250 \mu\text{m/s}$) is quite different from that of the latter one (i.e. $3000 \mu\text{m/s}$), the resulting bends look like recovery and effective strokes.

The simulation results also suggest that there are two time-intervals that correspond to the starts of both the recovery and effective strokes. Sugino and Naitoh (1982) pointed out the presence of these two distinguishable time-

intervals during the beat cycle of a cilium based on their computer simulations (see Fig. 5.29). Hence there may be two switching mechanisms for activation in the ciliary beat-cycle. In our present model, these two time-intervals are realized only when the elastic component is combined with the mono-stable system as it is undergoing an all-or-none response to an imposed sliding magnitude of the filaments. Therefore, to generate ciliary motion, combining the system with the elastic component is much more important than adopting 'ciliary' boundary conditions. This may provide a plausible explanation for the two time-intervals observed in the ciliary motion.

Goldstein (1979) observed starting transients of flagella, in which nearly straight flagella began to beat symmetrically or asymmetrically depending on the pH of the medium. These starting transients resemble the formation of new bends during steady-state beating. This means that steady-state waveforms are spontaneously realized as the first bend reaches the distal end. As described in Section 6.5.2, our model was able to simulate steady-state symmetric beating patterns as well as the starting transients of symmetric motion.

In the present section, we have shown that asymmetric steady-state bending patterns were also obtained within the first full cycle. The recovery stroke precedes the effective stroke and a full cycle is spontaneously realized when computer simulation starts from the nearly straight form of the flagellum in its resting state.

Computer simulations of Blum and Hines (1979) involve the initial transients for a while, and are therefore quite different from the observed starting transients of steady-state waveforms. This inconsistency results from the fact that the model of Blum and Hines (1979) is based on the self-oscillatory properties of the opposed cross-bridge system and that it takes time to synchronize all the oscillators.

In contrast, in the present model the triggered event that corresponds to active sliding of cross-bridges occurs successively along the length of the flagellum; therefore, steady-state beating is directly attained without the initial transients. In conclusion, the present model can generate various waveforms for flagella and cilia, both based on similar dynein-tubulin mechanisms at zero external viscosity.

Notes

- 1 Setting $C_N = 0$ in equation (5.36a) and integrating twice with respect to s , we get the following force-balance equation:

$$S_a + S_p + S_v + E_B \frac{\partial^2 \sigma}{\partial s^2} = 0.$$

We use the simple relationship $\theta = \sigma$, because in the absence of the external viscous force the flagellar configuration is determined only by the internal

environment of the axoneme and so the flagellar orientation is arbitrarily determined. When the internal viscous force, S_v , is given by

$$S_v = -\gamma \frac{\partial \sigma}{\partial t}$$

then equation (6.1) is obtained.

- 2 It is necessary to consider a few hundred cross-bridges, because cross-bridges are statistically treated as one distribution. An alternative approach is a 'Monte Carlo' (or a stochastic) one, in which the behaviour of an individual cross-bridge is examined in detail and after that a population of cross-bridges is averaged (see Brokaw, 1982). Of course either approach can lead to the same results.
- 3 The equations (6.6) are the description that we follow for a distribution of cross-bridges at the same velocity as the sliding. An alternative but equivalent description is that we concentrate our attention on a region between x and $x + \Delta x$ where cross-bridges move in and out of this region. For this description, the total derivatives in the equations (6.6) are expanded by the chain rule to become (see p. 288 of Hill (1974))

$$\frac{dn_i(x,t)}{dt} = \frac{\partial n_i(x,t)}{\partial t} + \frac{\partial n_i(x,t)}{\partial x} \frac{\partial x}{\partial t} \quad \text{for } i = 0, 1 \text{ and } 2.$$

- 4 This assumption may not be true when there are two detached states in the cross-bridge as in the model by Brokaw (1982). Because two different positions are assigned to the detached cross-bridge, it is difficult to estimate the mean position of the cross-bridge distribution at a given shear displacement. However, in the present three-state model, only one detached state is considered (i.e. a unique position is assigned to the detached cross-bridge), and so the mean position of the distribution is uniquely specified.
- 5 In the case of muscle, it is generally assumed that with the load applied the active force caused by the cross-bridges is balanced, and that internal viscosity is negligible. Sliding movement is established when the forces are balanced. However, no significant change appears in the sliding motion even when considering the resisting force caused by internal viscosity. So, I tentatively proposed that the internal viscous resistance is balanced with the total shear forces.

Setting $E_b = 0$ in equation (6.1), we have

$$\gamma \frac{d\sigma}{dt} = S_a + S_p.$$

Note this equation is equivalent to equation (6.8a) since $u = h\sigma$, $\gamma' = \gamma/h$ and $S_a = Q_I S_I + Q_{II} S_{II}$.

7 Simplified models for flagellar dynamics

In the previous chapter we introduced the excitable dynein system based on a three-state mechano-chemical cycle, as a possible model to account for bend propagation in the absence of a curvature control mechanism. Flagellar-like base-to-tip waveforms and ciliary-like repetitive beats have been successfully demonstrated by using a model that has excitable properties in the limit of zero external viscosity.

We are now interested in studying whether this class of models also operate in the presence of external viscosity. The dynamics of a flagellum suspended in a viscous fluid are described by the fourth-order partial differential equation (see Section 5.3.1):

$$\frac{\partial^2 S}{\partial s^2} + E_B \frac{\partial^4 \sigma}{\partial s^4} + C_N \frac{\partial \sigma}{\partial t} = 0. \quad (7.0)$$

where S is the total shear force, σ the shear angle (as a function of arc length s and time t), E_B the bending resistance and C_N the external viscous-drag coefficient. The problem in demonstrating various wave phenomena in flagella, is thus ascribed to the problem of how to specify S such that equation (7.0) satisfies various types of travelling wave solutions.

In the present chapter we prefer to use a formal dynein model rather than a more realistic three- or four-state model, so that we do not have to simultaneously deal with the numerous parameters required to specify a realistic mechano-chemical cycle. Section 7.1 describes the formal model. The key concept is that the total shear force S is assumed to be a nonlinear function of σ and $\dot{\sigma}$ (see below) in such a way that the formal model displays the excitable and oscillatory behaviours similar to those obtained by the original three-state model. The similarity in these dynamical behaviours between the two models is discussed in Section 7.2 (with $E_B = 0$ and $C_N = 0$), and in Section 7.3 (with $E_B \neq 0$ and $C_N = 0$). In Section 7.4 we show that the model described by equation (7.0) with $E_B \neq 0$ and $C_N \neq 0$ not only demonstrates normal wave phenomena such as base-to-tip bend propagation,

but also shows other dynamical behaviours such as tip-to-base bend propagation, the reversal of the propagation direction, and soliton-like behaviour (i.e. two waves propagating in opposite directions passing through each other on collision).

For simplicity, our attention is focused on the small-amplitude oscillations and bend propagation where maximal shear displacement is generally less than a single stroke-distance (i.e. 24 nm). Once the essential features of the force-generating system required for bend propagation without a curvature control mechanism are understood, it is possible to extend the model to large-amplitude waves (see Chapter 9).

7.1 The simplified excitable dynein model

The original three-state model (Murase and Shimizu, 1986) has two important features. First, a dynein cross-bridge undergoes a *unidirectional mechanochemical cycle* of *resting state* (attachment) \rightarrow *active state* (power stroke) \rightarrow *inactive state* (detachment). The presence of the inactive state is responsible for the *refractoriness*, in which the responsiveness to external stimuli is reduced or absent depending on the timing with which the stimuli are delivered (see Section 6.4.5). Second, a resting dynein has an *excitable* nature. The transition to an active state (called *dynein activation*) is only triggered by sliding in the forward direction past a *threshold*, but not in the backward direction (characterized by the *directional sensitivity*). This temporal responsiveness and directional sensitivity may amount to the *mechano-sensitivity* of a dynein.

Suppose that the sliding coordinate, x , is defined as a distance between a cross-bridge on one microtubule and a reference point on its adjacent microtubule. Then the *unidirectional cycle* arises as a result of the x -dependent transition rate constants among the three states. The force generated by the attached cross-bridge is given by the space derivative of the potential-energy function ($F_1 = -dU_1/dx$, $F_2 = -dU_2/dx$), as shown in Figure 7.1. Excitability arises in the resting dynein when there is a threshold position at x_c , below which x goes to one stable state at x_1 (resting) and above which it goes to the other state at x_2 (dynein activation).

The essence of this three-state model is contained within the formal excitable-dynein model (Murase *et al.*, 1989) in the following way. First, let resting and active states be regarded as a single ‘on’ state, and the inactive state be an ‘off’ state. A dynein switches between these two states when the shear (or sliding displacement) passes critical values (called *switching points*). When the shear falls below S_1 the dynein is turned ‘on’ and maintains its state until the shear rises above S_2 , and turns the dynein ‘off’. By setting $S_1 \neq S_2$, either ‘on’ or ‘off’ can occur depending on the ‘history’ of the dynein behaviour. This history-dependent characteristic (called *hysteresis*) of the dynein refers to the unidirectional dynein cycle.

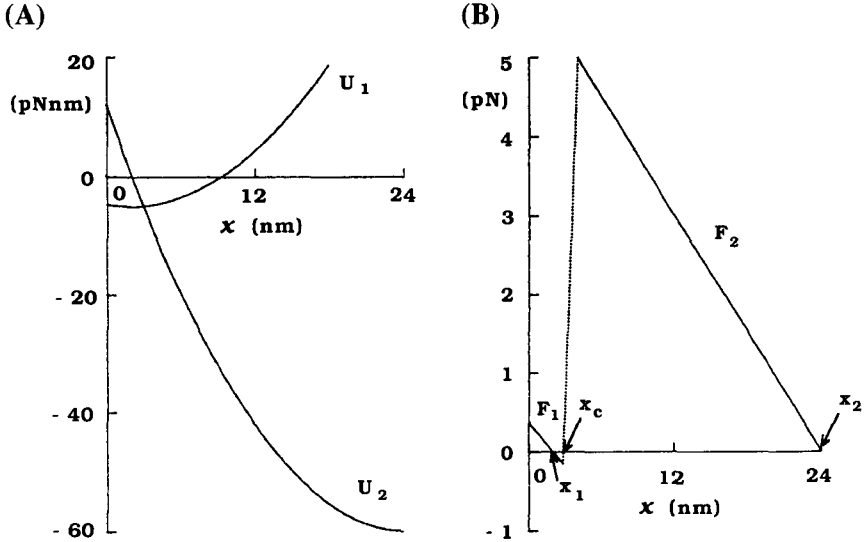


Figure 7.1 The three-state model of Murase and Shimizu (1986). (A): The potential-energy curve of the attached states as a function of the sliding coordinate, x . U_1 and U_2 denote the potential-energy of the resting and active states, respectively. (B): F_1 and F_2 denote the force generated by a dynein attached in the resting and active states, respectively, where $F_1 = -dU_1/dx$ and $F_2 = -dU_2/dx$. The dotted line represents the transition between the two states, which is determined by the transition rate constants (not shown). The stable positions of the dynein cross-bridges are at $x_1 = 2$ nm and $x_2 = 24$ nm, and the transition occurs at $x_c = 2.9$ nm. From Murase *et al.* (1989). Reprinted with permission.

The axoneme is treated as consisting of two opposing dynein subsystems, n_I being the fraction of subsystem I attached with force F_I and n_{II} the fraction of subsystem II attached with force F_{II} . Suppose that n_I and n_{II} act as 'on-off' switches with hysteresis. This hysteresis switching process can be described by the following *binary* function of x (see Fig. 7.2B). For sliding in the backward direction ($\dot{x} < 0$), if initially $n_I = 0$ for $x > S_I$, n_I switches from 0 to 1 at $x = S_I$ as follows:

$$n_I(x) = \begin{cases} 1 & 0 < x \leq S_I \\ 0 & S_I < x < l \end{cases} \quad (7.1a)$$

Here we assume that switching occurs instantaneously. Once $n_I = 1$ at $x = S_I$, n_I is always 1 even when x becomes larger than S_I . For sliding in the forward direction ($\dot{x} > 0$), if initially $n_I = 1$ for $x < S_2$, n_I switches from 1 to 0 at $x = S_2$ as follows:

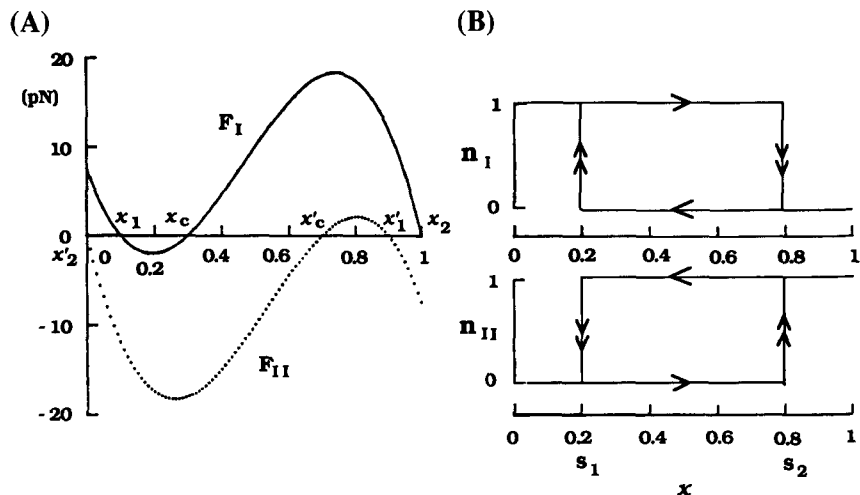


Figure 7.2 The cubic force–distance and hysteresis switching functions. (A): The active force is shown as a function of the (dimensionless) sliding coordinate, x . The solid line shows the force, F_I , for sliding in the forward direction (increasing x), and the dotted line the force, F_{II} , for sliding in the backward direction (decreasing x). The force–distance functions are: $F_I = Q_I(x - 0.1)(x - 1)(0.3 - x)$, and $F_{II} = Q_{II}(x - 0.9)(x - 0.7 - x)$ with $Q_I = Q_{II} = 250$ pN. (B): The fraction for attachment of a cross-bridge is shown as a function of x . The fraction is a two-valued function in the region $S_1 < x < S_2$, where $S_1 = 0.2$ and $S_2 = 0.8$. The value depends on the direction in which the region is entered. Note that $n_I + n_{II} = 1$ for each direction of movement. From Murase *et al.* (1989). Reprinted with permission.

$$n_I(x) = \begin{cases} 1 & 0 < x < S_2 \\ 0 & S_2 \leq x < 1 \end{cases} \quad (7.1b)$$

Once $n_I = 0$ at $x = S_2$, n_I is always 0 even when x becomes smaller than S_1 .

It is further required that $n_I + n_{II} = 1$, so that only one of the opposed subsystems is in the ‘on’ state at any time.¹ Thus a dynein in subsystem I is turned ‘on’ (and hence a dynein in subsystem II is turned ‘off’) during the forward sliding, while the dynein in subsystem I is turned ‘off’ (and hence the dynein in subsystem II is turned ‘on’) during the backward sliding.

The key features of dynein excitability are captured by any force–distance function for the ‘on’ state which crosses the x -axis three times with a negative slope (see Fig. 7.2A). (Such zeros are steady states.) We choose a cubic force–distance function,²

$$F_I(x) = Q_I(x - x_1)(x - x_2)(x_c - x) \quad (7.2a)$$

where Q_I is the scaling factor corresponding to the number of cross-bridges in subsystem I, x_1 and x_2 are the two stable positions and x_c is a threshold position analogous to the location of the transition between resting and active states of Figure 7.1. For all $x < x_c$, $x \rightarrow x_1$, while for all $x > x_c$, $x \rightarrow x_2$. For subsystem II, an oppositely directed force–distance function, F_{II} , is defined:

$$F_{II}(x) = Q_{II}(x - x'_1)(x - x'_2)(x'_c - x) \quad (7.2b)$$

where Q_{II} is the scaling factor, x'_1 and x'_2 are the two stable positions and x'_c is an unstable position.

7.2 Dynamics of a segment model

It is instructive to look first at a small segment of axoneme in which sliding movement is generated by the dynein force. This allows us to focus on the switching properties of the system in the absence of interactions with other segments. In the multi-segment simulations such interactions affect the switching dynamics leading to spatio-temporal patterns. The behaviour of a single segment, consisting of opposed dyneins and passive elastic links, can be simulated by solving the force-balance equation:³

$$\gamma \frac{d\sigma}{dt} = F_I(x)n_I(x) + F_{II}(x)n_{II}(x) - K_e(\sigma - \sigma_0) \quad (7.3a)$$

$$x = \sigma \quad (7.3b)$$

where K_e is the force constant for the passive elastic elements (e.g. nexin links which may exert a restoring force proportional to their shear), σ_0 is their location in the unstretched state, and γ is an internal viscosity introduced to allow force balance at a finite sliding velocity. When $K_e = 0$, there is bi-stability. Either a stable state at $\sigma = x_1$ or x'_1 can be present, depending on the initial shear displacement. When σ_0 is located in the unstable region and K_e is large enough, oscillatory behaviour occurs (see Fig. 7.3).

The qualitative behaviour of the cubic force-generating system with a hysteresis switching mechanism is, therefore, similar to the behaviour of the three-state dynein model of Murase and Shimizu (1986) discussed in the previous chapter in that it can display both bi-stable and oscillatory behaviour.

7.3 Bend propagation at zero external viscosity

Before attempting to demonstrate wave phenomena at *non-zero* external viscosity by solving equation (7.0), it is useful to examine whether the formal excitable-dynein model gives rise to bend propagation at *zero* external viscosity as expected in the context of the previous chapter. In such an ideal

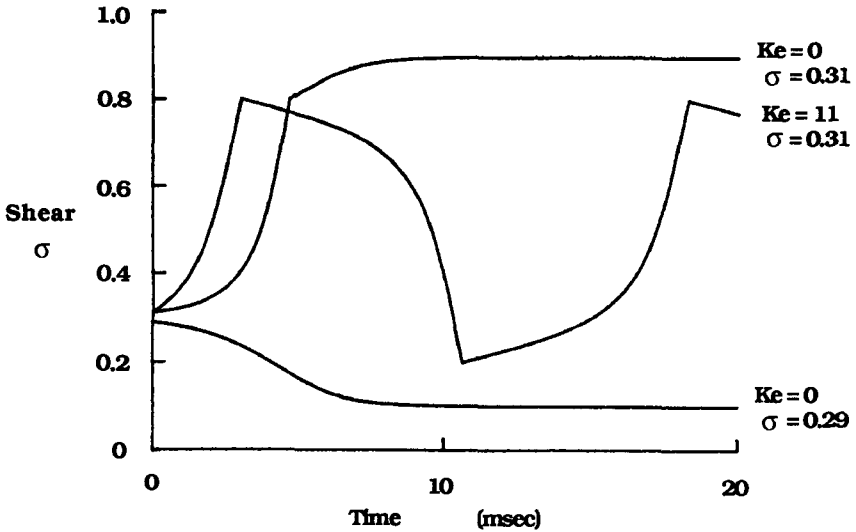


Figure 7.3 Shear in a single segment as a function of time for the cubic force–distance system. The shear, σ , is plotted for two values of K_e (the force constant for the passive elastic links, in pN/24 nm) and two initial values of σ . These values are shown in the figure. When $K_e = 0$, the system exhibits bi-stable behaviour since it approaches one of the two stable states, depending on the initial value of σ . As K_e is increased through some critical value, oscillatory behaviour appears. In these simulations $\sigma_0 = 0.5$ and $\gamma = 50$ pN ms/24 nm. Modified from Murase *et al.* (1989). Reprinted with permission.

situation, the flagellar dynamics are described by the so-called reaction–diffusion equation⁴ (see Chapter 6).

The complete system of equations and boundary conditions has the form:

$$\gamma \frac{\partial \sigma}{\partial t} = E_B \frac{\partial^2 \sigma}{\partial s^2} + S \tag{7.4a}$$

$$x = \sigma \tag{7.4b}$$

$$S = F_I n_I + F_{II}(1 - n_I) - K_e(\sigma - \sigma_0) \tag{7.4c}$$

$$F_I = Q_I(x - x_1)(x - x_2)(x_c - x) \tag{7.4d}$$

$$F_{II} = Q_{II}(x - x'_1)(x - x'_2)(x'_c - x) \tag{7.4e}$$

$$n_I = \begin{cases} 1 & 0 < x \leq S_1 \\ 0 & S_1 < x < 1 \end{cases} \text{ for } \dot{x} < 0 \tag{7.4f}$$

$$n_I = \begin{cases} 1 & 0 < x < S_2 \\ 0 & S_2 \leq x < 1 \end{cases} \text{ for } \dot{x} > 0 \tag{7.4g}$$

$$\frac{\partial\sigma(0)}{\partial s} = 0 \quad (7.4h)$$

$$\frac{\partial\sigma(L)}{\partial s} = 0. \quad (7.4i)$$

Here, s is the arc length along the axoneme. Boundary conditions (7.4h, i) mean that both ends are free, i.e. zero curvature at $s = 0$ and L , where L is the length of the axoneme.

A 50 μm model flagellum is divided into 50 segments of length 1 μm . In the model, a self-oscillatory basal end is combined with 49 segments exhibiting bi-stable behaviour. This type of model is easily developed by adopting $K_e = 60 \text{ pN}/24 \text{ nm}$ at $s = 1 \mu\text{m}$ and $K_e = 1 \text{ pN}/24 \text{ nm}$ for $1 < s < 50 \mu\text{m}$, because the proximal segment with a large K_e value acts as a pacemaker which can periodically stimulate the rest of the flagellum. The simulations were performed starting from a straight flagellum under free-end boundary conditions.

The left side of Figure 7.4 shows shear σ (or sliding x) as a function of arc length, s , along the axoneme at 5 ms intervals during self-organization of bending waves, while the right side of Figure 7.4 shows the corresponding shapes. As this figure shows, the basal pacemaker region repetitively stimulates the excitable region leading to periodic travelling excitation waves of equal amplitude.

For the convenience of the following discussion, we shall introduce the space–time diagram in Figure 7.5. This figure depicts the positions of waves (where the regions $\sigma > 0.5$ in the left side of Figure 7.4 are plotted by bars) as a function of time, t , and space, s . There is only a single bar at a given time for $0 < t < 45 \text{ ms}$ corresponding to a single bend. As time proceeds, the bar moves to the right which is associated with bend propagation. A steady-state waveform is attained as the first bend reaches the tip. As a result there are two bars (corresponding to two bends) at any time for $t > 45 \text{ ms}$. They continuously move to the right. The degree of successive shifts of bars in the space–time diagram indicates the velocity of bend propagation. The regular spatio-temporal patterns suggest that the system reaches a stable cycle of steady-state bend initiation and propagation.

7.4 Bend propagation at non-zero external viscosity

In the previous section we showed that the simple axoneme with excitable behaviour, when connected to a basal self-oscillatory region, displayed bend propagation initiating from the so-called pacemaker region at the base. These simulations were performed at zero external viscosity, but only in the presence of internal viscosity. Now consider what happens when external viscosity is present. We will focus our attention on the effects of the

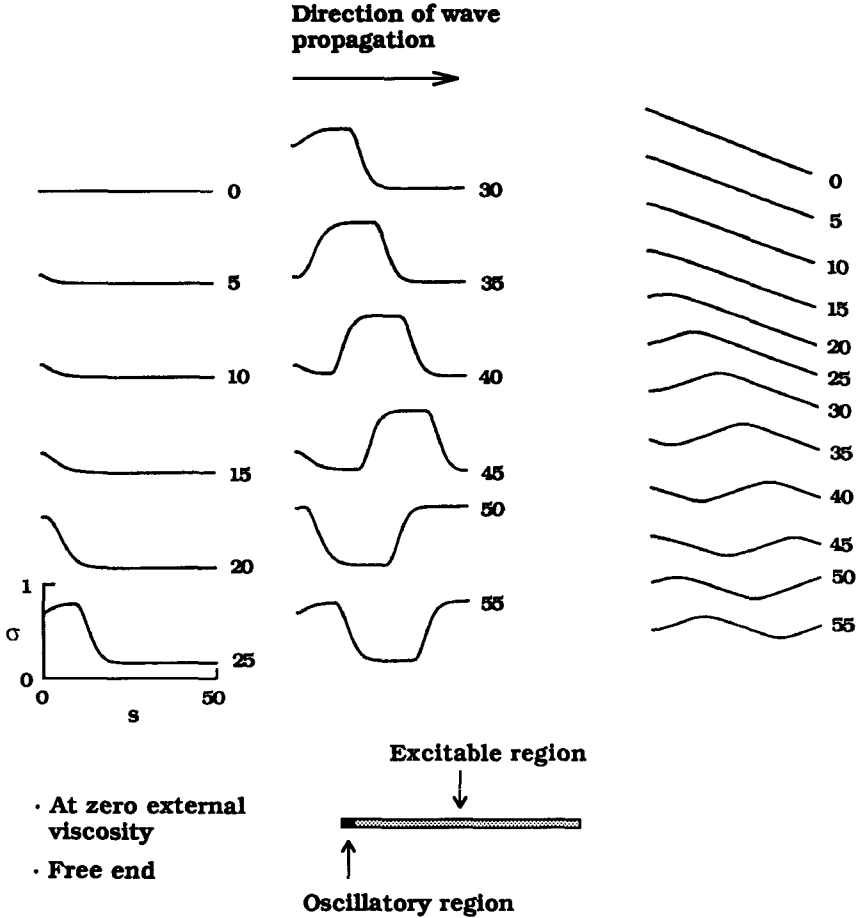


Figure 7.4 Bend propagation under free-end boundary conditions for the cubic force–distance function similar to that in Figure 7.2. The parameters are: $E_B = 300 \text{ pN } \mu\text{m}^2$, $\gamma = 100 \text{ pN ms}/24 \text{ nm}$, $Q_I = Q_{II} = 300 \text{ pN}$, $x_1 = 0.15$, $x_2 = 1$, $x_c = 0.25$, $x'_1 = 0.85$, $x'_2 = 0$, and $x'_c = 0.75$. The properties of the axoneme vary along its length as follows: $K_c = 60 \text{ pN}/24 \text{ nm}$ for $s = 1 \text{ } \mu\text{m}$ and $K_c = 1 \text{ pN}/24 \text{ nm}$ for $1 < s < 50 \text{ } \mu\text{m}$. This is equivalent to an oscillatory region in the first segment, an excitable region in segments 2–50. The initially straight axoneme was allowed to develop its bending waves. The shear is shown in ms at the indicated times on the left side of the figure, while the corresponding axonemal shapes are presented on the right side. The flagellar shapes in the (x, y) coordinates are obtained by:

$$x(s) = \int_0^s \cos(\sigma - 0.5) ds, \quad y(s) = \int_0^s \sin(\sigma - 0.5) ds.$$

The direction of the bend propagation is indicated by the arrow. The schematic representation of this axoneme is shown in the bottom panel.

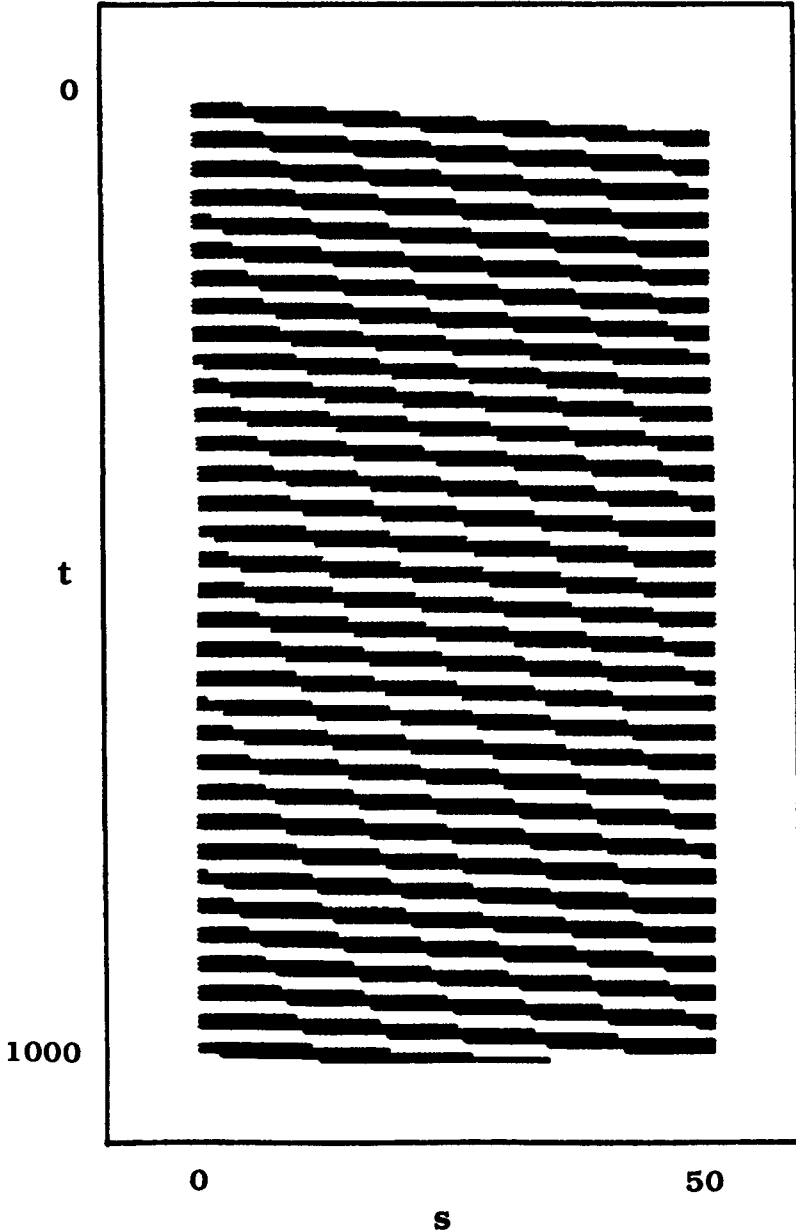


Figure 7.5 Positions of waves as a function of time, t (in ms), and space, s (in μm). The regions $\sigma > 0.5$ in the left of Figure 7.4 are plotted by bars. As time proceeds, the groups of bars move toward the right reflecting the fact that bending waves initiated at the base (at the left end) propagate toward the tip (the right end).

Table 7.1 Boundary conditions of the axoneme at the base

Free	$\begin{cases} F_N(0) = 0 \\ M_V(0) = 0 \end{cases}$
Clamped	$\begin{cases} V_N(0) = 0 \\ \frac{\partial V_N(0)}{\partial s} = 0 \end{cases}$
Pinned	$\begin{cases} V_N(0) = 0 \\ M_V(0) = 0 \end{cases}$

boundary conditions and axonemal structure on the dynamical behaviour of the model.

7.4.1 Boundary conditions for cilia and flagella

In obtaining equation (7.0) from its original equation (5.36), we have assumed that

$$\sigma(s) = \theta(s) \quad \text{for } 0 < s < L \quad (7.5)$$

where σ is the shear angle, θ the angle the flagellum makes to a fixed external coordinate system and L the length of the axoneme (see Section 5.3.1). As illustrated in Figure 5.9D, the sliding filament mechanism provides the following equation:

$$\frac{\partial \sigma(s)}{\partial s} = \frac{\partial \theta(s)}{\partial s} \quad \text{for } 0 < s < L. \quad (7.6)$$

The integration of equation (7.6) with respect to space, s , leads to

$$\sigma(s) - \theta(s) = \sigma(0) - \theta(0). \quad (7.7)$$

This suggests that the boundary conditions at the basal end play an important role in determining the relationship between σ and θ .

It is possible to consider three types of boundary conditions according as the basal end is *free to move*, *clamped rigidly* or *pinned at a point* (Table 7.1). In addition to these boundary conditions, a further boundary condition relating relative motion of the filaments is required for the sliding filament models. There is the possibility of three different constraints – the filaments are allowed to *slide freely*, are *tied together*, or are *individually pinned* (Table 7.2).

To get a solution to equation (7.0) or its original equation (5.36), we must specify one of several combinations of the boundary conditions – one from Table 7.1 and the other from Table 7.2. We shall discuss all the combinations in the context of constraint (7.5) as follows.

Table 7.2 Boundary conditions of the filaments at the base

Free	$\frac{\partial \sigma(0)}{\partial s} = 0$
Fixed	$\sigma(0) = 0$
Pinned	$\sigma(0) = \theta(0)$

First consider the axoneme freely suspended in a viscous fluid like a cut flagellum. The external viscous force, F_N , and moment, M_v , must be zero at the base (see the top row of Table 7.1). Note that these free-end boundary conditions are always required at the tip of cilia or flagella, irrespective of the boundary conditions at the base. Now we must specify one of the three conditions from Table 7.2 – free, fixed or pinned – relating to sliding movement of the filaments at the base. On one hand, Hines and Blum (1978; 1979) considered that the filaments were free to slide, i.e. $\partial \sigma(0)/\partial s = 0$ (see the top row of Table 7.2). In this case $(\sigma(0) - \theta(0))$ becomes an additional undetermined quantity (see Blum and Hines, 1979). This must be implicitly determined by the requirement that the total shear force along the length of the axoneme be zero:

$$\int_0^L S ds = 0. \quad (7.8)$$

Then we get exact solution to equation (5.36).

On the other hand, Brokaw (1972b; 1975; 1985) assumed that the filaments were tied together, i.e. $\sigma(0) = 0$ (see Fig. 5.21; and the middle row of Table 7.2). This means that the short region near the base, which effectively contains a very high shear resistance, absorbs all the shear forces along the length of the flagellum, and hence equation (7.8) holds. A variable $\theta(0)$ remaining in equation (7.7) is then specified, and exact solution to equation (5.36) is obtained.

Contrary to the above two cases, no attempt has been made to assume a pinned condition for the filaments, i.e. $\sigma(0) = \theta(0)$ (see the bottom row of Table 7.2). The pinned condition leads to equation (7.5) via equation (7.7) irrespective of equation (7.8). In a freely suspended flagellum, however, equation (7.8) must be always satisfied. Thus this condition is not appropriate to the flagellum. Now we shall consider another constraint described by equation (7.5) instead of equation (7.8). Generally, equation (7.5) is incompatible with equation (7.8). However, if there are two developing bends on the axoneme that are increasing in angle at equal but opposite rates, the average bend angle along the axoneme will be approximately zero, and hence equation (7.8) satisfied. Thus equation (7.5) appears to be a good approximation to constraint (7.8) under these conditions. Equation (7.0) is then a first-order approximation to the original equation (5.36).

As a second type of boundary conditions, let us consider the clamped-end conditions at the base, i.e. $V_N(0) = 0$ and $\partial V_N(0)/\partial s = 0$ (see the middle row of Table 7.1). This could be appropriate to a cilium which may be attached rigidly to the cell surface. Since $\partial F_N/\partial s = -C_N V_N$ from equations (5.29) and (5.31), $V_N(0) = 0$ is equivalent to $\partial F_N(0)/\partial s = 0$. Since the axoneme is continuous, one can get $\partial V_N/\partial s = -\partial\theta/\partial t$ (see Fig. 2 of Lubliner and Blum, 1971). Thus $\partial V_N/\partial s = 0$ is equivalent to $\theta(0) = 0$, so that only the condition $\sigma(0) = 0$ (see the middle row of Table 7.2) seems to be consistent with these clamped conditions. These conditions are usually taken into account for analyses of ciliary movement such as simulations in Figures 5.24 and 5.25 given by Blum and Hines (1979). Under these conditions, equation (7.5) is consistent with equation (7.7), so that we get exact solution of equation (5.36) by solving just equation (7.0).

The third conditions assume that the axoneme is pinned at the base, which may be equally applicable to a cilium, given our lack of detailed information of the transitional region at the base (see the bottom row of Table 7.1). This seems to be somewhere between the above two extremes. If, in addition, the filaments are individually pinned, i.e. $\sigma(0) = \theta(0)$ (see the bottom row of Table 7.2), equation (7.5) holds automatically from equation (7.7). From $M_v(0) = 0$, we have also $\partial\theta(0)/\partial s = \partial\sigma(0)/\partial s = 0$, which is implying that the filaments slide freely at the basal end since $\partial\sigma(0)/\partial s = 0$ (see the top row of Table 7.2). As a result, the conditions that the filaments are free or pinned at the base are not mutually exclusive, but are equivalent to each other as long as the axoneme is pinned, because we can get exact solution to equation (5.36) by solving equation (7.0) under either of the two conditions. The condition that the filaments are fixed, i.e. $\sigma(0) = 0$ (see the bottom row of Table 7.2), however, seems to be inconsistent with these pinned conditions.

In the present chapter we consider either of the first two conditions at the base: (i) the axoneme is free to move and the filaments are free to slide; or (ii) the axoneme is clamped and the filaments are fixed. The third conditions that (iii) the axoneme and the filaments are both pinned are reserved until Chapter 8.

7.4.2 Bend propagation with clamped-end boundary conditions

It is of interest to ascertain whether a bending wave would initiate and propagate if the basal end of the axoneme is held fixed, i.e. the clamped-end boundary conditions. Under these conditions, and on the assumption $\sigma(s) = \theta(s)$, the original basic equation (5.36) is solved exactly. Numerical simulations revealed that the model presented here displayed tip-to-base bend propagation as well as base-to-tip bend propagation, depending on the *structural asymmetry* along the length of the axoneme.

The full system of equations and boundary conditions has the form:

$$\frac{\partial^2 S}{\partial s^2} + E_B \frac{\partial^4 \sigma}{\partial s^4} + C_N \frac{\partial \sigma}{\partial t} = 0 \quad (7.9a)$$

$$x = \sigma \quad (7.9b)$$

$$S = F_I n_1 + F_{II}(1 - n_1) - K_e(\sigma - \sigma_0) \quad (7.9c)$$

$$F_I = Q_I(x - x_1)(x - x_2)(x_c - x) \quad (7.9d)$$

$$F_{II} = Q_{II}(x - x'_1)(x - x'_2)(x'_c - x) \quad (7.9e)$$

$$n_1 = \begin{cases} 1 & 0 < x \leq S_1 \\ 0 & S_1 < x < 1 \end{cases} \quad \text{for } \dot{x} < 0 \quad (7.9f)$$

$$n_1 = \begin{cases} 1 & 0 < x < S_2 \\ 0 & S_2 \leq x < 1 \end{cases} \quad \text{for } \dot{x} > 0 \quad (7.9g)$$

$$\frac{\partial^3 \sigma(0)}{\partial s^3} = 0; \quad \sigma(0) = \sigma_0 \quad (7.9h)$$

$$\frac{\partial^2 \sigma(L)}{\partial s^2} = 0; \quad \frac{\partial \sigma(L)}{\partial \sigma} = 0. \quad (7.9i)$$

The clamped-basal-end and free-distal-end boundary conditions are represented by (7.9h) and (7.9i), respectively.

Tip-to-base bend propagation. When sliding is not allowed at the basal end, the dyneins there will be unable to reach their switching points and will therefore continuously generate a large shear force in a single direction, thus preventing the formation of symmetric bends. To eliminate this problem, we removed the dynein from a short basal region. The resultant region without dyneins is referred to as a 'passive' region. The minimum size of the passive region depends on the strength of the dynein force and on the bending resistance. Of course, a passive proximal region is not necessary if the filaments are allowed to slide at the basal end (see Chapter 8). The cubic force-distance function was used for the excitable dynein system. The axoneme under consideration had the passive basal region and excitable dyneins uniformly distributed from the end of the passive region to the distal end.

After transient behaviours had died away starting from any initial conditions, bends initiated at the tip and propagated towards the base (Fig. 7.6). This phenomenon provides an interesting problem of how rhythmic bend propagation is organized even though none of these segments alone has a self-oscillatory property. At zero external viscosity, as studied in Section 6.5.3, the 'homogeneous' excitable axoneme does not exhibit sustained movement, rather it becomes 'quiescent' as time proceeds irrespective of initial conditions (see also Section 7.4.5).

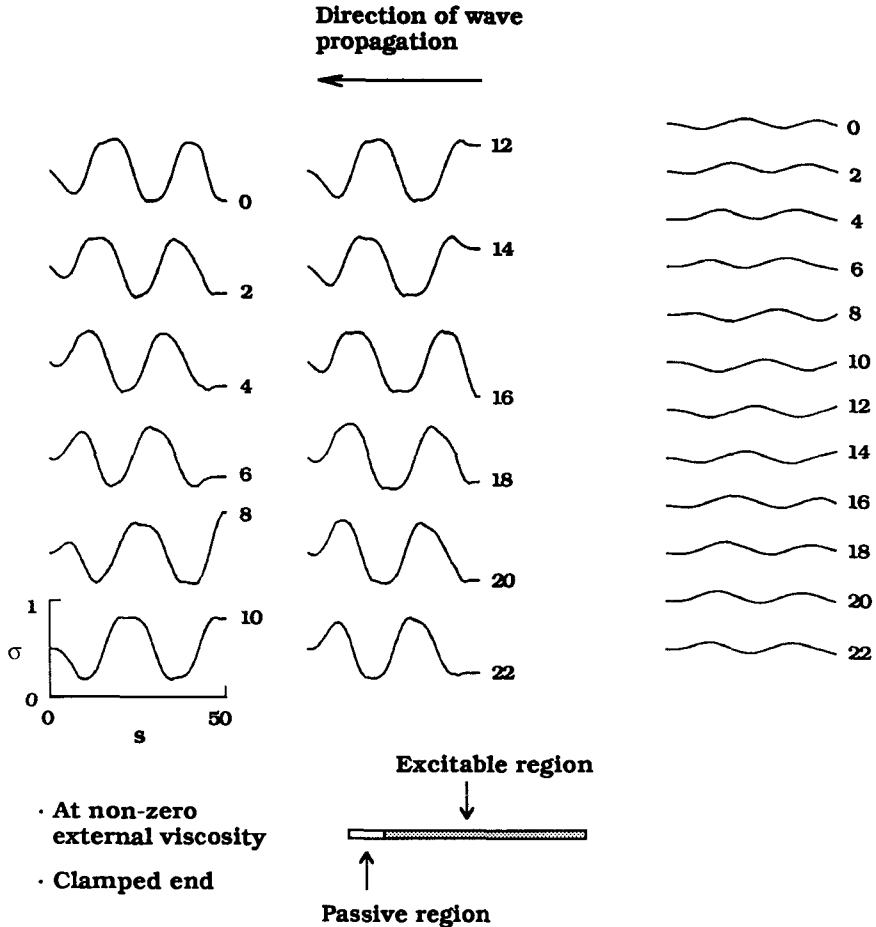


Figure 7.6 Tip-to-base bend propagation under clamped-end boundary conditions for the cubic force–distance function shown in Figure 7.2. The parameters are: $E_B = 400 \text{ pN } \mu\text{m}^2$, $C_N = 5 \text{ pN ms}/\mu\text{m}^2$. The properties of the axoneme vary along its length as follows: $Q_I = Q_{II} = 0$, $K_e = 1 \text{ pN}/24 \text{ nm}$ for $0 < s < 8 \mu\text{m}$ and $Q_I = Q_{II} = 270 \text{ pN}$, $K_e = 1 \text{ pN}/24 \text{ nm}$ for $8 \leq s \leq 50 \mu\text{m}$. This represents an axoneme with a short passive region at the basal end and bi-stable segments elsewhere. The schematic representation of this axoneme is shown in the bottom panel. From Murase *et al.* (1989). Reprinted with permission.

There seems to be an external viscosity-induced instability leading to tip-to-base bend propagation. To understand such a viscosity-induced instability two types of simulations were performed, either with only internal viscosity or only external viscosity. In the following simulations the axoneme had only passive elastic links along its entire length (i.e. $Q_I = Q_{II} = 0$), and a completely straight form was used as an initial condition. In the first type of

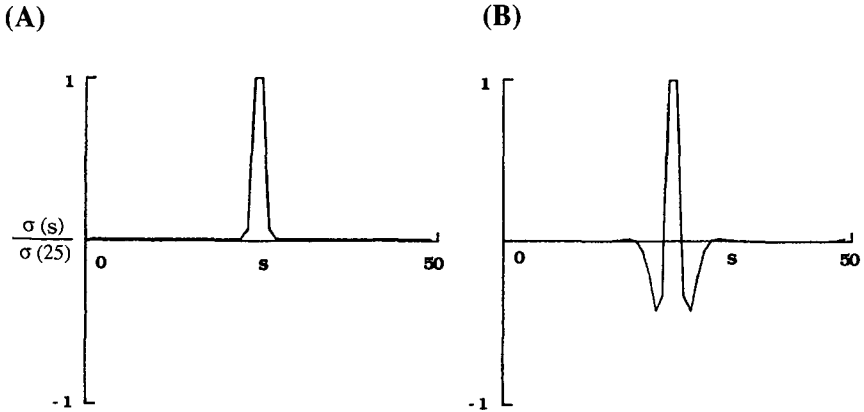


Figure 7.7 Relative shear, $\sigma(s)/\sigma(25)$, as a function of space, s , after an application of a point force of 50 pN at $s = 25 \mu\text{m}$ under free-end boundary conditions. An initially straight axoneme has only passive elastic links, i.e. $K_e = 1 \text{ pN}/24 \text{ nm}$, $Q_I = Q_{II} = 0$ and $E_B = 400 \text{ pN } \mu\text{m}^2$. A single point force of 50 pN is applied to the middle segment at $s = 25 \mu\text{m}$. The relative shear is plotted 0.01 ms after the stimulus. (A): There is only internal viscosity, i.e. $\gamma = 50 \text{ pN ms}/24 \text{ nm}$ and $C_N = 0$. Positive shear force always causes positive shear. (B): There is only external viscosity, i.e. $\gamma = 0$ and $C_N = 5 \text{ pN ms}/\mu\text{m}^2$. Positive shear force induces negative shear in the nearby region.

simulation, a positive shear force ($S = 50 \text{ pN}$) was applied to the middle segment of the axoneme (at $s = 25 \mu\text{m}$) under free-end boundary conditions.

Figure 7.7 illustrates the relative shear displacement plotted against the arc length, s , immediately (0.01 ms) after a step increase in shear force at $s = 25 \mu\text{m}$. The simulated shear distribution is spiky because a short time-interval is allowed between the onset of the shear force and the time when the resultant shear distribution is calculated. By adopting this simulation technique we can ignore the effects of the elastic bending resistance, and hence neglect the effects of the terms involving E_B in equation (7.4a) or (7.9a). At zero external viscosity but with internal viscosity, a positive shear force can only lead to positive shear displacements (Fig. 7.7A). In the presence of external viscosity only, positive shear force can lead to negative shear in nearby regions (Fig. 7.7B). This difference is clearly understood by considering the finite-difference approximation as follows.

Let space, s , and time, t , be made discrete by adopting $s = i\Delta s$ and $t = j\Delta t$, where i and j are integers, and Δs and Δt are the respective steps of the mesh along the s - and t -axes. Now $\sigma_{i,j}$ is used to denote $\sigma(i\Delta s, j\Delta t)$. Similarly, let S_i denote $S(s = i\Delta s)$. For convenience we assume $\Delta s = \Delta t = 1$. The final form of the finite-difference scheme for equation (7.4a) under a single point force at the i -th segment (at $s = 25 \mu\text{m}$ in Fig. 7.7) is:

$$\sigma_{i,j+1} = \sigma_{i,j} + S_i \quad (7.10)$$

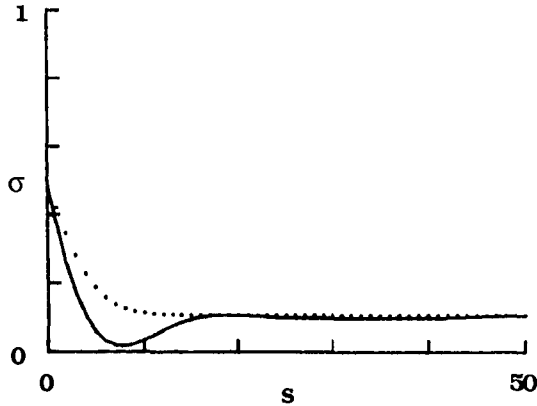


Figure 7.8 Shear, σ , as a function of s after an abrupt change of shear at the basal end, such that $\sigma(s=0) = 0.5$ under the clamped-end boundary conditions. An initially straight axoneme with only passive elastic links $K_e = 1 \text{ pN}/24 \text{ nm}$ and $E_B = 400 \text{ pN } \mu\text{m}^2$ is subjected to an abrupt change in the shear at the base. The distribution of shear 1 ms after the proximal end is displaced. Note that $\sigma(t=0) = 0.1$ for $0 < s < 50 \text{ } \mu\text{m}$. The dotted line shows $\sigma(s)$ with only internal viscosity, i.e. $\gamma = 50 \text{ pN ms}/24 \text{ nm}$ and $C_N = 0$. The solid line shows $\sigma(s)$ with only external viscosity, i.e. $\gamma = 0$ and $C_N = 5 \text{ pN ms}/\mu\text{m}^2$. From Murase *et al.* (1989). Reprinted with permission.

and equation (7.9a) is written as follows:

$$\sigma_{i,j+1} = \sigma_{i,j} + 2S_i \quad (7.11a)$$

$$\sigma_{i-1,j+1} = \sigma_{i-1,j} - S_i \quad (7.11b)$$

$$\sigma_{i+1,j+1} = \sigma_{i+1,j} - S_i \quad (7.11c)$$

Equation (7.10) predicts that σ_i increases when $S_i > 0$. In contrast equations (7.11) predict that σ_i increases, but at the same time σ_{i-1} and σ_{i+1} decrease even if $S_i > 0$.

In the second type of simulation, an abrupt change in shear (not shear force) was applied at $s = 0$ under the clamped-end condition. Figure 7.8 shows shear distribution some time (1 ms) after a step change in shear at $s = 0$. Since all the segments are passive, the shear force, S , is almost zero. The terms involving S can be neglected in equations (7.4a) and (7.9a). An abrupt change in shear at $s = 0$ is transmitted via an elastic coupling. A long period (1 ms) was allowed to proceed in order to obtain the shear distribution affected by the secondary effects of the elastic coupling. If there is only an internal viscosity, then shear is always in the same direction as the abrupt change (Fig. 7.8A). If, however, an external viscosity is present (with no internal viscosity), an external shear force develops in a distal region which causes shear in the opposite direction, though shear in the segment closer to the basal end is in the same direction as the abrupt change (Fig. 7.8B).

This difference is again understood by considering the finite-difference form for each original partial differential equation. The finite-difference form of equation (7.4a) is:

$$\sigma_{i,j+1} = \sigma_{i,j} + E_B(\sigma_{i-1,j} - 2\sigma_{i,j} + \sigma_{i+1,j}) \quad (7.12)$$

and the form of equation (7.9a) is written as

$$\begin{aligned} \sigma_{i,j+1} = \sigma_{i,j} - E_B[(\sigma_{i-2,j} - 2\sigma_{i-1,j} + \sigma_{i,j}) - 2(\sigma_{i-1,j} - 2\sigma_{i,j} + \sigma_{i+1,j}) \\ + (\sigma_{i,j} - 2\sigma_{i+1,j} + \sigma_{i+2,j})]. \end{aligned} \quad (7.13)$$

Equations (7.12) and (7.13) show the *attractive* interaction between the nearest-neighbour segments, because the right-hand side of equation (7.12) is decomposed into

$$E_B(\sigma_{i-1,j} - 2\sigma_{i,j} + \sigma_{i+1,j}) = -E_B(\sigma_{i,j} - \sigma_{i+1,j}) - E_B(\sigma_{i,j} - \sigma_{i-1,j}). \quad (7.14)$$

As a result, positive shear at $s = 0$ always induces positive shear in regions nearby. On the contrary, the average shear defined by

$$\bar{\sigma}_{i,j} = \sigma_{i-1,j} - 2\sigma_{i,j} + \sigma_{i+1,j} \quad (7.15)$$

shows the *repulsive* interactions between the average regions nearby, because the right-hand side of equation (7.13) is decomposed into

$$-E_B(\bar{\sigma}_{i-1,j} - 2\bar{\sigma}_{i,j} + \bar{\sigma}_{i+1,j}) = E_B(\bar{\sigma}_{i,j} - \bar{\sigma}_{i+1,j}) + E_B(\bar{\sigma}_{i,j} - \bar{\sigma}_{i-1,j}). \quad (7.16)$$

Equation (7.13) suggests that positive shear at $s = 0$ induces positive shear in the region nearby, yet at the same time negative shear via its average shear. This situation seems to be somewhat analogous to phenomena with *short-range activation* and *long-range inhibition* in neurophysiology, population dynamics, and morphogenesis (Murray, 1989). For real simulations, three terms in equations (7.4a) or (7.9a) must be taken into account. Especially, in solving equation (7.9a), complex dynamical behaviour can appear.

We can now understand how the tip-to-base bend propagation appears. Under the free-end boundary conditions at the distal end, both the external viscous force and external viscous moment are zero, thereby the tip can move and rotate freely relative to the other segments. Once the tip happens to swing due to active sliding in the positive direction, a viscous shear force is generated which in turn affects more proximal regions and triggers successive active sliding in the same direction via an elastic coupling. Since there is inhibitory viscous interaction between segments (see Fig. 7.8), active sliding of one segment acts to inhibit active sliding of the other in the same direction, but induces sliding in the opposite direction. This mutual inhibition provides a so-called 'flip-flop' switch. As a result, the axoneme as a whole exhibits a coordinated bending pattern, even though individual segments do not have oscillatory properties (see Fig. 7.15 for a concrete simulation).

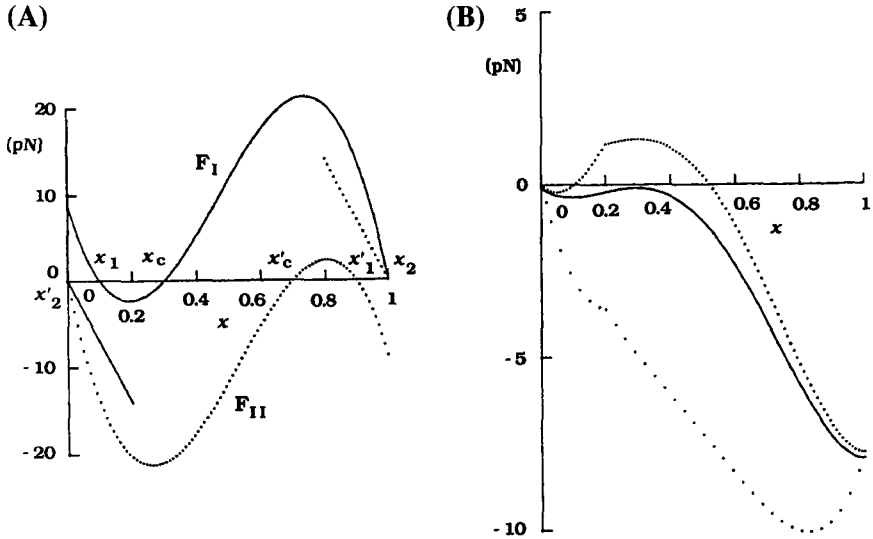


Figure 7.9 Modified force–distance function and energy diagram for the force–distance functions. (A): The force–distance function is the sum of the cubic force function shown in Fig. 7.2 plus the linear functions $-k_1 \cdot x$ for subsystem I in the region $0 \leq x \leq 0.2$ and $-k_{II} \cdot (1 - x_1)$ for subsystem II in the region $0.8 \leq x \leq 1$. In the figure $Q_1 = Q_{II} = 290$ pN and $k_1 = k_{II} = 70$ pN/24 nm in equations (7.17). For further details, see the legend to Fig. 7.2. (B): The ordinate is the integral of the force–distance function. Since x is dimensionless, the units of energy in this diagram are pN. The solid line is the energy diagram for the cubic force–distance function, with $Q_1 = Q_{II} = 250$ pN in equation (7.2). The upper dotted line is the energy diagram for the modified force–distance function of Fig. 7.9A. The lower dotted line differs from the upper one only in that a passive link with $K_c = 60$ pN/24 nm is also present in the first segment, leading to self-oscillatory behaviour. From Murase *et al.* (1989). Reprinted with permission.

Base-to-tip bend propagation. Three major modifications are necessary in demonstrating base-to-tip propagating waves along an axoneme. First, a self-oscillatory segment is placed immediately distal to the passive region at the basal end. This self-oscillatory segment acts as a pacemaker. Second, a passive terminal region is included at the tip without any dyneins. The passive region prevents bends from initiating at the tip. In fact, sea urchin sperm flagella of approximately $42 \mu\text{m}$ length have terminal regions of $5\text{--}8 \mu\text{m}$ (see Rikmenspoel, 1982). Third, the stability of the resting state is increased in order to reduce viscosity-induced perturbations. This can be achieved by increasing the force constant in the neighbourhood of the resting position at x_1 , as shown in Figure 7.9A. The modified force–distance functions are written as follows:

$$F_I(x) = \begin{cases} Q_I(x - x_1)(x - x_2)(x_c - x) - k_I(x - x_1) & 0 < x \leq S_1 \\ Q_I(x - x_1)(x - x_2)(x_c - x) & S_1 < x < 1 \end{cases} \quad (7.17a)$$

$$F_{II}(x) = \begin{cases} Q_{II}(x - x'_1)(x - x'_2)(x'_c - x) & 0 < x < S_2 \\ Q_{II}(x - x'_1)(x - x'_2)(x'_c - x) - k_{II}(x - x_1) & S_2 \leq x < 1 \end{cases}. \quad (7.17b)$$

The energy diagrams corresponding to the modified force–distance function and the original cubic force–distance function are shown in Figure 7.9B.

Figure 7.10 illustrates the result obtained when the above modifications are incorporated into the model under clamped boundary conditions. The viscosity-induced perturbations are remarkably reduced so that base-to-tip propagating waves occur successfully in the axoneme. The size of the passive terminal region at the tip seems to be a key factor in determining the direction of the bend propagation.

Since two different boundary conditions are adopted at the base and tip (i.e. the clamped basal end and free distal end), it is difficult to study the effects of the structural asymmetry inherent in the axoneme. For this reason, the next section deals with free-end boundary conditions at both ends.

7.4.3 Bend propagation with free-end boundary conditions

Bend initiation and propagation are studied under conditions where both basal and distal ends are free (see Table 7.1), and filaments are sliding freely at the base (see Table 7.2). First, we study the effects of the axonemal structure on the spatio-temporal patterns of sliding occurring within the axoneme. Then, the viscosity-induced perturbations are examined deeply, and finally the role of the curvature-control mechanism adopted in the previous models (see Table 6.1) is discussed.

Base-to-tip bend propagation. We are interested in the spatio-temporal sliding patterns, but not the exact shapes of the flagellum, so that the positions of waves are depicted as a function of time and space in Figure 7.11. This representation is comparable to that in Fig. 7.5. The model has three regions along the length of the axoneme: (i) the self-oscillatory region at $s = 1 \mu\text{m}$; (ii) the excitable region for $1 < s < 40 \mu\text{m}$; and (iii) the passive region for $40 \leq s \leq 50 \mu\text{m}$. For self-organization of bending waves, the model is started from a straight configuration at $t = 0$ by turning on subsystem I throughout the axoneme. Once a bend initiates at the basal end, it propagates towards the tip. The passive region at the tip ensures that bends do not initiate at the tip.

The patterns in Figure 7.11 are slightly different from those in Figure 7.5 in the following ways. First, the velocity of bend propagation would fluctuate as the slope of successive bars is not constant. There is some experimental evidence that the bend propagation velocity in the basal and distal regions is

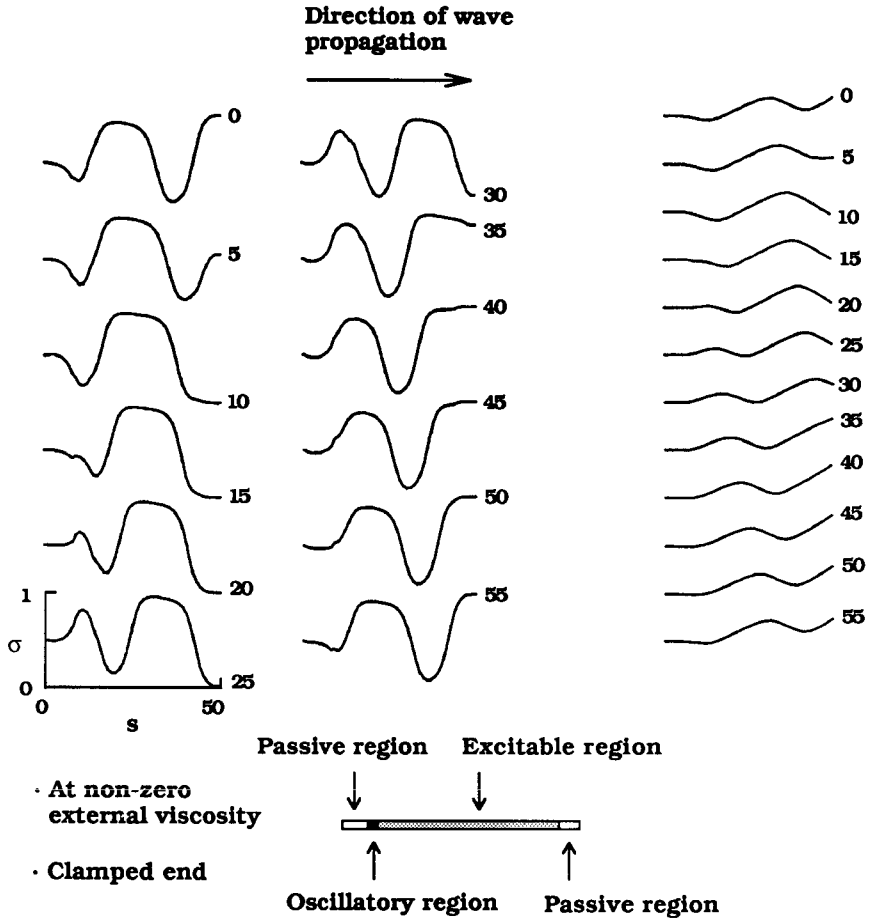


Figure 7.10 Base-to-tip bend propagation under clamped-end boundary conditions for the modified cubic force–distance function shown in Figure 7.9A. The parameters are: $E_B = 350 \text{ pN } \mu\text{m}^2$, $C_N = 5 \text{ pN ms}/\mu\text{m}^2$. The properties of the axoneme vary along its length as follows: $Q_I = Q_{II} = 0$, $K_e = 60 \text{ pN}/24 \text{ nm}$ for $0 < s < 8 \text{ } \mu\text{m}$; $Q_I = Q_{II} = 350 \text{ pN}$, $K_e = 60 \text{ pN}/24 \text{ nm}$ at $s = 8 \text{ } \mu\text{m}$; $Q_I = Q_{II} = 290 \text{ pN}$, $K_e = 1 \text{ pN}/24 \text{ nm}$ for $8 < s < 45 \text{ } \mu\text{m}$; and $Q_I = Q_{II} = 0$, $K_e = 1 \text{ pN}/24 \text{ nm}$ for $45 \leq s < 50 \text{ } \mu\text{m}$. The schematic representation of this axoneme is shown in the bottom panel.

lower than the velocity in the mid-region of the flagellum. This refers to non-uniform bend propagation (Brokaw, 1970). Our results may be relevant to this experimental observation. Second, the wavelength would fluctuate as the width of the bars along the s -axis is not constant. Third, the beat frequency would fluctuate as the ‘black–white’ interval along the t -axis is not constant.

These three characteristics are not obvious as long as we take only a small number of snapshots of flagellar shape at different instants. Furthermore, the

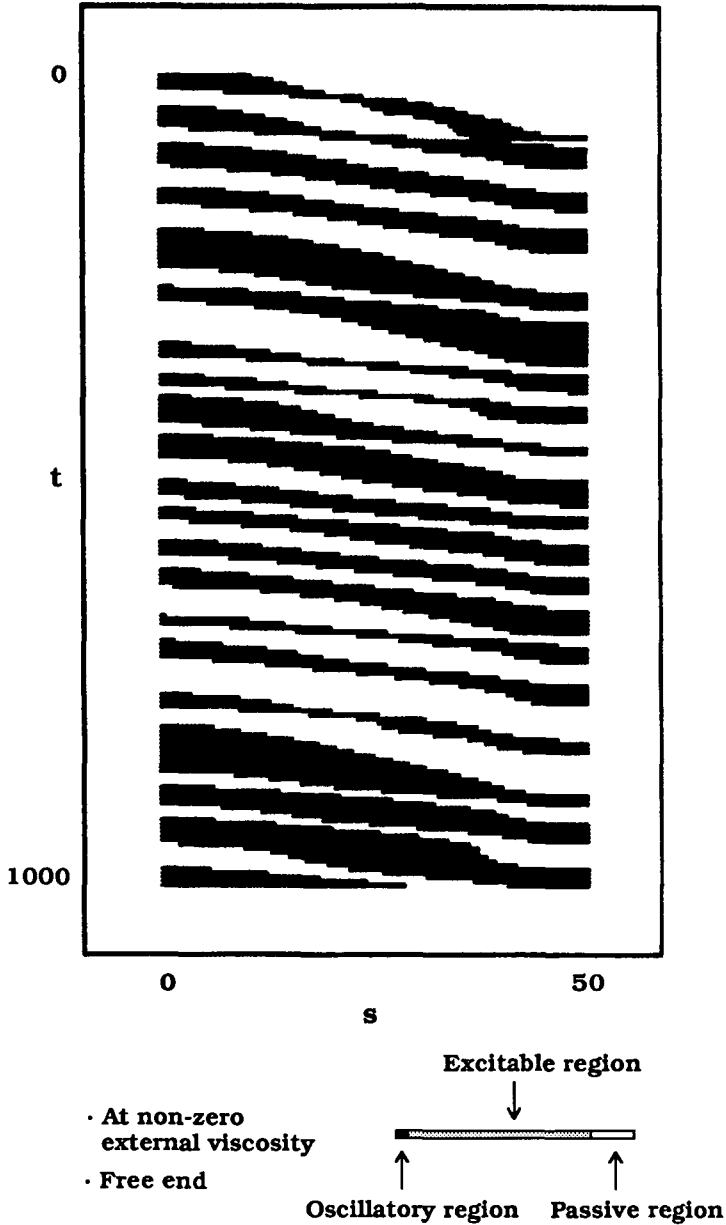


Figure 7.11 Base-to-tip bend propagation under free-end boundary conditions for modified cubic force–distance function shown in Figure 7.9A. Positions of waves are depicted as a function of time, t (in ms), and space, s (in μm). The regions $\sigma > 0.5$ are plotted by bars. The parameters are: $E_b = 400 \text{ pN } \mu\text{m}^2$, $C_N = 5 \text{ pN ms}/\mu\text{m}^2$. The properties of the axoneme vary along its length as follows: $Q_I = Q_{II} = 290 \text{ pN}$, $K_e = 60 \text{ pN}/24 \text{ nm}$ at $s = 1 \mu\text{m}$; $Q_I = Q_{II} = 290 \text{ pN}$, $K_e = 1 \text{ pN}/24 \text{ nm}$ for $1 < s < 40 \mu\text{m}$; and $Q_I = Q_{II} = 0 \text{ pN}$, $K_e = 1 \text{ pN}/24 \text{ nm}$ for $40 < s < 50 \mu\text{m}$. As time proceeds, the groups of bars move toward the right, which reflects that bending waves initiated at the base (at the left end) propagate toward the tip (the right end). The schematic representation of this axoneme is shown in the bottom panel.

flagellar shapes are obtained by an integral form (see legend to Fig. 7.4), so that if there are spatial fluctuations on the sliding patterns they smooth away when they are transformed into the shapes (see Fig. 4 of Murase *et al.*, 1989). For these reasons the above characteristics have not been discussed deeply.

Although experimental data corresponding to Figure 7.11 shows irregularity, it is ascribed to the nature of random noise (Brokaw, 1970). However, the present study suggests that these fluctuations arise in a deterministic mathematical model. It seems that they are not caused by random noise nor numerical errors, but are inherent in the system under the influence of external viscosity (cf. Sivashinsky and Michelson, 1980). Indeed, the curvature-controlled models also displayed non-uniform bend propagation (see Fig. 6 of Brokaw, 1972). There is the possibility that the model displays 'chaotic behaviour' (see Section 7.4.5).

Reversal of the direction of propagating waves. It is of interest to know what happens in the absence of the passive region at the tip. With the same parameters as those in Figure 7.11, except for the exclusion of the passive region, the model is started from a straight configuration at $t = 0$. Figure 7.12 shows that bend propagation occurs first from base to tip and then the direction is reversed at the first arrow (about $t = 300$ ms). These tip-to-base propagating waves are further replaced by the base-to-tip propagating waves at the second arrow (about $t = 600$ ms). This kind of reversal of bend propagation occurs at ~ 300 – 400 ms intervals as long as the computer simulation persists.

The frequency of this reversal depends on two factors: (i) the size of the passive region; and (ii) the stiffness of the elastic component at the base. On one hand, the passive region acts as 'buffer' which absorbs viscosity-induced perturbations. For example, the model with a passive region $5 \mu\text{m}$ long shows shorter duration of the reversal than the model without the passive region. As the length of the passive region is increased, the possibility for the reversal of bend propagation decreases markedly. A $10 \mu\text{m}$ passive region is sufficient to ensure unidirectional bend propagation (see Fig. 7.11). On the other hand, the stiffness of the basal elastic component determines the characteristic frequency of the self-oscillation, so that the basal region affects the duration of the reversal.

Suppose we have a 'homogeneous' axoneme without the passive or the self-oscillatory region, but with excitability throughout the length of the axoneme. This model is obtained when the stiffness at the basal segment is reduced from $K_c = 60$ to $1 \text{ pN}/24 \text{ nm}$. Of course this 'homogeneous' excitable axoneme cannot develop bending waves without superthreshold perturbations if the axoneme is initially straight. Once the axoneme was slightly deformed, however, bending waves were developed (cf. Fig. 7.15B). Under these conditions the model showed the reversal of propagating waves at about 1200 ms intervals.

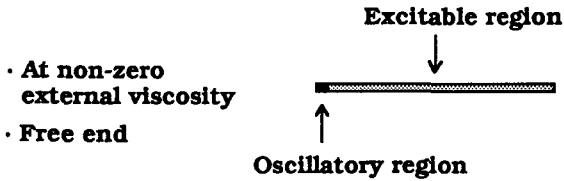
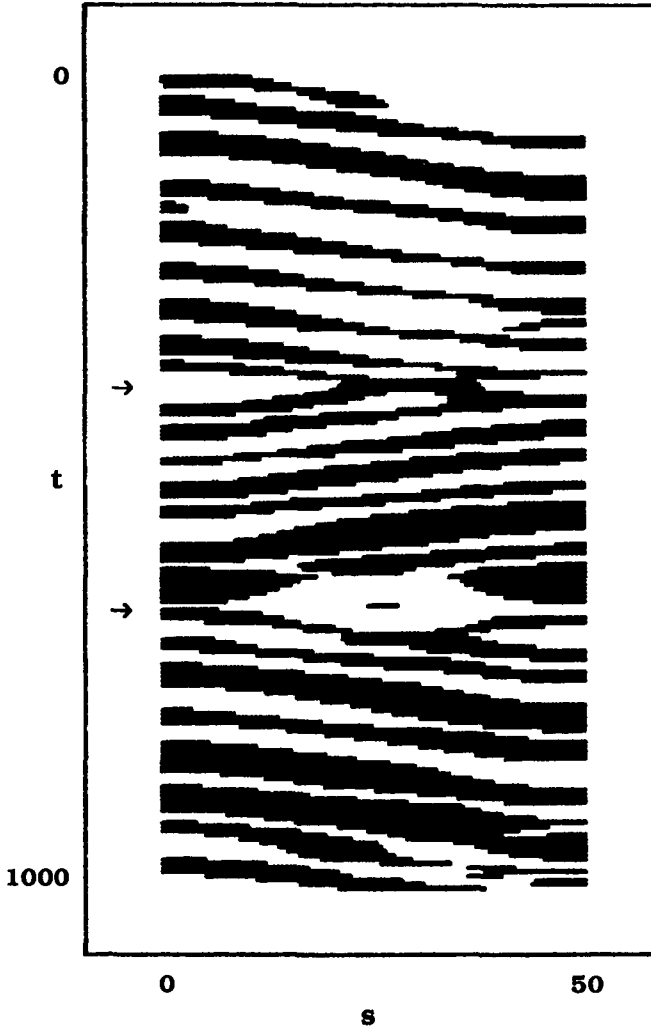


Figure 7.12 Reversal of the direction of propagating waves under free-end boundary conditions for modified cubic force–distance function shown in Figure 7.9A. Positions of waves are depicted as a function of time, t (in ms), and space, s (in μm). The regions $\sigma > 0.5$ are plotted by bars. The parameters are the same as those in Figure 7.11 except for the exclusion of the passive region. As time proceeds, first base-to-tip bend propagation occurs and then tip-to-base bend propagation appears at about $t = 300$ ms. At about $t = 600$ ms base-to-tip bend propagation occurs. The schematic representation of this axoneme is shown in the bottom panel.

These simulations suggest that the axonemal structure is highly responsible for the dynamical behaviour. Boundary conditions seem to be of secondary importance. Indeed there was an interesting observation by Brokaw (1965), in which removal of the normal distal end of the flagellum interfered with its ability to generate base-to-tip propagating waves. Omoto and Brokaw (1982) also observed a clear 'end effect', which involves a rapid unbending of bends that have reached the distal end of the flagellum lacking a 'terminal' region.

As described in Section 4.5.5, flagella of trypanosomatids show an unusual ability to propagate bending waves from either the base or the tip. Sea-urchin sperm flagella of *Tripneustes gratilla* show intermittent swimming that involves stopping and starting transients. From the above simulations it is possible to interpret these observations in terms of the structural asymmetry along the axoneme, such as the size of the passive region at the tip. A detailed comparison between model behaviours and experimental observations will provide insights into the role of a passive region at the tip of the axoneme.

7.4.4 Interaction of two waves propagating in opposite directions

As discussed in Section 4.5.5, there are interesting observations that record two waves travelling in opposite directions along the flagellum under abnormal conditions where the viscosity of the medium is increased (Holwill, 1965) or when some chemical agent is added (Alexander and Burns, 1983). When two such waves meet they appear to be frozen, but do not annihilate each other. These observations raise a problem concerning the interaction between the two waves. From a theoretical modelling point of view, however, no attempts have been made to solve this problem. It is, therefore, important to know whether or not two waves moving in opposite directions annihilate each other.

Simulations were carried out under two different situations: (i) with only internal viscosity; and (ii) with only external viscosity. The model was allowed to develop two bends propagating in opposite directions by applying stimuli at both ends. If there is only internal viscosity, two oppositely directed bends annihilate each other upon collision (Fig. 7.13). Each bend has a leading edge and a trailing edge. In the leading edge of each bend, subsystem I is turned 'on' and subsystem II is turned 'off', while in the trailing edge the reverse holds. The waves move in accordance with the operation of these 'on-off' switches. This switching operation continuously propagates, so that the system is completely reset after the bend passes through. As a result, the two waves seem to annihilate, leaving the system at rest. This phenomenon is analogous to the annihilation of action potentials in nerve systems (Tasaki, 1949; Matsumoto, et al., 1982) and chemical waves such as the Belousov-Zhabotinsky reaction (Kuramoto and Yamada, 1976; see also books by Winfree, 1980, 1987; Zykov, 1987; and Glass and Mackey, 1988).

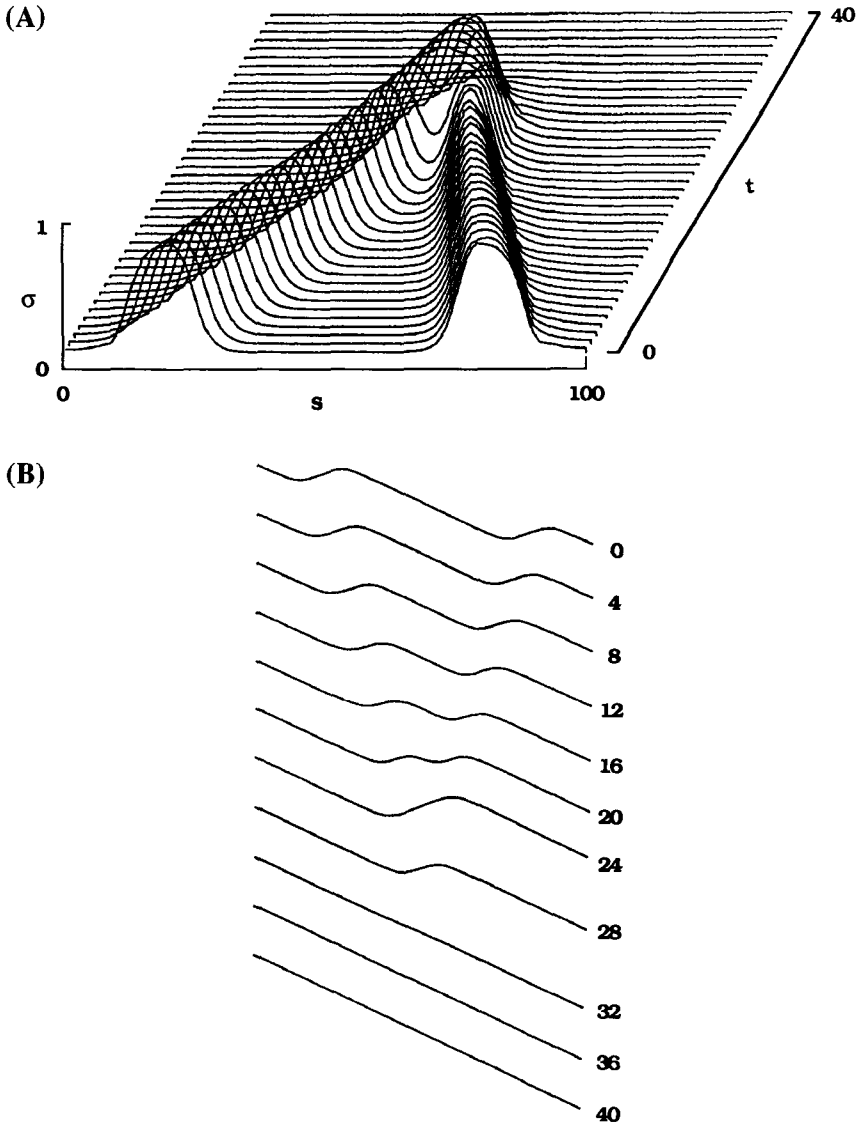


Figure 7.13 Annihilation of two waves propagating in opposite directions at zero external viscosity under free-end boundary conditions. The cubic force–distance function in Fig. 7.2 is used with the same parameters, except for $Q_I = Q_{II} = 290$ pN. Other parameters are: $E_B = 300$ pN μm^2 , $L = 100$ μm , $C_N = 0$, $\gamma = 100$ pN ms/24 nm, and $K_c = 1$ pN/24 nm. (A): σ is plotted as a function of space, s , at 1 ms intervals. Time proceeds from front to back. (B): Successive changes in the shape of the flagellum at 4 ms intervals.

If there is external viscosity, instead of internal viscosity, the waves appear to pass through one another (Fig. 7.14). The waves move slowly because only a small region at the trailing edge of each bend contributes to active sliding. The active region is small because viscous forces oppose the force required to reach the switching point. Thus both peak height and width in the σ - s curves become smaller as the waves approach one another, as indicated by less smoothness in Figure 7.14A. As the waves approach sufficiently close, the bends appear to merge, and switching occurs in many segments in the region of the collision. Since the resting state is not stable enough in these segments, sliding in the opposite direction, caused by subsystem II, occurs. After the collision, the number of segments contributing to active sliding is four times larger than before the collision, so wave speed is about fourfold faster.

Non-annihilating waves appear because the operation of ‘on-off’ switches is not continuously propagated but sometimes skips several segments due to viscosity-induced perturbations. As a result, the system never returns to the resting state, but instead some segments are spontaneously activating. By using the two-component reaction-diffusion model, Tuckwell (1980) found solitary wave solutions with soliton-like properties when ‘on-off’ switches were introduced into the model. Because the system ‘sees’ the new source functions during the collision of two solitary waves due to a number of ‘on-off’ switches, it is possible that solitary waves emerge from the collision (see Fig. 1.17).

Tuckwell (1980) also found that with slightly asymmetric initial data, when two waves collided, one wave more or less destroyed the other and continued to propagate after the collision. Similar phenomena appeared in the present model behaviour when the direction of bend propagation was reversed. As already shown in Figure 7.12, the axoneme happened to initiate the tip-to-base propagating wave. This destroyed the base-to-tip propagating wave since the two waves are slightly different in shape.

In the simulation shown in Figure 7.14, the cubic force-distance function was used. When the same simulation was performed but using the modified force-distance function of Figure 7.9, the two waves merged to form one bend similar to that shown at $t = 64$ ms in Figure 7.9B. However, because the resting state is more stable for this system, the waves do not continue on but instead the merged region slowly increases in width until the flagellum becomes straight. If external viscosity is high enough as examined by Holwill (1965), the merged region appears to be frozen.

7.4.5 External viscosity-induced perturbations

To understand the dynamical aspects of external viscosity-induced perturbations, the model is started from the same initial conditions with only internal viscosity (Fig. 7.15A) or only external viscosity (Fig. 7.15B). If there is only

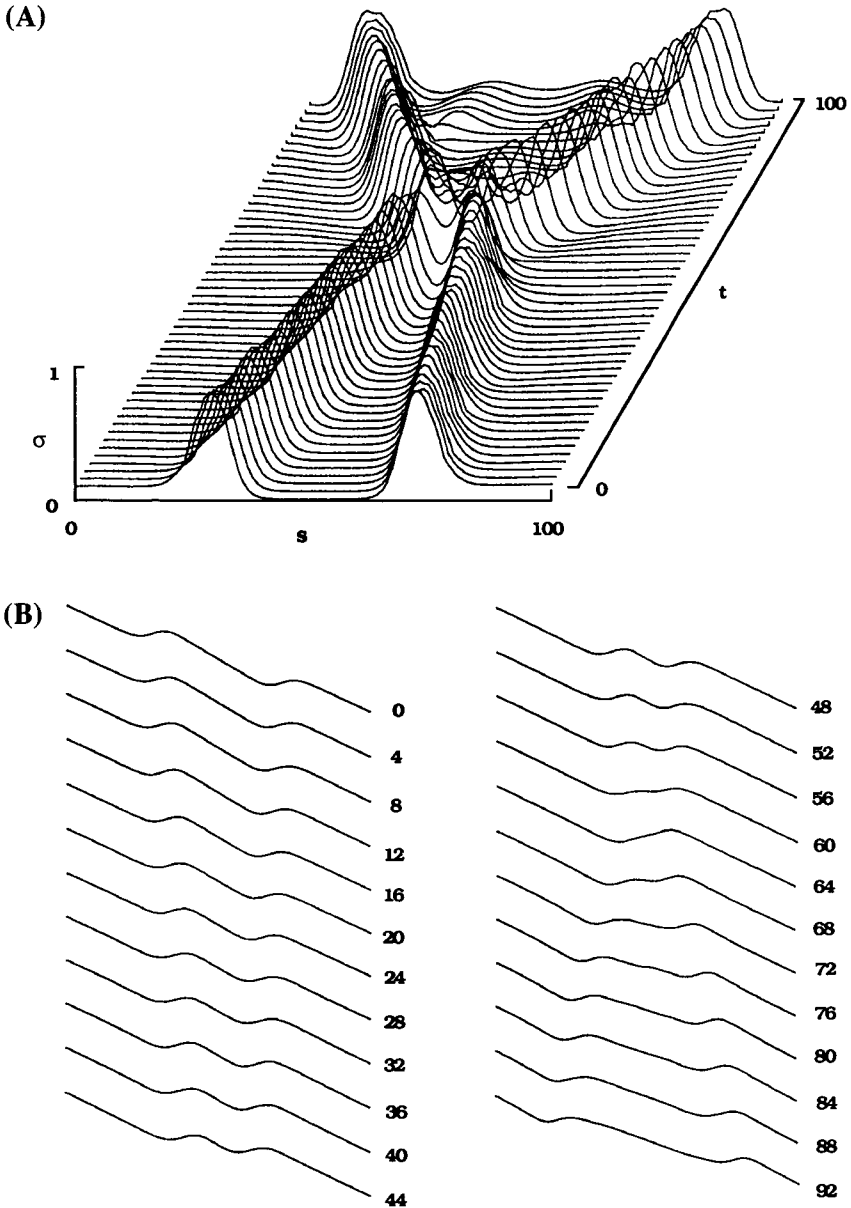


Figure 7.14 Soliton-like behaviour at non-zero external viscosity under free-end boundary conditions. The cubic force–distance function in Fig. 7.2 is used with the same parameters, except for $Q_{\text{I}} = Q_{\text{II}} = 400$ pN. Other parameters are: $E_{\text{B}} = 400$ pN μm^2 , $L = 100$ μm , $C_{\text{N}} = 5$ pN ms/ μm^2 , $\gamma = 0$, and $K_{\text{e}} = 1$ pN/24 nm. (A): σ is plotted as a function of space, s , at 2 ms intervals. Time proceeds from front to back. (B): Successive changes in the shape of the flagellum at 4 ms intervals.

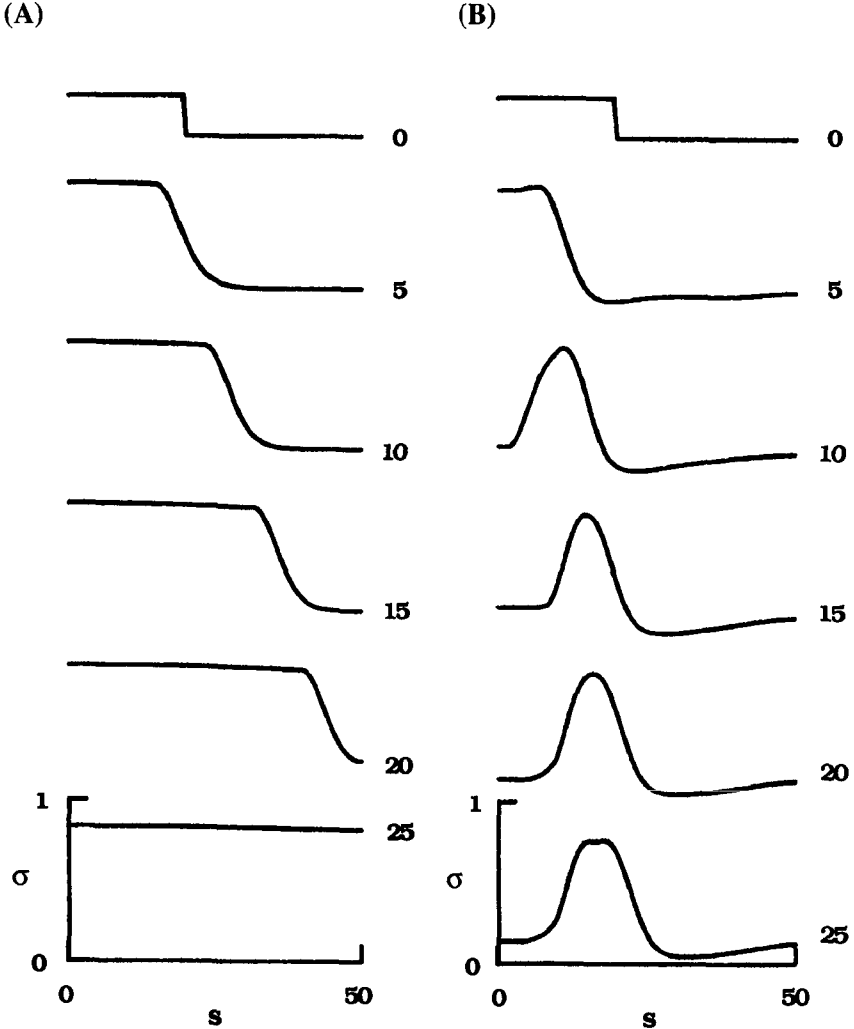


Figure 7.15 Dynamical behaviour of a ‘homogeneous’ excitable axoneme under free-end boundary conditions. σ is plotted as a function of space, s , at 5 ms intervals. The axoneme has only excitable segments, i.e. $K_c = 1 \text{ pN}/24 \text{ nm}$, $Q_I = Q_{II} = 250 \text{ pN}$ and $E_B = 400 \text{ pN } \mu\text{m}^2$ for $0 < s < 50 \text{ } \mu\text{m}$. The cubic force–distance function in Fig. 7.2 is used with the same parameter values. The model is started from the same initial conditions. (A): There is only internal viscosity, i.e. $\gamma = 100 \text{ pN ms}/24 \text{ nm}$ and $C_N = 0$. The flagellum becomes ‘quiescent’ when the bend propagates to the tip. (B): There is only external viscosity, i.e. $\gamma = 0$ and $C_N = 5 \text{ pN ms}/\mu\text{m}^2$. Due to external viscosity-induced perturbations the basal end beats up and down, which leads to continuous bend initiation.

internal viscosity, the axoneme becomes quiescent when the bend reaches the tip. On the contrary, if there is only external viscosity, viscosity-induced perturbations strongly influence the basal end to move up and down. Since this rhythmic motion continues for ever, the axoneme never returns to the resting state.

For the purpose of the following discussion, we shall consider more general equations instead of equation (7.9a):

$$\frac{\partial^2(S - \gamma\sigma)}{\partial s^2} + E_B \frac{\partial^4\sigma}{\partial s^4} + C_N \frac{\partial\sigma}{\partial t} = 0. \quad (7.18)$$

The ratio between γ and C_N plays an important role in determining the dynamical behaviour of the model described by equation (7.18). If $\gamma \gg C_N$ the term $-\gamma\sigma$ stabilizes the solution, and hence the dynamical behaviour is similar to that obtained by equation (7.4a). If $\gamma \ll C_N$ the behaviour is analogous to that generated by equation (7.9a).

The fourth-order partial differential equations of this kind appear in various ways (see Section 1.2.3). The general form of these equations is:

$$\frac{\partial\phi}{\partial t} = A \frac{\partial^2\phi}{\partial s^2} - B \frac{\partial^4\phi}{\partial s^4} + F(\phi) \quad (7.19)$$

where ϕ is a state variable defined at space, s , and time, t ; A and B are constants, and $F(\phi)$ is some nonlinear function. This type of equation is sometimes called the *generalized reaction-diffusion* equation (Cohen and Murray, 1981; Lara Ochoa, 1984; Murray, 1989), but also named the *Kuramoto-Sivashinsky* equation (Sivashinsky, 1977, 1979; 1980; Michelson and Sivashinsky, 1977; Sivashinsky and Michelson, 1980; Kuramoto, 1984; Hyman and Nicolaenko, 1986). Similar equations are also proposed in quite different contexts (Pumir *et al.*, 1983; Hooper and Grimshaw, 1985; Chang, 1986; Chen and Chang, 1986; Thompson and Virgin, 1988). The second order term in equation (7.19) corresponds to the diffusion process. When $A > 0$ spatial perturbations are stabilized (*normal diffusion*), though when $A < 0$ they are destabilized (*negative diffusion*).

It is instructive to consider that the internal shear force, S , is proportional to the shear, σ , as a linearized form of the cubic force-distance function in equation (7.2), or as a limit of zero time-delay in equation (5.88). Then, equation (7.18) is analogous to equation (7.19) when $\gamma = 0$. This situation corresponds to negative diffusion, leading to instability. Indeed, Brokaw (1972b, 1975) pointed out that the presence of internal viscosity (i.e. $\gamma > 0$) can stabilize the wavelength. The stable wavelength arises because the situation $\gamma > 0$ amounts to the normal diffusion, and hence stabilization.

Now consider the effects of curvature control on solutions to equation (7.9a). There are only even powers of the space derivatives, so that symmetry holds with respect to space, s . (Both the equation and boundary conditions are invariant under the spatial inversion $s \rightarrow -s$.) As a result, base-to-tip and tip-to-base waves are potentially equivalent (see Fig. 5.19). One way

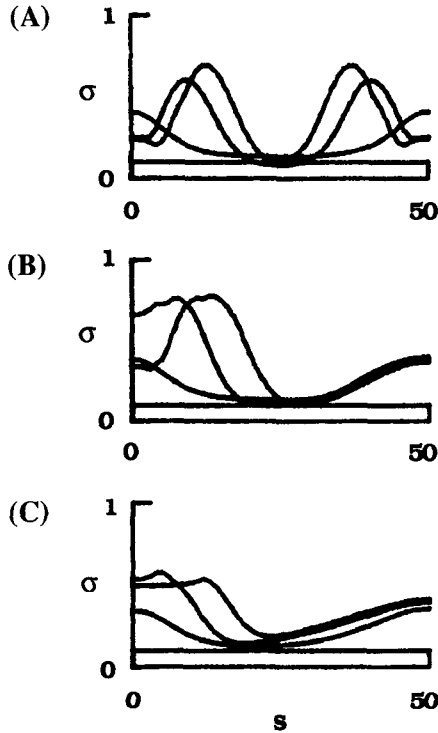


Figure 7.16 Dynamical behaviour of the self-oscillatory axoneme under free-end boundary conditions. σ is plotted as a function of space, s , at 20 ms intervals. The axoneme has only self-oscillatory segments, i.e. $K_e = 60$ pN/24 nm, $Q_I = Q_{II} = 250$ pN and $E_B = 400$ pN μm^2 for $0 < s < 50$ μm . The cubic force–distance function in Fig. 7.2 is used with the same parameter values. The model is started from the same straight configuration. (A): The ‘homogeneous’ self-oscillatory axoneme is allowed to develop bending waves. (B): The self-oscillatory axoneme with a 10 μm -long passive region at the tip. Unidirectional bend propagation results from this asymmetric structure. (C): The ‘homogeneous’ self-oscillatory axoneme under the influence of the curvature-control mechanism, in which $Q_I = 0$ for $\kappa > 0$ and $Q_{II} = 0$ for $\kappa < 0$. Unidirectional bend propagation is caused by the feedback function which is asymmetric about $\kappa = 0$.

by which unidirectional propagated waves are obtained is to introduce the curvature feedback control. The curvature of the axoneme can only be defined when two separate positions are specified (or mathematically, the curvature, κ , is defined as a space derivative of shear: $\kappa = \partial\sigma/\partial s$). This automatically induces the spatial coordination in violation of the $s \rightarrow -s$ symmetry because of the first space derivative, $\partial\sigma/\partial s$, which is necessary in maintaining bend propagation in one direction (see Fig. 5.18). An alternative way of demonstrating unidirectional bend propagation is to take into account the structural asymmetry such as the basal elastic component and the passive terminal piece.

As a concrete example, let us consider an axoneme with self-oscillatory behaviour. By adopting $K_c = 60 \text{ pN/24 nm}$ and the cubic force-distance function for $0 < s < 50 \mu\text{m}$, we can obtain a model with 'homogeneously' distributed self-oscillatory segments. Simulations were carried out from straight-line initial conditions in the following three cases. When the axoneme is 'homogeneous' two waves initiate at both ends and propagate in opposite directions (Fig. 7.16A). If the distal $10 \mu\text{m}$ of the axoneme was replaced by the passive region without active force-generating systems, then unidirectional bend propagation can occur (Fig. 7.16B). If the curvature-control mechanisms are introduced such that subsystem I is turned 'off' when $\kappa > 0$ and turned 'on' when $\kappa < 0$, unidirectional bend propagation can also occur (Fig. 7.16C).

By incorporating the curvature feedback control into theoretical models, unidirectional bend propagation has been demonstrated. Although these models successfully generate bend propagation from base to tip, important and interesting aspects have been missed. In the absence of the curvature-control mechanism, models lose their ability to propagate bending waves in one direction. The failure of unidirectional bend propagation is not a 'defect' of the models, but a 'merit' inherent in the system suspended in the viscous medium (cf. Sivashinsky and Michelson, 1980). There is the possibility that such a system shows a wide variety of spatio-temporal behaviours. Complex dynamical behaviour of this kind is one of the most interesting topics in modern physics, biology and chemistry, (see books by Manneville *et al.*, 1989; Jen, 1990; Serra and Zanarini, 1990; Weisbuch, 1991; see also Murase and Matsuo, 1991).

Notes

- 1 It is possible to introduce a time delay between the turning 'off' of subsystem I and the turning 'on' of subsystem II. In this case, $n_I + n_{II} \neq 1$, so that the time delay explicitly defines the refractory period.
- 2 The 24 nm interval of attachment sites (corresponding to a stroke distance of a dynein) is taken as unity for convenience. The sliding coordinate x is then defined as a distance between a dynein and an attachment site within the unity (i.e. $0 < x < 1$).
- 3 In Chapters 7 and 8 only a single unit of sliding is allowed ($0 < \sigma < 1$). Although this limits the model to simulation of the small-amplitude oscillations, equation (7.3b) holds and hence the model is easy to analyse. Chapter 9 deals with an extension of the present model for the large-amplitude oscillations. In this case, equation (7.3b) must be replaced by $x = \text{mod}(\sigma, 1)$.
- 4 Provided that only a single unit of sliding is allowed (i.e. $0 < x < 1$), the dimensionless sliding coordinate, x , and the shear angle, σ , are related by the proportionality constant $h/24 \text{ nm}$, where h is the interval between adjacent microtubules in the plane of bending and 24 nm is the interval between adjacent attachment sites (Hines and Blum, 1979). For convenience, $h = 24 \text{ nm}$ is assumed and then $\sigma = x$.

8 Simplified models for ciliary dynamics

In this chapter the excitable dynein model developed for flagellar movement is modified to display ciliary-like beating patterns. To generate asymmetric beating patterns typical of cilia, two types of asymmetries are introduced to the dynein force-generating system: (i) a *circumference asymmetry* between the two opposed dyneins; and (ii) a *longitudinal asymmetry* along the axoneme. Besides the above asymmetries concerning dyneins, a *structural asymmetry* is further incorporated into the model reflecting the basal structure and passive region at the tip.

In Section 8.1 we summarize the theoretical and experimental studies. In Section 8.2 we develop an isolated-segment model which involves two opposed dyneins with circumference asymmetry. This segment model serves as a functional unit of an intact ciliary system. In response to externally imposed stimuli the unit exhibits three types of dynamical behaviours: (i) an *oscillatory* type with rhythmic activity; (ii) a *quiescent* type, i.e. cessation of rhythmic activity; and (iii) an *excitable* type, in which superthreshold stimuli trigger a single active response. The responsiveness of this unit to a stimulus depends not only on its direction (*directional sensitivity*), but also on its timing (*refractoriness*). The term *mechano-sensitivity* is used to describe this kind of responsiveness.

Keeping the longitudinal and structural asymmetry along a cilium in mind, many such units are arranged *one-dimensionally* to form a ciliary system in Section 8.3. Like bend propagation in the flagellar system, the activity of dyneins is coordinated via functional interactions so that a bending wave propagates along the cilium. Of particular interest is the functional hierarchy in ciliary dynamics, which is discussed in Section 8.4. Depending on parameter values, the ciliary system also displays three types of behaviours: (i) an *oscillatory* type, which refers to an intrinsic repetitive activity with alternate effective and recovery strokes; (ii) a *quiescent* type, which refers to a resting state at the end of the effective or recovery stroke; and (iii) an *excitable* type, which refers to the *mechano-sensitivity* of a quiescent cilium to external stimuli leading to a single beat-cycle.

In order to emphasize the functional hierarchy mentioned above, let us consider a 'field' over which many cilia are arranged (Fig. 8.1). The activity of cilia will be coordinated via hydrodynamic interactions so that a wave of ciliary activity (known as the *metachronal wave*) passes over the 'field'. We now know that there are two waves at different levels: (i) a bending wave that propagates along a cilium; and (ii) a metachronal wave that propagates over a ciliated 'field'. Both wave phenomena seem to be based on similar excitable/oscillatory units with mechano-sensitivity (i.e. units as excitable dyneins for bending waves and as individual cilia for metachronal waves). This suggests that a universal principle can be applied to different wave phenomena.

8.1 Introduction

For a ciliary cycle to have an alternate effective and recovery stroke, there must be some asymmetry between the two opposite sides of the axoneme. Rikmenspoel and Rudd (1973) assumed two different types of active moments – *standing* and *travelling* moments. Sugino and Naitoh (1982) estimated two different sliding patterns (see Section 5.3.5). Their estimated patterns suggest that dynein activity is initiated at the base of a doublet and propagates toward the tip (see Fig. 5.29). Averaging this active region in doublets on each half of the axoneme, one finds that the active region on one half is distributed almost over the whole length of the axoneme during most of the effective stroke, whereas the active region on the other half propagates gradually to the tip during the recovery stroke. The two different sliding patterns have been termed *synchronous* and *metachronous* sliding (Sleigh and Barlow, 1982; Brokaw, 1989).

Although different cilia and flagella show different types of dynamical behaviour (see Chapter 4), it is possible that the same axoneme also exhibits a wide variety of beating patterns under different conditions. It is now accepted that intraciliary Ca^{2+} ions play an important role in controlling physiological parameters such as the beat pattern (Naitoh and Kaneko, 1972; 1973), activity (Satir, 1975; Gibbons and Gibbons, 1980a; Stommel, 1986) and direction of the bend propagation (Holwill and McGregor, 1975; 1976).

Naitoh and Kaneko (1972; 1973) observed that detergent-treated *Paramecium* are able to swim forward at low Ca^{2+} concentrations ($< 10^{-6}$ M Ca^{2+}) and backward at high Ca^{2+} concentrations ($> 10^{-6}$ M Ca^{2+}) because of *ciliary reversal* (Fig. 8.2A). Lateral cilia of mussel gill (Fig. 8.2B) are quiescent (Satir, 1975; Stommel, 1986) as Ca^{2+} concentration increases above 10^{-6} M, although they beat continuously below this concentration. The resultant quiescent cilia show strong mechano-sensitivity, in which mechanical displacement of quiescent cilia with a microneedle induces one or more normal beat-cycles

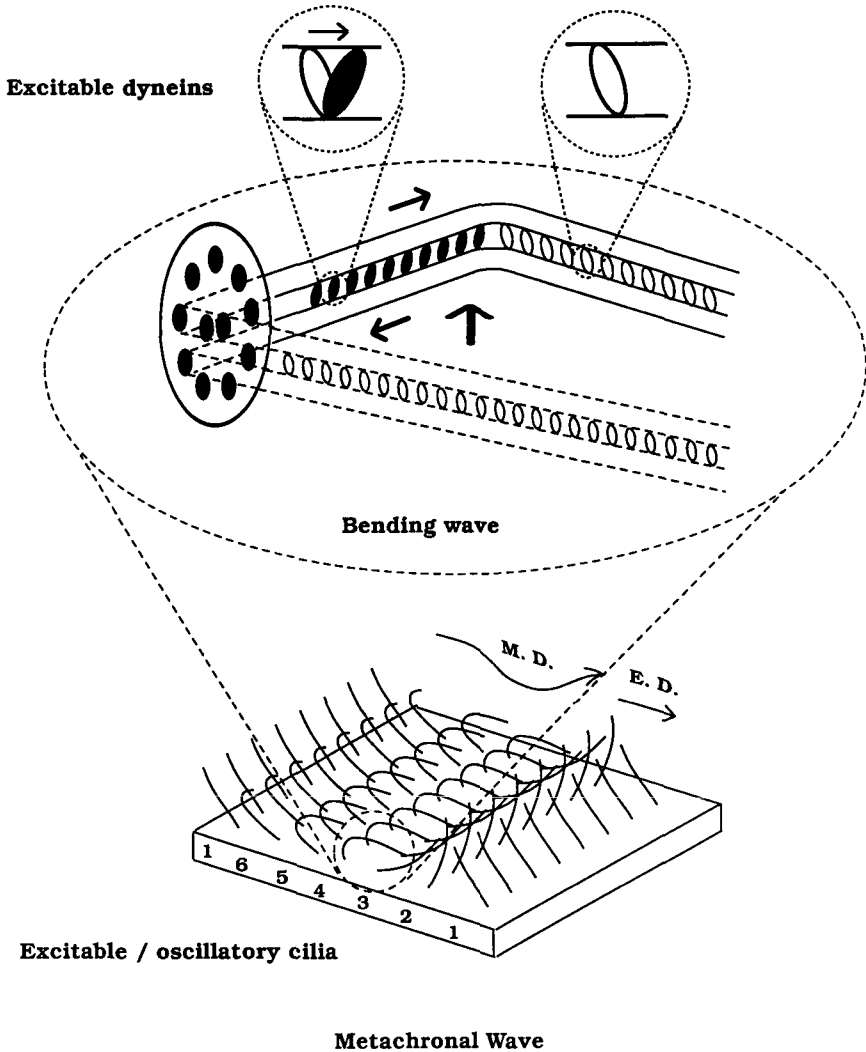


Figure 8.1 Two waves at different levels. The upper panel: Dynein cross-bridges are arranged along each doublet in the axoneme. Dark and white circles indicate active and preactive dynein cross-bridges. The coordination in time and space of the activity of 'excitable' dyneins gives rise to bending-wave propagation at the level of a cilium. The lower panel: Cilia are arranged in rows across and along the 'field'. In one direction, cilia beat *synchronously*; while in another direction they beat *metachronously*. Thus the coordination in time and space of the activity of individual 'excitable/oscillatory' cilia leads to metachronal wave propagation over a dense mat of cilia. M.D. and E.D. represent the directions of the metachronal wave and the effective stroke, respectively. A full cycle is conveniently divided into 6 stages to which the numbers 1, 2, ..., and 6 are assigned. From Murase (1990). Reprinted with permission.

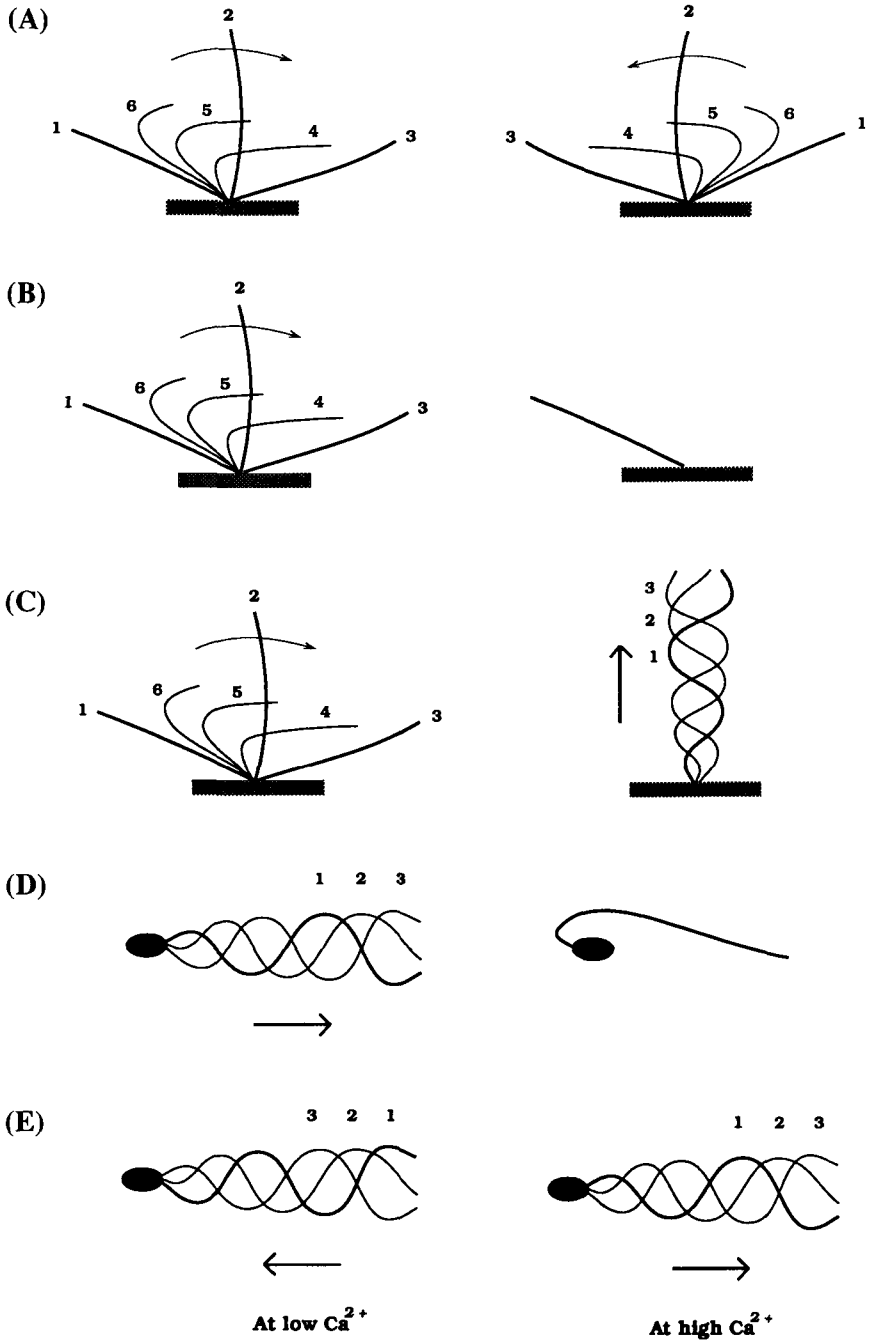


Figure 8.2 Ca^{2+} -induced behavioural changes in cilia and flagella. For each panel, the situation at low Ca^{2+} concentrations is on the left; the high case is on the right, with several different stages of a beat cycle numbered. (A): *Paramecium*. (B): *Mytilus* gill. (C): *Chlamydomonas*. (D): Sea-urchin sperm. (E) *Crithidia*.

(Stommel, 1986). Isolated axonemes of *Chlamydomonas* flagella (Fig. 8.2C) beat asymmetrically at low Ca^{2+} concentrations ($< 10^{-7}$ M Ca^{2+}), whereas they beat symmetrically at high Ca^{2+} concentrations ($> 10^{-6}$ M Ca^{2+}). Between the two dynamical states, there is a range of Ca^{2+} concentrations where the isolated axonemes are quiescent (Bessen *et al.*, 1980). Sea-urchin sperm flagella, normally beating, becomes quiescent at high Ca^{2+} concentrations (Fig. 8.2D; Gibbons and Gibbons, 1980a). In demembrated cells of *Crithidia*, two distinct modes of tip-to-base or base-to-tip bend propagation occur depending on Ca^{2+} concentrations (Fig. 8.2E; Holwill and McGregor, 1975; 1976).

The studies on *Chlamydomonas* flagella suggest that the Ca^{2+} responses are inherent in the axoneme itself, and cannot be assigned to the basal body components. The central tubules in these *Chlamydomonas* axonemes seem to regulate beating patterns, because axonemes lacking central tubules beat symmetrically, quite independent of Ca^{2+} concentrations (Hosokawa and Miki-Noumura, 1987), and there is a structural asymmetry inherent in the central tubules–central sheath complex (Witman *et al.*, 1978).

Although continuous rotation of central tubules was observed in *Paramecium* (Omoto and Kung, 1979) and *Chlamydomonas* (Kamiya, 1982), this was not the case for the compound cilia in the ctenophore *Pleurobrachia* (Tamm and Tamm, 1981). Nevertheless the compound cilia did exhibit similar – or usually more complex – Ca^{2+} -induced changes in waveform (Sleigh and Barlow, 1982). Thus, the effect of the continuous rotation of central tubules on the waveform is not clear.

Change in waveform must involve some change in the pattern of interdoublet sliding. Ca^{2+} ions are, therefore, considered to act on either the dynein force-generating system (Mohri and Yano, 1982) or the radial-spoke control system (Warner and Satir, 1974; Witman *et al.*, 1978), or perhaps even both systems at once (Summers and Gibbons, 1971). At present, it is not known where the Ca^{2+} -binding component is located within the axoneme.

In this chapter, we do not attempt to explain how Ca^{2+} affects flagellar and ciliary behaviours. Instead, the model for flagellar beating is modified in such a way that it describes various types of ciliary-like beatings. Once a close correlation is specified between changes in parameter values and behavioural changes in the model, it will then be possible to make a comparison between the response of the model to changes in parameters and the response of real flagella to changes in Ca^{2+} ions.

8.2 Dynamic properties of the opposed dyneins

As the first step in developing a model for ciliary beats, let us consider an isolated ciliary segment which involves the asymmetrically opposed dynein subsystems I and II. This allows us to focus on functional properties necessary for asymmetric ciliary beating.

8.2.1 A segment model

Suppose that internal shear force, S , is balanced to internal viscous shear force, $\gamma d\sigma/dt$, and an external shear force, Z . The full system of equations has the form:

$$\gamma \frac{d\sigma}{dt} = S + Z \quad (8.1a)$$

$$x = \sigma \quad (8.1b)$$

$$S = F_{\text{I}}n_1 + F_{\text{II}}(1 - n_1) - K_e(\sigma - \sigma_0) \quad (8.1c)$$

$$F_{\text{I}} = Q_{\text{I}}(x - x_1)(x - x_2)(x_c - x) \quad (8.1d)$$

$$F_{\text{II}} = Q_{\text{II}}(x - x'_1)(x - x'_2)(x'_c - x) \quad (8.1e)$$

$$n_1 = \begin{cases} 1 & 0 < x \leq S_1 \\ 0 & S_1 < x < 1 \end{cases} \quad \text{for } \dot{x} < 0 \quad (8.1f)$$

$$n_1 = \begin{cases} 1 & 0 < x < S_2 \\ 0 & S_2 \leq x < 1 \end{cases} \quad \text{for } \dot{x} > 0. \quad (8.1g)$$

Equation (8.1a) describes the force balance within the segment. Like in Chapter 7, the analysis in the present chapter is limited to the range of small-amplitude movement $0 < \sigma < 1$, so that equation (8.1b) holds. Equation (8.1c) defines the internal shear force. Cubic force–distance functions are used as defined by equations (8.1d) and (8.1e). Hysteresis switching functions are described by equations (8.1f) and (8.1g). Note that $n_1 + n_{\text{II}} = 1$, where n_1 and n_{II} are fractions in the ‘on’ state for subsystems I and II, respectively. The parameters used are: $x_1 = 0.1$, $x_2 = 0.3$, $x_3 = 1.0$, $x'_1 = x'_2 = 1.1$, $x'_3 = 0$; $Q_{\text{I}} = 300$ pN, $Q_{\text{II}} = 100$ pN; $S_1 = 0.2$, $S_2 = 0.8$; $k_1 = k_{\text{II}} = 0$; $K_e = 1$ pN/24 nm, $\sigma_0 = 0.7$; $\gamma = 50$ pN ms/24 nm. Initial conditions are: $\sigma = 0.3$ and $n_1 = 1$ at $t = 0$.

Only the internal viscosity is considered in this section. The external shear force, Z , is just introduced to examine the behaviour of this system. The external force, Z , may be interpreted as an active shear force produced by a dynein in the axoneme proximal to the segment under consideration. Although such an external force must be cancelled out in the normally beating cilium because of the continuity of the sliding microtubules (cf. Newton’s third law), the study of this ‘artificial’ isolated system would help us to understand not only how excitable–oscillatory behaviour appears but also how mechano-sensitivity occurs at the level of dynein system.

Experimentally the external force, Z , may arise when bending movements are constrained (cf. Kamimura and Takahashi, 1981; Kamimura and Kamiya, 1989) so that only sliding movements are allowed to occur against the stiffness of the microneedle. Here the resistive force of the microneedle may contribute to the external shear force.

For the purpose of the following discussion, let us introduce potential-energy functions U_I for subsystem I and U_{II} for subsystem II. They are obtained by integrating the force–distance functions F_I and F_{II} (see equation (7.2)) with respect to x , respectively:

$$U_i(x) = - \int_0^x F_i(x) dx \quad i = I, II. \quad (8.2)$$

The total potential-energy functions U'_I and U'_{II} are also defined as a sum of the original potential-energy functions given by equation (8.2) and the potential function obtained by integrating the elastic shear resistance:

$$U'_i(x) = - \int_0^x \{F_i(x) - K_e(\sigma - \sigma_0)\} dx \quad i = I, II. \quad (8.2')$$

When K_e is taken to be a small value (say 1 pN/24 nm) there is little difference between the potential-energy functions for the dynein system only as defined by equation (8.2), and the total potential-energy functions as defined by equation (8.2').¹

8.2.2 Excitable behaviour of the segment model

Figure 8.3 depicts how an excitable behaviour arises in the opposed-dynein system. To understand the behaviour of this system, potential-energy functions and corresponding ‘on–off’ switch dynamics are shown in the upper part. Potential-energy functions U_I and U_{II} are denoted by solid and broken curves, respectively. Panels a, b, c and d correspond to stages denoted by a, b, c and d in the time-course of $x (= \sigma)$. A hysteresis switching function for a dynein in subsystem I, n_I , is shown in the inset. Note that $n_{II} = 1 - n_I$.

Initially, the dynein in subsystem I is shifted above the threshold (≈ 0.3) as denoted by panel a. Active sliding takes place until the dynein reaches the switching point $S_2 (= 0.8)$ at which the dynein in subsystem I is turned ‘off’ (denoted by a white ball), and instead, a dynein in subsystem II is turned ‘on’ (denoted by a black ball) (panel b). Since the state at $x = S_2$ in subsystem II is less stable, the backward sliding spontaneously occurs until the dynein reaches the other switching point $S_1 (= 0.2)$ and the dynein in subsystem II is turned ‘off’ and the dynein in subsystem I is turned ‘on’ again (panel c). Since the location of the switching point $S_1 (= 0.2)$ is less than the threshold value (≈ 0.3) on the sliding coordinate, x , the dynein in subsystem I moves to the left as indicated by a leftward arrow in panel c. Finally the system returns to its resting state, and becomes quiescent (panel d).

The resulting time-course of x looks like an ‘impulse’ or an ‘action potential’ of the nervous system. A single action of this kind arises only when a momentary shift in shear is applied in a certain direction, though not in the opposite direction. This amounts to directional sensitivity. In addition, there is a time-interval (i.e. a *refractory period*) during which the responsiveness of the system to a second stimulus is reduced or absent (cf. Section 6.4.5).

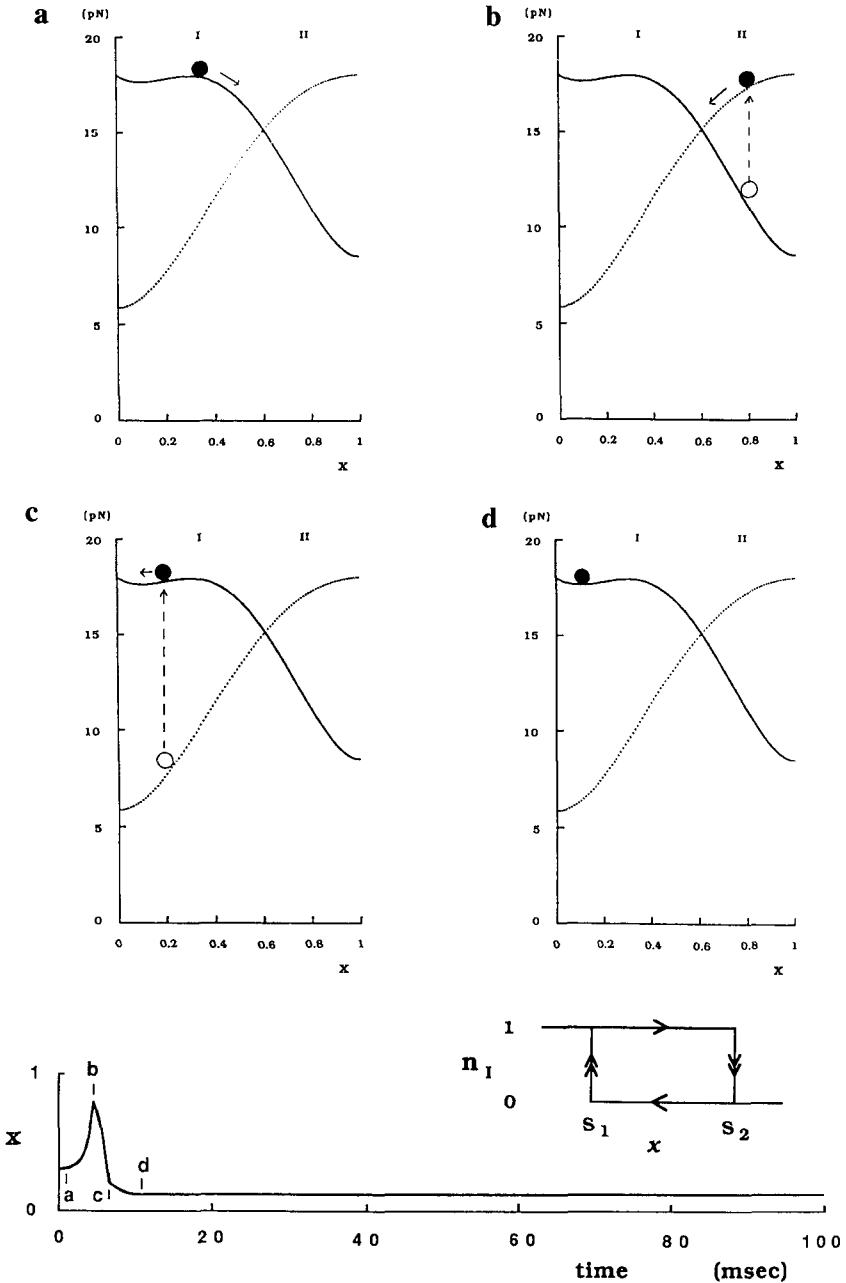


Figure 8.3 Behaviour of the ciliary segment model. The time-course of $x (= \sigma)$ is shown in the lower panel where typical stages are marked by a, b, c and d. The upper part shows potential-energy functions U_I for subsystem I (plotted by solid curves) and U_{II} for subsystem II (plotted by broken curves) given as a function of sliding coordinate x . On these potential functions black and white balls are drawn. Black balls indicate dyneins in the 'on' state and white balls indicate dyneins which have just turned 'off'. These switching dynamics are described by a hysteresis function as shown in the inset. Note that $n_I + n_{II} = 1$, where n_I and n_{II} are fractions in the 'on' state for subsystems I and II, respectively. Each panel corresponds to each stage in the lower panel (see text for details).

8.2.3 Mechano-sensitivity of the segment model to external stimuli

It is interesting to investigate how oscillations appear in this ‘quiescent’ system. Also of interest is to understand how this system is characterized by directional sensitivity. To study these dynamic properties of the system, a step change of an external force, Z , is applied to the system.

Figure 8.4 shows the responsiveness of the system to different values of external force steps beginning at $t = 30$ ms (panel B). In each case, the external force is initially set at zero (i.e. $Z = 0$ at $t = 0$) and calculations are started with the same parameter values and initial conditions as those in the previous subsection. At $t = 30$ ms, a sudden change occurs in the external force from zero to a new level at which it is held constant. The magnitude of the force applied to this system is shown in each panel.

When $Z = 2.0$ pN (or less than this critical value), active sliding is not triggered. Of course a negative value of Z (say $Z = -2.0$ pN) causes no significant effects on this ‘quiescent’ system. However, when $Z = 2.1$ pN, this ‘quiescent’ system shows ‘impulse trains’ or ‘oscillations’ with low frequency. At $Z = 3.0$ pN, the frequency is increased without change in the shape of each ‘impulse’. At $Z = 6.0$ pN, the time-course of x seems to be reversed with respect to $x = 0.5$ (i.e. the sharp peaks appear at $x = S_1$ instead of S_2 as in the case of $Z = 3.0$ pN), but the frequency remains almost constant. At $Z = 8.0$ pN, the system is forced to move into another stable state and becomes quiescent.

The functional properties mentioned above can be interpreted in terms of the modified form of a potential-energy curve in the presence of external shear force, Z . Figure 8.5 and panels A and C of Figure 8.4 show the ‘effective’ potential-energy functions under the influence of various values of the constant external force, Z . Integration of constant force Z with respect to x leads to $-Zx$. Thus the ‘effective’ potential function is obtained when $-Zx$ is superimposed upon U_I or U_{II} .

The positive value of Z decreases the potential barrier of the ‘effective’ potential-energy function for subsystem I, which causes instability of a metastable state leading to oscillations similar to the case of $Z = 2.1$ pN in Figure 8.4B. The forms of potential-energy curves for subsystems I and II are exchanged as Z is increasing (see also Fig. 8.4A,C), so that the time-variation of x is exchanged as seen in the cases of $Z = 3.0$ and 6.0 pN in Figure 8.4B. A further increase in Z causes a new stable state at $x = 1.0$ in subsystem II (since shear is restricted to the range 0–1). Once the dynein is trapped in this stable position, it cannot overcome the ‘effective’ potential-energy barrier. As a result, oscillations are no longer sustained and the system becomes quiescent for $Z = 8.0$ pN in Figure 8.4B.

In contrast, the negative value of Z increases the potential-energy barrier in subsystem I and increases the slope of the potential-energy curve in subsystem II (see the panel denoted by $Z = -2.0$ pN in Fig. 8.5), so that no qualitative

(A)

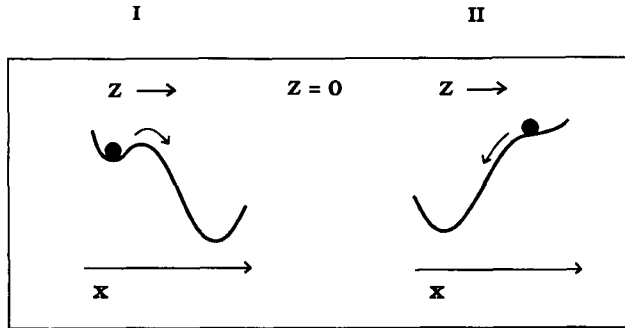


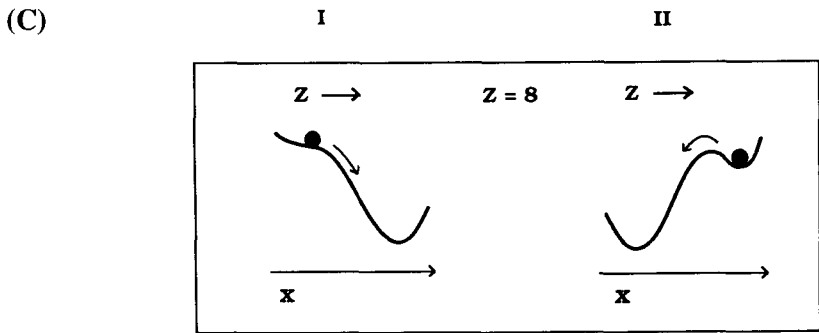
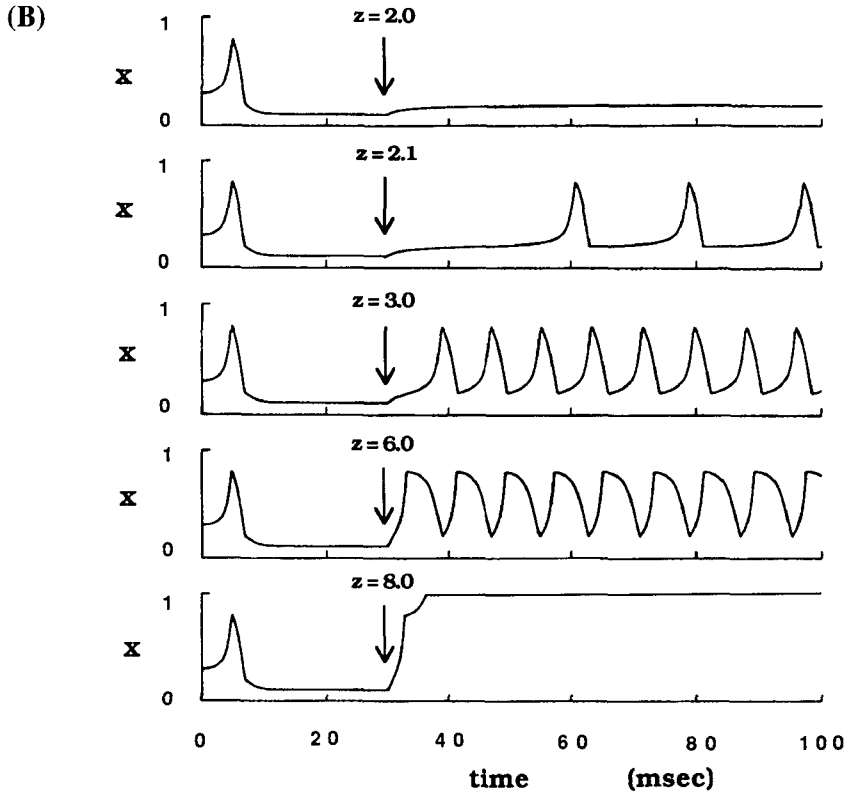
Figure 8.4 Panels A and C illustrate ‘effective’ potential-energy functions for subsystems I and II at different values of Z (see also Fig. 8.5). Panel B shows time variation of x ($= \sigma$) for various step changes in the external shear force, Z . All simulations start with the same initial conditions and $Z = 0$. The system exhibits a single action, and becomes quiescent. At $t = 30$ ms, a sudden step change in Z is applied to the quiescent system whose value is shown in each panel. No response occurs when $Z \leq 2.0$ pN, but the system exhibits oscillations with low frequency at $Z = 2.1$ pN. With increasing Z up to 3.0 pN the frequency is increased. When Z is further increased the slowly increasing phase in x gives way to the rapidly increasing phase, so that at $Z = 6.0$ pN, the shape of the time variation of x is reversed with respect to $x = 0.5$. That is, the slowly decreasing phase is followed by the rapidly decreasing phase. At $Z = 8.0$ pN, the system no longer exhibits oscillations, and becomes quiescent.

change appears in the asymmetric form of the potential-energy functions, even though the strong negative value of Z is imposed. Thus, directional sensitivity is ascribed to the asymmetric form of potential-energy functions.

8.3 Ciliary dynamics

8.3.1 A ciliary model

A $10 \mu\text{m}$ long ciliary axoneme is assumed to be ‘inhomogeneous’ reflecting the longitudinal and structural asymmetry (Fig. 8.6). A typical set of parameter values for each region is given as follows. $E_B = 300 \text{ pN } \mu\text{m}^2$. For the basal active region ($0 < s \leq 0.2 \mu\text{m}$): $Q_I = 300 \text{ pN}$, $K_e = 300 \text{ pN}/24 \text{ nm}$; $x_1 = 0.1$, $x_2 = 0.3$, $x_3 = 1.0$, $x'_1 = x'_2 = 0.85$, $x'_3 = 0$; $S_1 = 0.2$, $S_2 = 0.8$; $k_I = k_{II} = 30 \text{ pN}/24 \text{ nm}$; $\sigma_0 = 0.7$. Potential-energy functions defined by equation (8.2'), U'_I and U'_{II} , are shown in the left panel of Figure 8.6B. Note that curves 1 and 2 correspond to the cases of $Q_{II} = 1000$ and 1100 pN , respectively. For the rest of the active region ($0.2 < s \leq 8 \mu\text{m}$): $Q_I = Q_{II} = 300 \text{ pN}$; $K_e = 1 \text{ pN}/24 \text{ nm}$; and the other parameters are the same as for the basal region. Potential-energy functions defined by equation (8.2), U_I and U_{II} , are shown in the right panel of Figure 8.6B. For the passive terminal region ($8 < s < 10 \mu\text{m}$): $Q_I = Q_{II} = 0$; $K_e = 1 \text{ pN}/24 \text{ nm}$; $\sigma_0 = 0.7$.



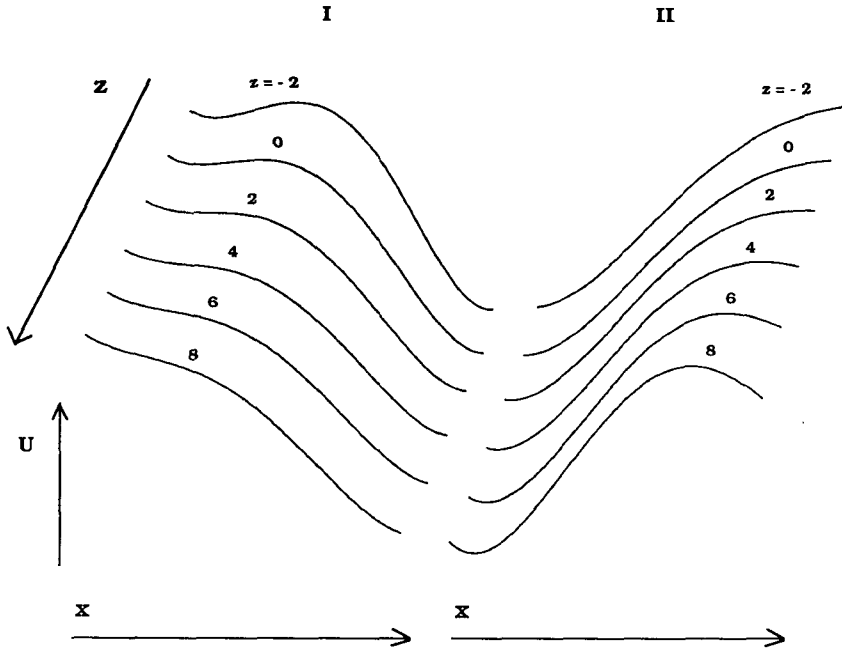


Figure 8.5 'Effective' potential-energy functions for subsystems I and II under the influence of the external force, Z , are plotted as a function of the sliding coordinate x at different Z values. 'Effective' potential-energy functions are obtained by superimposing $-Z \cdot x$ upon U_I or U_{II} . The left and right figures depict these effective potential functions for subsystem I and II, respectively. As Z is increased from -2.0 to 8.0 pN, the shape of the potential energy for subsystem I is exchanged for that of subsystem II.

Only a single unit of sliding (i.e. $0 \leq \sigma \leq 1$) is allowed; thus the model is limited to simulation of small-amplitude oscillations. Sliding coordinate, x , and shear angle, σ , are related by the proportionality constant $h/24$ nm, where h is the separation between adjacent doublets in the plane of bending and 24 nm is the interval between adjacent attachment sites (Hines and Blum, 1979). For convenience, $h = 24$ nm is assumed and then $\sigma = x$ is obtained.

For all simulations, a $10 \mu\text{m}$ -long cilium was divided into 50 segments of length $0.2 \mu\text{m}$. As the initial conditions, the cilium was straight ($\partial\sigma/\partial s = 0$ at $t = 0$ for $0 < s < 10 \mu\text{m}$), dyneins in subsystem I were in the 'on' state for all the active region of the axoneme ($n_1 = 1$ at $t = 0$ for $0 < s \leq 8 \mu\text{m}$), and all the segments were in the same sliding coordinate ($x = 0.1$ at $t = 0$ for $0 < s < 10 \mu\text{m}$).

Boundary conditions at the distal (free) end of a cilium require that external forces and moments vanish. A vanishing moment at the free end implies that the curvature vanishes (cf. Table 7.1). Thus

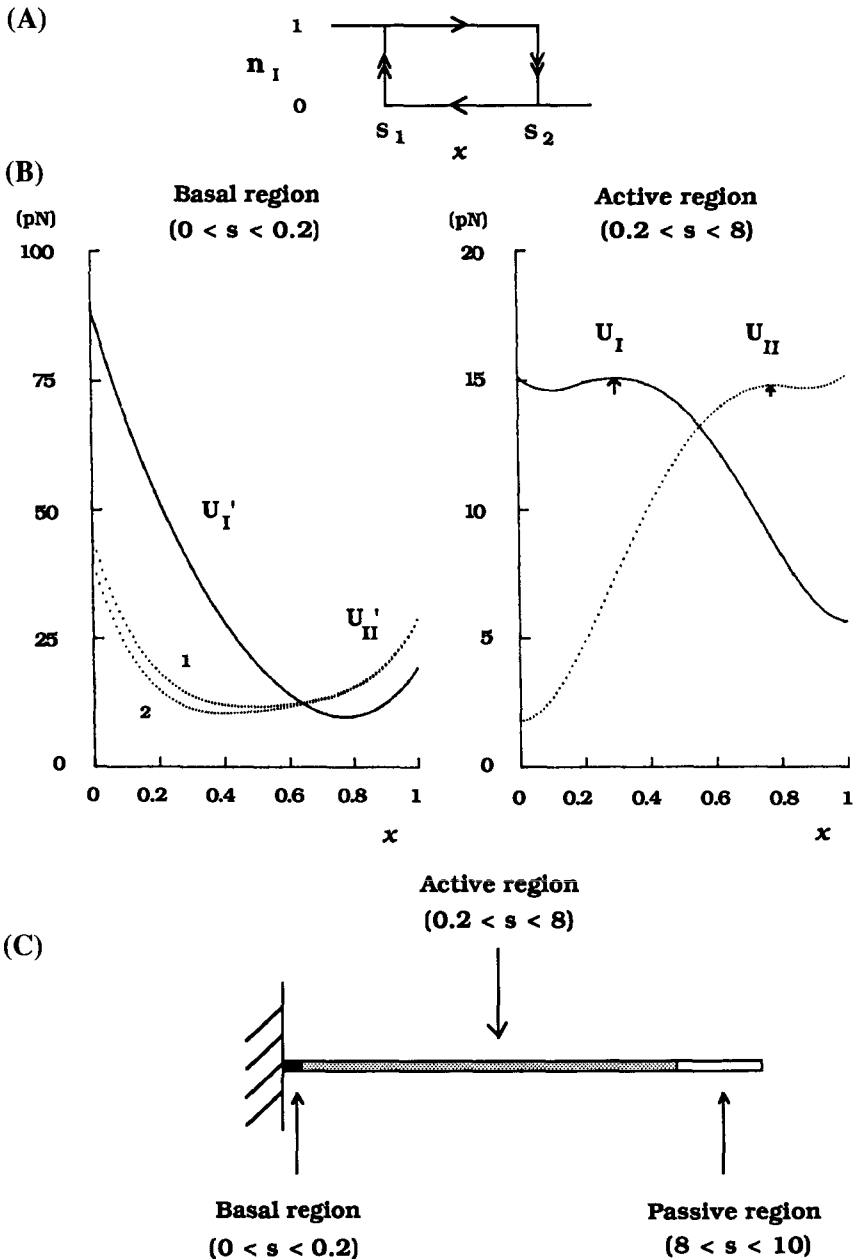


Figure 8.6 Ciliary model showing the structural, longitudinal and circumference asymmetry. (A): A hysteresis switching function for a dynein in subsystem I. (B): The left panel shows potential-energy functions U_I' and U_{II}' which are the sum of each original potential-energy function and the potential-energy function due to a basal elastic component. Curves 1 and 2 correspond to the cases of $Q_{II} = 1000$ and 1100 pN, respectively. The right panel shows potential-energy functions U_I and U_{II} . The potential-energy barriers are indicated by the arrows. Since the potential-energy function for a passive elastic component in the rest of the active basal region is small, U_I' and U_{II}' are almost equivalent to U_I and U_{II} . (C): A schematic representation of a ciliary axoneme. The basal active region ($0 < s \leq 0.2 \mu\text{m}$), the active region ($0.2 < s \leq 8 \mu\text{m}$) and passive region without dyneins ($8 < s < 10 \mu\text{m}$). From Murase (1990). Reprinted with

$$F_N(s = L) = 0, \quad \frac{\partial \sigma(s = L)}{\partial s} = 0. \quad (8.3)$$

The boundary conditions at the proximal (pinned) end require that the velocity and moments vanish. Since $-C_N V_N = \partial F_N / \partial s$ from equations (5.29) and (5.31), the pinned conditions are

$$\frac{\partial F_N(s = 0)}{\partial s} = 0, \quad \frac{\partial \theta(s = 0)}{\partial s} = 0. \quad (8.4a)$$

If the filaments are individually pinned at the base, then

$$\sigma(0) = \theta(0). \quad (8.4b)$$

An alternative set of boundary conditions are that the axoneme is clamped at the base:

$$\frac{\partial F_N(s = 0)}{\partial s} = 0, \quad \theta(s = 0) = 0. \quad (8.5a)$$

If the filaments are tied together at the base, then

$$\sigma(0) = 0. \quad (8.5b)$$

In both sets of boundary conditions one can assume $\sigma(s) = \theta(s)$ at any point, s , along the axoneme from equation (7.7), and similar results can be obtained. Of course, in the clamped-end case one must introduce a short passive region at the basal region to allow sufficient sliding over a full dynein cycle, as discussed in Chapter 7. In the present chapter we will consider the pinned boundary conditions at the proximal end.

The complete system of equations and boundary conditions have the form:

$$\frac{\partial^2 S}{\partial s^2} + E_B \frac{\partial^4 \sigma}{\partial s^4} + C_N \frac{\partial \sigma}{\partial t} = 0 \quad (8.6a)$$

$$x = \sigma \quad (8.6b)$$

$$S = F_I n_I + F_{II}(1 - n_I) - K_e(\sigma - \sigma_0) \quad (8.6c)$$

$$F_I = \begin{cases} Q_I(x - x_1)(x - x_2)(x_c - x) - k_I(x - x_1) & 0 < x \leq S_1 \\ Q_I(x - x_1)(x - x_2)(x_c - x) & S_1 < x < 1 \end{cases} \quad (8.6d)$$

$$F_{II} = \begin{cases} Q_{II}(x - x'_1)(x - x'_2)(x'_c - x) & 0 < x < S_2 \\ Q_{II}(x - x_1)(x - x_2)(x_c - x) - k_{II}(x - x_1) & S_2 \leq x < 1 \end{cases} \quad (8.6e)$$

$$n_I = \begin{cases} 1 & 0 < x \leq S_1 \\ 0 & S_1 < x < 1 \end{cases} \quad \text{for } \dot{x} < 0 \quad (8.6f)$$

$$n_I = \begin{cases} 1 & 0 < x < S_2 \\ 0 & S_2 \leq x < 1 \end{cases} \quad \text{for } \dot{x} > 0 \quad (8.6g)$$

$$\frac{\partial^3 \sigma(0)}{\partial s^3} = 0; \quad \frac{\partial \sigma(0)}{\partial s} = 0 \quad (8.6h)$$

$$\frac{\partial^2 \sigma(L)}{\partial s^2} = 0; \quad \frac{\partial \sigma(L)}{\partial s} = 0. \quad (8.6i)$$

Equation (8.6a) describes the moment-balance equation. Modified cubic force-balance functions are used for subsystems I and II, as defined by equations (8.6d) and (8.6e), respectively. The pinned-basal-end and free-distal-end conditions are represented by (8.6h) and (8.6i), respectively.

In this chapter in order to obtain larger angles as a result of a single unit of sliding, the total angle shown in the figures was amplified twofold.

8.3.2 Repetitive beat-cycle

Figure 8.7 shows a full cycle of the model behaviour when the parameter values listed in the previous section, and $Q_{II} = 1100$ pN ($0 < s \leq 0.2 \mu\text{m}$) were used (see Fig. 8.6). Figure 8.7A shows a recovery stroke of a cilium (right) and sliding patterns plotted against space, s , and time, t (left). Each contour plot of the sliding patterns corresponds to each stage during successive changes in the shape of a cilium. Time, t , develops backward (from 0 to 35 ms) as indicated by the arrow. Sliding is initiated at the base and triggered successively to the distal part in accordance with the propagation of a bend. This sliding pattern may account for the metachronous sliding. The model cilium pauses at the end of the recovery stroke and commences the beat-cycle with a full effective stroke.

Figure 8.7B shows an effective stroke (right) and sliding patterns (left). Unlike the upper left panel, time, t , develops forward (from 35 to 55 ms) as indicated by the arrow. Sliding is initiated in the basal region and spread out rapidly along the length of the axoneme. This sliding pattern may account for the synchronous sliding.

These simulation results are interpreted in terms of ‘on–off’ switches and triggering events in the following way. Since initially all the dyneins in subsystem I are in the ‘on’ state ($n_I = 1$), the dynein in the basal region would prefer to stay at about $x = 0.75$, whereas the dynein in the rest of the active region would prefer to stay at about $x = 0.1$. (Note that, as shown in Fig. 8.6, a stable position in subsystem I for the basal active region ($0 < s \leq 0.2 \mu\text{m}$) is at about $x = 0.75$, whereas that in subsystem I for the rest of the active region ($0.2 < s \leq 8 \mu\text{m}$) is at about $x = 0.1$.) Thus there seems to be ‘mutual instability’ between the basal region and the rest of the cilium with respect to the stable position of dyneins (see Section 6.6). As a result of a strong inclination toward the stable position at about $x = 0.75$, sliding in the forward direction (i.e. the direction of increasing x) is initiated. Since there is a relatively high potential barrier in each dynein, active sliding is triggered

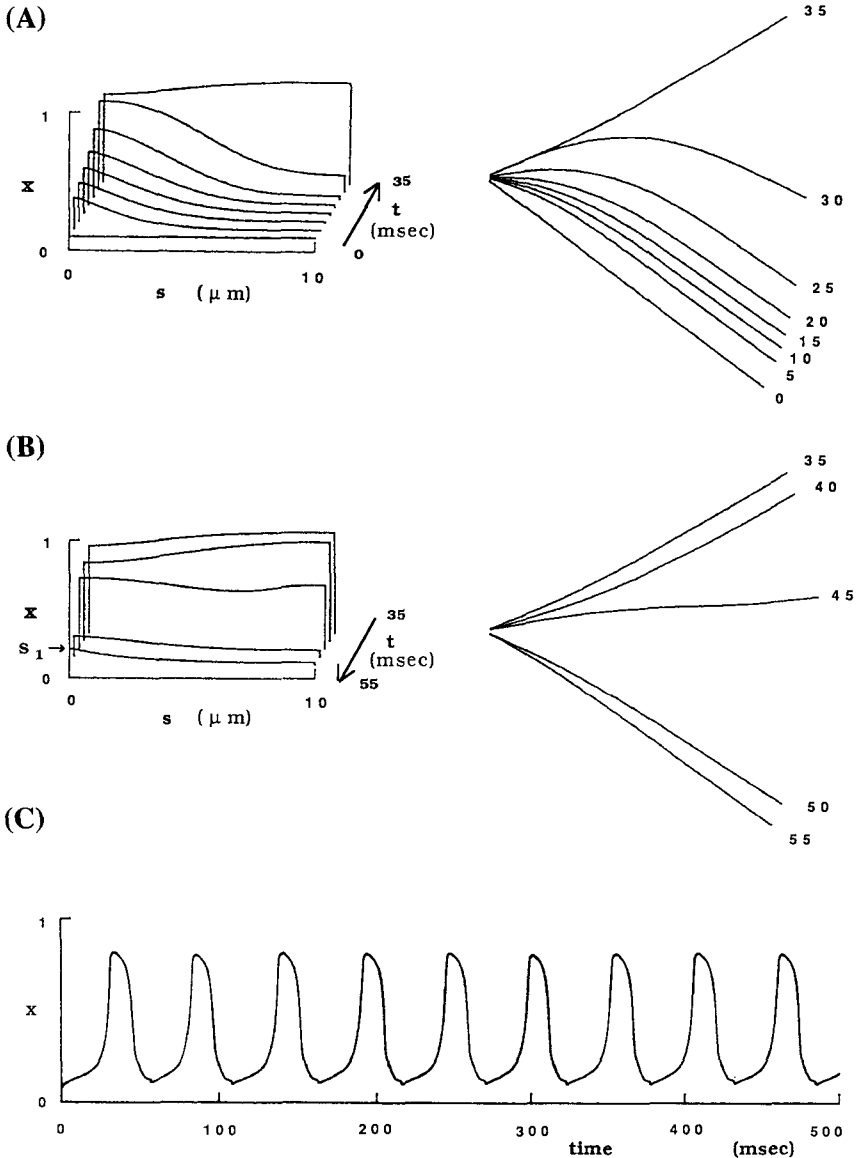


Figure 8.7 Repetitive beating solution of a ciliary model. (A): A 'recovery' stroke (right) and sliding patterns plotted as a function of space, s , along a length of the cilium and time, t (left). (B): An 'effective' stroke (right) and sliding patterns (left). (C): The time-course of x at $s = 5 \mu\text{m}$. This model oscillated with a frequency of 18 Hz. Parameters are as in Section 8.3.1. Note that $Q_{11} = 1100 \text{ pN}$ for the basal active region ($0 < s \leq 0.2 \mu\text{m}$), which corresponds to curve 2 in Fig. 8.6. From Murase (1990). Reprinted with permission.

successively along the axoneme. These metachronous or ‘slow’ triggering events account for a ‘recovery’ stroke.

After the recovery stroke, dyneins in subsystem I are turned ‘off’ and dyneins in subsystem II are turned ‘on’. As shown in Figure 8.6B, most of the active region is in a stable position at about $x = 0.9$, whereas the basal region is in a stable position at about $x = 0.3$. There appears to be ‘mutual instability’ again between the basal region and the rest of this system. As a result of this ‘mutual instability’, active sliding in the backward direction (i.e. the direction of decreasing x) is initiated. Since the potential barrier in subsystem II is relatively smaller than that in subsystem I (see right panel of Fig. 8.6B), active sliding is rapidly triggered along the length of the axoneme. These synchronous or ‘fast’ triggering events account for an ‘effective’ stroke. This effective stroke leaves the cilium in a position to begin the next recovery stroke.

The arrow in the left panel of Figure 8.7B indicates the switching point at $x = S_1$. At $t = 55$ ms, it is found that the sliding displacements in all the segments are below this switching point, so that all the dyneins in subsystem II are turned ‘off’ (and those in subsystem I are turned ‘on’) and the initial conditions are regained. Since the system is completely reset after a full cycle, it exhibits repetitive beat-cycles. Figure 8.7C shows the time-course of x at position $s = 5 \mu\text{m}$ to show that the system exhibits repetitive beat-cycles.

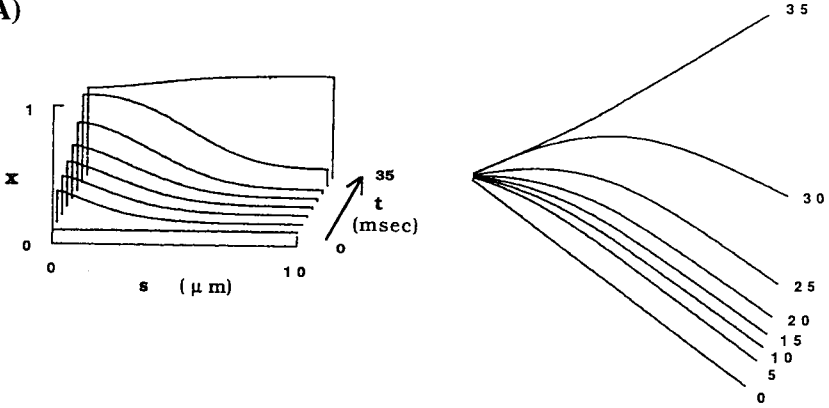
The basic mechanism underlying the repetitive ciliary beating mentioned above is similar to that discussed in Section 6.6, though the previous model was studied at the limit of zero external viscosity.

8.3.3 Discontinuous beat-cycle

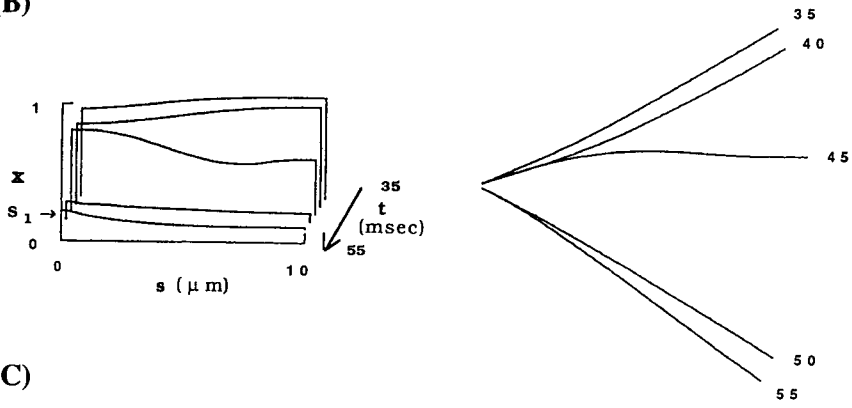
Quiescence due to ‘on–off’ switch failure. The ‘switch-point hypothesis’ by Satir (1984; 1985) suggests that failure of the operation of one of the switches will produce a quiescence of ciliary beat in a specific stroke position. To ascertain whether the ciliary model stops beating due to the failure of one of the switches, the same parameters as in Figure 8.7 are used except for $Q_{II} = 1000$ pN in the basal region such that the slope of curve 1 of U'_{II} in Figure 8.6 is set to be high enough to prevent dyneins in subsystem I from switching ‘on’ in the basal region after the effective stroke.

Figure 8.8 shows the case in which after a single beat-cycle the cilium is quiescent at the end of the effective stroke. Only the value of Q_{II} is decreased from the previous case, which affects the behaviour of the basal region in subsystem II, so that the recovery stroke is the same as that in Figure 8.7. However, the effective stroke is somewhat different. Especially after the effective stroke when one switch at the base fails as indicated by the arrow in the left panel in Figure 8.8B. The basal region is slightly above this switching point, so that subsystem I is not completely turned ‘on’ though the other parts of subsystem I are turned ‘on’. As illustrated in Figure 8.6,

(A)



(B)



(C)

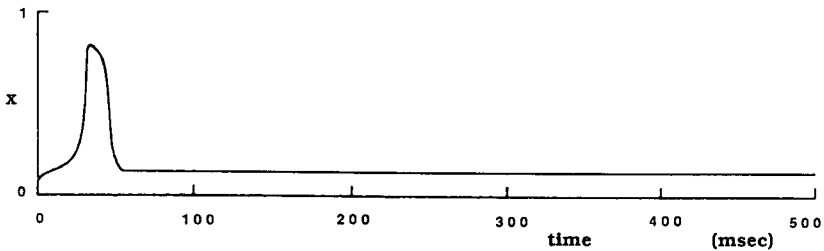


Figure 8.8 Discontinuous beat-cycle of a ciliary model. Each panel corresponds to that in Fig. 8.7. As shown in the lower panel, the model cilium is quiescent after a single beat-cycle. Parameters are as in Section 8.3.1. Note that $Q_{II} = 1000$ pN for the basal active region ($0 < s \leq 0.2 \mu\text{m}$), which corresponds to curve 1 in Fig. 8.6. From Murase (1990). Reprinted with permission.

the basal region is in a stable position at about $x = 0.3$ in subsystem II and the rest of the cilium is in a stable position at about $x = 0.1$ in subsystem I. As a result, there is weak ‘mutual instability’ between the basal region and the rest of the cilium. Thus the model cilium cannot initiate its next stroke.

Quiescence due to the failure of dynein activation. A slight change in a single parameter at the basal region appeared to cause a quiescent mode in the ciliary model. It is, therefore, interesting to know whether another quiescent mode arises if a parameter in the other part, say the rest of the active region, changes. For this purpose, we study what happens as the potential-energy barrier for subsystem I, k_I , is increased.

Figure 8.9A shows the effects of changing k_I on the shape of potential-energy functions. The left and right panels indicate the potential-energy functions of the basal region and of the rest of the active region, respectively. The parameter k_I in equation (8.6d) is kept at 30 pN/24 nm in the basal segment but the rest of the axoneme varies from 0 to 80 to 120 pN/24 nm in panels B, C, and D, respectively.

As the potential-energy barrier for subsystem I increases everywhere except for the basal segment, it becomes progressively more difficult to overcome that barrier, and hence the duration of the pause at the beginning of the recovery stroke increases markedly. For $k_I = 120$ pN/24 nm, the cilium becomes quiescent early in the recovery stroke. Unlike in the quiescent cilia in Figure 8.8, it is the failure of dyneins to activate in subsystem I that causes a quiescence of ciliary beat.

Another quiescent mode occurs when we change the potential-energy barrier for subsystem II, k_{II} , throughout most of the length of the axoneme (Fig. 8.10). When increasing the potential barrier for subsystem II the cilium becomes increasingly stable at the end of the recovery stroke. When $k_{II} = 120$ pN/24 nm the cilium stops beating at the end of the recovery stroke as shown in Figure 8.10D. The cilium becomes quiescent because dynein activation in subsystem II fails.

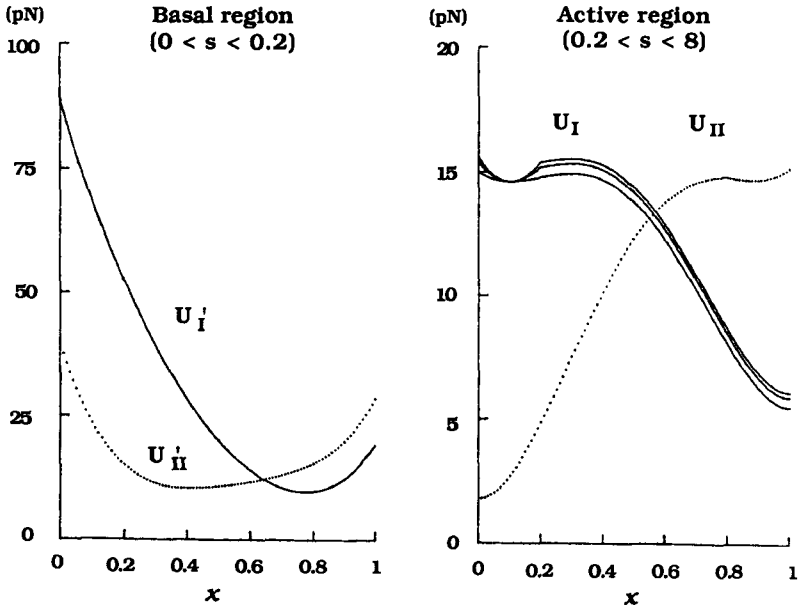
8.4 Ciliary dynamics under the influence of fluid flow

As noted above, at least three different sets of parameters can be found for which a cilium becomes quiescent at the end of either the recovery or the effective stroke. The question naturally arises as to whether fluid flow past such a cilium, such as occurs during a metachronal wave over closely packed cilia, might act to trigger repetitive beating. To solve this question we must modify the ciliary model.

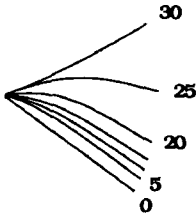
8.4.1 A modified ciliary model

Figure 8.11 depicts a schematic representation of a cilium under the influence of fluid flow. When fluid flow at velocity, V , is externally imposed on a

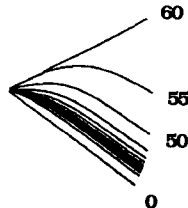
(A)



(B)



(C)



(D)

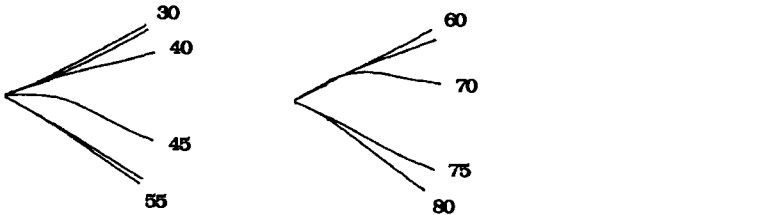


Figure 8.9 Beat patterns for an axoneme showing the effect of differences in the potential-energy function for subsystem I, U_I , throughout most of the length of the axoneme. Parameters are as in Fig. 8.6 except that $k_I = 0, 80$ and 120 pN/24 nm for curves 1, 2 and 3, respectively. The simulations corresponding to curves 1, 2 and 3 are shown in panels B, C and D, respectively. From Murase (1990). Reprinted with permission.

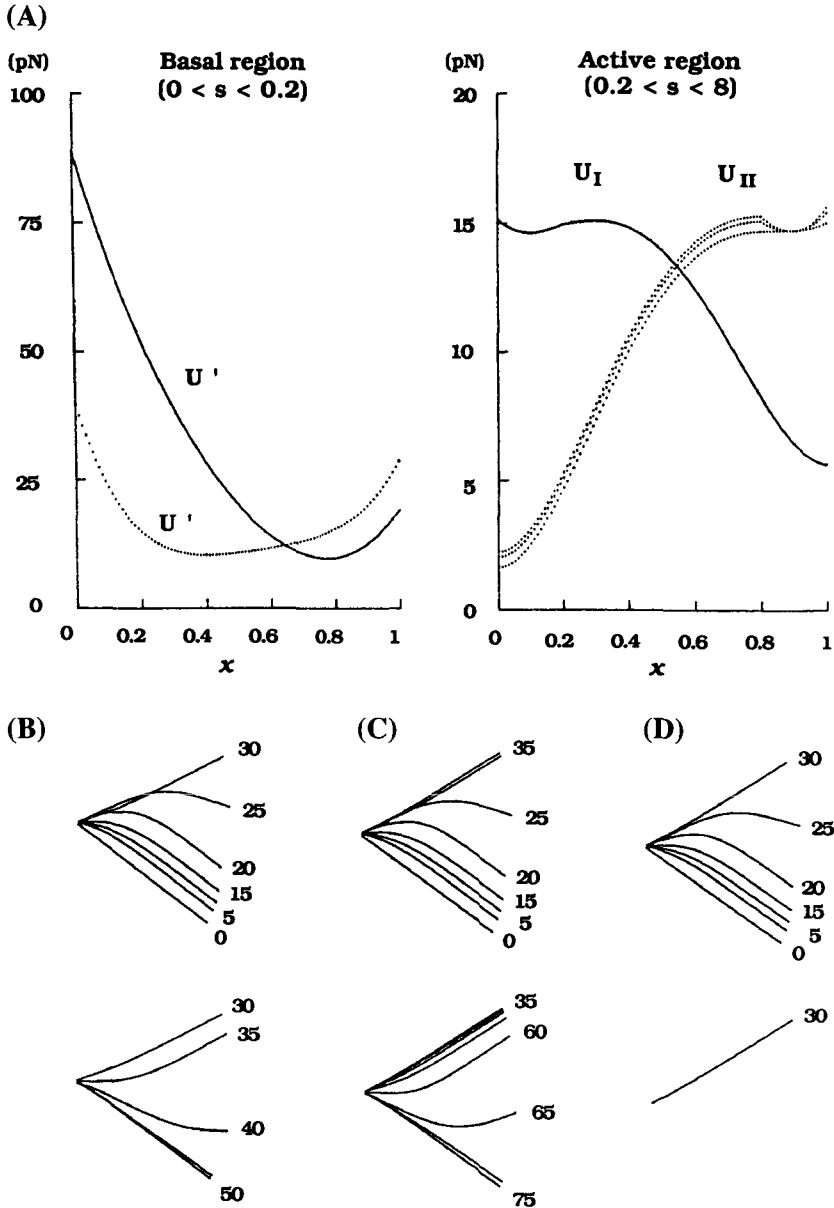


Figure 8.10 Beat patterns for an axoneme showing the effect of differences in the potential-energy function for subsystem II, U_{II} , throughout most of the length of the axoneme. Parameters are as in Fig. 8.7 except that $E_B = 200 \text{ pN } \mu\text{m}^2$ and $k_{II} = 0, 80$ or $120 \text{ pN}/24 \text{ nm}$ for curves 1, 2 and 3, respectively. The simulations corresponding to curves 1, 2 and 3 are shown in panels B, C and D, respectively. From Murase (1990). Reprinted with permission.

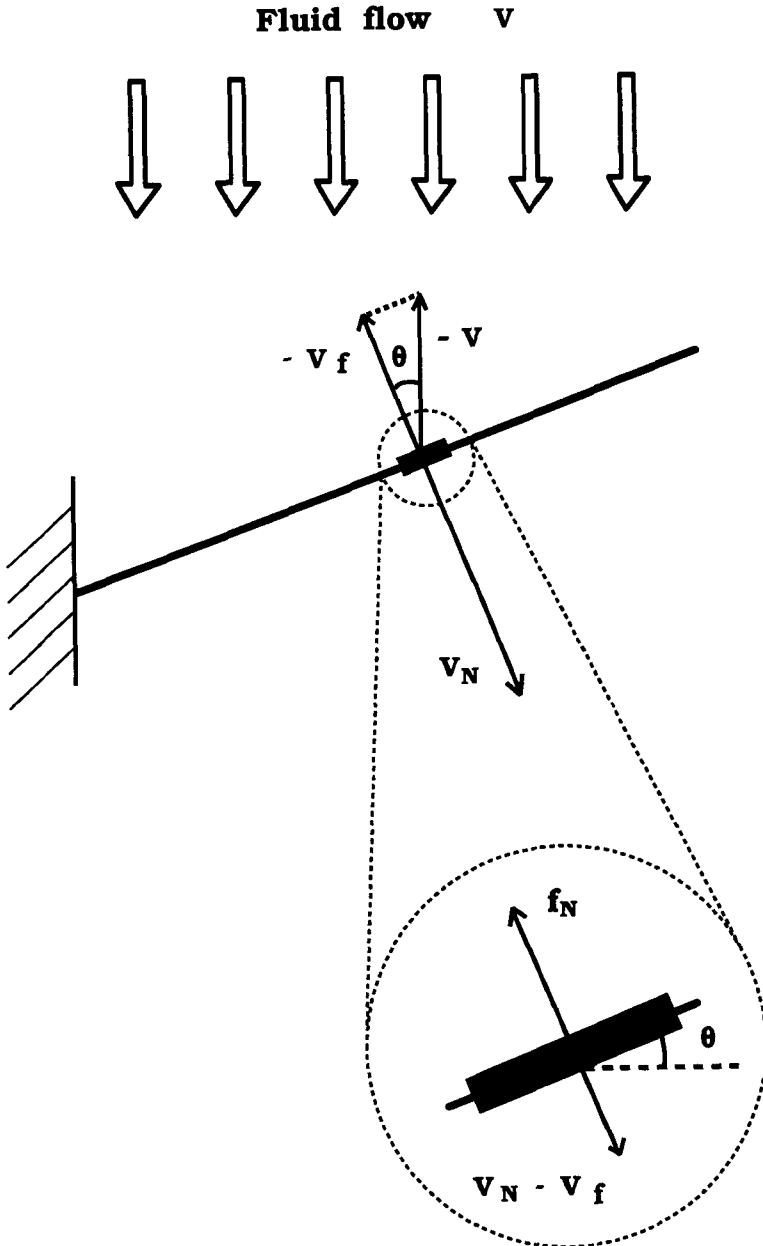


Figure 8.11 Diagram showing fluid flow at velocity V being applied to a beating cilium. Suppose that a segment with bend angle θ moves at velocity, V_N , in the normal direction. The normal component of the velocity of the fluid at the segment is: $V_f = V \cdot \cos\theta$. Thus the external viscous force per unit length, f_N , is proportional to the net velocity, $V_N - V_f$ according to the Gray and Hancock (1955) approximation.

cilium the net velocity of the cilium through the fluid is the difference between the normal component of the velocity of the cilium, V_N , in a fixed coordinate system, minus the normal component of the velocity of the fluid, $V_f = V \cdot \cos\theta$. Thus the external viscous force per unit length, f_N , is given by the following equation

$$f_N = -C_N(V_N - V_f). \quad (8.7)$$

From equations (5.28), (5.29), (5.30) and (5.32), the basic equation becomes

$$C_N \left(\frac{\partial \theta}{\partial t} - \frac{\partial V_f}{\partial s} \right) + \frac{\partial^2 S}{\partial s^2} + E_B \frac{\partial^4 \theta}{\partial s^4} = 0. \quad (8.8)$$

The initial conditions and the boundary conditions at the tip are the same as those in Section 8.3.1. But it is necessary to change one of the boundary conditions at the base as follows:

$$\frac{\partial F_N(s=0)}{\partial s} = -C_N V_f. \quad (8.9)$$

8.4.2 Responsiveness of a quiescent cilium to fluid flow

In the simulations shown in Figure 8.12, the parameters for the cilium were the same as in Section 8.3.1, except that $Q_{II} = 1000$ pN for the basal region. The cilium executed only a single beat, and stopped at the end of its effective stroke. The position of this resting cilium is shown at the top of Figure 8.12. A constant flow of water in the direction of the effective stroke and over a particular location ($6 < s < 8 \mu\text{m}$) shown was then assumed to begin at $t = 200$ ms.

When the fluid velocity was $23 \mu\text{m/s}$, the cilium remained stationary. When V was increased to $24 \mu\text{m/s}$, repetitive beating was initiated. Beat frequency was decreased with an increase in V to $100 \mu\text{m/s}$. Thus, fluid flow above a certain threshold value can initiate a repetitive beating pattern in a cilium which would otherwise be quiescent. If fluid flow increases further, the beat frequency is decreased (e.g. $V = 120 \mu\text{m/s}$) and finally the cilium cannot overcome the fluid force and hence beating ceases (e.g. $V = 150 \mu\text{m/s}$). Fluid flow with proper magnitude and direction can accommodate the 'on-off' switches at the basal region and thus facilitate repetitive beat-cycles.

8.4.3 Fluid flow induced beating patterns of quiescent cilia

The same quiescent cilium examined in Section 8.4.2 shows similar responsiveness to fluid flow even if the fluid flow is applied to a different location. For example, if the fluid is applied to location ($2 < s < 4 \mu\text{m}$) the essential features are not altered but the threshold value for the fluid velocity to induce repetitive beating is increased to $33 \mu\text{m/s}$. Figure 8.13A shows the shape of

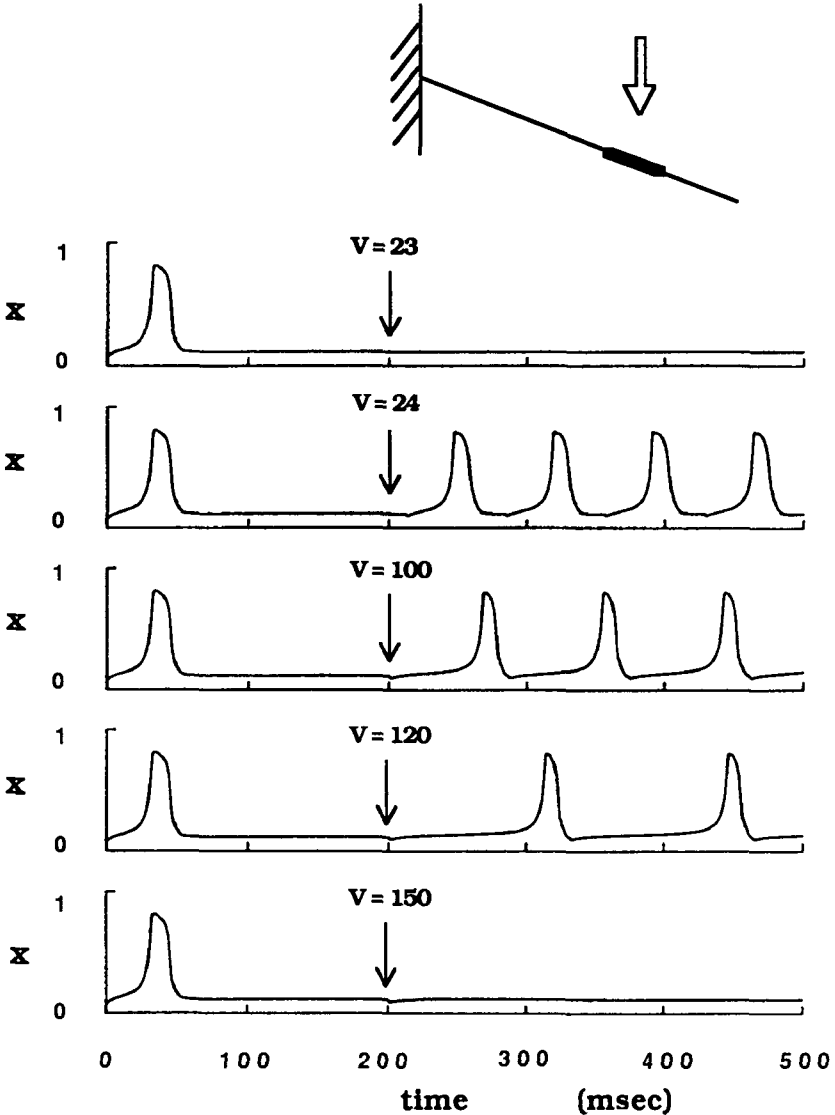


Figure 8.12 Effect of fluid flow on a cilium that did not have a repetitive beat-cycle. x (at $s = 5 \mu\text{m}$) is plotted as a function of time in order to illustrate ciliary motility. The cilium in Fig. 8.8 showed only a single beat and stopped at the end of the effective stroke. The inset shows the position of this resting cilium, the direction of flow of a fluid with the viscosity of water and its location ($6 < s < 8 \mu\text{m}$). Fluid begins flowing at $t = 200$ ms. Repetitive beating did not occur for $V = 23 \mu\text{m/s}$. Repetitive beating occurred for $V = 24 \mu\text{m/s}$. An increase in V to $100 \mu\text{m/s}$ caused a slight decrease in frequency. A further increase in V to $120 \mu\text{m/s}$ caused a further decrease in frequency and finally no beating was obtained for $V = 150 \mu\text{m/s}$. From Murase (1990). Reprinted with permission.

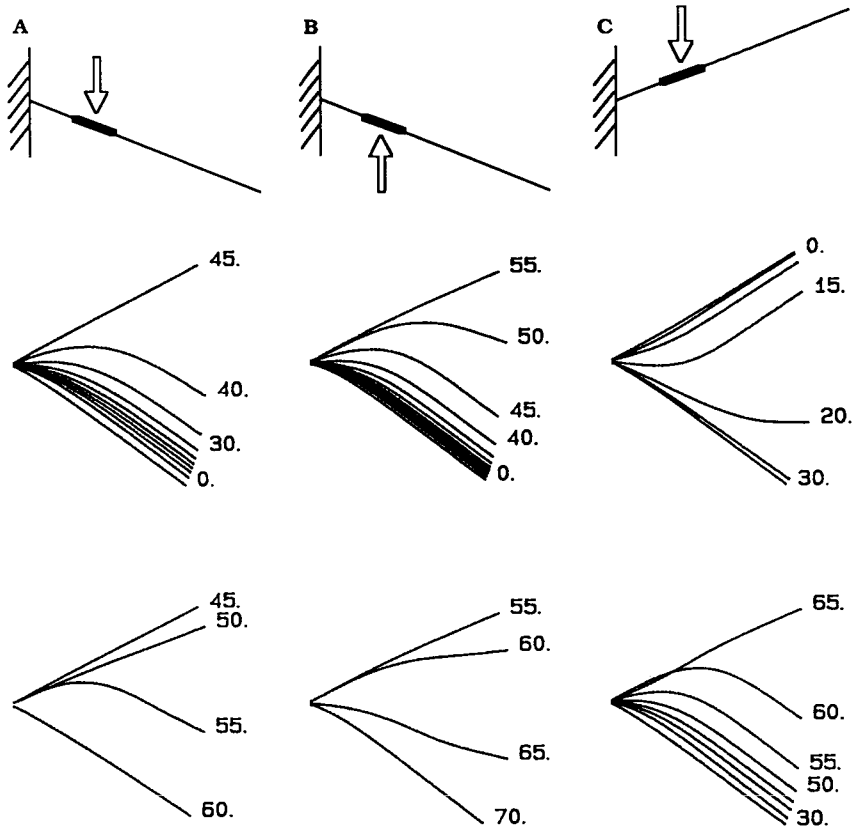


Figure 8.13 Beat patterns for axonemes induced by fluid flow to beat repetitively. The direction of fluid flow ($V = 100 \mu\text{m/s}$, location $2 < s < 4 \mu\text{m}$) and the resting position of the cilium are shown at the top of each of the three panels. Panel A shows the beat pattern for the cilium described in Fig. 8.8, which had stopped at the end of its effective stroke. Panel B shows the beat pattern induced by the fluid flow for the cilium shown in Fig. 8.9, which had stopped at the beginning of its recovery stroke. Panel C shows the beat pattern for the cilium shown in Fig. 8.10, which had stopped at the end of its recovery stroke. From Murase (1990). Reprinted with permission.

this cilium throughout its beat when fluid flow is applied to location ($2 < s < 4 \mu\text{m}$) at $V = 100 \mu\text{m/s}$. This beating pattern should be compared with the following two cases (Figs. 8.13B and C) where fluid flow is applied to the same location ($2 < s < 4 \mu\text{m}$) at the same velocity ($V = 100 \mu\text{m/s}$) but in the 'preferred' direction.

The simulation in Figure 8.9D stopped at the beginning of its recovery stroke, for reasons discussed above. Figure 8.13B shows that fluid flow with a velocity $100 \mu\text{m/s}$ in the direction of the recovery stroke initiated repetitive beating.

Figure 8.13C shows the effect of fluid flow on the cilium in Figure 8.10D where the cilium had failed to beat repetitively because the parameters were such that bend initiation did not occur either at the tip or the base. When fluid flowed ($V = 100 \mu\text{m/s}$) past this cilium in the direction of the effective stroke, repetitive beating occurred.

For each of the simulations shown in Figure 8.13, if the direction of flow of fluid was opposite to that shown, the cilium remained quiescent. Thus initiation of repetitive beating by fluid flow requires both that the speed of flow be above a threshold value and that it be in the appropriate direction.

The quiescent cilia illustrated in the upper part of Figure 8.13A and B indicate similar resting positions at the end of the effective or at the onset of the recovery stroke. But they exhibit quite different directional mechano-sensitivity as indicated by the arrows. This difference can be clearly explained in terms of 'on-off' switches between the opposed subsystems and dynein activation in subsystem I. On one hand, the cilium (Fig. 8.8 and the upper panel of Fig. 8.13A) is held in its resting position because a single switch fails at the base. Thus fluid flow is effective in initiating a recovery stroke only if it is applied to the cilium in the direction to facilitate the switch that failed. On the other hand, the cilium (Fig. 8.9 and the upper panel of Fig. 8.13B) is at rest at the onset of the recovery stroke because dynein activation in subsystem I cannot be triggered even though dyneins are already turned 'on' due to a high potential-energy barrier. Thus fluid flow in the direction that facilitates the activation is very effective.

Similarly to the dynamical behaviour of an isolated segment as examined in Section 8.2, the present ciliary model also displays refractoriness in which its responsiveness to the momentary shift in the bend angle is reduced or absent depending on the time when the stimulus is applied. There seems to be a hierarchy in the nature of the ciliary dynamics. At a component system level, an isolated segment shows mechano-sensitivity. At a ciliary system level, the cilium also possesses mechano-sensitivity.

Since the ciliary model is developed when similar components are connected to each other in a one-dimensional array, it is reasonable to consider that dynamical properties inherent in the unit are amplified into macroscopic behaviour of the cilium. The resultant multi-segment system, however, displayed more variety in the behaviour than does the single-segment system. An example was that quiescent cilia resting almost in the same position showed two different types of mechano-sensitivity (Fig. 8.13A and B).

8.4.4 *A bridge between experimental observations and simulation results*

When considering the effects of Ca^{2+} on the function of an axoneme, the simulation results in the present chapter offer some predictions. To obtain the ciliary-like asymmetric beatings, it is necessary to assume that (i) the length of the axoneme is short enough; (ii) the dynein force-generating system has

both circumference and longitudinal asymmetries; and (iii) the axoneme has structural asymmetry.

Assumption (i) is equivalent to the increase in bending resistance, E_B , in its effect on the wavelength as discussed in Section 6.6. We can therefore expect that the stiffness of an axoneme may change, or probably increase with the increase in Ca^{2+} concentrations. Assumption (ii) may be possible when regulatory sites, say Ca^{2+} -binding sites are distributed inhomogeneously along and around the axoneme. Assumption (iii) for the structural asymmetry can be ascribed to assumption (ii) for the functional asymmetry, so that the present model can be also applicable to an isolated axoneme without basal structure.

It is well known that the direction of bend propagation is controlled by Ca^{2+} concentrations: at low Ca^{2+} concentrations only tip-to-base bend propagation occurs, while at high Ca^{2+} concentrations only base-to-tip bend propagation appears (see Section 4.5.5). As we have discussed in Chapter 7, the direction of bend propagation depends on the structural asymmetry along the axoneme. It is, however, possible to ascribe this structural asymmetry to the functional asymmetry in dyneins via Ca^{2+} ions.

Interestingly a slight change in a single parameter causes qualitative changes in the ciliary dynamics such as the transition from oscillatory mode to quiescent mode. From a point of view of the control theory, the model behaviours of this kind are worth discussing because it is very efficient to change dynamics of 'distributed systems' like cilia via a slight change in a single parameter. The present model analysis would give us a bridge between experimental observations under different Ca^{2+} concentrations and simulation results with different parameter values.

Note

- 1 This is not always the case for the ciliary model, which will be examined in the next section, because there is a basal region involving a strong shear resistance in the model.

9 Large-amplitude oscillations and bend propagation

Having developed simplified models for small-amplitude flagellar- and ciliary-like beating patterns in a viscous medium (Chapters 7 and 8), we now turn to a more realistic model to account for large-amplitude oscillations and bend propagation. Key assumptions in developing the model are that (i) each dynein arm has multiple active sites or 'heads', which are distributed along most of the 24 nm distance between adjacent B-subtubule attachment sites; and (ii) any given dynein molecule tends to produce force continuously during interdoublet sliding in one direction and to produce little force during sliding in the opposite direction. Assumption (i) ensures that sliding movement occurs smoothly, because a single dynein is capable of producing active force continuously via multiple heads. Assumption (ii) describes directional sensitivity of the dynein system, which is necessary for regulation of flagellar oscillations and bend propagation.

Section 9.1 outlines the recent experimental data concerning dynein mechano-chemistry. Indeed, it is necessary to have virtually complete information about dynein mechano-chemistry. However, there has been controversy concerning dynein substructure and function as reviewed by Goodenough and Heuser (1985a), by Johnson *et al.* (1986), and by Brokaw and Johnson (1989). Thus I believe that any theory directed at elucidating the essence of mechano-chemistry is valuable and necessary at the present time. Section 9.2 summarizes the experimental study of periodically forced flagellar oscillators. Since this study has a short history, little is understood about the underlying mechanisms. Section 9.3 outlines the previous excitable-dynein model. As a model for a short segment, two opposed dyneins are combined with a passive elastic component in Section 9.4. Likewise in Chapters 6 and 7 the segment model displays bi-stable and oscillatory behaviours depending on the magnitude of the elastic components, but differs at large amplitudes. This is discussed in Section 9.5. Many such segment models are arranged one-dimensionally in order to develop a model for a whole flagellum. In Section 9.6 the model flagellum is tested for its ability to describe bend propagation.

When forced oscillations are applied to the basal end of the flagellum by the sliding displacement, successive bend propagation can occur even in the absence of a curvature-control mechanism. In Section 9.7 we emphasize the characteristics of the present model in comparison with the other model.

9.1 Dynein substructure and function

Two distinct interpretations of experimental studies have been proposed for the two rows of dyneins referred to as outer and inner arms along the A-subtubule of each outer doublet (see Fig. 4.3). The classical interpretation is that the inner and outer arms contribute equally to the beating as well as the sliding movement. This is based on the observations that removal of the outer dyneins from sea-urchin sperm flagella results in a 50% reduction in beat frequency without a significant change in beat pattern (Gibbons and Gibbons, 1973), and also results in a 50% reduction of sliding velocity (Yano and Miki-Noumura, 1981). Recent technical developments in biochemistry and electron microscopy, however, have provided a new interpretation that the two types of arms are significantly different in structure and function, and this has caused a good deal of controversy.

9.1.1 Outer dyneins

The study of outer dyneins has a rich history, and it is a subject of controversy. Here we begin with different types of models for outer dyneins.

A traditional model of outer dyneins is illustrated in Figure 9.1A. Goodenough and Heuser (1982), however, proposed another model from the studies of quick-frozen deep-etched replicas of *Tetrahymena* and *Chlamydomonas* axonemes, which is depicted in Figure 9.1B, C, D. The Goodenough and Heuser model assumed that (i) each dynein arm has five morphologically discrete components; (ii) a single point of the components interacts with the adjacent B-subtubule; and (iii) the conformational changes of a dynein from a rigor (Fig. 9.1B) to a relaxed state (Fig. 9.1C) are responsible for the power stroke (Fig. 9.1D).

On the contrary, another model was provided from studies on the dyneins of *Tetrahymena* by scanning-transmission electron microscopy (Johnson and Wall, 1983a; 1983b) and by kinetic analysis (Shimizu and Johnson, 1983). The model assumed that (i) each dynein has three active sites called 'heads'; (ii) there is one *ATPase* site on each dynein head; and (iii) all the three heads interact functionally with the B-subtubule in an ATP-sensitive manner. Besides the above models, there are many others to account for outer dynein substructure as shown in Figure 9.1E.

The spate of controversy described above probably results from a diversity in dynein substructure from one species to the next: there are three heads in the outer dynein arms of *Chlamydomonas* (Witman *et al.*, 1982) and

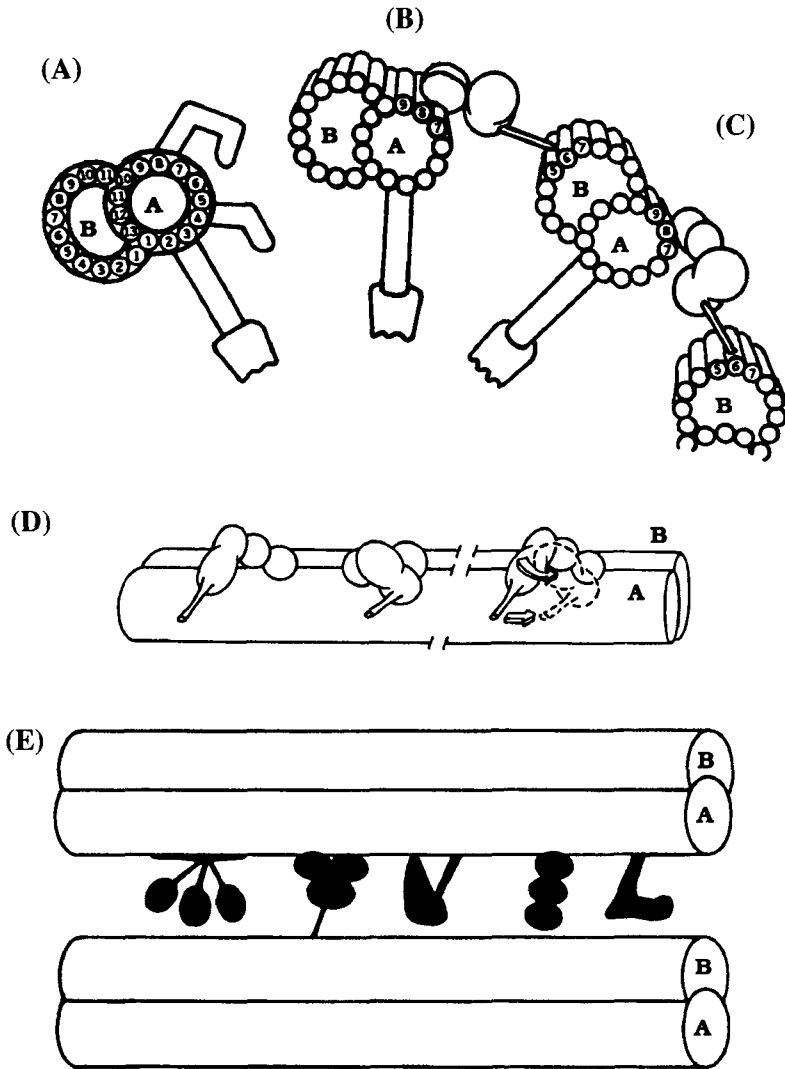


Figure 9.1 Schematic representations of various models of the dynein arm. A and B are the A- and B-subtubules. (A): Traditional representation of outer and inner arms (see Figs. 4.3 and 4.4). Diagrams (B)–(D) show the model by Goodenough and Heuser (1982). (B): Outer arm in the rigor state. (C): Outer arm in the relaxed state. (D): Power stroke of outer arm. The transition from relaxed (left) to rigor state (middle) is associated with the power stroke (right). The observer is facing the side of an A-subtubule, seeing the arms from the perspective of the neighbouring B-subtubule. (E): Other models of dynein. Left to right: Three-headed bouquet model by Johnson and Wall (1983b); three-subunit mouse model by Heuser and Goodenough (1981); club model by Witman and Minervini (1982); Three-subunit rod model by Warner *et al.* (1977); and hook model by Allen (1968). From: (A)–(D) Goodenough and Heuser (1982). Reprinted with permission of the Rockefeller University Press. (E) Johnson and Wall (1983a). Reprinted with permission.

Tetrahymena (Johnson and Wall, 1983a; 1983b), and two heads in the outer dynein arms of sea-urchin sperm flagella (Sale *et al.*, 1985). What is even more complicated, there do not appear to be any significant kinetic differences between the three dynein heads of *Chlamydomonas* and *Tetrahymena* (Johnson *et al.*, 1986), though there are functional differences between two-dynein heads of sea-urchin sperm flagella (Penningroth and Peterson, 1986).

Despite the spate of controversy over structure and function of outer dyneins, the role of outer dyneins in the control of bend propagation is considered to be of less importance. One reason is that sea-urchin sperm flagella (Gibbons and Gibbons, 1973) and some *Chlamydomonas* mutants (Kamiya and Okamoto, 1985; Mitchell and Rosenbaum, 1985), which are lacking the entire outer arm, are still capable of swimming. Another reason is that other *Chlamydomonas* mutants with large defects in inner dyneins lack beating motility (Kamiya *et al.*, 1989). It is therefore concluded that (i) the inner arms alone are necessary for motility, probably in concert with the radial-spoke system, and that (ii) the outer arms just amplify this activity.

9.1.2 Inner dyneins

Goodenough and Heuser (1985b) analysed the inner dynein arms of several different organisms such as sea-urchin, *Chlamydomonas* and *Tetrahymena* by using a quick-freeze, deep-etch technique. Whereas sea urchin 'outer' arms have two heads and *Chlamydomonas* and *Tetrahymena* 'outer' arms have three heads (see Section 9.1.1), all three organisms have common 'inner'-dynein substructure. As shown in Figure 9.2, the common features are that (i) there are two distinct species of inner arm, one with two heads and the other with three; (ii) these heads fan out into the interdoubtlet space; and (iii) they bind to the A-subtubule with a 24–32–40 nm sequence of intervals rather than the regular 24 nm interval of outer arms.

Through electron-microscopic analyses of *Chlamydomonas* flagella, however, Piperno *et al.* (1990) provided the new aspects of the molecular composition of inner dyneins as follows. (i) The inner arms are distinguished as three distinct structures. (ii) Each inner arm has two 'heads', each having an ATPase site. (iii) Three distinct inner arms are located in precise positions relative to the radial spokes, which leads to the 24–32–40 nm sequence of intervals. Though observations (i) and (ii) are inconsistent with those obtained by Goodenough and Heuser (1985b), observation (iii) is in agreement with the model shown in Figure 9.2. Since binding sites on the B-subtubule are available at 24 nm intervals (Takahashi and Tonomura, 1978), the irregular intervals of inner dyneins ensure that sliding movement occurs smoothly. If, in addition, multiple heads of inner dyneins are functionally equivalent, they may be causing continuous force generation.

An important observation is that some *Chlamydomonas* flagellar mutants with large defects in inner dynein arms that lack beating motility, still

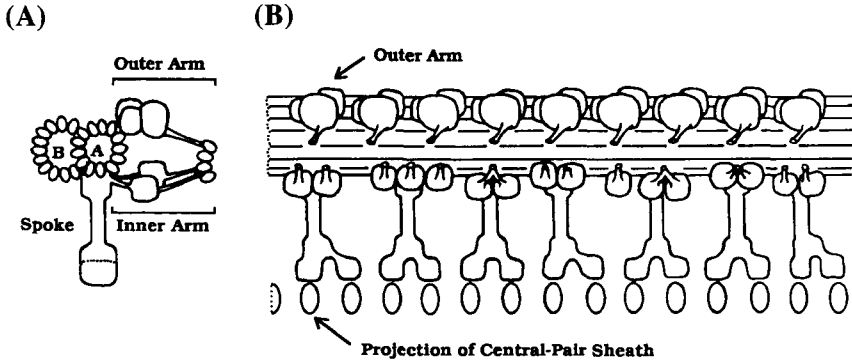


Figure 9.2 (A): Cross-sectional diagram of a set of A- and B-subtubule, outer and inner arms, and a radial spoke. (B): Longitudinal configuration of the same set as in (A) as viewed from right to left. Outer arms are spaced at 24 nm (upper part). The two-headed inner arms are in register with the outer arms, whereas the three-headed inner arms span the distance between the two outer arms (lower part). The mismatch between the heads of outer arms and heads of the inner arms would contribute to a smooth sliding movement. Y-shaped rods represent radial spokes. From Goodenough and Heuser (1985b). Reprinted with permission of the Rockefeller University Press.

undergo sliding motility upon perfusion with Mg-ATP and protease (Kamiya *et al.*, 1989). This observation suggests that (i) non-motile axonemes result from the loss of a control mechanism, but not from the lack of sliding motility, and (ii) the locus of control mechanism is in the inner arm. Much work must be done against external viscosity when axonemes beat in a viscous medium (cf. Brokaw and Benedict, 1968) as compared with sliding motion alone (cf. Kamimura *et al.*, 1985). It is, therefore, possible to consider that (i) the mechanism that controls sliding is quite different from that of beating, (ii) the functional difference between the sliding and beating motility is ascribed to the structural and/or functional difference between the inner and outer arms, and (iii) the irregular intervals of inner arms affect the control mechanism which converts sliding into bending motion.

9.2 Regulation of flagellar oscillations

It is clear that the minimal requirement for bend propagation is the inner dyneins in concert with resistive components such as nexin links and radial spokes. However, little is known about the regulation of sliding among the nine doublets of the cylindrical axoneme as they are converted into planar bending waves. Gibbons *et al.* (1987) investigated these regulatory mechanisms by using a new technique in which the sperm head is held in the tip of a vibrating micropipette (Fig. 9.3A). The micropipette is capable of vibrating along any axis at frequencies up to 150 Hz. In the following experiments, the

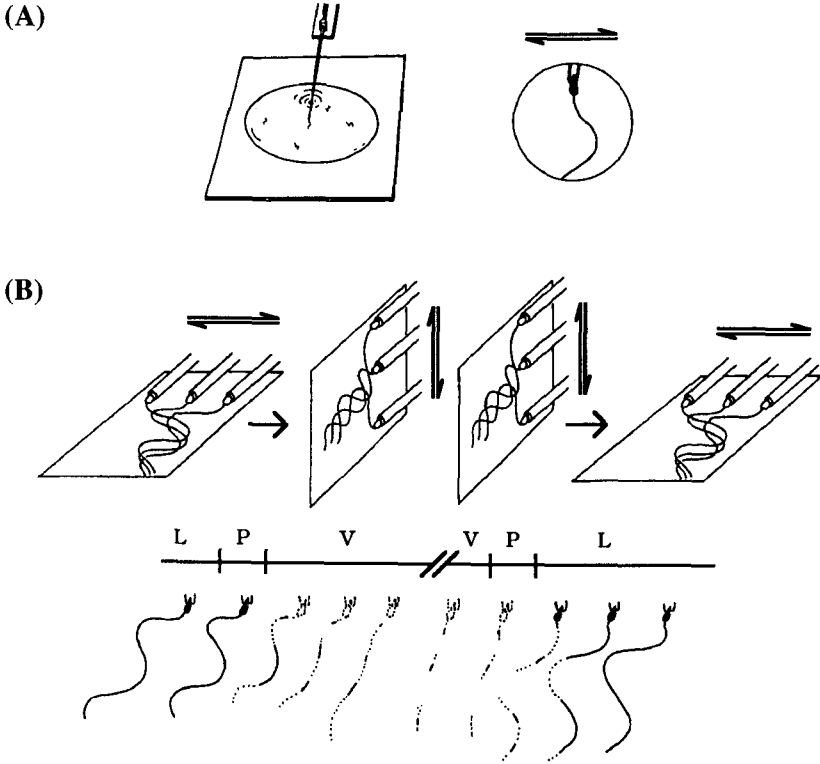


Figure 9.3 (A): Forced-oscillation apparatus. The tip of the sperm head is held in the tip of a micropipette by gentle suction (left). The micropipette can be oscillated along any axis. The planar flagellar beat is approximately in the focal plane of the microscope when the pipette vibration is set to be in the lateral direction (right). From Takahashi and Shingyoji (1989). (B): Experiments of abrupt change in the direction of pipette vibration. The direction of pipette vibration is abruptly changed from lateral (L) to vertical (V) and back, with a brief stationary period (P) of ~20 ms between the two directions of vibration. Upper panel: The three successive images are schematically shown for each direction of pipette vibration. Modified from Takahashi and Shingyoji (1989). Lower panel: Videotaped flagellar images are traced. Broken lines represent regions of the flagellum that are out of focus. From Gibbons *et al.* (1987). Reprinted with permission. Copyright © Macmillan Magazines Ltd.

vibration frequency was kept almost equal to the natural beat frequency of the flagellum. The direction of pipette vibration was then changed either abruptly or gradually.

Gibbons *et al.* first examined the effects of an abrupt change in the direction of pipette vibration (Fig. 9.3B). The pipette was initially vibrated in the direction of pipette vibration (Fig. 9.3B). The imposed movement of the head was within the plane of flagellar beat. Changing the direction of pipette vibration abruptly from

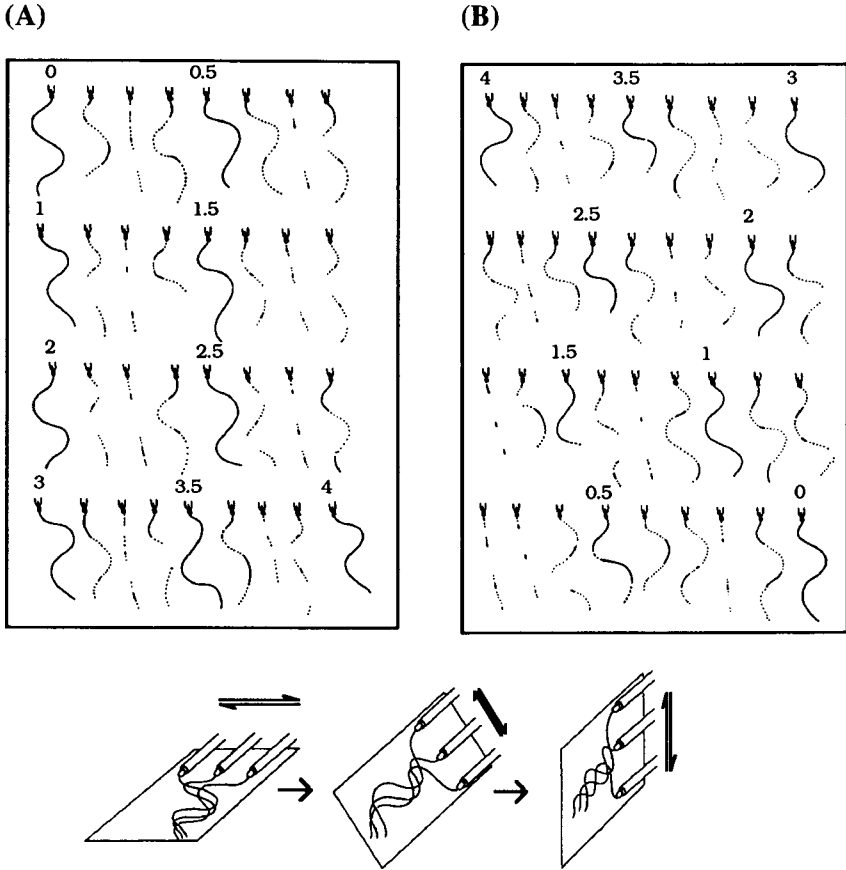


Figure 9.4 Experiments of gradual change in the direction of pipette vibration. The direction of pipette vibration is gradually rotated clockwise (lower panel). The numbers indicate the rotational sequence (upper panel). Broken lines represent regions of the flagellum that are out of focus. (A): Four complete cycles of rotation of the direction of pipette vibration are performed. The flagellar beat plane is wound up by four rotational cycles. (B): Cessation of the pipette vibration leads to the spontaneous unwinding of the flagellar beat plane. From Takahashi and Shingyoji (1989). Reprinted with permission.

lateral to vertical, the beating flagellum responds by forming the new beating plane as the imposed plane of the pipette vibration. This occurs within 50 ms (~ 2 beat-cycles). After resetting the vibration direction to lateral, the flagellar beat plane returned equally as quickly.

The second type of experiments were performed by changing the vibration direction gradually in a clockwise direction for several cycles (Fig. 9.4A). The vibration direction was initially set to be lateral and then rotated

gradually and continuously. The beat plane of the flagellum followed the vibration plane of the pipette for at least four complete cycles. Fig. 9.4A shows selected tracings of a beating flagellum over four cycles. The number assigned indicates the sequence of rotation. When the vibration was stopped after the completion of four rotations, the flagellum rotated back anti-clockwise for the same number of cycles (Fig. 9.4B). An interpretation of these results is that the pattern of active sliding among nine outer microtubules can rotate relative to the sperm head. Gibbons *et al.* (1987) considered that this active sliding was partially regulated by the central tubule complex, though the underlying mechanisms are still unknown.

9.3 Brief outline of the previous model

The behaviour of the previous model proposed in Chapter 7 is summarized by the movement of a 'ball' on the double-minimum-potential as a function of x (Fig. 9.5). Assuming that attachment sites are in register with dynein arms, a population of dyneins in a small segment of the flagellum is approximated by a localized distribution within a single sliding unit (see Fig. 9.7A). Let x ($0 < x < 1$) be a dimensionless distance between the dynein arm and its corresponding attachment site such that $x = 1$ corresponds to 24 nm. x_1 , x_2 and x_c are positions at which the original cubic force function of one dynein (say, subsystem I) crosses the x -axis (i.e. x_1 , x_2 and x_c are boundaries of force function changes). x_1 corresponds to the position where the attachment site is located within a single sliding unit for subsystem I. Similarly, x'_1 , x'_2 and x'_c are defined for the opposed dynein (say, subsystem II). These x (or x') values give either stable or unstable positions on the potential-energy curve obtained from the integration of the cubic force function of subsystem I (or subsystem II). To produce symmetric beating patterns typical of flagella, two opposed subsystems are assumed to be the mirror image of each other (i.e. $x_i = 1 - x'_i$ where $i = 1, 2$ and 3).

The upper and lower hysteresis functions in Figure 9.5 show the switching 'on' and 'off' of dynein activity in subsystems I and II, respectively. n_I and n_{II} are probabilities of attachment. S_1 and S_2 are sites of attachment and detachment in subsystem I, while the reverse is true in subsystem II because one subsystem is the mirror image of the other. This hysteresis switching function reflects the transition of dyneins, in which, for example, dyneins in subsystem I are in the 'on' state near attachment site at $x = x_1$ and are turned 'off' after power stroke for $x > S_2$. Consequently, 'on' and 'off' in opposed dyneins depend on the direction of sliding.

Suppose that the sliding displacement of x_1 is given such that dyneins in subsystem I are in the 'on' state (denoted by a black ball) and those in subsystem II are in the 'off' state (denoted by a white ball) (Fig. 9.5(1)). Perturbations with superthreshold x values ($> x_c$) cause 'active' sliding in the forward direction (increasing x) to amplify the initially applied displacement

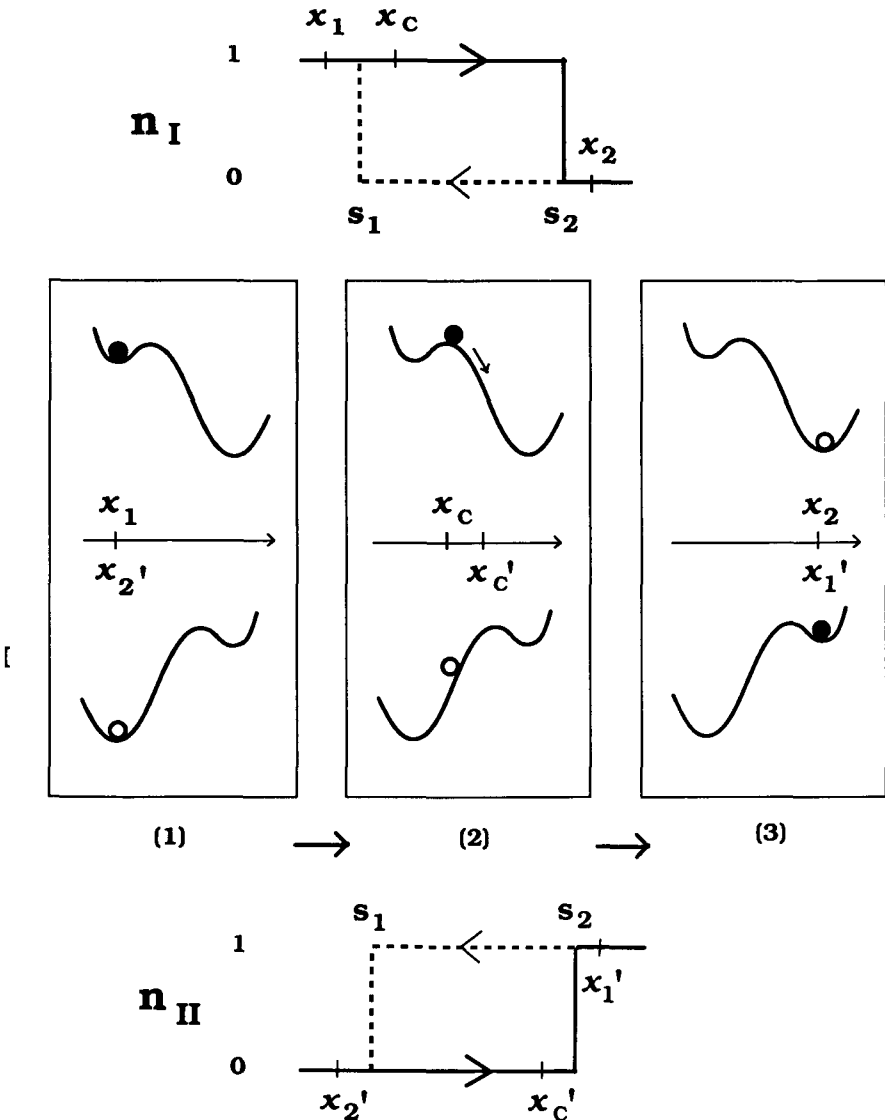


Figure 9.5 Diagrams showing hysteresis switching functions and potential-energy functions for opposed dyneins. The upper and lower panels show hysteresis switching curves n_I (for subsystem I) and n_{II} (for subsystem II), respectively, as a function of the sliding displacement x . The switching 'on' and 'off' of dynein activity is represented by discrete 1 and 0 values. The solid and dotted lines represent the states of dyneins in the forward (indicated by right-ward arrows) and backward (indicated by left-ward arrows) directions, respectively. The middle panel shows movements of a 'ball' on the potential-energy function, in which the upper part denoted by I indicates the dynamics in subsystem I and the lower part denoted by II shows dynamics of dyneins in subsystem II. For $x = x_1$, dyneins in subsystem I are initially in the 'on' state as indicated by the black ball and those in subsystem II are in the 'off' state as indicated by the white ball (in panel (1)). The superthreshold perturbation applied ($x > x_c$) causes active sliding in the forward direction (in panel (2)). When the sliding displacement exceeds $x = x_2$, dyneins in subsystem I are turned 'off' and those in subsystem II are turned 'on' (in panel (3)). From Murase (1991a). Reprinted with permission.

in this direction (Fig. 9.5(2)). The transition of a dynein to the force-generating state is referred to as *dynein excitation* or *dynein activation*. Note that dynein excitation occurs within the 'on' state (see Section 7.1). When sliding occurs further to exceed $x = S_2$ (where $0 < x_1 < S_1 < x_c < S_2 < x_2 < 1$), dyneins in subsystem I are turned 'off' and at the same time dyneins in subsystem II are turned 'on' following the solid lines in the direction shown in the n_I and n_{II} hysteresis functions, respectively. The occurrence of the switching 'on' and 'off' of dynein activity is indicated by a black ball and a white ball, respectively (Fig. 9.5(3)). The resultant sliding from x_1 to x_2 corresponds to a 'single' power stroke of the dynein and no further sliding occurs in the forward direction because of a lack of 'active' force enhancing the sliding in this direction (cf. low-amplitude assumption).

Because of the symmetric structure of the two opposed dyneins with respect to $x = 0.5$, both x_1 (or x'_2) and x_2 (or x'_1) are metastable positions so that backward sliding (decreasing x) does not occur without superthreshold perturbations in the form of the sliding in this direction. As a result, this model shows bi-stable behaviour in the absence of any other constraint (cf. Murase and Shimizu, 1986). However, once the passive elastic component is introduced with proper magnitude and with the proper equilibrium position, metastable positions are no longer 'stable' due to the disappearance of the potential barrier located near x_c (or x'_c). Then forward and backward sliding occur alternately, resulting in oscillations with small amplitude. Note that sliding direction is associated with the switching 'on' and 'off' of dynein activity, which is characterized by *directional sensitivity* (see Section 7.1).

9.4 A segment model for large-amplitude motion

For convenience, the cubic function is replaced by a piece-wise linear function without changing any other essential features of the previous model as follows:

$$F_1(x) = \begin{cases} Q_1 \cdot (-0.1x) & (0 \leq x < S_1) \\ Q_1 \cdot k_1(x - a_1) & (S_1 \leq x < a_2) \\ Q_1 \cdot (-0.1(x - 1)) & (a_2 \leq x < 1) \end{cases} \quad (9.1)$$

where x is a dimensionless distance between a dynein arm and its corresponding attachment site, $k_1 = 0.1(1 - a_2 + S_1)/(a_2 - S_1)$, $a_1 = S_1/(1 - a_2 + S_1)$ and Q_1 is the factor corresponding to the number of dyneins. The magnitude of parameters is in the order: $0 < S_1 < a_1 < a_2 < S_2 < 1$. We define x by $x = \text{mod}(\sigma, 1)$, where σ is the shear angle between the two adjacent doublets along which F_1 functions are periodically arranged (the middle panel of Fig. 9.6). This means that the attachment sites are periodically arranged along the microtubule as indicated by $\sigma = -1, 0, 1$ and 2 (which correspond to $-24, 0, 24$ and 48 nm, respectively). The potential-energy curve for each F_1 function is schematically drawn (the upper panel of Fig. 9.6).

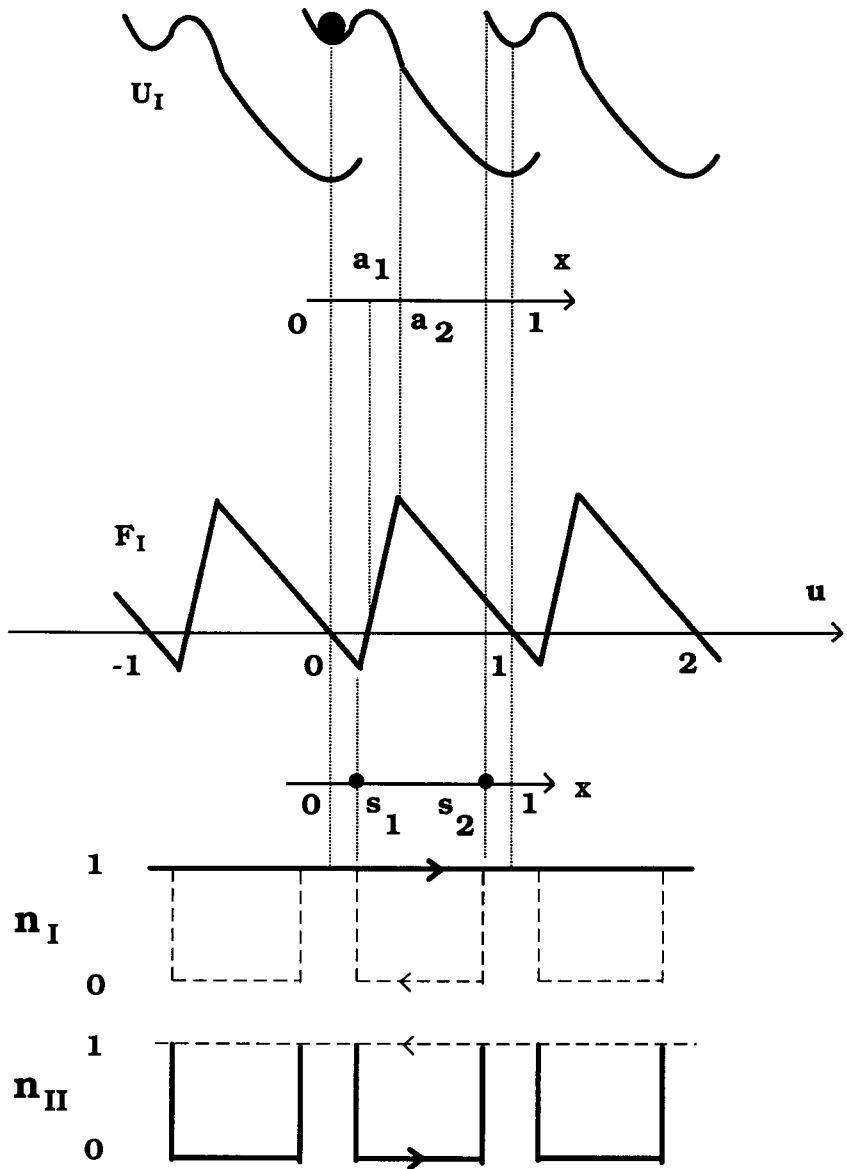


Figure 9.6 Diagrams showing potential-energy functions (upper panel), force functions (middle panel) and hysteresis switching functions (lower panel) for the modified excitable model. The sliding displacement x is defined by $x = \text{mod}(\sigma, 1)$, where σ is the 'net' sliding displacement. Reflecting the periodic structure of microtubules, each function has the periodic form with respect to the net sliding displacement. Functions n_I and n_{II} represent the 'on-off' switches in subsystems I and II, respectively. Solid and dotted lines in n_I and n_{II} indicate states of dyneins during the forward and backward sliding, respectively. $\sigma = -1, 0, 1$ and 2 correspond to $-24, 0, 24$ and 48 nm, respectively. a_1 defines the threshold value for sliding in the forward direction. From Murase (1991a). Reprinted with permission.

Successive attachment of dyneins is allowed to occur by modifying the hysteresis switching mechanism (the lower panel of Fig. 9.6). After this modification, the model possesses the ability to generate large sliding displacement. Note that the n_I (or n_{II}) function represents the switching dynamics for subsystem I (or subsystem II), and that each solid (or dotted) line shows dynamics of dyneins in each subsystem during the forward (or backward) sliding motion. Similarly to the previous model for flagellar dynamics, both dynein subsystems are assumed to be the mirror image of each other so that they generate symmetric beating patterns.

Let us consider imposed sliding starting from $\sigma = 0$ (i.e. $x = 0$) in the forward direction. In the previous model, dyneins in subsystem I initially in the 'on' state are turned 'off' when they exceed the switching point at $x = S_2$, and at the same time the opposed dyneins in subsystem II are turned 'on' following each solid line in the direction indicated by the arrow (see Fig. 9.5(3)). In the present model, however, dyneins in subsystem I initially in the 'on' state are assumed to be in the 'on' state as long as sliding occurs in the forward direction. This is based on the assumption that detachment and re-attachment processes occur very rapidly at $x = S_2$ in comparison with the velocity of sliding. On the contrary, dyneins in subsystem II initially in the 'on' state are turned 'off' at $x = S_1$ and 'on' at $x = S_2$ during forward sliding. As a result, the time-dependent 'on-off' patterns of dynein activity in subsystem I are quite different from those in subsystem II. Asymmetric 'on-off' patterns of this kind can be ascribed to directional sensitivity of dyneins. For each dynein subsystem, the combination of force-distance function and hysteresis mechanism results in *threshold phenomena*.

If there were multiple active sites within a single dynein, they would contribute to producing continuous sliding in one direction over a single sliding unit. In the present model, two or three active sites are introduced instead of a single active site within a single dynein arm (Fig. 9.7), so that the number of 'balls' on the potential-energy curve shown in the upper panel of Figure 9.6 should be changed to two or three. Note that two or three active sites are turned 'on' only when they pass through attachment sites reflecting the ATP-driven mechano-chemical cycle. This dynamic property results from the hysteresis switching mechanism of dynein activity. As a result, the multiple-active-site system shows directional sensitivity.

If all the 'heads' of the outer dyneins were not functionally equivalent, the inner dynein 'arms' could compensate for the lack of multiple interactions between the 'heads' of the outer dyneins and the B-subtubule. Suppose the situation is as illustrated in Figure 9.8A. Now consider a small segment of length Δs (say, $\Delta s = 1 \mu\text{m}$). There are a lot of inner dynein arms within this segment. Many such inner arms generate forces which contribute to sliding movement via the continuity of filaments. The most important variable is the distance between each dynein arm and its nearest-neighbour attachment site. If the distribution of the inner dynein active arms within the

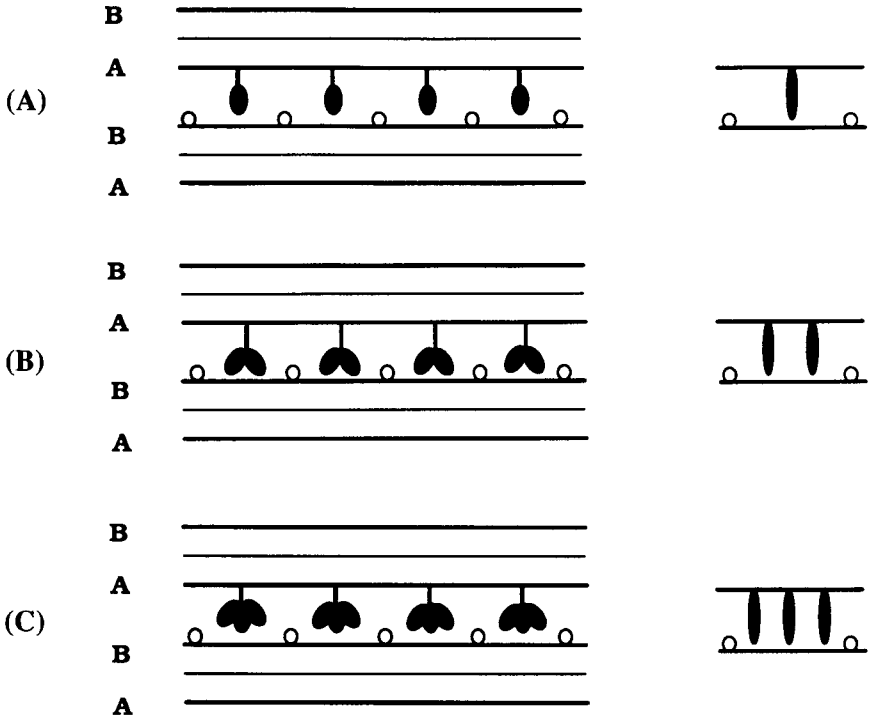


Figure 9.7 Schematic diagrams showing the arrangements of outer dynein arms. Outer dyneins, denoted by filled ellipses, are located on the A-subtubule at 24 nm intervals. The attachment sites, denoted by open circles, are located on the neighbouring B-subtubule at 24 nm intervals. (A): If only a single active site (or 'head') is available on a single dynein (left), a single distribution can be a good approximation of the population of dyneins within a small segment (right). (B): Outer arms of sea-urchin sperm flagella have two heads (left). If two such heads are functionally equivalent, the distribution splits into two subsets (right). (C): Outer arms of *Chlamydomonas* and *Tetrahymena* flagella have three heads (left). If three such heads are functionally equivalent, the distribution splits into three subsets (right). From Murase (1991a). Reprinted with permission.

segment is plotted against the distance between the nearest-neighbour sites, the distribution is not localized like Figure 9.7A, but it splits into two subsets (see right panel of Fig. 9.8A) because the inner arms are partially staggered by 8 nm. This corresponds to the situation where each outer dynein has two functionally equivalent active sites as illustrated in Figure 9.7B. Therefore, the fundamental formulation of the present model would remain unchanged, except for the distance between the two split distributions. If each inner arm has two or three heads (Fig. 9.8B,C), the number of the distribution of inner dynein active sites is increased but the essential features do not change.

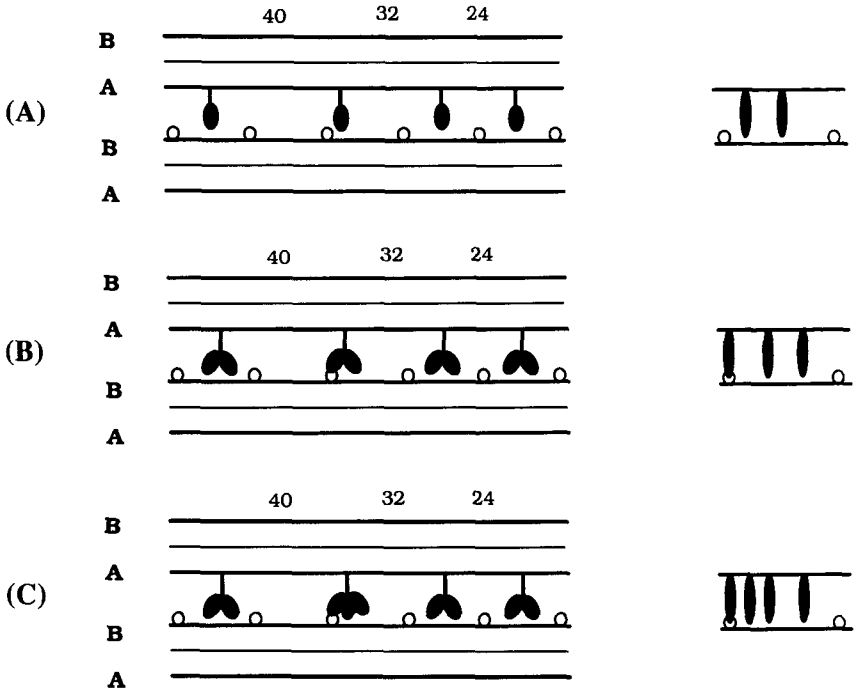


Figure 9.8 Schematic diagrams showing the arrangements of inner dynein arms. The inner arms, denoted by filled ellipses, are spaced at repeating intervals of 24, 32 and 40 nm on the A-subtubule, the same period as the radial spokes. The attachment sites, denoted by open circles, are located on the neighbouring B-subtubule at 24 nm intervals. (A): Even though a single active site (or 'head') is available on a single dynein (left), the population of dyneins within a small segment is approximated by two distinct distributions because the inner dynein arms are staggered by 8 nm relative to the attachment sites (right). (B): If each inner arm has two heads as reported by Piperno *et al.* (1990) (left), the distribution splits into three subsets (right). (C): If inner arms have two or three heads as reported by Goodenough and Heuser (1985b) (left), the distribution splits into four subsets (right). From Murase (1991a). Reprinted with permission.

Consequently, it does not matter whether multiple heads of outer dyneins are functionally equivalent. The significant requirement for the present model is that active sites, either 'heads' or 'arms', are distributed over the adjacent sites on the B-subtubule.

9.5 Large-amplitude sliding motion

The behaviour of a single segment is simulated by solving the following complete system of equations:

$$\gamma \frac{d\sigma}{dt} = \Sigma[F_I(x)n_I(x) + F_{II}(x)n_{II}(x)] - K_e(\sigma - \sigma_0) \quad (9.2a)$$

$$x = \text{mod}(\sigma, 1) \quad (9.2b)$$

$$F_I(x) = \begin{cases} Q_1 \cdot (-0.1x) & (0 \leq x < S_1) \\ Q_1 \cdot k_1(x - a_1) & (S_1 \leq x < a_2) \\ Q_1 \cdot (-0.1(x - 1)) & (a_2 \leq x < 1) \end{cases} \quad (9.2c)$$

$$F_{II}(x) = -F_I(-x) \quad (9.2d)$$

$$n_I(x) = 1 \quad \text{for } \dot{x} > 0 \quad (9.2e)$$

$$n_I(x) = \begin{cases} 1 & 0 < x \leq S_1 \text{ or } S_2 < x \leq 1 \\ 0 & S_1 < x < S_2 \end{cases} \quad \text{for } \dot{x} < 0 \quad (9.2f)$$

$$n_{II}(x) = 1 \quad \text{for } \dot{x} < 0 \quad (9.2g)$$

$$n_{II}(x) = \begin{cases} 1 & 0 < x \leq S_1 \text{ or } S_2 < x \leq 1 \\ 0 & S_1 < x < S_2 \end{cases} \quad \text{for } \dot{x} > 0 \quad (9.2h)$$

Equation (9.2a) describes the balance of all the shear forces. The contribution of multiple active sites must be summed up (see the first term of right-hand side of equation (9.2a)). γ is internal viscosity for sliding motion (taken as 30 pN ms/24 nm). K_e is the force constant of the passive elastic components. For large-amplitude sliding motion the sliding coordinate, x , is determined by the shear angle, σ , via equation (9.2b). Equation (9.2d) reflects the mirror image of the two subsystems I and II. Hysteresis switching mechanisms are represented by equations (9.2e–h).

9.5.1 Free sliding motion

The model proposed here was first tested for its ability to describe free sliding motion similar to that of the experiment by Summers and Gibbons (1971). For this purpose, $K_e = 0$.

As shown in Figure 9.9, this model exhibits steady-state sliding motion during which dyneins in subsystem I are successively turned ‘on’ while those in subsystem II are essentially turned ‘off’ to facilitate active sliding motion in one direction. It should be noted that this model would amplify the initially applied displacement in the same direction.

9.5.2 Excitability and oscillations with large amplitude

It is interesting to investigate the dynamic behaviours of this model when internal shear resistance is imposed corresponding to radial link systems like the nexin links and radial spokes. In practice, K_e is set to be non-zero.

When the value of K_e is relatively small (say 6 pN/24 nm), the system reaches a stable state after sliding occurs in several units (Fig. 9.10). The reverse is obtained when the initial sliding displacement is imposed in the

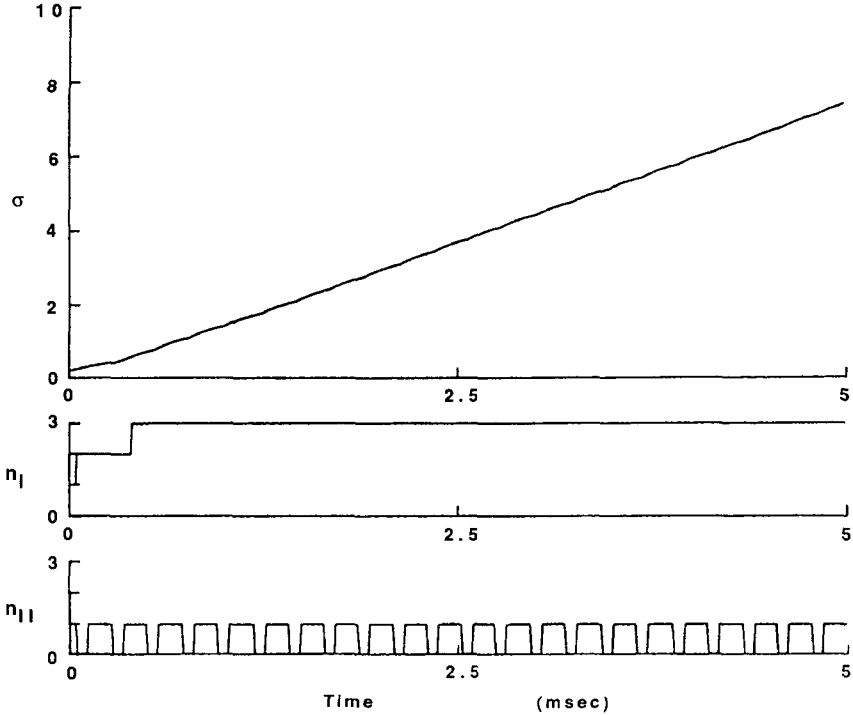


Figure 9.9 Free sliding movement of opposed dyneins. The net sliding displacement σ (upper), the total number of activated sites within a dynein in subsystem I (middle) and in subsystem II (lower) are plotted as a function of time t , where $\sigma = 0, 2, 4, \dots$ correspond to $0, 48, 96, \dots$ (nm), respectively. Steady-state sliding movement takes place when three sites are active within a dynein in subsystem I. During active sliding, one of the three sites within a dynein in subsystem II is alternately turned ‘on’ and ‘off’. This effect can be seen as the wavy line of the net sliding displacement σ . The parameters are: $\gamma = 30 \text{ pN ms}/24 \text{ nm}$, $Q_1 = 250 \text{ pN}$, $a_2 = 0.3$, $s_1 = 0.1$ and $s_2 = 0.9$. From Murase (1991a). Reprinted with permission.

opposite direction. Of course, no sliding occurs without initial perturbation. This behaviour is thus ascribed to ‘excitability’.

When the value of K_c is relatively large (say $8 \text{ pN}/24 \text{ nm}$), the state achieved after active sliding is no longer ‘stable’ and oscillations with large amplitude appear (Fig. 9.11). Therefore, this system resembles the previous model (Chapter 7) with respect to the excitability and oscillations, but differs in the sliding magnitude.

9.6 Bend propagation without curvature control

The most interesting thing to investigate was whether bend propagation can occur without a curvature-control mechanism. For this purpose, forced

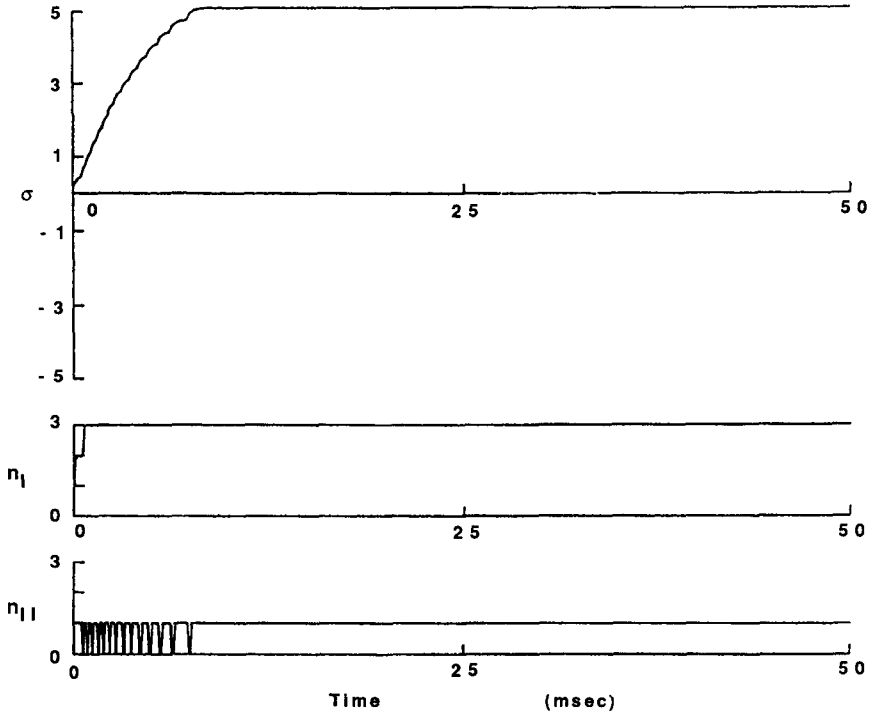


Figure 9.10 Sliding movement coupled with the passive elastic component. Parameters are the same as those in Figure 9.9 except for $K_c = 6 \text{ pN/24 nm}$. See the legend to Figure 9.9. From Murase (1991a). Reprinted with permission.

oscillations were applied to the basal end by sliding displacement to initiate successive bends.

The complete system of equations and boundary conditions has the form:

$$\frac{\partial^2 S}{\partial s^2} + E_B \frac{\partial^4 \sigma}{\partial s^4} + C_N \frac{\partial \sigma}{\partial t} = 0 \quad (9.3a)$$

$$x = \text{mod}(\sigma, 1) \quad (9.3b)$$

$$S = \Sigma[F_I n_I + F_{II} n_{II}] - K_e(\sigma - \sigma_0) \quad (9.3c)$$

$$\frac{\partial \sigma^3(0)}{\partial s^3} = 0; \quad \frac{\partial \sigma(0)}{\partial s} = 0 \quad (9.3d)$$

$$\frac{\partial \sigma^2(L)}{\partial s^2} = 0; \quad \frac{\partial \sigma(L)}{\partial s} = 0 \quad (9.3e)$$

$$\sigma(s = 0) = A \cdot \sin\left(\frac{2\pi}{T} t\right), \quad (9.3f)$$

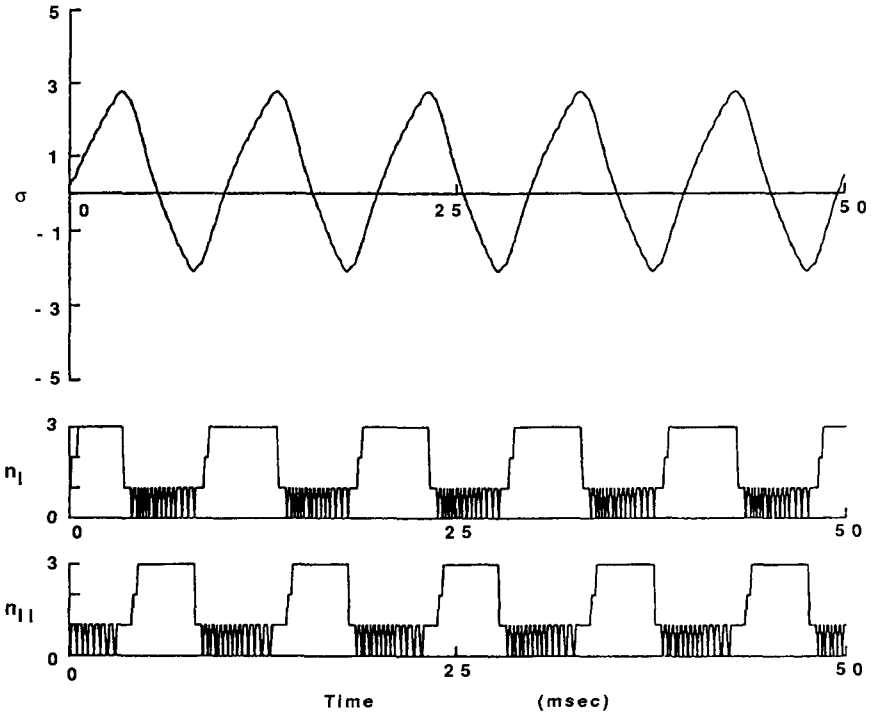


Figure 9.11 Large-amplitude oscillations. Parameters are the same as those in Figure 9.9 except for $K_c = 8 \text{ pN}/24 \text{ nm}$. Depending on the direction of active sliding, the ‘on-off’ patterns of subsystem I are quite different from those of subsystem II. See the legend to Figure 9.9. From Murase (1991a). Reprinted with permission.

where C_N and E_B are the external viscous coefficient (taken as $5 \text{ pN ms}/\mu\text{m}^2$) and the elastic bending resistance (taken as $1000 \text{ pN } \mu\text{m}^2$). L is the length of the flagellum (taken as $50 \mu\text{m}$). F_I , F_{II} , n_I and n_{II} are given by equations (9.2c–h). The axoneme is assumed to be pinned at the base and free at the tip as represented by equations (9.3d) and (9.3e), respectively. Equation (9.3f) describes the periodic driving stimulation at the base. Here A and T are the amplitude and the period of forced oscillation (taken as 0.5 and 40 ms , respectively).

Figure 9.12B shows the simulated flagellar shape at 5 ms intervals during bend propagation without a curvature-control mechanism. The simulated waves were constructed of circular arcs and straight lines as observed in real flagella (Brokaw, 1965). Figure 9.12A shows the shear angle, σ , as a function of the arc length, s , at 5 ms intervals. Although the peak-to-peak amplitude of the forced oscillations is equal to a single sliding unit (i.e. $2A = 1$ corresponds to 24 nm), the peak-to-peak amplitude of propagated waves is larger

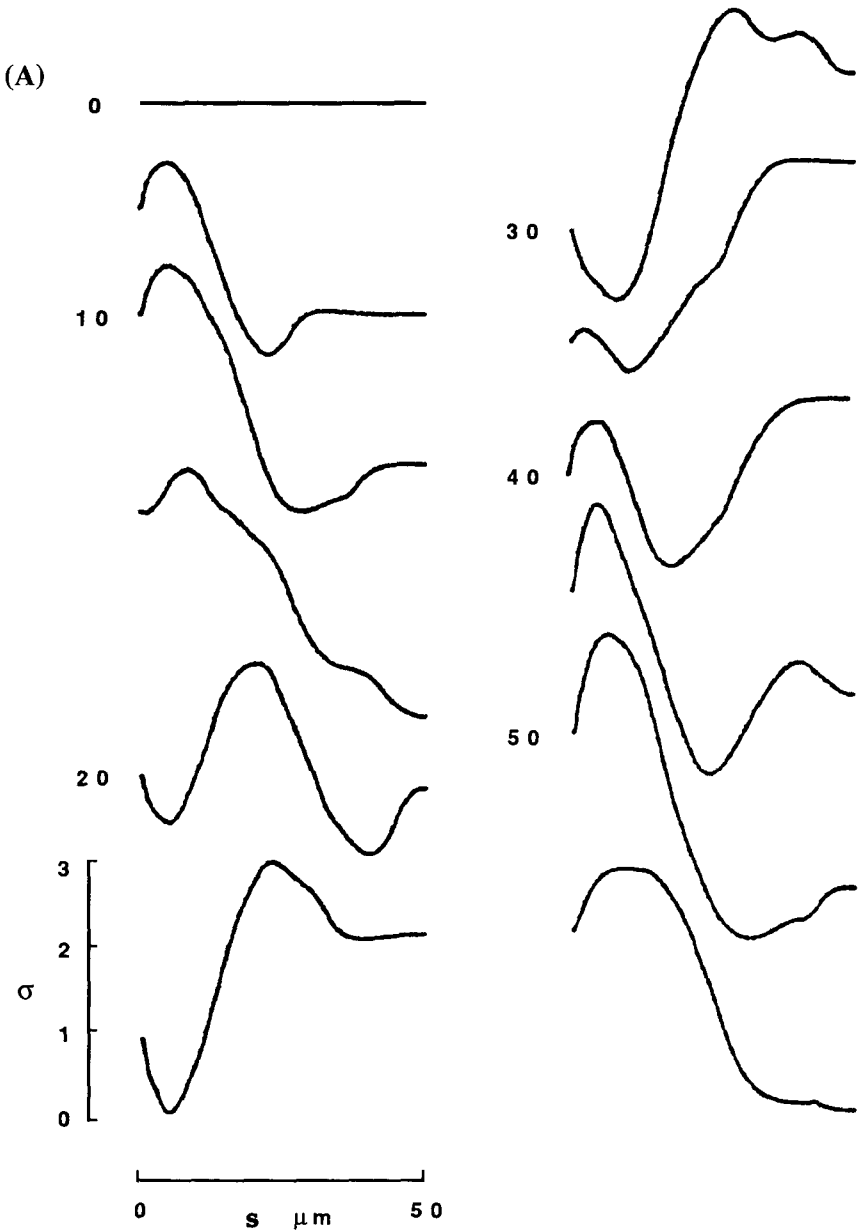
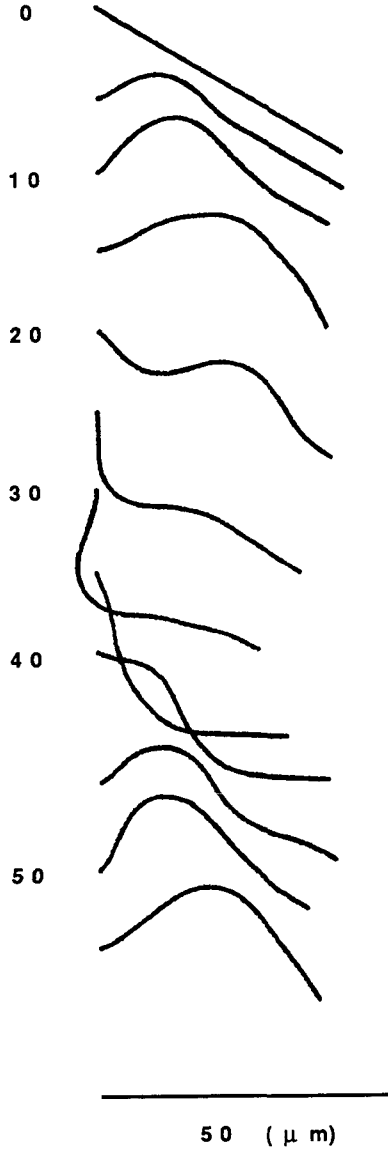


Figure 9.12 Large-amplitude bend propagation in response to a periodic forced oscillation at the basal end. (A): The net sliding displacement, σ , as a function of the arc distance, s , along the flagellum from the head. Successive σ - s distributions are displaced at 5 ms intervals. (B): The simulated waveforms of the flagellum. The left end corresponds to the basal end to which the forced oscillation is applied. Successive snapshots, taken at 5 ms intervals, are displaced downward. In equations (9.3), parameters are: $C_N = 5 \text{ pN ms}/\mu\text{m}^2$, $E_B = 1000 \text{ pN } \mu\text{m}^2$, $k = 5 \text{ pN}/24 \text{ nm}$, $Q_1 = 250 \text{ pN}$, $a_2 = 0.3$, $S_1 = 0.1$, $S_2 = 0.9$. The period of the applied oscillation is 40 ms. From Murase (1991a). Reprinted with permission.

(B)



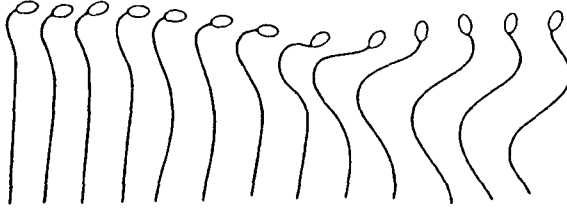


Figure 9.13 Starting transients of a sea-urchin sperm from rest to motion. The tracings, at intervals of 5 ms, of an observed sperm. From Rikmenspoel (1978). Reprinted with permission.

than this sliding unit. As shown in Figure 9.12A, sliding occurs in almost three units (which corresponds to 72 nm) in the axoneme except for the basal region.

Starting from a completely straight configuration, the model showed a short duration of starting transients (from $t = 0$ to 20 ms). The simulated starting transients partially resembled the observed transients, in which the motion was started by an increase of the bend near the proximal region as shown in Figure 9.13. After the transients, steady-state waveforms (from $t = 20$ to 55 ms) with large amplitude were obtained. There are one or two bends on the axoneme. The period of the steady-state waveforms was 40 ms, which was equal to the period of forced oscillation applied at the base. Unlike the previous model (Chapter 7), it was not necessary to introduce structural asymmetry such as a long passive terminal region at the tip. This is because multiple active sites stabilize the bending waves to get rid of perturbations induced by external viscosity, and also because forced oscillations are applied to the basal end.

9.7 Essence of the model behaviour

9.7.1 Dynamical behaviours of dyneins with multiple active sites

The formal dynein model with multiple active sites accounts for large-amplitude oscillations and bend propagation. Even though the two opposed dyneins initially possess symmetric ‘on-off’ patterns, the applied displacement causes *symmetry breaking* when the applied displacement is above a threshold value. The present model does not require that a population of dyneins be treated as a single distribution as in previous studies (Chapters 6, 7 and 8). Instead, the individual active site of a dynein is assumed to possess both the directional sensitivity (or hysteresis mechanism) and the displacement sensitivity.

Figure 9.14 illustrates how symmetry breaking occurs in response to superthreshold perturbations in the form of the sliding displacement. Let us consider the case of three active sites within a single dynein. Similarly to

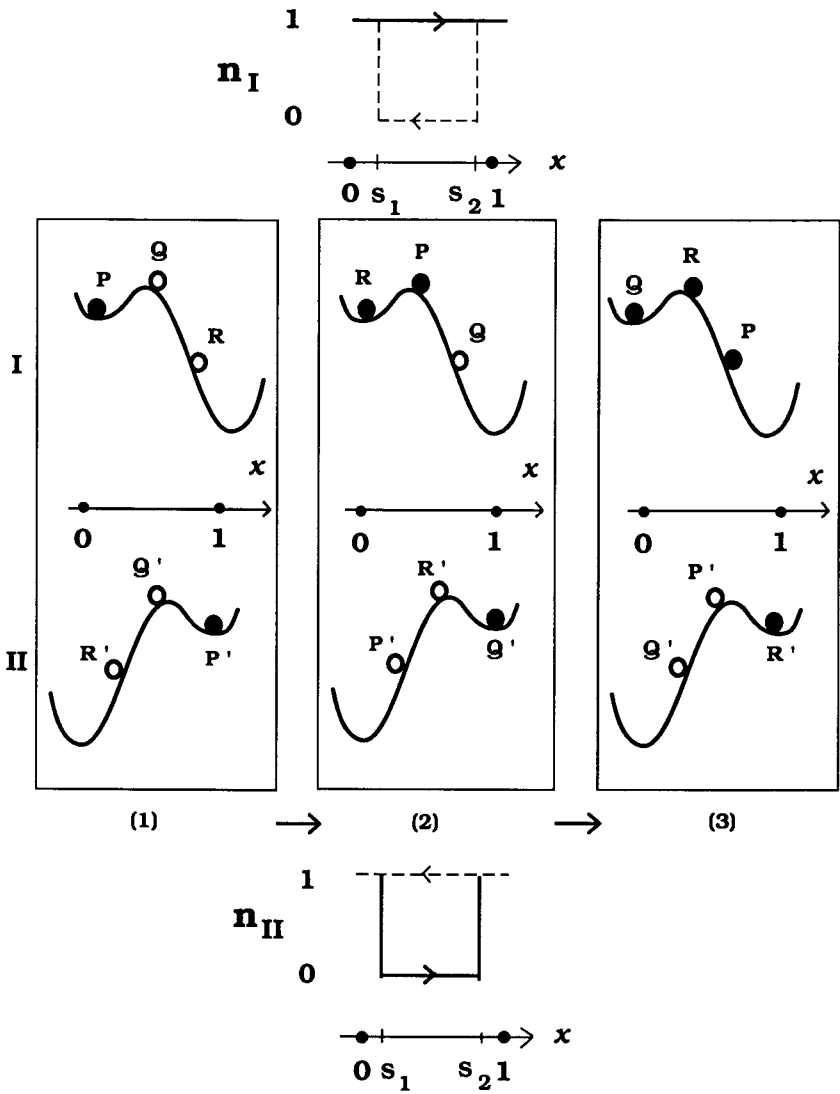


Figure 9.14 Diagrams showing hysteresis switching functions and potential-energy functions for modified dynein model. The upper and lower panels show hysteresis switching curves n_I for subsystem I and n_{II} for subsystem II, respectively as a function of the sliding displacement x . The 'on' and 'off' states are represented by 1 and 0 values, respectively. Solid and dotted lines show states of dyneins during forward and backward sliding, respectively. The middle panel shows movements of balls on the potential-energy functions, in which the upper part, denoted by I, indicates the dynamics of three active sites within a dynein in subsystem I and the lower part, denoted by II, shows the dynamics of three active sites within a dynein in subsystem II. As sliding movement takes place, the 'on-off' patterns of opposed subsystems become asymmetrical; that is, for subsystem I three sites are in the 'on' state, while for subsystem II only one of the three is in the 'on' state as indicated by panel (3). See text for details. From Murase (1991a). Reprinted with permission.

Figure 9.5, 'on' and 'off' states are represented by black and white balls on the potential-energy functions. Initially, the 'on-off' patterns of opposed dyneins are taken to be symmetric because one of the sites (say site P for subsystem I and site P' for subsystem II) close to the attachment site can only be in the 'on' state (in panel (1)). Suppose that a superthreshold perturbation, say, $x = 1/3$ ($> a_2$) is introduced; each site shifts its position by this displacement; that is, in subsystem I sites P at $x = 0$, Q at $x = 1/3$ and R at $x = 2/3$ (in panel (1)) change their positions at $x = 1/3$, $2/3$ and 0 , respectively like the 'circular relation' due to the periodic structure (in panel (2)). The reverse is obtained for the dynamics of dyneins in subsystem II. As a result of this superthreshold sliding displacement, the 'on-off' patterns become slightly asymmetric (in panel (2)). Then active sliding takes place automatically in this direction since the active force in subsystem I is larger than that in subsystem II. When the sliding displacement is $2/3$, the 'on-off' patterns become quite asymmetrical; that is, three sites are in the 'on' state for subsystem I while a single site is in the 'on' state for subsystem II (in panel (3)).

A similar discussion is available even when three active sites are replaced by two sites. One can understand that qualitative behaviour is retained when the balls R and R' are omitted from each panel in Figure 9.14.

The active sliding once initiated would persist until the sliding in this direction is interrupted by, for example, the passive elastic component. Depending on the magnitude of this passive elasticity, oscillations with large amplitude occur. The present model, therefore, seems to mimic the model behaviours studied in Chapters 6 and 7 with respect to excitability and oscillations.

9.7.2 Controversy over structure and function of dynein arms

Recent structural analyses of the outer dynein arms have revealed the presence of two or three heads which are associated with ATPase sites (Johnson *et al.*, 1986; Brokaw and Johnson, 1989). There has been controversy over the role of these multiple heads (see Johnson *et al.*, 1986). One group considered that there are functional differences between two dynein ATPases of sea-urchin sperm flagella (Penningroth and Peterson, 1986), and that all heads did not attach to the B-subtubule (Goodenough and Heuser, 1982; Sale *et al.*, 1985). Another group suggested that there do not appear to be any significant kinetic differences between the three heads of outer dynein arms from *Chlamydomonas* flagella (Shimizu and Johnson, 1983), and that all three heads interacted functionally with the B-subtubule in the ATP-sensitive way (Johnson *et al.*, 1986).

If the present study were based on the former consideration, the presence of inner dynein arms would compensate for the loss of outer dynein arms (Gibbons and Gibbons, 1973; Yano and Miki-Nomura, 1981). This is probably true because the inner dyneins are partially staggered, as occurs in

Chlamydomonas flagella (see Goodenough and Heuser, 1985b; Piperno *et al.*, 1990). As a result, dynein arms may be distributed along the distance between adjacent B-subtubule attachment sites. The distribution of dynein arms between the adjacent attachment sites is roughly equivalent to the situation where each dynein has multiple heads (or active sites) which are distributed between the attachment sites (compare Figs. 9.7 and 9.8).

Consequently, it does not matter whether multiple heads of the outer dyneins are functionally equivalent or not. Of importance is the assumption that more than one site (head or arm) can interact with the B-subtubule. This assumption is consistent with the previous assumption that two rows of dyneins are staggered at 4 nm relative to the rows of attachment sites (Brokaw, 1982), and that there is a continuous distribution of dyneins between adjacent attachment sites (Hines and Blum, 1978).

9.7.3 *Difference between Satir's model and the present model*

Satir (1984; 1985) has detailed a switching-point hypothesis in which he associates sliding direction with 'on' and 'off' of dynein activity. The present excitable-dynein mechanism is similar to Satir's switching dynein cycle with respect to the 'on' and 'off' of dynein activity. However, there is a significant difference between them. In Satir's dynein cycle, a dynein in the 'on' state produces an active force that leads to sliding; while in the present excitable-dynein cycle, a dynein in the 'on' state does not produce active sliding force unless it passes a threshold. This occurs because the 'on' state contains both 'preactive' and 'active' states in the original three-state cross-bridge cycle (Murase and Shimizu, 1986; Murase *et al.*, 1989). In other words, the present model assumes that a 'switching point' at $x = S_1$ is slightly different from a 'threshold point' at $x = a_1$ (see Fig. 9.6). Satir's dynein cycle, however, assumes that the turning 'on' of dynein activity and the onset of active sliding occur at the same point, which implies that a 'switching point' is equal to a 'threshold point'; that is, $S_1 = a_1$ in Figure 9.6.

9.7.4 *Some future work*

Simulated waveforms shown in Figure 9.12B mimic actual flagellar waves. However, several problems remain. First, the present system is driven back and forth by the periodic changes of sliding displacement on the assumption that the bend angle, θ , is equal to the sliding displacement, σ . As long as the forced oscillations are applied at the basal end, it is not necessary to consider the constraint concerning the relation of θ and σ (cf. Blum and Hines, 1979). The assumption that $\theta = \sigma$ is thus reasonably acceptable. Nevertheless an interesting extension of this study is to include pacemaker sites or autonomous oscillators at the basal region of the axoneme with excitable properties.

The study of such systems is necessary to understand the nature of free-swimming flagella.

Secondly, equation (9.3a) describing the balance of moments omits the higher order of nonlinearity (see Hines and Blum, 1979). To study large-amplitude wave propagation, we cannot neglect these nonlinear terms completely.

Finally, bends are allowed to occur only in a predetermined plane, since the present model has just two opposed dynein subsystems. To demonstrate the effects of change in the direction of pipette vibration as examined by Gibbons *et al.* (1987), we need to modify the model in such a way that it has nine doublets and accounts for three-dimensional bends.

In spite of the problems mentioned above, the present model is potentially extensible to get rid of the problems. It is possible that the excitable mechanism of the dynein force-generating system will be established by future studies.

10 From simple to complex dynamical behaviours in mechano-chemical cycles: hyperoscillations, bursting and chaos

We have studied the overall behaviours of flagella and cilia based on the simplified model of an elementary dynein–tubulin, mechano-chemical cycle (Chapters 7, 8 and 9). One of the most remarkable results of this approach is that a flagellum or a cilium described as an ensemble of these very simple elements can display surprisingly complex dynamical behaviours. The unsolved problem, however, is what sort of complexity arises in a single mechano-chemical system.

This chapter describes experimental and theoretical results in order to solve the above problem. Section 10.1 summarizes recent experimental data concerning *hyperoscillations* characterized by their high frequencies (~ 300 Hz) and low amplitudes (~ 4 nm) at the level of the dynein–tubulin dynamics. In Section 10.2 we develop the model of dynein–tubulin interactions, which is more realistic than the formal excitable-dynein model developed previously, *but still simple enough to deal with*. Section 10.3 discusses the overall dynamical behaviours of the model in the context of nonlinear dynamics. In Section 10.4 we explain how hyperoscillations appear and disappear in terms of the model behaviour. Section 10.5 discusses the more complex dynamical behaviours, such as *bursting* and *chaos*, arising in the model in response to periodic stimuli.

10.1 Mechano-chemical hyperoscillations

Kamimura and Kamiya (1989) developed a highly sensitive measurement technique in order to look more closely at the mechano-chemical conversion mechanism. Flagellar axonemes of demembrated sea-urchin sperm were fragmented and placed between a glass slide and a coverslip. Beads of sub-micrometre diameter were attached to the microtubules to act as indicators of microtubule sliding. These fragmented axonemes did not beat, instead they displayed high-frequency (~ 300 Hz), low-amplitude (~ 4 nm) oscillations – namely, *hyperoscillations* (Brokaw, 1990) – when reactivated.

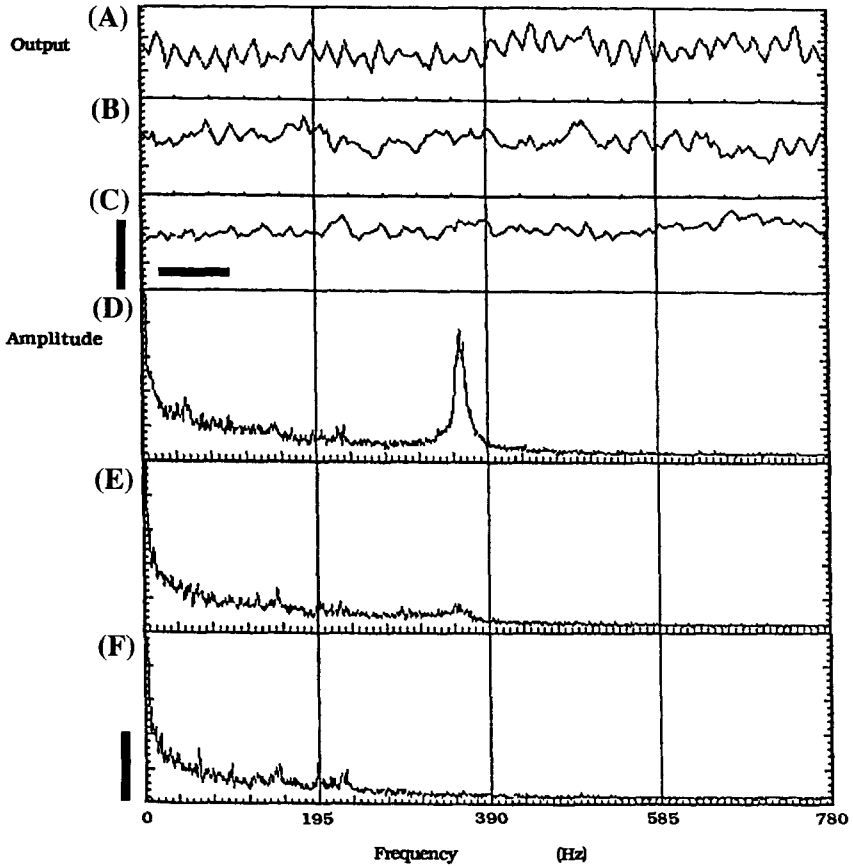


Figure 10.1 Movements of a microbead attached to an axoneme fragment under different chemical conditions. (A): Output from the optical detector showing hyperoscillations in the presence of 1 mM ATP. Vertical bar, 9 nm; horizontal bar, 10 ms. (B): Output from the same bead as in (A) in the presence of 1 mM ATP and 0.5 μ M vanadate. (C): Output from the same bead as in (A) in the absence of ATP. (D), (E) and (F) show FFT patterns obtained from the outputs shown in (A), (B) and (C), respectively. From Kamimura and Kamiya (1989). Reprinted with permission. Copyright © Macmillan Magazines Ltd.

Figure 10.1 shows the movements of a microbead attached to an axoneme fragment (in panels A–C) and the frequency spectra of these movements (in panels D–F) under different conditions. In the presence of 1 μ M ATP hyperoscillations appeared (Fig. 10.1A) as revealed by a sharp peak in the fast Fourier transform (FFT) spectra (Fig. 10.1D).

As biochemical conditions were changed, these hyperoscillations disappeared, and were replaced by an erratic movement attributed to *noise* (i.e. random thermal fluctuations). There were two ways by which hyperoscillations disappeared. In one, 0.5 μ M vanadate (a potent inhibitor of dynein ATPase)

was added (Fig.10.1B). This caused the remarkable decrease in the amplitude of the sharp peak shown in Figure 10.1D resulting in the FFT patterns in Figure 10.1E. The disappearance of hyperoscillations probably occurred as a result of the decrease in the fraction of the dynein attached in the force-generating state causing the decrease in the active force.

The second way by which hyperoscillations disappeared was through the reduction of the Mg-ATP concentration. As the Mg-ATP concentration was decreased, the vibration frequency decreased as can be seen in the shift of the peak in Figure 10.1D toward the left (i.e. low-frequency region) though without a remarkable change in its peak amplitude. In the absence of ATP the oscillatory movement disappeared (Fig. 10.1C and F). This ATP-dependence suggests that the bead movements reflect ATP-driven dynein-tubulin interactions.

The question that arises is how the dynein-tubulin system displays hyperoscillations. In the rest of this chapter I try to answer this question based on a simple model for the dynein-tubulin interactions, and then try to predict more complex dynamical phenomena.

10.2 The model

10.2.1 Mathematical description

The essential features of the original three-state model (Chapter 6) were approximated by the formal excitable-dynein model (Chapters 7 and 8) on the assumption that (i) a dynein undergoes 'spontaneous' transition between the 'on' and 'off' states, depending on the history of the dynein behaviour (characterized by hysteresis); and (ii) the dynein in the 'on' state obeys a cubic (or modified cubic) force-distance relationship (characterized by excitability). If, in addition to these two assumptions, multiple active sites within a single dynein head and/or the irregular intervals of inner dyneins were taken into account, shear oscillations of large amplitudes occurred (Chapter 9).

The present model assumes that (i) the fraction of the dynein attached changes 'gradually' rather than 'spontaneously'; (ii) the dynein attached shows a cubic force-distance function; and (iii) there are passive elastic and external shear forces. Let x , n and Z be the dimensionless sliding displacement ($x = 1$ corresponds to 24 nm), the fraction of dyneins attached (varying continuously between 0 and 1), and the external shear force, respectively. Then, the model can be expressed as:

$$\gamma \frac{dx}{dt} = nf(x) - K_c x + Z \quad (10.1a)$$

$$\frac{dn}{dt} = \begin{cases} b(1-n) & (x \leq x_a) \\ -cn & (x > x_a) \end{cases} \quad (10.1b)$$

where

$$f(x) = Ax^2(1 - x). \quad (10.1c)$$

A , b , c , K_e , x_a and γ are the force constant of the active dynein, the attachment rate constant, the detachment rate constant, the force constant of the passive elastic component, the attachment region and the internal viscous shear resistance, respectively. Here b and c are in ms^{-1} ; A , K_e and Z in pN per cross-bridge; and γ in pN·ms per cross-bridge. Equation (10.1a) describes the balance of all the shear forces. Equation (10.1b) shows that n is allowed to change continuously between 0 (completely lacking in excitability) and 1 (maximal excitability), depending on x . The x -dependence of the dynein behaviour reflects the x -dependent transition rate constants in the original three-state model.¹

There are several ways by which dynamical properties of the model can be represented. One way to predict the model behaviour is by numerical integration of equations (10.1). This numerical technique is useful in describing quantitatively the time evolution of state variables x and n . In addition to using numerical techniques, it is also useful to deduce important qualitative properties of the solutions to equations (10.1) without explicitly solving them. Examples of such qualitative visualizations are the force–distance representation, the potential-surface representation, and the phase-plane representation. The next three subsections describe these three qualitative analytical methods.

10.2.2 Force–distance relationship

By setting $dx/dt = 0$ in equation (10.1a), we have the following steady-state force–distance relationship for the model:

$$Z = -nf(x) + K_e x. \quad (10.2)$$

Figure 10.2 illustrates such force–distance relationships in the (x, Z) plane. When $n = 1$, there is a cubic force–distance relationship which has three intersections, P_1 , P_2 and P_3 , with the x -axis. These three points are the actual steady-state points when $Z = 0$. Intersection P_1 corresponds to a stable resting state, P_2 to an unstable threshold state, and P_3 to a stable excited state. Superthreshold x values lead to the excited state, P_3 , while subthreshold x values lead to the resting state, P_1 . This model, thus, accounts for a threshold phenomenon.

Instead of applying the superthreshold x values, an excited state is also achieved by increasing Z . As Z is increased (say, $Z = 0.004$), the intersections P_1 and P_2 approach each other. A sufficiently large value of Z makes P_1 and P_2 disappear. As a result, the phase point moves toward P_3 .

It is clear that the excited state is obtained by the shift of either x or Z . However, this excited state is not definitely stable because n begins to decrease according to equation (10.1b). We set $x_a = 0.2$, so that the excited

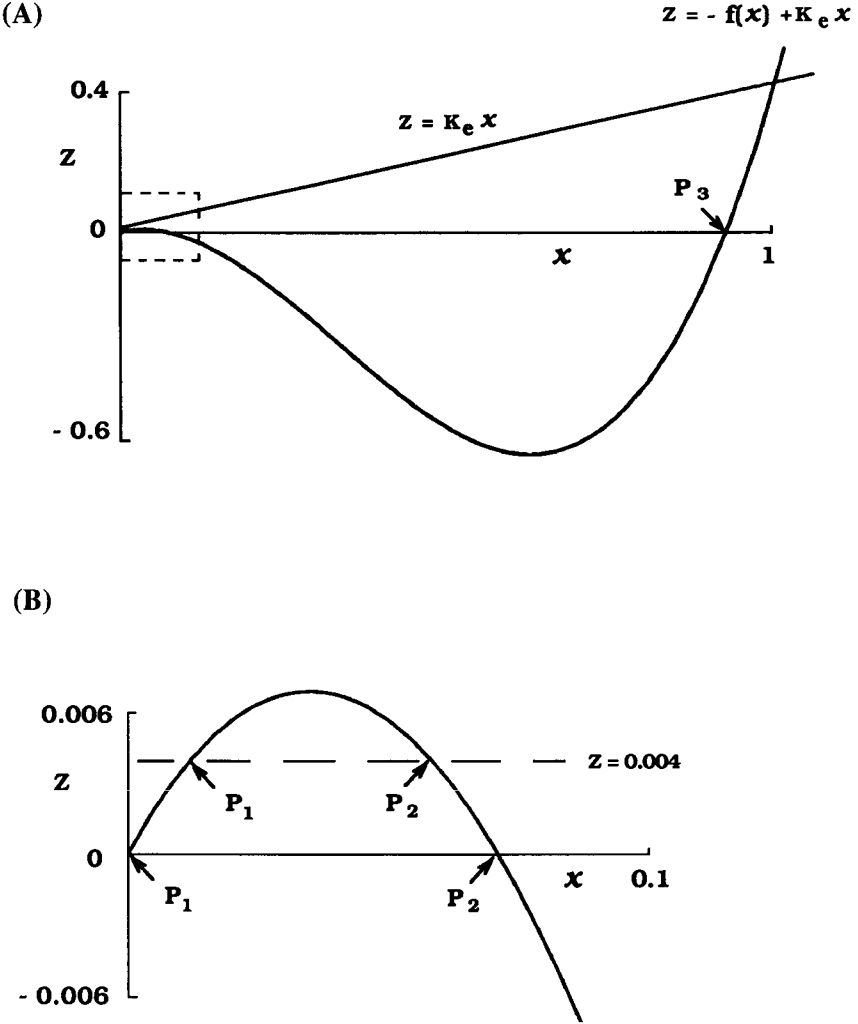


Figure 10.2 Force–distance characteristics. The area denoted by a broken square in panel (A) is enlarged in panel (B). When $Z = 0$ and $n = 1$, there are three steady states with two stable states, P_1 and P_3 , and one unstable state, P_2 . As n decreases from 1 to 0, the cubic function is replaced by a monotonic function. Interestingly, these force–distance characteristics are analogous to the well-known current–voltage characteristics of excitable membranes (see Fig. 3.19).

state exists in the region where detachment takes place (i.e. the decrease in n toward 0). The force–distance relationship changes dynamically from $Z = -f(x) + K_e x$ to $Z = K_e x$. The resultant force–distance relationship has only a single steady state at the origin, and so the system returns to this state. There is a refractory period during which the cubic force–distance relationship disappears, and hence there is no threshold phenomenon.

If Z is set at a value that causes the two intersections P_1 and P_2 to vanish, the system no longer stays in a stable steady state, but instead displays oscillatory behaviours. Depending on the constant values of Z , a number of different rhythms arise in which low- and high-amplitude oscillations can be observed (see Fig. 10.7).

Now it should be noted that, if the external force, Z , the sliding displacement, x , and the fraction of dynein attached, n , are viewed as the external current, I , the transmembrane voltage, V , and the generalized excitability parameter, Y (where Y can be considered as summing up the whole behaviour of the sodium activation m , sodium inactivation h , and potassium activation n , of the Hodgkin–Huxley model), then $Z = -f(x) + K_e x$ and $Z = K_e x$ are analogous to the current–voltage relationship for a maximally excitable membrane and that for a completely inexcitable membrane. In this analogy, the model described by equations (10.1) also accounts for the electrical excitability phenomena (see Section 3.6 and Fig. 3.19). Indeed this model resembles the simple version of the Hodgkin–Huxley model for an excitable membrane presented by van Capelle and Durrer (1980) and extended by Landau *et al.* (1987).

10.2.3 Potential-energy surface

The qualitative behaviour of the model described by equations (10.1) is predicted by the movement of a ‘ball’ on the potential-energy surface, $U(x, n)$. The energy surface is:

$$\begin{aligned} U(x, n) &= - \int_0^x (f(x) - K_e x) dx \\ &= An \left(\frac{x^4}{4} - \frac{x^3}{3} \right) + K_e \frac{x^2}{2}. \end{aligned} \quad (10.3)$$

Figure 10.3A illustrates the energy surface. When $n = 1$, there are two valleys separated by a peak, and the ‘ball’ will move to one or the other depending on its initial position. If it is placed to the left of the peak, it will move to the left minimum. If it is placed to the right of the peak (labelled 1), it will move to the right minimum (labelled 2). This corresponds to the monotonic increase in x (upper panel in Fig. 10.3B). Since the ‘ball’ leaves the activation region ($x > x_a$), n decreases monotonically (lower panel in Fig. 10.3B). As a result, the potential-energy function has a single valley and so

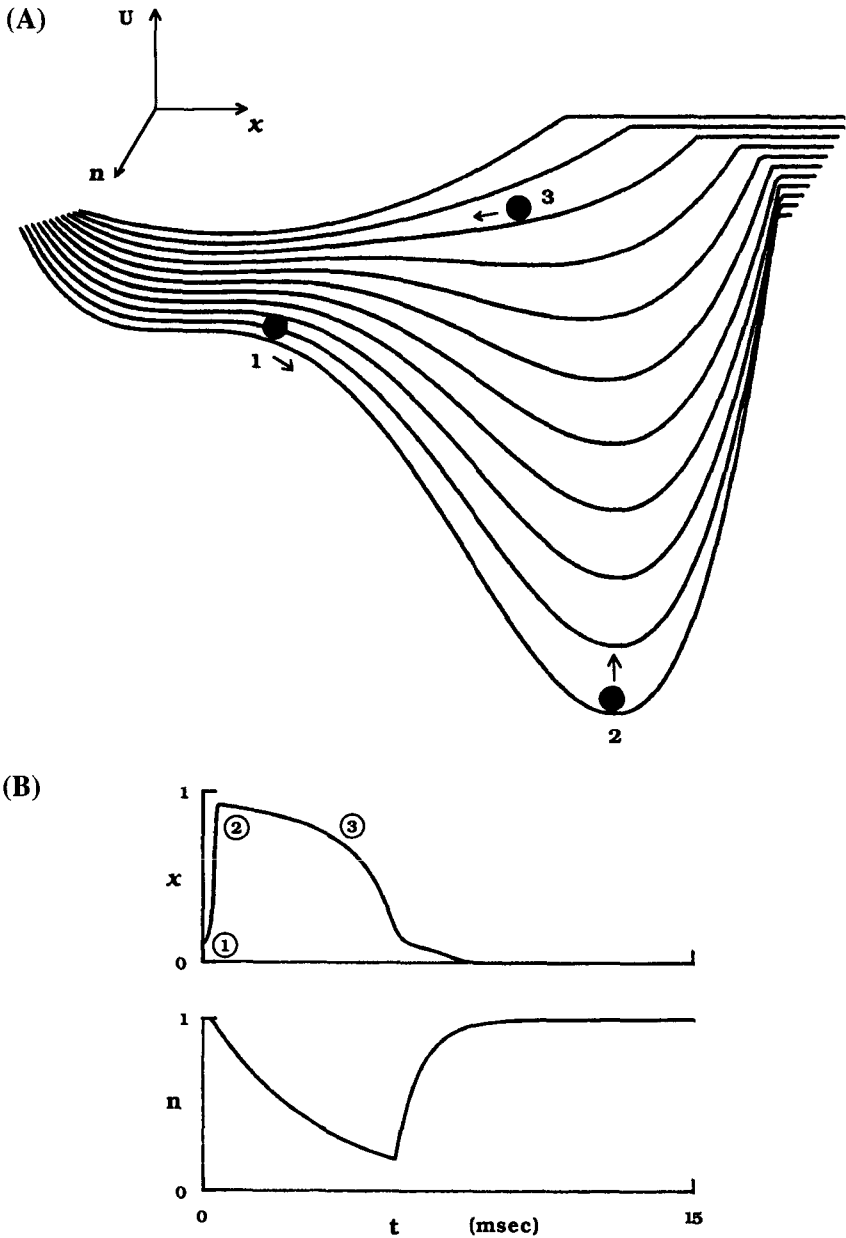


Figure 10.3 (A): Potential-energy surface, $U(x, n)$. There are three 'balls'. Numbers correspond to stages of the model behaviour, similarly marked in Figures 10.3B and 10.4. When $n = 1$, the potential has two valleys. As n decreases, however, the deeper valley disappears, leaving a single valley. The remaining valley corresponds to the resting state. (B): The time-course of x and n : x shows an 'action-potential'-like behaviour in nerve membrane. The circled numbers correspond to those in panel (A). Parameters are: $A = 6 \text{ pN}$, $b = 1.3 \text{ ms}^{-1}$, $c = 0.3 \text{ ms}^{-1}$, $K_c = 0.4 \text{ pN}$, $x_a = 0.2$, $\gamma = 0.1 \text{ pN ms}$, and $Z = 0$. Initial conditions are: $n = 1$ and $x = 0.1$.

the ‘ball’ moves to the minimum (labelled 3). Thus, the energy surface nicely summarizes the qualitative dynamics of x (see Section 8.2 and Figs. 8.3 to 8.5).

10.2.4 Phase-plane representation

The model behaviour is completely described by the state variables x and n . Solutions to equations (10.1) can be represented as trajectories in the (x, n) phase plane. A typical trajectory is given in Figure 10.4, which corresponds to the solution in Figure 10.3B. This figure also represents the vertical isocline or the x -nullcline (i.e. $\dot{x} = 0$) and the horizontal isocline or the n -nullcline ($\dot{n} = 0$). These nullclines are written as follows:

$$\dot{x} = 0 \quad n = \frac{K_e x - Z}{Ax^2(1-x)} \quad (10.4a)$$

$$\dot{n} = 0 \quad n = \begin{cases} 1 & (x \leq x_a) \\ 0 & (x > x_a) \end{cases} \quad (10.4b)$$

The intersections of the two nullclines give the steady-state points, P_1 , P_2 and P_u , where P_1 is a stable node (i.e. resting point), P_2 a saddle point (i.e. threshold point), and P_u an unstable point. Starting from the point (circled number 1), the phase point moves rapidly along a horizontal path. This part of the trajectory corresponds to the dynein power stroke – or the upstroke of the ‘action-potential’-like behaviour – in Figure 10.3B. This dynein power stroke is followed by its detachment (or inactivation), leading to a decrease in n . As a result, the trajectory turns downward. When the phase point enters the local attachment (or activation) region, it ascends vertically toward the resting point, P_1 , resulting in the completion of the loop.

The last part of this trajectory determines the key features of the model behaviour. The next section discusses how this part of the trajectory in the phase plane is influenced by the vector field and/or the shape of isoclines (see Section 6.4.5 and Figs 6.14 to 6.17).

10.3 Excitability and oscillations in the dynein-tubulin system

10.3.1 Homoclinic orbit

Let us first consider the effect of a change in the vector field. For this purpose we shall change the value of attachment rate b . For small values of b (say $b = 1.3$ as in Fig. 10.4), the phase point moves toward the resting point, P_1 . As b increases from 1.3, the trajectory in the region for $x \leq x_a$ moves slightly upward (Fig. 10.5A for $b = 1.320$), and at the critical value of b it touches the saddle point. This is known as a *homoclinic orbit*. The homoclinic connection may be considered as a limit cycle of infinite period.

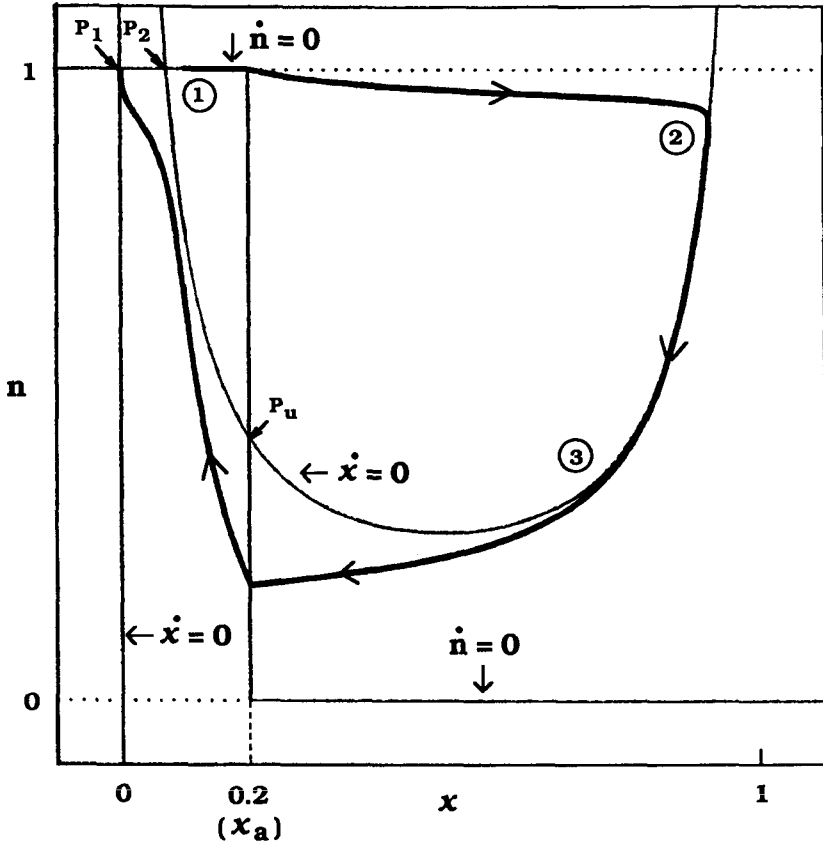


Figure 10.4 Phase plane of the model described by equations (10.1). One solution to these equations is represented by a trajectory marked with arrowheads. The circled numbers correspond to those in Figure 10.3. Three singular points, P_1, P_2 and P_u , occur at these intersections of x - and n -nullclines. P_1 is a stable node, P_2 a saddle point, and P_u an unstable point. The two intersections P_1 and P_2 correspond to those in Fig. 10.2. A threshold phenomenon appears at the saddle point. Parameters and initial conditions are as in Fig. 10.3.

As b continues to increase to $b = 1.322$, the phase point no longer moves toward the resting point, leaving a stable limit-cycle oscillation with an amplitude of about 0.4 and a frequency of 133 Hz.

Although the vector field given by equations (10.1) varies continuously with b , there is a sudden appearance of a stable limit cycle across a threshold value of b . Figure 10.6 illustrates how a limit cycle appears as the parameter, b , is increased. When $b = 1.3$, a stable node, P_1 , a saddle point, P_2 , and an unstable fixed point, P_u coexist (left panel). The saddle point has a stable and an unstable separatrix as indicated by the arrowheads. As b is increased to

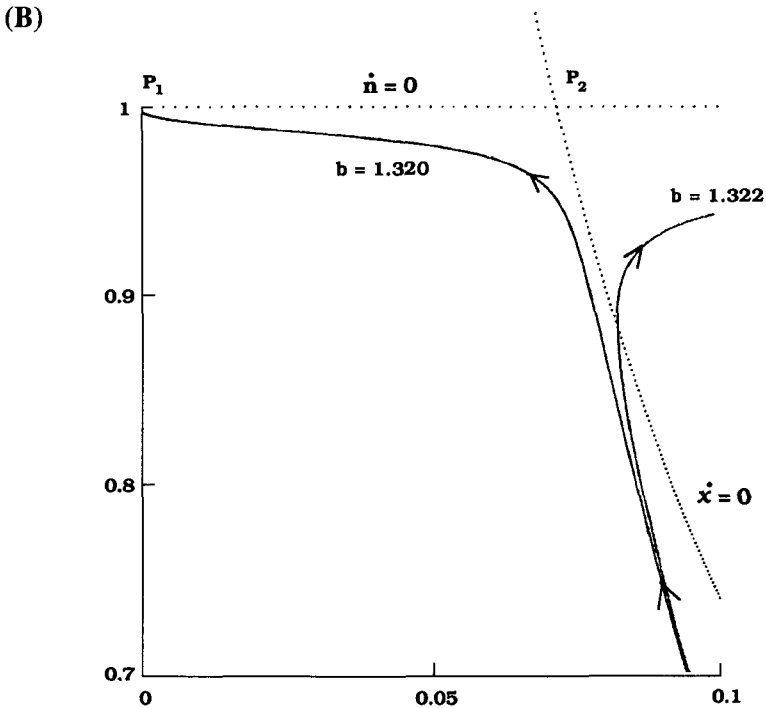
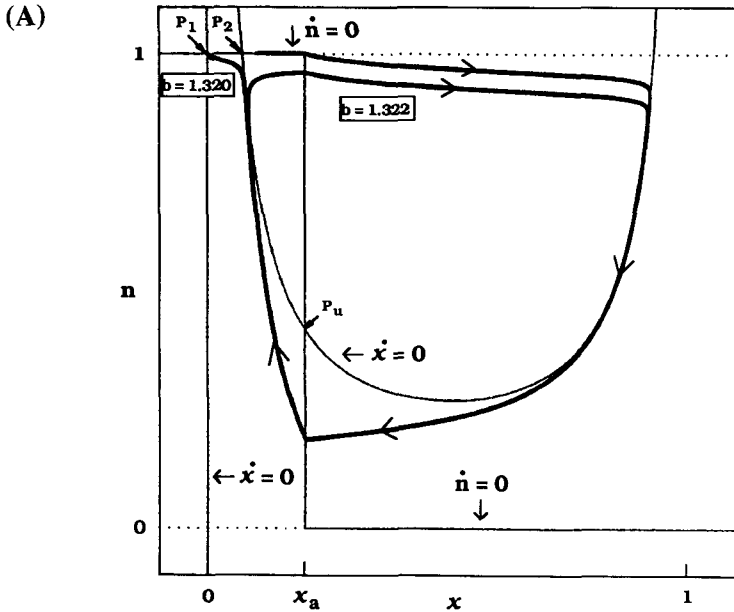


Figure 10.5 Influence of the parameter b . (A): For small parameter values ($b = 1.320$), the trajectory starts from the superthreshold initial conditions and returns to the stable point, P_1 . This excitable behaviour is similar to the previous case shown in Fig. 10.4. When b is slightly larger ($b = 1.322$), there appears a closed trajectory on which a phase point circulates clockwise around the unstable point, P_u . This corresponds to a stable limit-cycle oscillation with an amplitude of about 0.4 and a frequency of 133 Hz. (B): Enlarged detail of panel (A) to show two separating trajectories.

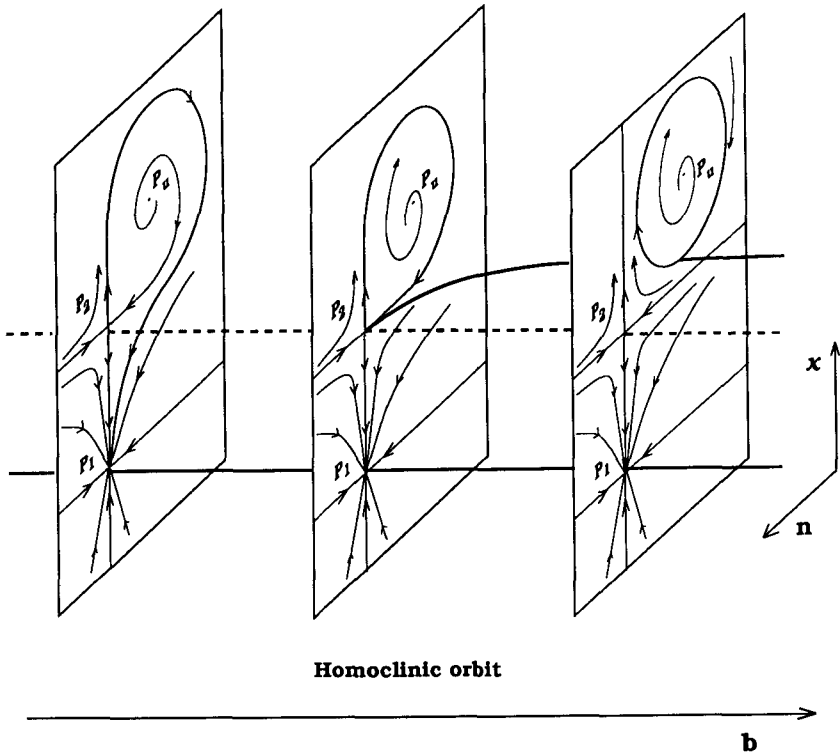


Figure 10.6 Sudden appearance of a limit cycle through a homoclinic connection. There is a stable node, P_1 , a saddle point, P_2 , and an unstable fixed point, P_u (left panel). As the parameter, b , is increased, the unstable separatrix of the saddle point meets with the stable separatrix, resulting in a homoclinic orbit (middle panel). The homoclinic orbit exists only for a single value of b . By increasing b , the limit-cycle oscillation suddenly appears (right panel). Inversely, decreasing b makes the limit-cycle disappear upon collision with the saddle point. This is the typical mechanism by which a limit cycle can abruptly vanish from a phase plane. The upper solid curve, middle broken line, and lower solid line represent the paths of the particular phase point of the limit cycle, of the saddle point and of the stable node, respectively. If b is replaced by Z , this figure represents the emergence of the homoclinic orbit as observed in Fig. 10.8.

the critical value ($b = 1.321$), the stable separatrix just touches the limit cycle, resulting in a homoclinic connection (middle panel). With further increases in b , the limit-cycle oscillation spontaneously appears. As a result, there is a stable limit cycle, a stable node, and a saddle point in the phase plane (right panel). By reversing the parameter and decreasing b , the limit cycle suddenly disappears upon collision with the saddle point. After the annihilation of the limit-cycle oscillation, there remains a saddle point and a stable node in the phase plane.

10.3.2 Dynamic hysteresis loop

It is also important to study the effect of changing the constant parameter, Z , on the x -nullcline. Figure 10.7 shows how the change in Z affects the shape of the x -nullcline, and hence the trajectories in the (x, n) phase plane. According to equation (10.4a), n is decreased by a positive change of Z for any x values. This change lowers the x -nullcline (Fig. 10.7A). Inversely, the x -nullcline is raised by a negative change of Z . The n -nullcline, however, is not modified by any of these changes.

Because of the short distance between the two intersections, P_1 and P_2 , the locations of these intersections are very sensitive to small changes in the x -nullcline. As Z is increased from zero, the x -nullcline is lowered, so that P_1 moves to the right and P_2 to the left. As a result, P_1 and P_2 meet with each other, and then vanish (e.g. $Z = 0.007$). The resulting x -nullcline is characterized by an S-shaped sigmoid. As long as the S-shaped characteristic exists, oscillations of any amplitude and frequency appear. Figure 10.7B shows one example of such oscillations when $Z = 0.02$. The amplitude and frequency are about 0.3 (corresponding to about 7 nm) and 280 Hz, respectively. As Z continues to increase to $Z = 0.04$, the S-shaped characteristic is replaced by a rather monotonic curve. Oscillatory behaviour ceased after oscillatory transients damped (Fig. 10.7C). If Z is further increased to $Z = 0.08$, non-oscillatory decay of the motion appears (Fig. 10.7D).

It is also interesting to note that the S-shaped x -nullcline in this model highly resembles nullclines of the biochemical models for excitability and oscillations (see e.g. Goldbeter, 1980), and those of the models for excitable membranes (see e.g. van Capelle and Durrer, 1980). There appear to be common features for excitability and oscillations among quite diverse biochemical, electrophysiological, and mechano-chemical systems.

Figure 10.8 depicts the bifurcation diagram as a function of Z . There are two types of dynamic hysteresis loops labelled as A and B. First consider the diagram labelled A. Starting in the oscillatory state (the upper solid curve) and decreasing Z , the limit cycle disappears through a homoclinic connection (see Fig. 10.6) and the system jumps to a stable node (the lower solid curve). If Z is now increased, the stable node will persist until it vanishes upon collision with a saddle (the middle broken curve). This is known as a saddle-node bifurcation or fold bifurcation as discussed in Section 6.4.5. Figure 10.9A illustrates how a saddle-node bifurcation occurs. Through this saddle-node bifurcation, the limit cycle reappears.

Next consider the diagram labelled B. For small values of Z (< 0.03), there is a stable limit cycle (the lower solid curve). When Z is increased to $Z > 0.03$, there is also a stable steady state at $x = 0.2$ (the upper solid line), but the dynamics will be stuck at the stable limit cycle. However, as Z is further increased, the limit cycle disappears suddenly. If Z is now decreased, a stable steady state persists until $Z < 0.03$, and then a stable limit-cycle oscillation

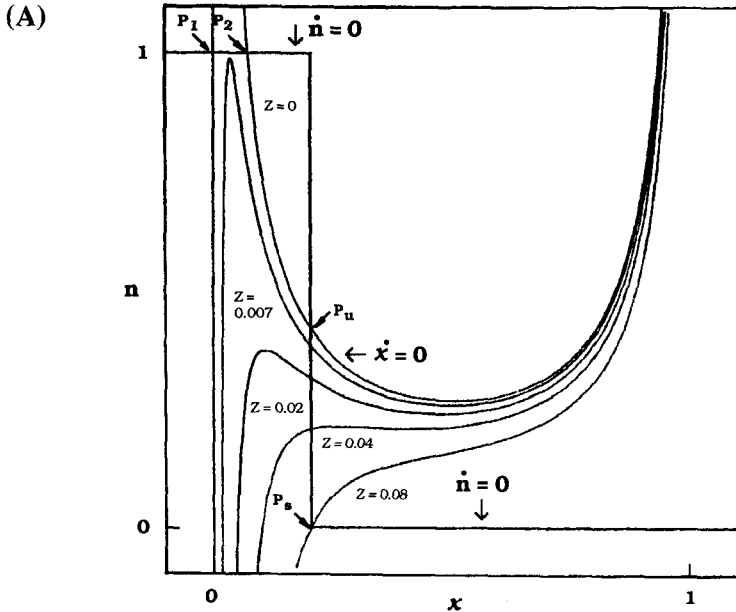
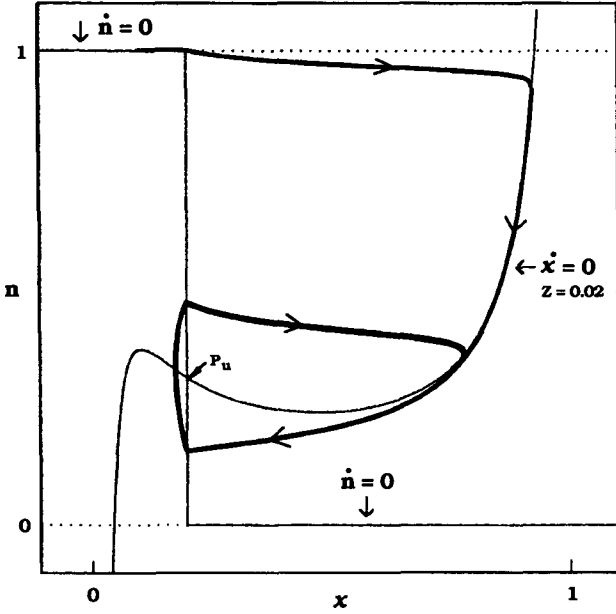


Figure 10.7 Influence of the parameter, Z . The parameters and initial conditions are as in Figures 10.3B and 10.4, except for the value of Z . (A): When $Z = 0$, there are three intersections, P_1 , P_2 and P_u , of the x - and n -nullclines. P_1 is a stable node, P_2 a saddle point, and P_u an unstable point. As Z is increased from 0, the x -nullcline is lowered without changing the n -nullcline. For $Z = 0.007$, the two intersections P_1 and P_2 vanish upon collision, though there still remains an unstable point, P_u . However, if Z is further increased to $Z = 0.03$, the unstable point, P_u , disappears, and instead there appears a stable point, P_s . For $Z > 0.03$, there is always the stable point, P_s , as a single intersection of the two nullclines. (B): Limit-cycle oscillation with an amplitude of about 0.3 and a frequency of 280 Hz for $Z = 0.02$. Starting from the initial conditions (i.e. $n = 1$ and $x = 0.1$), the trajectory converges on the stable limit cycle as shown by a solid curve with arrowheads. (C): Damped oscillation leading to a stable point, P_s , for $Z = 0.04$. The trajectory starts with the same initial conditions. (D): Non-oscillatory decay of the model behaviour for $Z = 0.08$.

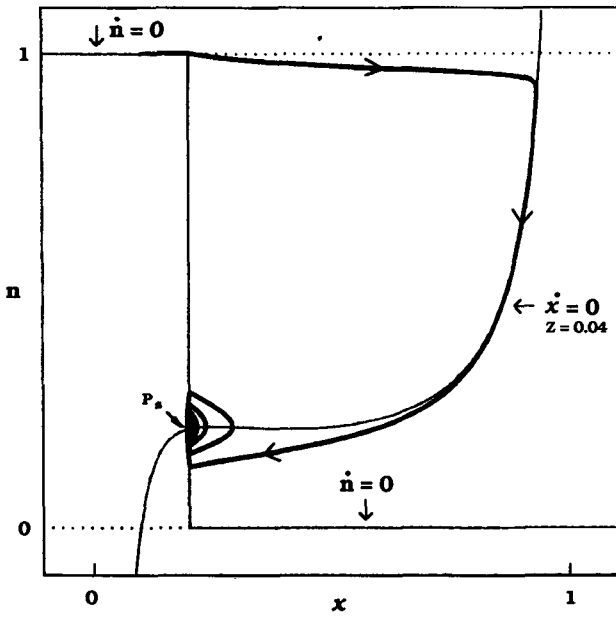
of finite amplitude and frequency suddenly appears. This is known as a *subcritical Hopf bifurcation* or *hard excitation* as illustrated in Figure 10.9B. Unlike the general Hopf bifurcation, the dotted curve of the unstable limit cycle does not rise vertically from an unstable steady state when increasing Z . This occurs because the system lacks differentiability at $x = 0.2$ (see equation (10.1b)).

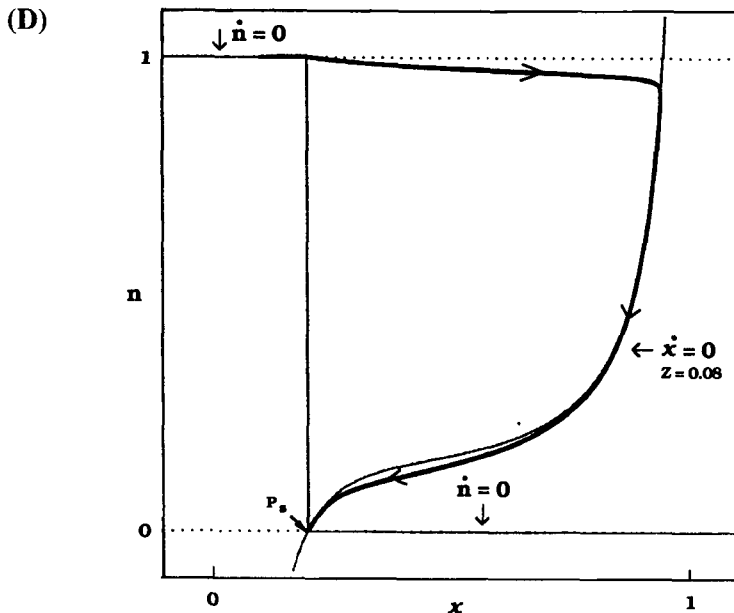
The important characteristic common to both bifurcation diagrams (labelled A and B) is that for some ranges of parameter values there is bi-stability (i.e. a stable steady state coexists with a stable limit cycle). For a system

(B)



(C)





possessing these types of characteristics, two interesting experiments are possible. In one, the system is subjected to an alternately increasing and decreasing control parameter. Either a stable steady state or a stable limit cycle might appear, depending on the history of the control parameter. Thus, the system dynamically switches oscillations ‘on’ and ‘off’. If the control parameter is increased and decreased slowly, compared with the frequency of the limit-cycle oscillation, then the system can exhibit distinct burst-like activity. This situation is discussed in more detail in Section 10.5.

In the second type of experiment, a brief stimulus of a certain strength is delivered at a critical phase of the ongoing limit cycle. It is possible that the system jumps to the stable state because of this stimulus, resulting in an abrupt loss of oscillation. Similarly, another stimulus can trigger oscillations when it is delivered to the quiescent system. The annihilation of oscillations induced by a single pulse-like perturbation has been discovered in cardiac pacemaker cells (Jalife and Antzelevitch, 1979) and in nerve cells (Guttman *et al.*, 1980), but it has not yet been observed in dynein-tubulin systems.

10.4 Onset and cessation of hyperoscillations

Analysis in the previous section reveals that (i) oscillations of any amplitude and frequency can be present by modifying the vector field and/or nullclines;

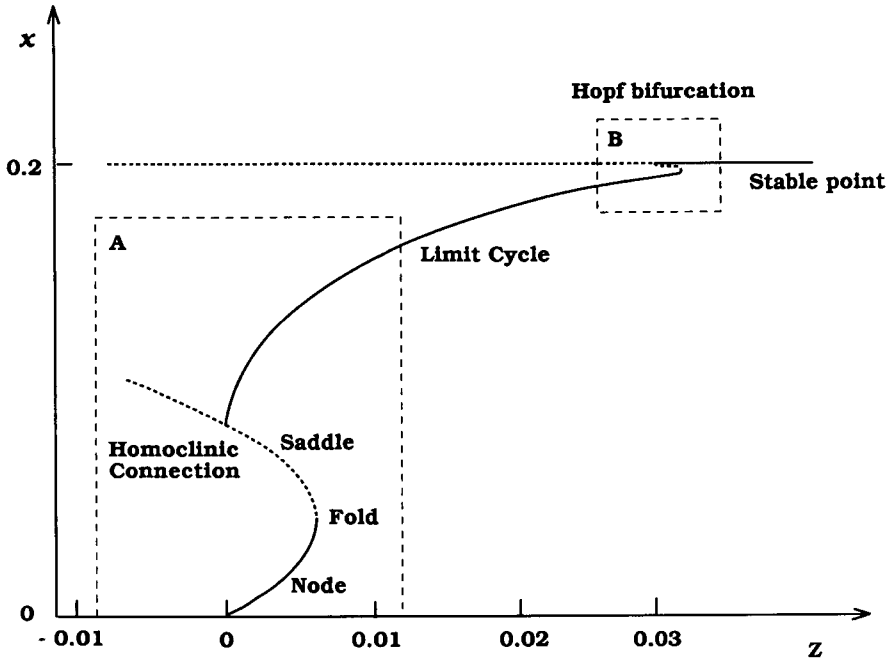


Figure 10.8 Bifurcation diagram for the model described by equations (10.1) as a function of the control parameter, Z . The parameters are as in Figures 10.3B, 10.4 and 10.7 except for the Z values. The upper broken line refers to an unstable fixed point. The lower broken curve refers to a saddle point. Besides them, there is a limit cycle, a stable node and a stable fixed point as indicated in the figure. The homoclinic connection in the broken rectangle labelled A resembles that in Figure 10.6. If b is viewed as Z , the same is true. The saddle–node bifurcation shown in the broken rectangle labelled A is detailed in Figure 10.9A. The Hopf bifurcation appears in the broken rectangle labelled B. This is detailed in Figure 10.9B.

and (ii) the initiation and termination of limit-cycle oscillations can be controlled by stimuli. Based on these considerations, we try to understand how hyperoscillations appear and disappear in the dynein–tubulin system.

As we have discussed, there are two ways by which hyperoscillations are annihilated: one is by the decrease in the frequency asymptotically toward 0, which is associated with a decrease in the ATP concentration; and the other is by the decrease in the fraction of the dynein in the force-generating state when vanadate is added.

Consider, for example, the stable limit-cycle oscillation shown in Figure 10.7B. Figure 10.10 re-draws the same limit-cycle trajectory (solid curve) as that in Figure 10.7B for $b = 1.3$ and $Z = 0.02$. We first consider the effects of lowering ATP concentration on hyperoscillations. For this purpose, we assume that the detachment rate constant, c , is roughly proportional to the

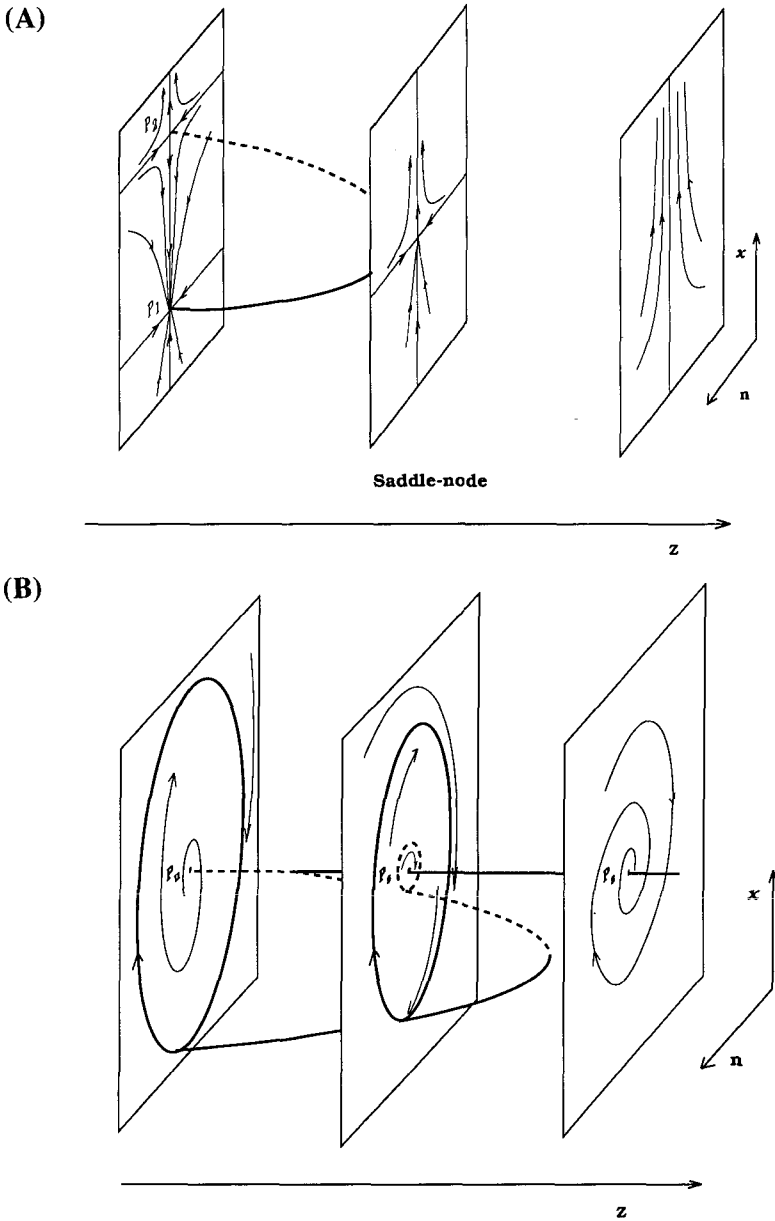


Figure 10.9 (A): Saddle–node bifurcation. The bifurcation diagram shown in the broken rectangle A of Figure 10.8 is detailed. The upper broken and the lower solid curves correspond to the paths of the saddle point, P_2 , and the stable node, P_1 , respectively. As Z is increased, the two steady-state points approach each other (left panel), and then vanish (middle panel). As a result, every trajectory goes away to infinity (right panel). (B): Subcritical Hopf bifurcation (or hard excitation). The bifurcation diagram shown in the broken rectangle B of Figure 10.8 is detailed. Initially, there is a stable limit-cycle oscillation (solid trajectory) and an unstable fixed point, P_u , for a relatively small value of Z (left panel). As Z is increased, the unstable point, P_u , is converted to an unstable limit cycle (broken circle), leaving a stable fixed point, P_s (middle panel). For a sufficiently large value of Z , the stable and unstable oscillations disappear and a single stable cycle remains (right panel). There is bi-stability (i.e. the stable point and stable limit-cycle coexist) in the middle panel, so that hysteresis appears when the control parameter, Z , is increased and decreased.

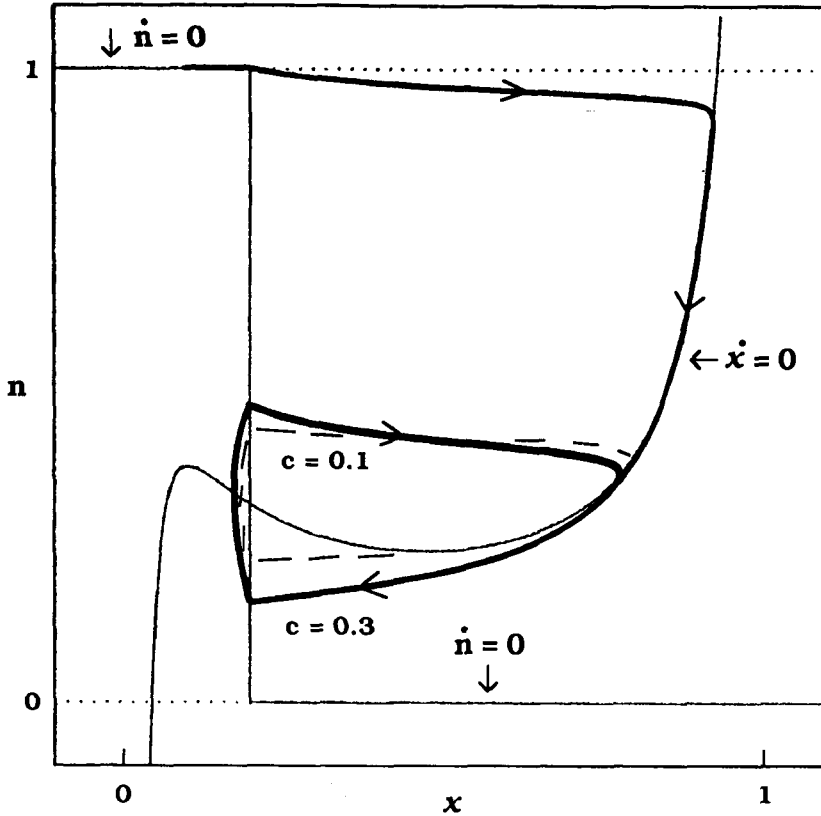


Figure 10.10 Annihilation of oscillations accompanied by the decrease in their frequencies. The parameters are as in Figure 10.7B except for the values of c . When $c = 0.3$, there is the same trajectory as in Fig. 10.7B. If c is decreased, the phase point moves slowly in the region of $x > x_*$ (see equation (10.1b)). As a result, the frequency of oscillation decreases. When $c = 0$, a trajectory approaches a stable point on the x -nullcline depending on the initial conditions. This means that oscillation is annihilated. This dynamical behaviour probably accounts for the effects of the change in ATP concentration in the experiments by Kamimura and Kamiya (1989).

ATP concentration. As c decreases, the trajectory along which a phase point is moving is changed (dotted line) and the phase point stays longer on the x -nullcline. This means that the detachment process becomes a rate-limiting step, and hence the limit-cycle oscillation slows down with the decrease of the frequency. When $c = 0$, the oscillation is completely annihilated. This model behaviour corresponds to the experimental observation that hyperoscillations are annihilated through the decrease in the frequency when ATP concentration is lowered.

How can we interpret the effects of vanadate in terms of the model

behaviour? In order to account for these effects, equation (10.1b) should be rewritten as follows:

$$\frac{dn}{dt} = \begin{cases} b(n_0 - n) & (x \leq x_a) \\ -cn & (x > x_a) \end{cases} \quad (10.5)$$

where n_0 is the maximal fraction of dyneins in the force-generating state. Previously, we have assumed that $n_0 = 1$. However, it is reasonable to consider that n_0 is inversely proportional to the concentration of vanadate. As n_0 is decreased from 1, the n -nullcline in the attachment region ($x \leq x_a$) is lowered as illustrated in Figure 10.11. There is no significant effect on the speed of motion of a phase point there, and so the frequency is not changed dramatically. At the critical value of n_0 , a homoclinic connection appears. With a slight decrease in n_0 , a limit-cycle oscillation completely disappears in the phase plane. This model behaviour, therefore, accounts for the cessation of hyperoscillations through the decrease in the fraction of dyneins in the active state when vanadate is added.

10.5 Complex dynamical behaviours

We have studied how the simple model displays the oscillatory and non-oscillatory modes, and how it undergoes the transition between the two modes. Our next interest is to know whether this model can exhibit more complex dynamical behaviours than these simple oscillatory and non-oscillatory modes. For this purpose, we first set $b = 1.35$ while leaving other parameters the same as in Figure 10.4, such that the model displays oscillations with a frequency of 150 Hz. Then, the parameter Z is periodically changed with extremely low (10 Hz) or high (1264 Hz) frequencies, compared with the ‘intrinsic’ frequency of 150 Hz.

10.5.1 *Bursting*

We assume the periodic change of Z as follows:

$$Z = AM \cdot \sin(2\pi ft) \quad (10.6)$$

where AM and f are the amplitude and frequency, respectively. We chose $AM = 0.01$ and $f = 10$ Hz for the following reasons. Because $AM = 0.01$, the homoclinic connection and the saddle–node bifurcation appear as the transition between the oscillatory mode and non-oscillatory mode (see Fig. 10.8). If, in addition to this change of size in Z , Z is forced to oscillate with a relatively low frequency (say, 10 Hz), two time-scales are introduced: one is the time-scale that comes from an intrinsic fast oscillation with a frequency of 150 Hz; and the other results from the extrinsic slow oscillation with a frequency of 10 Hz. In this situation, the slowly changing parameter, Z , influences the dynamics given by the fast variables, n and x . Through the

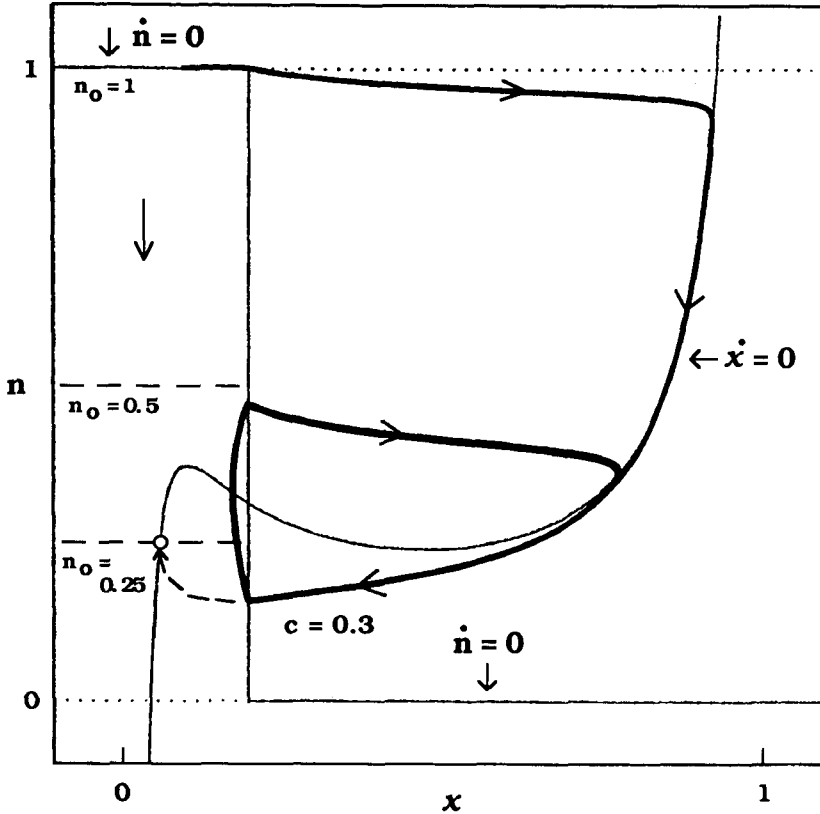


Figure 10.11 Annihilation of oscillations due to the decrease in the fraction of the dynein in the force-generating state. The parameters are as in Figure 10.7B except for n_0 . As n_0 is decreased from 1, the n -nullcline in the region for $x \leq x_a$ is lowered. When $n_0 = 0.5$, there is little difference in the trajectory, so that the frequency is not changed significantly. As n_0 is decreased, the homoclinic connection appears. For $n_0 = 0.25$, the phase point moves toward the stable fixed point. Thus, the oscillation is annihilated without changing its frequency. This behaviour may account for the effects of vanadate in the experiments by Kamimura and Kamiya (1989).

saddle–node bifurcation, the fast oscillations are turned ‘on’; while through the homoclinic connection, the fast oscillations are turned ‘off’. Consequently, clusters of bursting activity are separated by relatively quiescent phases as illustrated in Figure 10.12.

10.5.2 Chaos

Now consider what happens when the parameter Z is forced to oscillate with a high frequency ($f = 1264$ Hz) and a large-amplitude ($AM = 0.08$). The large-

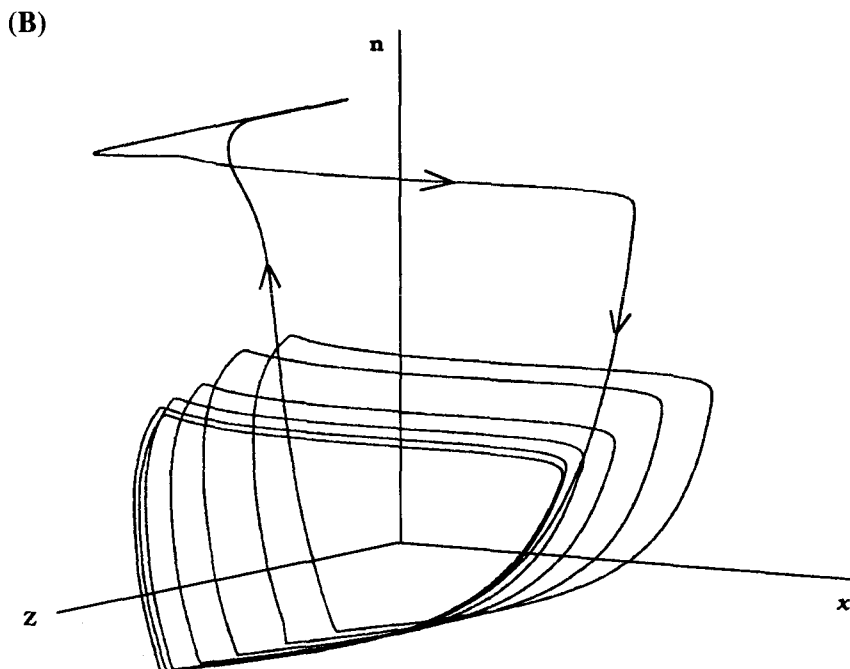
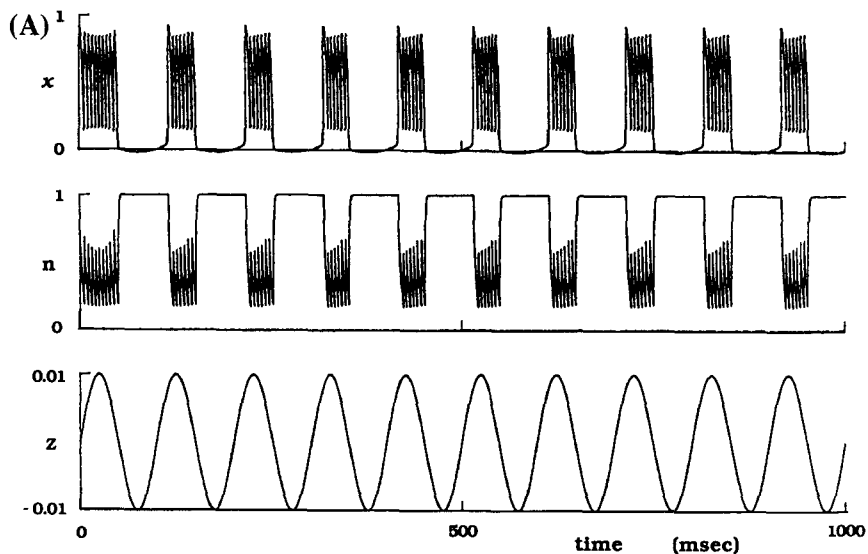
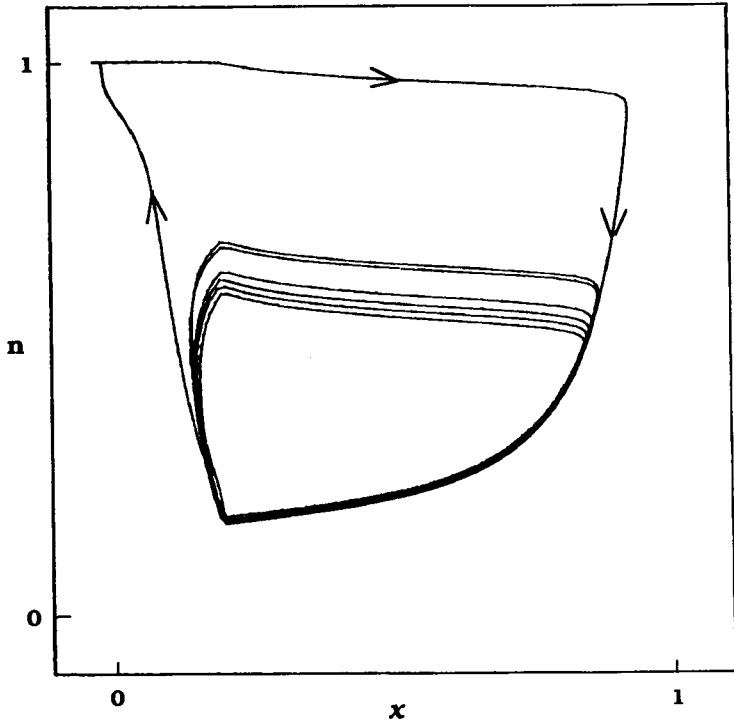
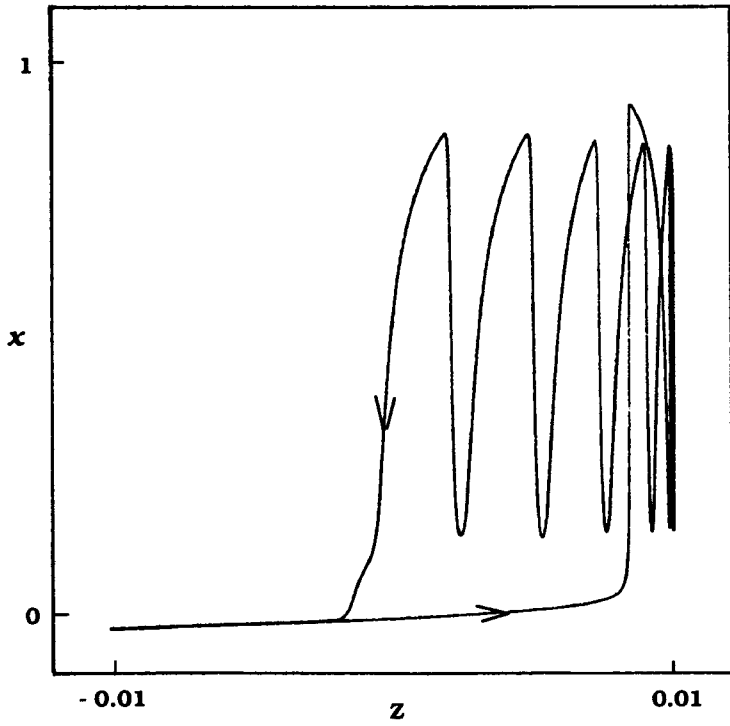


Figure 10.12 Bursting behaviour in the model of the dynein-tubulin cycle. The parameters are: $b = 1.35$, $AM = 0.01$, and $f = 10$ Hz. Other parameters are as in Figures 10.3B and 10.4. There are two time-scales: one corresponds to a relatively high frequency (150 Hz for $Z = 0$) of variables x and n ; and the other is a relatively slow forced oscillation (10 Hz). (A): The time-courses of x , n and Z . Complex periodic behaviour occurs in the form of bursting in which clusters of spikes are separated by quiescent phases. (B): Phase-space representation of bursting in the three-variable coordinate. (C): Projection of the trajectory in panel B onto the (x, n) phase plane. (D): Projection of the trajectory in panel B onto the (Z, x) phase plane. It is clear that the saddle-node bifurcation determines the rising phase of Z leading to bursting, and the homoclinic connection determines the loss of bursting activity.

(C)



(D)



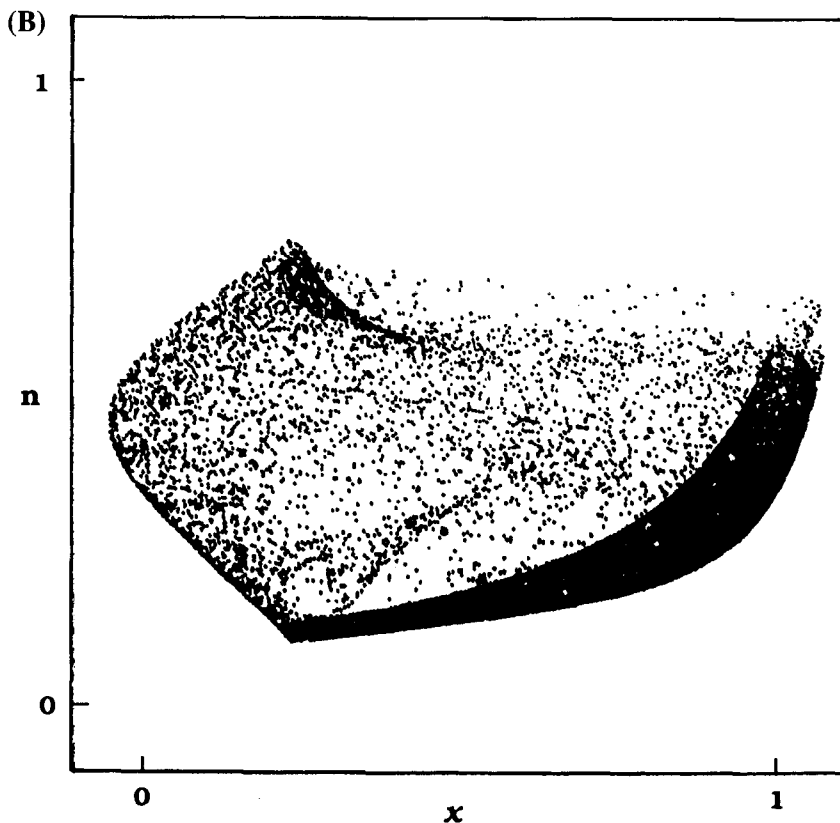
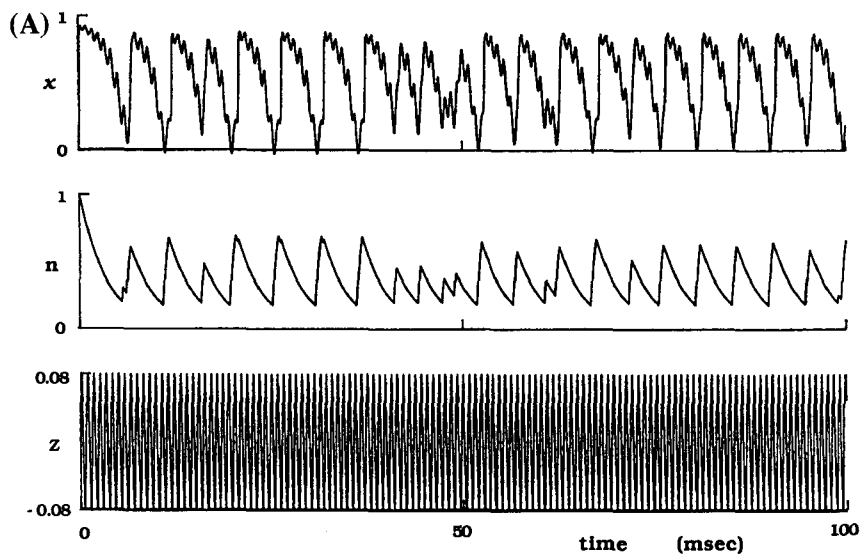


Figure 10.13 Chaotic behaviour in the model of the dynein-tubulin cycle. The parameters are: $b = 1.35$, $AM = 0.08$, and $f = 1264$ Hz. Other parameters are as in Figures 10.3B and 10.4. There are two time-scales: one corresponds to a relatively slow frequency (150 Hz for $Z = 0$) of variables x and n , and the other is an extremely high forced oscillation (1264 Hz). (A): The time-courses of x , n and Z . Chaotic dynamical behaviour appears.

amplitude perturbation covers the whole bifurcation diagram shown in Figure 10.8, so that complex behaviour can be expected. Furthermore, extremely high frequencies would strongly perturb the system, which would play an important role in generating complexity.

Figure 10.13 shows one typical example of chaotic behaviours computed in the present model. It is possible to investigate the detailed 'map' for chaos and bursting as well as synchronization in the (AM, f) plane. However, I am interested in predicting complex dynamical behaviours as an important first step to gaining insight into the underlying mechanism of the dynein-tubulin cycle, but not in studying this specific model too deeply. So this problem seems to be of secondary importance at this stage.

10.5.3 Discussion

The theoretical model proposed in this chapter accounts not only for simple modes of excitability and oscillations, but also more complex dynamical behaviours such as bursting and chaos. Unfortunately, flagellar and ciliary dynamics have not been studied along this line, although some cilia actually show bursts of repeated cycles of beating (see Sleight and Barlow, 1982). One reason for this is that many cell biologists have been interested in the regular behaviours, such as the symmetric steady-state bend propagation typical of flagella and the asymmetric beat-cycle with an effective and a recovery stroke typical of cilia, but not in the potential irregular behaviours. Although periodic-perturbation methods have been applied to the flagellum (Okuno and Hiramoto, 1976, Gibbons *et al.*, 1987), no one has ever investigated its aperiodic responsiveness. Another reason is that theoretical biologists have not tried to develop simple mathematical models in this field, but instead have aimed to develop complicated models. They have been interested in quantitatively explaining specific modes of cilia and flagella. It is, therefore, very difficult to understand the essential features of the model.

I think it is much better to have any 'qualitative' agreement with experimental data than to make efforts to do 'quantitative' curve fitting. So the point in this chapter is that (i) a very simple model can explain qualitative behaviours observed in experiments, and (ii) this model can potentially exhibit complex dynamics which may be observed in experiments in future.²

Before ending this chapter, I would like to reiterate the common features among the diverse living systems. The force-distance characteristics shown in Figure 10.2 resemble the well-known current-voltage characteristics. Furthermore, the nullclines in this model strikingly resemble those in the models for biochemical excitability and oscillations (see Goldbeter, 1980) and in the models for excitable membranes (see van Capelle and Durrer, 1980). As they are similar, it is not surprising that the present model gives rise to bursting

and chaos as many models predict such behaviour (Decroly and Goldbeter, 1987; Rinzel and Lee, 1987). Many attractive problems are open to you!

Notes

- 1 In the formal excitable-dynein model (Chapters 7, 8 and 9), this x -dependence refers to the hysteresis 'on-off' switching function.
- 2 Kamimura and Kamiya further investigated hyperoscillations under various conditions. For details see S. Kamimura and R. Kamiya. High-frequency vibration in flagellar axonemes with amplitudes reflecting the size of tubulin, *J. Cell Biol.* (submitted).

References

- Abbott, R. H. An interpretation of the effects of fiber length and calcium on the mechanical properties of insect flight muscle, *Cold Spring Harbor Symp. Quant. Biol.* **37**, 647–654 (1973).
- Afzelius, B. A. Electron microscopy of the sperm tail. Results obtained with a new fixative, *J. Biophys. Biochem. Cytol.* **5**, 269–278 (1959).
- Alexander, J. and Burns, R. G. Differential inhibition by erythro-9-[3-(2-hydroxyonyl)] adenine of flagella-like and cilia-like movement of *Leishmania* promastigotes, *Nature* **305**, 313–315 (1983).
- Allen, R. D. A reinvestigation of cross-sections of cilia, *J. Cell Biol.* **37**, 825–831 (1968).
- Amos, L. A. and Klug, A. Arrangement of subunits in flagellar microtubules, *J. Cell Sci.* **14**, 523–549 (1974).
- Armstrong, C. F., Huxley, A. F. and Julian, F. J. Oscillatory responses in frog skeletal muscle fibres, *J. Physiol.* **186**, 26–27 (1966).
- Baba, S. A. Ciliary and flagellar movement: function and structure. In *Cell Motility*, pp. 79–97, University of Tokyo Press, Tokyo (1974).
- Baba, S. A. Regular steps in bending cilia during the effective stroke, *Nature* **282**, 717–720 (1979).
- Babloyantz, A. Self-organization phenomena resulting from cell–cell contact, *J. Theor. Biol.* **68**, 551–561 (1977).
- Babloyantz, A. *Molecules, Dynamics and Life: An Introduction to Self-organization of Matter*. Wiley, New York (1986).
- Baker, G. L. and Gollub, J. P. *Chaotic Dynamics: An Introduction*. Cambridge University Press, Cambridge (1990).
- Berg, H. C. *Random Walks in Biology*. Princeton University Press, Princeton, NJ (1983).
- Bergé, P., Pomeau, Y. and Vidal, C. *Order within Chaos. Towards a Deterministic Approach to Turbulence*. Wiley, New York (1986).
- Bessen, M., Fay, R. B. and Witman, G. B. Calcium control of waveform in isolated flagellar axonemes of *Chlamydomonas*, *J. Cell Biol.* **86**, 446–455 (1980).
- Blake, J. R. Hydrodynamic calculations on the movements of cilia and flagella. II. *Opalina*. *J. Theor. Biol.* **52**, 67–82 (1975).
- Blake, J. R. and Sleigh, M. A. Mechanics of ciliary locomotion, *Biol. Rev.* **49**, 85–125 (1974).
- Blum, J. J. and Hines, M. Biophysics of flagellar motility, *Quart. Rev. Biophys.* **12**, 103–180 (1979).

- Brennen, C. and Winet, H. Fluid mechanics of propulsion by cilia and flagella, *Ann. Rev. Fluid Mech.* **9**, 339–398 (1977).
- Brokaw, C. J. Movement and nucleoside polyphosphatase activity of isolated flagella from *Polytoma uvella*, *Expl. Cell Res.* **22**, 151–162 (1961).
- Brokaw, C. J. Non-sinusoidal bending waves of sperm flagella, *J. Exp. Biol.* **43**, 155–169 (1965).
- Brokaw, C. J. Effects of increased viscosity on the movements of some invertebrate spermatozoa, *J. Exp. Biol.* **45**, 113–139 (1966).
- Brokaw, C. J. Bending moments in free-swimming flagella, *J. Exp. Biol.* **53**, 445–464 (1970).
- Brokaw, C. J. Bend propagation by a sliding filament model for flagella, *J. Exp. Biol.* **55**, 289–304 (1971).
- Brokaw, C. J. Flagellar movement: a sliding filament model. *Science* **178**, 455–462 (1972a).
- Brokaw, C. J. Computer simulation of flagellar movement. I. Demonstration of stable bend propagation and bend initiation by the sliding filament model, *Biophys. J.* **12**, 564–586 (1972b).
- Brokaw, C. J. Molecular mechanism for oscillation in flagella and muscle, *Proc. Nat. Acad. Sci. U.S.A.* **72**, 3102–3106 (1975).
- Brokaw, C. J. Computer simulation of flagellar movement. IV. Properties of an oscillatory two-state cross-bridge model, *Biophys. J.* **16**, 1029–1041 (1976).
- Brokaw, C. J. Models for oscillation and bend propagation by flagella, *Symp. Soc. Exp. Biol.* **35**, 313–338 (1982).
- Brokaw, C. J. Computer simulation of flagellar movement. VI. Simple curvature-controlled models are incompletely specified, *Biophys. J.* **48**, 633–642 (1985).
- Brokaw, C. J. Operation and regulation of the flagellar oscillation. In *Cell Movement*, eds. F. D. Warner, P. Satir and I. R. Gibbons, pp. 267–279, Alan R. Liss, New York (1989).
- Brokaw, C. J. Flagellar oscillation: new vibes from beads, *J. Cell Sci.* **95**, 527–530 (1990).
- Brokaw, C. J. and Benedict, B. Mechanochemical coupling in flagella. I. Movement-dependent dephosphorylation of ATP by glycerinated spermatozoa, *Arch. Biochem. Biophys.* **125**, 770–778 (1968).
- Brokaw, C. J. and Gibbons, I. R. Localized activation of bending in proximal, medial, and distal regions of sea-urchin sperm flagella. *J. Cell Sci.* **13**, 1–10 (1973).
- Brokaw, C. J. and Johnson, K. A. *Perspective* dynein-induced microtubule sliding and force generation. In *Cell Movement, Vol. 1*, eds. F. D. Warner, P. Satir and I. R. Gibbons, pp. 191–198, Alan R. Liss, New York (1989).
- Chang, H.-C. Nonlinear waves on liquid film surfaces I. Flooding in a vertical tube, *Chem. Eng. Sci.* **41**, 2463–2476 (1986).
- Chen, L.-H. and Chang, H.-C. Nonlinear waves on liquid film surfaces II. Bifurcation analyses of the long-wave equation, *Chem. Eng. Sci.* **41**, 2477–2486 (1986).
- Childress, S. *Mechanics of Swimming and Flying*. Cambridge University Press, Cambridge (1981).
- Cohen, D. S. and Murray, J. D. A generalized diffusion model for growth and dispersal in a population, *J. Math. Biol.* **12**, 237–249 (1981).
- Cole, K. S. *Membranes, Ions and Impulses*. University of California Press, Berkeley (1968).
- Cook, P. A. *Nonlinear Dynamical Systems*. Prentice-Hall, Englewood Cliffs, NJ (1986).
- Crowley, P. H., Benham, C. J., Lehnart, S. M. and Morgan, J. L. Peripheral doublet microtubules and wave generation in eukaryotic flagella, *J. Theor. Biol.* **93**, 769–784 (1981).
- Davydov, A. S. *Biology and Quantum Mechanics*. Pergamon Press, New York (1982).

- Decroly, O. and Goldbeter, A. From simple to complex oscillatory behaviour: analysis of bursting in a multiply regulated biochemical system, *J. Theor. Biol.* **124**, 219–250 (1987).
- Devaney, R. L. *An Introduction to Chaotic Dynamical Systems*, 2nd edn. Addison-Wesley, Redwood City (1989).
- Douglas, G. J. and Holwill, M. E. J. Behaviour of flagella isolated from *Crithidia oncopelti*, *J. Mechanochem. Cell Motility*, **1**, 213–223 (1972).
- Feller, W. *An Introduction to Probability Theory and Its Applications. Vol. 1*. Wiley, New York (1968).
- Feynman, R. P., Leighton, R. B. and Sands, M. *The Feynman Lectures on Physics. Vol. II*. Addison-Wesley, Reading, Mass (1964).
- FitzHugh, R. Mathematical models of threshold phenomena in the nerve membrane, *Bull. Math. Biophys.* **17**, 257–278 (1955).
- FitzHugh, R. Thresholds and plateaus in the Hodgkin–Huxley nerve equations, *J. Gen. Phys.* **43**, 867–896 (1960).
- FitzHugh, R. Impulses and physiological states in theoretical models of nerve membrane, *Biophys. J.* **1**, 445–466 (1961).
- FitzHugh, R. Mathematical models of excitation and propagation in nerve. In *Biological Engineering*, ed. H. P. Schwan, pp. 1–85, McGraw-Hill, New York (1969).
- Fluford, G. R. and Blake, G. R. Muco-ciliary transport in the lung, *J. Theor. Biol.* **121**, 381–402 (1986).
- Gibbons, B. H. Intermittent swimming in live sea urchin sperm, *J. Cell Biol.* **84**, 1–12 (1980).
- Gibbons, B. H. and Gibbons, I. R. Flagellar movement and adenosine triphosphatase activity in sea urchin sperm extracted with Triton X-100, *J. Cell Biol.* **54**, 75–97 (1972).
- Gibbons, B. H. and Gibbons, I. R. The effect of partial extraction of dynein arms on the movement of reactivated sea-urchin sperm, *J. Cell Sci.* **13**, 337–357 (1973).
- Gibbons, B. H. and Gibbons, I. R. Calcium-induced quiescence in reactivated sea urchin sperm, *J. Cell Biol.* **84**, 13–27 (1980a).
- Gibbons, I. R. Cilia and flagella of eukaryotes, *J. Cell Biol.* **91**, 107s–124s (1981a).
- Gibbons, I. R. Transient flagellar waveforms during intermittent swimming in sea urchin sperm. II. Analysis of tubule sliding, *J. Musc. Res. Cell Motility* **2**, 83–130 (1981b).
- Gibbons, I. R. Transient flagellar waveforms in reactivated sea urchin sperm, *J. Musc. Res. Cell Motility* **7**, 245–250 (1986).
- Gibbons, I. R. and Gibbons, B. H. Transient flagellar waveforms during intermittent swimming in sea urchin sperm. I. Wave parameters, *J. Musc. Res. Cell Motility* **1**, 31–59 (1980b).
- Gibbons, I. R., Shingyoji, C., Murakami, A. and Takahashi, K. Spontaneous recovery after experimental manipulation of the plane of beat in sperm flagella, *Nature* **325**, 351–352 (1987).
- Gierer, A. and Meinhardt, H. A theory of biological pattern formation, *Kybernetik* **12**, 30–39 (1972).
- Gilula, N. B. and Satir, P. The ciliary necklace. A ciliary membrane specialization, *J. Cell Biol.* **53**, 494–504 (1972).
- Glass, L. and Mackey, M. C. *From Clocks to Chaos: The Rhythms of Life*. Princeton University Press, Princeton, NJ (1988).
- Goldbeter, A. Models for oscillations and excitability in biochemical systems. In *Mathematical Models in Molecular and Cellular Biology*, ed. L. A. Segel, Cambridge University Press, Cambridge (1980).

- Goldstein, S. F. Irradiation of sperm tails by laser microbeam, *J. Exp. Biol.* **51**, 431–441 (1969).
- Goldstein, S. F. Isolated, reactivated and laser-irradiated cilia and flagella. In *Cilia and Flagella*, ed. M. A. Sleight, pp. 111–130, Academic Press, London (1974).
- Goldstein, S. F. Starting transients in sea urchin sperm flagella, *J. Cell Biol.* **80**, 61–68 (1979).
- Goldstein, S. F., Holwill, M. E. J. and Silvester, N. R. The effects of laser microbeam irradiation of the flagellum of *Crithidia (Strigomonas) oncopelti*, *J. Exp. Biol.* **53**, 401–409 (1970).
- Goodall, M. C. Auto-oscillations in extracted muscle fibre systems, *Nature* **177**, 1238–1239 (1956).
- Goodenough, U. W. and Heuser, J. E. Substructure of the outer dynein arm, *J. Cell Biol.* **95**, 798–815 (1982).
- Goodenough, U. W. and Heuser, J. E. Outer and inner dynein arms of cilia and flagella, *Cell* **41**, 341–342 (1985a).
- Goodenough, U. W. and Heuser, J. E. Substructure of inner dynein arms, radial spokes, and the central pair/projection complex of cilia and flagella, *J. Cell Biol.* **100**, 2008–2018 (1985b).
- Gray, J. *Ciliary Movement*. Cambridge University Press, Cambridge (1928).
- Gray, J. The movement of sea-urchin spermatozoa, *J. Exp. Biol.* **32**, 775–801 (1955).
- Gray, J. and Hancock, G. J. The propulsion of sea-urchin spermatozoa, *J. Exp. Biol.* **32**, 802–814 (1955).
- Guckenheimer, J. and Holmes, P. *Nonlinear Oscillations, Dynamical Systems, and Bifurcations of Vector Fields*. Springer, New York (1983).
- Guttman, R., Lewis, S. and Rinzel, J. Control of repetitive firing in squid axon membrane as a model for a neuron oscillator, *J. Physiol.* **305**, 377–395 (1980).
- Haken, H. *Synergetics – An Introduction. Nonequilibrium Phase Transitions and Self-Organization, in Physics, Chemistry and Biology*. Springer, Berlin (1977).
- Heinl, P., Kuhn, H. J. and Rüegg, J. C. Tension responses to quick length changes of glycerinated skeletal muscle fibers from the frog and tortoise, *J. Physiol.* **237**, 243–258 (1974).
- Herzig, J. W. A model of stretch activation based on stiffness measurements in glycerol extracted insect fibrillar flight muscle. In *Insect Flight Muscle*, ed. R. T. Trigear, pp. 209–219, North-Holland, Amsterdam (1977).
- Heuser, J. E. and Goodenough, U. W. Three-dimensional structure of axonemal dynein, *J. Cell Biol.* **91**, 49a (1981).
- Hill, A. V. Excitation and accommodation in nerve, *Proc. Roy. Soc. B* **119**, 305–355 (1936).
- Hill, A. V. The heat of shortening and the dynamic constants of muscle, *Proc. Roy. Soc. B* **126**, 136–195 (1938).
- Hill, T. L. Theoretical formalism for the sliding filament model of contraction of striated muscle. Part I. *Prog. Biophys. Molec. Biol.* **28**, 267–340 (1974).
- Hill, T. L., Eisenberg, E., Chen, Y. and Podolsky, R. J. Some self-consistent two-state sliding filament models of muscle contraction, *Biophys. J.* **15**, 335–372 (1975).
- Hines, M. and Blum, J. J. Bend propagation in flagella. I. Derivation of equations of motion and their simulation, *Biophys. J.* **23**, 41–57 (1978).
- Hines, M. and Blum, J. J. Bend propagation in flagella. II. Incorporation of dynein cross-bridge kinetics into the equations of motion. *Biophys. J.* **25**, 421–442 (1979).
- Hiramoto, Y. and Baba, S. A. A quantitative analysis of flagellar movement in echinoderm spermatozoa, *J. Exp. Biol.* **76**, 85–104 (1978).
- Hodgkin, A. L. and Huxley, A. F. A quantitative description of membrane current and its application to conduction and excitation in nerve, *J. Physiol.* **117**, 500–544 (1952).

- Holden, A. V. (ed.) *Chaos*. Manchester University Press, Manchester (1986).
- Holwill, M. E. J. The motion of *Strigomonas oncopelti*, *J. Exp. Biol.* **42**, 125–137 (1965).
- Holwill, M. E. J. and McGregor, J. L. Micromanipulation of the flagellum of *Crithidia oncopelti*. I. Mechanical effects, *J. Exp. Biol.* **60**, 437–444 (1974).
- Holwill, M. E. J. and McGregor, J. L. Control of flagellar wave movement in *Crithidia oncopelti*, *Nature* **255**, 157–158 (1975).
- Holwill, M. E. J. and McGregor, J. L. Effects of calcium of flagellar movement in the trypanosome *Crithidia oncopelti*, *J. Exp. Biol.* **65**, 229–242 (1976).
- Hooper, A. P. and Grimshaw, R. Nonlinear instability at the interface between two viscous fluids, *Phys. Fluids* **28**, 37–45 (1985).
- Hosokawa, Y. and Miki-Noumura, T. Bending motion of *Chlamydomonas* axonemes after extrusion of central-pair microtubules, *J. Cell Biol.* **105**, 1297–1301 (1987).
- Huxley, A. F. Muscle structure and theories of contraction, *Prog. Biophys.* **7**, 255–318 (1957).
- Huxley, A. F. Muscular contraction, *J. Physiol.* **243**, 1–43 (1974).
- Huxley, A. F. and Simmons, R. M. Proposed mechanism of force generation in striated muscle, *Nature* **233**, 533–538 (1971).
- Huxley, H. E. Sliding filaments and molecular motility systems, *J. Biol. Chem.* **265**, 8347–8350 (1990).
- Huxley, H. E. and Brown, W. The low angle X-ray diagram of vertebrate striated muscle and its behaviour during contraction and rigor, *J. Mol. Biol.* **30**, 383–434 (1967).
- Hyman, J. M. and Nicolaenko, B. The Kuramoto–Sivashinsky equation: a bridge between PDE's and dynamical systems, *Physica* **18D**, 113–126 (1986).
- Infeld, E. and Rowlands, G. *Nonlinear Waves, Solitons and Chaos*. Cambridge University Press, Cambridge (1990).
- Jackson, E. A. *Perspectives of Nonlinear Dynamics Vol. 1*, Cambridge University Press (1989).
- Jackson, E. A. *Perspectives of Nonlinear Dynamics Vol. 2*, Cambridge University Press (1990).
- Jalife, J. and Antzelevitch, C. Phase resetting and annihilation of pacemaker activity in cardiac tissue, *Science* **206**, 695–697 (1979).
- Jen, E. (ed.) *1989 Lectures in Complex Systems*. Addison-Wesley, New York (1990).
- Jewell, B. R. and Rüegg, J. C. Oscillatory contraction of insect fibrillar muscle after glycerol extraction, *Proc. Roy. Soc. B* **164**, 428–459 (1966).
- Johnson, K. A. and Wall, J. S. Structure and molecular weight of the dynein ATPase, *J. Cell Biol.* **96**, 669–678 (1983a).
- Johnson, K. A. and Wall, J. S. Structural and mass analysis of dynein by scanning transmission electron microscopy, *J. Submicrosc. Cytol.* **15**, 181–186 (1983b).
- Johnson, K. A., Marchese-Ragona, S. P., Clutter, D. B., Holzbauer, E. L. F. and Chilcote, T. J. Dynein structure and function, *J. Cell Sci. Suppl.* **5**, 189–196 (1986).
- Johnson, R. E. and Brokaw, C. J. Flagellar hydrodynamics. A comparison between resistive-force theory and slender-body theory, *Biophys. J.* **25**, 113–127 (1979).
- Julian, F. J. Activation in a skeletal muscle contraction model with a modification for insect fibrillar muscle, *Biophys. J.* **9**, 547–570 (1969).
- Kamimura, S. and Kamiya, R. High-frequency nanometre-scale vibration in 'quiescent' flagellar axonemes, *Nature* **340**, 476–478 (1989).
- Kamimura, S. and Takahashi, K. Direct measurement of the force of microtubule sliding in flagella, *Nature* **293**, 566–568 (1981).
- Kamimura, S., Yano, M. and Shimizu, H. ATP hydrolysis coupled to microtubule sliding in sea-urchin sperm flagella, *J. Biochem.* **97**, 1509–1515 (1985).
- Kamiya, R. Extrusion and rotation of the central-pair microtubules in detergent-treated *Chlamydomonas* flagella, *Cell Motil. Suppl.* **1**, 169–173 (1982).

- Kamiya, R. and Okamoto, M. A mutant of *Chlamydomonas reinhardtii* that lacks the flagellar outer dynein arm but can swim, *J. Cell Sci.* **74**, 181–191 (1985).
- Kamiya, R., Kurimoto, E., Sakakibara, H. and Okagaki, T. A genetic approach to the function of inner and outer arm dynein. In *Cell Movement, Vol. 1*, eds. F. D. Warner, P. Satir and I. R. Gibbons, pp. 209–218, Alan R. Liss, New York (1989).
- Katchalsky, A. and Spangler, R. Dynamics of membrane processes, *Quart. Rev. Biophys.* **1**, 127–175 (1968).
- Kawai, M. and Brandt, P. W. Sinusoidal analysis: a high resolution method for correlating biochemical reactions with physiological processes in activated skeletal muscles of rabbit, frog and crayfish, *J. Musc. Res. Cell Motility*, **1**, 279–303 (1980).
- Knight-Jones, E. W. Relations between metachronism and the direction of ciliary beat in Metazoa, *Quart. J. Microscop. Sci.* **95**, 503–521 (1954).
- Koshland, D. E., Nemethy, G. and Filmer, D. Comparison of experimental binding data and theoretical models in proteins containing subunits, *Biochemistry* **5**, 365–385 (1966).
- Krinsky, V. I. (ed.) *Self-Organization. Autowaves and Structures far from Equilibrium*. Springer, Berlin (1984).
- Kuramoto, Y. *Chemical Oscillations, Waves, and Turbulence*. Springer, Berlin (1984).
- Kuramoto, Y. and Yamada, T. Pattern formation in oscillatory chemical reactions, *Prog. Theor. Phys.* **56**, 724–740 (1976).
- Landau, M., Lorente, P., Henry, J. and Canu, S. Hysteresis phenomena between periodic and stationary solutions in a model of pacemaker and nonpacemaker coupled cardiac cells, *J. Math. Biol.* **25**, 491–509 (1987).
- Lara Ochoa, F. A generalized reaction diffusion model for spatial structure formed by motile cells, *Biosystem* **17**, 35–50 (1984).
- Li, Y.-X. and Goldbeter, A. Oscillatory isozymes as the simplest model for coupled biochemical oscillators, *J. Theor. Biol.* **138**, 149–174 (1989).
- Lighthill, J. Flagellar hydrodynamics, *SIAM Rev.* **18**, 161–230 (1976).
- Linck, R. W. and Langevin, G. L. Reassembly of flagellar B($\alpha\beta$) tubulin into singlet microtubules: consequences for cytoplasmic microtubule structure and assembly, *J. Cell Biol.* **89**, 323–337 (1981).
- Linck, R. W., Olson, G. E. and Langevin, G. L. Arrangement of tubulin subunits and microtubule-associated proteins in the central-pair microtubule apparatus of squid (*Loligo pealei*) sperm flagella, *J. Cell Biol.* **89**, 309–322 (1981).
- Lindemann, C. B. and Rikmenspoel, R. Sperm flagellar motion maintained by ADP, *Exp. Cell Res.* **73**, 255–259 (1972).
- Lorand, L. and Moos, C. Auto-oscillations in extracted muscle fibre systems, *Nature* **177**, 1239 (1956).
- Lubliner, J. An analysis of interfilament shear in flagella, *J. Theor. Biol.* **41**, 119–125 (1973).
- Lubliner, J. and Blum, J. J. Model for bend propagation in flagella, *J. Theor. Biol.* **31**, 1–24 (1971).
- Lubliner, J. and Blum, J. J. Analysis of bend initiation in cilia according to a sliding filament model, *J. Theor. Biol.* **69**, 87–99 (1977).
- Lunec, J. Fluid flow induced by smooth flagella. In *Swimming and Flying in Nature Vol. 1*, eds. T. Y. T. Wu, C. J. Brokaw and C. Brennen, pp. 143–159, Plenum Press, New York (1975).
- Machemer, H. Mechanical conditions of flagellar and ciliary metachronism. In *Swimming and Flying in Nature. Vol. 1*, eds. T. Y. T. Wu, C. J. Brokaw and C. Brennen, pp. 211–221, Plenum Press, New York (1975).
- Machin, K. E. Wave propagation along flagella, *J. Exp. Biol.* **35**, 796–806 (1958).
- Machin, K. E. The control and synchronization of flagellar movement, *Proc. Roy. Soc. B* **158**, 88–104 (1963).

- Machin, K. E. Feedback theory and its application to biological systems, *Symp. Soc. Exp. Biol.* **18**, 421–446 (1964).
- Machin, K. E. and Pringle, F. R. S. The physiology of insect fibrillar muscle III. The effect of sinusoidal changes of length on a beetle flight muscle, *Proc. Roy. Soc. B* **152**, 311–330 (1960).
- Mandelkow, E.-M., Schultheiss, R., Rapp, R., Müller, M. and Mandelkow, E. On the surface lattice of microtubules: helix starts, protofilament number, seam, and handedness, *J. Cell Biol.* **102**, 1067–1073 (1986).
- Manneville, P., Boccara, N., vichniac, G. Y. and Bidaux, R. (eds) *Cellular Automata and Modeling of Complex Physical Systems*. Springer, Berlin (1989).
- Matsumoto, G., Aihara, K. and Utsunomiya, T. A spatially-ordered pacemaker observed in squid giant axons, *J. Phys. Soc. Jpn.* **51**, 942–950 (1982).
- Matsumoto, K. and Tsuda, I. Noise-induced order, *J. Stat. Phys.* **31**, 87–106 (1983).
- Meinhardt, H. *Models of Biological Pattern Formation*. Academic Press, New York (1982).
- Michelson, D. M. and Sivashinsky, G. I. Nonlinear analysis of hydrodynamic instability in lamina flames – II. Numerical experiments, *Acta Astronautica* **4**, 1207–1221 (1977).
- Minorsky, N. *Introduction to Non-Linear Mechanics*. J. W. Edwards, Ann Arbor, Mich. (1947).
- Mitchell, D. R. and Rosenbaum, J. L. A motile *Chlamydomonas* flagellar mutant that lacks outer dynein arms. *J. Cell Biol.* **100**, 1228–1234 (1985).
- Mohri, H. and Yano, Y. Reactivation and microtubule sliding in rodent spermatozoa, *Cell Motil. Suppl.* **1**, 143–147 (1982).
- Monod, J., Wyman, J. and Changeux, J.-P. On the nature of allosteric transition: a plausible model, *J. Mol. Biol.* **12**, 88–118 (1965).
- Moon, F. C. *Chaotic Vibrations: An Introduction for Applied Scientists and Engineers*. Wiley, New York (1987).
- Murakami, A. Analysis of metachronal coordination in ciliary pads of *Mytilus* gill, *J. Fac. Sci. Tokyo Univ. IV* **10**, 23–35 (1963).
- Murakami, A. Ciliary and flagellar movement: control mechanism. In *Cell Motility*, pp. 131–156, University of Tokyo Press, Tokyo (1974).
- Murase, M. Simulation of ciliary beating by an excitable dynein model: oscillations, quiescence and mechano-sensitivity, *J. Theor. Biol.* **146**, 209–231 (1990).
- Murase, M. Excitable dynein model with multiple active sites for large-amplitude oscillations and bend propagation in flagella, *J. Theor. Biol.* **149**, 181–202 (1991a).
- Murase, M. Complex dynamical behaviors in cilia and flagella: motility and mechano-sensitivity. In *Physics of Living State – Dynamics of Information and Fluctuation in Biological Systems*, eds T. Musha, Y. Sawada, T. Kawakubo, T. Kushida, and H. Shimizu, Ohmsha, Tokyo (1991b).
- Murase, M. Hyperoscillations in mechanochemical systems, *J. Theor. Biol.* (1991c).
- Murase, M. and Matsuo, M. Mathematical modeling for the aging process: normal, abnormal and self-terminating phenomena in spatio-temporal organization, *Mech. Aging Devel.* (1991).
- Murase, M. and Shimizu, H. Computer simulation of the stepwise sliding in cilia and flagella, *J. Musc. Res. Cell Motility* **6**, 380 (1985a).
- Murase, M. and Shimizu, H. Dissipative structures for cell movement: excitable phenomena and soliton. *Proceedings of International Symposium on Mathematical Biology*, pp. 174–175 (1985b).
- Murase, M. and Shimizu, H. A model of flagellar movement based on cooperative dynamics of dynein-tubulin cross-bridges, *J. Theor. Biol.* **119**, 409–433 (1986).
- Murase, M., Hines, M. and Blum, J. J. Properties of an excitable dynein model for bend propagation in cilia and flagella, *J. Theor. Biol.* **139**, 413–430 (1989).

- Murase, M., Tanaka, H., Nishiyama, K. and Shimizu, H. A three-state model for oscillation in muscle: sinusoidal analysis, *J. Musc. Res. Cell Motility* **7**, 2–10 (1986).
- Murata, T., Yano, M. and Shimizu, H. A model for bacterial flagellar motor: free energy transduction and self-organization of rotational motion, *J. Theor. Biol.* **139**, 531–559 (1989).
- Murray, J. D. *Mathematical Biology*. Springer, Berlin (1989).
- Nagumo, J., Arimoto, S. and Yoshizawa, S. An active pulse transmission line simulating nerve axon, *Proc. IRE* **50**, 2061–2070 (1962).
- Naitoh, Y. and Kaneko, H. Reactivated Triton extracted models of Paramecium: modification of ciliary movement by calcium ions, *Science* **176**, 523–524 (1972).
- Naitoh, Y. and Kaneko, H. Control of ciliary activities by adenosinetriphosphate and divalent cations in triton-extracted models of *Paramecium caudatum*, *J. Exp. Biol.* **58**, 657–676 (1973).
- Nicolis, G. and Prigogine, I. *Self-Organization in Nonequilibrium Systems – From Dissipative Structures to Order through Fluctuations*. Wiley, New York (1977).
- Nishiyama, K. and Shimizu, H. Dynamic analysis of the structure and function of sarcomeres, *Biochim. Biophys. Acta* **587**, 540–555 (1979).
- Nishiyama, K. and Shimizu, H. A monte carlo study of stochastic phenomena in biological systems. I. Mathematical treatment of the geometrical structure of muscle, *Math. Biosci.* **54**, 115–135 (1981).
- Nishiyama, K., Shimizu, H., Kometani, K. and Chaen, S. The three-state model for the elementary process of energy conversion in muscle, *Biochim. Biophys. Acta* **460**, 523–536 (1977).
- Okuno, M. and Hiramoto, Y. Mechanical stimulation of starfish sperm flagella, *J. Exp. Biol.* **65**, 401–413 (1976).
- Olver, P. J. and Sattinger, D. H. (eds) *Solitons in Physics, Mathematics, and Nonlinear Optics*. Springer, New York (1990).
- Omoto, C. K. and Brokaw, C. J. Structure and behavior of the sperm terminal filament, *J. Cell Sci.* **58**, 385–409 (1982).
- Omoto, C. K. and Kung, C. The pair of central tubules rotated during ciliary beat in *Paramecium*, *Nature* **279**, 532–534 (1979).
- Penningroth, S. M. and Peterson, D. D. Evidence for functional differences between two flagellar dynein ATPases, *Cell Motil. Cytoskeleton* **6**, 586–594 (1986).
- Phillips, D. M. Structural variants in invertebrate sperm flagella and their relationship to motility. In *Cilia and Flagella*, ed. M. A. Sleight, pp. 379–402, Academic Press, London (1974).
- Piperno, G., Ramanis, Z., Smith, E. F. and Sale, W. S. Three distinct inner dynein arms in *Chlamydomonas* flagella: molecular composition and location in the axoneme, *J. Cell Biol.* **110**, 379–389 (1990).
- Pitelka, D. R. Basal bodies and root structures. In *Cilia and Flagella*, ed. M. A. Sleight, pp. 437–469, Academic Press, London (1974).
- Prigogine, I., Lefever, R., Goldbeter, A. and Herschkowitz-Kaufman, M. Symmetry breaking instabilities in biological systems, *Nature* **223**, 913–916 (1969).
- Pringle, J. W. S. The excitation and contraction of the flight muscles of insects, *J. Physiol.* **108**, 226–232 (1949).
- Pringle, J. W. S. *Insect Flight*. Cambridge University Press, Cambridge (1957).
- Pringle, J. W. S. Stretch activation of muscle: function and mechanism, *Proc. Roy. Soc. B* **201**, 107–130 (1978).
- Pumir, A., Mannerille, P. and Pomeau, Y. On solitary waves running down an inclined plane. *J. Fluid Mech.* **135**, 27–50 (1983).
- Rasband, S. N. *Chaotic Dynamics of Nonlinear Systems*. Wiley, New York (1990).
- Rashevsky, N. Outline of a physico-mathematical theory of excitation and inhibition, *Protoplasma* **20**, 42–56 (1933).

- Rashevsky, N. An approach to the mathematical biophysics of biological self-regulation and of cell polarity, *Bull. Math. Biophys.* **2**, 15–25 (1940).
- Rikmenspoel, R. Movement of sea urchin sperm flagella, *J. Cell Biol.* **76**, 310–322 (1978).
- Rikmenspoel, R. Ciliary contractile model applied to sperm flagellar motion, *J. Theor. Biol.* **96**, 617–645 (1982).
- Rikmenspoel, R. and Rudd, W. G. The contractile mechanism in cilia, *Biophys. J.* **13**, 955–993 (1973).
- Rikmenspoel, R. and Sleigh, M. A. Bending moments and elastic constants in cilia, *J. Theor. Biol.* **28**, 81–100 (1970).
- Rinzal, J. and Lee, Y. S. Dissection of a model for neuronal parabolic bursting, *J. Math. Biol.* **25**, 653–675 (1987).
- Rüegg, J. C. Oscillatory mechanism in fibrillar insect flight muscle, *Experientia* **24**, 529–640 (1968).
- Sale, W. S. and Satir, P. Direction of active sliding of microtubules in *Tetrahymena* cilia, *Proc. Nat. Acad. Sci. U.S.A.* **74**, 2045–2049 (1977).
- Sale, W. S., Goodenough, U. W. and Heuser, J. E. The substructure of isolated and in situ outer dynein arms of sea urchin sperm flagella, *J. Cell Biol.* **101**, 1400–1412 (1985).
- Sanderson, M. J. and Sleigh, M. A. Ciliary activity of cultured rabbit tracheal epithelium: beat pattern and metachrony, *J. Cell Sci.* **47**, 331–347 (1981).
- Satir, P. Studies on cilia. II. Examination of the distal region of the ciliary shaft and the role of the filaments in motility, *J. Cell Biol.* **26**, 805–834 (1965).
- Satir, P. Studies on cilia. III. Further studies on the cilium tip and a 'sliding filament' model of ciliary motility, *J. Cell Biol.* **39**, 77–94 (1968).
- Satir, P. How cilia move, *Sci. Amer.* **231**, 44–52 (1974).
- Satir, P. Ionophore-mediated calcium entry induces mussel gill ciliary arrest, *Science* **190**, 587–588 (1975).
- Satir, P. The generation of ciliary motion, *J. Protozool.* **31**, 8–12 (1984).
- Satir, P. Switching mechanisms in the control of ciliary motility, *Modern Cell Biol.* **4**, 1–46 (1985).
- Satir, P., Wais-Steider, J., Lebduska, S., Nasr, A. and Avolio, J. The mechanochemical cycle of the dynein arm, *Cell Motility* **1**, 303–327 (1981).
- Scarborough, J. B. *Differential Equations and Applications*. Waverly Press, Baltimore (1965).
- Schmidt, G. and Tondl, I. A. *Non-Linear Vibrations*. Cambridge University Press, Cambridge (1986).
- Schroeder, M. *Fractals, Chaos, Power Laws: Minutes from an Infinite Paradise*. W. H. Freeman, New York (1991).
- Scott, A. C. Introduction to nonlinear waves. In *Nonlinear Phenomena in Physics and Biology*, Nato Advanced Study Institutes Series B: Physics, pp. 7–82, Plenum Press, New York (1981).
- Serra, R. and Zanarini, G. *Complex Systems and Cognitive Processes*. Springer, Berlin (1990).
- Shimizu, H. Dynamic cooperativity of molecular processes in active streaming, muscle contraction, and subcellular dynamics, *Adv. Biophys.* **13**, 195–278 (1979).
- Shimizu, T. and Johnson, K. A. Kinetic evidence for multiple dynein ATPase sites, *J. Biol. Chem.* **258**, 13841–13848 (1983).
- Shingyoji, C., Murakami, A. and Takahashi, K. Local reactivation of triton-extracted flagella by iontophoretic application of ATP, *Nature* **265**, 269–270 (1977).
- Sivashinsky, G. I. Nonlinear analysis of hydrodynamic instability in lamina flames – I. Derivation of basic equations, *Acta Astronautica* **4**, 1177–1206 (1977).

- Sivashinsky, G. I. On self-turbulization of a laminar flame, *Acta Astronautica* **6**, 569–591 (1979).
- Sivashinsky, G. I. On flame propagation under conditions of stoichiometry, *SIAM J. Appl. Math.* **39**, 67–82 (1980).
- Sivashinsky, G. I. and Michelson, D. M. On irregular wavy flow of a liquid film down a vertical plane, *Prog. Theor. Phys.* **63**, 2112–2114 (1980).
- Sleigh, M. A. *The Biology of Cilia and Flagella*. Pergamon Press, Oxford (1962).
- Sleigh, M. A. Fluid propulsion by cilia and the physiology of ciliary systems. In *Perspectives in Experimental Biology. Vol. 1*, ed. P. S. Davies, pp. 125–134, Pergamon Press, Oxford (1976).
- Sleigh, M. A. and Barlow, D. I. How are different ciliary beat patterns produced? *Symp. Soc. Exp. Biol.* **35**, 139–157 (1982).
- Sleigh, M. A. and Jarman, M. Graded responses in ciliary activity of ctenophores compared with the 'staircase' of cardiac muscle, *J. Mechanochem. Cell Motility* **2**, 61–68 (1973).
- Steiger, G. J. Stretch activation and tension transients in cardiac, skeletal and insect flight muscle. In *Insect Flight Muscle*, ed. R. T. Trigear, pp. 221–268, North-Holland, Amsterdam (1977).
- Steiger, G. J. and Rüegg, J. C. Energetics and 'efficiency' in the isolated contractile machinery of an insect fibrillar muscle at various frequencies of oscillation, *Pflügers Arch.* **307**, 1–21 (1969).
- Stephens, R. E. Enzymatic and structural proteins of the axoneme. In *Cilia and Flagella*, ed. M. A. Sleigh, pp. 39–76, Academic Press, London (1974).
- Stommel, E. Mechanical stimulation activates beating in calcium-arrested lateral cilia of *Mytilus edulis* gill, *J. Musc. Res. Cell Motility* **7**, 237–244 (1986).
- Struble, R. A. *Nonlinear Differential Equations*. McGraw-Hill, New York (1962).
- Sugino, K. and Naitoh, Y. Simulated cross-bridge patterns corresponding to ciliary beating in *Paramecium*, *Nature* **295**, 609–611 (1982).
- Summers, K. E. The role of flagellar structures in motility, *Biochim. Biophys. Acta* **416**, 153–168 (1975).
- Summers, K. E. and Gibbons, I. R. Adenosine triphosphate-induced sliding of tubules in trypsin-treated flagella of sea-urchin sperm, *Proc. Nat. Acad. Sci. U.S.A.* **68**, 3092–3096 (1971).
- Takahashi, K. and Shingyoji, C. 'Rotation' in eukaryotic flagellar movement, *Biophys.* **27**, 145–150 (1989).
- Takahashi, M. and Tonomura, Y. Binding of 30S dynein with the B-tubule of the outer doublet of axonemes from *Tetrahymena pyriformis* and adenosine triphosphate-induced dissociation of the complex, *J. Biochem.* **84**, 1339–1355 (1978).
- Tamm, S. L. Motility and mechanosensitivity of macrocilia in the ctenophore *Beroë*, *Nature* **305**, 430–433 (1983).
- Tamm, S. L. and Tamm, S. Ciliary reversal without rotation of axonemal structures in ctenophore comb plates, *J. Cell Biol.* **89**, 495–509 (1981).
- Tasaki, I. Collision of two nerve impulses in the nerve fibre, *Biochem. Biophys. Acta* **3**, 494–497 (1949).
- Taylor, G. I. Analysis of the swimming of microscopic organisms, *Proc. R. Soc. Lond.* **A209**, 447–461 (1951).
- Thompson, J. M. T. and Stewart, H. B. *Nonlinear Dynamics and Chaos*. Wiley, New York (1986).
- Thompson, J. M. T. and Virgin, L. N. Spatial chaos and localization phenomena in nonlinear elasticity, *Phys. Lett. A* **126**, 491–496 (1988).
- Thorson, J. and White, D. C. S. Distributed representations for actin-myosin interaction in the oscillatory contraction of muscle, *Biophys. J.* **9**, 360–390 (1969).

- Thorson, J. and White, D. C. S. Role of cross-bridge distortion in the small-signal mechanical dynamics of insect and rabbit striated muscle, *J. Physiol.* **343**, 59–84 (1983).
- Tsukita, S. and Yano, M. Actomyosin structure in contracting muscle detected by rapid freezing, *Nature* **317**, 182–184 (1985).
- Tuckwell, H. C. Evidence of soliton-like behavior of solitary waves in a nonlinear reaction-diffusion system, *SIAM J. Appl. Math.* **39**, 310–322 (1980).
- Turing, A. M. The chemical basis for morphogenesis, *Phil. Trans. R. Soc.* **B237**, 37–72 (1952).
- van Capelle, F. J. L. and Durrer, D. Computer simulation of arrhythmias in a network of coupled excitable elements, *Circ. Res.* **47**, 454–466 (1980).
- van der Pol, B. On relaxation oscillations, *Phil. Mag.* **2**, 978–992 (1926).
- van der Pol, B. and van der Mark, J. The heartbeat considered as a relaxation oscillator, and an electrical model of the heart, *Phil. Mag.* **6**, suppl., 763–775 (1928).
- Varela, F. J., Rowley III, J. C. and Moran, D. T. The control of ciliary movements: an application of the cusp catastrophe, *J. Theor. Biol.* **65**, 531–553 (1977).
- Warner, F. D. The fine structure of the ciliary and flagellar axoneme. In *Cilia and Flagella*. ed. M. A. Sleight, pp. 11–37, Academic Press, London (1974).
- Warner, F. D. and Satir, P. The structural basis of ciliary bend formation. Radial spoke positional changes accompanying microtubule sliding, *J. Cell Biol.* **63**, 35–63 (1974).
- Warner, F. D., Mitchell, D. R. and Perkins, C. R. Structural conformation of the ciliary ATPase dynein, *J. Mol. Biol.* **114**, 367–384 (1977).
- Weisbuch, G. *Complex Systems Dynamics*. Addison-Wesley, New York (1991).
- White, D. C. S. and Thorson, J. Phosphate starvation and the nonlinear dynamics of insect fibrillar flight muscle, *J. Gen. Physiol.* **60**, 307–336 (1972).
- White, D. C. S. and Thorson, J. The kinetics of muscle, *Prog. Biophys. Molec. Biol.* **27**, 173–255 (1973).
- Wiggins, S. *Introduction to Applied Nonlinear Dynamical Systems and Chaos*. Springer, New York (1990).
- Winfree, A. T. *The Geometry of Biological Time*. Springer, Berlin (1980).
- Winfree, A. T. *When Time Breaks Down. The Three-Dimensional Dynamics of Electrochemical Waves and Cardiac Arrhythmias*. Princeton University Press, Princeton, NJ (1987).
- Witman, G. B. and Minervini, N. M. Dynein arm conformation and mechanochemical transduction in the eukaryotic flagella, *Symp. Soc. Exp. Biol.* **35**, 203–223 (1982).
- Witman, G. B., Plummer, J. and Sander, G. *Chlamydomonas* flagellar mutants lacking radial spokes and central tubules. Structure, composition and function of specific axonemal components, *J. Cell Biol.* **76**, 729–747 (1978).
- Witman, G. B., Johnson, K. A., Pfister, K. K. and Wall, J. S. Fine structure and molecular weight of the outer arms of dyneins of *Chlamydomonas*, *J. Submicrosc. Cytol.* **15**, 193–197 (1982).
- Wray, J. S. Filament geometry and the activation of insect flight muscles, *Nature* **280**, 325–326 (1979).
- Yanagida, T., Arata, T. and Oosawa, F. Sliding distance of actin filament induced by a myosin crossbridge during one ATP hydrolysis cycle, *Nature* **316**, 366–369 (1985).
- Yano, Y. and Miki-Noumura, T. Recovery of sliding ability in arm-depleted flagellar axonemes after recombination with extracted dynein I, *J. Cell Sci.* **48**, 223–239 (1981).
- Zeeman, E. C. Differential equations for the heartbeat and nerve impulse. In *Towards a Theoretical Biology. Vol. IV*. ed. C. H. Waddington, pp. 8–67, Edinburgh University Press, Edinburgh (1972).
- Zykov, V. S. *Simulation of Wave Processes in Excitable Media*. Manchester University Press, Manchester (1987).

Author index

(Numbers in *italics* refer to figure legends.)

- Abbott, R. H., 61
Afzelius, B. A., 99
Alexander, J. and Burns, R. G., 120,
247, 4.20
Allen, R. D., 9.1
Amos, L. A. and Klug, A., 94, 4.4
Armstrong, C. F. *et al.*, 85
- Baba, S. A., 117, 195, 4.2, 4.18–4.19
Babloyantz, A., 21, 170
Baker, G. L. and Gollub, J. P., 25n
Berg, H. C., 90
Bergé, P. *et al.*, 25n
Bessen, M. *et al.*, 192, 259
Blake, J. R., 5.30
Blake, J. R. and Sleight, M. A., 144,
189, 5.3, 5.5
Blum, J. J. and Hines, M., 178, 183,
190n, 192–3, 220, 222, 234–5,
5.24–5.25
Brennen, C. and Winet, H., 136–7, 5.8,
5.30–5.32
Brokaw, C. J., 63–4, 96, 99, 101, 123,
153, 167–9, 176, 192, 223n, 234,
243, 245, 247, 252, 256, 299, 305,
307, 3.6, 3.8 3.10, 4.23, 5.9, 5.17,
5.20–5.21, 5.23
Brokaw, C. J. and Benedict, B., 286
Brokaw, C. J. and Gibbons, I. R., 193
Brokaw, C. J. and Johnson, K. A., 282,
304
- Chang, H. -C., 252
Chen, L. -H. and Chang, H. -C., 252
- Childress, S., 136, 140, 190n
Cohen, D. S. and Murray, J. D., 252
Cole, K. S., Table 5.2
Cook, P. A., 3
Crowley, P. H. *et al.*, 215
- Davydov, A. S., 2.1–2.2
Decroly, O. and Goldbeter, A., 17, 331,
1.14
Devaney, R. L., 25n
Douglas, G. J. and Holwill, M. E. J.,
122, 178, 193
- Feller, W., 11–13
Feynman, R. P. *et al.*, 137
FitzHugh, R., 8, 83, 219, 211
Fluford, G. R. and Blake, G. R., 4.29
- Gibbons, B. H., 123
Gibbons, B. H. and Gibbons, I. R., 95,
99, 117, 123, 256–9, 283, 285, 304
Gibbons, I. R., 96, 123, 4.22
Gibbons, I. R. and Gibbons, B. H., 123
Gibbons, I. R. *et al.*, 286–9, 306, 330,
9.3
Gierer, A. and Meinhardt, H., 19
Gilula, N. B. and Satir, P., 4.2
Glass, L. and Mackey, M. C., 25n, 247
Goldbeter, A., 13, 334
Goldstein, S. F., 111, 121, 215–16
Goldstein, S. F. *et al.*, 121, 4.21
Goodall, M. C., 31, 37
Goodenough, U. W. and Heuser, J. E.,
282–3, 285, 304, 9.1–9.2, 9.8

- Gray, J., 91, 96, 123, 4.24
 Gray, J. and Hancock, G. J., 144–6,
 150, 5.7, 8.11
 Guckenheimer, J. and Holmes, P., 25n
 Guttman, R. *et al.*, 321
- Haken, H., 6
 Heintz, P. *et al.*, 2.15
 Herzig, J. W., 51, 2.22–2.23
 Heuser, J. E. and Goodenough, U. W.,
 9.1
 Hill, A. V., 24n, 47, 223n
 Hill, T. L., 64
 Hill, T. L. *et al.*, 64
 Hines, M. and Blum, J. J., 169–70,
 190n, 176–9, 192, 196, 234, 254n,
 305–6
 Hiramoto, Y. and Baba, S. A., 214
 Hodgkin, A. L. and Huxley, A. F., 8
 Holden, A. V., 25n
 Holwill, M. E. J., 120, 247, 249
 Holwill, M. E. J. and McGregor, J. L.,
 120, 122–3, 219, 256–9
 Hooper, A. P. and Grimshaw, R., 252
 Hosokawa, Y. and Miki-Noumura, T.,
 192, 259
 Huxley, A. F., 54, 64, 69, 2.18, 3.1–3.2,
 3.6–3.7
 Huxley, A. F. and Simmons, R. M., 46,
 50, 68, 2.17
 Huxley, H. E., 36
 Huxley, H. E. and Brown, W., 33, 194
 Hyman, J. M. and Nicolaenko, B., 252
- Infeld, E. and Rowlands, G., 22, 131
- Jackson, E. A., 22, 131, 25n
 Jalife, J. and Antzelevitch, C., 321
 Jen, E., 254
 Jewell, B. R. and Rüegg, J. C., 37, 41,
 2.9, 2.12, 2.14
 Johnson, K. A. and Wall, J. S., 283–5,
 9.1
 Johnson, K. A. *et al.*, 282, 285, 304
 Johnson, R. E. and Brokaw, C. J., 150
 Julian, F. J., 57, 85n
- Kamimura, S. and Kamiya, R., 260, 307,
 10.10–10.11
 Kamimura, S. and Takahashi, K., 260
 Kamimura, S. *et al.*, 286
- Kamiya, R., 259
 Kamiya, R. and Okamoto, M., 285
 Kamiya, R. *et al.*, 95, 285–6
 Katchalsky, A. and Spangler, R., 206
 Kawai, M. and Brandt, P. W., 41, 73,
 2.13, 2.16
 Knight-Jones, E. W., 126
 Koshland, D. E., 25n
 Krinsky, V. I., 8
 Kuramoto, Y., 23, 1.18
 Kuramoto, Y. and Yamada, T., 247
- Landau, M. *et al.*, 312
 Lara Ochoa, F., 252
 Li, Y. -X. and Goldbeter, A., 14, 1.12
 Lighthill, J., 137, 149–50, 190n
 Linck, R. W. and Langevin, G. L., 94,
 4.4
 Linck, R. W. *et al.*, 94
 Lindemann, C. B. and Rikmenspoel, R.,
 193, 216–19
 Lorand, L. and Moos, C., 31, 37
 Lubliner, J., 154, 196
 Lubliner, J. and Blum, J. J., 215
 Lunec, J., 138
- Machemer, H., 126
 Machin, K. E., 97–8, 154, 158, 179, 4.5,
 5.12–5.16
 Machin, K. E. and Pringle, F. R. S., 40
 Mandelkow, E. -M. *et al.*, 94
 Manneville, P. *et al.*, 254
 Matsumoto, G. *et al.*, 247
 Matsumoto, K. and Tsuda, I., 10, 1.8
 Meinhardt, H., 19
 Michelson, D. M. and Sivashinsky,
 G. I., 252
 Minorsky, N., 7
 Mitchell, D. R. and Rosenbaum, J. L.,
 285
 Mohri, H. and Yano, Y., 259
 Monod, J. *et al.*, 13, 25n
 Moon, F. C., 25n
 Murakami, A., 112–13, 130, 4.15, 4.25,
 4.27–4.28
 Murase, M., 8.1, 8.6–8.10, 8.12–8.13,
 9.5–9.12, 9.14
 Murase, M. and Matsuo, M., 254
 Murase, M. and Shimizu, H., 191, 194,
 203, 225, 228, 291, 305, 6.1–6.2,
 6.4–6.5, 6.7–6.13, 6.18, 7.1

- Murase, M. *et al.*, 68–80, 225, 245, 305,
 3.11, 3.13–3.18, 7.1–7.3, 7.6,
 7.8–7.9
 Murata, T. *et al.*, 90
 Murray, J. D., 252

 Nagumo, J. *et al.*, 8
 Naitoh, Y. and Kaneko, H., 256
 Nicolis, G. and Prigogine, I., 1
 Nishiyama, K. *et al.*, 68
 Nishiyama, K. and Shimizu, H., 68

 Okuno, M. and Hiramoto, Y., 111, 194,
 217, 330
 Olver, P. J. and Sattinger, D. H., 22,
 131
 Omoto, C. K. and Brokaw, C. J., 247
 Omoto, C. K. and Kung, C., 259

 Penningroth, S. M. and Peterson, D. D.,
 285, 304
 Phillips, D. M., 89
 Piperno, G. *et al.*, 285, 305, 9.8
 Pitelka, D. R., 96
 Prigogine, I. *et al.*, 1
 Pringle, J. W. S., 29, 38, 50, 2.3
 Pumir, A. *et al.*, 252

 Rasband, S. N., 25n
 Rashevsky, N., 18, 24n
 Rikmenspoel, R., 183, 193, 214, 241
 Rikmenspoel, R. and Rudd, W. G., 183,
 193, 256, 5.28
 Rikmenspoel, R. and Sleigh, M. A., 111
 Rinzel, J. and Lee, Y. S., 331
 Rüegg, J. C., 2.8, 2.10

 Sale, W. S. and Satir, P., 102, 107
 Sale, W. S. *et al.*, 285, 304
 Sanderson, M. J. and Sleigh, M. A., 112,
 131, 134, 4.29
 Satir, P., 96, 101, 195, 271, 305, 4.26
 Satir, P. *et al.*, 103, 256
 Scarborough, J. B., 3
 Schmidt, G. and Tondl, I. A., 4
 Schroeder, M., 25n
 Scott, A. C., 22, 131
 Serra, R. and Zanarini, G., 254
 Shimizu, H., 217
 Shimizu, T. and Johnson, K. A., 283,
 304

 Shingyoji, C. *et al.*, 99, 111, 219, 4.7
 Sivashinsky, G. I., 23, 252
 Sivashinsky, G. I. and Michelson,
 D. M., 245, 254
 Sleigh, M. A. and Barlow, D. I., 111,
 112, 256–9, 330
 Sleigh, M. A. and Jarman, M., 112, 117,
 194
 Sleigh, M. A., 126, 128, 4.26
 Steiger, G. J. and Rüegg, J. C., 47, 73,
 2.20–2.21
 Steiger, G. J., 81
 Stephens, R. E., 94
 Stommel, E., 256–9
 Struble, R. A., 3
 Sugino, K. and Naitoh, Y., 183, 221,
 256, 5.29
 Summers, K. E., 91, 201
 Summers, K. E. and Gibbons, I. R.,
 101–2, 203, 259, 296

 Takahashi, K. and Shingyoji, C., 9.3–9.4
 Takahashi, M. and Tonomura, Y., 119,
 194, 285
 Tamm, S. L., 112–13
 Tamm, S. L. and Tamm, S., 259
 Tasaki, I., 131, 247
 Taylor, G. I., 138, 140, 150
 Thompson, J. M. T. and Stewart, H. B.,
 6, 25n
 Thompson, J. M. T. and Virgin, L. N.,
 252
 Thorson, J. and White, D. C. S., 61
 Tsukita, S. and Yano, M., 35
 Tuckwell, H. C., 21, 249, 1.17
 Turing, A. M., 18

 van Capelle, F. J. L. and Durrer, D., 318
 van der Pol, B. and van der Mark, J.,
 24n
 van der Pol, B., 24n
 Varela, F. J. *et al.*, 179

 Warner, F. D., 89, 94
 Warner, F. D. *et al.*, 9.1
 Warner, F. D. and Satir, P., 119, 195,
 259
 Weisbuch, G., 254
 White, D. C. S. and Thorson, J., 61

- Wiggins, S., 25n
Winfrey, A. T., 247
Witman, G. B. and Minervini, N. M.,
9.1
Witman, G. B. *et al.*, 259, 283
Wray, J. S., 33
- Yanagida, T. *et al.*, 34
Yano, Y. and Miki-Noumura, T., 283,
304
- Zeeman, E. C., 181, 183
Zykov, V. S., 8, 247

Subject index

(Numbers in *italics* refer to figure legends.)

- A-filament, 33; *see also* thick filament
- A-subtubule, 283, 4.4 4.10, 6.3, 9.7–9.8
- abfrontal cilia, 117, 4.18
- absolute
 - and relative refractory period, 88, 112–14
 - refractory period, 212
 - temperature, 71
- actin filaments, 33
- action potentials, 1, 85, 131, 261, 6.10
- activation, 57, 219
- activator, 19–21
- active
 - contractile microtubule mechanism, 96, 98–9
 - shear force, 154
 - sliding microtubule mechanism, 96, 99
- afibrillar muscle, 53n
- aggregative behaviour, 24
- all-or-none response(s), 1, 206, 217, 222
- allosteric enzyme, 13, 15, 1.9
- amplitude, 7, 139, 148
- anal cirri, 112
- angular
 - frequency, 2, 44
 - mechanical impedance, 160
 - velocity, 7
- annihilating waves, 88
- annihilation, 130–1
- antagonistic muscles, 41
 - pair of cross-bridges, 65
 - pairs of direct flight muscles, 29
- antilaeplectic, 134
- antiplectic, 126, 130, 189, 4.25, 4.28
- aperiodic, 8, 330
- arc length, 224
- asynchronous, 29, 53n, 2.2–2.3
- ATP, 68, 99, 101, 111, 4.11
 - AMP, 99
 - induced force generation, 102
 - hydrolysis, 27, 33, 196, 2.6–2.7
- ATPase
 - activity, 72, 3.14
 - site, 283
- attractive
 - interaction, 240
 - type of interaction, 2
- auto-catalytic
 - activation, 19
 - enzyme reaction, 1.9
 - isozyme reactions, 1.11
 - process, 200
- autonomous motility, 97
- average shear, 240
- axoneme(s), 89, 91–3, 103, 4.3

- B-subtubule, 283–5, 4.4, 4.10, 9.7–9.8
- bacteria, 136
- bacterial flagella, 89
- basal
 - body, 91, 96
 - plate, 96
- base-to-tip bend propagation, 241–5, 7.10–7.11

- basic equations of flagellar dynamics, 152–6
- Belousov–Zhabotinsky reaction(s), 8, 10, 1.7
- bend
 angle, 5.11
 initiation and bend propagation, 97, 168, 192
 propagation, 230–47, 5.18, 7.4, 7.6, 7.10
- bending
 resistance, 183, 191, 224
 waves, 1, 89
- Bernoulli trials, 11, 25n
- Beroë, 112, 114, 4.17
- bi-stability, 228, 319, 6.7, 10.9
- bi-stable, 203–6, 211, 217, 219, 282, 291, 6.8, 7.3
- bifurcation parameter, 10
- binary function, 226
- biochemical systems, 1
- birhythmicity, 13
- black box, 185
- Boltzmann constant, 71
- Bonhoeffer–van der Pol model, 8; *see also* BVP model
- boundary
 conditions, 138, 178, 233–5, 266, 4.5
 layer, 135
- Brokaw (1972) model, 167–9
- Brokaw (1985) model, 172–5
- Brokaw model, 68, 3.8–3.10
- burst-like activity, 321
- bursting, 2, 17–18, 307, 325–6
- bursts, 112
- butterflies, 29
- BVP model, 8, 84–5, 1.6; *see also* Bonhoeffer–van der Pol model
- C-filament, 33, 2.5
- C-subtubule, 96
- Ca²⁺, 36–7, 47–8, 122, 256, 280, 2.20–2.21, 8.2
 binding, 57, 259, 281
 concentration, 73
- catastrophe model, 179–83
- cell membrane, 91
- cell-body-flagella interactions, 150
- central pair, 91, 6.3
- centre-to-centre distance, 120, 4.19
- centrioles, 96
- chain rule, 55, 223n
- chance fluctuations, 11
- chaos, 2, 88, 307, 326–30
- chaotic behaviour(s), 18, 23
- characteristic
 equation, 172
 frequency, 43, 73–4, 3.13
 function, 4
- chemical
 energy, 196
 waves, 1
- Chlamydomonas*, 259, 283, 8.2
- cilia sublayer model, 189
- ciliary
 metachronism, 141
 model, 178–85, 264–9
 necklace, 4.2
 pads, 112
 propulsion, 185–9
- ciliated micro-organisms, 136
- circular relation, 304
- circumference asymmetry, 255
- clamped
 end, 159
 -end boundary conditions, 235–42, 7.6, 7.8, 7.10
- classical paradox, 144
- clefts, 134
- cleavage divisions, 96
- comb plates, 112, 128
- complete system, 83
- complex
 conjugate, 6, 190n
 dynamical behaviour(s), 2, 254, 307, 325–31
 plane, 162
 temporal patterns, 2
- compound cilia, 112, 117, 259
- concerted transition model, 13, 25n
- conformation change, 25n
- continuity condition, 138
- contractile elements, 156, 4.6, 5.13
- control
 mechanisms, 103
 system, 195
- cooperative, 200
- interactions, 25n
- coupled
 limit-cycle oscillator(s), 1.18, 10.7
 -oscillator system, 23
- Crithidia*, 120, 256, 4.21
- ctenophores, 112, 114–15, 4.17
- cubic

- elastic resistance, 168
- force-distance function(s), 227, 254, 260, 309–10, 7.6, 7.9, 7.13–7.16
- current
 - clamp, 85
 - voltage relationship, 85, 312
- curvature, 150, 156, 168, 170
 - controlled model(s), 167–75, 192
 - feedback control, 178
- cusp catastrophe, 182
- cylinder, 136
- cytoplasm, 91

- damping parameter, 4
- dark-field micrographs, 101
- defence system, 134
- delay, 43, 58
- delayed
 - activation, 206
 - elasticity, 156, 158
 - stretch-activation, 176; *see also* stretch activation
 - tension change, 51
 - tension development, 54, 57; *see also* stretch activation
 - tension fall, 41; *see also* de-activation
 - tension rise, 41; *see also* delayed
 - tension development, stretch activation
- dense mat, 129
- destabilization, 2, 24
- deterministic system, 8
- dexioplectic, 126, 4.25
- diffusion, 1, 18
 - constants, 19
 - coupled limit-cycle oscillators, 23
 - instability, 19
 - process, 252
- dimer, 94
- Dirac delta function, 142, 209
- direct
 - action, 3
 - cell-cell interactions, 21
- directional
 - mechano-sensitivity, 114, 131
 - sensitivity, 197, 200, 225, 255, 261, 293, 302
- discontinuous beat-cycle, 271
- discriminant, 6
- dispersion relation, 24
- displacement, 3, 61
 - sensitivity, 302
 - velocity plot, 3.10, 5.22
 - velocity relationship, 67
- double
 - length-step experiment, 50–3, 2.22
 - minimum-potential, 289
- doublet, 91
 - subsets, 108
- dragonflies, 2.2
- driven-oscillation experiment, 38–41
- driving force, 3
- dynamic cooperativity, 217
- dynein
 - activation, 225, 291
 - active force, 191
 - cross-bridge cycle, 195
 - cross-bridges, 95–6
 - excitation, 291

- eels, 99
- effective stroke, 91, 180, 185, 256, 269
- egg, 96
- elastic
 - and viscous moduli, 40
 - bending moment, 156
 - coupling, 1, 239
 - resistance, 176
 - spring, 3, 1.2
- elasticity, 38, 2.8
- electron microscopy, 102
- electrotonic coupling, 1
- elementary cycles, 72–3, 3.14
- elongated inert body, 144
- end effect, 247
- energy
 - absorption, 162
 - accumulating process, 8
 - barrier, 206
 - dissipation, 162
 - source, 162
 - supplying process, 8
- envelope model, 138, 185–9
- equilibrium, 19, 136, 152
 - position, 3
 - state, 180
- eukaryotic cells, 89
- Euplotes*, 112
- excitability, 1, 8, 13, 111–12, 296–7, 310, 314–21
- excitable, 191, 225
 - cilia, 112
 - dynein models, 193
 - dynein system, 236

- oscillatory phenomena, 203–9
- properties, 203
- type, 255
- excitation, 24n
- external
 - force, 144
 - load, 34
 - stimuli, 1
 - viscous force, 138, 152
 - viscous moment, 152
 - viscous-drag coefficient, 224
- extra ATPase activity, 47, 2.20–2.21
- F-actin, 33, 2.4
- fast
 - action, 181, 5.26–5.27
 - equation, 1.5
 - oscillation, 325
- feedback
 - loop, 18, 197
 - relationship, 167, 172
- fertilization, 96
- fibrillar muscle, 53n
- finite-difference approximation, 238
- first
 - order delay, 61
 - order equations, 6
 - order kinetic equation, 55
 - order rate process(es), 43–4, 81, 169
 - order reaction, 1.9
 - quadrant, 162
- flagellar configuration, 152, 5.9
- flagellum-flagellum interactions, 150
- flip-flop, 240
- fluid
 - dynamics, 135, 138–50
 - flow, 273–80
 - motion, 144
- flying
 - birds, 136
 - insects, 27, 136
- focus, 6, 1.4
- fold bifurcation, 211, 318
- force
 - balance equation, 67, 81, 142, 152, 165
 - distribution, 144, 5.4
 - equilibrium, 138
 - generating mechanisms, 102–3
 - length relationship, 173; *see also* tension-length relationship
 - velocity behaviour, 3.10
 - velocity curve, 54, 64–5, 85n, 2.19
 - velocity relationship, 47, 55–7, 173–4, 176, 3.2, 3.6, 5.22; *see also* force-velocity curve, force-velocity behaviour
- forced oscillation, 3, 4.5
- forcing function, 183
- Fourier transform, 2, 73, 308
- fractions, 55, 3.1
- free
 - end, 159
 - oscillation, 2.8–2.9
 - sliding motion, 203, 296
 - end boundary conditions, 215, 230, 7.4, 7.7, 7.11–7.16
 - oscillation experiment, 36–8
- friction-force function, 3, 1.2
- functional
 - hierarchy, 255
 - unit, 2
- G-actin, 33, 2.4
- Gaussian distribution, 201, 209
- generalized reaction-diffusion equations, 24
- global inactivation, 197
- glycerinated
 - insect muscles, 2.9
 - vertebrate muscle, 2.13
- glycerol-extraction, 36
- glycolytic systems, 8
- goblet cells, 4.29
- Gray and Hancock approach, 144, 146–9
- half-sarcomere, 55
- hard excitation, 319; *see also* subcritical Hopf bifurcation
- harmonic
 - motion, 185
 - oscillator, 6,
- heads, 282–3
- heart beats, 27, 181
- helical structure, 94
- heterodimers, 94
- hierarchy, 89, 280
- Hill's force-velocity relationship, 47; *see also* force-velocity relationship
- Hines-Blum (1978) model, 169–72
- histogram, 117, 4.18
- Hodgkin-Huxley
 - model, 312
 - nerve equations, 209

- Hoffmann-Berling, 99
 homoclinic orbit, 314–17, 10.6
 homogeneous system, 19
 Huxley model, 54–8, 63, 3.2–3.3, 3.6
 hydrodynamic
 forces, 131
 instability, 23
 interactions, 87, 255
 hyperoscillations, 307
 hysteresis, 206, 225, 309
 functions, 291; *see also* hysteresis
 switching functions
 loop, 318–21
 switching function(s), 260–1, 9.5, 9.14
 switching mechanism, 228
- I-filament, 33; *see also* thin filament
 immediate elastic responses, 50
 impulse(s), 131, 219, 261
 in phase, 126
 in-phase and quadrature component, 40
 inactivation, 219
 inactive, 196
 indirect
 action, 3
 flight muscles, 29
 inert body, 144
 inertial
 effects, 135
 forces, 3, 137
 load, 31, 37
 inhibition, 19, 24n
 inhibitor, 19–21
 inhomogeneous structures, 19
 initial
 condition, 215
 transients, 46, 222
 inner
 and outer arms, 95, 194; *see also*
 inner dyneins, outer dyneins
 dynein arms, 9.8
 dyneins, 285–6; *see also* inner and
 outer arms
 insect flight muscle, 29, 33–4
 insensitivity, 112; *see also* refractoriness
 instability, 1, 217, 1.2
 intermittent
 beating, 88
 flagellar beating, 120–3
 oscillations, 123
 swimming, 123, 4.22
 internal
 -clock model, 183
 shear resistances, 168
 viscosity, 228
 viscous resistance, 178, 191
 viscous shear force, 154, 190n
 viscous shear resistance, 202
 intrinsic rhythm, 114
 inverse pendulum, 3, 1.1
 irregular duration of pauses, 123
 irregularity, 88
 isocline, 8, 211, 314; *see also* nullcline
 isometric
 conditions, 56, 58, 80, 85
 force, 173, 176; *see also* isometric
 tension
 steady state tension, 63
 tension, 43, 46–7, 81; *see also*
 isometric force
 isozyme, 1.10
- Julian model, 58, 3.4
- Karman vortices, 136, 5.1
 kinematic viscosity, 136
 kinetic equation(s), 13, 72, 75, 77, 200
 Kuramoto-Sivashinsky equation, 23
- laeoplectic, 126, 4.25
 laminar flame, 23
 laser irradiation, 121, 4.21
Leishmania, 120
 length
 -step analysis, 43; *see also* length-step
 experiment
 -step experiment, 41–6
 -tension loop(s), 40, 2.11
 -tension relationship, 72–3, 3.12
 Liénard's transformation, 7
 ligand molecule, 25n
 limit cycle(s), 68, 314, 1.12, 5.22
 limit-cycle oscillation(s), 208–9, 211,
 1.4
 linear
 -response theory, 43
 stability analysis, 23, 170
 tension-length relationship, 158–62
 local
 activation, 197
 hydrodynamic interactions, 150
 long-range
 hydrodynamic interactions, 150
 inhibition, 19, 24, 240, 1.16

- longitudinal
 - asymmetry, 255
 - motion, 139
 - wave, 141, 187
- lung function, 134
- Machin model, 156–67
- macrofilia, 112
- manifold, 182, 5.26–5.27
- mass, 3, 38, 2.8
- mastigonemes, 148, 5.8
- Mathieu equation, 3
- maximal sliding velocity, 34
- mean position, 201
- mechanical
 - constraint, 111
 - impedance, 156, 159–60
 - potential, 69, 197; *see also*
 - potential-energy function
 - properties, 36–47
 - stimulus, 112
- mechano-chemical
 - cycle(s), 29, 34–6, 87, 111, 112, 307, 4.11
 - system, 1, 307
- mechano-sensitivity, 112–17, 225, 255–6, 263–4, 280
- membrane
 - current, 85
 - potential, 85
- metabolic pathways, 1
- metachronal wave(s), 87, 126, 138, 255, 273
- metachronism, 123–9, 4.24
- metachronous sliding, 108, 111, 220, 269
- metastable positions, 291
- Mg-ATP, 36
- Mg²⁺, 91, 99, 101
- micro-reversibility, 21
- microneedle, 111, 113, 114, 260
- microtubules, 89, 93–4
- mitochondria, 31, 91
- mitotic spindle, 96
- model system, 36, 99
- modified
 - cubic force-distance function(s), 269, 7.10–7.12
 - Huxley model, 3.6–3.7
 - two-state model, 3.5
- moment-balance equation(s), 152, 170, 269
- mono-stability, 6.10
- mono-stable behaviour, 206–8, 217, 219, 6.11
- monomer, 94
- Monte Carlo, 223
- morphogenes, 19
- morphogenesis, 18, 24, 240
- mosquitos, 29, 2.2
- muco-ciliary
 - clearance, 134
 - system, 4.29
 - transport system, 134
- mucus, 134, 4.29
 - layer, 134
 - propelling cilia, 112, 131–4
 - transporting epithelia, 131
- multicellular system, 24
- multiple
 - active sites, 282
 - stable states, 120
 - steady-state transitions, 1
 - time-scales, 18
- muscle
 - fibres, 31, 2.4
 - structure, 31–4
- mutual instability, 220, 269, 271, 273
- myofibrils, 31, 53n, 2.4
- myofilament array, 33
- myosin helices, 33
- Mytilus* gill, 112, 117, 126, 130, 4.18, 4.27, 8.2
- N-shaped current-voltage curve, 85
- Navier-Stokes equations, 190n
- nearest-neighbour segments, 240
- negative
 - diffusion, 24, 252
 - friction, 3
 - stiffness, 162
- nerve
 - excitation, 84–5
 - impulse(s), 29, 181, 183
 - membrane, 131, 10.3
- nervous system, 1, 8, 84, 261, 3.19
- neurophysiology, 240
- Newton's third laws, 260
- Newton's laws, 135, 144, 152, 190n, 5.5
- nexin links, 91, 101, 210, 228, 296
- no-slip boundary condition, 143
- node, 7, 211, 314, 10.4
- noise, 11, 308
 - induced order, 8–13

- non-annihilating wave(s), 88, 249
- non-equilibrium open systems, 1
- non-uniform bend propagation, 243
- nonlinear
 - oscillators, 123
 - tension-length relationship, 162–7
- normal diffusion, 252
- nuclei, 31
- nullcline(s), 8, 314, 318, *1.10, 10.4*; *see also* isocline
- Nyquist plot, 40, 69, 73, *2.11, 2.16, 3.13, 5.14*
- Ochromonas*, 148
- ‘off’ state, 225
- oligomer, 25n
- ‘on’ and ‘off’ switch(es), 21, 108
- ‘on’ state, 225
- ‘on-off’ switch(es), 249, 269, 280
 - dynamics, 261
 - failure, 271
- one-dimensional array, 23, *1.18*
- Opalina*, 91, 112, 189
- opposing cross-bridge pair system, 194; *see also* antagonistic pair of cross-bridges
- orbit, 141
- oscillating lever system, 40
- oscillation-induced ATPase, 29, 47–50
- oscillation, 1, 8, 111–12, 296, 314–21
- oscillatory
 - behaviour, 68, 81, *6.13, 7.3*
 - contraction, 27, 54
 - element, 158
 - phenomena, 206
 - power, 47, *2.20–2.21*
 - Reynolds number, 137
 - type, 255
 - work, 40, 158
 - cilia, 112
- out of phase, 126, 128
- outer
 - and inner arms, *4.3*
 - dynein arms, *9.7*
 - dyneins, 283–5; *see also* inner and outer arms
- pacemaker(s), 193, 230, 305, 321
- Paramecium*, 91, 112, 185, 256, *8.2*
- parametrically excited system, 2
- passive
 - elastic elements, 228
 - elastic shear force, 154
 - microtubule mechanism, 96–8
 - terminal piece, 253
- pattern formation, 18
- peak-to-peak amplitude, *2.13*
- pendulum, 2, *1.1*
 - clocks, 123
- periodic
 - behaviour, 2
 - stimuli, 307
- permanent bridge, 95–6
- phase, 7, 38
 - advance(s), 39, 73–4, 77–80
 - angle, 40, *2.11*
 - delay, 73, 77
 - instability, 23
 - plane, 6, 8, 210, *1.5, 10.4*
 - plane analysis, 209–13
 - plane representation, 314
 - point(s), 8, 210, 314, 324, *1.5*
 - shift, 39–40, 139, *2.11*
- phenomenological equation, 61, 81
- piece-wise linear function, 291
- pinned end, 159
- planar waves, 146
- Pleurobrachia*, 112, 115, 128, 194, 259, *4.17*
- Poincaré section, *10.13*
- polar coordinates, 6
- polarity, 33, 102
- population dynamics, 24, 240
- potassium activation, 312
- potential
 - barrier, 269, 291; *see also* potential-energy barrier
 - energy barrier, 263, 280
 - energy curve, 289
 - energy function(s), 7, 55, 261, 263, *3.1, 3.11, 8.3–8.5, 9.5–9.6, 9.14*; *see also* mechanical potential
 - energy surface, 312–14
 - field, 6
 - function, 8
- power
 - output, 72–3, *3.14*
 - series, 140
 - spectrum, 11
 - stroke, 34, 283, 289, 314
- pressure, 136
 - field, 138
- principal and reverse bend, 117

- product, 13, *1.9*
 - activated allosteric enzyme, 13
- propulsive motion, 162
- protofilaments, 94
- protomers, 25n
- protozoa, 120
- pulsed-laser microbeam, 111

- quantal steps, 117–20
- quick-release and quick-stretch
 - experiment, *see* length-step experiment
- quiescence, 271–3
- quiescent, 123, 252, 255, 261, 263, 321

- radial
 - link systems, 296
 - spokes, 91, 101, 117, 296
 - spoke cycle, 195
 - spoke system, 195, 200, 285
- random fluctuation, 8
- rapid-freezing electron-microscope, 35
- rate
 - constant(s), 56, 61, 69, 77, *3.1*
 - function, 13, 15
 - limiting process, 75, 77, 80
 - limiting step, 324
- reaction-diffusion
 - equation, 229
 - model, 249
 - system, 19–22, 191
- reactivation, 99
- recovery stroke, 91, 180, 185, 256, 269
- reduced system(s), 83, 209
- refractoriness, 85, 131, 255; *see also*
 - insensitivity
- refractory period, 261, 312
- relative
 - dry friction, 3
 - refractory period, 213
 - velocity, 3
- relax, 34
- relaxation
 - oscillation(s), 7, 176, *1.3, 1.5*
 - time, 61, 170
- release de-activation, 41, 51; *see also*
 - stretch activation; stretch de-activation
- repetitive
 - beat-cycle, 269–71
 - firing, 85
- repulsive
 - interactions, 240
 - type of interaction, 2
- resistive-force theory, 146–50
- resonant
 - frequency, 37
 - lever system, *2.8*
- responsiveness, 277
- resting, 196
 - phase, 134
 - position, 280
 - state, 206
- reversal of the direction
 - of propagating waves, 245–7
 - of wave propagation, 88
- reverse rate constants, 64
- Reynolds numbers, 135–7, 146
- rhythms, 2, 312
- rigor state, *9.1*
- rotational
 - inertia, 152
 - potential function, *1.4*

- S-shaped sigmoid, 318, *1.10*
- saddle
 - point, 211, 314, *10.4, 10.6*
 - node bifurcation, 211, 318, *10.9*; *see also* fold bifurcation
- sarcomeres, 33, *2.4*
- scaling factor, 228
- sea-urchin sperm, 101, 111, 123, 241, 256, 302, *4.22*
- second-order velocity, 140
- self-organization, 1, 242, *5.17*
- self-oscillation(s), 65, 158
- self-oscillatory
 - model(s), 175–8, 192
 - properties, 222
- self-propelling
 - body, 144
 - micro-organisms, 144
- self-turbulization phenomena, 2, 24
- separatrix, 211, 315, *10.6*
- sequential transition model, 25n
- serous layer, 134
- shear
 - angle, 150, 224, *5.11*
 - controlled feedback mechanism, 172
 - displacement, 152, 196, *5.11, 6.3*
 - resistance, 101, 173, 183
- sheath, 91, *4.3, 4.19, 6.3*
- short-range activation, 19, 24, 240, *1.16*
- single point-force, 143, *5.4*

- singular
 - point(s), 6–7, 211, 1.4
 - solutions, 138
- sinusoidal analysis, 38, 43–4, 72, 2.11
- slender-body theory, 150
- sliding
 - coordinate, 55, 196
 - displacement, 152
 - filament mechanism, 27
 - filament models, 233
 - microtubule model, 156
- slit camera, 112
- slow
 - equation, 1.5
 - oscillation(s), 18, 325
- small- and large-amplitude oscillations 15
- snakes, 99
- sodium
 - activation, 312
 - inactivation, 312
- solitons, 21–2, 88, 131
- space
 - clamp, 1
 - dependent patterns, 1
 - time diagram, 230
- spatial
 - control mechanism, 108–11
 - order, 18–24
 - structure, 21
- spatio-temporal
 - chaos, 2
 - distributions, 74–80, 3.15–3.17
 - structures, 2
- spermatozoa, 120, 136
- Spirochaeta balbianii*, 4.24
- spring constant, 3, 55, 1.2
- stability, 164
- stabilization, 21, 24
- stable point, 8, 1.10
- standard deviation, 201
- standing
 - and travelling moments, 256
 - wave modes, 162
- starting transients, 222
- stationary state, 1
- steady state wave-forms, 222
- steady-state
 - attached cross-bridge distribution, 56, 58
 - beating, 222
 - conditions, 55, 61
 - muscle contraction, 56
 - points, 211
 - shortening, 46–7
- step analysis, 44
- step-length change, 81, 3.3–3.4, 3.9, 3.18
- stiffness, 33, 260
 - measurements, 50, 2.22
- stimulus intensity, 8
- Stokes equations, 138–40, 142, 190n
- Stokeslet, 142–4
 - velocity field, 142
- stopping and starting transients, 88, 123
- strain, 61
- strange behaviour, 129–34
- stream function, 140
- streamlines, 143, 5.4
- stretch
 - activation, 51, 54, 57, 80–1, 158, 172, 3.4–3.5; *see also* delayed tension development; release de-activation
 - de-activation, 65; *see also* release de-activation
- stroke distance, 196
- structural asymmetry, 91, 219, 235, 242, 253, 255, 281
- structurally stable, 8
- subcritical Hopf bifurcation, 319, 10.9; *see also* hard excitation
- substrate, 13, 1.9
- subsystem, 1
- subthreshold, 6.7, 6.10
- subunits, 13, 15, 25n
- Sugino-Naitoh model, 183–5
- superthreshold, 217, 289, 6.7
 - perturbations, 112
- surface forces, 136
- suspension, 2–3
- sustained
 - oscillations, 27
 - oscillator, 220
- swimming-sheet model, 138–42, 185, 5.2
- swing, 2
- switch-point hypothesis, 271
- switching
 - mechanisms, 222
 - point(s), 225, 249, 305
- symmetry breaking, 302
- symplectic, 126, 130, 189, 4.25, 4.28
- synchronism, 123–9, 4.24
- synchronization, 50, 123, 125, 164–7

- synchronous, 29, 53n, 2.1, 2.3
 and metachronous sliding, 256
 sliding, 108, 111, 220, 269
- T_1 and T_2 curves, 44, 47
- temporal
 control mechanism, 107–8
 order(s), 1–18
 responsiveness, 225
- tension
 transients, 2.14–2.16
 -length relationship, 85; *see also*
 force-length relationship
 -step experiment, 46–7
- Tetrahymena*, 96, 283
- thermal noise, 8; *see also* noise
- thick filament(s), 33, 2.4; *see also*
 A-filament
- thin filament(s), 33, 2.4; *see also*
 I-filament
- third quadrant, 162
- thorax, 29
 -wing system, 37
- three-dimensional trajectory, 18
- three-state
 cross-bridge cycle, 198
 model, 68–80, 195–200, 225, 3.11
- threshold., 180–1, 193, 225, 5.26–5.27
 phenomena, 203, 293, 310
 point, 305
 separatrix, 211, 213
 value, 280
- thrusting and dragging forces, 144
- time
 constant, 61
 delay, 112, 156, 172, 206, 254n
 -intervals, 221
 -scales, 1.5
- tip-to-base bend propagation, 236–40,
 7.6
- total shear force, 224
- tracheal epithelium, 112, 131
- trajectory, 68, 211, 314, 1.5, 10.4–10.5
- transfer function, 158
- transients, 3.3–3.4, 3.18
- transition zone, 91
- translational motion, 144
- transverse
 mechanical impedance, 160
 motion, 139
 wave, 141, 187
- triggering events, 269, 271
- triplet, 91, 96
- Tripneustes gratilla*, 123, 4.22
- Triton X-100, 99
- trypsin, 101, 4.9
- tubulin, 94, 4.4
- turbulent flow, 136
- Turing instability, 19; *see also* diffusion
 instability
- two-component system, 18
- two-dimensional
 sheet, 138
 wave, 23
- two-factor model, 24n
- two-filament system, 107–8
- two-state model, 54–68
- undulatory motion, 144
- unidirectional
 active sliding, 102–3
 bend propagation, 245
 mechano-chemical cycle, 103, 200
- unstable oscillation, 15
- van der Pol equation, 4, 24n, 1.3
- vanadate, 308, 322
- vector
 field, 314
 modulus plot, 40
- vertebrate
 muscle, 29, 31–3
 skeletal muscle, 27
- vibration, 2
- viscoelastic, 134, 176
- viscosity-induced
 instability, 237; *see also*
 viscosity-induced perturbations
 perturbations, 241–2, 249; *see also*
 viscosity-induced instability
- viscous
 bending moment, 156
 coupling, 128, 4.26
 drag coefficients, 146
 forces, 137
 resistance, 101, 176
 stress, 136
- voltage-clamp, 85
- volume forces, 135
- water-propelling cilia, 130–1
- waterbugs, 37
- wave

- front, 219
- generating function, 150, 5.9
- number, 24, 5.18
- velocity, 140, 148
- wavelength, 24, 148
- waving sheet, 144
- weak coupling, 127
- wing
 - beats, 27
 - beat frequencies, 29
- Y-V curve, 68; *see also*
 - displacement-velocity plot
- Z-lines, 33
- zero-thrust swimming condition, 148

NONLINEAR SCIENCE THEORY AND APPLICATIONS

Series editor **Arun V. Holden**, Centre for Nonlinear Studies,
University of Leeds

The Dynamics of Cellular Motility

MASATOSHI MURASE

The processes that underlie cellular motility—the contraction of muscle and the beating of cilia and flagella—not only share a common mechanism, based on sliding filaments, but can also share oscillatory dynamics.

The dynamics of cellular motility uses nonlinear dynamics as a framework to approach oscillations in motile systems and presents mechano-chemical oscillatory systems as a prototype of nonlinear science. The key idea from nonlinear dynamics is that very simple nonlinear models can have complicated behaviours and that although biological systems do have intricate and complicated structures and behaviours, simple nonlinear models can quantitatively describe these behaviours and a mathematical analysis of such simple models can help in the understanding of biological processes.

The book surveys up-to-date experimental and theoretical results and provides an excellent foundation and introduction to this field and to the literature, from which interdisciplinary research can be developed.

With over 200 illustrations, it is an attractive and readable volume, invaluable to scientists working in the field and of interest to graduate students of cellular biology, chemistry, physics and applied mathematics.

Masatoshi Murase is Theoretical Biologist at Tokyo Metropolitan Institute of Gerontology, Japan, and is Visiting Professor in the Department of Mathematics at the University of California, USA

ISBN 0-471-93576-X



9 780471 935766

JOHN WILEY & SONS

Chichester · New York · Brisbane · Toronto · Singapore